SIONYX1403000015.0092
SAMSUNG EX. 1002 - 1293/4148

Global CT Market

ANALOGIC
The World Resource for Health & Security Technology

Note: U.S. data in orders

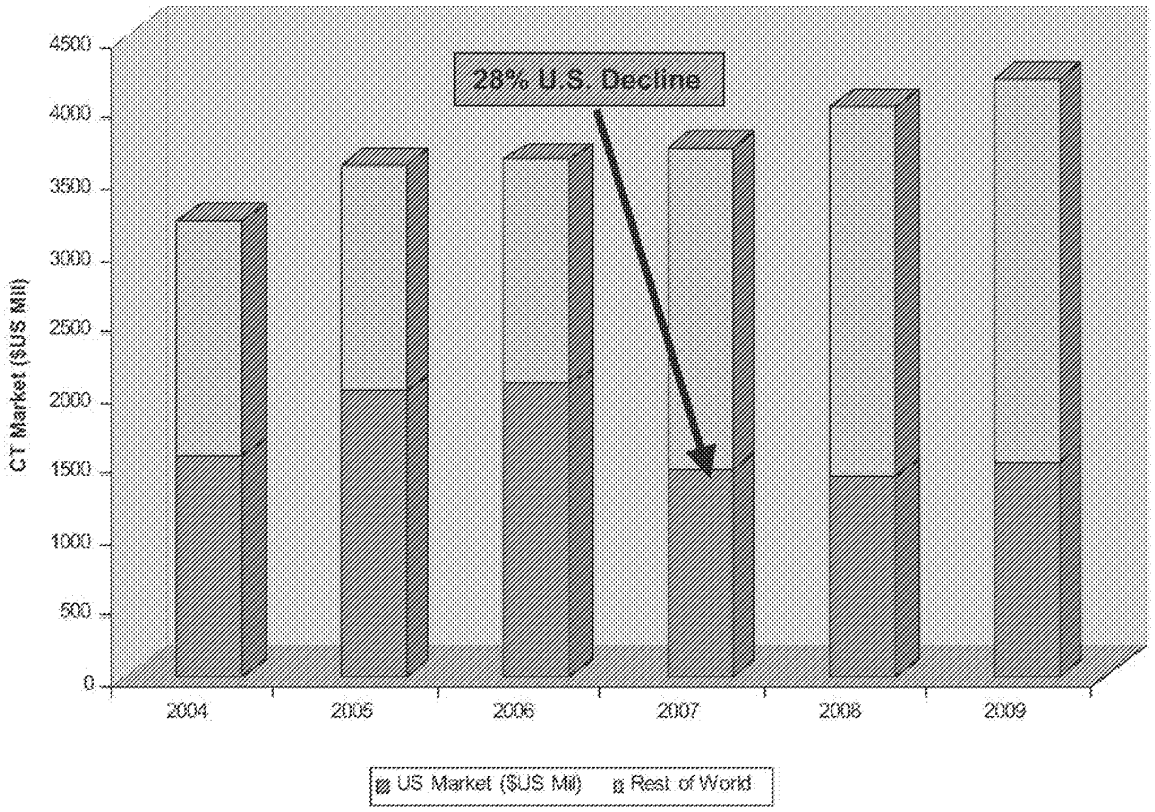

Source: Philips Medical, Fuji-Kezai, Analogic

SAMSUNG EX. 1002 - 1294/4148
SIONYX1403000016.0001

US CT Market Distribution

ANALOGIC
The World Resource for Health & Security Technology

Market Share by Product Tier (2006) Based on unit volume

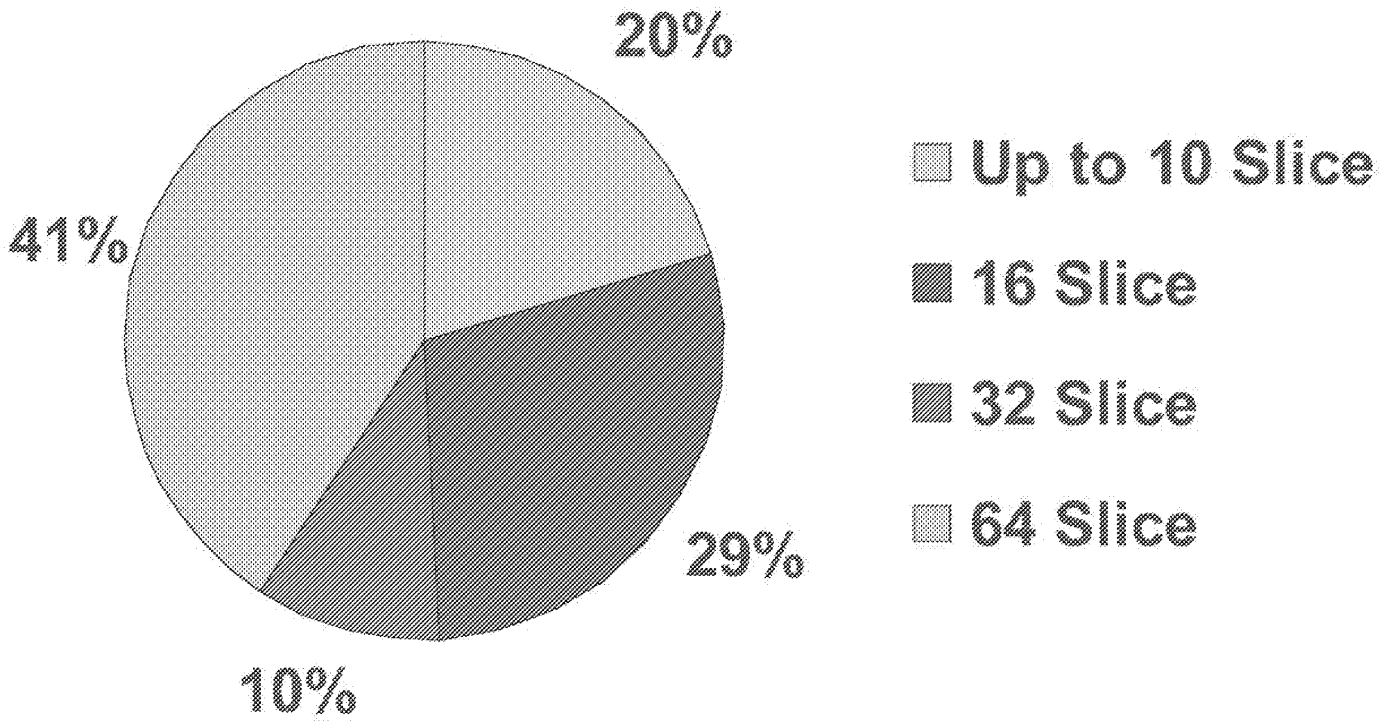

Source: 2006 Frost & Sullivan

SIONYX1403000016.0002
SAMSUNG EX. 1002 - 1295/4148

ANALOGIC
The World Resource for Health & Security Technology

CT Market Pricing Trends

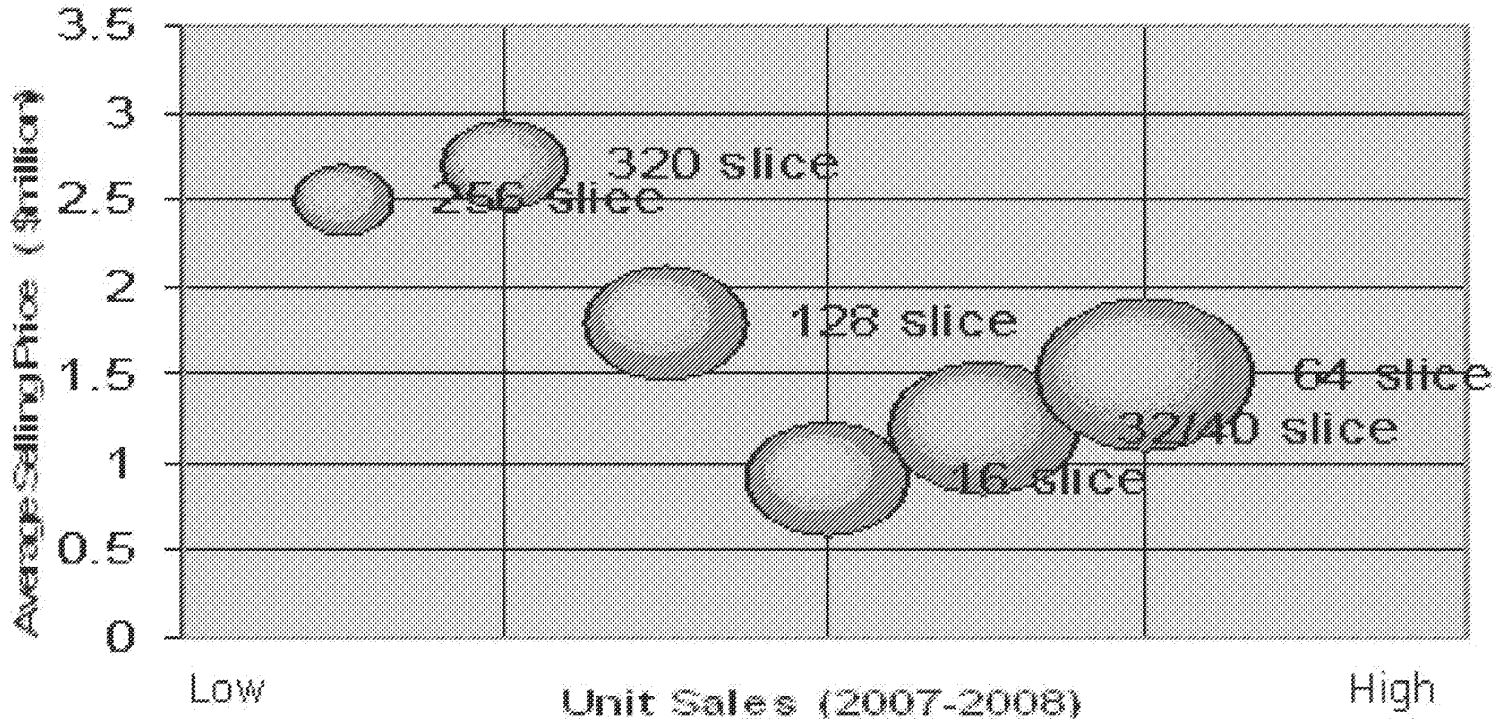

Source: 2008 Frost & Sullivan

SIONYX1403000016.0003
SAMSUNG EX. 1002 - 1296/4148

ANALOGIC®
The World Resource for Health & Security Technology

Evolution and Present Status of Medical X-Ray CT Imaging

Medical CT

ANALOGIC

The World Resource for Health & Security Technology

SIONYX1403000016.0004

SAMSUNG EX. 1002 - 1297/4148

SIONYX1403000016.0005

SAMSUNG EX. 1002 - 1298/4148

Analogic in CT

ANALOGIC
The World Resource
for Health & Security Technology

- CT Subsystems
  - Data Management Systems (DMS)
  - Data Acquisition Systems (DAS)
  - Detector Arrays
  - Gantries
  - PowerLink – Non-Contact Power Transfer
  - Collimators
  - Reconstruction Software
  - Motion Control
  - Patient Table
  - Operator Contol Station

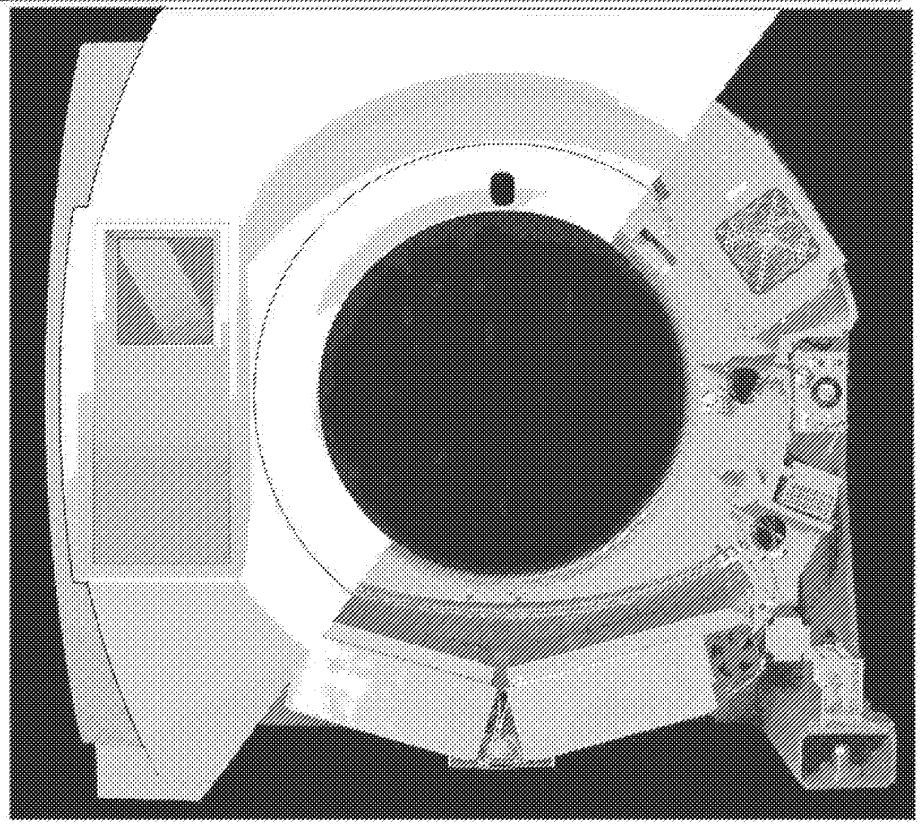

SIONYX1403000016.0006
SAMSUNG EX. 1002 - 1299/4148

ANALOGIC®

The World Resource for Health & Security Technology

CT Systems Security

Milestones in X-ray CT

ANALOGIC
The World Resource for Health & Security Technology

- **Sequential scanning of consecutive slices: 1970s**
- **Spiral scanning-CT acquisition with continuous translation of patient: beginning of 1990s**
- **Multislice spiral CT: end of 1990s**
- **Dual source CT: 2000s**

- ***Main trend: increasing speed of acquisition and axial coverage (slices)***

SIONYX1403000016.0008
SAMSUNG EX. 1002 - 1301/4148

SIONYX1403000016.0009
SAMSUNG EX. 1002 - 1302/4148

ANALOGIC
The World Resource for Health & Security Technology

Multislice Spiral CT Scanning

- Mid 1990s: 300 mm lung or abdominal examination with narrow slice requires 200 s long scan
- Mid 2000s: same examination takes 1-3 sec
- High speed of CT allows large scan within one breath hold, and to acquire images of moving organs, such as heart.

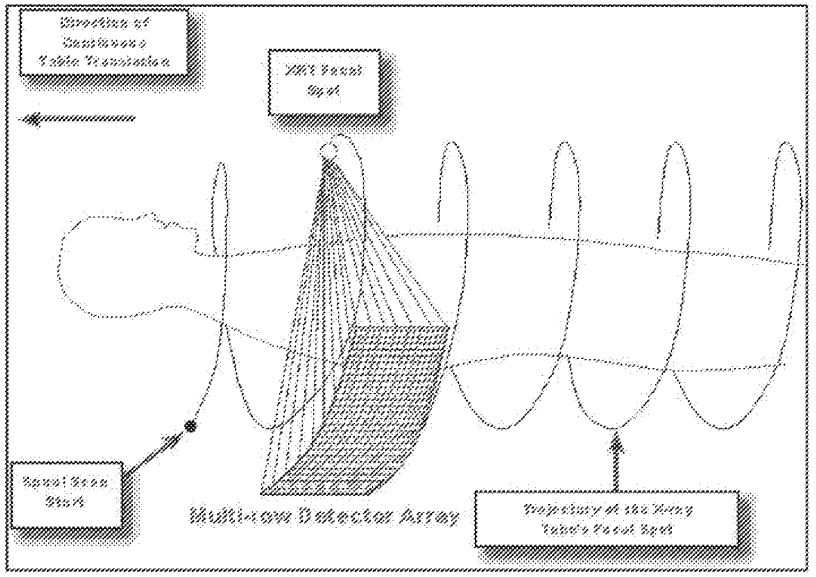

SIONYX1403000016.0010
SAMSUNG EX. 1002 - 1303/4148

CT applications

ANALOGIC
The World Resource for Health & Security Technology

- **Coronary Angiography**
  - Rest phase of coronary arteries is 60 msec!
  - Non-invasive emergency diagnosis for cause of chest pain: coronary blockage, pulmonary embolism, aortic aneurism.
  - Alternative: 6 hour long invasive catheterization procedure with 1% risk of serious complications, including death.

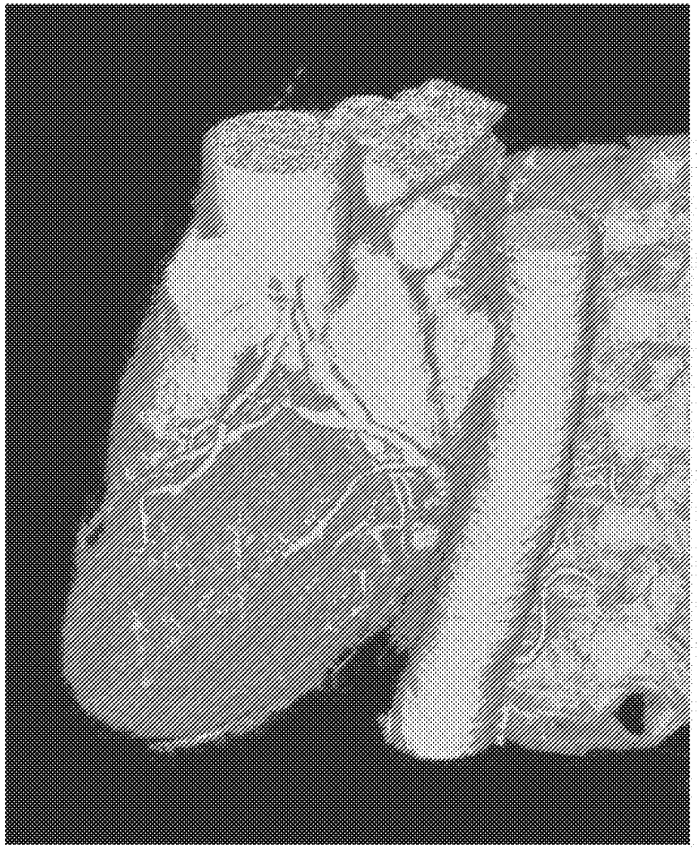

SAMSUNG EX. 1002 - 1304/4148
SIONYX1403000016.0011

ANALOGIC
The World Resource for Health & Security Technology

Main drivers in X-ray CT

- Short scan time and large axial coverage for reliable anatomical and functional measurements of whole organs (perfusion of heart, brain, lung)
- Ultra-High spatial resolution
- Anatomical/Functional multi-modality imaging in SPECT-CT, PET-CT
- Patient dose reduction

- Is slice war over?

SIONYX1403000016.0012
SAMSUNG EX. 1002 - 1305/4148

DMS for X-Ray CT

ANALOGIC
The World Resource for Health & Security Technology

- Scan time: 0.3 sec
- XRT Power: 100 kW
- Axial coverage: 40-160 mm at isocenter
- Spatial resolution: ~0.5 mm
- Remarkable progress in X-Ray CT in the past decade is largely explained by fast development of the Data Measurement System (DMS)

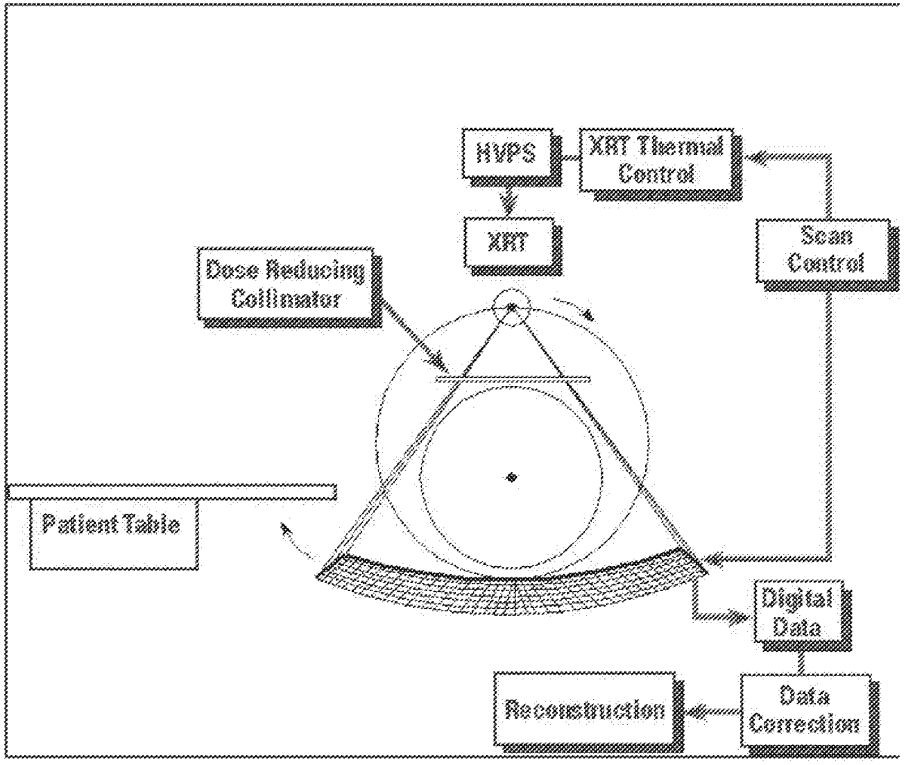

SAMSUNG EX. 1002 - 1306/4148
SIONYX1403000016.0013

Main DMS Parameters

ANALOGIC
The World Resource for Health & Security Technology

Parameter	Typical value	Parameter	Typical value
X-ray energy, kVp	80-140	Rotation time, sec	0.3
XRT power, kW	100	Data transfer rate, GBit/sec	10
FOV, cm	50	Operational temperature range	15-45°C
Isotropic resolution at isocenter, mm	0.5-0.6	Number of x-ray photons per sample at peak power	300,000
Number of channels per row	700-1000	Conversion efficiency, el/eV	0.01-0.02
Number of rows	64, 128, 320	Sampling rate, Hz	3000
Typical element size, mm	1x1	Data resolution, bit	18-20
Typical detector distance from XRT focal spot, mm	1000	Dynamic range, bit	16-18

SIONYX1403000016.0014
SAMSUNG EX. 1002 - 1307/4148

ANALOGIC
The World Resource for Imaging & Security Technology

Detector Channels per CT - 2008

High End (128-320 slices)	up to 300,000
Mid Range (16 slices)	57,00
Low End (single slice)	1000

Analogic DAS/DMS

- From 400-1000 channels in 1993 to 300,000 channels in 2008
- DAS/DMS complexity increases at constant:
  - Cost
  - Power consumption
  - and almost same Mechanical Envelope

SAMSUNG EX. 1002 - 1308/4148
SIONYX1403000016.0015

ANALOGIC
The World Resource for Health & Security Technology

Charge Integrating CT Detector

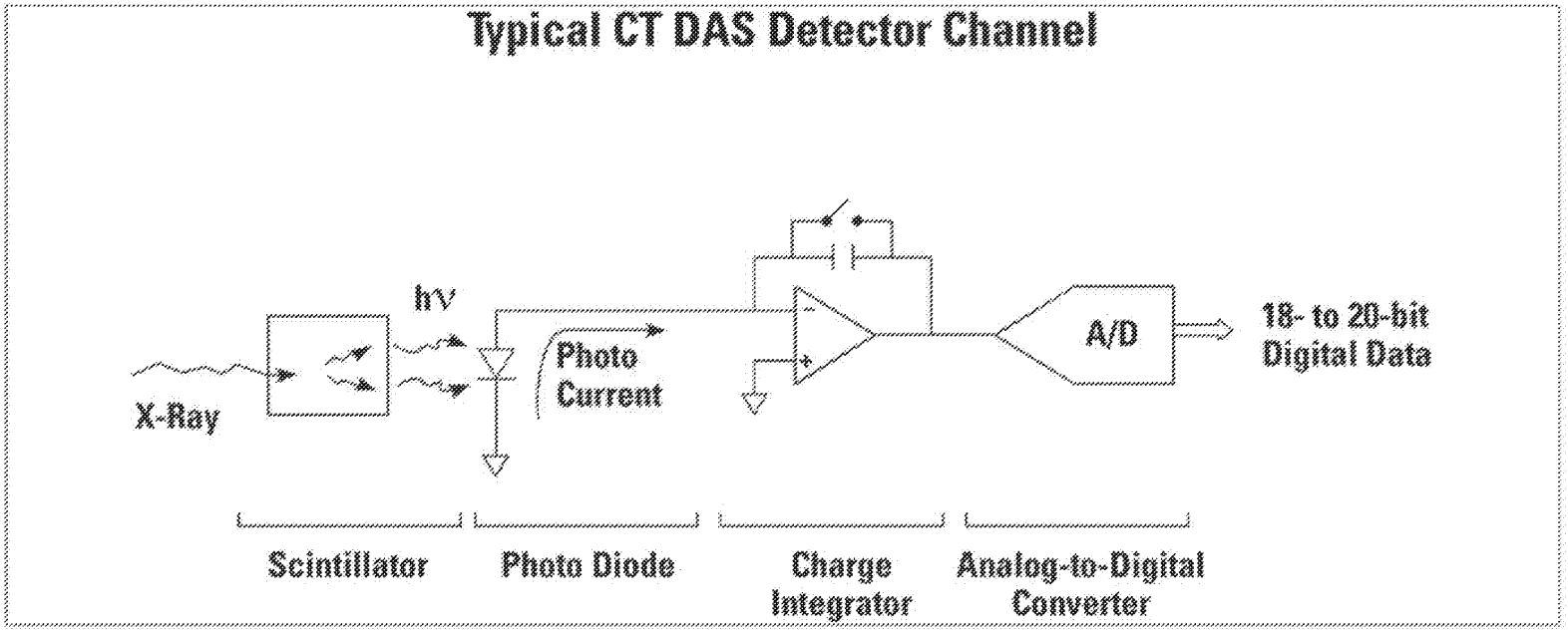

Uniform and Adaptive Detector Configurations

ANALOGIC
The World Resource for Health & Security Technology

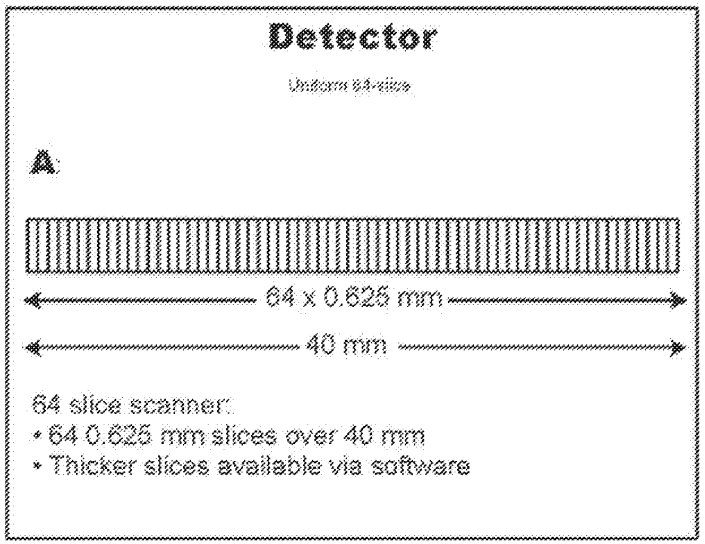

Uniform coverage in axial direction. Used in most 64, 128, 256 slice Scanners.

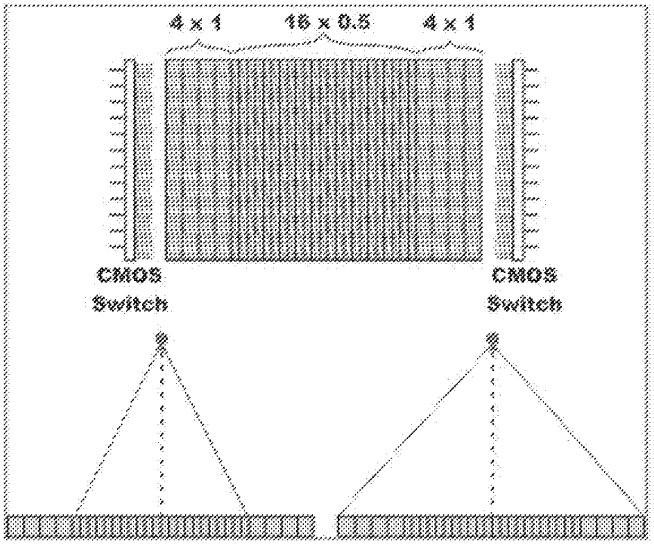

Adaptive arrays have fewer septa and DAS channels. Used in CT with 16 or fewer slices.

SIONYX1403000016.0016
SAMSUNG EX. 1002 - 1309/4148

SIONYX1403000016.0017

SAMSUNG EX. 1002 - 1310/4148

ANALOGIC®

The World Resource for Health & Security Technology

CT Subsystems

- **DMS**
  - 1 – 64 Slice+
  - Integrated DAS and Detector Assemblies
  - X-ray Beamline Design

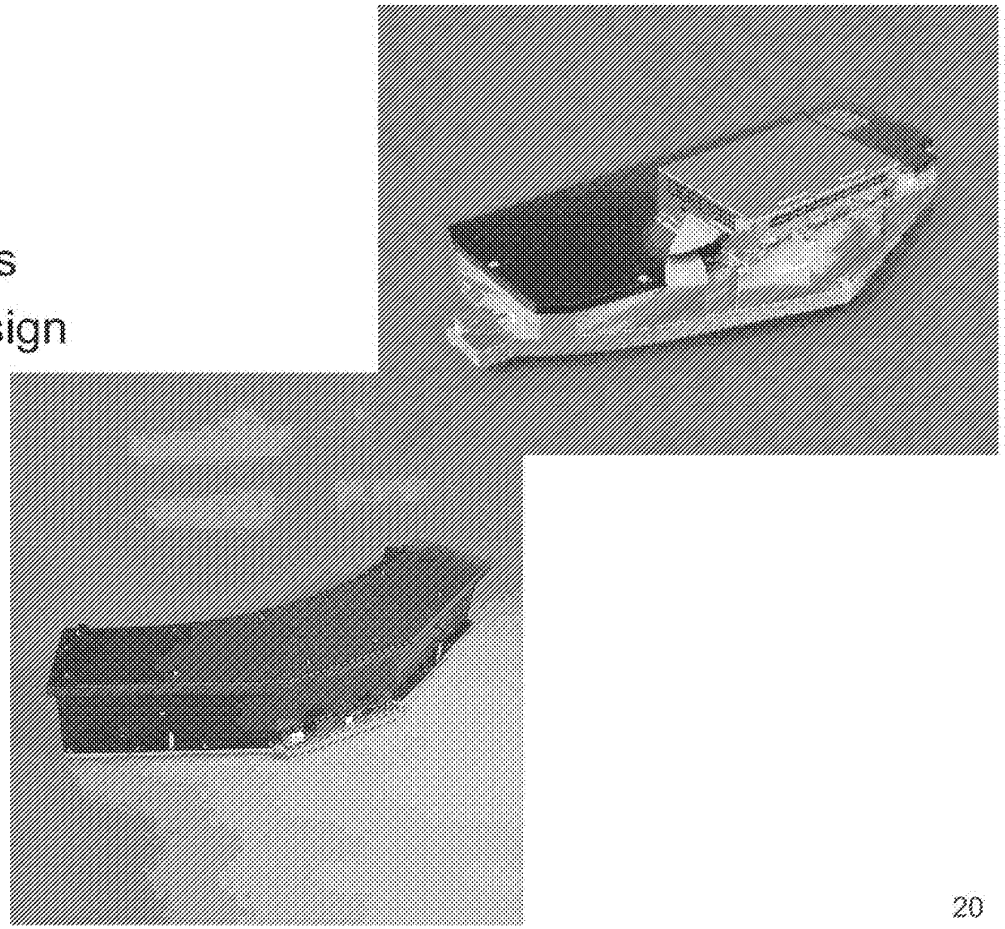

16x64 CT Detector

ANALOGIC
The World Resource for Health & Security Technology

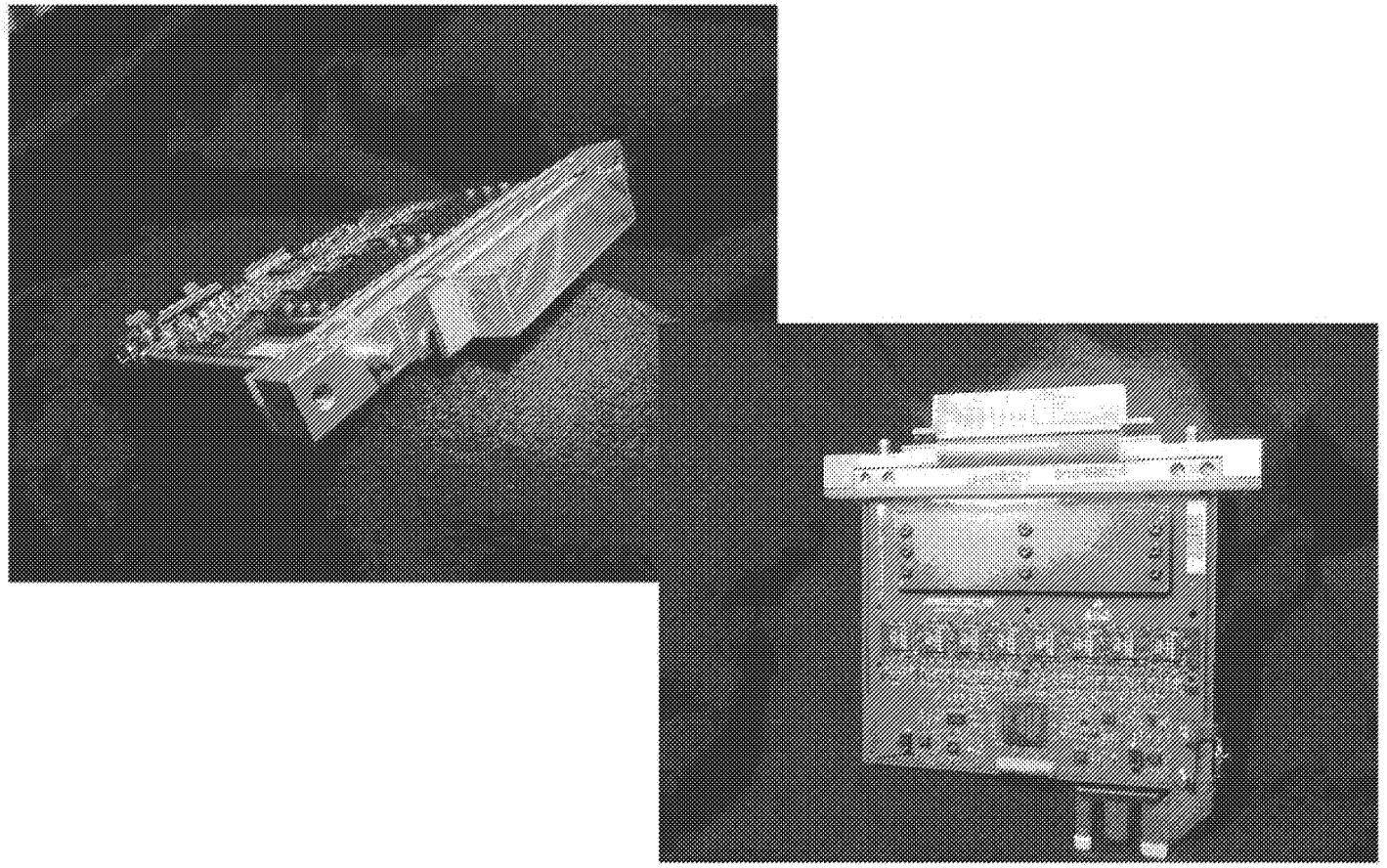

SIONYX1403000016.0018

SAMSUNG EX. 1002 - 1311/4148

Requirements for Scintillators in X-Ray CT

ANALOGIC
The World Resource for Health & Security Technology

Parameter	Requirement	Importance
Energy range	20-140 keV	
DQE (0)	>95 %	Image noise, dose reduction
Dose rates at detector	~0.1 Gy/s	
Lifetime dose	100 kGy	
Light output (LO)	>40,000 ph/MeV	Image noise at high attenuation
Emission spectrum, nm	400-1000	Used with Si photodiodes
Decay time	<10 µs	To support >10 kHz DAS rates
Afterglow	<10 ppm at 3 ms	Image artifacts
Susceptibility to radiation damage	<1 %/Gy	Image artifacts if channels non-uniform
Lifetime degradation	<20 %	Dynamic range reduction
LO temperature coefficient	<0.3 %/°C	Image artifacts if channels non-uniform
Low cost, non-toxic		DMS cost, cost of removal

SIONYX1403000016.0019
SAMSUNG EX. 1002 - 1312/4148

SIONYX1403000016.0020
SAMSUNG EX. 1002 - 1313/4148

ANALOGIC
The World Resource for Health & Security Technology

Main Scintillators in X-Ray CT

Scintillator	Density (g/cm^3)	Thickness [a] to stop 99 % (mm)	Relative Light output[b]	Emission band maximum	Primary decay (µs)	Afterglow (% at 3 ms)
$CdWO_4$	7.9	2.6	1	495	2, 15	<0.1
$Gd_2O_3:Eu^{+3}$	7.55	2.6	-	610	-	-
$(Y,Gd)_2O_3:Eu$	5.9	6.1	1.52	610	1000	5
$Gd_2O_2S:Pr,Ce,$	7.34	2.9	1.8	520	2.4	<0.1
$Gd_2O_2S:Tb(Ce)$	7.34	2.9	1.8	550	600	≤0.7
$La_2HfO_7:Ti$	7.9	2.8	0.45	475	10	-
$Gd_3Ga_5O_{12}:Cr,$	7.09	4.5	1.38	730	150	<0.1

[a] Thickness to absorb 99 % of x-ray photons generated by tungsten anode x-ray tube at 140 kVp.

[b] Relative light output measured using silicon photodiode, under 140 kVp tungsten anode XRT excitation.

General Electric introduced fast "Gemstone" garnet based ceramic scintillator in 2007.

Limited data in public domain.

Silicon Photodiodes for X-Ray & LOGIC
Main Requirements

The World Resource for Health & Security Technology

Parameter	Value
Mode of operation	P-i-n structure, Photovoltaic, 0V bias
Elements number per chip, typ	512
Interconnect density	>64 per pitch
Pitch in x-axis, typ	1.0 mm
Pitch in z-axis, typ	1.0 mm
NEP	$<3 \cdot 10^{-15}$ W/√ Hz
Rise, fall time	<1 μs
Spectral response range	320-1060 nm
Photosensitivity, typ	0.3 A/W at 500 nm
Uniformity of photosensitivity	+/-2% ch-to-ch
Leakage current for 1x1 mm^2	5 pA, max,@10 mV bias, 25 C,
Cross-talk	0.1 %, max
Terminal capacitance for 1x1 mm^2	20 pF, max, @0V, 10 kHz

SIONYX1403000016.0021
SAMSUNG EX. 1002 - 1314/4148

Data Acquisition Electronics Main Requirements

ANALOGIC
The World Resource for Health & Security Technology

Parameter	Performance	Note
Electronic Noise σ_e	≤ (1/2) $\sigma_{\gamma,m}$	$\sigma_{\gamma,m}$ = Minimum Photon Noise
Digitization Interval δ	≤ (1/6) $(\sigma_\gamma^2 + \sigma_e^2)^{1/2}$	σ_γ = Photon Noise
Sampling Rate	≥ 10 kHz	
Offset Stability	≤ 1.5 ppm FSR /°C	FSR = Full Scale Reading
Gain Stability	≤ ± 50 ppm FSR /°C	
Integral Non Linearity	≤ 200 ppm R /°C ± 2 ppm FSR	R = Reading
Differential Non Linearity	≤ 30 ppm R /°C ± 1 ppm FSR	
Power Consumption	≤ 3 mW / Channel	
Packaging	64-128 Channels AMP/ADC	ASIC

SIONYX1403000016.0022
SAMSUNG EX. 1002 - 1315/4148

SIONYX1403000016.0023

SAMSUNG EX. 1002 - 1316/4148

ANALOGIC
The World Resource for Health & Security Technology

Trends in Medical CT

1. **New CT scanning geometry: Dual-Source, Multi-Source, Inverse-geometry**
   - Advantages: Faster acquisition, Cone-beam artifact reduction
   - Requires multiple DMS, or area detector, expensive

2. **Energy-sensitive CT**
   - Advantages: elimination of beam hardening artifacts, material discrimination, better contrast at lower dose
   - Solutions
     - Dual-layered detectors
     - Dual-source CT, kVp switching
     - Photon Counting Detectors with multiple energy bins

3. **Multimodality CT: SPECT/CT, PET/CT, Preclinical systems**

ANALOGIC
The World Resource
for Health & Security Technology

SIONYX1403000016.0024

SAMSUNG EX. 1002 - 1317/4148

4. Phase-contrast imaging (more distant future)

- Phase-contrast imaging, based on difraction is more sensitive in 10-150 keV range then attenuation based imaging.
- Requires interferometry and difractometry detection technique.

Multiple Source CT

ANALOGIC
The World Resource for Health & Security Technology

- Multiple source/detector systems-old idea becomes a desirable development
- Higher rotation rates require increase in X-Ray power, not achievable with present X-Ray technology
- Fraction of rotation is required for a full scan
- Issues: scatter reduction, high cost
- Siemens introduced commercial Dual Source CT in 2004

SIONYX1403000016.0025
SAMSUNG EX. 1002 - 1318/4148

Energy sensitive CT: Dual Energy Detector

ANALOGIC
The World Resource for Health & Security Technology

- **Two crystals with different emission bands are used.**
- **Radiation is hardened by the first crystal.**
- **Optical band pass filters limit diodes to see signal from only one crystal.**
- **Advantages:**
  - Simultaneous acquisition of Low and High Energy samples.
  - High Quantum Efficiency
  - Planar silicon PDA technology

R. Deych, US Patent 7,388,208 B2 2008

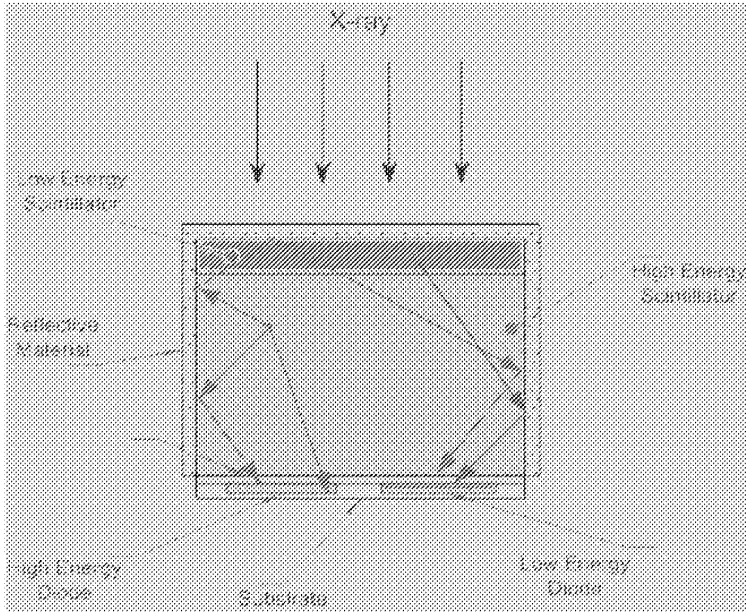

Incident X-ray Photons
Light Photons from High Energy Scintillator
Light Photons from Low Energy Scintillator

SIONYX1403000016.0026
SAMSUNG EX. 1002 - 1319/4148

Contrast-to-Noise Model Results

ANALOGIC
The World Resource for Health & Security Technology

(Teflon detail in water background)

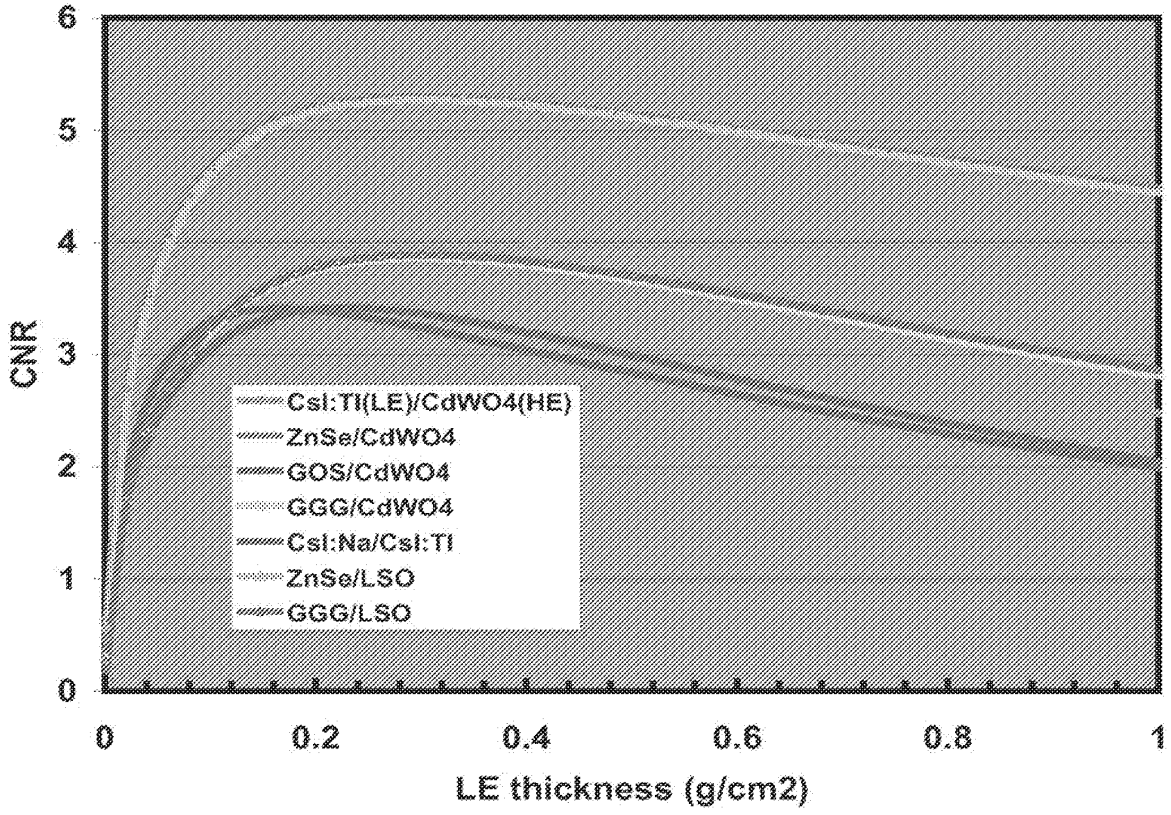

SIONYX1403000016.0027
SAMSUNG EX. 1002 - 1320/4148

Energy sensitive CT, Single photon counting

ANALOGIC

The World Resource for Health & Security Technology

SIONYX1403000016.0028

SAMSUNG EX. 1002 - 1321/4148

SAMSUNG EX. 1002 - 1322/4148
SIONYX1403000016.0029

ANALOGIC
The World Resource for Health & Security Technology

SPC in Computed Tomography

- **New medical applications and capabilities**
  - Contrast media removal in images
  - Multiple contrast agents
  - Reduction of beam hardening artifacts
  - Patient dose reduction
- **Requires high counting rates up to 10^9 (!) photons/sec/mm^2**

SAMSUNG EX. 1002 - 1323/4148
SIONYX1403000016.0030

ANALOGIC
The World Resource for Health & Security Technology

Direct Conversion Detectors

- **Dual energy CZT based detector tested in LightSpeed GE CT scanner, *IEEE 2007***
- **Pre-clinical CT scanner with 6 energy bands based on CZT technology tested by Philips, *IEEE 2008***
- **Main drawbacks:**
  - Long carrier transit time, insufficient speed
  - Material polarization at high exposure rates

SAMSUNG EX. 1002 - 1324/4148
SIONYX1403000016.0031

ANALOGIC
The World Resource for Health & Security Technology

Scintillator Based SPC

- X-ray CT will require fast scintillators and internal gain in photodetectors
- Fast scintillators with Solid State PM are being proposed for CT
- Potential Available Fast Scintillators: LSO, LYSO, $LaBr_3$
- New faster scintillators with 1-10 nsec decay time are required

Multimodality CT: SPECT/CT, PET/CT

ANALOGIC
The World Resource for Health & Security Technology

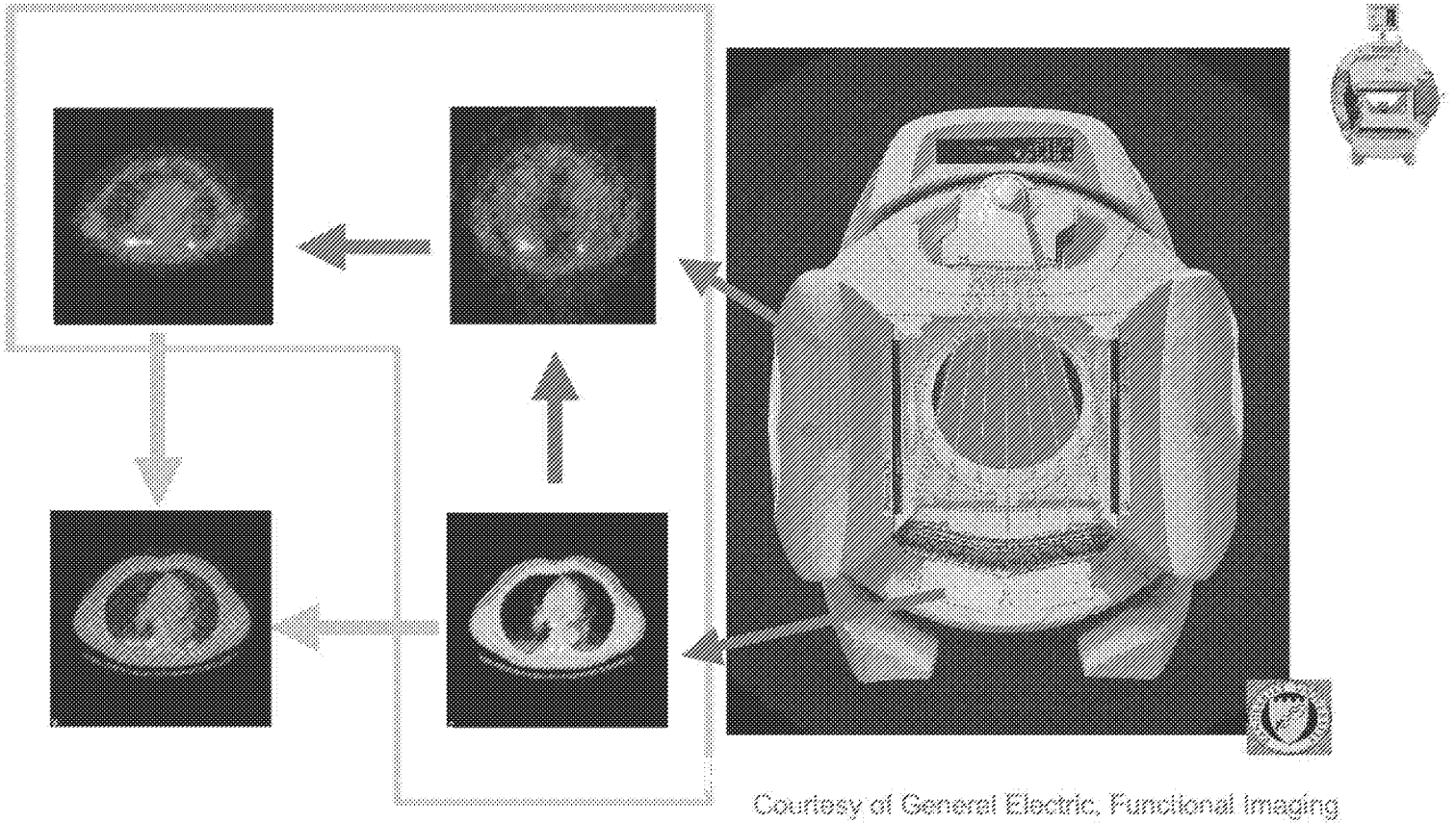

Courtesy of General Electric, Functional Imaging

SIONYX1403000016.0032
SAMSUNG EX. 1002 - 1325/4148

Advances in X-ray CT: Conclusions and Predictions

ANALOGIC
The World Resource for Health & Security Technology

- CT scanners with 320 slice acquisition in 0.3 sec are available
- The "slice war" between major medical imaging companies is over!
- New CT systems will include novel scanning techniques: multiple sources, inverse geometries
- Multi-energy CT will be needed to obtain better tissue discrimination at lower patient dose.
- Photon counting detection may replace charge integration
- X-ray CT will become new market for ultrafast nanosecond scintillators.

SIONYX1403000016.0033
SAMSUNG EX. 1002 - 1326/4148

Advances in Digital Mammography

ANALOGIC

The World Resource for Health & Security Technology

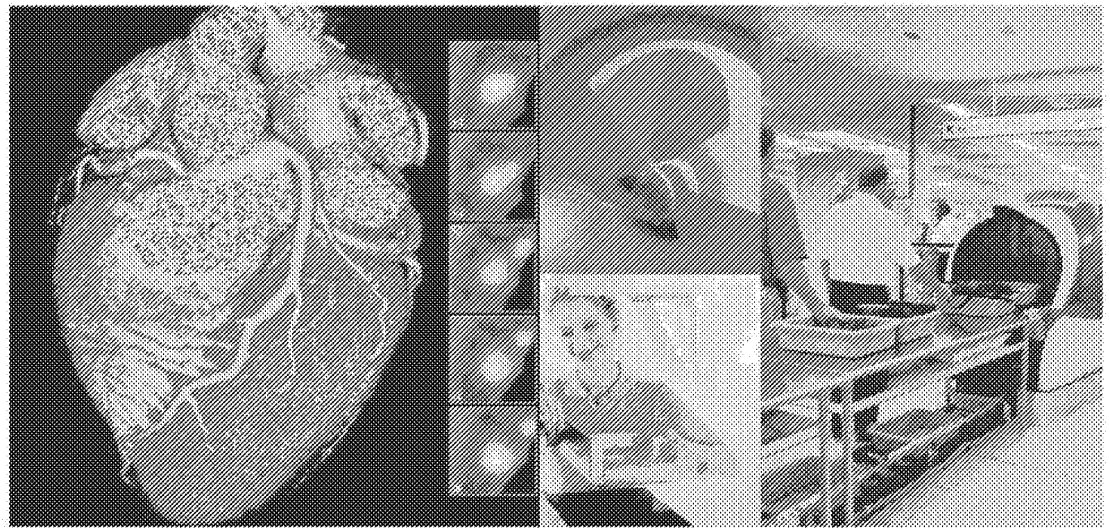

SIONYX1403000016.0034

SAMSUNG EX. 1002 - 1327/4148

Stating the Problem

ANALOGIC
The World Resource
for Health & Security Technology

Increasing mammography clinical diagnostic's sensitivity and specificity while optimizing patients' flow and reducing operational costs.

SIONYX1403000016.0035
SAMSUNG EX. 1002 - 1328/4148

SAMSUNG EX. 1002 - 1329/4148
SIONYX1403000016.0036

ANALOGIC
The World Resource for Digital Security Technology

Digital Mammography Installed Units

2005	450
2006	900
2007	1650
2008	2000 est.
2009	2100 est.

Average Time/Patient

ANALOGIC
The World Resource for Health & Security Technology

Film-based analog mammography:

12 – 15 minutes

Se-based digital mammography:

5 – 6 minutes

SIONYX1403000016.0037

SAMSUNG EX. 1002 - 1330/4148

Digital Radiography

ANALOGIC
The World Resource for Health & Security Technology

- **Two Step Conversion - INDIRECT**
  X-Ray to light to electrical charge

- **One Step Conversion - DIRECT**
  X-Ray to electrical charge

SIONYX1403000016.0038
SAMSUNG EX. 1002 - 1331/4148

SAMSUNG EX. 1002 - 1332/4148
SIONYX1403000016.0039

a: Se Technologies

ANALOGIC
The World Resource for Health & Security Technology

- **Generation I:**

  dielectric isolation layer deposited on top of two layer "p" Se structure

- **Generation II:**

  single Se deposition process with real time doping to create three layer pin or nip structures

SIONYX1403000016.0040

SAMSUNG EX. 1002 - 1333/4148

Mammography Detector

ANALOGIC
The World Resource for Health & Security Technology

General Characteristics

Technology:	amorphous Selenium
Active area:	24 cm x 30 cm
Resolution:	2816 x 3584 pixels
Pixel pitch:	85 µm
Acquisition speed:	2 frames/second
Digitization:	14 bits

Se Characteristics

ANALOGIC
The World Resource for Health & Security Technology

- Atomic Number: 34
- Conversion Efficiency: 50 eV / e-h
- Evaporation Temperature: 217 deg. C
- Crystallization Temperature: 60 deg. C
- Expansion Coefficient: 40 ppm/deg. C

SIONYX1403000016.0041
SAMSUNG EX. 1002 - 1334/4148

SIONYX1403000016.0042
SAMSUNG EX. 1002 - 1335/4148

ANALOGIC
The World Resource for Health & Security Technology

a: Selenium Detector Structure

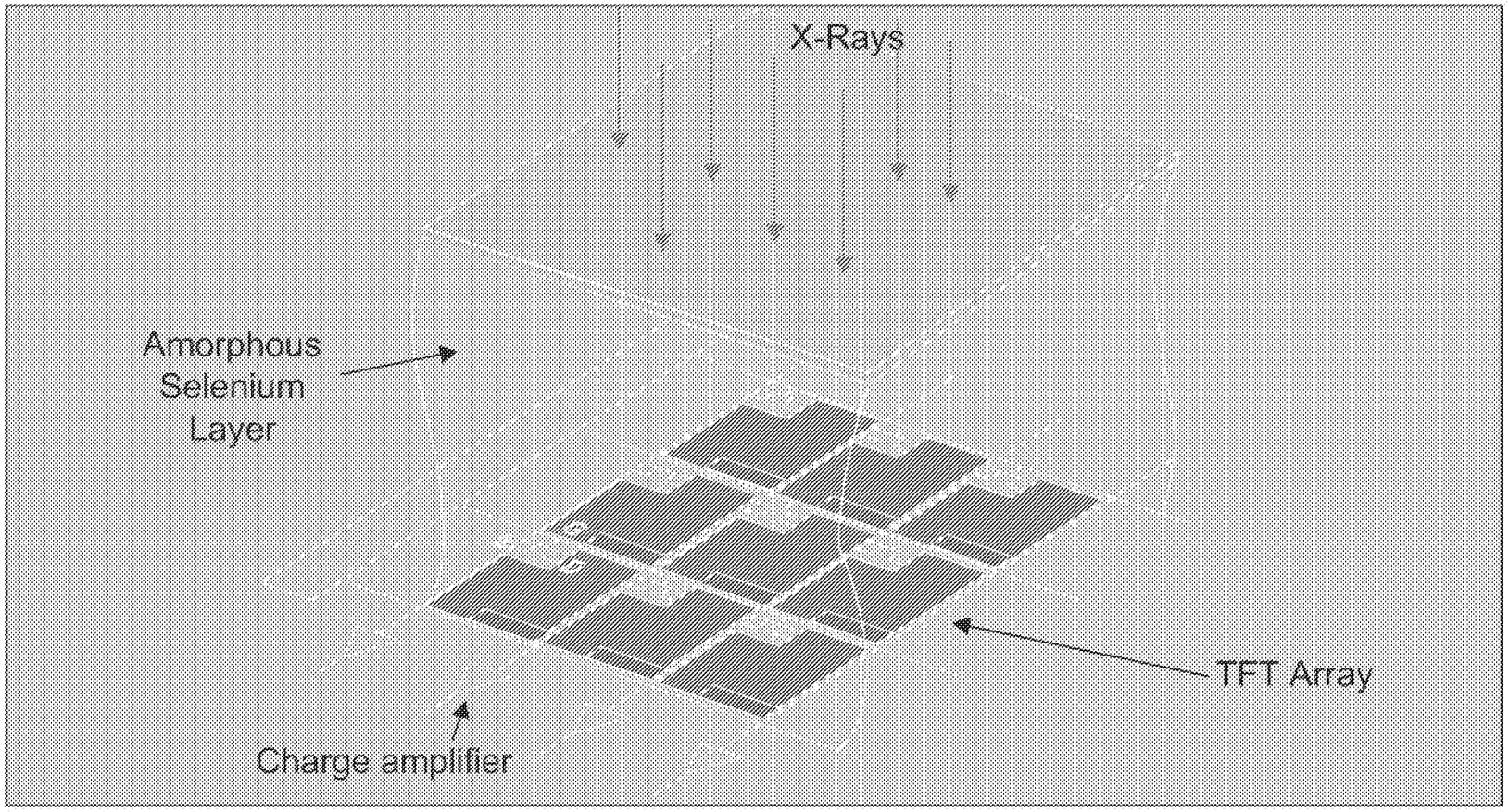

SIONYX1403000016.0043
SAMSUNG EX. 1002 - 1336/4148

X-Ray Absorption

ANALOGIC
The World Resource for Health & Security Technology

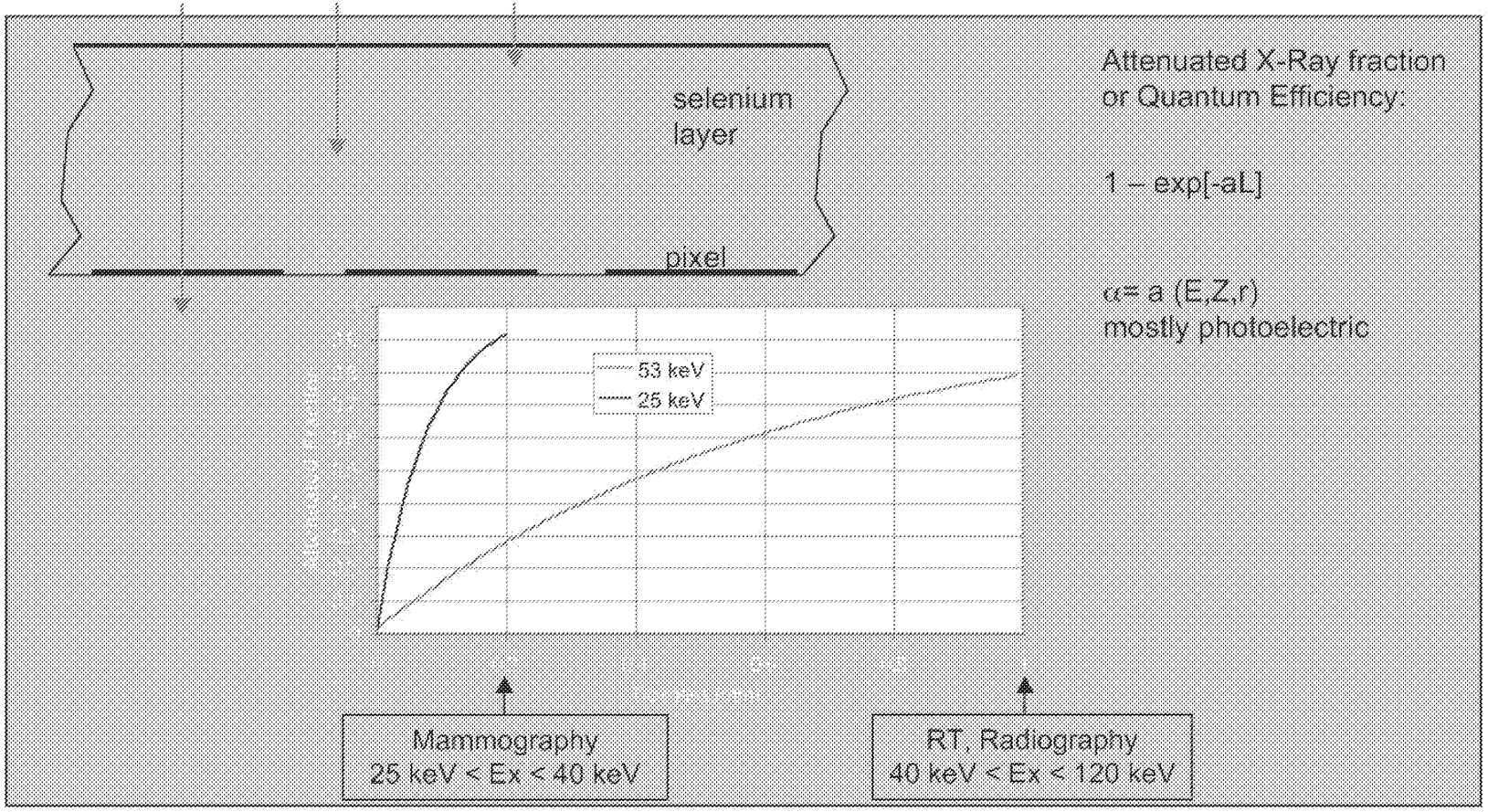

Attenuated X-Ray fraction or Quantum Efficiency:

$1 - \exp[-aL]$

$\alpha = a\,(E,Z,r)$
mostly photoelectric

SIONYX1403000016.0044
SAMSUNG EX. 1002 - 1337/4148

Charge Generation

ANALOGIC
The World Resource for Health & Security Technology

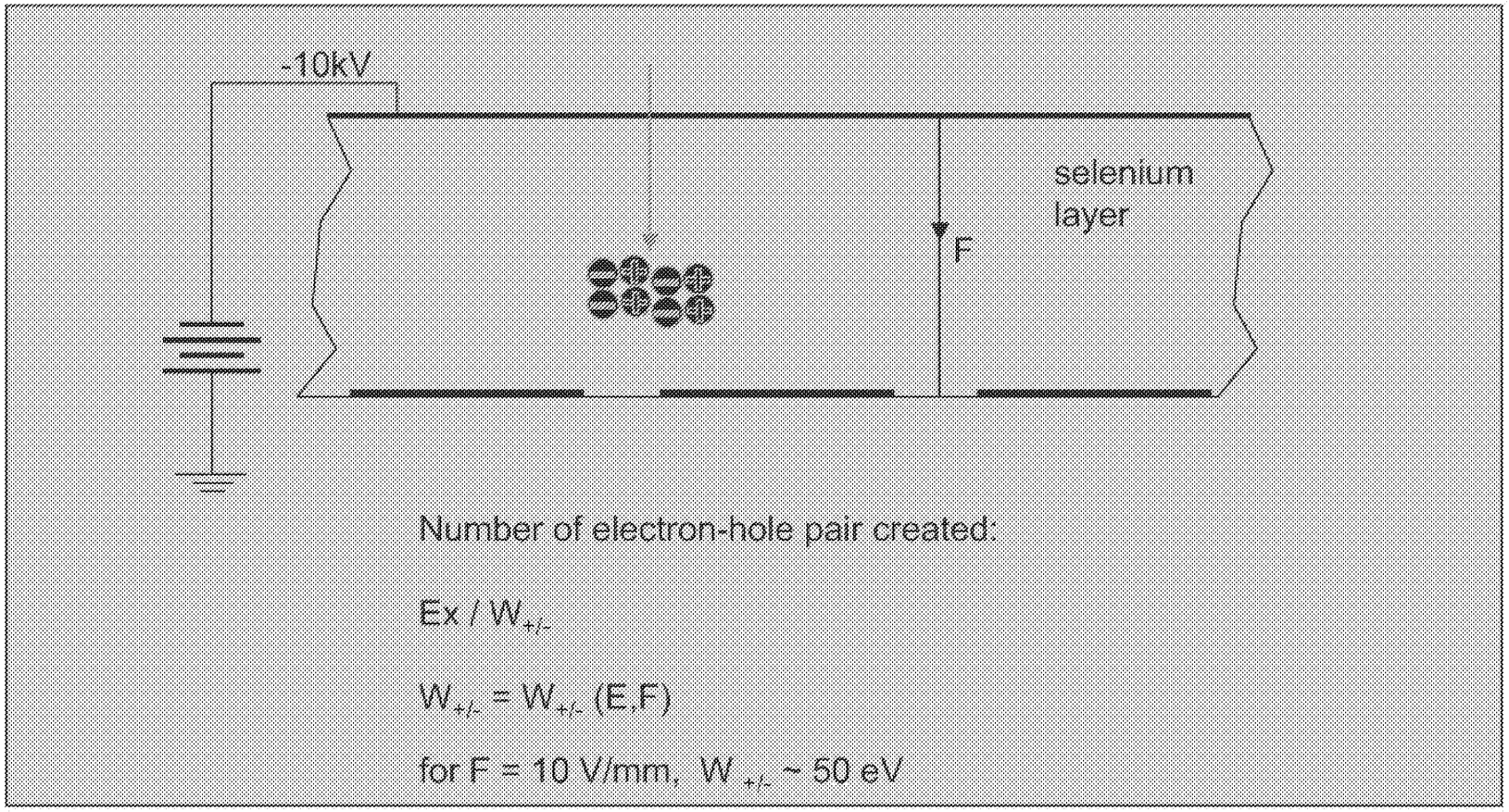

Number of electron-hole pair created:

$Ex / W_{+/-}$

$W_{+/-} = W_{+/-}(E,F)$

for F = 10 V/mm, $W_{+/-} \sim 50$ eV

SIONYX1403000016.0045
SAMSUNG EX. 1002 - 1338/4148

Charge Drift

ANALOGIC
The World Resource for Health & Security Technology

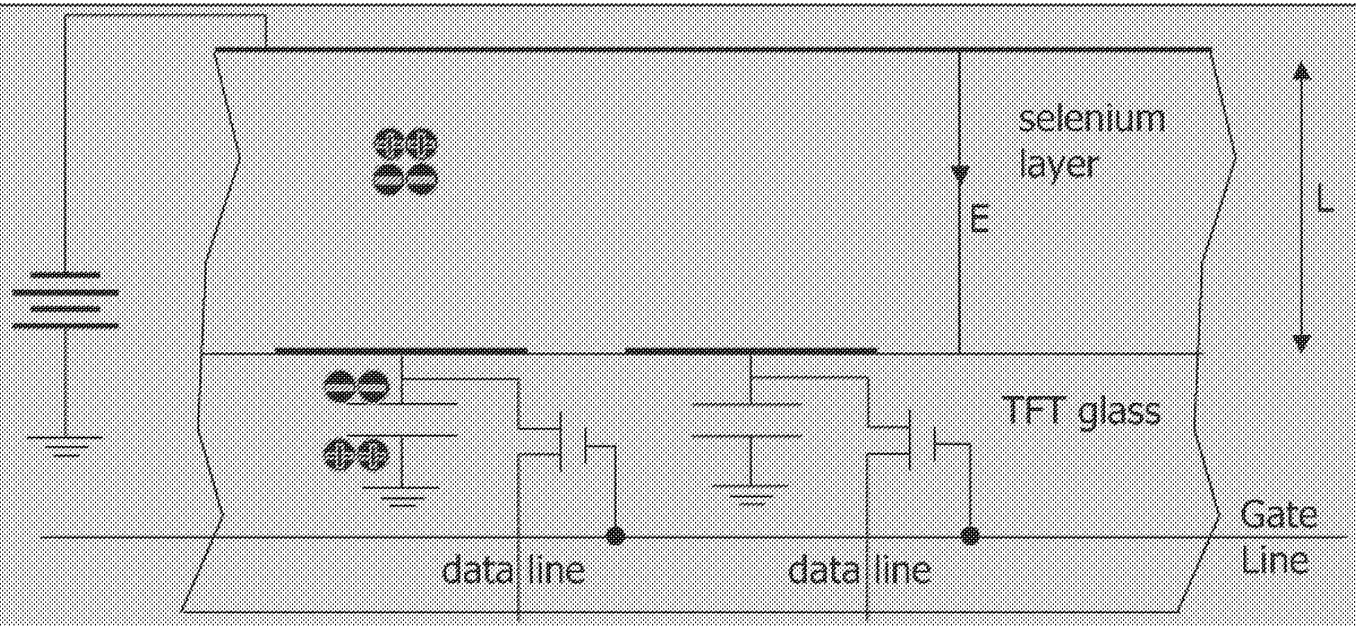

Charge Collection (induction) efficiency:

$\eta = \mu\tau E/L \{ 1-\exp[-L/\mu\tau E] \}$

μ: mobility
τ: lifetime
$\mu\tau E$: mean free path

Typical values for a-Se:

$\mu\tau E(e)$ = 3-4 mm
$\mu\tau E(h)$ = 3-20 mm

For a good detector $\mu\tau E >> L$

SAMSUNG EX. 1002 - 1339/4148
SIONYX1403000016.0046

TFT Pixel Architecture

ANALOGIC
The World Resource for Health & Security Technology

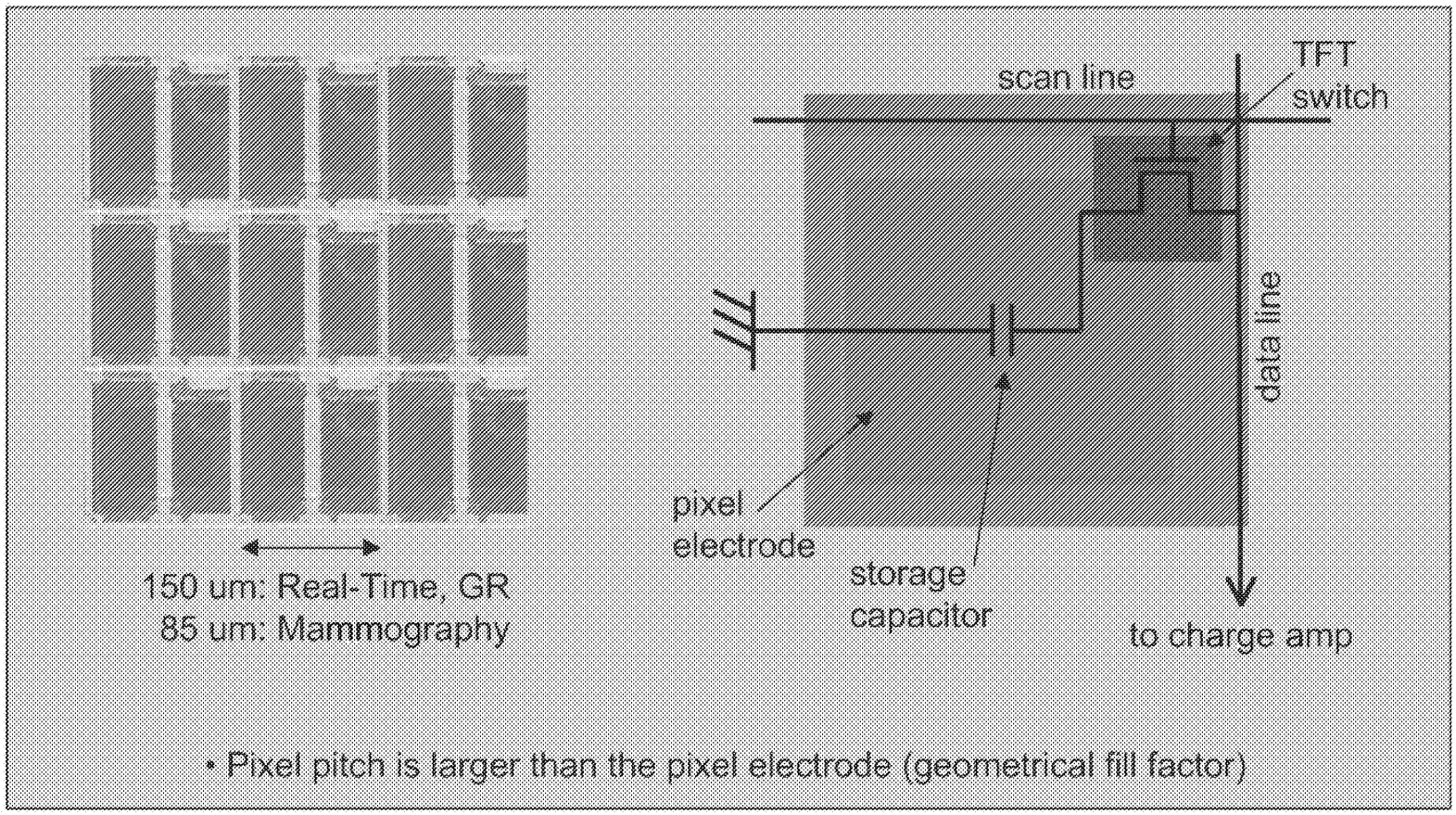

• Pixel pitch is larger than the pixel electrode (geometrical fill factor)

SIONYX1403000016.0047
SAMSUNG EX. 1002 - 1340/4148

ANALOGIC
The World Resource for Health & Security Technology

TFT Array Sequential Readout

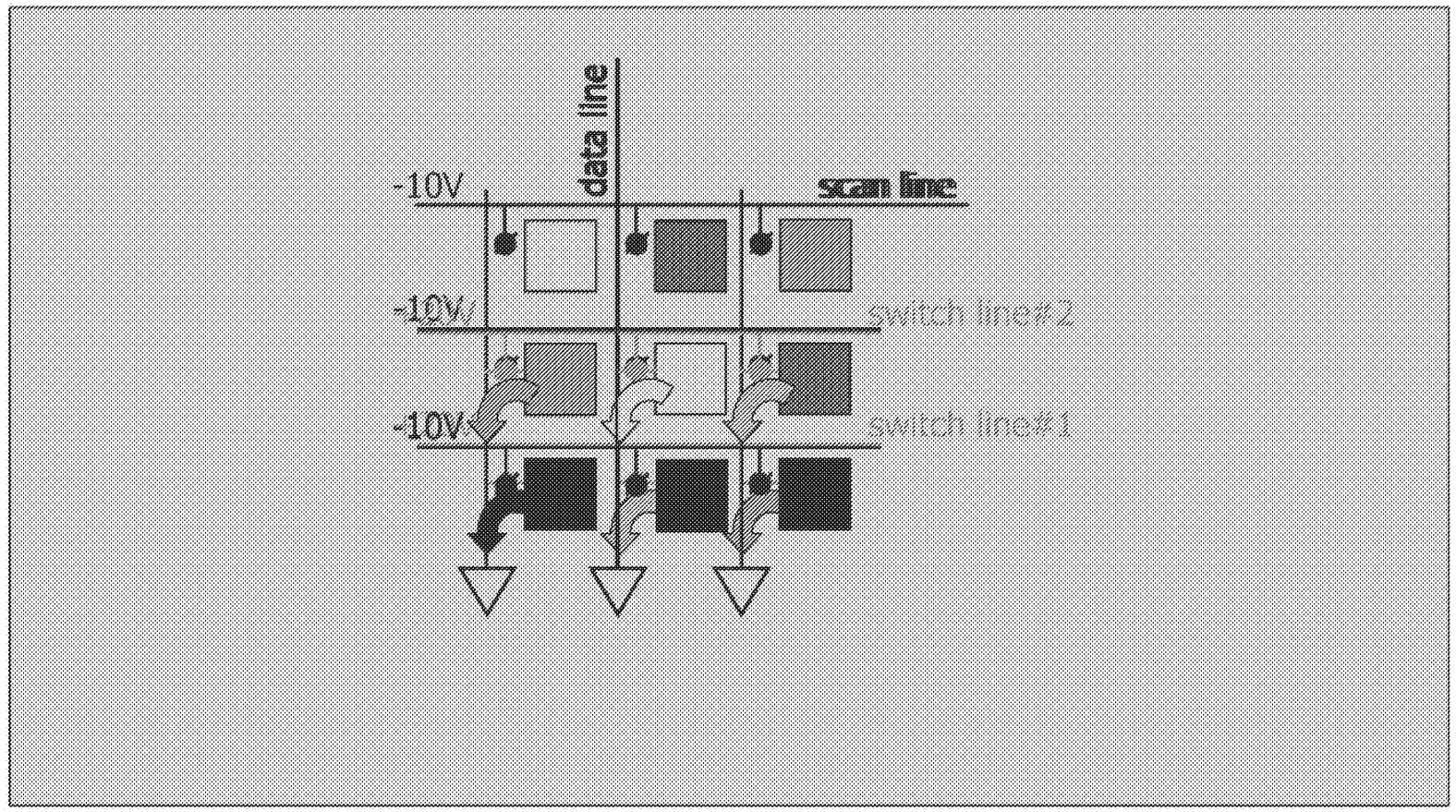

SIONYX1403000016.0048
SAMSUNG EX. 1002 - 1341/4148

ANALOGIC
The World Resource for Health & Security Technology

Detector Spatial Resolution

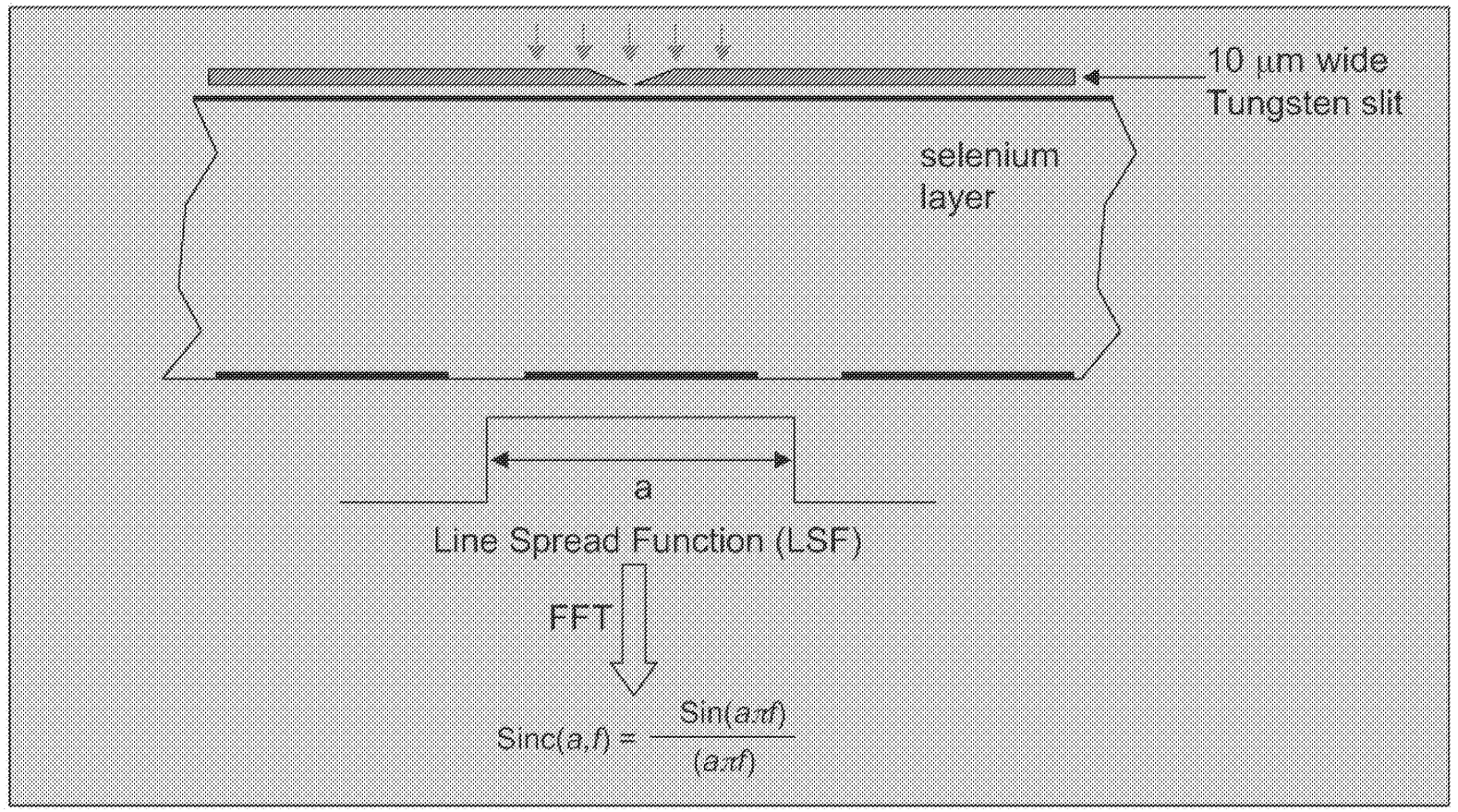

Detector Modulation Transfer Function (MTF)

ANALOGIC
The World Resource for Health & Security Technology

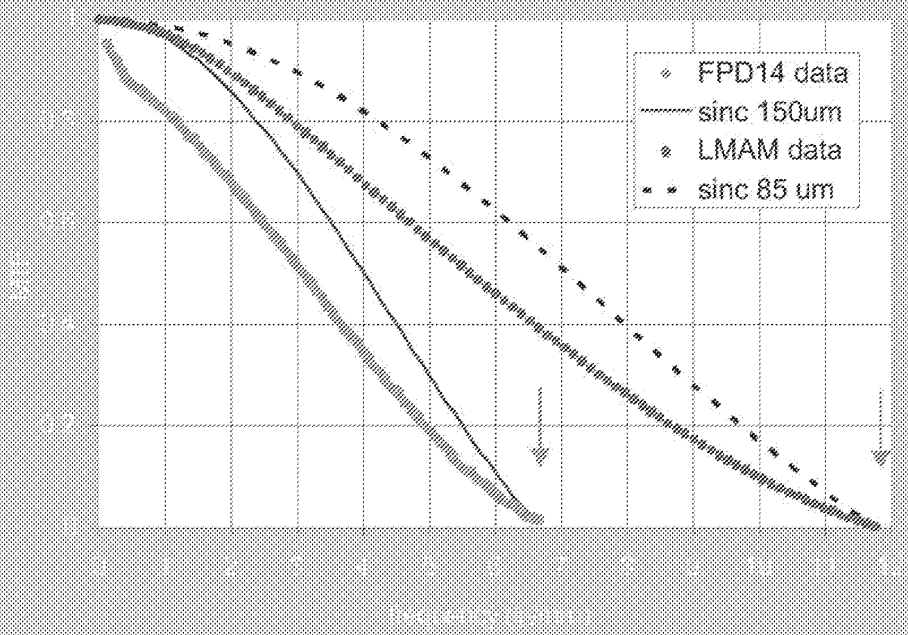

- Experimental MTF's are close to their corresponding sinc functions
- The first zero-crossing of each sinc function corresponds to physical pixel pitch:
  6.6 lp/mm for 150 μm pixel
  11.7 lp/mm for 85 μm pixel

SIONYX1403000016.0049
SAMSUNG EX. 1002 - 1342/4148

Detector Performance: Signal to Noise Ratio (SNR)

ANALOGIC
The World Resource for Health & Security Technology

If γ is the number of X-Ray incident on the detector then $SNR = \frac{\gamma}{\sqrt{N_e^2 + \gamma}}$
where N_e is the electronic noise

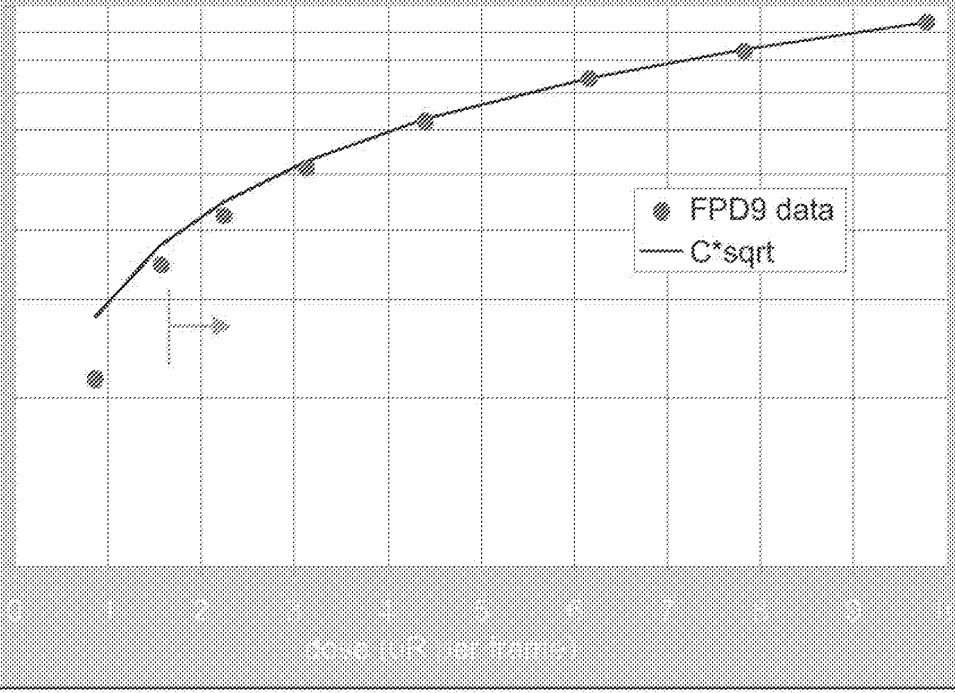

The SNR curve follow a sqrt behavior above $2\mu R$

SIONYX1403000016.0050
SAMSUNG EX. 1002 - 1343/4148

Detector Detective Quantum Efficiency (DQE)

ANALOGIC
The World Resource for Health & Security Technology

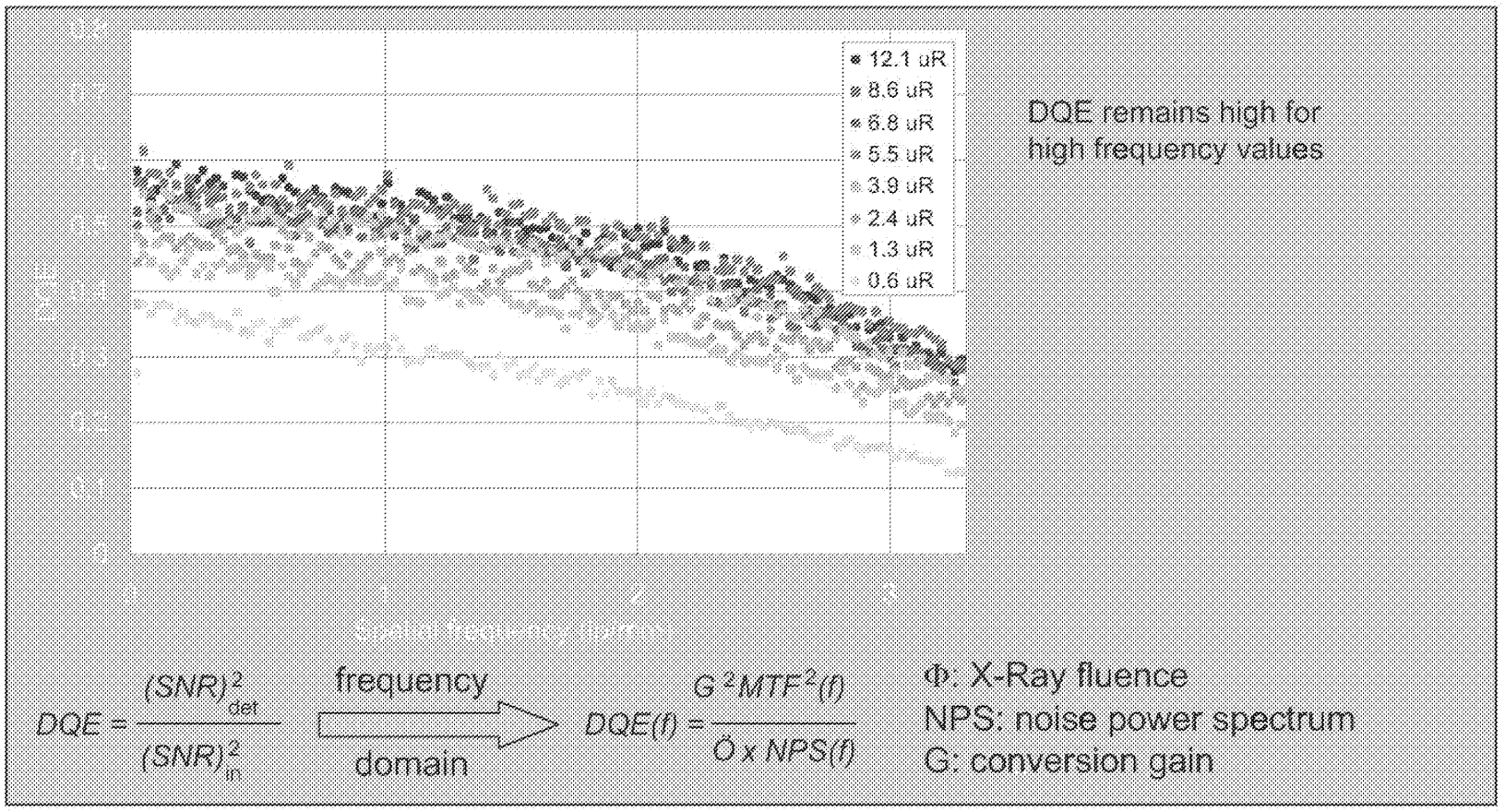

DQE remains high for high frequency values

$$DQE = \frac{(SNR)^2_{det}}{(SNR)^2_{in}} \xrightarrow[\text{domain}]{\text{frequency}} DQE(f) = \frac{G^2 MTF^2(f)}{\Phi \times NPS(f)}$$

Φ: X-Ray fluence
NPS: noise power spectrum
G: conversion gain

SIONYX1403000016.0051
SAMSUNG EX. 1002 - 1344/4148

SIONYX1403000016.0052
SAMSUNG EX. 1002 - 1345/4148

Manufacturing Steps

ANALOGIC
The World Resource for Health & Security Technology

- Deposit in vacuum amorphous Se on TFT
- Deposit top metal electrode on a-Se the
- Attach high voltage contact to electrode
- Deposit isolation on multi-layer structure
- Attach peripheral ASIC electronics to TFT
- Assembly the detector in final enclosure
- Perform parametric and imaging tests

Selenium Coater

ANALOGIC
The World Resource
for Health & Security Technology

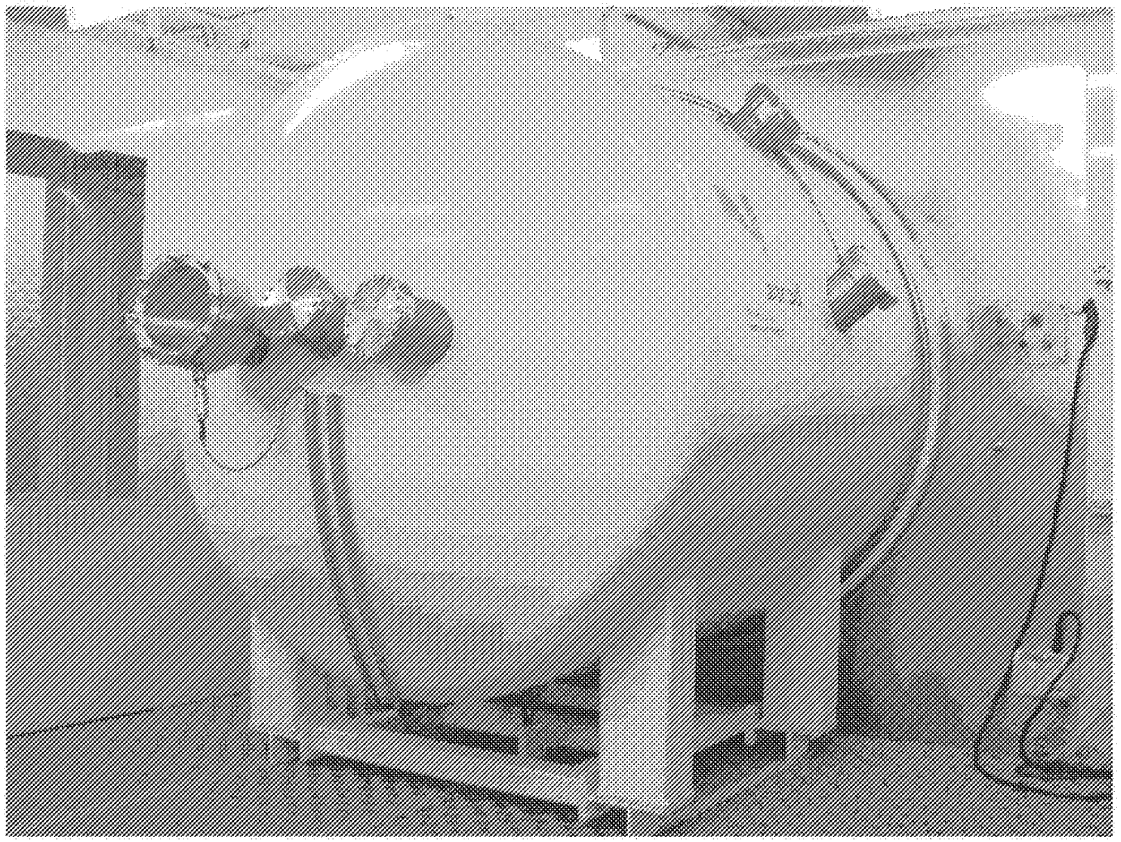

SIONYX1403000016.0053
SAMSUNG EX. 1002 - 1346/4148

Selenium Coater

ANALOGIC
The World Resource
for Health & Security Technology

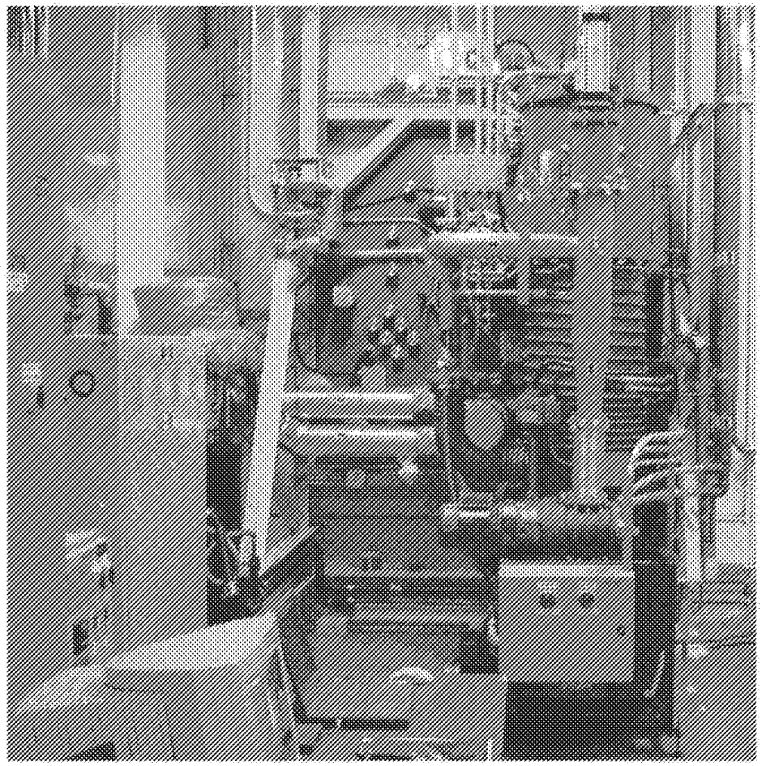

SIONYX1403000016.0054
SAMSUNG EX. 1002 - 1347/4148

SIONYX1403000016.0055
SAMSUNG EX. 1002 - 1348/4148

Mammography Detector

ANALOGIC
The World Resource for Health & Security Technology

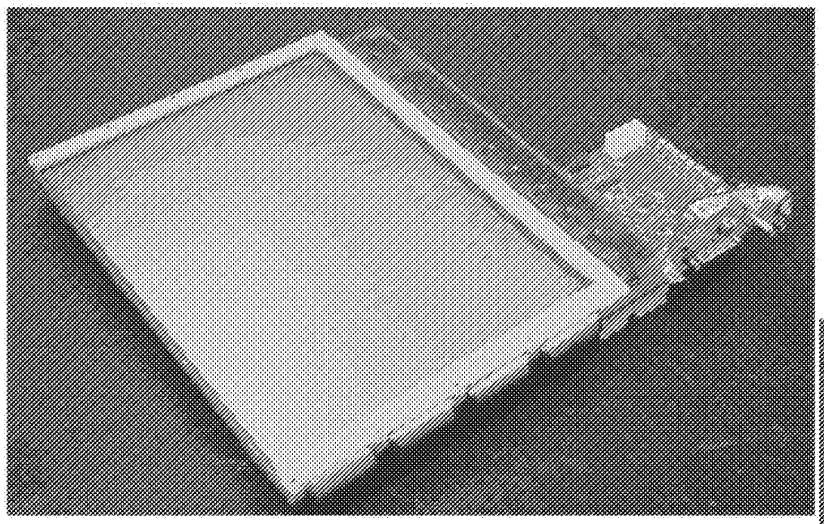

Electronic sub-assembly

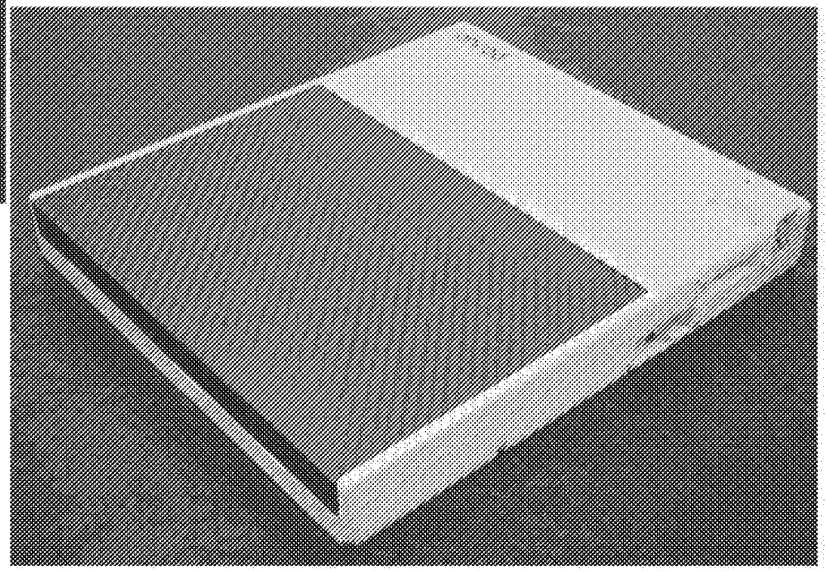

Packaged detector

ANALOGIC

The World Resource for Health & Security Technology

Tomosynthesis

SAMSUNG EX. 1002 - 1350/4148
SIONYX1403000016.0057

Acknowledgements

ANALOGIC
The World Resource for Health & Security Technology

The author acknowledges the contribution of Dr. Olivier Tousignant, Anrad Corporation, Saint-Laurent, QC, Canada who made the characteristic parameters measurements of the LMAM detectors.

Minimization of reflected light in photovoltaic modules

March 01, 2008 | 0 Comments

Maximum photovoltaic module efficiency requires that incident sunlight is not reflected en route to the absorber layer ...

by Dan M.J. Doble, John W. Graff, Fraunhofer Center For Sustainable Energy Systems, Massachusetts Institute of Technology, Cambridge MA USA

Maximum photovoltaic module efficiency requires that incident sunlight is not reflected en route to the absorber layer, and that light that does enter this layer is not subsequently reflected back out, or transmitted through the cell.

A variety of anti-reflection technologies have been deployed in PV modules and the topic remains the subject of active research. Anti-reflection technologies can be broadly split into two categories: 1) Anti-reflective coatings (ARCs) reduce reflection at interfaces above the light absorbing layer of cells; and 2) Texturized surfaces serve the dual purpose of increasing light transmittance and also trapping light within the absorber layer. Often the most effective strategies employ a combination of these techniques.

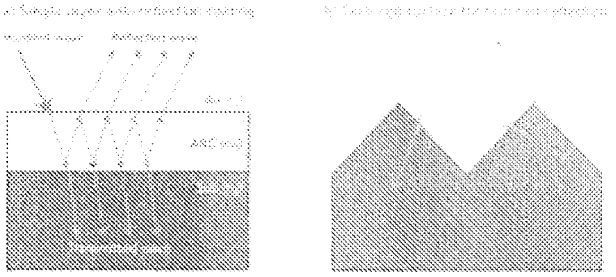

Figure 1: Reducing reflection by a) exploiting interference effects with a single-layer ARC; b) a textured surface for reduced reflection.

Click here to enlarge image

The choice of appropriate anti-reflection technology is a complex optimization of factors that includes more than just performance, but also reliability, manufacturability, and ultimately cost.

Background

The Fresnel equations describe what happens when light travels between two optical media of differing refractive index. Two possibilities are allowed, transmission and reflection, and their ratio depends upon the index of refraction of the materials and the angle of incidence.

An interface with a large mismatch in refractive index will result in strong Fresnel reflection. All of the common cell absorber materials (silicon, cadmium telluride, and copper indium gallium diselenide) exhibit relatively high refractive index. In the case of bare silicon, for example, this causes over 30% of the incident light to be reflected with the remainder transmitted through the interface.

Traditional ARCs are employed to reduce reflection by exploiting interference effects. Consider a thin coating on top of a silicon wafer (Fig. 1a). Incident light partially reflects at the first interface, and partially transmits. The same thing happens at the second interface. A series of multiple reflections takes place within the ARC layer, which add together to form a composite reflected and transmitted wave.

It can be shown mathematically that reflection is minimized when the optical thickness is one quarter of the wavelength of incident light and when the refractive index of the intermediate layer is

$$(n_1 * n_3)^{\frac{1}{2}}$$

A single layer cannot be a quarter wavelength over the entire spectral or angular range of interest, and this means that best performance is only achieved at one wavelength and angle. To determine the optimal thickness, the spectral response of the cell and the spectral content of the incident radiation must be considered, as well as the expected incident angle distribution. These factors themselves are often approximations.

The availability of materials can be an additional constraint; materials with the necessary properties that can be economically deposited may not exist, or good candidates may not exhibit sufficient durability. These problems can be partially overcome by applying a multi-layer ARC structure with more traditional materials.

An alternate method to achieve an ARC structure features a continuous and gradual transition in refractive index between the materials either side. This graded index approach can be approximated by multiple discrete layers, each with slightly different index than the preceding layer. As the effective index is an average of the parent bulk material and air, recent developments in materials with nano-scale porosity have enabled a wide range of available refractive index. Solutions for both cells and module glass have been applied that utilize this technique [1].

Another method to reduce reflection losses involves larger scale texturing of a surface. This approach increases the transmission at the interface by allowing light that is initially reflected to try again (Fig. 1b). When combined with a reflective surface on the back of the cell, texturing can significantly increase optical path length in the semiconductor, and therefore the probability of absorption. In this way, the path length of light in crystalline silicon cells can be increased by a factor of 6 or more.

SIONYX1403000016.0058

SAMSUNG EX. 1002 - 1351/4148

The geometric structure of the surface texture is very important for optimizing transmission of incoming light and the trapping of internally reflected light. Inverted pyramid structures have been shown to be particularly effective for this purpose.

Modules and cells

While the semiconductor-air interface receives quite a bit of attention, in practice nearly all PV modules consist of two interfaces for which Fresnel reflection is the greatest concern: first, between air and the glass sheet, and second, as light enters the high-refractive index cell structure absorber. Reflection at both of these interfaces must be addressed in order to maximize performance.

An example of an air-glass ARC successfully used in modules features alternating layers of physical vapor deposited (PVD) silicon nitride and silicon oxide. In addition to reduced reflectance, this hard coating stack can improve the durability of the modules to weather, abrasion, and pollution. Also, the coating reduces transmission of infrared light below the band-gap of most absorber materials, which can increase module efficiency due to reduced operating temperature [2].

Texturing techniques have also been applied to modules, using glass cutting and grinding processes to produce a variety of different patterns. The greatest improvements are reported for inverted pyramid structures, with an efficiency gain of 3% under standard conditions and 10% for light that is incident at 70°. Of course, there is the risk that such features may trap dust and rainwater in certain locations, resulting in soiling of the module and power loss. For this reason, grooved patterning is also available, which allows the free flow of water from the module surface.

Reflection from the second interface (at the absorber surface) is managed with similar techniques, though the index contrast is typically more significant. In the case of amorphous silicon thin film cells, the surface of the overlying transparent conducting oxide is usually textured, which ensures a textured surface to the subsequently deposited amorphous silicon. For crystalline silicon cells, silicon nitride coatings formed by chemical vapor deposition (CVD) are commonly used as single layer ARCs. It is interesting to note that due to the high index of the encapsulant, thin films of materials with higher refractive index, such as titanium dioxide, actually produce lower reflectance. However, manufacturing issues favor silicon nitride, as well as the additional benefit of supplying excess hydrogen, a proven bulk-passivation agent.

Visual observation will show that cells using a single layer silicon nitride ARC are shiny blue or purple, indicating that although reflection is greatly reduced, there is nevertheless reflection at some wavelengths. In advanced crystalline silicon solar cells, surface texturing is often combined with an ARC to give an exceptionally low total reflectivity and black appearance.

Outlook

Some recent innovations in antireflection take inspiration from nature. When examined under an SEM, the surface of the cornea on a moth's eye is seen to have a textured surface in which features are which are roughly 200nm in height and spaced in a hexagonal pattern with centers approximately 300nm apart. This sub-wavelength profile is equivalent to a graded index, which reflects very little light because there are no abrupt index changes. The result is exceptionally low reflectance and high transmission of light from any direction, which is important for the moth's night vision capability as well as reducing its visibility to predators. Similar nanoscale texturization has been experimentally applied to surfaces used in photovoltaics via holographic lithography processing, sol-gel liquid processing, and plasma etching techniques [3].

Conclusion

The choice of anti-reflection technology depends upon many factors. In addition to the gain in light transmission, and hence improved efficiency, the cost, manufacturability, side benefits and environmental stability are all critically important. Looking to the future and the anticipated reduced cost of solar photovoltaics, any further improvements in anti-reflection technology will have to be balanced against cost. Whereas there is obviously much need for improvement in module efficiency, there will be progressively diminishing returns from further improvements in anti-reflection. It may be that in the future, the most significant innovations in anti-reflection will not be those that result in the transmission of incrementally more light, but rather those that can be manufactured on a massive scale at a significantly reduced cost.

References

1. http://www.epa.qld.gov.au/publications/p01865aa.pdf/Antireflection_coatings_for_solar_collectors.pdf
2. http://www.ivr-energy.de/docs/uopp.pdf.
3. http://www.fraunhofer.de/fhg/images/magazine2-2005-08ff_tcm8-43669.pdf.

Dan M.J. Doble received his PhD in chemistry from the U. of Nottingham in the UK. He is group leader, photovoltaics, at the Fraunhofer Center For Sustainable Energy Systems, Massachusetts Institute of Technology, Cambridge, MA, USA; ddoble@fraunhofer.org; www.fraunhofer.org. John W. Graff received his PhD in electrical engineering from Boston U. He is group leader for energy device prototyping at the Fraunhofer Center For Sustainable Energy Systems, MIT.

0 COMMENTS

REGISTER TO COMMENT

RENEWABLE ENERGY WORLD

http://www.renewableenergyworld.com/rea/news/article/2009/03/minimization-of-reflected-light-in-photovoltaic-modules

JOURNAL OF MATERIALS PROCESSING TECHNOLOGY 201 (2008) 291–296

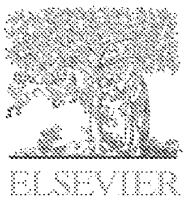

journal homepage: www.elsevier.com/locate/jmatprotec

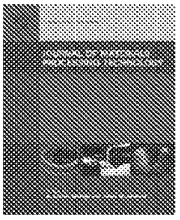

Laser surface treatment of multicrystalline silicon for enhancing optical properties

L.A. Dobrzański[a,*], *A. Drygała*[a], *K. Gołombek*[a], *P. Panek*[b], *E. Bielańska*[b], *P. Zięba*[b]

[a] *Division of Materials Processing Technology, Management and Computer Techniques in Materials Science, Institute of Engineering Materials and Biomaterials, Silesian University of Technology, Konarskiego Street 18a, 44-100 Gliwice, Poland*

[b] *Institute of Metallurgy and Materials Science, Polish Academy of Sciences, Reymonta Street 25, 30-059 Cracow, Poland*

ARTICLE INFO

Keywords:
Surface treatment
Laser processing
Multicrystalline silicon
Photovoltaics

ABSTRACT

To minimise reflection from the flat surface, the multicrystalline silicon wafers were textured. This means creating a roughened surface so that incident light may have a larger probability of being absorbed into the solar cell. Due to grains of random crystallographic orientation, most of the texturing methods used for monocrystalline silicon are ineffective in case of multicrystalline silicon. Therefore, in the present paper a new approach to surface texturisation was developed. Texturisation of multicrystalline silicon wafers was carried out by means of laser surface treatment. Then, a special etching procedure was applied to remove laser-damaged layer. The reflectance of produced textures was measured by PerkinElmer Lambda spectrophotometer with an integrating sphere. The topography of laser-textured surface was investigated using ZEISS SUPRA 25 and PHILIPS XL 30 scanning electron microscopes. The laser treatment and etching in alkaline solution ensured obtaining texture of regular structure that was insensitive to random crystallographic orientation of different grains. The laser processing parameters were adjusted by performing a number of experiments for different values of processing parameters. It is a new approach to texturisation problem of multicrystalline silicon.

© 2007 Elsevier B.V. All rights reserved.

1. Introduction

Taking into account rapidly growing demand for energy and the fast depletion of deposits of conventional sources of energy, the development of new sources of energy has become a challenge to today's world. Moreover, what is even more important is that the use of fossil fuels such as coal and crude oil, being nowadays prevailing sources of energy, leads to unacceptably high concentration of harmful gases in the atmosphere. This, in turn, leads to ozone depletion and global warming that may destructively influence natural environment (Goetzberger and Hoffmann, 2005; Rodacki and Kandyba, 2000; Green, 2000).

One of the most important alternatives for conventional source of energy is solar energy. It is referred to as solar radiation that reaches the earth. Solar energy can be converted directly or indirectly into other forms of energy such as heat and electricity. A direct conversion of solar energy into electricity is performed by photovoltaic devices referred to as solar cells. The main drawback in the use of photovoltaic technology is the intermittent and variable character of solar light. However, this technology has many significant advantages

* *Corresponding author.*
E-mail address: leszek.dobrzanski@polsl.pl (L.A. Dobrzański).
0924-0136/$ – see front matter © 2007 Elsevier B.V. All rights reserved.
doi:10.1016/j.jmatprotec.2007.11.278

SIONYX1403000016.0060

SAMSUNG EX. 1002 - 1353/4148

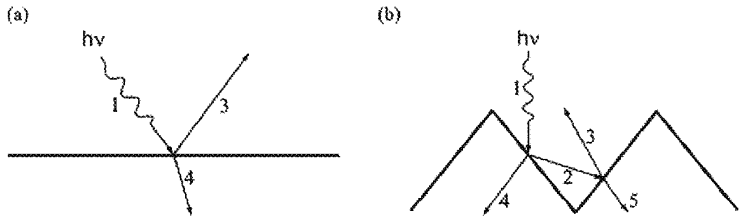

Fig. 1 – The influence of surface texture on light reflection: (a) planar surface and (b) textured surface. (1) Incident light, (2 and 3) reflected light and (4 and 5) absorbed light (Goetzberger and Hoffmann, 2005; Klugmann, 1999).

compared with conventional sources of energy. It is pollution free and clean, has no moving parts, produces no noise and requires very little maintenance. It does not require connection to a power grid since it can operate as a standing alone system. It is very promising alternative as far as environment protection is concerned since the use of this technology may significantly reduce chemical, radioactive and thermal pollution. Therefore, it may be helpful in reducing the greenhouse effect. In addition, it may be treated as a renewable and virtually inexhaustible source of energy in the context of expected duration of sun activity (Green, 2000; Nijs et al., 2001; Klugmann, 1999).

As a consequence, it is very attractive new technology for power generation. So far, it is not competitive with conventional sources of energy because of high production costs of solar cells but experts predict that with mass production and improvement in technology the unit price will drop and the significance of this technology in the energy production will systematically increase in future (Klugmann, 1999). In order to decrease production costs of photovoltaic systems intensive research in the area of multicrystalline silicon solar cells is carried out. It is one of the most environmental-friendly material of high abundance in the crust of the earth. It is competitive material for photovoltaics compared with monocrystalline silicon due to relatively low production cost and acceptable efficiency of cells (Dekkers et al., 2004; Hauser et al., 2003; Panek et al., 2005; Park et al., 2002; de Wolf et al., 2000; Dobrzański et al., 2007; Dobrzański and Drygała, 2007).

Electrical current is produced in the solar cell as a result of interaction between the incident sunlight and semiconductor that the cell is made of. Sunlight is composed of photons whose energy corresponds to their wavelengths. The flux of incident photons is generally separated into three disjoint parts: reflected photons, photons passing through the cell and absorbed photons. The influence of surface texture on light reflection is depicted in Fig. 1. Only absorbed photons of energy greater than the energy gap of semiconductor that cell is made of may generate electricity. During the operation of solar cells, optical losses appear that deteriorate light to electric conversion. Optical losses consist in reflection of the part of incident light from the front surface of the cell. As a result a smaller number of photons can generate electron–hole pairs and contribute in a photovoltaic conversion decreasing solar cell performance. When the flux of incident photons (1) reaches the planar front surface (Fig. 1a) it is divided into the absorbed (4) and reflected flux (3). To minimise the number of photons in reflected flux, surface texturing is accomplished. Texturing consists in expanding the front surface by roughening (Fig. 1b). In that case, the flux of incident photons (1) is again divided into absorbed (4) and reflected flux (2). However, because of the slope of textured surface, reflected flux (2) has another chance to bounce the front surface once again. As a result, the reflected ray (2) reaches the surface again and the second absorbed flux (5) can penetrate into the bulk of material. Consequently, the probability with greater amount of incident light to be absorbed is increased (Goetzberger and Hoffmann, 2005; Klugmann, 1999).

There are many publications relevant to the increase of incident sunlight absorption by means of surface texturisation (Dekkers et al., 2004; Hauser et al., 2003; Panek et al., 2005; Park et al., 2002; de Wolf et al., 2000). However, most of the texturing methods used for monocrystalline silicon appear to be ineffective for multicrystalline silicon. Therefore, we take up in this paper the research on texturisation of multicrystalline silicon by means of laser technology. Laser processing may be applied in the production of crystalline solar cells in the areas such as doping, scribing, cutting, drilling, joining of cells and laser fired contacts (Dobrzański et al., 2007). The principle of laser processing consists of material removal resulting from laser-induced melting and evaporation (Dobrzański and Drygała, 2007; Abbott et al., 2005; Klimpel et al., 2007; Major, 2002). The interaction between laser beam and material depends on both the laser type and its parameters. Therefore, they must be selected to match specific properties of material under processing (Allmen and Blatter, 1995; Bonek et al., 2007; Jackson and O'Neill, 2003; Jackson and Robinson, 2007). In the present paper, laser-textured surface of multicrystalline silicon has been studied. Microstructure and reflectivity of various textures as well as their influence of electrical properties of solar cells have been evaluated.

2. Experimental

Material used as a substrate was "as cut", p-type, boron-doped multicrystalline silicon wafers manufactured by casting method. Experiments were carried out on wafers of thickness ~330 μm, area 5 cm × 5 cm and resistivity 1 Ω cm. Damage on the surface induced by wire-cutting was removed by etching in 20% KOH solution at 80 °C. Typically, about 11 μm of distorted material were etched away creating damage-free surface.

To minimise reflection losses from the front surface, texturisation of wafers by means of ALLPRINT DN50A Q-switched

SIONYX1403000016.0061

SAMSUNG EX. 1002 - 1354/4148

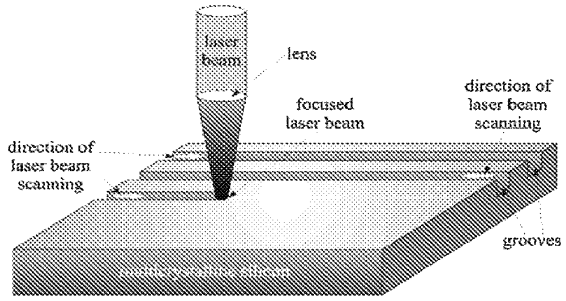

Fig. 2 – Schematic diagram of laser texturisation.

Nd:YAG laser was performed. Fig. 2 shows the schematic diagram of the employed laser processing. Successive grooves were scribed with constant spacing within consecutive scanning of the wafer surface by laser beam in the opposite directions. Many trials for different values of laser parameters were carried out. On the basis of these trials optimum parameters of laser treatment were adjusted and assumed to take the following values: maximum output power ($P = 50$ W), speed of laser beam $\upsilon = 20$ mm/s, pulse repetition frequency $f = 15$ kHz. The texture consisting of parallel grooves as well as a criss-cross of perpendicular grooves with spacing of 90 μm was produced.

A wet etching treatment after laser texturisation was performed in 20% KOH at 80 °C for 10 and 20 min to remove laser-damaged layer. The topography of laser-textured surfaces was investigated using ZEISS SUPRA 25 and PHILIPS XL 30 scanning electron microscopes. The reflectance of produced textures was measured by PerkinElmer Lambda spectrophotometer with an integrating sphere. The illuminated *I–V* parameters were measured under standard AM 1.5 radiation.

3. Results and discussions

For comparison, scanning electron microscope micrographs showing treated surface after consecutive steps of technological process are presented. Surface of multicrystalline silicon wafer before laser texturisation and after etching step to remove saw damage is depicted in Figs. 3a and 4a.

In general, there are many factors influencing the interaction between laser beam and treated surface. On the one hand, it depends on the material properties such as absorption coefficient, thermal diffusivity, thermal expansion coefficient and melting and evaporation point. On the other hand, laser parameters such as power, wavelength, pulse duration, repetition frequency and beam translation influence the results of laser treatment.

The research was carried out to improve performance of multicrystalline silicon solar cells. The main idea of enhancement was to reduce reflection losses from the front surface by means of texture produced in the process of laser treatment.

The parameters of the laser processing were selected to obtain required structure of texture and minimise disadvantageous influence of high temperature of laser treatment on the material. Therefore, many trials were performed to obtain optimum parameters of laser treatment.

In addition, since pulsed laser was used in experiments, repetition frequency and beam translation had to be adjusted to guarantee the achievement of assumed pattern of texture. Pulsed laser removes by ablation only a small amount of material with single pulse. The amount of removed material is proportional to power density and the area of laser beam spot. Repetition frequency ($f = 15$ kHz) and beam translation ($\upsilon = 20$ mm/s) were adjusted so that pulses were overlapping. Consequently, continuous lines placed parallel side by side with constant spacing (0.09 mm) were laser scribed on the wafers surface and the texture shown in Fig. 4b was produced. Moreover, textures in the form of criss-cross grooves were laser scribed (Fig. 5a).

Fig. 3b demonstrates in macroscopic scale that performed laser processing allowed for obtaining uniform texture with no impact due to the random crystallographic orientation of different grains. However, residual ablation slag at the surface of scribed grooves and laser-damaged silicon layer were observed in the textured surface (Fig. 4b). Therefore, post-scribe alkaline etching in 20% KOH solution at temperature 80 °C was applied to remove these undesirable side effects of laser texturing. It should be pointed out that if the grooves are too deep it is difficult to remove all of the slag from their bottom unless long etching time is applied. This, however, increases flattening of post-etching texture and reflection from the front surface for the textures with parallel grooves. This disadvantageous effect was not observed for the criss-cross textures (Fig. 5). In this case, after etching process, textures in the form of inverted pyramids were obtained (Fig. 5b–d). To remove the ablation

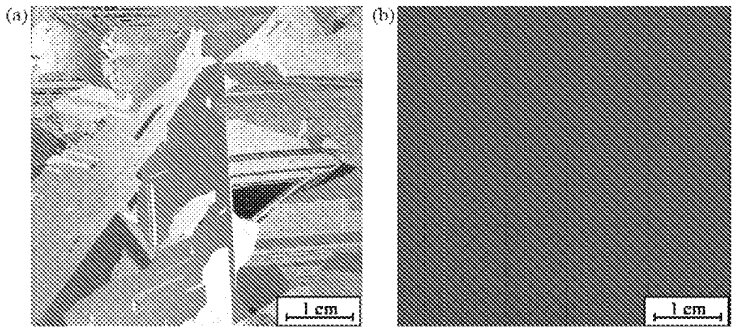

Fig. 3 – Optical images of the multicrystalline silicon wafer of area 5 cm × 5 cm (a) before laser processing and (b) after laser processing.

SIONYX1403000016.0062

SAMSUNG EX. 1002 - 1355/4148

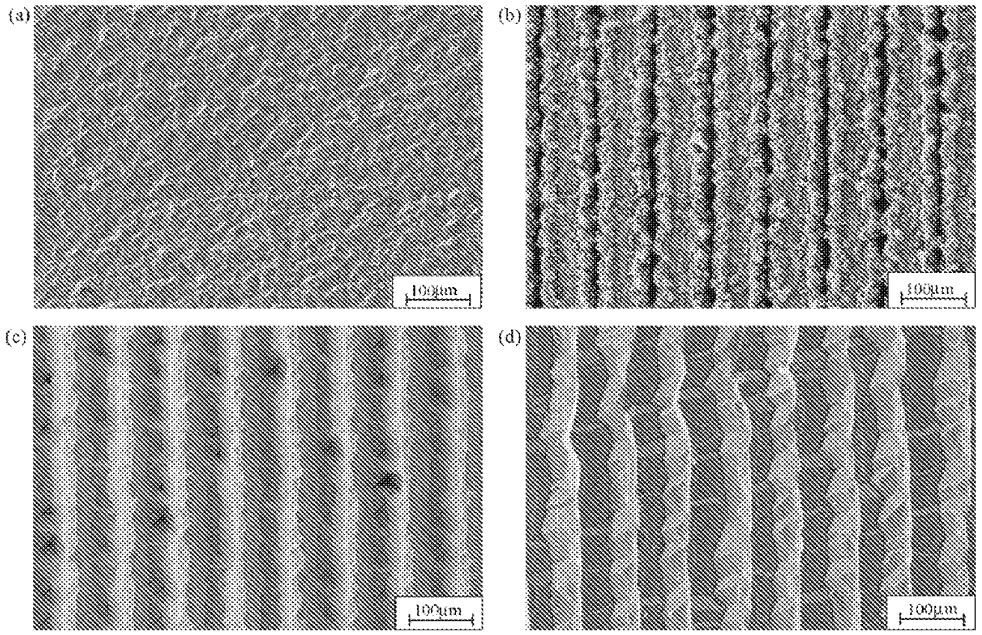

Fig. 4 – SEM images of multicrystalline silicon surface with texture in the form of parallel grooves: (a) after saw damage etching but before laser texturisation, (b) after laser texturisation, (c) after laser texturisation and 10 min etching and (d) after laser texturisation and 20 min etching.

slag form textured surface, the appropriate etching time had to be applied. The grooves were scribed with the depth making it possible to remove all the residual ablation slag and minimise flattening of texture. It can be observed that with the progress of etching process, angle between sidewalls of the grooves becomes more and more obtuse. Consequently, final texture takes the form of interlocking grooves (Fig. 4c and d).

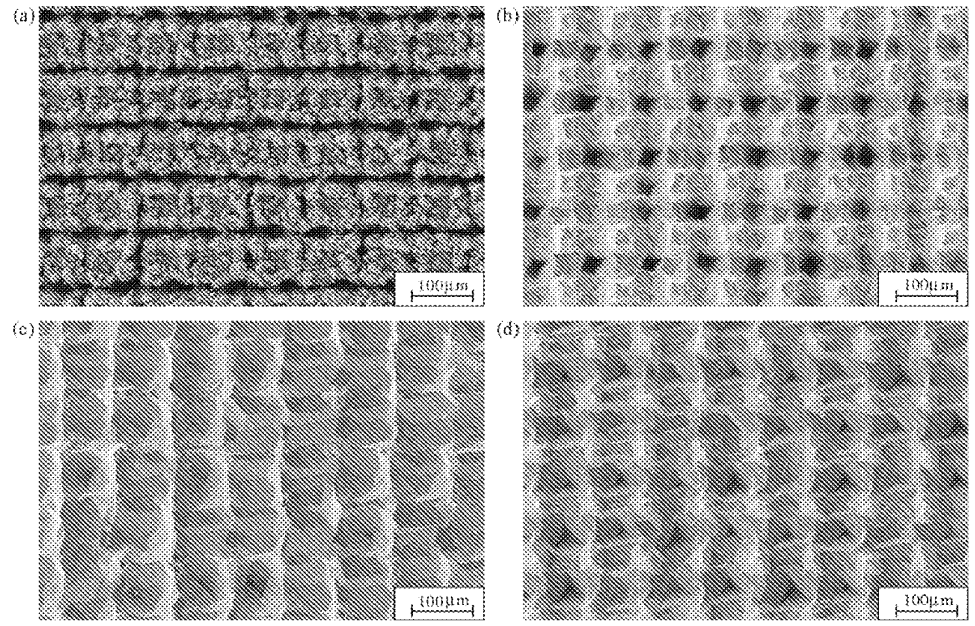

Fig. 5 – SEM images of multicrystalline silicon surface with texture in the form of perpendicular grooves: (a) after laser texturisation, (b) after laser texturisation and 10 min etching and (c and d) after laser texturisation and 20 min etching.

SIONYX1403000016.0063

SAMSUNG EX. 1002 - 1356/4148

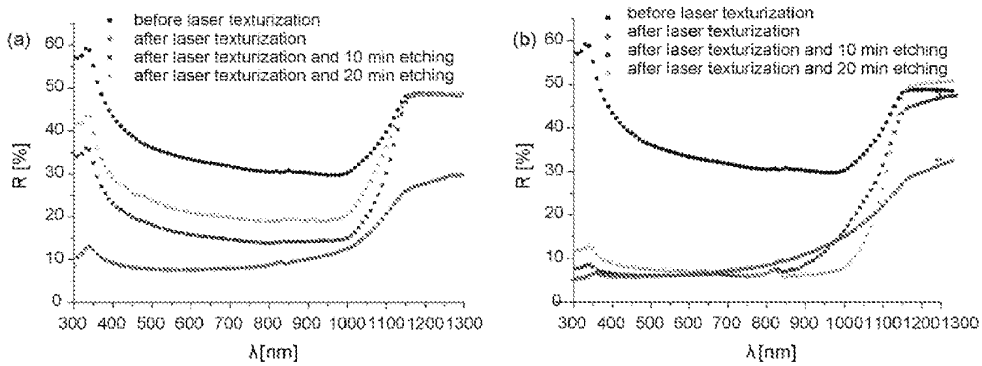

Fig. 6 – Reflection curves for wafers with texture in the form of (a) parallel grooves and (b) perpendicular grooves.

Table 1 – Calculated effective reflectance for surfaces under investigation and the parameters of current–voltage characteristics of solar cell with and without laser texturisation

No.	Texture type	R_{eff} (%)	I_{SC} (mA)	V_{OC} (mV)	FF	E_{ff} (%)
1	Without texture	34.1	630	551	0.74	10.2
2	PG* laser texture	11.6	190	259	0.48	0.9
3	PG* laser texture and 10 min etching	18.2	507	537	0.62	6.7
4	PG* laser texture and 20 min etching	23.6	679	561	0.73	11.1
5	CC** laser texture	9	120	214	0.39	0.4
6	CC** laser texture and 10 min etching	9.1	657	522	0.63	8.6
7	CC** laser texture and 20 min etching	8.3	724	575	0.72	11.9

*Parallel grooves, **criss-cross.

To confirm effectiveness of produced textures, total reflection curves were measured with spectrophotometer equipped with an integrating sphere for wavelengths covering the range 300–1300 nm. Fig. 6a shows the graph of reflectance of silicon wafer without texture, wafer after laser texturisation, textured wafer after 10 and 20 min of alkaline etching for textures consisting of parallel grooves. It can be seen that the longer the etching time the higher the reflectivity of the surface. It results from the flattening of the texture during etching.

The total reflectance curves for the criss-cross texture are depicted in Fig. 6b. In that case, etching process did not influence the increase of reflectance as much as for the textures consisting of parallel grooves. After etching, regions of increased reflectance may be observed, but there also exist regions where etching decreases reflectance.

Additionally, the reduction of reflectance was characterized by effective reflectance defined as (Menna et al., 1995):

$$R_{eff} = \frac{\int_{300}^{1100} R(\lambda)N(\lambda)\,d\lambda}{\int_{300}^{1100} N(\lambda)\,d\lambda} \quad (1)$$

where $R(\lambda)$ is reflectance, $N(\lambda)$ is the solar flux under AM1,5 standard conditions. Calculated results are presented in the Table 1.

In the calculation of effective reflectance, spectral irradiance of sun is taken into account. Consequently, it gives adequate information about the fitting of reflectance curve of the surface to the spectrum of solar incident light.

It can be seen that laser texturing reduced effective reflectance even more than four times compared with raw and untextured wafers. However, due to ablation slag and laser-damaged layer significant decrease in electrical performance of solar cells was observed. Therefore, chemical etching was conducted to remove the top layer of distorted silicon.

Moreover, for texture with parallel grooves, the longer etching time the higher effective reflectance. The criss-cross texture revealed quite different behavior in the etching process. It was possible to reduce the effective reflectance of criss-cross texture to 8.3% by applying 10 min alkaline etching.

4. Conclusions

In the paper, laser texturing method developed to obtain the uniform texture on multicrystalline silicon was presented. Surfaces of laser-textured multicrystalline silicon wafers were investigated. Various textures for different laser parameters and etching steps were fabricated. Then, the structures of textures were observed under SEM. Investigations carried out revealed serious laser-induced damage layer on the treated surface. Therefore, to remove the distorted layer wet etching was applied. Etching step after texturing has to be a trade-off between improvement of electrical and deterioration of optical properties of the cell. Textures were characterized by reflectance measurement and electrical parameters of manufactured solar cells. The cell of the best conversion efficiency was obtained for criss-cross texture after 20 min alkaline etching. Produced textures seem to be useful for

SIONYX1403000016.0064

SAMSUNG EX. 1002 - 1357/4148

multicrystalline silicon solar cells since their fabrication by means of laser processing is insensitive to random crystallographic orientation of different grains and significantly decrease the reflectance of the surface.

Acknowledgement

The research was partially financed in the frame of the Polish State Committee for Scientific Research project no. 3 T08C 048 29 headed by Prof. L.A. Dobrzański.

REFERENCES

Abbott, M., Cousins, P., Chen, F., Cotter, J., 2005. Laser-induced defects in crystalline silicon solar cells. In: Proceedings of the 31st IEEE Photovoltaic Specialist Conference, Orlando, pp. 1241–1244.

Allmen, M.V., Blatter, A., 1995. Laser-Beam Interactions with Materials. Springer-Verlag, Berlin.

Bonek, M., Dobrzański, L.A., Piec, M., Hajduczek, E., Klimpel, A., 2007. Crystallisation mechanism of laser alloyed gradient layer on tool steel. J. Achievements Mater. Manuf. Eng. 20 (411), 414.

de Wolf, S., Choulat, P., Vazsonyi, E., Einhaus, R., van Kerschaver, K., de Dlercq, K., Szlufcik, J., 2000. Towards industrial application of isotropic texturing for multi-crystalline silicon solar cells. In: Proceedings of the 16th European Photovoltaic Solar Energy Conference, Glasgow, pp. 1521–1524.

Dekkers, H.F.W., Agostinelli, G., Dehertoghe, D., Beaucame, G., 2004. Improved performance of mc-Si solar cells by isotropic plasma texturing. In: Proceeding of the 19th European Photovoltaic Solar Energy Conference and Exhibition, Paris, pp. 412–415.

Dobrzański, L.A., Drygała, A., 2007. Laser processing of multicrystalline silicon for texturization of solar cells. J. Mater. Process. Technol. 191, 228–231.

Dobrzański, L.A., Drygała, A., Panek, P., Lipiński, M., Zięba, P., 2007. Application of laser in silicon surface processing. J. Achievements Mater. Manuf. Eng. 24, 179–182.

Goetzberger, A., Hoffmann, V.U., 2005. Photovoltaic Solar Energy Generation. Springer-Verlag, Berlin.

Green, M.A., 2000. Photovoltaics: technology overview. Energy Policy 28, 989–998.

Hauser, A., Melnyk, I., Fath, P., Narayanan, S., Roberts, S., Bruton, T.M., 2003. A simplified process for isotropic texturing of mc-Si. In: Proceedings of the 3rd World Conference on Photovoltaic Energy Conversion, Osaka, pp. 1447–1450.

Jackson, M.J., O'Neill, W., 2003. Laser micro drilling of tool steel using Nd:YAG lasers. J. Mater. Process. Technol. 142, 517–525.

Jackson, M.J., Robinson, G.M., 2007. Micromachining electrical grade steel using pulsed Nd-YAG lasers. J. Achievements Mater. Manuf. Eng. 20, 451–454.

Klimpel, A., Luksa, K., Kik, T., 2007. GTA remelting of surface spot defects. J. Achievements Mater. Manuf. Eng. 25, 73–76.

Klugmann, E., Klugmann-Radziemska, E., 1999. Alternative sources of energy. Photovoltaic energy. Econ. & Environ., Białystok (in Polish).

Major, B., 2002. Ablation and Deposition by Pulsed Laser. Akapit, Kraków (in Polish).

Menna, P., Di Francia, G., La Ferrara, V., 1995. Porous silicon in solar cells: a review and description of its application as an AR coating. Solar Energy Mater. Solar Cells 37, 13–24.

Nijs, J.F., Szlufcik, J., Poortmans, J., Sivoththaman, S., Mertens, R.P., 2001. Advanced cost-effective crystalline silicon solar cell technologies. Solar Energy Mater. Solar Cells 65, 249–259.

Panek, P., Lipinski, M., Dutkiewicz, J., 2005. Texturization of multicrystalline silicon by wet chemical etching for silicon solar cells. J. Mater. Sci. 40, 1459–1463.

Park, S.W., Kim, J., Lee, S.H., 2002. Application of acid texturing to multi-crystalline silicon wafers. J. Korean Phys. Soc. 43, 423–426.

Rodacki, T., Kandyba, A., 2000. Energy Conversion in Solar Power Station. Silesian University of Technology, Gliwice (in Polish).

SIONYX1403000016.0065

SAMSUNG EX. 1002 - 1358/4148

C9

Appl. Phys. A 73, 177–181 (2001) / Digital Object Identifier (DOI) 10.1007/s003390100530

Applied Physics A
Materials
Science & Processing

Formation of conical microstructures upon laser evaporation of solids

S.I. Dolgaev, S.V. Lavrishev, A.A. Lyalin, A.V. Simakin, V.V. Voronov, G.A. Shafeev*

General Physics Institute of the Russian Academy of Sciences, 38, Vavilov street, 117942, Moscow, Russia

Received: 12 February 2000/Accepted: 28 March 2000/Published online: 20 June 2001 – © Springer-Verlag 2001

Abstract. The formation and development of the large-scale periodic structures on a single crystal Si surface are studied upon its evaporation by pulsed radiation of a copper vapor laser (wavelength of 510.6 nm, pulse duration of 20 ns). The development of structures occurs at a high number of laser shots ($\sim 10^4$) at laser fluence of 1–2 J/cm^2 below optical breakdown in a wide pressure range of surrounding atmosphere from 1 to 10^5 Pa. The structures are cones with angles of 20–25°, which grow towards the laser beam and protrude above the initial surface for 20–30 μm. It is suggested that the spatial period of the structures (10–20 μm) is determined by the capillary waves period on the molten surface. The X-ray diffractometry reveals that the modified area of the Si substrate has a polycrystalline structure and consists of Si nanoparticles with a size of 40–70 nm, depending on the pressure of surrounding gas. Similar structures are also observed on Ge and Ti.

PACS: 42.62.-b; 79.20.D; 81.15.Fg

The action of laser radiation on the solids is a significantly non-equilibrium process due to both high temperature gradients and high heating rates. Even under continuous wave laser irradiation a solid surface undergoes peculiar changes to its morphology. To mention a few, these are the formation of the dendritic V_2O_5 crystals or "giant" Cu_2O crystals, which grow towards the beam of a continuous wave CO_2 laser [1–3]. Pulsed laser irradiation typically results in the appearance of periodic structures, in particular, of large-scale periodic structures [4]. This type of structure, having the spatial period of tens of mμ, is usually associated with the instabilities of the melt produced on a solid surface during laser heating, and have been observed on Ge, Ni, Sn, Al, Cu, etc. [4–6]. The hydrodynamic instabilities of the melt, such as Kelvin-Helmholtz or Reyleigh-Tailor ones, are due to its interaction with the expanding plasma plume. The development of the instability requires of sufficiently high number of laser shots, from tens to hundreds, and the structure period depends on the ambient pressure, as well as on the laser spot size.

Recently, laser microstructuring of the Si surface has been reported upon its ablation by the radiation of an excimer KrF laser [6, 7]. The observed structure appears in a rather narrow window of processing parameters and consists of columns protruding above the initial surface of the Si wafer. The formation of the structure in [7] is assigned to the specific interaction of Si vapors with the oxidizing atmosphere and requires a sufficiently high number of laser shots, of the order of 10^3, to be delivered to each point of the Si surface. The specific relief might be associated with one of the above-mentioned instabilities. This is suggested by a similar morphology of the columns, which have a rounded tip whose diameter is even larger than that of the column, like it was observed on brass [5]. The authors consider the known "vapor-liquid-solid" mechanism [8] to explain the growth of Si columns, along with suggested chemical interaction of the vapor with the surrounding atmosphere. The formation of columns is reported only in reactive atmospheres – such as O_2 or SF_6 – at pressure not less than 1 atm.

In the present paper we show that the development of the column-like structure is due to the presence of capillary waves on the molten solid surface, which serve as a starting inhomogeneity for the development of the specific cone-like morphology of the surface. The development of high (20–30 μm) cones is due to the variation of the optical absorptivity of the solid surface with the formation of the surface relief. Since the growth of the cones requires an elevated number of laser pulses, we use a high-repetition rate Cu vapor laser for the microstructuring of both single crystal Si and Ge and polycrystalline Ti targets. It is shown that the modified surface of a single crystal of Si contains Si particles of the size of 40–70 nm.

1 Experimental

Single crystal Si and Ge of (100) orientation and polycrystalline Ti targets were subjected to laser irradiation either in

*Corresponding author. (E-mail: shafeev@kapella.gpi.ru)

SIONYX1403000016.0066

SAMSUNG EX. 1002 - 1359/4148

air or in low vacuum (1 Pa). A Cu vapor laser was used for irradiation, with a repetition rate of 10 kHz, pulse duration of 20 ns, and laser wavelength of 510.6 nm with some fraction of 578.2 nm, depending on the pumping current. To increase the modified area the sample was mounted on a computer-driven X-Y stage to allow its displacement under the laser beam with pre-set scanning velocity and overlap between the consecutive scans. Typically, non-polarized laser radiation was focused on a sample surface into a 40 mμ spot. The angle of incidence of the laser beam was varied from 90 to 60°. No optical breakdown took place for any laser parameters used in this work. The morphology of the samples was studied with the help of a scanning electron microscope (SEM), Jeol. The modifications of the crystallographic structure of the samples after laser irradiation were investigated using an X-ray diffractometer.

2 Results

Under laser fluence exceeding the melting threshold for Si at the wavelength of 510.6 nm (about 0.38 J/cm^2), a significant change of the surface morphology is observed. The Si surface irradiated in vacuum is covered by a dense array of a cone-like structures (Fig. 1). The spacing between the adjacent cones is almost independent of the overlap of the laser beam between the consecutive scans and is of 10–15 μm. Typically, the necessary number of laser pulses is about 10^4 at a laser fluence of 1–2 J/cm^2. Due to the high repetition rate of a Cu vapor laser, this number of pulses is delivered to the sample during the dwell time of about 1 s. More pulses are needed to develop the structure shown in Fig. 1 at lower laser fluence. On the contrary, at higher fluences and dwell times a hole is formed in the Si surface, whose depth increases with the dwell time.

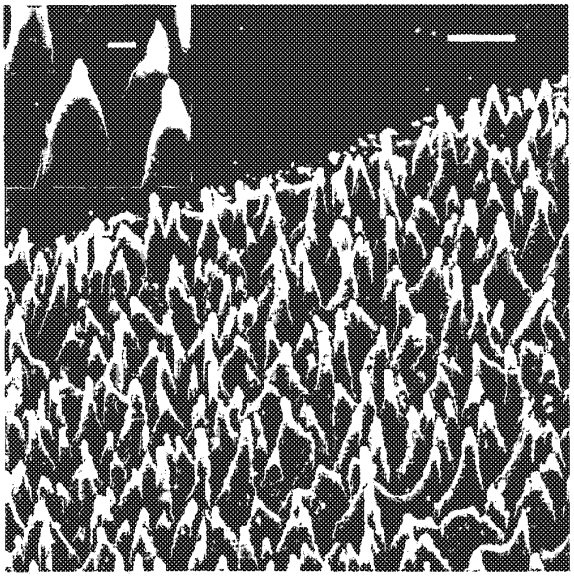

Fig. 1. Morphology of a single crystal Si wafer after exposure to 10^4 pulses of a Cu vapor laser. Laser fluence of 1 J/cm^2, scale bar denotes 25 μm. The *inset* shows the enlarged view of the column tips, scale bar denotes 4 μm

The Si surface irradiated in air at the same laser fluence is covered by a thick loose layer of its oxide. However, the dissolution of the oxide in an aqueous solution of HF reveals a similar cone-like structure of the surface, though the tips of the cones are less pointed. Apparently, the modified Si surface has high specific area, since the bubble emission accompanying the dissolution of the oxide in HF is observed over several days. The cleavage of the modified Si wafer shows that the conical structures protrude above the wafer surface for 20–30 μm, while the wafer areas between the cones are deepened by approximately the same value (Fig. 2).

The structures on the Si surface grow towards the axis of the laser beam. This is observed in a wide range of incidence angles from 90 to 60° (Fig. 3). This feature is new, since this

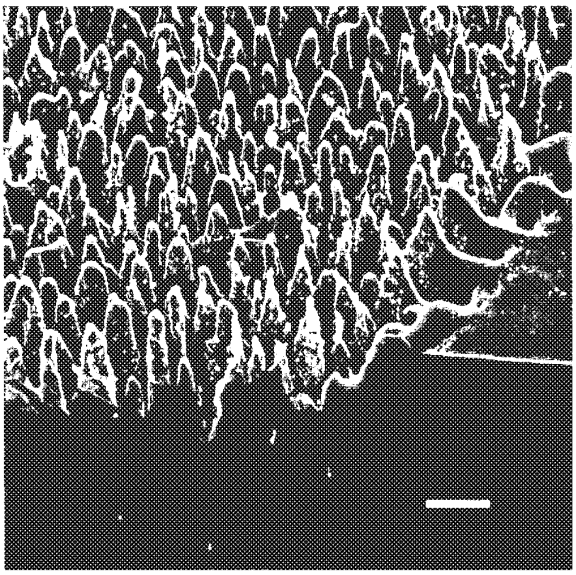

Fig. 2. Cleaved Si wafer exposed to a Cu vapor laser radiation in air and then processed in aqueous solution of HF to remove the oxide layer. Laser shot number of 5×10^3 at fluence of 2 J/cm^2, scale bar denotes 40 μm

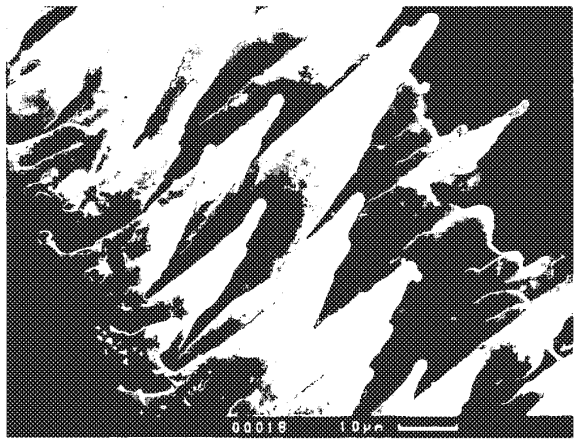

Fig. 3. Microsructures produced in Si wafer at an incident angle of the laser beam of 60°. Scale bar denotes 10 μm

SIONYX1403000016.0067

SAMSUNG EX. 1002 - 1360/4148

type of structure has never been reported before in experiments with optical breakdown.

The modification of the morphology is accompanied by the modification of the crystallographic structure of the sample. This is illustrated by diffractograms of the structured Si surface shown in Fig. 4. The oxide formed on the Si wafer upon irradiation in air is amorphous and does not give any observable diffraction peaks. The polycrystalline Si peaks are widened, which allows the estimate of the average size of Si particles in the modified surface as 70 nm. The relative intensities of the polycrystalline Si peaks suggest no texture on the modified area of the sample. The Si samples structured by laser irradiation in a vacuum show a similar diffractogram, but the widening of the polycrystalline peaks is more pronounced. The average size of Si particles in this case is about 40 nm.

An intermmediate stage of the structure development is that of the waves on the sample surface. The example of these waves and their transition to the cone-like structure on the surface of a single Si crystal is shown in Fig. 5. One can see the proximity of the period of the waves to that of the cones. With an increase in the number of laser pulses (from left to right), holes appear in the minima of the surface relief, while the summits of the waves transform into cones. The formation of the structures is accompanied by intense speckle–like scattering of laser radiation on the modified surface. The scattered signal reaches its maximum during the formation of the waves, then the signal drops down with the development of the conical structure of the surface. The modified areas look completely black in appearence due to multiple reflections of the incident light on the structure.

The cone angle can be estimated as 20–25°. The conical shape of the structures observed in the present work differs from that observed in previous experiments, where optical breakdown and plasma formation above the solid surface was detected. In the latter case, instead of pointed cones, the structures are columns with rounded mushroom-like tips [5].

Similar conical structures are observed on the surface of other solids exposed to a sufficiently high number of laser pulses at a fluence exceeding the melting threshold. Figure 6 shows the SEM view of these structures on Ge and Ti. One can see that the spatial period of the microcones is about 10 μm and it does not depend on the overlap of the laser spot during scanning. Note that the tips of cones in Fig. 6a – like the tips on Si (Fig. 1) – look brighter than the cone itself. This is due to enhanced electron emission from the tips of the

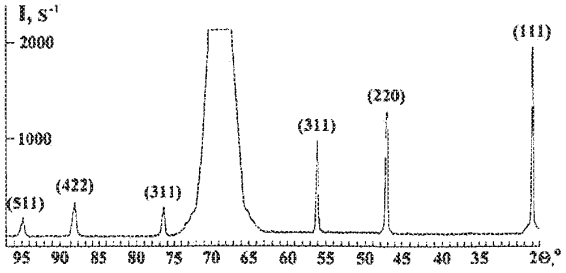

Fig. 4. X-ray $\theta/2\theta$-diffractogram of a single crystal Si (100) with microstructures formed upon exposure in air. One can see the numerous peaks of polycrystalline Si. The saturated peak corresponds to the single crystal wafer

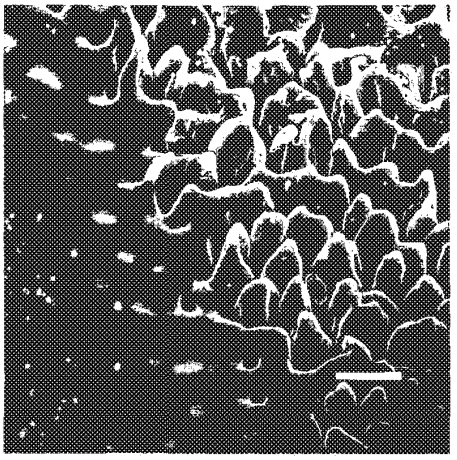

Fig. 5. Evolution of the surface morphology of Si exposed to radiation of a Cu vapor laser from waves to an array of micro-cones with the increase of the number of laser pulses. The surface is covered by condensed particles of the evaporated material. Laser fluence of 1 J/cm^2, scale bar denotes 20 μm

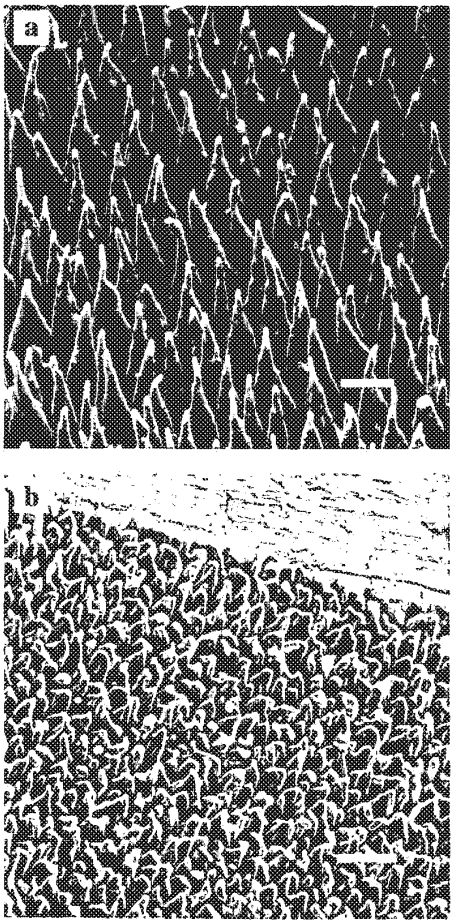

Fig. 6a,b. Conical structures on the surface of a single crystal Ge (a) and polycrystalline Ti (b). Irradiation in vacuum, laser fluence of 1 J/cm^2. Space bar denotes 20 μm (a) and 40 μm (b)

SIONYX1403000016.0068

SAMSUNG EX. 1002 - 1361/4148

structures [9]. Similar to Si, the microcones on Ge and Ti substrates are also oriented towards the laser beam at an inclined incidence of laser radiation.

3 Discussion

The height of the structures may be associated with the height of a vapor cloud above the solid surface during its heating by the laser radiation. The geometrical estimations show that about 10^{12} Si atoms are evaporated and re-deposited at each laser pulse. The temperature of the vapor is close to the melting point of Si (1668 K, [10]), and the vapor diffuse from the substrate for the distance about the structure height (20 μm). Assuming that the vapor is an ideal gas, one can estimate its pressure $p = nkT$ as 30 atm. Here n stands for the density of Si vapor, k is the Boltzmann constant and T is the temperature. This value of pressure in the vapor implies a minor influence of normal atmospheric pressure on the process of structure formation, except for, of course, its possible chemical interaction with vapor. The evaporated material condenses mostly on the top of the cones. The reason for this re-arrangement of material is the feedback between the surface morphology and its absorptivity (see Fig. 7). At homogeneous distribution of the laser beam intensity, the maxima of the temperature will be gained in those areas of the surface, which are oriented perpendicular to the laser beam axis. Direct measurements show that the reflection coefficient of the laser beam from Si is 0.38 at normal incidence and 0.72 at the incident angle of 78°. The latter angle corresponds to the incidence angle of laser radiation on the cone surface. This variation of the reflectivity provides the preservation of the conical structure at laser fluence close to the threshold of melting. In this sense the structures are self-organized ones. Moreover, laser radiation is reflected from the cones to the valleys between them (see Fig. 7), thus increasing the local laser fluence in the intercones area.

Figure 5 demonstrates that microstructures develop from the waves, and the proximity of their spatial period to one of the structures supports this suggestion. These waves serve as the starting inhomogeneity of the absorptivity of the surface. The origin of the waves requires further investigations.

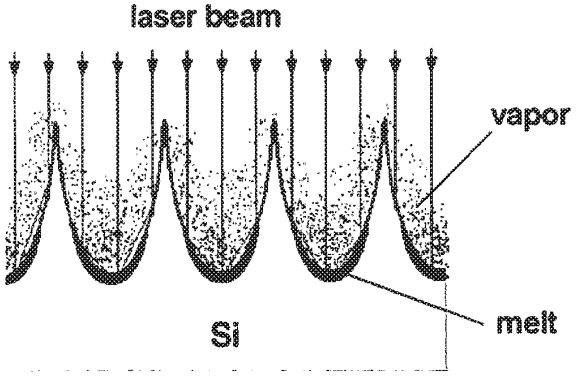

Fig. 7. The schematic view of the development of the conical structure during laser evaporation. The *black areas* indicate the molten Si in the valleys during the laser pulse, while the cones remain solid

The capillary waves can be responsible for the formation of the initial periodic structure. Let us estimate the spatial period of capillary waves on the surface of molten Si. The dispersion relation for shallow capillary waves on a liquid surface is given by the following expression [11]:

$$\omega^2 = \frac{\sigma}{\varrho} hk^4, \tag{1}$$

where h is the thickness of the liquid, ω is the frequency of the wave, σ is the coefficient of surface tension of the melt and k stands for the wave vector of the capillary wave ($k = 2\pi/\lambda$, λ is the wavelength of the capillary wave). Since Si solidifies between consecutive laser pulses, one can take the period of the wave ($T = 2\pi/\omega$) as the time of existence of the melt.

This time depends on the overheating of the surface above the melting point of a solid and should be close to the duration of the laser pulse near the threshold of melting. Assuming $T = 20$ ns, $h = 1$ μm (this is of an order of the heat diffusion depth in Si during laser pulse), $\sigma = 850$ mN/m at 1550 °C, one gets $\lambda = 1$ μm, which is significantly lower than the observed spatial period of the structures. However, the above-mentioned dispersion relation is not applicable in our experimental conditions, since it is valid only for infinite liquid surface. The finite dimensions of the molten area confined to laser spot modify the spectrum of capillary waves. It becomes discrete, and the eigenvalues of the wave vector k are defined by the following equation: $k^2 = \pi^2(m^2/a^2 + n^2/b^2)$, where $m, n = 1, 2, 3\ldots$, a, b stand for the dimensions of the laser spot [11].

The other possible reasons for initial surface inhomogeneity could be Benard cells, Rayleigh-Tailor, and Kelvin-Helmholtz instabilities [5]. The last two effects are unlikely because of the low density of the surronding medium under our experimental conditions.

Note that for Ge and Ti the coefficient of surface tension is of the same order of magnitude: $\sigma = 558$ and 1558 mN/m at 1550 and 1670 °C [10], respectively, so the spatial period of structures observed on these materials is also of the order of 10 μm. Figure 5 directly points out that the conical structure is developed from initial melt instability with an increase in the number of laser shots. This stage of the instability is out of range of the perturbation theory, where the perturbation amplitude is supposed to be small.

The material evaporated during the laser pulse re-condenses on the solidified surface as clusters with the size depending on the ambient pressure. Apparently, the clusters coalesce above the wafer surface, and in case of irradiation in air they are partially oxidized. These clusters are responsible for the observed polycrystalline structure of the laser-evaporated surface. The clusters should be located on the surface of the cones, though this point requires further studies.

The difference in the cone morphology observed in the present work compared to previously observed ones is the absence of the rounded mushroom-like tip, whose diameter may exceed the diameter of the column. The experimental data suggest that this difference is due to the absence of the plasma above the solid surface during the irradiation. Si columns formed in air upon laser ablation with an excimer KrF laser are free of oxide [7], and this implies its removal by the shock wave of the optical breakdown. On the contrary, in the present conditions the Si surface is covered by a thick layer of Si

SIONYX1403000016.0069

SAMSUNG EX. 1002 - 1362/4148

oxide, as it was observed on SiC ceramics in similar experimental conditions [12]. The fact of optical breakdown is not addressed directly in [7], but presence is suggested indirectly by the absence of structures at an ambient pressure lower than 1 atm, where the breakdown occurs at lower laser fluence. In the present conditions, the breakdown does not occur due to, first, the lower energy of the laser photon and, second, due to a longer laser pulse. Both factors do not favor the development of the electron avalanche, and in our experimental conditions the structuring of the surface is gained via laser evaporation. Moreover, the growth of the structures towards the laser beam is hardly possible in presence of plasma, since the pressure of the plasma expanding perpendicular to the target surface would break the inclined structures with high aspect ratios like those shown in Fig. 3. Apparently, the chemical interaction of vapors with surrounding atmosphere does not play any significant role in the formation of the conical structure by laser evaporation.

It is interesting to note the difference in the cone tip shape observed on Si and Ge. On the latter material the tips are less pointed than on Si. Since the tips of the cones are oriented perpendicular to the laser beam axis, they could be molten during the laser pulse. The temperature of the tip during the laser pulse should depend on the absorption coefficient of the material. Since the extinction coefficient of Ge at 510.6 nm is higher than that of Si (2.0 against 0.1, [13]), and the melting temperature of Ge is lower than that of Si, one can suppose that Ge tips are molten in the typical experimental conditions.

4 Conclusions

Thus, laser-assisted formation of a dense array of conical structures upon laser evaporation of solids has been demonstrated. In the experimental conditions of the present work no optical breakdown above the solid surface occurs, and this leads to a new morphology of periodic cones on the laser-evaporated solid surface with pointed tips protruding above the initial surface of the wafer for 20–30 μm. The cones grow from the capillary waves towards the laser beam axis, so their spatial period is determined by the melt parameter. The formation of elongated cone-like structures is possible owing to the increase of reflectivity of the surface with the increase of the incident angle, so that the melting and evaporation of the surface occurs mostly in those areas of the wafer that are oriented to the normal of the laser beam axis, that is between the cones. The crystallographic structure of the cones differs from that of the initial wafer, the laser-structured surface contains a significant amount of polycrystalline nanophase material. The structures are obtained in a wide range of the surrounding atmosphere (from 1 to 10^5 Pa), which suggest the negligible contribution of its chemical interaction with vapors.

The process of surface structuring via laser evaporation has a wide spectrum of potential applications. For instance, the modified Si surface has a high absorption coefficient in the visible light due to multiple scattering of light in the cones, which can be used in fabrication of solar batteries instead of anti-reflecting coatings. The structures on Si surface are of potential interest as field emitters of electrons, which can be easily integrated into Si-based electronic devices. These studies are now ongoing [9]. Note that the structures previously observed in presence of plasma formation can hardly be used as cold emitters because of the rounded tips. Finally, laser structuring of the solid surface leads to noticable increase of its specific surface, which is of potential interest in catalysis and sensors. The laser-structured surface of biocompatible metal alloys might be interesting as a template for biological tissues.

Acknowledgements. We thank V.P. Ageev, V.I. Luchin, and A.J. Pedraza for helpful discussions. The work was partially supported by the Russian Foundation of Basic Research, grants 01-02-17724 and 01-02-16495.

References

1. L. Nanai, I. Hevesi, N.F. Bunkin, B.A. Zon, S.V. Lavrishev, B.S. Luk'yanchuk, G.A. Shafeev: Appl. Phys. A **50**, 27 (1990)
2. L. Nanai, I. Hevesi, N.F. Bunkin, B.A. Zon, S.V. Lavrishev, B.S. Luk'yanchuk, G.A. Shafeev: Appl. Phys. A **50**, 101 (1990)
3. L. Nanai, I. Hevesi, F.V. Bunkin, B.S. Luk'yanchuk, G.A. Shafeev, D.T. Alimov: Infrared Phys. **25**, 141 (1985)
4. T.J. Bastow: Nature **222**, 1058 (1969)
5. A.B. Brailovsky, S.V. Gaponov, V.I. Luchin: Appl. Phys. A **61**, 81 (1995)
6. F. Sanches, J.L. Morenza, R. Aguiar, J.C. Delgado, M. Varela: Appl. Phys. Lett. **69**, 620 (1996); F. Sanches, J.L. Morenza, R. Aguiar, J.C. Delgado, M. Varela: Appl. Phys. A **66**, 83 (1998)
7. A.J. Pedraza, J.D. Fowlkes, D.H. Lowndes: Appl. Phys. Lett. **74**, 2322 (1999)
8. E.I. Givargizov: Curr. Top. Mater.Sci. **1**, 79 (1978)
9. S.I. Dolgaev, V.D. Frolov, A.V. Karabutov, V.V. Voronov, G.A. Shafeev: to be published
10. I.S. Grigoriev, E.Z. Meilikhov (Eds.): *Handbook on Physical Data* (Energoatomizdat, Moscow 1991)
11. L.D. Landau, E.M. Lifshits: *Hydrodynamics* (Nauka, Moscow 1988)
12. S.I. Dolgaev, A.A. Lyalin, G.A. Shafeev, V.V. Voronov: Appl. Phys. A **63**, 75 (1996)
13. V.M. Zolotaryov, V.N. Morozov, E.V. Smirnova (Eds.): *Handbook on Optical Constants of natural and artificial media* (Leningrad, Khimia 1984)

SIONYX1403000016.0070

SAMSUNG EX. 1002 - 1363/4148

OPTICAL PATH LENGTH ENHANCEMENT FOR > 13% SCREENPRINTED THIN FILM SILICON SOLAR CELLS

F. Duerinckx*[1], I. Kuzma Filipek[1], K. Van Nieuwenhuysen[1], G. Beaucarne[1],
J. Poortmans[1], F. Leloup[2], J. Versluys[2], P. Hanselaer[2]
[1]IMEC vzw, Kapeldreef 75, B-3001 Heverlee, Belgium
[2]KaHo Sint-Lieven, Gebroeders Desmetstraat 1, B-9000 Gent, Belgium
*Corresponding author: Tel: +32 16 281923 Fax: + 32 16 281501 E-mail: filip.duerinckx@imec.be

ABSTRACT: Epitaxial thin film silicon solar cells, consisting of a thin epitaxially grown active layer on a low quality silicon substrate, suffer from a low short-circuit current compared to bulk silicon mono- or multicrystalline cells. To counteract this disadvantage, the optical path length in the thin active epitaxial layer has to be increased. Two separate developments to accomplish this have been implemented on cell level. The first one consists of a plasma textured epitaxial surface resulting in a lambertian-like texture that not only decreases the front surface reflection but also increases the optical path length of the photons in the layer by a factor of 2. To avoid the transmission loss of low energy photons into the silicon substrate, a conductive optical reflector consisting of a porous Si stack of high/low porosity layers is grown on the substrate prior to epitaxy. An internal reflection of 80% has been measured at the epi/substrate interface, which translates, in combination with the oblique light coupling into the layer, into an optical path length enhancement factor of 14. Implementation of these features for screen printed epitaxial cells with a 20 μm active layer on low quality substrates (UMG or offspec Si) has resulted in short-circuit currents approaching 30 mA/cm^2 and efficiencies of 13.5%.
Keywords: Texturisation, porous silicon, epitaxy

1 INTRODUCTION

Epitaxial thin film silicon solar cells, consisting of a thin epitaxially grown active layer on a low quality silicon substrate (Figure 1), incorporate many attractive features usually associated with their sister cells based on bulk silicon [1]. In addition, the epi/substrate structure ("wafer equivalent" [2]) could be processed in state-of-the-art production lines since most of the cell process is very similar to current screen printing processes. However, their moderate efficiency of 12% for semi-industrial screen printed cells [3] currently limits the attention that is paid to this cell type by the PV Community. Compared to bulk silicon solar cells, similar levels of open-circuit voltage and Fill factor can be obtained. The short-circuit current (Jsc) however is held back by the optically thin active layer (W ≤ 20 μm). Light that traverses the epitaxial layer is lost for collection in the highly doped, low quality substrate. As a consequence, a difference in Jsc of 7 mA/cm^2 between both cell technologies is not uncommon (Table 1). This work concentrates on removing this bottleneck by improving the optical path length for long wavelength light by working on 2 levels:

(i) Texturing of the front surface to achieve light scattering at an oblique angle in the epitaxial layer (section 2).
(ii) Growth of an intermediate reflector between the epi-layer and the substrate (section 3).

The results of the epitaxial thin film cells, including both advances described above, are presented in section 4.

Technology	Jsc (mA/cm^2)	Eff. (%)
Epitaxial thin film cells	~ 26	12.3
Bulk Si cells (multi)	~ 33	15.6

Table 1: Comparison of typical results for Jsc and efficiency for standard epitaxial thin film cells and multicrystalline silicon solar cells (Open-circuit voltage and fill factor are taken as 615 mV and 77% for both technologies).

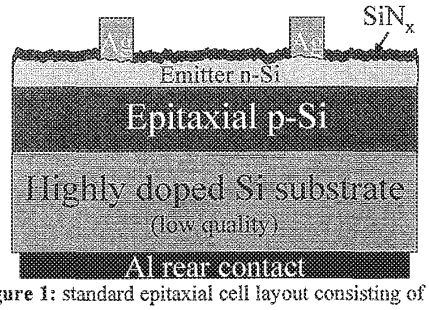

Figure 1: standard epitaxial cell layout consisting of a 20 μm active epitaxial layer on a highly doped low-quality substrate.

2 FRONT SURFACE LIGHT SCATTERING BY PLASMA TEXTURING

Since the epitaxial layer is quite thin, the silicon removal during the texturing step has to be limited. In addition, the texturing should work reliably and reproducibly on smooth epitaxial surfaces and it should scatter the impinging light. Ideally, the surface should be a lambertian refractor. Fluorine based plasma texturing [4] turned out to be the ideal technique to achieve these objectives. We have been able to reduce the surface reflection to levels of 10-15% (30-35% before texturing) with a very limited removal of silicon.

In order to assess the scattering behaviour of our textures, the reflected light was measured at KaHo Sint-Lieven using angular resolved reflection measurements by means of a BSDF (Bi-directional Scatter Distribution Function) set-up [5]. The scattering efficiency was shown to be dependent on the duration of the texturing process (Figure 2) and on the wavelength of the impinging light (Figure 3). These figures show the spectral radiance coefficient (q) as a function of the angle of the reflected light. This coefficient is defined as:

SIONYX1403000016.0071

SAMSUNG EX. 1002 - 1364/4148

$$q = \frac{dL_{e,\lambda}}{dE_{e,\lambda}} \quad (1/sr)$$

with $L_{e,\lambda}$:Spectral radiance (W/m^2.sr.nm)
$E_{e,\lambda}$: Spectral irradiance (W/m^2.nm)

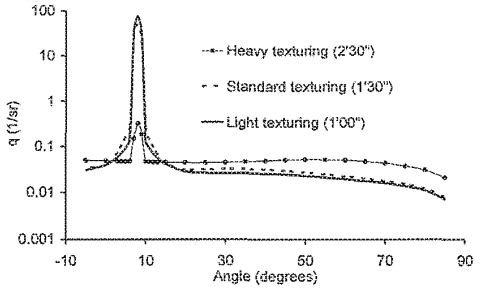

Figure 2: Effect of texturing time on spectral radiance coefficient (q) for a wavelength of 800 nm.

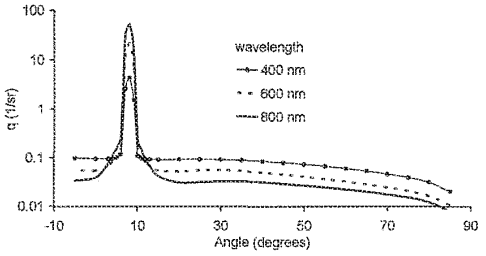

Figure 3: Wavelength dependence of spectral radiance coefficient (q) for a standard texturing process (1'30").

Figure 2 clearly shows that the duration of the texturing has a strong influence on the scattering behaviour. The peak at +8° is the specular reflected light (impinging light at –8°). The stronger the texturing, the more diffusive the light behaviour and the smaller the specular peak becomes. The response is also dependent on the wavelength of the impinging light (Figure 3). At 800 nm the specular response is clearly stronger than at 400 nm. This dependence is probably related to the size of the textured features versus the wavelength of the light.

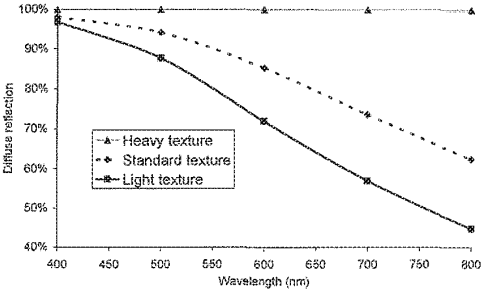

Figure 4: Diffuse percentage of reflected light as function of wavelength for 3 texturing conditions (Diffuse + specular reflection = 100%).

An estimation of the specular versus diffused percentage of reflected light can be made by assuming axial symmetry around the axis of specular reflected light. The outcome is shown in Figure 4: if only a very limited amount of silicon is removed (short texturing) then the specular reflective component increases at higher wavelengths thereby limiting the diffusive behaviour. A longer texturing rectifies this problem at the cost of more silicon being removed. Consequently, a compromise must be made between light scattering and the absorption volume of the epitaxial layer. In practice it has been found that complete light scattering can be achieved for a Si removal of only 1.75 µm. A good uniform texturing with a limited removal of only 0.5 -1.0 µm is possible but then the requirement of a lambertian surface texture (100% diffusive) cannot be fulfilled.

For the case of a completely lambertian texture, the photons move through the active epitaxial layer at a average angle of 60° to the normal. The optical path length enhancement is then equal to 2 (= 1/cos(60°)). In other words, a 20 µm epitaxial layer behaves optically as a 40 µm silicon slab.

The plasma texture brings a lot of advantages on cell level: a lower reflection, oblique light coupling and a lower contact resistance (higher Ag/Si contact area). The improvement in Jsc can be quantified as 1.0 - 1.5 mA/cm^2. On the other hand, the larger surface area usually results in a small loss in Voc (a few mV). The effect on efficiency is clearly positive (around 0.5 – 1.0 % absolute).

3 POROUS SI BRAGG REFLECTORS FOR INTERNAL LIGHT TRAPPING

To decrease the transmittance of long wavelength light into the substrate, an intermediate reflector could be positioned at the epi/substrate interface. Photons reaching this interface can now be reflected and pass a second time through the active layer. Since the light is diffuse from the moment it has entered the cell (due to the lambertian nature of the plasma texture), a large part of the photons will strike the front surface outside the escape angle. Therefore, most of the photons will be reflected internally due Total Internal Reflectance (TIR) for a 3rd pass. The story repeats itself from that moment on so that multiple passes through the epitaxial layer become possible (Figure 5).

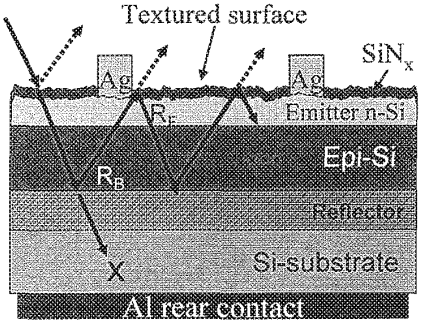

Figure 5: Advanced epitaxial cell layout illustrating the concept of an intermediate reflector. The internal reflections R_B and R_F are detailed in the following paragraphs.

In practice, the reflector is made by electrochemical growth [6] of a porous silicon stack of alternating high

SAMSUNG EX. 1002 - 1365/4148

and low porosity layers (a multiple Bragg reflector). During the epitaxial growth on top of the porous Si stack, the individual layers reorganize into Quasi Monocrystalline Silicon (QMS). The nanoporous layers are transformed into thin silicon layers with large voids. This process is driven by a minimization of surface energy. The original layout of the stack however is maintained, resulting in alternating layers consisting of small and large voids (Figure 6). This structure has been proved to be ideal for the concept of a reflector based on constructive interference [3].

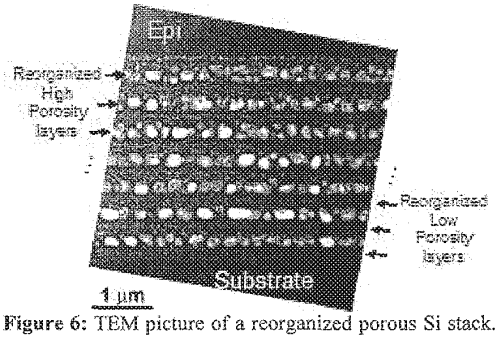

Figure 6: TEM picture of a reorganized porous Si stack. The epitaxial layer, substrate and the individual layers of the stack are indicated.

The measured external reflectance of the epi/porous Si/substrate structure has been analytically linked to the internal reflection R_B (Figure 5) at the porous silicon stack [3]. The rear internal reflection strongly increases with the number of alternating high/low porosity layers in the porous silicon stack. An internal reflectance of approximately 80% has been achieved for a porous Si stack of 15 layers. This allows the calculation of the optical path length enhancement, which is defined as [7]:

$$Z = \frac{1 + R_B}{1 - R_B R_F}$$

with R_B : Internal reflectance at the rear of the epitaxial layer (at the epi/porous Si interface).

R_F: Internal reflectance at the front of the epitaxial layer (Figure 5).

With the assumption of a perfect lambertian diffuser on the front of the cell, R_F can be calculated as [8]:

$$R_F = 1 - \frac{1 - R_{Front}}{n_{Si}^2}$$

with R_{Front}: externally reflected light at air/silicon interface.

n_{Si}: refractive index of silicon.

This calculation gives approximately 93% for R_F and a Z-factor of 7.0 for the case of a 15-layer porous silicon stack (R_B =80%). Like stated in section 2, a perfect light diffuser at the front gives an additional Z-factor of 2. Therefore the final path length enhancement from the combination of a lambertian front surface and an internal reflector efficiency of 80% will be 14. This would mean that a 15 µm thick epitaxial layer behaves optically as a 210 µm thick slab of silicon.

4 CELL RESULTS BASED ON SCREENPRINTING PROCESSES

Three different substrates were used as carrier for our epitaxial cells: mono-Si (for proof of concept), low quality offspec-Si and low quality Upgraded Metallurgic Grade (UMG) Si. The 2 latter substrates are both multicrystalline wafers. The complete cell process follows the following process sequence:

- Wafer preparation (saw damage removal + cleaning)
- Porous Si stack formation (optional)
- Epitaxial deposition (APCVD system, thickness: 20 µm, doping level: 10^{17} cm^{-3})
- Plasma texturing of front surface
- $POCl_3$-diffusion +glass removal
- PECVD SiNx deposition
- Screenprinting of front and rear contacts + IR-firing
- Parasitic junction removal

The cell results on the different substrates are tabulated in tables 2-3. On mono-si substrates the reflector gives a 3 mA/cm^2 increase in short-circuit current. This agrees very well with our predictions based on optical measurements and confirms that the epitaxial quality on porous Si is as good as for the case without reflector. The cell efficiency has increased by 1.5% absolute to 13.5%. Remark the good Fill Factor for the cells with reflector indicating that there is no problem with conduction through the reorganized porous Si stack [9].

Reflector?	Jsc (mA/cm^2)	Voc (mV)	FF (%)	Eff. (%)
No	25.5	611	76.9	12.0
Yes	28.6	611	77.1	13.5

Table 2: Effect of the porous Si reflector for epitaxial cells on mono-Si substrates (Cell size: 18 cm^2).

Reflector?	Jsc (mA/cm^2)	Voc (mV)	FF (%)	Eff. (%)
No	26.4	606	76.6	12.3
Yes	27.7	597	76.7	12.7

Table 3: Effect of the porous Si reflector for epitaxial cells on low quality Offspec-Si substrates (Cell size: 18 cm^2).

The gain for the offspec-Si cells is lower, which can be explained by the as yet non-optimised status of the process on multicrystalline silicon material. Characterization of the finished cells has pointed out 2 problems, optical and electrical, that limit at the moment the improvement from the porous silicon reflector on these substrates:

- The porous silicon growth is most probably not identical on different grain orientations as is the case for the multicrystalline offspec material. An internal reflectance around 75% has been extracted for the offspec cells with porous silicon. The best cells with porous silicon on mono give an internal reflection of 85%. Although this difference is seemingly not so large, it would already result in a Jsc difference of about 0.7 mA/cm^2. Nevertheless, an internal reflectance of 75% should, according to our calculation, still give a 2.5 mA/cm^2 increase in Jsc compared to the condition without reflection. As can be seen in the table, only a 1.3 mA/cm2 increase is achieved for the offspec cells.
- The 9 mV loss in Voc indicates a problem with the epitaxial quality for these cells. This is further

SIONYX1403000016.0073

SAMSUNG EX. 1002 - 1366/4148

illustrated in Figure 7 by a comparison of the internal quantum efficiency (IQE) for cells on multicrystalline substrates with/without reflector. On the one hand, the large improvement in the long wavelength region (800-1100 nm) is readily apparent. This can be completely attributed to the positive effect of the reflector. However, in the shorter wavelength region, the IQE of the cell with reflector is lower than the one without reflector. This effect has been noticed in the case of offspec Si as well as UMG-Si. and visualizes the problem with the epitaxial quality on porous Si/multi-Si structures. It explains the loss in Voc and also the reason for the lower-than-expected increase in Jsc (see above).

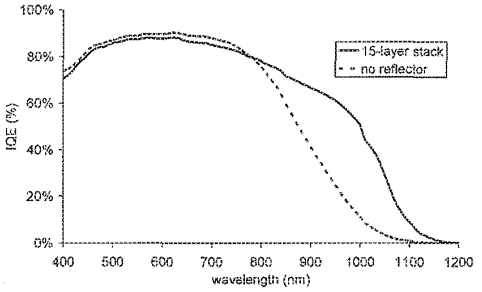

Figure 7: Internal Quantum Efficiency of epitaxial cells with/without porous Si reflector on low quality multicrystalline substrates.

Nevertheless, the offspec cells with porous silicon reflector already give a very promising 0.4% absolute higher efficiency compared to the cells without reflector. Table 4 gives the top results of another screen printing cell process which differs from the previous process only in the use of a shallow emitter diffusion. An efficiency of ***13.3%*** with a high Jsc of 29.7 mA/cm^2 has been reached for epi-on-offspec screenprinted cells. Furthermore, a similar screen printing process for epitaxial cells on UMG-Si has resulted in a top efficiency of ***13.5%***. In the case of mono-Si as substrate, ***13.8%*** with a high Voc of 621 mV has been obtained. It is expected that additional understanding of the porous silicon growth on multi-Si and especially an improved epitaxial growth will lead to higher efficiencies on the low quality substrates. In parallel to that development, our work will be concentrated on enlarging the size of our epitaxial cells which, at the moment, are limited by the porous Si formation apparatus.

Substrate	Jsc (mA/cm^2)	Voc (mV)	FF (%)	Eff. (%)
Offspec	29.7	595	75.1	13.3
UMG	28.7	606	77.7	13.5
Mono	28.7	621	77.8	13.8

Table 4: Best epitaxial cells with porous Si reflector on UMG and Offspec Si substrates (Cell size: 18 cm^2).

5 CONCLUSION

In order to increase the efficiency of thin film epitaxial silicon solar cells, 2 improvements have been implemented on cell level. On the front surface of the cell, plasma texturing enables a strong reflection reduction while limiting the amount of removed silicon. The textured surface diffuses the refracted light entering the cell. This results in a lambertian-like surface and an optical path length enhancement of 2.

On the rear of the epitaxial layer, a reorganized porous Si stack is implemented to reflect the non-absorbed photons for consecutive passes through the active layer. Reflectance values up to 85% have been measured for this internal reflector. Together with the total internal reflection on the front surface, this lead to an additional optical path length enhancement of 7.

On cell level, the porous Si reflector has given considerable increases in Jsc (between 1.4 and 3.1 mA/cm^2) combined with a small drop in Voc (only for the case of low quality multicrystalline substrates). Cell efficiencies have crossed 13% for epitaxial screenprinted cells on the 3 substrates that are investigated: 13.8% on mono-Si, 13.5% on UMG-Si and 13.3% on offspec Si.

6 ACKNOWLEDGEMENTS

The cells were measured against a reference cell which is calibrated (traceable) to the World Radiometric Reference by the European Solar Test Installation (ESTI) of the European Commission Joint Research Centre, an ISO 17025 accredited calibration laboratory. The financial support from the European Community is acknowledged for the following FP5/FP6 projects: ENK6-CT2002-00618 (EPIMETSI), ENK6-CT2002-00613 (SWEET) and SES6-CT 2003-502583 (Crystal Clear).

7 REFERENCES

[1] Poortmans J., Beaucarne G., Mertens R., Technical Digest of the International PVSEC, Bangkok, Thailand 2004, 13-16.

[2] Reber S., Schmidhuber H., Lautenschlager H., Rentsch J., Lutz F., 19th European Photovoltaic Solar Energy Conference and Exhibition, Paris (France), 2004, 1311-1314.

[3] Duerinckx F., Van Nieuwenhuysen K., Kim H., Kuzma-Filipek I., Dekkers H., Beaucarne G., Poortmans J., Progress in Photovoltaics: Research and Applications 13, pp 673-690, 2005.

[4] Dekkers H.F.W., Agostinelli G., Dehertoghe D., Beaucarne G., Traxlmayr U., Walther G., 19th European Photovoltaic Solar Energy Conference and Exhibition, Paris (France), 2004, 412-415.

[5] Leloup L., De Waele T., Versluys J., Hanselaer P., Pointer M., Proc. ISCC/CIE Expert Symposium, Ottawa (Canada), 2006 (in press)

[6] Stalmans L., Poortmans J., Caymax M., Bender H., Jin S., Nijs J. Mertens R., 2nd World Conference and Exhibition on Photovoltaic Solar Energy Conversion, Vienna (Austria)), 1998, 124-127.

[7] Campbell P., Green M.A., J. Appl. Phys. 62(1), 1987, 243-249.

[8] Tobias I., Rodriguez J.M., Luque A., Progress in Photovoltaics: Research and Applications 3, 1995, 177-187.

[9] Kuzma-Filipek I., Duerinckx F., Van Nieuwenhuysen K., Beaucarne G., Poortmans J., Mertens R., Proc. Of PSST, Barcelona (Spain), 2006 (in press).

SIONYX1403000016.0074

SAMSUNG EX. 1002 - 1367/4148

Available online at www.sciencedirect.com
SCIENCE DIRECT®
Nuclear Instruments and Methods in Physics Research A 546 (2005) 274–280
NUCLEAR INSTRUMENTS & METHODS IN PHYSICS RESEARCH Section A
www.elsevier.com/locate/nima

Tests of a backside illuminated monolithic CMOS pixel sensor in an HPD set-up ☆

Wojciech Dulinski[a,*], Andrea Braem[b], Massimo Caccia[c], Gilles Claus[a], Grzegorz Deptuch[a], Damien Grandjean[d], Christian Joram[b], Jacques Séguinot[b], Marc Winter[d]

[a]*LEPSI, IN2P3/ULP, 23, rue de Loess, BP20, F-67037 Strasbourg, France*
[b]*CERN, PH Division, CH-1211 Geneve 23, Switzerland*
[c]*Universita degli Studi dell' Insubria, Como, Italy*
[d]*IReS, IN2P3/ULP, 23, rue de Loess, BP20, F-67037 Strasbourg, France*

Available online 19 April 2005

Abstract

A backside illuminated, monolithic CMOS pixel sensor for direct detection of low energy electrons has been developed and is proposed as an active element for a non-destructive hadron beam monitor. In this application, the device is used as an imager of secondary electrons emitted from an aluminium foil of sub-micrometer thick intersecting the beam and accelerated in an electrostatic field to ~20–30 keV energy. The sensitivity to these electron energies (a few microns range in silicon) is obtained by back-thinning the detector, fabricated in the form of standard VLSI chip, down to the radiation sensitive epitaxial layer. The original thinning procedure was applied for processing of a large area, one million pixels prototype. The prototype has been tested using low-energy electrons inside an HPD structure. Tests results proving the device imaging capabilities of such a radiation are presented.
© 2005 Elsevier B.V. All rights reserved.

Keywords: Monolithic active pixel sensors; CMOS; Backside illuminated; Low energy electrons detection; HPD

1. Introduction

A Monolithic Active Pixel Sensor (MAPS) integrates on the same substrate the detector element with the processing electronics. The device is fabricated in a standard CMOS process available through many commercial microelectronics companies. The idea of using MAPS for the detection of ionizing radiation, in particular for high-energy charged particles tracking, has been proposed by the IReS-LEPSI team in the beginning of 1999. The ability of the monolithic CMOS sensors to provide charged particle tracking has

☆Work supported under SUCIMA E.C. Contract N. GIRD-CT-2001-00561.
*Corresponding author. Tel.: +33 3 90 24 28 68.
E-mail address: dulinski@lepsi.in2p3.fr (W. Dulinski).

0168-9002/$ - see front matter © 2005 Elsevier B.V. All rights reserved.
doi:10.1016/j.nima.2005.03.116

SIONYX1403000016.0075

SAMSUNG EX. 1002 - 1368/4148

been demonstrated on a series of Minimum Ionizing MOS Active sensor (MIMOSA) chip prototypes [1–5]. The development of a backside illuminated MAPS device was done within the framework of the SUCIMA FP5 European Project [6]. One of two tasks of the collaboration is the development of a non-destructive beam monitoring in a hadron-therapy centre. This requires a direct imaging of secondary emission electrons emitted from a sub-micrometer thick Al foil intersecting the beam and accelerated in electrostatic field up to an energy of around 30 keV, corresponding to a few micrometers range in silicon [7]. In order to adapt a standard MAPS device for efficient detection of such electrons, the thickness of the passive entrance window of the device must be reduced to much less than 1 μm. This operation is done after the device has been fabricated by a standard CMOS process provider; it is usually executed by another party and therefore is called post-processing.

2. Backside illuminated monolithic CMOS sensor

2.1. Standard MAPS

The key element of the Monolithic CMOS Active Pixel Sensor is the use of an N_well/P_substrate diode to collect through thermal diffusion the charge generated by the impinging particle in the thin, undepleted silicon underneath the readout electronics (Fig. 1). This solution allows 100% fill factor, as required in tracking applications. In a standard MAPS sensor, a thin radiation sensitive volume (~10 μm of high quality epitaxial silicon) is sitting on top of a thick (hundreds of micrometers) low quality silicon substrate simply serving as mechanical support. The front side of the epitaxial layer is covered by a passive material, made of several layers of metal and silicon oxide used for circuit electrical interconnection. This structure is well adapted to the detection of penetrating, high-energy particles, but is not compatible with a short range of low-energy (tens of keV) electrons. The sensitivity to such electrons may be obtained by back-thinning the device down to the epitaxial layer, by removing all

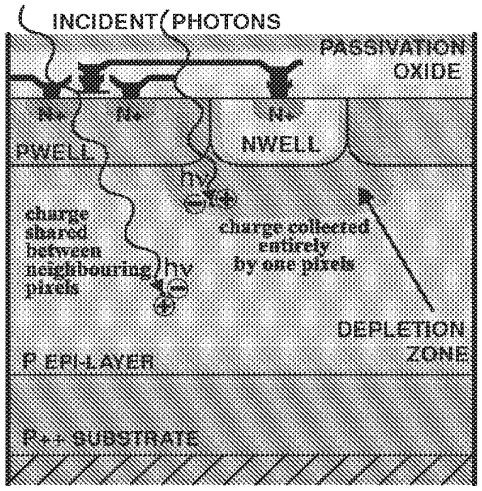

Fig. 1. Cross-section of a silicon wafer showing the principle of a standard CMOS Monolithic Pixel Sensor integrated on the top surface.

of the silicon bulk material. After thinning, the active volume of the detector is directly exposed to the incident radiation. There remains a passive entrance window (mainly silicon oxide for the passivation) with a thickness of the order of 100 nm.

2.2. Post-processing

The back-thinning procedure was developed in collaboration with industry and successfully used for processing of large area ($1.7 \times 1.7\,cm^2$, one million pixels) Mimosa5 MAPS prototypes [8,13]. Before the thinning, the mechanical structure of the chip was reinforced by attaching a several hundreds of microns thick support to the entire front surface. Then the original P++ layer was removed. The exposed surface of epitaxial silicon was passivated, resulting in a thin SiO_2 entrance window. Because of the reinforcing structure, access to the bonding pads of the chip from the original front side was blocked. In order to allow for electrical connections to the chip, a new access path for bonding wires was created from the opposite side, by etching deep trenches in front of bonding pads across the entire thickness of the remaining epitaxial layer (Fig. 2). The

SIONYX1403000016.0076

SAMSUNG EX. 1002 - 1369/4148

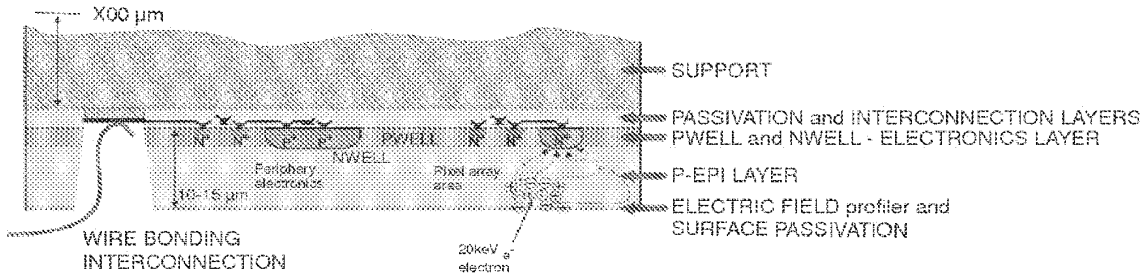

Fig. 2. Cross-section of the back-thinned CMOS monolithic pixel sensor. The low energy electrons impinge on the back (bottom) side of the structure.

post-processing yield was fully satisfactory and several operational chips were obtained. Because of limited area of original bonging metal pads ($90 \times 90\,\mu m^2$), assembly was not trivial and required the use of a 17 μm diameter Al wire and a deep access, fine pitch wedge bonding tool. The chip mounting to the test PCB and following bonding service was provided by a specialized company [9].

2.3. Device calibration using soft X-ray photons

A calibration, performed with a ^{55}Fe 5.9 keV X-ray source, allows to measure the conversion gain and the charge collection characteristics of the device. X-ray photons interact via photoelectric effect inside the active detector volume, and generate an average number of charge carriers of 1640 e/h pairs in silicon. This gives rise to a characteristic peak in the collected charge distribution. For detectors having close to 100% charge collection efficiency, the position of this peak can be directly used for measurements of the conversion gain. This is not the case for the presented device, where the carrier transport mechanism goes mainly through thermal diffusion. Because of a relatively long collection time (in the order of hundred of nanoseconds), some charge losses are therefore expected. The charge is also naturally spread among several pixels. However, the assumption of a fully efficient charge collection is justified for a small sub-sample of photons that convert directly inside the depleted volume of the charge collecting p–n junction. This explains the existence of the small statistics peaks, visible on the right side of the energy spectrum of an individual pixel (Fig. 3, top), in addition to the main peak representing the partially collected charge from photons converted anywhere in the epitaxial volume. The left-side small peak was attributed to the K_α 5.9 keV line and provides the conversion gain. The position of the main peak and its evolution with the number of pixel included in the reconstructed cluster (Fig. 3 middle and bottom) may be used as a tool to estimate the charge collection efficiency from the epitaxial zone. Our previous (still unpublished) measurements with a standard non-thinned Mimosa5 chip shows that 3×3 pixel clusters may account for more than 90% of the charge generated anywhere inside the epitaxial layer.

The basic parameters, like charge-to-voltage conversion factor, noise and leakage current of the thinned devices were found similar to these characterizing non-thinned ones. The total charge collected by a 3×3 pixels cluster amounts for about 60% of the calibration peak value, showing a clear difference with respect to a non-thinned Mimosa5. This may be understood from the particular doping profile close to the $P^{++}_{substrate}/P^{-}_{epi}$ and P^{+}_{well}/P^{-}_{epi} interface. Such an interface provides a potential barrier high enough to act as a "mirror" for diffusing electrons, keeping them close to the middle of the epitaxial layer and limiting their volume spread. In the process used for Mimosa5 fabrication (AMS 0.6 μm), the initial thickness of the epitaxial layer is 14 μm. However, because of several high temperature processing steps, p-dopant diffusion from the substrate forms a 4 μm thick "transition" layer, where the doping

SIONYX1403000016.0077

SAMSUNG EX. 1002 - 1370/4148

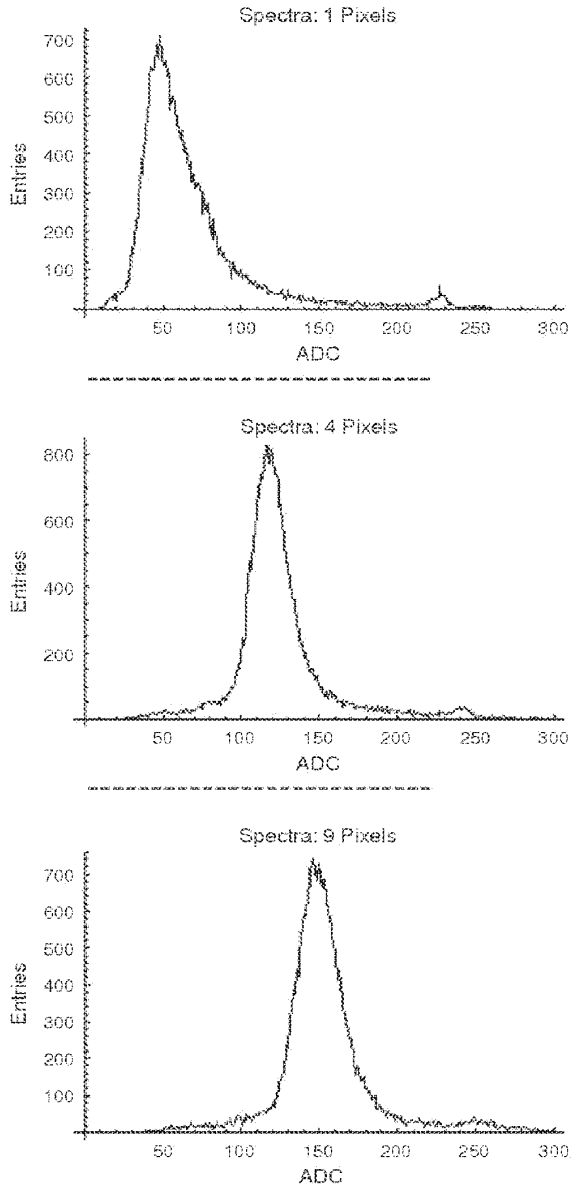

Fig. 3. Collected charge distribution of back-thinned Mimosa5, illuminated with a ^{55}Fe 5.9 keV photons source. Top to bottom: single pixel cluster (central pixel, highest signal), 2×2 and 3×3 clusters.

density decreases smoothly by four orders of magnitude. But, according to microscope inspection of the thinned device edge, this transition layer seems to be entirely etched away, leaving only a 10 μm thick, high resistivity epitaxial layer as active volume. It is therefore possible that such a sharp transition is less efficient as a reflecting layer and part of the charge is lost at the Si/SiO_2 interface. Preliminary results from the beam test [10] show also a substantial decrease of the total charge generated by passing minimum ionising particle, confirming a reduction of the active layer thickness during the back-thinning step.

3. Tests using low energy electrons

3.1. HPD set-up

The used low-energies electrons test set-up contains all basic element of a Hybrid Photon Detectors [11], except for the vacuum tank which is not sealed but connected instead to a pumping system (Fig. 4). The testing of the solid state detector prototype can therefore be done with increased flexibility. A semi-transparent CsI photocathode converts light quanta from a pulsed deuterium filled UV lamp into electrons. These photoelectrons are accelerated by a potential difference between photocathode and a sensor kept at ground potential. A metal plate close to the detector with a circular opening in front of the sensitive area protects the chip periphery (bonding wires) and improves the uniformity of electric field in the central region. During these tests the sensor was kept at room temperature.

According to the electric field simulation (Fig. 5) using the SIMION 3D package [12], the total width of electron position distribution at the detector surface, corresponding to a point-like source at the photocathode, is of the order of 1.5 mm. This is several orders of magnitude more than the expected detector resolution; therefore this electrostatics setting may be used to prove the sensor detection efficiency, but is not appropriate for testing its ultimate spatial resolution.

Back-thinned pixel sensor tests with tunable 5–25 keV mono-energetic electrons were crucial for assessing the feasibility of the beam monitoring system developed within the SUCIMA Collaboration framework.

SIONYX1403000016.0078

SAMSUNG EX. 1002 - 1371/4148

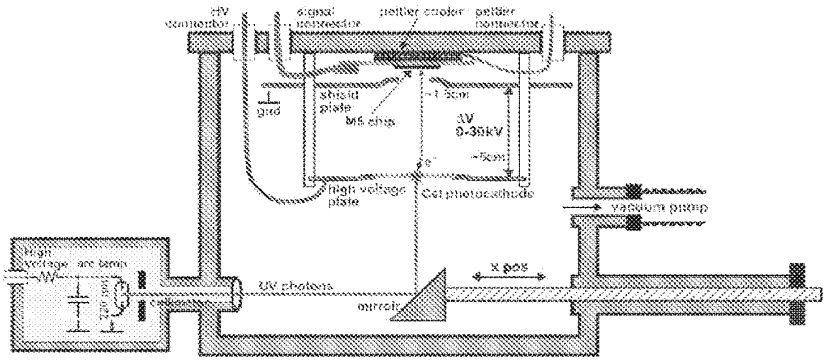

Fig. 4. Schematic of the HPD set-up used at CERN.

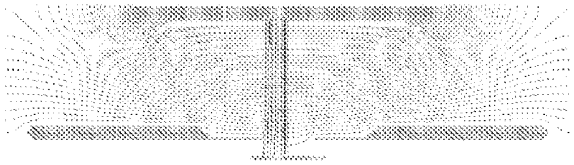

Fig. 5. Simulation (SIMION 3D) of the electric potential distribution and electron trajectories between the CsI photocathode and the Mimosa5 detector.

Fig. 6 shows an overall external and internal view of CERN HPD set-up used for described measurements.

3.2. HPD set-up tests results

Fig. 7 shows typical pulse-high spectra of reconstructed 15 keV electrons, representing the total signal from the central pixel in the cluster (top), cluster of 2×2 pixels (middle) and cluster of 3×3 pixels (bottom). A clear separation of the signal peak from noise is visible.

Fig. 8 shows the measured single electron peak position as a function of the accelerating voltage. In the measured range (from 7.5 up to 20 kV) this dependence is linear. The extrapolated line intercepts the x-axis at 2.48 kV, which may be interpreted as energy loss (~2.5 keV) in the non-active entrance window. The estimation of the entrance window thickness of this tested detector given by the back-thinning process provider is 160 nm. Detectors

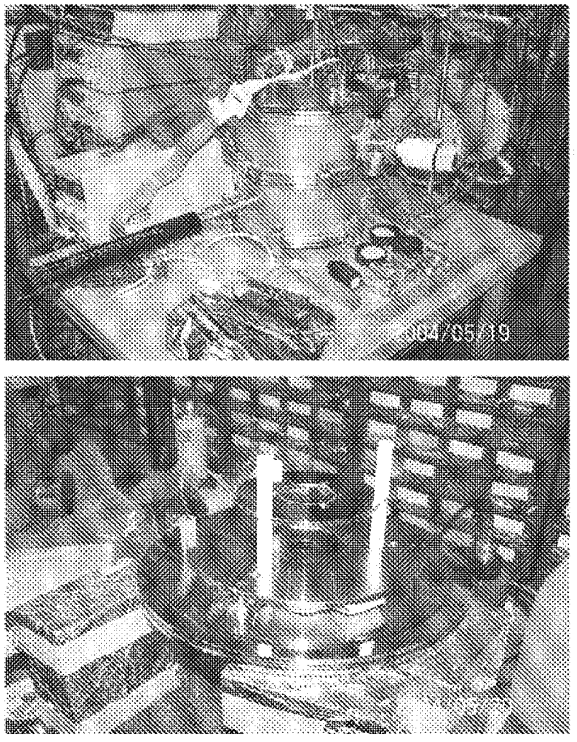

Fig. 6. External (top) and internal view of the HPD set-up at CERN.

with several other window thicknesses (from 75 to 160 nm) were also manufactured and will be tested soon.

SIONYX1403000016.0079

SAMSUNG EX. 1002 - 1372/4148

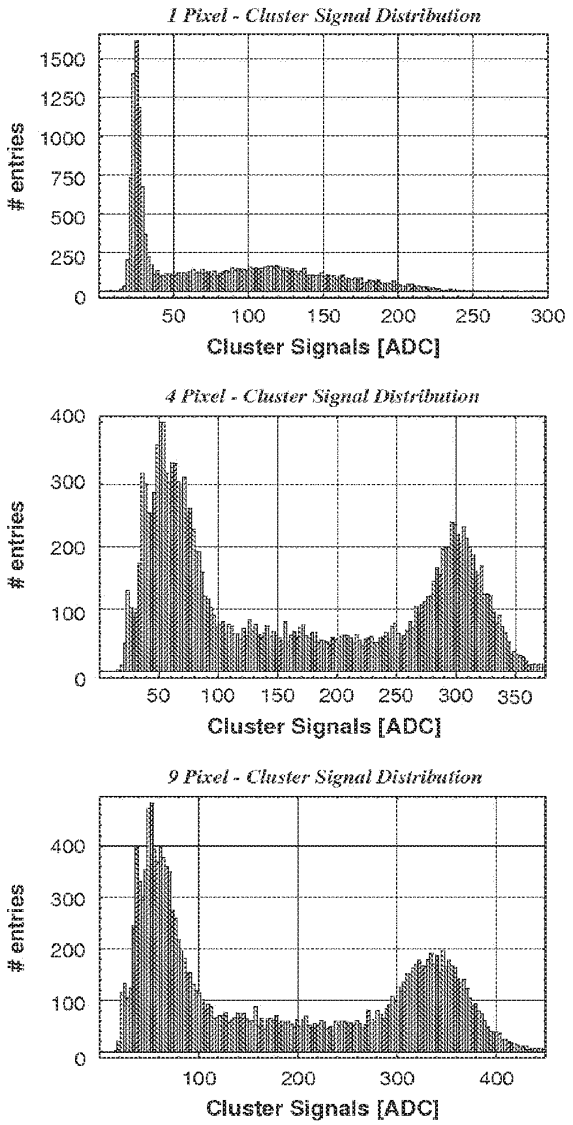

Fig. 7. Collected charge distribution for 15 keV electrons obtained with the back-thinned Mimosa5.

4. Summary and conclusion

An original industrial process was developed and successfully used for back thinning of standard CMOS monolithic pixel sensors down to the epitaxial radiation sensitive layer. The ability of a thinned and backside illuminated sensor to efficiently detect electrons in the energy range between 7.5 and 20 keV has been clearly demonstrated. Such a backside illuminated imager may find a number of new applications, in addition to its role as electron imaging device in a non-destructive beam monitor using the SLIM scheme for which it was developed. Some of them, namely autoradiography using a tritium beta source and electron microscopy, have already been explored and results will be published soon [13]. Other applications include thermal neutron imaging with a converter layer deposited directly on the sensor entrance window and single visible light photon imaging using the Hybrid Photon Detector scheme. Still another one which may be considered is sub-micron precision, single particle tracking in proton and ion micro-beam facilities.

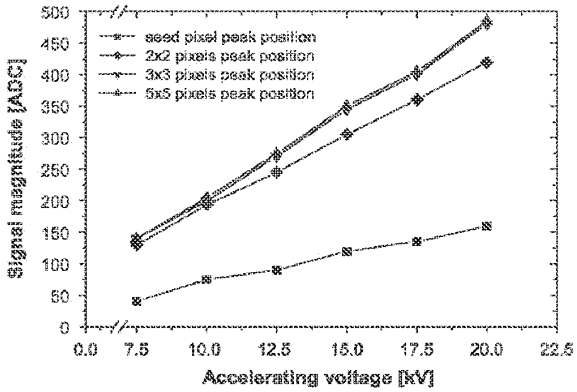

Fig. 8. Total charge amplitude (peak position) of reconstructed hits as a function of accelerating voltage (~electron energy) and cluster size.

Acknowledgments

This work was possible thanks to a continuous support of the SUCIMA team from INP Krakow (Adam Czermak, Barbara Dulny and Bogdan Sowicki) which developed and provided us with the SUCIMA USB DAQ board; a powerful, flexible and easy to use compact data acquisition system [14].

SIONYX1403000016.0080

SAMSUNG EX. 1002 - 1373/4148

References

[1] R. Turchetta, et al., Nucl. Instr. and Meth. A 458 (2001) 677.
[2] G. Claus, et al., Nucl. Instr. and Meth. A 465 (2001) 120.
[3] G. Deptuch, et al., IEEE Trans. Nucl. Sci. NS-49 (2) (2002) 601.
[4] Yu. Gornushkin, et al., Nucl. Instr. and Meth. A 478 (2002) 311.
[5] G. Deptuch, et al., Nucl. Instr. and Meth. A 511 (2003) 240.
[6] M. Caccia, et al., Nucl. Phys. B (Proc. Suppl.) 125 (2003) 133.
[7] L. Badano, O. Ferrando, M. Pezzetta, G. Molinari, SLIM (sem for low interception monitoring) an innovative non-destructive beam monitor for the extraction lines of a hadrontheraphy centre, in Proceeding of DIPAC, 5–7 May, Mainz, Germany, 2003, pp. 77.
[8] Yu. Gornushkin, et al., Nucl. Instr. and Meth. A 513 (2003) 291.
[9] S.A. Microbonding., rue de l'Areuse 1a, CH 2103 Noiraigue, Switzerland.
[10] A. Besson, Recent progress on Mimosa sensors, presented at the ECFA Meeting, Durham, September 2004, to be published.
[11] C. Joram, Nucl. Phys. B (Proc. Suppl.) 78 (1999) 407.
[12] SIMION 3D Ion Source Software. http://www.srv.net/klack/simion.htm.
[13] G. Deptuch, Tritium autoradiography with thinned and back-side illuminated monolithic active pixel sensor device, preprint LEPSI-2004, Nucl. Instr. and Meth. A 543 (2005) 537.
[14] A. Czermak, et al., Data acquisition system for silicon ultra fast cameras, in: Proceedings of the Seventh International Conference on Advanced Technology and Particle Physics, Villa Olmo, Como, 15–19 October 2001.

SIONYX1403000016.0081

SAMSUNG EX. 1002 - 1374/4148

Texturing, reflectivity, diffuse scattering and light trapping in silicon solar cells

Leonard Forbes

L. Forbes and Associate LLC, 7340 NW Mountain View Drive, PO Box 1716
Corvallis, OR 97339-1716 USA, lenforbes@forbes4.com, 1-541-753-1409

Abstract

The energy conversion efficiency is a critical consideration in the application of silicon solar cells. Texturing both front side and backside have been used to increase the absorption of infrared sun light energy in silicon solar cells. A review is given of some of the basic concepts and then a design described for the optimal textured structure and some of the practical limitations described in realizing this structure in silicon technology.

1.0 Introduction

Texturing and light trapping of infrared light energy are in reality old topics and the concepts and often discussed in relationship to silicon solar cells where the absorption coefficient of infrared light is very low. A separate but related issue has also been the use of texturing to reduce the reflectivity of silicon to visible light to improve particularly the blue response, this may not in general reduce the reflectivity to infrared light and if it does this will not result in infrared light trapping. The conflicting requirements for reduced reflectivity particularly for visible light and the requirement for light trapping of infrared light have often resulted in confusion among professionals working in the field of silicon solar energy. Light trapping requires high reflectivity of light at the internal side of the front surface for the light reflected from the backside of the solar cell.

A review is given of some of the basic concepts in terms of a simple model and then a design described for the optimal textured structure for infrared light trapping.

2.0 Front side and backside texturing

Texturing has been used as a technique to improve the efficiency of photodetectors and solar cells due to a reduction in reflections at the front surface. Most of the literature available describes the use of front side texturing of photodiodes to improve the absorption of visible light energy. Regularly textured front side surfaces have been described for solar cells by Arndt et al. (1975). The majority of silicon solar cells currently use single front side textured surfaces. Front side texturing not only serves to reduce the reflectivity of the silicon surface due to multiple attempts at transmission through the front surface as has been described by Arndt et al. (1975) but also results in longer path lengths for light that is scattered at large angles.

A light anti-reflecting region of pillars has also been described as an air-substrate index of refraction matching layer by Boden and Bagnall (2009) when considering the anti-reflecting characteristics of the "moth's eye." In some cases this anti-reflecting layer also acts like a light

SAMSUNG EX. 1002 - 1375/4148

diffusing layer with features configured to increase the effective absorption efficiency and energy conversion efficiency of the solar cell or photodetector. The anti-reflecting features may be cones, pyramids, pillars, and other features, and, when such features are used for diffusion and for the scattering of light may they be distributed in a random fashion. It should be noted that any feature that produces the desired diffusive light scattering is one that closely approximates a Lambertian scattering surface at the desired wavelengths of radiation. Lambertian scattering is ideal diffuse scattering providing light distributed over the whole half sphere or solid angle of 2π sterradians. Manipulating the feature sizes, dimensions, etc. allows the light anti-reflecting and light diffusing region to be tunable for a specific wavelength. Varying the material near or deposited upon the anti-reflecting and light diffusing region can also be used to enhance these characteristics.

2.1 Front side texturing

Consider now the effect of front side texturing on the near infrared wavelength response where absorption is very low; texturing will also change the absorption in the remaining part of the infrared and the visible light regions but this will not yet be considered. In the near infrared the index of refraction of silicon is η=3.42 and the reflectance is about R = 30% from a single surface and transmittance through a single surface is T = 70% for normal incident waves. The absorption coefficient of silicon is very low in the near infrared. If there is no backside reflector radiation under normal incidence is reflected first from the first surface . There are successive reflections from both the back and internal reflections from the front surface resulting in a total transmittance, if there is no reflective layer or the oxide layer , of

$$T_{tot} = (T\ T)(1 + R^2 + R^4 + ...) = (T\ T) / (1 - R^2) \quad (1)$$

This result has been obtained using the sum of a geometric series. If both top and back surfaces are just polished silicon-air then this results in a total transmittance of 54% and a reflectance of 46%. The internal absorption, A, of infrared light where the absorption coefficient, α, is very low due multiple internal reflections in a sample of thickness, d, with a polished backside is

$$A = \alpha d\ (1 + R_2)(1 + R_1 R_2 + R_1^2 R_2^2 + ...) = \alpha d\ (1 + R_2) / (1 - R_1 R_2) \quad (2)$$

The enhancement, Enh, in internal absorption by multiple internal reflections with a polished backside is

$$Enh = (1 + R_2) / (1 - R_1 R_2) \quad (3)$$

The back surface can be coated with a thin oxide or conductive oxide and metal reflector to produce an internal reflection that is specular. If the backside is a perfect reflector, a condition that can't be achieved in general by placing metal directly on the semiconductor [3], but that can be achieved by metal over an oxide, then R_1 = 0.3 and R_2 = 1.0 and

$$Enh = (1 + R_2) / (1 - R_1 R_2) = 3 \quad (4)$$

and the external quantum efficiency, EQE is

SAMSUNG EX. 1002 - 1376/4148

$$EQE = \alpha d\ T_1\ (1 + R_2)/(1 - R_1 R_2) = 2\alpha d\ T_1 \quad (5)$$

where T_1 is the fraction of the incident light transmitted through the first surface, for specular reflections light $T_1 = (1 - R_1)$. However, for simplicity in further analysis and notation we will designate R_1 to be the fraction of light incident from the backside on the front surface and reflected back internally from the front surface. This need not be simply related as previously to the fraction of incident light transmitted from outside the sample through the front side surface.

Now consider the case as shown in Fig. 1(a) with a textured front surface and backside reflector. For simplicity if we neglect the increase in individual path lengths due to scattering by a textured front surface and count only the number of reflections then if the front side is textured and an antireflecting film added to minimize, $R_1 \sim 0$. If the reflectivity of the front surface to incident radiation is very low then the reflectivity to radiation incident from the backside is also very low. This results in only two passes of the incident radiation and then the Enh = 2 and EQE = 2 α d. This underestimates the possible improvement possible due to front side texturing but apparently describes the where the front side is textured as porous silicon but there is little scattering (Yuan et al., 2009). Neglecting the increase in individual path lengths due to scattering by a textured front surface underestimates the improvement possible due to front side texturing but a more important practical consideration is the backside reflectivity. Estimates are that the reflectivity of aluminum directly on silicon may be as low as $R_2 = 0.3$.

If the absorption is not low then from Fig. 1(a) the absorption on two successive paths where, $R_1 \sim 0$, and, $R_2 = 1$, can be expressed as

$$A = (1 - \exp(-\alpha d))(1 + \exp(-\alpha d)) = (1 - \exp(-2\alpha d)) \quad (6)$$

If the absorption, αd, is low, $A = 2\alpha d$ and if the absorption is high , αd, is large, A =1. Eqn. 6 will be used later in comparing the absorption due to front side texturing to the absorption due to backside texturing.

2.2 Backside texturing

Backside texturing, Fig. 1(b) has also been used as a technique to improve the efficiency of photodetectors and solar cells due to backside light scattering and light trapping by improving the absorption of near infrared light energy. Backside texturing can result in multiple internal reflections and light trapping. One of the first descriptions of using this technique in photodetectors was by St. John(1969). Another description was provided by Cotter (1998). A more recent description of the same technique on ultra-thin solar cells has been given by Aberle et al. (2007). They disclosed the use of white paint as the backside diffuse reflector. Their initial results show a large increase in the absorption with the white paint as a back

SAMSUNG EX. 1002 - 1377/4148

surface reflector but only a modest ten or twenty percent increase in the quantum efficiency. We have also investigated the use of white paint as a diffuse reflector (Forbes and Louie, 2010). A later result by Aberle et al. (2007) indicated that a twenty to forty percent enhancement in conversion efficiency can be obtained on thin film microcrystalline solar cells by adding more titanium dioxide to the white paint. However, thick layers of the order 80 μm or more of paint are required on thin film solar cells which in themselves are only a few micrometers thick.

If the increase in the individual path lengths caused by the diffuse scattering at the backside is neglected and if the absorption coefficient is very low then the total effective path length is determined by just the number of reflections. If then as before R_1 is designated to be the fraction of light incident from the backside on the front surface that is reflected back internally from the front surface, the total absorption can be shown to be

$$A = \alpha d\ (1 + R_2)(1 + R_1 R_2 + R_1^2 R_2^2 + \ldots) = \alpha d\ (1 + R_2)/(1 - R_1 R_2) \qquad (7)$$

The effective increase in absorption is $Enh = (1 + R_2)/(1 - R_1 R_2)$. The internal quantum efficiency, IQE, in the infrared where the absorption in silicon is low is then, $IQE = \alpha d\ Enh$. The external quantum efficiency, EQE, is $EQE = T_1\ IQE$ and $EQE = T_1\ \alpha d\ Enh$. T_1 is the fraction of light incident on the front surface from outside the sample that is transmitted through the front surface, 0.7, for an air-silicon interface.

A technique that improves the infrared response has the top side polished but the back side textured with an oxide like silicon oxide or transparent conductive oxides like zinc oxide, indium oxide, or tin oxide, and a metal like aluminum or silver or mirror reflector. The texturing is realized in a fashion to produce a true diffuse scattering, Lambertian scattering at infrared wavelengths. This diffuse scattering layer and reflecting layer combination, in essence, yields $R_2 = 100\%$, an ideal diffuse reflector. The reflectance of the polished front side to the scattered light radiation is determined by solid angle considerations. Any incident light with an angle of incidence greater than the critical angle θ, will be totally internal reflected. If the backside scattering is totally diffuse or Lambertian, the transmittance is then determined by the area of the surface, πr^2, within the critical angle, θ, in this case 17° for silicon and air. The radius of the circle is $r = d \sin(17)$, where, d, is the thickness of the sample. This area is divided by the area of the half sphere, $2\ \pi d^2$. If the backside scattering is totally diffuse the transmittance of the front planar surface is then roughly 3% to internally reflected light from the backside and the reflectance $R_1 = 97\%$. The path length enhancement factor can be very large

$$Enh = (1 + R_2)/(1 - R_1 R_2) = 66 \qquad (8)$$

This would result in an internal quantum efficiency, $IQE = 66\ \alpha d$ and since T_1 is still 0.7 and $EQE = 46\ \alpha d$. This is consistent with the estimate by Cotter (1998) that was defined as, $4\eta^2$, where, η, is the optical index of refraction of the semiconductor, then for a backside textured silicon photodetector $4\eta^2 = 51$ in the near infrared where the index of refraction for silicon $\eta = 3.42$. If the backside is a textured and truly diffusive scattering surface and a mirror like

SAMSUNG EX. 1002 - 1378/4148

surface is used behind the back side, a very large enhancement of absorption in the near infrared can be achieved.

If the absorption in the silicon layer is not assumed to be small but rather taken into account it can be shown that the enhancement factor for the internal quantum efficiency due to multiple reflections is modified from Eqn. 8 and becomes

$$Enh = (1- \exp(-\alpha d))(1 + R_2 \exp(-\alpha d))/(1 - R_1 R_2 \exp(-2\alpha d)) \quad (9)$$

This allows a calculation of the responsivity, in terms of the electrical current in Amperes per incident light power in Watts, of solar cells of different thickness, d, for different wavelengths, λ, since the absorption coefficient, $\alpha(\lambda)$, is a function of wavelength. If it is assumed that the backside is an ideal reflector, $R_2 = 1.0$, and the amount of diffusive scattering of the back surface varies from that of a planar surface then the fraction of light reflected back from the front surface will vary. If the back surface is planar then there is only specular reflection and, $R_1 = 0.3$, if the back surface is an ideal Lambertian diffusive surface then the fraction of light reflected back from the front surface will be very large, $R_1 = 0.97$. Several values of R_1 are discussed herein for a diffuse reflector, these represent the fraction of light internally reflected back at the front surface. For purposes of the present description, values of $R_1 \geq 0.9$ are deemed particularly useful. The enhancement in absorption described by Eqn . 9 then varies with the fraction of light radiation reflected back from the front surface and thickness of the sample. These results are compared in Fig. 2(a) for a thin 2 micrometer thick sample to those for front side texturing as described by Eqn. 6 . The same assumptions have been used in both cases with respect to radiation path length. As can be seen from the calculated responsivity in Fig. 2(a) backside texturing is much more effective in enhancing the absorption of infrared light energy.

The analysis for backside texturing can also be performed for thick silicon solar cells or photodetectors, and compared to published results by Yamamoto et al., (2010) in Fig. 2(b). Eqn. 9 has been used in this comparison where $R_1 = 0.93$, and $R_2 = 1.0$, indicating a very effective backside scattering by a laser ablated surface.

3.0 Practical realizations

3.1 Backside reflectors

One of the difficulties in silicon technology is realizing a backside reflector. Metal directly on a silicon backside has been found in practice not be a good reflector. One approach in thin film technology has been to deposit silicon on a oxide over a textured metal. In doing so the desire has been to use thicker oxides to try to planarize the oxide top surface for silicon deposition. One of the difficulties with this approach is illustrated in Fig. 3(a), while the metal may be a diffusive reflector but the reflected light is defracted towards the normal upon entering the silicon. The light in the silicon will not appear to originate from a Lambertian scattering source. In Fig. 3(b) the backside of the silicon is textured and a thin oxide or dielectric used before metal deposition. If the oxide is thin, much less than a quarter

SAMSUNG EX. 1002 - 1379/4148

wavelength then the reflected light is not affected by the thin oxide and the reflection into the silicon can be Lambertian scattering.

3.2 Diffuse light scattering

Diffuse scattering at even one wavelength is in general not easily achieved and is not realized by pyramidal structures, random pyramidal structures nor gratings. Ideal reflective Lambetrian scattering provides light distributed over the whole half sphere or a solid angle of 2π sterradians. Herein the use backside texturing provides diffusive reflective light scattering at the backside and planar front side surfaces to provide for total internal reflections at the front side and multiple passes of red and infrared light in silicon solar cells. The front surface preferably has an anti-reflecting layer for visible light, but this layer does not significantly effect the reflectivity of the front surface to infrared light.

Thus, a solar cell or photodetector has been described that provides optimal conversion of visible light and infrared energy to electricity. Backside texturing with diffusive scattering and frontside internal reflection produce a large enhancement of conversion efficiency. The preferred structure uses a set of cusps etched into the backside of solar cells to provide diffusive scattering. One of the best examples of the scattering and diffraction of light is the classical treatment of the interaction of light with narrow slits such as given by Born and Wolf (1999). Here we will replace the slits by reflective strips in an absorbing material. Consider firstly light of one particular wavelength, or wavenumber, k. For an array of n strips of width, s, and equal spacing, d, with the light vertically incident ,the intensity of the diffracted light on a screen, I, is proportional to:

$$I \sim (H(n d k p /2) \quad \text{sinc}(s k p/2))^2 \qquad (10)$$

where sinc(x) is the the ratio, sin(x)/x , and $p = \sin\theta$, θ is the angle from the vertical at which the light is diffracted. The formula for the intensity is valid if the observing screen is much farther away then, s or d , or namely the Fraunhofer diffraction regime. In this case, the diffraction pattern is equivalent to the Fourier transform of the diffraction grating. For a single strip of finite width, the diffraction pattern has the well-known form of a sinc function. For multiple slits of finite width, the diffraction is a pattern of peaks and troughs of the aperture, n d, whose locations are described by the interference function, H, and whose intensity is modulated by the sinc function pattern arising from a single strip. The envelope of the intensities of the regular diffraction pattern observed on the screen is a sinc function. An alternative derivation to that in Born and Wolf (1999) given by Falloon (2011) is to firstly recognize that a set of narrow strips are described by the convolution of a series of delta functions with a single strip so the Fourier transform of the grating is the product of the transform of a series of delta functions, which yields H, times the Fourier transform of a single strip the sinc function, sinc(s q/2). This yields $H \sim \sin(n d q/2)/ \sin(d q /2)$. Here, q, is the normalized wave number, $q = k\ p = k \sin\theta$.

SAMSUNG EX. 1002 - 1380/4148

Consider now a solar cell as shown in Fig. 4 , where light incident on the top or front surface passes through the cell and strikes a textured reflective surface at the bottom or back of the cell, Fig. 4(b). Lambertian scattering by a single element into a semicircle will, as shown in Fig. 4(b), result in a Lorentzian intensity pattern , Fig. 4(a) on a flat screen. Light will be scattered large distances in the, x, direction as a result of the uniform intensity on the semicircle. Here the normalized wavenumber is, $q = k\,p = k\,\sin(\theta)$. In order to achieve Lambertian scattering then one must find the inverse Fourier transform of the Lorentzian and use this for the shape of a single element providing scattering or for each element providing diffraction in an array. The Fourier transform of each element providing scattering will then give uniform illumination of a semicircle and a Lorentzian shape on the flat screen. The inverse Fourier transform of a Lorentzian is a "cusp" as shown in Fig. 4(c). A series or array of strips of such regular "cusps" will result in a series of dots on the screen with a nearly uniform intensity described by a Lorentzian envelope for the intensities over a wide range of distances, each dot will have the shape and location described by the interference function, H, of the aperture defining the region occupied by the "cusps." A regular array of strips of cusps will produce a regular diffraction pattern of dots on the front surface where the intensity is determined by the Fourier transform of the single "cusp" shown in Fig. 4(a). It is fairly straightforward to demonstrate this in two dimensions in a qualitative manner by considering an array of strips of cusps and using numerical calculations on a computer that does Fourier transforms. This has also been illustrated in Fig,. 5(a) as was experimentally shown by Born and Wolf (1999) by illuminating a aperture with punched holes, top illustration, on a dark screen as in the bottom part of each illustration. Likewise an random array of "cusps" will also work as well, these will produce a random array of dots on the front surface or a "fuzzy" pattern as shown in Fig. 5(b) as was experimentally shown by Born and Wolf (1999).

In the case of a solar cell with very wide features there is essentially no aperture. A regular array or random arrangement of strips of "cusps" on the backside will result in Lambertian scattering from each element separately and optimal scattering. In the case of solar cells there need be no concern about the accumulative effect of a large number of "cusps" and whether or not they form a regular diffraction pattern. We need only be concerned here that the scattering from each element be Lambertian, this will insure a maximum of total internal reflection back from the silicon side of the front surface. The solar cells are however three dimensional, to affect a practical realization of the "cusp" features we need to rotate the cusps to give scattering in three dimensions. It is easier to make random isolated individual "cusps" rather than strips of "cusps".

The size of the "cusps" are chosen to optimize a particular wavelength, λ, the wavelength in silicon. For instance, $1/a$, the height of the "cusps" is chosen to be some multiple factor of the wavelength. The maximum slope for a normalized cusp is minus one so the maximum scattering angle is ninety degrees. Since the height of the cusps does not have to be any particular multiple factor of the wavelength for nearby infrared wavelengths the scattering will also be Lambertian. For infrared sunlight energy the scattering from each cusp in a random

SAMSUNG EX. 1002 - 1381/4148

array will be diffusive or nearly diffusive scattering resulting in light trapping (Forbes 2011) and a significant increase in the conversion efficiency of solar silicon cells.

4.0 Conclusions

A random array of such etched "cusps" into the backside of a silicon wafer can be provided by porous silicon and chemical etches. A porous silicon or metal catalyst etch can provide vertical holes at random locations, these can then be etched with a conventional isotropic silicon etch to round off the shape corners resulting in a cusp like structure. A thin layer of oxide can either be grown or oxide or another dielectric deposited and the backside covered by a reflective metal. In this manner a random array of cusp like scattering centers can be formed on the back of silicon solar cells.

Backside texturing and reflective structures have the potential of making large improvements in the energy conversion, from 10% to 20% on thick crystalline or multi-crystalline silicon (Forbes and Louie 2010) and from 20% to 40% on thin film microcrystalline and amorphous silicon (Aberle et al., 2007) solar cells. Backside texturing and light trapping may be necessary to realize the full potential of thin film silicon solar cells in comparison to other competitive technologies as is evident from the review by Razykov et al. (2011).

References

Aberle, A. G.. Berger, O., and Inns, D., 2007. Commercial white paint as back surface reflector for thin-film solar cells. Solar Energy Materials & Solar Cells. 91, 1215–1221.

Arndt, R.A., Allison J.F., Haynos, J.G., and Meulenberg, Jr., A. , 1975. Optical properties of the COMSAT non-reflective cell. 11th IEEE Photovoltaic Spec. Conf. 40-43.

Boden, S.A., and Bagnall, D.M., 2009. SPIE Optics and Photonics. Nanostructured biomimetic moth-eye arrays in silicon by nanoimprint lithography. SPIE Optics and Photonics. 74010J-1 - 74010J-12.

Born, M., and Wolf, E., 1999. Principles of Optics, seventh ed. Cambridge University Press, Cambridge, pp. 446-455.

Cotter, J.E., 1998. Optical intensity of light in layers of silicon with rear diffuse reflectors. J. Appl. Phys. 84, 618-624.

Forbes, L., and Louie, M.Y., 2010. Backside Nanoscale Texturing to Improve IR Response of Silicon Photodetectors and Solar Cells. Nanotech. 2, 9-12.

SAMSUNG EX. 1002 - 1382/4148

St. John, A.E., 1969., Multiple Internal Reflection Structure in a Silicon Detector which is Obtained by Sandblasting. U.S. Patent 3,487,223.

Razykov, T.M., Ferekides, C.S., Morel D., Stefanakos E., Ullal, H.S., and Upadhyaya, H.M., 2011. Solar photovoltaic electricity: Current status and future prospects. Solar Energy. 85, 1580-1608.

Yamamoto, K., Sakamoto, A., Nagano, T., Fukumitsu, K., 2010. NIR sensitivity enhancement by laser treatment for Si detectors. Nuclear Instr. and Meth. Phys. A624, 520-523.

Yuan, H.-C., Yost, V.E., Page, M.R., Stradins, P., Meier, D.L., and Branz, H.M., 2009. Efficient black silicon solar cell with a density-graded nanoporous surface: Optical properties, performance limitations, and design rules. Appl. Phys. Lett. 95, 123501.

Falloon, P., "Multiple Slit Diffraction Pattern" from the Wolfram Demonstrations Project http://demonstrations.wolfram.com/MultipleSlitDiffractionPattern/ last accessed July 2011.

Forbes, L., 2011. Continuation in Part of US Patent Publication 201110140106 Backside texturing by cusps to improve IR response of silicon solar cells, to be published Dec. 2012. http://appft1.uspto.gov/netahtml/PTO/search-adv.html last accessed July 2011.

SAMSUNG EX. 1002 - 1383/4148

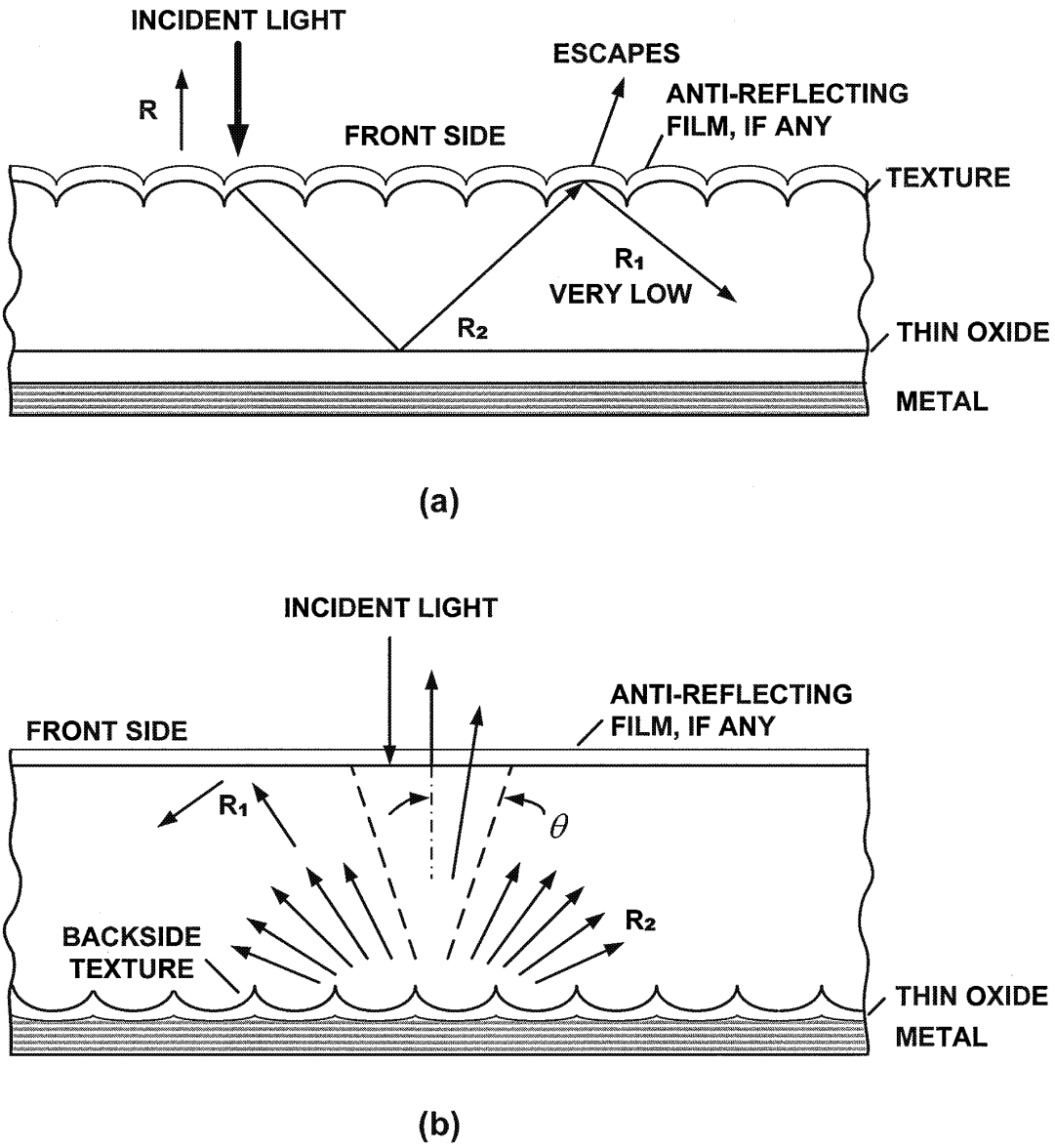

Fig. 1. (a) Front side textured solar cell,
(b) Backside textured solar cell.

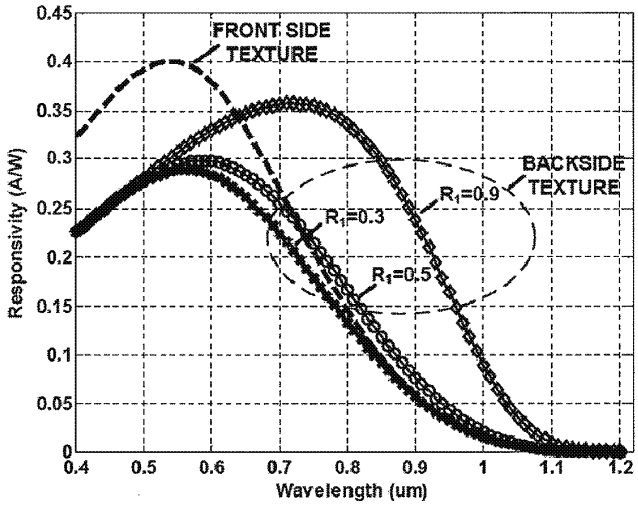

(a)

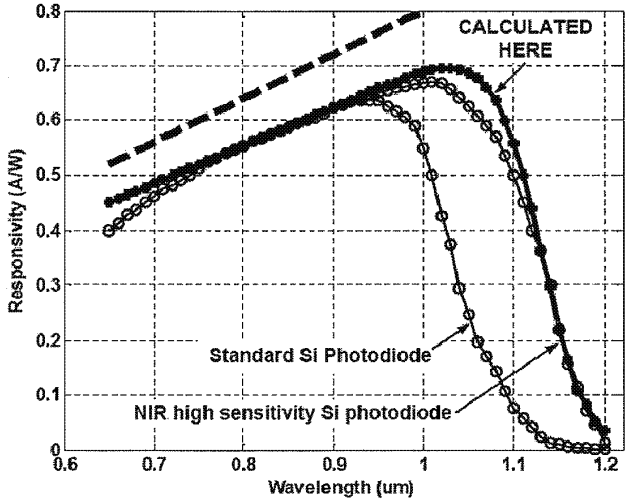

(b)

Fig. 2 (a) Comparison of front and backside texture on thin film silicon solar cells , (b) Matching of our model with R2=1 and R1=0.93 to data by Yamamoto et al.,(2010) 270 μm silicon wafer, backside texture.

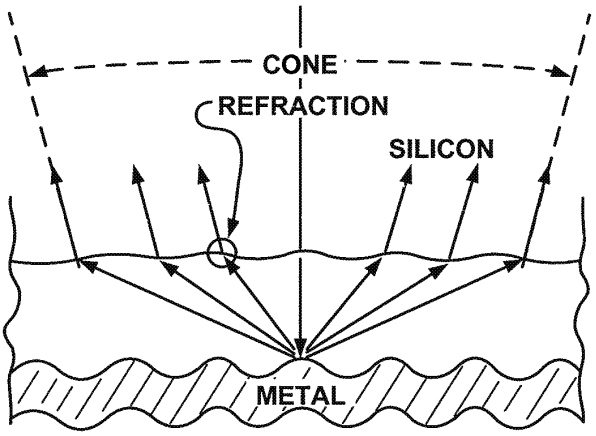

(a)

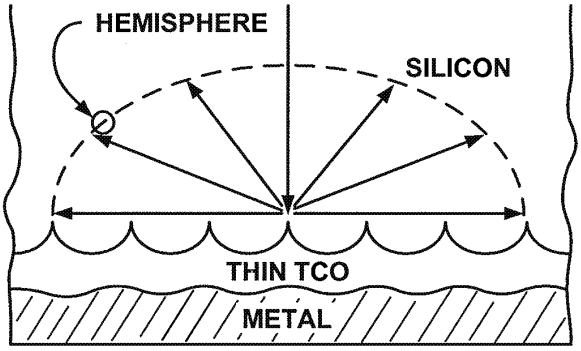

(b)

Fig. 3. (a) Silicon grown on textured metal,
(b) Metal reflector deposited on the backside of textured silicon.

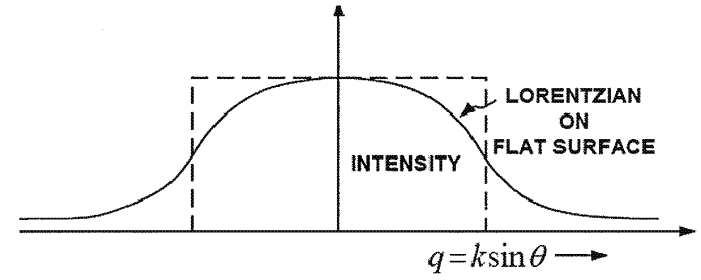

(a)

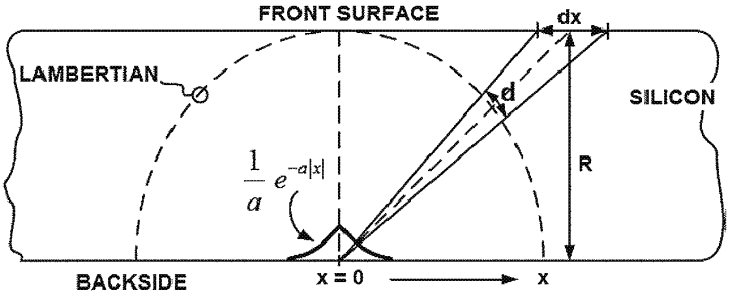

(b)

AREAS

$$\frac{d\,dz}{dx\,dz} = \frac{1}{1 + \left(\frac{x}{R}\right)^2}$$

$$FT\left(\frac{a}{2} \cdot e^{-a|x|}\right) = \frac{1}{1 + \left(\frac{k}{a}\right)^2}$$

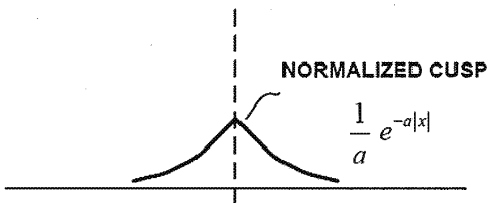

(c)

Fig. 4. (a) Scattered light amplitude at front side,
(b) Light scattering by backside texture,
(c) Normalized cusp and Fourier transform.

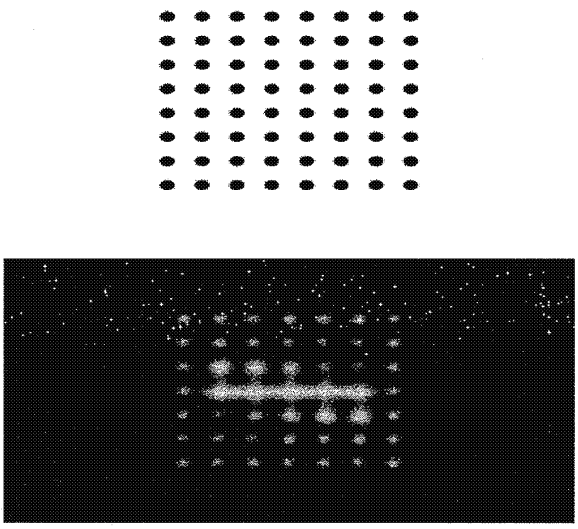

(a)

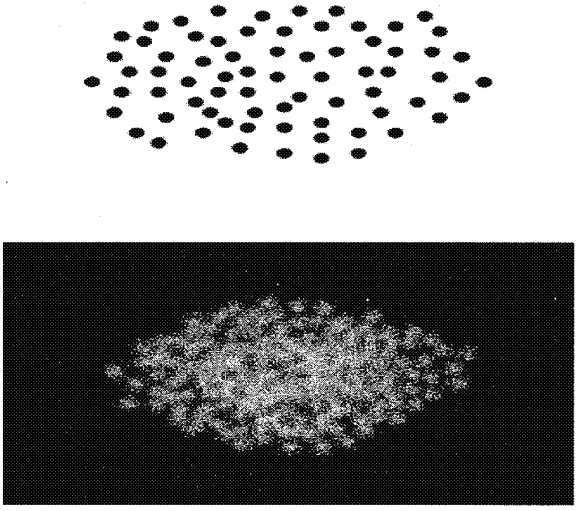

(b)

Fig. 5. (a) Diffraction pattern of a regular array,
(b) Diffraction pattern of a random array.

Backside Nanoscale Texturing to Improve IR Response of Silicon Solar Cells and Photodetectors

Leonard Forbes* and Michael Y. Louie

Electrical Engineering and Computer Science
Oregon State University, Corvallis, OR 97331-5501
* also with L. Forbes and Associates LLC
PO Box 1716, Corvallis, OR 97339-1716 prof@forbes4.com

ABSTRACT

Texturing has been widely used as a technique for light trapping and to improve the efficiency of solar cells by utilizing multiple internal reflections and light trapping. Unfortunately there are conflicting infrared light trapping and visible light antireflection criteria in solar cells. A portion of the publications and reports on solar cells describes the use of backside texturing of the solar photodiodes to improve the absorption of near infrared light energy in the solar cell. Here a distinction is made between the antireflective properties of surfaces and their scattering properties. It is demonstrated that for absorption of near infrared sun light energy that backside texturing of solar cells is most efficient.

Keywords: solar cells, texturing, infrared response

1 INTRODUCTION

Backside textured surfaces were described for increasing the efficiency of silicon detectors over forty years ago[1] and more recently texturing has been used on solar cells.[2] Backside textured surfaces have been previously described for solar cells [3,4], as well as front side[5] double side textured surfaces[6,7]. There are a variety of texturing techniques[8-11]. Front side texturing serves to reduce the reflectivity of the silicon surface, in analogy to the moth's eye[10], when the silicon is strongly absorbing in the visible spectrum. When the silicon is not strongly absorbing in the near infrared a back side textured surface[2] works in conjunction with a totally internally reflecting front side surface to best increase the absorption of near infrared photons. This results in multiple internal reflections and light trapping. From the previous description it should be apparent that there are conflicting requirements for the absorption of infrared light energy and visible light energy. Front side texturing is required to maximize absorption of visible light energy, the backside condition is irrelevant since visible radiation is strongly absorbed near the front surface. On the other hand a smooth front side and textured backside is needed to maximize the utilization of infrared light energy.

2 BACKSIDE TEXTURING

Texturing has been widely used as a technique for light trapping and to improve the efficiency of solar cells due to multiple internal reflections and light trapping. A portion of the literature on solar cells describes the use of backside texturing of the solar photodiodes to improve the absorption of near infrared light energy in the solar cell. One of the first descriptions of using this technique was given by A.E. St John in US Patent 3,487,223 30 Dec. 1969. [1] Another description was provided by J.E. Cotter[3]," Optical intensity of light in layers of silicon with rear diffuse reflectors," Journal of Applied Physics,vol.84, no.1, pp. 618-24, 1 July 1998. A more recent description of the same technique on ultra-thin solar cells has been given by O. Berger, D. Inns, and A. G. Aberle[4] , "Commercial white paint as back surface reflector for thin-film solar cells," Solar Energy Materials & Solar Cells, vol. 91, pp. 1215–1221, 2007, they used white paint as the backside diffuse reflector. Their initial results show a large increase in the absorption with the white paint as a back surface reflector but only a modest ten or twenty percent increase in the quantum efficiency. Their later results just quoted but not shown indicate that a twenty to forty percent enhancement in conversion efficiency can be obtained on thin film microcrystalline solar cells by adding more titanium dioxide to the white paint.

SIONYX1403000016.0096

SAMSUNG EX. 1002 - 1389/4148

3 ANALYSIS

A very recent analysis of the enhancement of infrared absorption in solar cells and photo detectors has been provided by the inventor, L. Forbes, "Conflicting Infrared Light Trapping and Visible Light Antireflection Criteria in Solar Cells," submitted to Appl. Phys. Lett., 2010, that is described in part again here.

Traditional or photodiodes and photo detectors in imagers use what is called FSI, or Front Side Illumination technology as shown in Fig. 1. In conventional CMOS imagers the substrates or wafers are hundreds of micrometers thick but epitaxial or silicon on insulator wafers are used to limit the depth of absorption of the incident radiation, CCD imagers are sometimes thinned to a few micrometers. Recently solar cells have been fabricated using thin films of microcrystalline silicon. As a result of the thin active film thickness the efficiency of the absorption of infrared and short wavelength visible light in thin silicon films has become important.

The preferred technique described here for near infrared, NIR, or short wavelength infrared, SWIR, detectors and imagers and thin film microcrystalline solar cells is front side illumination with backside texturing. We will consider only the effect of texturing on the near infrared wavelength response, texturing will also change the absorption in the remaining part of the visible region but this will not be considered here. In the near infrared the index of refraction of silicon is η=3.42 and the reflectance is about R = 30% from a single surface and transmittance through a single surface is T = 70% for normal incident waves. The absorption coefficient of silicon very low in the near infrared. In Fig. 1 light under normal incidence is reflected from the first surface and then there are successive reflections from both the back and front surface resulting in a total transmittance of

$$T_{tot} = (T\ T)(1 + R^2 + R^4 + \ldots\ldots) =$$

$$(T\ T) / (1 - R^2) \qquad (1)$$

The last result has been obtained using the sum of a geometric series. If both surfaces are just polished silicon-air then this results in a total transmittance of 54% and a reflectance of 46%.

If we neglect the increase in the individual path lengths caused by the diffuse scattering and if the absorption coefficient is very low then the total effective path length is determined by just the number of reflections and the total absorption can be shown to be

$$A = \alpha d\ (1 + R_2\ )\ (1 + R_1\ R_2 + R_1^2\ R_2^2 +$$

$$\ldots\ldots) = \alpha d\ (1 + R_2\ ) / (1 - R_1\ R_2\ ) \qquad (2)$$

Here, α, is the absorption coefficient in reciprocal cm and, d, is the thickness of the sample in cm, and the effective increase in path length is Enh = $(1 + R_2\ ) / (1 - R_1\ R_2\ )$. The internal quantum efficiency in the infrared where the absorption in silicon is low is then, IQE = α d Enh, and the external quantum efficiency is EQE= T_1 IQE = $T_1\ \alpha$ d Enh. If both sides of an infrared photo detector or thin film silicon solar cell are polished then $T_1 = T_2 = 0.70$ and $R_1 = R_2 = 0.3$ which gives Enh = 1.4, IQE = 1.4 α d and EQE = α d.

A configuration to improve the infrared response is to have the front side polished but the back side textured with a metal or mirror reflector behind it to give R_2 = 100% as a diffuse reflector. The reflectance of the polished front side to the scattered light will be determined by solid angle considerations. Any incident light with an angle of incidence greater than the critical angle will be totally internal reflected. If the backside scattering is totally diffuse or Lambertian the transmittance will then be determined by the area of the surface, $\pi\ r^2$, within the critical angle, in this case 17 degrees for silicon and air. The radius of the circle is r= d sin(17). This area is divided by the area of the half sphere, $2\ \pi\ d^2$. If the backside scattering is totally diffuse the transmittance of the front planar surface is then roughly T_1 = 3% and the reflectance R_1 = 97%. The path length enhancement factor can be very large

$$Enh = (1 + R_2\ ) / (1 - R_1\ R_2\ ) = 66 \qquad (3)$$

This would result in an IQE = 66 α d and an EQE = 46, this is consistent with Cotter's estimate[3] for a backside textured silicon photo detector of $4\ \eta^2 = 51$ in the near infrared where for silicon η = 3.42. As shown in Fig. 1 if the backside is textured and a mirror like surface is used behind the back side a very large enhancement of absorption in the near infrared can be achieved.

SIONYX1403000016.0097

SAMSUNG EX. 1002 - 1390/4148

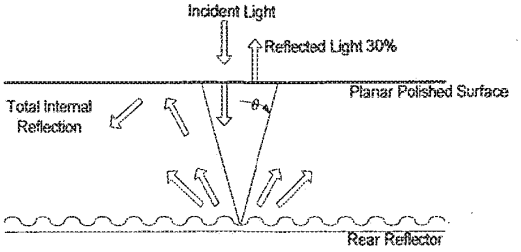

Fig. 1 Scattered back side total reflection from a textured back side and backside mirror-like reflector. There is total internal reflection at the front surface for light scattered outside the critical angle for the silicon-air surface, 17^0.

4 SOLAR CELLS

The results for single solar cells or photodetectors are shown in Fig. 2. These can be either a crystalline silicon p-i-n diode or a microcrystalline silicon p-i-n diode. The semiconductor junctions at the bottom and top can either be conventional implanted or diffused junctions or doped amorphous silicon layers can be used to form heterojunctions. For optimum infrared response The backside is textured while the front side is a reflective planar surface. A large enhancement can be obtained in the infrared response.

Fig. 2(a) shows a thin film silicon solar cell[4] that either has a white paint diffuse reflector(PDR) on the back or no reflector. A 10% to 20% increase in the conversion efficiency was obtained by just commercial white paint, even larger 40% increases were obtained with a special paint on the back. Fig. 2(b) shows our results on a thick silicon diode with a gold backside reflector or a white paint on the backside. The white paint is a simple but not a very effective PDR, a large thickness of paint and high titanium oxide concentration is required.

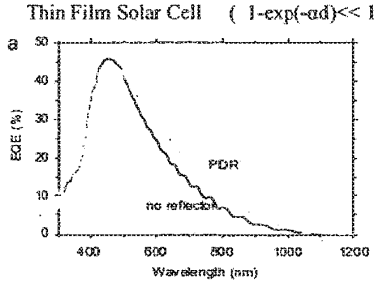

(a)External quantum efficiency with diffuse back surface reflector(PDR, white paint) and without; from O.Berger, D. Inns and A. G. Aberle[12]

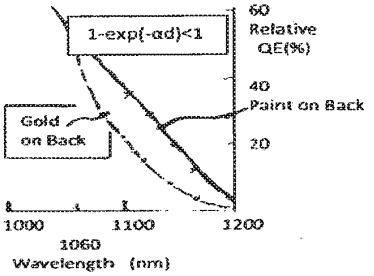

(b) Our thick silicon photodetector diode, with gold on back versus white paint on the backside

Fig. 2. Solar cells with and without white paint on the back, thick photodiode with metal on the

For solar cells the maximum benefits of texturing can be achieved by using a structure consisting of two stacked solar cells, as shown in Fig. 4.[2] The top solar cell having a textured front, to transmit and allow absorption of visible light, and textured back. The bottom solar cell would have a smooth front surface and textured back to absorb infrared light energy. Most infrared light will just pass through the top solar cell and not be absorbed, the textured surfaces in the top solar cell transmit infrared light. The bottom solar cell will absorb most of the infrared light energy due to multiple internal reflections and trapping of the infrared light. The efficiency of stacked or tandem cells will be high.

5 PHOTODETECTORS

The results for a better backside textured surface on a photodiode detector in the near infrared are not shown here. However results for a single pass of a 100 um thick epitaxial sample have been compared to backside texturing with total internal reflections at the front side and light trapping. The enhancement factor observed is at least a factor of twenty, the 100um backside textured sample appears like a 700um sample with no texturing. Multiple internal reflections without texturing but an ideal metal backside reflector will result in an enhancement factor from Eqn. 3 of about three. The 700um thick sample with no texturing but a backside metal reflector will then have an apparent of effective thickness of 2000um. The 100um sample could ideally have an enhancement of over 60 but in the practice this is

SIONYX1403000016.0098

SAMSUNG EX. 1002 - 1391/4148

limited by non-ideal losses so than the actual enhancement is around twenty and both samples have an apparent thickness of 2000um. This results in a useful absorption in silicon out to 1100nm or the indirect bandgap energy of silicon.

6 CONCLUSIONS

This paper describes a simple analysis technique and design considerations in the use of backside texturing to improve the near infrared(IR) response of silicon photodiodes, photodetectors, imagers and solar cells. A large enhancement in the absorption of infrared and near infrared light can be achieved in silicon photodetectors and solar cells with an optimum backside diffuse reflector. If the silicon substrates are thin then enhancement of the longer wavelength visible light components can also be achieved.

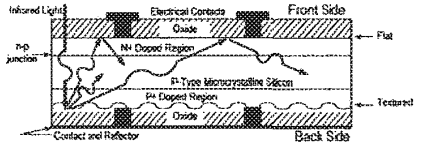

Fig. 3. Crystalline or microcrystalline silicon solar cell with textured backside and multiple internal reflections of infrared light, increased path length and enhancement of absorption of infrared light.

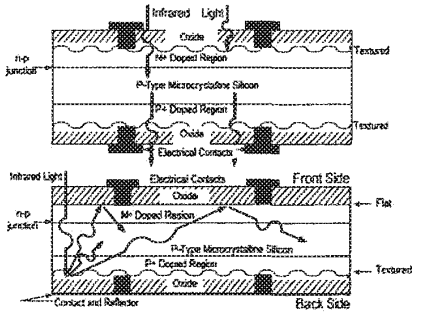

Fig. 4. Crystalline or microcrystalline stacked solar cells for absorption of visible light in the top cell and absorption of infrared light in the bottom solar cell. The top cell is transparent to infrared light.

REFERENCES

[1] US Patent 3,487,223 30 Dec. 1969 A.E. St John
[2] L. Forbes, Appl. Phys. Lett., submitted
[3] J.E. Cotter, J. Appl. Phys., **84**, 618(1998).
[4] O. Berger, D. Inns and A. G. Aberle, Solar Energy Materials & Solar Cells, **91** , 1215--1221(2007)
[5] R.A. Arndt, J.F. Allison, J.G. Haynos, and A. Meulenberg, Jr., 11th IEEE Photovoltaic Spec. Conf., 40(1975)
[6] E. Yablonovitch, and G.D. Cody, IEEE Trans. Electron Dev., **29**, 300 (1982).
[7] P. Campbell and M.A. Green, J. Appl. Phys., **62**, 243 (1987).
[8] E. Mazur et al., Appl. Phys. Lett., **78**, 1850 (2001).
[9] B. Vallejo, M. González-Mañas, J. Martínez-López and M.A. Caballero, Solar Energy, **81**, 565 (2007)
[10] S.A. Boden and D.M. Bagnall, SPIE Optics and Photonics, 74010J-1(2009).
[11] A. Goetzberger, J.C. Goldschmidt, M. Peters and P. Loper, Solar Enrgy Mtrls & Solar Cells, **92**, 1570 (2008).

SIONYX1403000016.0099

SAMSUNG EX. 1002 - 1392/4148

APPLIED PHYSICS LETTERS VOLUME 80, NUMBER 20 20 MAY 2002

Surface microstructuring and long-range ordering of silicon nanoparticles

J. D. Fowlkes and A. J. Pedraza[a)]
Department of Materials Science and Engineering, The University of Tennessee, Knoxville, Tennessee 37996-2200

D. A. Blom and H. M. Meyer III
High Temperature Materials Laboratory, Oak Ridge National Laboratory, Oak Ridge, Tennessee 37831-6064

(Received 14 November 2001; accepted for publication 21 March 2002)

Pulsed-laser irradiation was used to induce the formation of linear arrays of nanoparticles that can extend over millimeter distances. On flat surfaces, the irradiation induces the fragmentation and clustering of a thin silicon film pulsed-laser deposited on silicon into nanoparticles that grow to 30–40 nm in diameter. The nanoparticles aggregate into clusters that migrate, forming short curvilinear groups that exhibit a short-range ordering. If a region containing a microscopic roughness is introduced, the nanoparticles are forced to align into long and remarkably straight lines with line spacing very close to the laser wavelength. A close connection is established between the nanoparticle alignment and the evolution of laser-induced periodic surface structures. The microscopic roughness solely serves as a trigger to produce the alignment. © *2002 American Institute of Physics.* [DOI: 10.1063/1.1480106]

Nanosecond pulsed-laser deposition (PLD) is a simple and fast technique to grow nanoparticles.[1–6] The very high photon flux impinging on a target produces the ejection of a high density of neutral atoms, ions, and electrons. The background gas pressure confines the ejected material to a certain distance from the target.[7] As a consequence of the continuous scattering, clusters and nanoparticles are formed ahead of the target and projected in the forward and backward directions, and can be collected on a substrate or redeposited on the target. In this letter, we describe a method that employs pulsed-laser irradiation to induce the formation of sets of linear arrays of nanoparticles that extend over large areas.

Irradiations were done in a high-vacuum chamber using 25 ns pulses of a 248-nm-wavelength laser. To ensure a high-purity gas environment, the vacuum chamber was pumped to a base pressure of 1×10^{-7} Torr prior to each experiment. Helium gas, 99.999% pure, was the primary inert gas used for the experiments, although argon gas yielded results similar to those described below. Single-crystal (001) silicon substrates were etched in 10:1 HF solution prior to laser treatment to remove the native oxide layer.

In a first set of experiments, silicon was laser irradiated at a fluence in the range of 0.6–1 J/cm^2, under a background pressure of He ranging from 10^{-1} to 10^2 Torr. After 100 pulses, high-resolution scanning electron microscopy (HRSEM) showed a clear contrast in the irradiated region that suggested the formation of a thin film on the surface. An extremely thin film intermixed with very fine nanoparticles, ~1 nm diam, was already detected by atomic-force microscopy (AFM) after 50 pulses, contrasting with nonirradiated specimens that have an AFM measured roughness of less than 1 nm. The roughness increased with the number of laser pulses and after 100 pulses the irradiated region showed an irregular distribution of uneven regions several hundreds of nm in diameter separated by 3–8 nm deep crevices. An irregularly shaped film, ~10 nm thick and extensively fragmented, was observed on the target surface after 400 pulses, whereas no film or particles were detected when specimens were irradiated at the same fluence in vacuum. It is the presence of the He atmosphere that produces the backscattered atoms and, possibly, nanoparticles that originate the deposited film.[7] Auger emission spectroscopy (AES) of a film produced after 200 pulses showed that silicon oxide was present in the first nanometer. The elemental Si signal grew very strong within the next nanometer, yielding thereafter 90% concentration, while the Si signal from the oxide decreased to undetectable levels.

After additional irradiation, in some regions of the laser spot, the contrast associated with the film disappeared and it was in these regions where a high density of nanoparticles appeared. By contrast, in regions where the film is seen the density is much less, but the immediate vicinity of most of these nanoparticles is depleted of film. Presently, it is not clear whether the nanoparticles nucleate in the film itself and grow at its expense, or if very fine nanoparticles form during ablation in the gas phase and once deposited on the surface act as clustering centers consuming the film.

Using a high-precision SEM stage positioning mechanism the same sets of particles were identified and their relative locations were followed after each laser irradiation treatment. Nanoparticles of 30–40 nm diam aggregated into curvilinear strings. Upon additional irradiation, some strings have clearly changed their position relative to other strings. The displacement of nanoparticles does not lead to any particular long-range pattern on the surface. As they changed position, two important features were apparent: (i) the nanoparticles were seen to maintain their distinctive shape and (ii) no additional particles aggregated to the strings. The sets of nanoparticles rotated and bended, apparently tending to align like pearls in a necklace, as seen in Fig. 1. The resulting

a)Electronic mail: apedraza@utk.edu

 © 2002 American Institute of Physics
Downloaded 06 Jun 2004 to 128.103.60.225. Redistribution subject to AIP license or copyright, see http://apl.aip.org/apl/copyright.jsp

SIONYX1403000016.0100

SAMSUNG EX. 1002 - 1393/4148

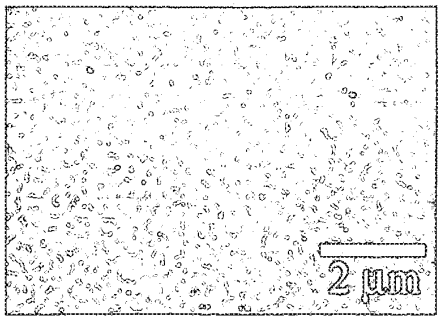

FIG. 1. HRSEM illustrating short-range ordering of silicon nanoparticles. Irradiation in 100 Torr He using 1000 pulses at E_d=1 J/cm^2.

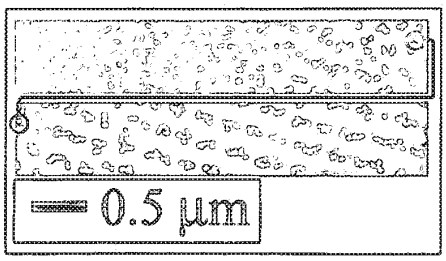

FIG. 3. SEM image showing the evolution, motion, and organization of nanoparticles into linear, well-organized arrays from a precursor silicon film. Substrate first irradiated in 650 Torr SF_6 with 2000 pulses (E_d =2.5 J/cm^2) to generate a cone/hole microstructure. Second irradiation followed in 100 Torr He with 200 pulses (E_d=1 J/cm^2).

structure has a short-range ordering in the sense that each nanoparticle has a high probability of having a first neighbor along a line and that each short line is separated from the next by a distance close to the wavelength of the incident light. Under the conditions of these experiments, laser-irradiation-promoted displacements of nanoparticles do not lead to any particular long-range-ordered pattern on the surface. The mechanism of nanoparticle motion is being investigated.

In another set of experiments, it was found that long-range ordering of nanoparticles occurs if a microhole–microcone structure is present. The cone array was produced first, by laser irradiating the single-crystal silicon substrates, typically, at 3 J/cm^2, in 375 Torr of SF_6.[8] Subsequently, the substrates were laser irradiated in the presence of an inert gas atmosphere under similar conditions as in the first set of experiments described above. The microcone–microhole structure occupied a rectangular area that was three times smaller than the area of the spot formed during the irradiation in He. The SF_6-treated region and the much larger region irradiated in He were chosen to be concentric. The cone microstructure remained essentially undisturbed during the irradiation under He because the laser fluence was much lower than the laser fluence used to generate the cones.

Figure 2 shows an image of the linear nanoparticle arrays formed inside the laser spot of the second irradiation cycle, adjacent to the area occupied by the cones. These arrays run over microscopic regions with few defects apparent in the array alignment. In some instances, the arrays extended over millimeter long distances, and were modestly curved over microscopic dimensions. The spacing between nanoparticle lines, as measured by SEM, was in many cases 248 nm, but it varied between 230 and 255 nm. A sevenfold increase in total gas pressure causes a twofold increase in the nanoparticle density. The average nanoparticle diameter seems to be independent of gas pressure, and remains in the range of 30–40 nm over the helium pressure range of 0.5–100 Torr.

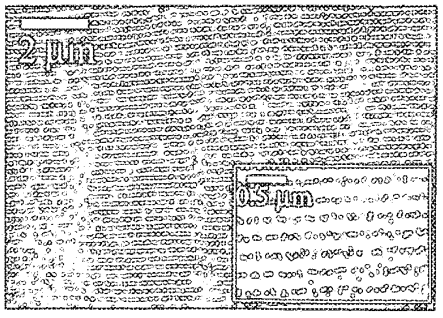

FIG. 2. SEM micrograph of a Si substrate first irradiated in 375 Torr SF_6 with 1500 pulses (E_d=3 J/cm^2) to generate a cone/hole microstructure. Second irradiation followed in 0.5 Torr He with 200 pulses (E_d =1 J/cm^2) producing the long-range nanoparticle ordering. Inset shows a higher magnification image of the silicon nanoparticle array.

The chemical composition of the nanoparticles was determined using AES. First, the substrate surface containing the linear arrays was Ar^+-ion sputtered to remove carbon surface contamination and the thin, SiO_2 surface layer that formed upon contact with air, exposing the inner core of the nanoparticles. After the sputtering, the substrate was tilted at a very steep angle to ensure that the electron beam reached only the nanoparticles. Quantitative analysis of the spectra following sputtering gave a chemical composition of ~3.5 at.% oxygen, indicating that most of the oxygen had been removed. More importantly, the only detected silicon signal was from elemental silicon.

Our experiments thus indicate a complex set of ablation-related phenomena: first a film forms and then nanoparticles form out of this film while the film is continuously being replenished during each ablation cycle. The nanoparticles grow larger with each laser pulse and it appears that they are required to reach a minimum size for the alignment to occur. Figure 3 is a collection of overlapping HRSEM images of a region close to the cone microstructure illustrating the progression from silicon film to fully developed nanoparticle array.

The spacing between nanoparticle lines has been precisely measured by AFM and found equal to the wavelength of the laser light, λ, when irradiation is performed at normal incidence, θ_i=0. AFM images also showed that the nanoparticles are located in valleys of a nanoroughness imprinted in the substrate. This nanoroughness is observed only in regions where nanoparticle alignment took place. These observations suggest that the alignment of nanoparticles could be associated with the laser-induced periodic surface structure (LIPSS).[9] Using polarized Nd:YAG laser light, Young *et al.*[9] observed that part of the damage pattern produced consists of parallel fringes with a spacing equal to $\lambda/(1 \mp \sin \theta_i)$. Also, similar to what it has been found for the LIPSS phenomenon,

Downloaded 06 Jun 2004 to 128.103.60.225. Redistribution subject to AIP license or copyright, see http://apl.aip.org/apl/copyright.jsp

SIONYX1403000016.0101

SAMSUNG EX. 1002 - 1394/4148

the alignment is initially observed just above the melting threshold, and occurs in a narrow laser fluence range. The models developed to explain LIPSS (Refs. 10–12) assumed the existence of a rough region naturally occurring on the surface of any specimen, confined to a much smaller scale than the laser light wavelength used to produce the periodic damage. The light scattered by this rough region interacts with the incident beam. The resulting interference would produce inhomogeneous energy deposition, and hence, LIPSS. It has also been found that the damage thus generated interacts with additional incident radiation, further reinforcing the initial effect.[13]

In the present case, the particles themselves seem to be acting as scattering centers, and the interaction between the scattered and the incident waves leads to nanoparticle ordering. The nanoparticles reach a maximum size of ~30 nm, which is almost one order of magnitude smaller than λ, and well within the roughness limits imposed by the LIPSS theory. For normal incidence the particles align along the rectangular beam (or laser aperture) short axis. For the laser beam used in these experiments, electric field E of the radiation along the beam short-axis direction is almost twice as intense as in the direction normal to it. Particles cluster and align along the maximum intensity of the incident radiation E field, independently of the specimen orientation relative to laboratory coordinates. It can be reasoned that as the nanoparticles align in the direction of the E field maximum intensity, the intensity modulation that results from the interference between "scattered" fields and the incident beam is intensified. This causes more nanoparticles to cluster on and along the lines, further reinforcing the initial effects.

In principle, light is scattered by each nanoparticle in all directions across the surface producing radial interference patterns with the incident beam. If many particles occur in a random distribution on the surface, a very complex interference pattern can develop, generating a structure with a short-range ordering as shown in Fig. 1. In this structure, although a tendency toward alignment can be seen, the structure becomes physically locked. The microcone/microhole structure seems to set off the organization of nanoparticles in its immediate vicinity. The role of scratches with a depth significantly less than the light wavelength in the formation of LIPSS has been well documented.[9] The cone structure has a dimension much larger than the laser wavelength, thus although the development of the aligned structure can be paralleled to LIPPS, its origin could be quite different. It is well documented that the microcone structure acts as a very good light absorber at wavelengths that include 248 nm,[14] and its role in the alignment phenomenon could be as a light absorber of part of the scattered laser light. We are actively investigating the self-organization mechanism prompted by this singular microstructure.

The question arises as to whether a surface perturbation as profound as the cone array is necessary to produce the long-range ordering. When a fine wire (100 μm in diameter) intercepting the beam was imaged on the substrate surface, the linear alignment of nanoclusters occurred as well, in the ridge of the first fringe of the pattern resulting from the diffraction of light by the wire. The nanoparticles became aligned in the direction of the E field maximum intensity *independently* of the orientation of the wire. Using a wire as an initiator of the nanoparticle alignment, the line spacing has been measured as a function of the angle of incidence of the laser beam. It was found that the spacing follows the law $\Lambda=\lambda/(1-\sin\theta)$, strongly emphasizing again the connection between LIPSS and the nanoparticle alignment phenomenon.

In summary, we have shown that pulsed-laser irradiation promotes fragmentation and clustering of a PLD silicon film, followed by the aggregation of very fine nanoparticles into ~30 nm clusters. The laser irradiation not only promotes cluster formation but also induces a *short-range ordering*. The presence of an extended rectangular region inside the laser-irradiated area having a microscopic roughness forces the nanoparticles to align along segments that can extend over millimeter distances. At normal laser beam incidence, *a line spacing equal to the laser wavelength characterizes this long-range ordering*. A close connection with the production of LIPSS is established.

This research was sponsored by National Science Foundation Grant No. DMR-9901238 and by the Oak Ridge National Laboratory, managed by UT-Battelle, LLC, for the U.S. Department of Energy under Contract No. DE-AC05-00OR22725.

[1] Y. Yamada, T. Orii, I. Umezu, and T. Yoshida, Jpn. J. Appl. Phys., Part 1 **35**, 1361 (1996).
[2] T. Yoshida, S. Takeyama, Y. Yamada, and K. Mutoh, Appl. Phys. Lett. **68**, 1772 (1996).
[3] T. Makimura, Y. Kunii, and K. Murakami, Jpn. J. Appl. Phys., Part 1 **35**, 4780 (1996).
[4] T. Makimura, T. Sakuramoto, and K. Murakami, Jpn. J. Appl. Phys., Part 2 **35**, L735 (1996).
[5] T. Makimura, Y. Kunii, N. Ono, and K. Murakami, Jpn. J. Appl. Phys., Part 2 **35**, L1703 (1996).
[6] D. H. Lowndes, C. M. Rouleau, T. Thundat, G. Duscher, E. A. Kenik, and S. J. Pennycook, J. Mater. Res. **14**, 359 (1999).
[7] D. B. Geohegan, in *Pulsed-Laser Deposition of Thin Films*, edited by D. B. Chrisey and G. K. Hubler (Wiley, New York, 1994), p. 115.
[8] A. J. Pedraza, J. D. Fowlkes, and D. H. Lowndes, Appl. Phys. Lett. **77**, 1629 (2000).
[9] J. F. Young, J. S. Preston, H. M. van Driel, and J. E. Sipe, Phys. Rev. B **27**, 1155 (1983).
[10] J. E. Sipe, J. F. Young, J. S. Preston, and H. M. van Driel, Phys. Rev. B **27**, 1141 (1983).
[11] Z. Guosheng, P. M. Fauchet, and A. E. Siegman, Phys. Rev. B **26**, 5366 (1982).
[12] S. R. J. Brueck and D. J. Ehrlich, Phys. Rev. Lett. **48**, 1678 (1982).
[13] J. F. Young, J. E. Sipe, and H. M. van Driel, Phys. Rev. B **30**, 2001 (1984).
[14] C. Wu, C. H. Crouch, L. Zhao, J. E. Carey, R. Younkin, J. A. Levinson, E. Mazur, R. M. Farrell, P. Gothoskar, and A. Karger, Appl. Phys. Lett. **78**, 1850 (2001).

Downloaded 06 Jun 2004 to 128.103.60.225. Redistribution subject to AIP license or copyright, see http://apl.aip.org/apl/copyright.jsp

SIONYX1403000016.0102

SAMSUNG EX. 1002 - 1395/4148

2D back-side diffraction grating for improved light trapping in thin silicon solar cells

Jo Gjessing,[1,2,3*] Erik Stensrud Marstein,[1,4] and Aasmund Sudbø[4,2]

[1] *Institute for Energy Technology, Pb 40, 2027 Kjeller, Norway*
[2] *University Graduate Center at Kjeller, Norway*
[3] *University of Oslo, Department of physics, Norway*
[4] *University of Oslo, Faculty of Mathematics and Sciences, Norway*
*jo.gjessing@ife.no

Abstract: Light-trapping techniques can be used to improve the efficiency of thin silicon solar cells. We report on numerical investigation of a light trapping design consisting of a 2D back-side diffraction grating in combination with an aluminum mirror and a spacing layer of low permittivity to minimize parasitic absorption in the aluminum. The light-trapping design was compared to a planar reference design with antireflection coating and back-side aluminum mirror. Both normally and obliquely incident light was investigated. For normal incidence, the light trapping structure increases the short circuit current density with 17% from 30.4 mA/cm^2 to 35.5 mA/cm^2 for a 20 μm thick silicon solar cell. Our design also increases the current density in thinner cells, and yields higher current density than two recently published designs for cell thickness of 2 and 5 μm, respectively. The increase in current may be attributed to two factors; increased path length due to in-coupling of light, and decreased parasitic absorption in the aluminum due to the spacing layer.

©2010 Optical Society of America

OCIS codes: (050.1950) Diffraction gratings; (350.6050) Solar energy.

References and links

1. F. Henley, A. Lamm, S. Kang, and L. Tian, "Direct film transfer (DFT) technology for kerf-free silicon wafering," Proc. 23rd PVSEC, Valencia Spain, 1090–1093 (2008).
2. J. Nelson, *The Physics of Solar Cells*, (Imperial College Press, London, 2003).
3. E. Yablonovitch, "Statistical ray optics," J. Opt. Soc. Am. 72(7), 899–907 (1982).
4. J. M. Gee, "Optically enhanced absorption in thin silicon layers using photonic crystals," Twenty-Ninth IEEE Photovolt. Spec. Conf., 150–153 (2002).
5. P. Sheng, A. N. Bloch, and R. S. Stepleman, "Wavelength-selective absorption enhancement in thin-film solar cells," Appl. Phys. Lett. 43(6), 579–581 (1983).
6. C. Heine, and R. H. Morf, "Submicrometeer gratings for solar energy applications," Appl. Opt. 34(14), 2476–2482 (1995).
7. M. T. Gale, B. Curtis, H. Kiess, and R. H. Morf, "Design and fabrication of submicron structures for light trapping in silicon solar cells," Proc. SPIE 1272, 60–66 (1990).
8. H. Sai, H. Fujiwara, and M. Kondo, "Back surface reflectors with periodic textures fabricated by self-ordering process for light trapping in thin-film microcrystalline silicon solar cells," Sol. Energy Mater. Sol. Cells 93(6-7), 1087–1090 (2009).
9. H. Sai, H. Fujiwara, M. Kondo, and Y. Kanamori, "Enhancement of light trapping in thin-film hydrogenated microcrystalline Si solar cells using back reflectors with self-ordered dimple pattern," Appl. Phys. Lett. 93(14), 143501 (2008).
10. H. Sai, Y. Kanamori, K. Arafune, Y. Ohshita, and M. Yamaguchi, "Light trapping effect of submicron surface textures in crystalline Si solar cells," Prog. Photovoltaics 15(5), 415–423 (2007).
11. R. Dewan, and D. Knipp, "Light-trapping in thin-film silicon solar cells with integrated diffraction grating," J. Appl. Phys. 106(7), 074901 (2009).
12. A. Čampa, J. Krč, F. Smole, and M. Topič, "Potential of diffraction gratings for implementation as a metal back reflector in thin-film silicon solar cells," Thin Solid Films 516(20), 6963–6967 (2008).
13. L. Zeng, Y. Yi, C. Hong, J. Liu, N. Feng, X. Duan, L. C. Kimerling, and B. A. Alamariu, "Efficiency enhancement in Si solar cells by textured photonic crystal back reflector," Appl. Phys. Lett. 89(11), 111111 (2006).

#119649 - $15.00 USD Received 6 Nov 2009; revised 24 Feb 2010; accepted 24 Feb 2010; published 3 Mar 2010
(C) 2010 OSA

SIONYX1403000016.0103

SAMSUNG EX. 1002 - 1396/4148

14. N.-N. Feng, J. Michel, L. Zeng, J. Liu, C.-Y. Hong, L. C. Kimerling, and X. Duan, "Design of Highly Efficient Light-Trapping Structures of Thin-Film Crystalline Silicon Solar Cells," IEEE Trans. Electron. Dev. 54(8), 1926–1933 (2007).
15. P. Bermel, C. Luo, L. Zeng, L. C. Kimerling, and J. D. Joannopoulos, "Improving thin-film crystalline silicon solar cell efficiencies with photonic crystals," Opt. Express 15(25), 16986–17000 (2007).
16. D. Zhou and R. Biswas, "Harvesting photons in thin film solar cells with photonic crystals," Mater. Res. Soc. Symp. Proc. 1101, (2008).
17. J. G. Mutitu, S. Shi, C. Chen, T. Creazzo, A. Barnett, C. Honsberg, and D. W. Prather, "Thin film solar cell design based on photonic crystal and diffractive grating structures," Opt. Express 16(19), 15238–15248 (2008).
18. C. Haase, and H. Stiebig, "Optical Properties of Thin-film Silicon Solar Cells with Grating Couplers," Prog. Photovoltaics 14(7), 629–641 (2006).
19. C. Haase, and H. Stiebig, "Thin-film silicon solar cells with efficient periodic light trapping texture," Appl. Phys. Lett. 91(6), 061116 (2007).
20. F.-J. Haug, T. Söderström, M. Python, V. Terrazzoni-Daudrix, X. Niquille, and C. Ballif, "Development of micromorph tandem solar cells on flexible low-cost plastic substrates," Sol. Energy Mater. Sol. Cells 93(6-7), 884–887 (2009).
21. J. Gjessing, E. S. Marstein, and A. Sudbø, "Modelling of light trapping in thin silicon solar cells with back side dielectric diffraction grating," Proc. 24th PVSEC, Hamburg Germany, 2604–2607 (2009).
22. http://software.kjinnovation.com/GD-Calc.html
23. L. Li, "Formulation and comparison of two recursive matrix algorithms for modeling layered diffraction gratings," J. Opt. Soc. Am. A 13(5), 1024–1035 (1996).
24. http://ab-initio.mit.edu/meep/
25. A. Taflove, and S. C. Hagness, *Computational Electrodynamics: The Finite-Difference Time-Domain Method*, (Artech House Publishers, Norwood MA, 2005).
26. J. D. Joannopoulos, S. G. Johnson, J. N. Winn, and R. D. Meade, *Photonic Crystals: Molding the Flow of Light*, (Princeton University Press, New Jersey 2008).
27. C. M. Herzinger, B. Johs, W. McGahan, J. Woollam, and W. Paulson, "Ellipsometric determination of optical constants for silicon and thermally grown silicon dioxide via a multi-sample, multi-wavelength, multi-angle investigation," J. Appl. Phys. 83(6), 3323–3336 (1998).
28. E. D. Palik ed., *Handbook of Optical Constants of Solids*, (Academic Press, San Diego, 1985).
29. http://rredc.nrel.gov/solar/spectra/am1.5/
30. M. A. Green, *Silicon Solar Cells – Advanced principles and practice*, (Centre for Photovoltaic Devices and Systems, Sydney, 1995).
31. H. A. Macleod, *Thin-Film Optical Filters*, (Institute of Physics Publishing, Bristol, 2001).
32. C. H. Henry, "Limiting efficiencies of ideal single and multiple energy gap terrestrial solar cells," J. Appl. Phys. 51(8), 4494–4500 (1980).
33. E. Schneiderlöchner, R. Preu, R. Lüdemann, and S. W. Glunz, "Laser-Fired Rear Contacts for Crystalline Silicon Solar Cells," Prog. Photovoltacis 10, 29–34 (2002).
34. http://www.mathworks.com/

1. Introduction

The cost per watt of solar cells needs to be reduced for solar electricity to become competitive with energy produced from fossil fuels. Thinner cells can reduce both the amount of material needed, and also demand on material quality, thereby reducing both production costs and energy consumption. Thin film technologies aim at reducing cost through decreased material consumption, but deposited thin film solar cells have inferior efficiency compared to the much thicker wafer based crystalline silicon (Si) cells. Recent discoveries have showed that it is also possible to make high quality crystalline Si substrates and solar cells with thickness down to 20 μm and below [1]. Although this approach holds much promise, one fundamental challenge must be overcome. Si exhibits an indirect band gap, and at this thickness a significant part of the light is lost due to insufficient absorption of the near infrared radiation. Thus, the decrease in cost obtained by using very thin Si substrates is offset by a decrease in efficiency. In order to avoid excessive optical losses, thin Si cells therefore need an efficient light-trapping scheme.

For monocrystalline Si the most common method in the industry today is alkaline anisotropic wet etching, which results in a random structure of pyramids [2]. This works well for [100] oriented wafers, but it is not as effective for the [111] orientation. This might pose a problem for wafers made by the technology used in [1] where wafers are [111] oriented. For multicrystalline Si, the use of isotropic acidic etches is more common. Especially the alkaline etching of monocrystalline Si has proved successful for front side light trapping. Both methods results in fairly large surface structures with sizes in the order of 2-10 μm. For deposited thin film Si cells, glass materials with textured transparent oxide coatings, are

#119649 - $15.00 USD Received 6 Nov 2009; revised 24 Feb 2010; accepted 24 Feb 2010; published 3 Mar 2010
(C) 2010 OSA

SIONYX1403000016.0104

SAMSUNG EX. 1002 - 1397/4148

popular substrates due to their potential for light trapping. These random structures have dimensions below 1 μm. Yablonovitch [3] showed that an ideal patterning with random total internal reflection, in the statistical limit would enhance absorption by $4n^2$, where n is the refractive index of the material ($4n^2$~50 for Si). However, it is not known whether nor how such ideal patterns can be fabricated.

Periodic structures have the potential of achieving better light trapping than random structures over a limited spectral range [4,5]. Periodic structures for light trapping in solar cells has been investigated earlier [5–7], and also in a number of recent works [8–19]. One type of such gratings is diffraction gratings made of metal. Such gratings are relative simple to fabricate. However, a problem with metal gratings is that they general suffer from strong narrowband absorption lines [7,12]. To overcome this problem, pure dielectric designs combining gratings and back reflectors made from Bragg stacks, have been proposed [13–17]. Zeng et al. [13] achieved good correspondence between the theoretical predictions and the measured short circuit current for a 5 μm thick c-Si solar cell. Low-cost fabrication of periodic structures has also been investigated. Haug et al. [20] made 2D structures on a low-cost substrate using hot embossing, while Sai et al. [8,9] has demonstrated a self ordered periodic structured back reflector with periods as small as 300 nm. With a period of 900 nm these structures showed better light-trapping properties than the Asahi U-type glass. The Asahi U-type glass is a state-of-the-art random texturing for thin-film solar cells. Most of the literature on the subject focuses on thin cells in the range of 0.5-5 μm. The effect of back-side light-trapping structures will in general be most prominent for such thin cells, due to low baseline absorption. Thicker cells on the other hand, will have the advantage that the solar spectrum that reaches the back side is more narrow-banded, which is an apparent advantage for periodic structures.

In [21] we presented a 2D-periodic back-side grating structure that combined a purely dielectric grating with a flat Al reflector, separated from the grating by a layer of SiO_2. The low refractive index of SiO_2 provides a large index contrast which gives the diffraction grating a spectrally broad response. Admittedly, air provides an even larger index contrast, but is impractical. In addition to reducing parasitic absorption in the Al, the oxide layer provides excellent surface passivation, a vital prerequisite for any highly efficient, thin, crystalline Si solar cell. High quality back-side surface passivation is especially important for thin cells where carrier excitation to a greater extent will occur close to the back side. In this paper we go into further details of the properties of the structure, and perform an optimization of the vital parameters grating period, fill factor, grating thickness and oxide thickness. We have also investigated how oblique incidence angle affects the light trapping properties. We focus in this work on a Si thickness of 20 μm, which is particularly relevant in the light of the recent findings of Henley et al. [1].

2. Numerical methods

To accurately predict the response of the back-side diffraction grating, rigorous electromagnetic modelling of the light is needed. Numerical modelling was performed with Grating Diffraction Calculator (GD-Calc) [22], a software package that uses rigorously coupled wave analysis (RCWA) [23]. GD-Calc is a fully vectorial solver and solves the Maxwell equations for a single frequency. The results from GD-Calc have been compared with results obtained with the software package Meep [24]. Meep uses the method of finite difference time domain (FDTD) [25,26] for solving the Maxwell equations numerically. Both methods (RCWA and FDTD) showed almost identical results for non-absorbing materials. However, with RCWA it is straightforward to analyze the strength of each diffraction order separately. This is imperative when analyzing the grating efficiency. Finally, RCWA is also better suited when the model structure contains layers with large differences in thickness.

There are at least two limiting cases that can be accurately described by simple scalar models for the propagation of light. These cases do not give us quantitative information about the light trapping design, but we have found the fast calculations allowed by the scalar models to be very useful in limiting the number of time-consuming RCWA simulations needed to do

#119649 - $15.00 USD Received 6 Nov 2009; revised 24 Feb 2010; accepted 24 Feb 2010; published 3 Mar 2010
(C) 2010 OSA

SIONYX1403000016.0105

SAMSUNG EX. 1002 - 1398/4148

the design. The fast calculations have allowed us to limit the size of the four-dimensional volume in parameter space that we had to map using RCWA simulations.

Figure 1 shows the structure that was modeled in GD-Calc. This structure has been compared with a reference model with equal thickness (e.g. 20 μm), single-layer AR coating, and a planar back-side Al mirror. Wavelength-dependent refractive index data (real and imaginary part) is used for absorbing materials (i.e. Si [27], Al and Ag [28]), while a refractive index of 1.5 and 1.95 is used for SiO_2 and Si_3N_4 respectively. The Si_3N_4 AR layer was designed to give a minimum reflectance at a wavelength just above 600 nm, which corresponds to a thickness of 78 nm.

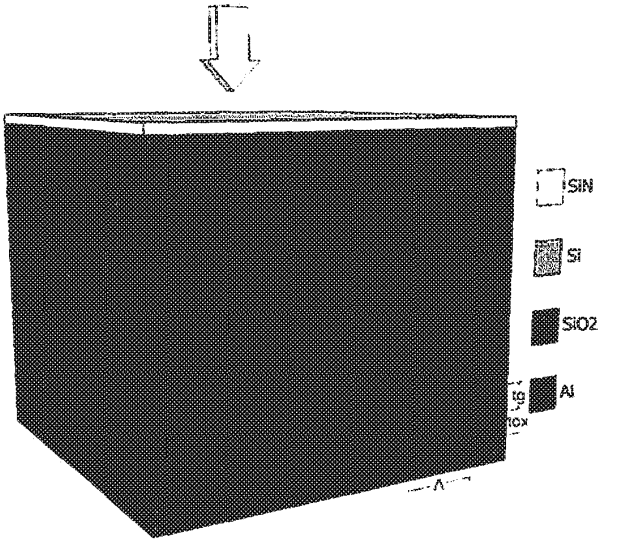

Fig. 1. Optical solar cell model structure used in the computations (not to scale). A single layer of Si_3N_4 is used as AR-coating. The reference structure is similar except that the SiO_2 and the grating layer are removed, and the Si is in direct contact with a planar Al-mirror.

A quantitative measure is needed for comparison of the different design parameters. The parameters as indicated in Fig. 1 are the grating period Λ, grating thickness t_g, thickness of the oxide layer t_{ox} and fill factor, here defined as the area covered by holes divided by the total area. A suitable measure of the performance of the structure is the short circuit current density (J_{sc}) excited by the AM 1.5 solar spectrum [29], which is calculated as shown in Eq. (1):

$$J_{sc} = q \int_0^\infty A(\lambda)\Phi(\lambda)d\lambda \qquad (1)$$

Equation (1) provides a limit for the maximum J_{sc} that would be obtained if all the generated electron hole pairs reach the contacts. Here, λ is the wavelength in [nm], q the elementary charge in [C], $A(\lambda)$ the absorbance which is a dimensionless wavelength dependent factor between zero and one, calculated by GD-calc and $\Phi(\lambda)$ is the spectral density of the photon irradiance with dimension [$s^{-1}m^{-2}nm^{-1}$] from the AM1.5 spectrum normalized so that the irradiance equals 1000 W/m^2. The integration is performed from 0 to ∞ but $\Phi(\lambda)$ is negligible for λ<300 nm while $A(\lambda)$ is negligible for λ>1100 nm due to the bandgap of Si.

Absorption in the Al-mirror may be substantial, but does not contribute to J_{sc}. This parasitic absorption is therefore subtracted from the total absorption. The decoupling of parasitic absorption from the absorption in the rest of the cell is calculated in a straightforward

#119649 - $15.00 USD Received 6 Nov 2009; revised 24 Feb 2010; accepted 24 Feb 2010; published 3 Mar 2010
(C) 2010 OSA

SIONYX1403000016.0106

SAMSUNG EX. 1002 - 1399/4148

manner in GD-Calc. The absorption is calculated by taking the difference in Poynting vector going into and out of the given plane.

Free carrier absorption (fca) [30] is not considered in this model. As long as the Si is lightly doped, as is common in the bulk Si, fca will not make a big contribution for solar cell applications.

3. Grating analysis

3.1 Grating equation

The most important property of the grating is to increase the path length of light inside the Si by coupling the light into higher diffraction orders. The angles of the diffracted orders are given by the two-dimensional grating equation. We use the word grating in this article to describe our bi-periodic pattern of cylinders as shown in Fig. 1. The direction of the incident beam may be described by the polar angle θ, defined as the angle between the beam and the normal to the plane, and the azimuth angle φ, which determines the orientation in the plane. The outgoing beam may be diffracted in either direction of periodicity and will be characterized by two diffraction orders m_x and m_y. For each pair of diffraction orders (m_x, m_y), the corresponding beam angles θ, and φ for the diffracted beam are different.

For a one-dimensional (linear) grating and an angle of incidence in the plane of periodicity, the grating equation takes the form of Eq. (2). The two-dimensional grating equation is a straight forward extension of the one dimensional equation.

$$n_o \sin(\theta_m) = n_i \sin(\theta_i) + \frac{m\lambda}{\Lambda} \tag{2}$$

n is the refractive index, θ the angle between the beam and the normal to the plane in the direction of periodicity (classical mount), Λ the grating period, λ the free-space wavelength, and m the diffraction order. m is also the subscript of the angle θ_m of the diffracted wave corresponding to diffraction order m. The incident beam and material have the subscript i while the outgoing material has the subscript o. In this case we have diffraction in Si, so that $n_i = n_o \approx 3.6$. From Snell's low of refraction, the critical angle where total internal reflection will occur at a Si-air boundary is $\theta_c = \sin^{-1}(1/n_{Si}) \sim 16$ degrees. Light from the Si incident at the Si-air boundary at a larger angle will be totally internally reflected back into the Si. Adding layers of other materials between the Si and air does not change the critical angle for escape into the air.

From Eq. (2) we see that at normal incidence ($\theta_i = 0$) the angle of the diffracted beam is given by $\sin(\theta_m) = m\lambda/(n\Lambda)$. For small periods (i.e. $\Lambda<\lambda/n$) the equation has a real solution only for the zeroth order ($m=0$), i.e. specular reflectance. If the period is larger than the wavelength of light, the angle of the lower diffraction orders will become too small to efficiently increase the path length, and the lowest diffraction order will also lie in the escape cone of Si (~16 degrees). This limits the optimal grating period to the interval $\Lambda \in (\lambda / n_{Si}, \lambda)$.

Since the terrestrial solar spectrum contains a wide band of wavelengths we define a mean wavelength $\bar{\lambda}$ as shown in Eq. (3):

$$\bar{\lambda} = \frac{\int_0^\infty \lambda(A_{base}(\lambda) - A_{opt}(\lambda))\Phi(\lambda)d\lambda}{\int_0^\infty (A_{base}(\lambda) - A_{opt}(\lambda))\Phi(\lambda)d\lambda} \tag{3}$$

A_{base} is the absorbance of light through a slab of thickness L (i.e. [1-exp(−2α(λ)L]). The factor 2 in the exponential derives from assuming a perfect back-side reflector, which doubles the path length of the light. A_{opt} is the optimum absorbance given by the Yablonovitch limit [3] for the same thickness, so that the factor 2 is replaced by $4n_{Si}^2$. The light which is absorbed in an optimal cell, but is not absorbed in the baseline cell, is of most relevance when optimizing the periodic structure. Equation (3) gives a weighted distribution that goes to zero for both

#119649 - $15.00 USD Received 6 Nov 2009; revised 24 Feb 2010; accepted 24 Feb 2010; published 3 Mar 2010
(C) 2010 OSA

SIONYX1403000016.0107

SAMSUNG EX. 1002 - 1400/4148

short and long wavelengths, and with a $\bar{\lambda}$ of 0.98 μm for a 20 μm thick Si slab. For simplicity, an ideal AR-layer with zero reflectance is assumed in this calculation.

3.2 Diffraction efficiency

The diffraction angles may be found from the grating equation, but the power distributed in each diffraction order is a sensitive function of the grating thickness t_g. A convenient measure of the suitability of the grating for light trapping purposes is the power fraction diffracted into higher orders, D_{HO}, which is a dimensionless number between zero and one, defined in Eq. (4) in the same way as in [10]:

$$D_{HO} = \sum_{m_x=-\infty}^{m_x=\infty} \sum_{m_y=-\infty}^{m_y=\infty} D_{m_x,m_y} - D_{00} \tag{4}$$

In order to calculate D_{HO}, a summation is done over all diffraction orders (m_x, m_y). Thereafter, the component in the zeroth order D_{00}, which represents specular reflection, is subtracted.

3.3 Large-period approximation

To maximize D_{HO}, the specular reflection power fraction D_{00} needs to be minimized. In the limit of a Λ much larger than λ, this is achieved by designing the grating thickness so that the reflection from the peaks and valleys of the grating interfere destructively. In a pure metal grating this is done by making the grooves $\lambda/4$ deep. In our design, however, the phase of the reflected light is dependent not only on the grating thickness t_g, but also upon the oxide thickness t_{ox}, which is the distance from the grating to the back-side Al-mirror. However, the principle of the $\lambda/4$ grating may be extended to the case of a multilayer structure by calculating the phase of the reflected wave from the peaks and valleys of the grating structure independently. The two phases can be calculated for two uniform multilayer slab structures, one representative for the peaks of the cylinders of Fig. 1, and the other representative of the space between the cylinders. For each slab structure, we used the method of transfer matrix [31] to calculate the phase of the reflected wave. This calculation is very much faster than an RCWA simulation.

3.4 Small-period (electrostatic) approximation

For small periods the light does not interact with the grating peaks and valleys independently. Instead, the EM-waves will behave as in a homogeneous material where the effective refractive index n_{eff} is determined by the distribution of the light between the low and the high dielectric. Thus, the phase of the light reflected from the grating structure behaves like the phase of the light reflected form a homogenous slab structure where the grating layer is replaced by a homogenous (so-called metamaterial) layer with an effective refractive index. Note that the grating structure will diffract light into higher orders as long as the period Λ is larger than λ/n_{Si}. Nevertheless we have found that we can use the small-period approximation to find the optimal grating thickness needed to minimize D_{00} also for Λ slightly larger than λ/n_{Si}. The thickness of the layers should be chosen so that the light reflected from the effective homogenous slab structure has a phase of π (or equivalently -π) relative to the top of the cylinders, referring to Fig. 1. With this condition satisfied D_{00} will be suppressed due to destructive interference. Again, the calculation of the effective refractive index of the metamaterials is much faster than an RCWA simulation.

4. Simulation results

4.1 Diffraction orders and phase plot

Figure 2 compares D_{HO} calculated with GD-Calc (a) as a function of t_g and t_{ox}, with the phase difference between grating peaks and valleys (b), as calculated for the large-period approximation explained above. The free space wavelength is 1 μm, while the period in the calculations with GD-Calc is 2 μm so it is closer to the large period regime than the small

#119649 - $15.00 USD Received 6 Nov 2009; revised 24 Feb 2010; accepted 24 Feb 2010; published 3 Mar 2010
(C) 2010 OSA

SIONYX1403000016.0108

SAMSUNG EX. 1002 - 1401/4148

period regime. The figure shows clear correlations between D_{HO}-maxima, and the parts of the phase plot where the phase difference is close to π (or equivalently $-\pi$). Increasing the period in GD-Calc to 5 μm gives an excellent correlation for the entire range of t_g, t_{ox} values shown in Fig. 2.

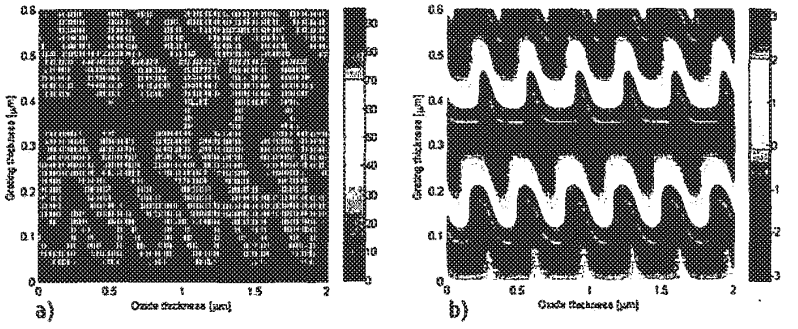

Fig. 2. Power fraction D_{HO} in higher-order diffracted beams (a), defined in Eq. (4) as a function of t_g and t_{ox} calculated with GD-calc using a period of 2 μm. (b) shows the phase difference between grating peaks and valleys calculated independently for the peaks and valleys by the transfer matrix method. A phase difference close to $+\pi$ or $-\pi$ indicates destructive interference at normal incidence, resulting in a corresponding maximum D_{HO}.

Figure 3 shows the small period case where the D_{HO} map (a) is calculated with a period of 0.3 μm (free-space wavelength of 1 μm), which is close to the minimum period that still allows higher diffraction orders to propagate in the Si superstrate. The phase map in Fig. 3(b) shows the reflected phase from a homogenous structure of layers where the grating layer is replaced by a slab of material with an effective refractive index n_{eff} of 3. We have written a Matlab [34] program to calculate the zero-frequency effective refractive index of a periodic pattern of parallel cylinders having the E-field perpendicular to the cylinder axes. We have used the standard angular harmonic solutions for Laplace's equation in cylindrical coordinates to set up a series expansion for the electric field, matched the electric field analytically at the surface of the cylinder, and imposed periodic boundary conditions by point matching of the electric field along the edges of a square unit cell. For this zero-frequency case we found a n_{eff} of 2.5 with a fill factor of 0.5. A general trend in the dispersion relation of the periodic structure is that the slope of the lowest band is reduced when the frequency increases. This corresponds to an increase in effective refractive index owing to accumulation of light in the dielectric with a high refractive index. Examples of such diagrams can be found in the book of Joannopoulos et a [26]. The discrepancy between the calculated value and the fitted value in Fig. 3(b) may be attributed to the fact that we are not comparing to a zero-frequency case. It is interesting to note that the grating structure has meta-material like properties also above the diffraction limit. For Λ between the two extreme cases, the D_{HO} map has features from both the small period phase map in Fig. 3 and the large period phase map in Fig. 2.

#119649 - $15.00 USD Received 6 Nov 2009; revised 24 Feb 2010; accepted 24 Feb 2010; published 3 Mar 2010
(C) 2010 OSA

SIONYX1403000016.0109

SAMSUNG EX. 1002 - 1402/4148

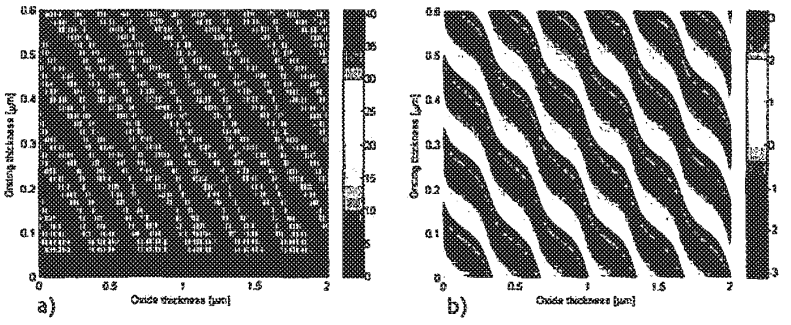

Fig. 3. (a) D_{HO} defined in Eq. (4) as a function of t_g and t_{ox} calculated with GD-calc using a period of 0.3 µm. Note that the magnitude of the higher order reflections is much lower than in figure Fig. 2(a). Figure 3(b) shows the phase plot of a reflected wave from a one dimensional stack of homogenous slabs where the grating layer have been substituted by a homogenous slab with an effective refractive index n_{eff} = 3. The calculation of phase is performed with the transfer matrix method.

The phase maps in Fig. 2(b) and Fig. 3(b) indicate the t_g and t_{ox} parameter space where we will expect to find D_{HO}-maxima. They also show us how the interactions between the layer thicknesses influence the positions of the maxima. However, the phase maps do not indicate the strength of the diffraction orders (as long as all phase maxima have the same phase e.g. ± π). In this case the analysis of the D_{HO} at the wavelength $\bar{\lambda}$ defined in Eq. (3) is a powerful tool. It provides the diffraction efficiency, and it can be performed without taking the 20 µm Si slab into account. The GD-calc simulations are faster without the slab on top. The presence of the slab with a thickness of many tens of wavelengths in the structure creates a need for a very fine wavelength sampling in every spectrum calculated, to be able to resolve the Fabry-Perot interference pattern from the 20-µm-thick Si slab. Correlation between the D_{HO}-map and absorption in the Si-slab is good, except that the D_{HO}-map seems to overestimate the light-trapping at shorter periods (not shown). To incorporate the effect of total internal reflections and secondary grating interactions simulations must be performed with the full model structure of Fig. 1.

4.2 Parasitic absorption

Al is the common choice as a back reflector for wafer based solar cells in industry today, mainly due to its low cost. However, Al reflectors suffer from a high absorption. Gratings may further enhance this problem by providing a means for coupling light to the reflector. To reduce parasitic absorption in the Al-mirror, we have placed a layer of SiO_2 between the grating and the Al mirror. Figure 4 shows the effect of t_{ox} on J_{sc} and parasitic J_{sc} (i.e. absorption current in the Al). We observe that the parasitic absorption in the Al, and therefore also the electric field strength in the Al, is only slightly effected by the thickness of the spacing layer for thicknesses above 0.2 µm. J_{sc} however continues to oscillate. This implies that it must be the *phase* of the light reflected from the Al that generates these oscillations. This is confirmed by seeing how the oscillations in J_{sc} match excellently with oscillations expected from Fabry-Perot interference in the oxide spacing layer. The same effect can also be seen in Fig. 2 and Fig. 3.

#119649 - $15.00 USD Received 6 Nov 2009; revised 24 Feb 2010; accepted 24 Feb 2010; published 3 Mar 2010
(C) 2010 OSA

SIONYX1403000016.0110

SAMSUNG EX. 1002 - 1403/4148

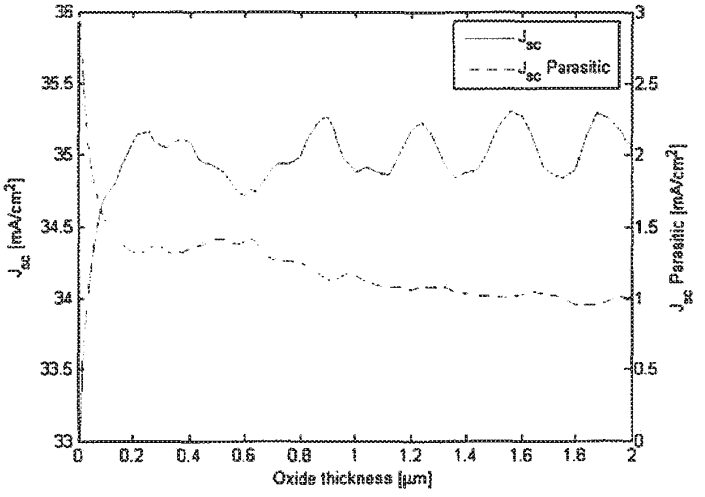

Fig. 4. The figure shows J_{sc} on the left axis, and parasitic absorption on the right axis as a function of thickness of the SiO_2 spacing layer t_{ox} between the grating and the Al mirror.

4.3 Short circuit current

Figure 5 displays a parameter scan over both Λ and fill factor for the full optical solar cell structure. A grating thickness t_g = 0.23 μm and spacing layer thickness t_{ox} = 0.2 μm was chosen on the basis of a D_{HO}-map similar to the ones shown in Fig. 2(a) and Fig. 3(a). We can see that highest values of J_{sc} are obtained over a broad parameter range with periods from 0.7 μm up to 1 μm. One should be aware that in general, for each t_g and t_{ox} we get a different version of Fig. 5, with different locations and values of the J_{sc} maxima. However, the highest J_{sc} values seem to be in the period range from around 0.6 μm to 1 μm also for other t_g and t_{ox} combinations (not shown). In addition, the trend that the ridges corresponding to high J_{sc} values moves towards higher period with increasing fill factor (most notable for small periods), remains the same also for other t_g and t_{ox} combinations. For thinner substrates Eq. (3) gives a smaller $\bar{\lambda}$, and the locations of the maxima in Fig. 5 will shift towards shorter periods.

#119649 - $15.00 USD Received 6 Nov 2009; revised 24 Feb 2010; accepted 24 Feb 2010; published 3 Mar 2010
(C) 2010 OSA

SIONYX1403000016.0111

SAMSUNG EX. 1002 - 1404/4148

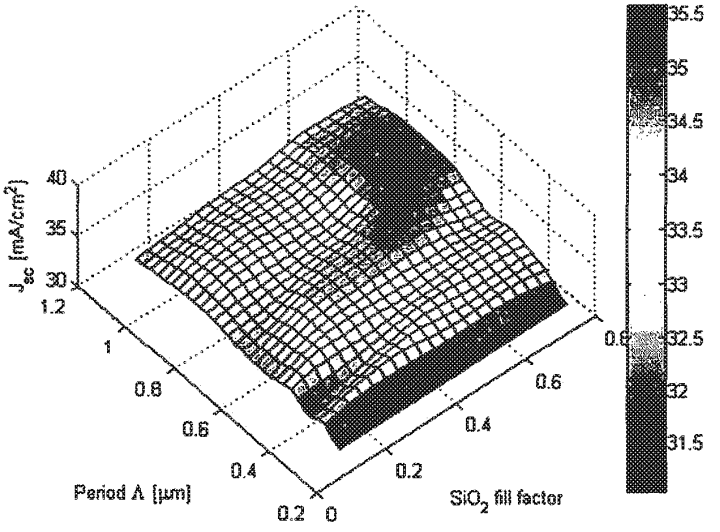

Fig. 5. The figure shows J_{sc} for different combinations of grating period Λ and fill factor for a grating thickness $t_g = 0.23$ μm and a spacing layer thickness $t_{sl} = 0.2$ μm.

For Λ outside the interval $\Lambda \in (\lambda / n_{Si}, \lambda)$ described earlier, J_{sc} drops significantly. For smaller periods J_{sc} drops because only the zeroth diffraction order remains and $D_{OH} = 0$. For periods larger than 1 μm there are still higher orders that may be diffracted at large angles, so the cut-off is not as sudden as the cut-off for small periods.

In Fig. 6 the spectral absorbance in the light-trapping structure from Fig. 1 is compared with the spectral absorbance in a reference cell having equal thickness and AR-coating, but a planar back side Al reflector. The figure shows a significant improvement in the wavelength range from 0.8 to 1.1 μm. At wavelengths below 0.7 μm there is no discernable difference in the absorption, and the front side reflectance is the limiting factor. Figure 6(a) shows the rapid Fabry-Perot oscillations resulting from interference in the 20 μm thick Si slab. A time-consuming dense wavelength sampling is required to resolve the oscillations. Analysis of the D_{HO} is therefore an efficient way to do a faster analysis of the structure. In Fig. 6(b) one can see remnants of these oscillations, after they have been reduced with the help of a digital low-pass filter (a moving average), for easier comparison of the curves.

#119649 - $15.00 USD Received 6 Nov 2009; revised 24 Feb 2010; accepted 24 Feb 2010; published 3 Mar 2010
(C) 2010 OSA

SIONYX1403000016.0112

SAMSUNG EX. 1002 - 1405/4148

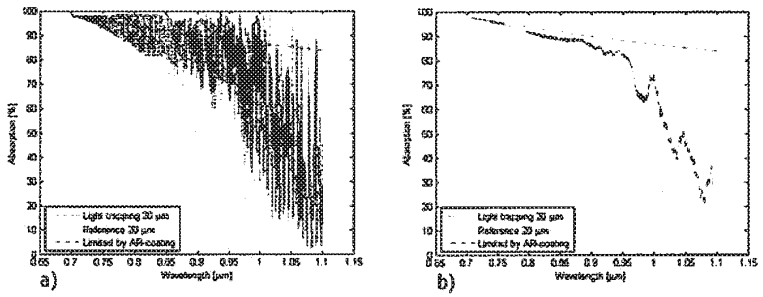

Fig. 6. The figure shows absorption as a function of wavelength for the light-trapping design (solid line) and the reference (dotted line), compared to the limitation imposed by the front-side reflectance from a single layer AR-coating on top of an infinite Si slab (dashed line). (a) shows the simulated spectral response, and (b) shows a moving average of the same data. A A of 0.7 µm, fill factor of 0.6, t_g of 0.23 µm and t_{ox} of 0.2 µm are used for the light trapping structure.

In Table 1 the absorbance in Fig. 6 is inserted in Eq. (1) to calculate the J_{sc}. We see that the light-trapping structure with Al reflector holds the potential to improve J_{sc} by 5.1 mA/cm^2, or 17% relative, compared to a 20 µm thick reference cell.

Table 1. Comparison of J_{sc} for different model structures assuming all excited charge carriers reach the contacts. The spectral response of the 20 µm reference and the light-trapping structure with Al-reflector is shown in Fig. 6. The same parameters are used for all light trapping three cells, varying only the back side reflector. The AM 1.5 absorbance is the percentage of the photons in the wavelength interval 300-1100 nm which are absorbed in the Si.

Structure	J_{sc} [mA/cm^2]	AM 1.5 absorbance
Light trapping 20 µm – ideal reflector	36.1	83.0%
Light trapping 20 µm – Ag reflector	35.9	82.5%
Light trapping 20 µm – Al reflector	35.5	81.6%
Reference 20 µm	30.4	69.9%
Reference 160 µm	36.6	84.1%

The reflectance of Ag is in general significantly better than for Al. Table 1 show us that we will gain 0.4 mA/cm^2 by replacing the Al reflector in Fig. 1 with Ag. Actually, the parasitic J_{sc} is reduced by 0.7 mA/cm^2 for the Ag reflector (not shown), but only a bit more than half of this is contributing to the J_{sc}. For a perfect reflector the J_{sc} reaches 36.1 mA/cm^2. The light-trapping cell with Al reflector from Table 1 actually achieves the same J_{sc} as a 5 times thicker planar reference cell with the same AR coating and an Al reflector. This is equivalent to an average absorption length of 180 µm in silicon, or an increase in optical thickness by a factor of 9. In other words, the number of photons absorbed in the light-trapping cell with an Al reflector is the same as what would be absorbed in the first 180 µm of an infinitely thick Si-slab with the same AR-coating as the light-trapping cell. The light-trapping structure with Ag reflector increases optical thickness by a factor of 11.

4.4 Comparison with literature

Comparison with different light-trapping concepts is not straight forward due to the differences in cell design, thickness, surface structures, and material and cell materials. To further complicate the picture, different authors use different parameters to describe the effect of their light-trapping design. Quantitative comparison of back-side light-trapping structures with AR-structures is unsuitable since the back-side structures address only the part of the solar spectrum that reaches the back side, while AR-structures address the whole solar spectrum. The predicted light-trapping effect in solar cells for periodic structures have been confirmed experimentally by other authors for 1D gratings [13,18]. No such comparison has

#119649 - $15.00 USD Received 6 Nov 2009; revised 24 Feb 2010; accepted 24 Feb 2010; published 3 Mar 2010
(C) 2010 OSA

SIONYX1403000016.0113

SAMSUNG EX. 1002 - 1406/4148

been found for 2D gratings. However, a 2D Al dimple pattern was recently compared to one of the best random structures available, and showed good results [9].

Most of the relevant data from literature focus on thinner cells. For comparison purposes we have modeled the light trapping response of our periodic structure on thinner cells. However, a separate optimization of AR-coating or grating parameters for the given thickness has not been performed. Therefore, a further improvement of light trapping could be expected from our structure by performing the optimization for the given thickness.

Mutitu et al. [17] found a J_{sc} of 30.3 mA/cm^2 for a 5 μm thick c-Si cell including both a 1D triangular shaped back-side grating with a dielectric Bragg reflector, and a front side binary grating with a double layer AR-coating. A J_{sc} of 27.4 mA/cm^2 was obtained with no front-side grating, and a binary grating together with the Bragg reflector on the back side. We obtain an equivalent J_{sc} (30.3 mA/cm^2) with a planer front-side AR-coating and our back-side structure. We observe that parasitic absorption in the Al-reflector has more than doubled at this thickness compared to the 20 μm cell. The use of Ag back reflector would be more advantageous at this thickness than for the 20 μm thick cell.

Bermel et al. [15] modeled a 2 μm c-Si cell with a dielectric Bragg back-reflector in combination with different types of periodic light scattering structures. Bermel used Henry's model [32] for radiative recombination as a loss mechanism, to get efficiency from J_{sc}. Bermel's best result was obtained for a 2D triangular back-side cylinders pattern, and showed an efficiency of 16.32% corresponding to a J_{sc} of 23.9 mA/cm^2 for a lossless model like ours. With our structure and the Al back reflector applied to a 2 μm thick cell we obtain a J_{sc} of 26.4 mA/cm^2, or an improvement of 10% over Bermel's structure.

4.5 Angular dependence

For non-tracking solar panels the angle of the incident light (i.e. the sun) varies with time. Thus, it is of great interest to study the response of the light-trapping structure at different incidence angles. The angle of incidence is in general specified by the polar angle θ and the azimuth angle φ. We have studied the effect of θ on the J_{sc} while keeping φ fixed so that the incidence plane is along one of the directions of periodicity. Both s-polarization and p-polarization are considered. For s-polarization the E-field is transverse to the normal of the layer structure, while for p-polarization the E-field is in the plane of incidence. The solar irradiance is unpolarized, thus the light incident at the solar cell contains equal amounts of s- and p-polarization. In real life, the solid angle captured by the module (as seen from the sun) decreases with $\cos(\theta)$. Small angles of incidence will therefore be relatively more important with respect to power generation than larger angles of incidence. In Fig. 7 a constant solid angle is assumed, so that each angle represents a solar panel with a different area.

Figure 7 shows the angular dependence of J_{sc} for both the light-trapping structure and the reference cell. Contrary to what one might assume, the average J_{sc} increases with incidence angle for both cell structures. For the light-trapping cell J_{sc} is notably higher at angles around 10 - 20 degrees than at normal incidence, before it starts to drop steadily cell for higher θ. The reference cell has a smaller J_{sc} increase at small θ, but it lasts all the way to 55 degrees.

#119649 - $15.00 USD Received 6 Nov 2009; revised 24 Feb 2010; accepted 24 Feb 2010; published 3 Mar 2010
(C) 2010 OSA

SIONYX1403000016.0114

SAMSUNG EX. 1002 - 1407/4148

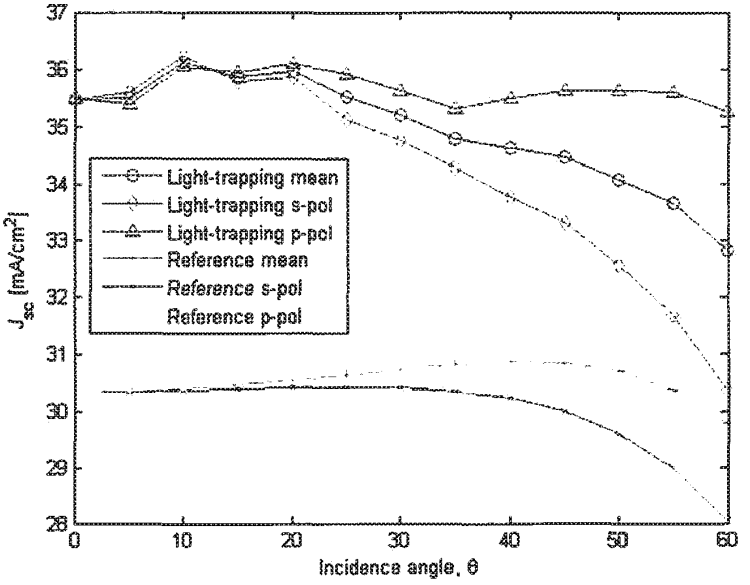

Fig. 7. The figure shows the effect of incidence angle on J_{sc} for the cell with light-trapping structure and for the reference cell. Both p-polarization and s-polarization and their mean are shown.

The increase in J_{sc} for the reference cell can be explained by the Brewster angle effect, where front-side reflectance will be reduced towards zero for p-polarization. The light-trapping cell will experience the same Brewster angle effect at the front surface. However, the improvement in J_{sc} is more than what would be expected from this effect at small θ while J_{sc} is significantly lower where the Brewster effect is at its strongest. An increase in J_{sc} at small θ was also reported in [17] for a 1D line grating. We believe this increase might be attributed to less out-coupling of light due to the reduced symmetry at oblique incidence. The problem of out-coupling is discussed in [6].

Varying the incidence angle θ_i in the grating equation (i.e. Eq. (2)) will also change the angles of the outgoing modes in the same plane. By inserting $\bar{\lambda}$ from Eq. (3) into Eq. (2) we find that at an incidence angle $\theta_i = 23.5$ degrees, the $m = -1$ mode (in the same plane) will no longer be totally internally reflected at the front surface. This gradual escape of diffraction orders is an effect which may explain parts of the reduction in J_{sc} that we observe for the light-trapping structure.

5. Discussion

Due to the recent advances in crystalline Si substrate manufacture described above, we have chosen to focus our attention on Si cells with a thickness of 20 μm. This is considerably thinner than state of the art wafer-based cells today (around 160 μm), but also well above the common thin-film technologies with layer thickness of only a few microns. The relative gain by adding a light trapping structure will of course be larger the thinner the cell, and most of the earlier works focus on cells significantly thinner than 20 μm. However, an advantage of the semi-thin (e.g. 20 μm) cells investigated in this work is that the spectrum of the light that is transmitted to the back side is narrower than for thinner cells, due to significantly stronger

#119649 - $15.00 USD Received 6 Nov 2009; revised 24 Feb 2010; accepted 24 Feb 2010; published 3 Mar 2010
(C) 2010 OSA

SIONYX1403000016.0115

SAMSUNG EX. 1002 - 1408/4148

absorption at shorter wavelengths. It is therefore possible to optimize the light trapping effect for the narrow spectral range that reaches the back side of the 20 μm thick Si-slab. Periodic structures are particularly well suited for this purpose, since they can easily be exploited to make a narrowband trapping response.

In general, the parasitic absorption in a metal mirror is higher, the higher the index of refraction is in the adjacent dielectric where the light propagates. The SiO_2-Al boundary reduces parasitic absorption of light in the metal compared to a Si-Al boundary. Another vital effect of the SiO_2-layer is to move the metal away from the grating, so that the evanescent waves from the grating that reach the metal are weaker. As we saw in Table 1, Ag may help to further reduce the parasitic absorption. However, the improvement of 1.1% by replacing the Al mirror with Ag is not as large as one would expect by looking at the reflecting properties of the two materials. The reason for this we believe to be that our structure is optimized both for light scattering and for reduced absorption, thus maximizing J_{sc}. We should point out that we have just simulated the performance of an Ag mirror used with a grating structure optimized for an Al mirror; we have not optimized the grating structure for an Ag mirror. The advantages of using Al as a back reflector instead of Ag are not just the material costs, but also that Al is directly compatible with the laser fired contact process [33], which is one obvious way of making the electrical contact at the back side of the cell.

We have focused in this work on binary cylindrical geometries with oxide cylinders in silicon as shown in Fig. 1. Binary structures have the advantage of requiring relatively short computation times with RCWA compared to more complex geometries. In addition they may be fabricated using conventional silicon micro-fabrication technology. The simplicity of such a binary system is also favorable for analyzing the interactions between light and the grating structure. Other geometries may possibly hold the potential for even more efficient light trapping. For example, it has been shown that blazed gratings perform better than binary gratings for a 1D structure when the grating structure was applied to both the front and the back side [6,18].

We have investigated different cylinder configurations; triangular lattice instead of square, and silicon cylinders instead of oxide cylinders. We found no significant difference in the maximum J_{sc} between the different configurations. We have found that a SiO_2 fill-factor above 0.5 (i.e., oxide cylinders with radius above 0.4A or Si cylinder with radius below 0.4A) is favorable for silicon cylinders as well as for oxide cylinders. On the other hand, Fig. 5 shows that there is a wide range of different periods and fill factor combinations that have the potential of providing a high J_{sc}. This freedom in design with respect to period, fill factor and material may be an advantage with respect to fabrication.

To further increase the light trapping a better AR-coating is needed. A double layer AR-coating would add more than 1 mA/cm^2 to all the J_{sc}-values of Table 1. Encapsulating the cell would also help reduce the front side reflectance by making the change in refractive index more gradual. To reduce the reflectance further, a front-side texturing of some sort is usually applied. Configurations with a 1D front and back-side periodic grating have been shown to increase light trapping compared to configurations with only a 1D back-side grating [11,17]. The effect of a randomly structured front side, however, is difficult to assess. Simulation of random structures with the RCWA method are very slow, because they are typically done with the help of very large unit cells that are many wavelengths on the side, but with adequate resolution to resolve the periodic structures.

6. Conclusion

We have presented a light-trapping design for a solar cell, incorporating a back-side bi-periodic pattern of silica (SiO_2) cylinders combined with a layer of SiO_2 to detach the grating from the back-side Al mirror. The grating increases the coupling of light into the Si solar cell, while the layer of SiO_2 reduces the parasitic absorption in the Al mirror and ensures a good surface passivation. Simple design criteria for optimizing grating performance have been presented. In particular the interaction between the EM-waves in the grating layer and oxide layer has been investigated for two extreme cases (i.e. large periods and short periods),

#119649 - $15.00 USD Received 6 Nov 2009; revised 24 Feb 2010; accepted 24 Feb 2010; published 3 Mar 2010
(C) 2010 OSA

SIONYX1403000016.0116

SAMSUNG EX. 1002 - 1409/4148

showing good agreement between fully vectorial EM-field simulation results and simple scalar optical field models. The scalar models are very helpful in limiting the parameter space for the numerical simulations. We have performed numerical simulations to quantify the light trapping in terms of the short circuit current density. Our simulations show that for an optimized 20 μm thick Si solar cell, a short circuit current density of 35.5 mA/cm^2 would be obtained if all the charge carriers are collected at the contacts. This is an increase of more than 17% compared to a reference cell with the same thickness and a planar back-side Al mirror. Our design is also effective for thinner cells, and we see an improvement compared to two recently published papers for cell thicknesses of 2 and 5 μm, respectively. The light-trapping design presented shows promising behavior over a wide range of incidence angles. To further improve the light trapping, the front-side reflection should be reduced.

Acknowledgments

The author acknowledges the Nordic Center of Excellence in PV and the Norwegian Research Council through the Nanomat program for the financial support.

#119649 - $15.00 USD Received 6 Nov 2009; revised 24 Feb 2010; accepted 24 Feb 2010; published 3 Mar 2010
(C) 2010 OSA

SIONYX1403000017.0001

SAMSUNG EX. 1002 - 1410/4148

2D blazed grating for light trapping in thin silicon solar cells

Jo Gjessing[1,2,3], Aasmund Sudbø[4,2], Erik Stensrud Marstein[1,4]
[1] *Institute for Energy Technology, Pb 40, 2027 Kjeller, Norway*
[2] *University Graduate Center at Kjeller, Norway*
[3] *University of Oslo, Department of physics, Norway*
[4] *University of Oslo, Faculty of Mathematics and Sciences, Norway*
Corresponding author e-mail address: [illegible]

Abstract: We propose a novel sub-micron back-side grating for light trapping in thin silicon solar cells. The 2D-blazed grating has the potential to increase the optical thickness of the solar cell by a factor of 17.
©2010 Optical Society of America
OCIS codes: (050.1970) Diffractive optics; (350.6050) Solar energy.

1. Introduction

Decreasing the thickness of Si solar cells appears to be one of the most promising ways of reducing the cost of solar electricity. Methods for making crystalline Si substrates with a thickness below 20μm, well below the 150 -200 μm commonly used today, have recently been demonstrated, using lift-off techniques based on proton implantation [1]. However, due to the poor absorption of crystalline Si in the near-infrared spectrum, light trapping is essential to avoid optical losses in such thin substrates.

The surface textures commonly used in the relatively thick cells of today are in general not suitable for cell thicknesses below 20μm, because of the large feature size of these textures (2-10 μm). For thin-film cells, typically having thicknesses on the order of 1 μm, textures of front side oxides have been developed. All of these textures are of a random nature. Yablonovitch [2] showed that for an ideal randomizing structure, the maximum theoretical intensity increase for a weakly absorbing material with an index of refraction of n is $4n^2$ (~50 for Si). In actual fabricated cells, this factor is more in the range of 10 [3]. Periodic structures have the potential to exceed the limit of the randomizing textures [4], and seem promising for light trapping in thin Si solar cells, as verified through both theoretical [5] and experimental studies [6].

According to Heine and Morf [7], a blazed 1D grating (i.e., regular grating with straight parallel grooves) on the back side of a solar cell is beneficial for light trapping. This is attributed to a reduced out-coupling of light by avoiding mirror symmetries in the grating. Unfortunately, a 1D grating can trap only one of the two polarizations present in sunlight efficiently. We overcome this limitation by designing a novel 2D blazed back-side grating structure with excellent light-trapping properties. In addition to the 2D blazed grating, our light-trapping scheme consists of a back-side Al mirror separated from the grating by a thin layer of SiO_2, as shown in [8]. The purpose of the SiO_2 layer is to reduce the absorption in the back-side metal by reducing the electromagnetic coupling from the Si and the grating to the metal. SiO_2 is also excellent for passivation of Si, which is especially important in thin crystalline Si solar cells, where more of the generation of charge carriers will occur close to the back side.

2. Methodology

Figure 1 shows the total, optical model structure that we have investigated numerically. We performed the electromagnetic computation with Grating Diffraction Calculator (GDC) [9]. GDC uses rigorously coupled wave analysis (RCWA), wherein the Maxwell equations are solved independently in horizontal layers in the Fourier space, before the solutions are coupled with the specific boundary conditions. This method is especially effective for computations where there are large differences in the thicknesses of the individual layers. The oblique planes of the blazed grating are represented by a staircase structure consisting of 10 steps.

We have optimized the structure by varying the following three different parameters illustrated in Figure 1; the grating period Λ, the grating thickness t_g, and the thickness t_{ox} of the oxide layer separating the grating from the back side metal. To limit the necessary computational time, the three-dimensional parameter scan was performed for an infinitely thick Si slab for a single wavelength. From the parameter scan we analyzed the diffraction into higher orders D_{HO} given by Eq. (1).

SAMSUNG EX. 1002 - 1411/4148

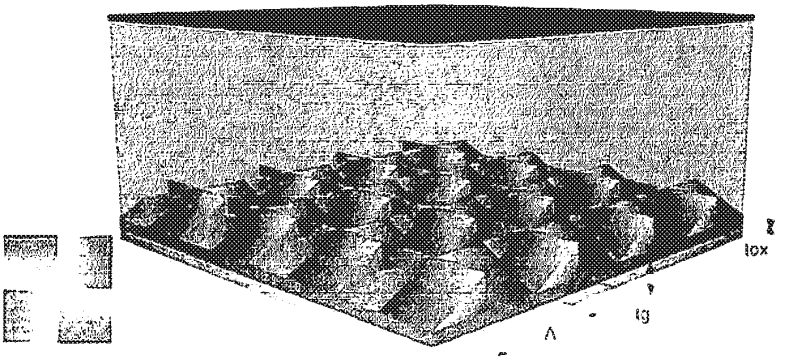

Figure 1: Model of the 2D blazed structure. Each unit cell consists of 4 quadrants with oblique planes sloping in different directions. The inset shows a false-color representation of one unit cell viewed from above, with color representing height. Beneath the grating is a layer of SiO_2, and an Al mirror. Above the grating is a 20 μm thick Si-slab with an anti-reflection coating. The model is not to scale.

$$D_{HO} = \sum_{m_x} \sum_{m_y} D_{m_x m_y} - D_{00} \qquad (1)$$

The summation is performed over a finite number of diffraction orders (m_x, m_y). Evanescent (non-propagating) diffraction orders transfer no power in a lossless Si slab, so all the power is contained within the propagating diffraction orders. The zero order (specular) reflection D_{00} is subtracted to get the power diffracted into higher orders. This method is useful for locating potential maxima where in-coupling is high and back-side absorption low. However, D_{HO} does not reveal the angles of diffraction and internal distribution of power between the higher diffraction orders. Neither will effects such as out-coupling be identified in the process. The maxima must therefore be explored in further detail before running the full structure computations.

We use the maximum short circuit current density J_{sc} (assuming that all photo-generated charge carriers are collected at the contacts) to quantify the light-trapping effect. J_{sc} is found by weighting the spectral absorption calculated with GDC with the photon flux from the AM1.5 spectrum corresponding to 1000 W/m^2. The integration needed to obtain J_{sc} is performed from 300 nm to 1100 nm due to low solar irradiance or absorption values outside this interval.

To study the effect of back-side absorption and front side reflection, we have investigated both Al and Ag mirrors and single- and double-layer antireflection coatings (SLAR and DLAR). Wavelength dependent optical data is used for Si [10], Al and Ag [11]. For the SLAR we used Si_3N_4 with a refractive index of n=1.95 and a thickness of 78 nm. The DLAR consisted of 108 nm of magnesium fluoride (MgF_2, n=1.37) and 60 nm of zinc selenide (ZnS, n=2.35).

3. Results and discussion

The maximum J_{sc} for the 2D blazed grating was found for a period Λ=0.95 μm, t_g =0.4 μm and t_{ox}=0.1μm. The spectral absorption with these parameters is shown in Figure 2. The corresponding J_{sc} is 36.8 mA/cm^2, which is more than 20 % higher than for the reference cell also shown in Figure 2. It is interesting to note that the spectral absorption makes a leap at exactly 950 nm, which is also the period of the grating. For wavelengths larger than the period, only the zeroth order is allowed to propagate in air, which reduces the number of allowed escape modes for the light. The resulting J_{sc} for the different configurations are summed up in Table I.

From Table I we see that a 20 μm thin solar cell with the light trapping supplied by the 2D blazed grating structure can produce more current than the 8 times thicker 160 μm reference cell. This is found to correspond to an increase in optical thickness of a factor of 17. In other words, an absorbing Si-slab with the same AR-coating would need a thickness of 340 μm to absorb the same amount of photons as the 20 μm thick cell with 2D blazed grating and

SAMSUNG EX. 1002 - 1412/4148

Al-mirror. This increase in optical thickness also implies that the light will have several interactions with the back side, thus the reflectivity of the mirror will be of special importance. Changing to a higher reflectivity metal like Ag reduces the parasitic absorption from 1.3 mA/cm^2 to 0.5 mA/cm^2 (not shown) giving a J_{sc} of 37.3 mA/cm^2, or equivalent to an increase in optical thickness of 22.

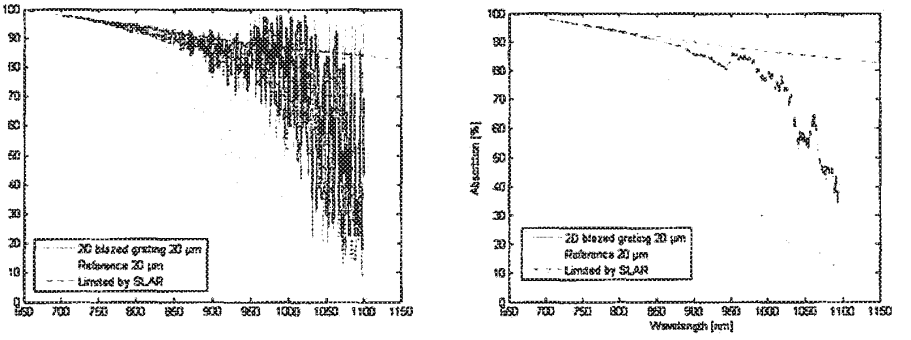

Figure 2: To the left is the spectral absorption in a 20 µm thick Si-cell with a 2D blazed grating with Al-mirror and SLAR (solid), the estimated absorption in a reference cell with equal thickness and a planar back side Al-mirror (dotted), and the limitation given by the front side reflection from a SLAR (dashed). The rapid oscillations in the figure to the left is caused by Fabry-Perot interference in the 20 µm thick Si-slab. To the right is a moving average of the values on the left.

Table I: Comparison of potential J_{sc} for different solar cell configurations.

Structure	J_{sc} with SLAR [mA/cm^2]	J_{sc} with DLAR [mA/cm^2]
2D Blazed 20 µm Al-mirror	36.8	38.7
2D Blazed 20 µm Ag-mirror	37.3	39.3
Reference 20 µm Al-mirror	30.4	31.8
Reference 160 µm Al-mirror	36.6	38.6

A comparison of the configurations from Table I reveals that the front-side reflection is a key to further improvement of light trapping. The change from SLAR to DLAR increases J_{sc} by 2 mA/cm^2. The best configuration with DLAR and Ag mirror gives a J_{sc} of 39.3 mA/cm^2, corresponding to absorption of more than 90 % of the photons in the solar spectrum in the interval 300-1100 nm. DLARs are not, however, commonly used in manufactured modules due to the cost of manufacture combined with the constraints imposed by the refractive index of the front-side cover glass. The encapsulated modules will have increased reflection losses compared to the DLAR, but compared to the SLAR reflection losses may actually be reduced due to a more gradual change in refractive index. However, absorption in the glass and the laminating polymer (EVA) must be accounted for in the case of an encapsulated cell.

We conclude that an extension of the blazed grating to two dimensions provides a successful light-trapping structure with an 8 times increase in optical thickness compared to a planar reference cell. Combined with a proper front-side anti-reflection coating this allows for high efficiency solar cells made of thin Si-wafers.

[1] F. Henley et al., "Direct film transfer (DFT) technology for kerf-free silicon wafering," 23rd PVSEC, Valencia, Spain (2008).
[2] E. Yablonovitch, "Statistical ray optics," J. Opt. Soc. Am., Vol 72, (1982).
[3] J. Nelson, "The Physics of Solar Cells," 1.Ed., World Scientific Publishing, (2003).
[4] P. Sheng et al., "Wavelength-selective absorption enhancement in thin-film solar cells," Appl. Phys. Lett. Vol. 43 (1983).
[5] D. Zhou and R. Biswas., "Harvesting photons in thin film solar cells with photonic crystals," Mater. Res. Soc. Symp. Proc., Vol. 1101, (2008).
[6] H. Sai et al., "Enhancement of light trapping in thin-film hydrogenated microcrystalline Si solar cells using back reflectors with self-ordered dimple pattern," Appl. Phys. Lett., Vol. 93, (2008).
[7] C. Heine and R.H. Morf, "Submicron gratings for solar energy applications," Applied Optics, Vol. 34, pp 2476-2482, (1995).
[8] J. Gjessing, E.S. Marstein, A. Sudbø, "Modelling of light trapping in thin silicon solar cells with back side dielectric diffraction grating,", presented at the 24th EU PVSEC, Hamburg, Germany, 21-25 Sept. (2009).
[9] http://software.kmnoptics.com/GID-Calc.html
[10] C.M. Herzinger et al., " Ellipsometric determination of optical constants for silicon and thermally grown silicon dioxide via a multi-sample, multi-wavelength, multi-angle investigation," J. Appl. Phys., Vol. 83, pp 3323-3336, (1998).
[11] E.D. Palik, "Handbook of Optical Constants of Solids," Academic press (1985).

SAMSUNG EX. 1002 - 1413/4148

Available online at www.sciencedirect.com
SCIENCE DIRECT®
Journal of Physics and Chemistry of Solids 66 (2005) 1891–1894
JOURNAL OF PHYSICS AND CHEMISTRY OF SOLIDS
www.elsevier.com/locate/jpcs

Band-gap grading in $Cu(In,Ga)Se_2$ solar cells

M. Gloeckler, J.R. Sites *

Department of Physics, Colorado State University, Fort Collins, CO 80523-1875, USA

Abstract

The quaternary system $Cu(In,Ga)Se_2$ (CIGS) allows the band gap of the semiconductor to be adjusted over a range of 1.04–1.67 eV. Using a non-uniform Ga/In ratio throughout the film thickness, additional fields can be built into p-type CIGS-based solar cells, and some researchers have asserted that these fields can enhance performance. The experimental evidence that grading improves device performance, however, has not been compelling, mostly because the addition of Ga itself improves device performance and hence a consistent separation of the grading benefit has not always been achieved. Numerical modeling tools are used in this contribution to show that (1) there can be a beneficial effect of grading, (2) in standard thickness CIGS cells the benefit is smaller than commonly believed, (3) there is also the strong possibility of reduced rather than of increased device performance, and (4) thin-absorber cells derive more substantial benefit.
© 2005 Elsevier Ltd. All rights reserved.

Keywords: A. Chalcogenides; A. Thin films; A. Semiconductors; D. Optical properties; D. Transport properties

1. Introduction

Record conversion efficiencies of CdS/CIGS thin-film solar cells are approaching 20% [1]. The absorber layers used in these cells are deposited by the three-stage process [2], which leads to non-uniform Ga/In composition versus absorber depth. Other methods commonly used, such as co-evaporation, allow the engineering of Ga/In profiles by varying the element fluxes during deposition. The effects of these non-uniform Ga/In compositions in $CuIn_{1-x}Ga_xSe_2$ have been broadly investigated by simulations and experiments. Prior simulations have predicted: (1) small ($<0.5\%$) to moderate ($<1\%$) improvements in efficiency with an increase in x towards the back contact, 'back grading' [3–7], (2) small to large ($>2\%$) improvements with an increase in x towards the junction, 'front grading' [4–8] (3) small to large improvements with an increase in x towards front and back and a minimum band-gap in between, 'double grading' [3–6,9,10]. Interpretation of experiments agree reasonably well with these results in showing moderate improvements due to back grading [7,11–13], moderate improvements due to front grading [7] and large improvements ($>3\%$) due to double grading [9–11]. Often however, there is a wide range of results available when simulation parameters or experimental conditions were varied, such that back [4,7,11], front [4,7,12], and double grading [10] have also been observed to reduce efficiency.

Substitution of Ga for In in $Cu(In,Ga)Se_2$ enlarges the band gap from 1.04 to 1.67 eV, with the change occurring primarily in the conduction band [14]. Simulated device efficiency η and open-circuit voltage V_{oc} are shown in Fig. 1 for solar cells with uniform band-gap energies (details of the model are discussed below). Typical high-efficiency devices have minimum band gaps of 1.1–1.2 eV. Addition of a Ga/In grading to an absorber with a minimum band gap $E_{min} < 1.4$ eV *may increase its performance due to either the grading benefit or the increase in average Ga content* (higher average band gap in Fig. 1). In fact, Dullweber [7] observed a close correlation between the average Ga-content and the device performance, independent of the Ga distribution. Except for references [4,7,13], uniform band-gaps equal to the graded band-gap minimum (1.04 eV 'CIS', in most cases) are used for comparison to determine the grading benefit. This unfortunate selection of the reference performance, results in overestimates of efficiency gains attributed to the grading benefit, especially for front and double grading structures where the band gap increases in high recombination regions. In Refs. [4] and [7] an average band-gap is used for comparison, and in Ref. [13] the results are normalized to the optical band-gap.

To eliminate the grading vs. average band-gap complication, graded device structures in this article are compared with ungraded devices with the same open-circuit voltages.

* Corresponding author. Tel.: +1 970 491 5850; fax: +1 970 491 7947.
E-mail address: sites@lamar.colostate.edu (M. Gloeckler).

0022-3697/$ - see front matter © 2005 Elsevier Ltd. All rights reserved.
doi:10.1016/j.jpcs.2005.09.087

SIONYX1403000017.0005

SAMSUNG EX. 1002 - 1414/4148

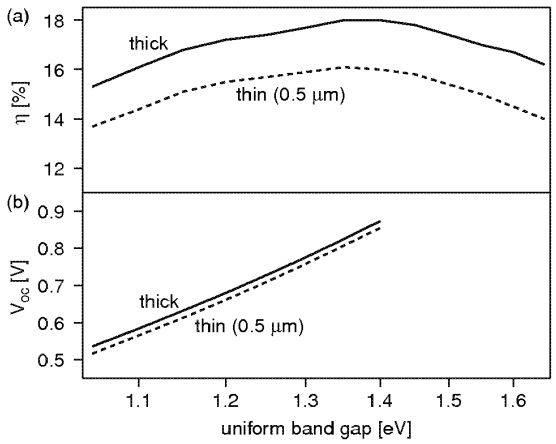

Fig. 1. (a) Simulated device efficiency, η and (b) open-circuit voltage, V_{oc}, for CIGS solar cells with uniform band-gap energies and thicknesses of 3 μm (solid) and 0.5 μm (dashed).

Because of the monotonic increase of the open-circuit voltage with band gap, this choice establishes an objective and absolute criteria for grading benefits, independent of changes in average Ga composition. The alternative comparison to the effective optical band-gap used in Ref. [13] would yield similar results.

2. Device model

The starting point for the simulations is a three layer CIGS model discussed earlier [15], with an additional mid-gap recombination center being present in the absorber. This baseline configuration includes a 200-nm ZnO window, 50-nm CdS buffer, and 3-μm CIGS absorber layer. The uniform Ga-content device efficiency with these parameters is shown as a function of the absorber-band gap in Fig. 1; $\eta(E_g=1.04\text{ eV})=15.1\%$ and $\eta(E_g=1.15\text{ eV})=16.8\%$, which is typical for good CIS and ungraded CIGS solar cells. Recombination at the CdS/CIGS interface is not included since earlier calculations have shown that for positive band offsets, interface recombination has a negligible effect [16]. For all cases considered here this criteria is fulfilled. A standard terrestrial AM1.5 spectrum is used for the simulated illumination [17].

Band-gap variations (front, back, and double gradings) are described in this paper by the parameters ΔE_{Fr} (linear E_g-increase towards the front), ΔE_{Ba} (linear E_g-increase towards the back), E_{min} (minimum band gap), and d_{min} (distance of the minimum from the junction). The numerical model approximates the linear variations by discrete layers of varying band gap and optical absorption spectrum. The band-gap difference between two adjacent layers is always less than $2kT$ and in most cases less than kT (26 meV). Hence, a graded device model typically consists of 10–25 layers of absorber material. The absorption spectrum used is that reported for 1.15 eV CIGS [18], and it is shifted on the energy axis according to the band-gap in each layer.

3. Results

3.1. Back grading

Back grading establishes an additional drift field for the minority electrons that assists carrier collection and reduces back contact recombination. Normalized current-voltage parameters for $E_{min}=1.04$ eV, $\Delta E_{Ba}=0$–0.6 eV, and $d_{min}=0.1$–2.5 μm are shown in Fig. 2. Normalization is achieved by studying the difference in short circuit current density ΔJ_{sc}, fill factor ΔFF, and efficiency $\Delta\eta$ between graded and ungraded absorber devices with the same open-circuit voltage ($\Delta V_{oc}=0$).

A small J_{sc} increase is observed once the back grading extends into the front half of the device ($d_{min}<1.5$ μm). The improvement is about 1–1.5 mA/cm^2 and weakly dependent on the parameter ΔE_{Ba}. FF shows a negligible decrease with large ΔE_{Ba} and small d_{min}. The net gain in efficiency is typically 0.5%. With $\Delta E_{Ba}>0.4$ eV and $d_{min}\approx 0.3$ μm, we observe a maximum $\Delta\eta=0.7\%$.

3.2. Thin CIGS absorbers

Material as well as deposition costs can be greatly reduced by thinning the absorber layers from the standard thickness of 2–3 μm. Optically, less than 0.5 μm is needed to absorb more than 90% of the light with $E_{ph} > E_g$, even without considering reflection of the light at the back contact. Lundberg et al. [19] investigated the performance of CIGS solar cells as a function of absorber thickness and found that the dominanting loss for thinner absorber layers is a reduction of J_{sc}, which exceeds the reduction in generation due to increased back contact recombination.

Predicted efficiencies for the constant band-gap model with a reduced absorber thickness of 0.5 μm are shown in Fig. 1. Efficiency is lowered by about 2%, and these losses are mostly in J_{sc}, followed by a lower FF, and a slightly reduced V_{oc}.

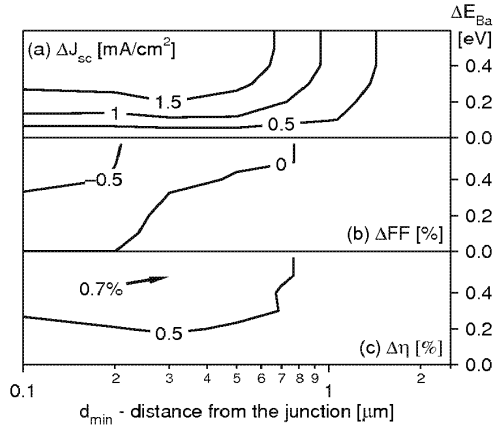

Fig. 2. Change in J_{sc} (a), FF (b), and η (c) due to the addition of back grading in 'thick' (3 μm) CIGS devices. The numbers shown are the differences to results found with uniform band-gap energies of equal V_{oc}.

SIONYX1403000017.0006

SAMSUNG EX. 1002 - 1415/4148

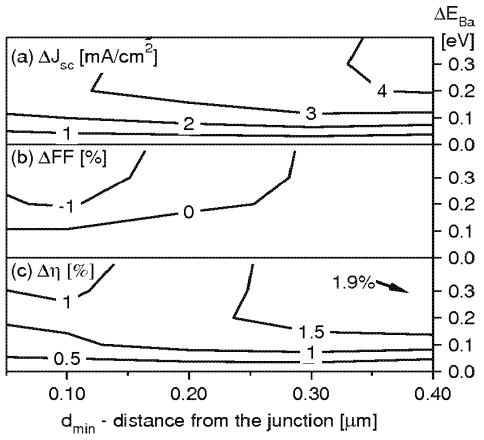

Fig. 3. Change in J_{sc} (a), FF (b), and η (c) due to the addition of back grading in thin (0.5 μm) CIGS devices.

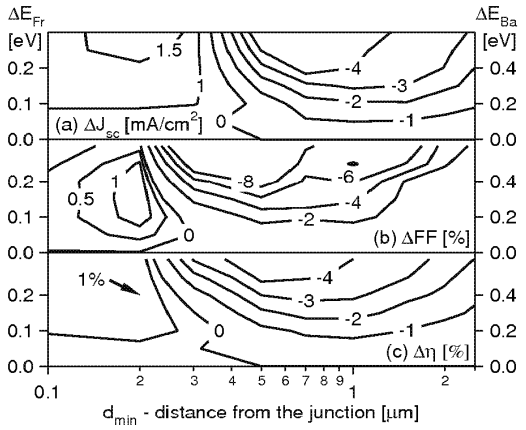

Fig. 4. Change in J_{sc} (a), FF (b), and η (c) due to the addition of double grading. E_g increases by ΔE_{Fr} towards the front and by ΔE_{Ba} towards the back of the device.

Experimentally, an efficiency loss closer to 6% has been observed for 0.5 μm CIGS [19]. This larger loss is most likely correlated to the experimental difficulties in adjusting the film thickness without changing other film parameters at the same time, especially morphology and defect structure.

When a thin CIGS absorber of 0.5 μm is simulated without consideration of material-quality changes, the effects of back contact passivation can be highlighted. Such results are shown in Fig. 3. The model predicts that J_{sc} losses can be fully recovered by a fairly steep back grading and, hence, absorber thinning is predicted to be practical without significant loss in efficiency.

3.3. Double grading

Conceptually, double grading allows increased performance by achieving a high J_{sc}, which is determined by the minimum band-gap in the device, and at the same time increased V_{oc} due to the locally increased band gap in the space-charge region. This principal of two band gaps was experimentally verified by Dullweber et al. [20]. The quantified η gains, reported in [10], however, used the minimum band-gap absorber as reference performance and overestimated the grading effect.

The *normalized* current-voltage parameters from our simulations, for $E_{min}=1.04$ eV, $\Delta E_{Ba}=0$–0.6 eV, $\Delta E_{Ba}/\Delta E_{Fr}=2$, and $d_{min}=0.1$–2.5 μm, show that the double grading benefits are rather modest (Fig. 4). For $d_{min}<0.3$ μm the simulations predict J_{sc} gains similar to those with the back grading. For larger d_{min}, however, J_{sc} is strongly reduced, as much as 5 mA/cm^2, depending on the height of ΔE_{Fr}. FF improves with small d_{min}, but it also shows considerable reduction for intermediate $d_{min}\approx 0.2$–1.5 μm. The highest efficiency gain should be close to 1% when the minimum band gap is located in the middle of the space charge region near 0.2 μm. Comparing this 1% increase with the 0.7% achieved by back grading alone, the gain achieved by the separation of electrical and optical band-gap is quite modest. Models in which only a front grading were implemented show similar losses in J_{sc} and FF, and under no circumstances was an efficiency gain observed.

3.4. Current-loss explanation

The losses in J_{sc} for intermediate values of d_{min} result approximately equally from the reduced absorption in the junction region and from the poorer collection due to the reduction and possible reversal of the drift field for minority carriers. Fig. 5 shows the conduction band for three different front gradings with $d_{min}=0.1$, 0.3, and 1 μm under zero bias (b) and at a voltage between the maximum power voltage and V_{oc} (a). For small d_{min} the front grading is completely contained in the space charge region and slightly reduces the field. With $d_{min}=0.3$ μm good collection is still possible at zero voltage (no reduction in J_{sc}). However, a barrier exists under forward bias that leads to poorer collection and is observed as a reduction in the FF. Larger values for d_{min} lead to barriers under all conditions, reducing J_{sc} and FF. For materials with lower carrier concentrations (here we used 2×10^{16} cm^{-3}

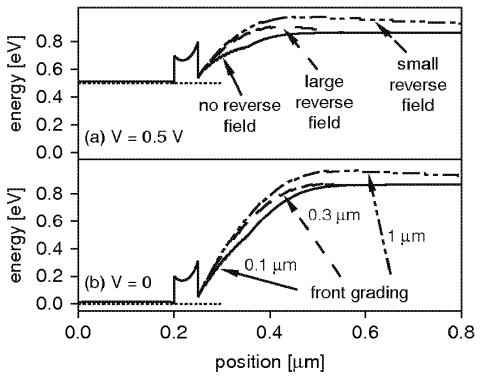

Fig. 5. Conduction band energy at zero voltage and under forward bias. Intermediate positions of the band-gap minimum lead to a significant reverse field for electrons.

SIONYX1403000017.0007

SAMSUNG EX. 1002 - 1416/4148

for the CIGS layer), the range of d_{min} that is unfavorable is expected to decrease.

4. Discussion and Conclusions

Back grading in CIGS solar cells is seen to improve simulated device efficiency compared to ungraded devices. For devices with standard thicknesses, the effect is small, around 0.5% in efficiency. The potential efficiency gain increases significantly as the absorber thickness is reduced. We predict $\Delta\eta \approx +2\%$ with a thickness of 0.5 μm, which means that the thinning losses are fully recovered. These efficiency gains are in good agreement with experimental work [13], but experimentally the thinning losses were greater and not fully recovered by adding back grading.

Double grading shows benefits similar to those from back grading, but the additional front grading can lead to large losses in FF and J_{sc}, if the band-gap minimum is not contained within the space charge region. The large FF loss has been observed by Topic et al. [3] and was argued to be due to the reverse drift field for the minority carriers. Our simulations confirm this conclusion.

With larger minimum band-gap energies of 1.2 eV (instead of 1.04 eV), slightly higher gains up to $\Delta\eta = 1.2\%$ are achieved, and the highest absolute efficiency of 18.6% exceeds the highest uniform band gap efficiency by 0.6%. Higher ratios $r = \Delta E_{Ba}/\Delta E_{Fr}$ also seem to be favorable: the highest efficiency gain ($E_{min} = 1.04$ eV) increased from 0.6% for $r = 1$, 1% for $r = 2$, and 1.2% for $r = 3$.

Although frequently believed to be a major contributor to high efficiency devices, we have shown that the benefit that can be expected by implementing back, front, or double grading in standard-thickness CIGS solar cells to be small. Large losses in FF and J_{sc} can be realized with front and double gradings. Thin CIGS devices, however, can benefit significantly from a back grading that reduces back contact recombination.

Acknowledgements

This research was supported by the US National Renewable Energy Laboratory. The modeling calculations for this work used the AMPS-1D software developed at the Pennsylvania State University supported by the Electric Power Research Institute.

References

[1] K. Ramanathan, M.A. Contreras, C.L. Perkins, S. Asher, F.S. Hasoon, J. Keane, D. Young, M. Romero, W. Metzger, R. Noufi, J. Ward, A. Duda, Properties of 19.2% efficiency ZnO/CdS/$CuInGaSe_2$ thin-film solar cells, Prog. Photovolt 11 (2003) 225–230.

[2] M.A. Contreras, B. Egaas, K. Ramanathan, J. Hiltner, A. Swartzlander, F. Hasoon, R. Noufi, Progress toward 20% efficiency in Cu(In,Ga)Se_2 polycrystalline thin-film solar cells, Prog. Photovolt 7 (1999) 311–316.

[3] M. Topič, F. Smole, J. Furlan, Band-gap engineering in CdS/Cu(In,Ga)Se_2 solar cells, J. Appl. Phys. 79 (1996) 8537–8540.

[4] A. Dhingra, A. Rothwarf, Computer simulation and modeling of graded bandgap $CuInSe_2$/CdS based solar cells, IEEE Trans. Electron Devices 43 (1996) 613–621.

[5] J.L. Gray, Y.J. Lee, Numerical modeling of graded band gap CIGS solar cells, in: Proceedings of the First World Conference on Photovoltaic Energy Conversion, 1994, pp. 123–126.

[6] J. Song, S.S. Li, C.H. Huang, O.D. Crisalle, T.J. Anderson, Device modeling and simulation of the performance of $Cu(In_{1-x},Ga_x)Se_2$, Solid-State Electron. 48 (2004) 73–79.

[7] T. Dullweber, G. Hanna, W. Shams-Kolahi, A. Schwartzlander, M.A. Contreras, R. Noufi, H.W. Schock, Study of the effect of gallium grading in Cu(In,Ga)Se_2, Thin Solid Films 361–362 (2000) 478–481.

[8] A.M. Gabor, J.R. Tuttle, M.H. Bode, A. Franz, A.L. Tennant, M.A. Contreras, R. Noufi, D.G. Jensen, A.M. Hermann, Band-gap engineering in Cu(In,Ga)Se_2 thin films grown from $(In,Ga)_2Se_3$ precursors, Solar Energy Mater. Sol. Cells 41–42 (1996) 247–260.

[9] T. Dullweber, O. Lundberg, J. Malmström, M. Bodegård, L. Stolt, U. Rau, H.W. Schock, J.H. Werner, Back surface band gap gradings in Cu(In,Ga)Se_2 solar cells, Thin Solid Films 387 (2001) 11–13.

[10] T. Dullweber, Optimierung des Wirkungsgrades von Cu(In,Ga)Se_2-Solarzellen mittels variablem Verlauf der Bandlücke, PhD thesis, Universität Stuttgart, 2002.

[11] M.A. Contreras, J. Tuttle, A. Gabor, A. Tennant, K. Ramanathan, S. Asher, A. Franz, J. Keane, L. Wang, R. Noufi, High efficiency graded bandgap thin-film polycrystalline Cu(In,Ga)Se_2-based solar cells, Solar Energy Mater. Sol. Cells 41–42 (1996) 231–246.

[12] M. Bodegård, O. Lundberg, J. Malmström, L. Stolt, High voltage Cu(In,Ga)Se_2 devices with Ga-profiling fabricated using co-evaporation, in: Proceedings of 28th IEEE Photovoltaic Specialist Conference, 2000, pp. 450–453.

[13] O. Lundberg, M. Edoff, L. Stolt, The effect of Ga-grading in CIGS thin film solar cells, Thin Solid Films 480–481 (2005) 520–525.

[14] S.-H. Wei, S.B. Zhang, A. Zunger, Effects of Ga addition to $CuInSe_2$ on its electronic, structural, and defect properties, Appl. Phys. Lett. 72 (1998) 3199–3201.

[15] M. Gloeckler, A.L. Fahrenbruch, J.R. Sites, Numerical modeling of CIGS and CdTe solar cells: Setting the baseline, in: Proceedings of Third World Conference on Photovoltaic Energy Conversion, 2003, pp. 491–494.

[16] M. Gloeckler, J.R. Sites, Efficiency limitations for wide-band-gap chalcopyrite solar cells, Thin Solid Films 480–481 (2005) 241–245.

[17] K. Emery, Handbook of Photovoltaic Science and Engineering in: A. Luque, S. Hegedus (Eds.), Wiley, Chichester, 2003, pp. 702–711. (Based on R. Bird, R. Hulstrom, C. Riordan, Solar Cells 14 (1985) 193).

[18] P.D. Paulson, R.W. Birkmire, W.N. Shafarman, Optical characterization of $CuIn_{1-x}Ga_xSe_2$ alloy thin films by spectroscopic ellipsometry, J. Appl. Phys. 94 (2003) 879–888.

[19] O. Lundberg, M. Bodegård, J. Malmström, L. Stolt, Influence of the Cu(In,Ga)Se_2 thickness and Ga grading on solar cell performance, Prog. Photovolt 11 (2003) 77–88.

[20] T. Dullweber, U. Rau, M.A. Contreras, R. Noufi, H.-W. Schock, Photogeneration and carrier recombination in graded gap Cu(In,Ga)Se_2 solar cells, IEEE Trans. Electron Devices 47 (2000) 2249–2254.

SIONYX1403000017.0008

SAMSUNG EX. 1002 - 1417/4148

Solar Energy Materials & Solar Cells 92 (2008) 1570–1578

Contents lists available at ScienceDirect

Solar Energy Materials & Solar Cells

journal homepage: www.elsevier.com/locate/solmat

Light trapping, a new approach to spectrum splitting

A. Goetzberger, J.C. Goldschmidt, M. Peters *, P. Löper

Fraunhofer Institute for Solar Energy Systems, Heidenhofstr. 2, 79110 Freiburg, Germany

ARTICLE INFO

Article history:
Received 14 April 2008
Accepted 4 July 2008
Available online 29 August 2008

Keywords:
Light trapping
Concentration
Photon management

ABSTRACT

In this paper, a novel type of light trap is introduced. It enables photovoltaic conversion with separate solar cells optimized for different frequency bands, which are covered by spectrally selective mirrors. Sunlight is coupled into a transparent medium and converted to diffuse radiation by randomization. It is well known that under these conditions light intensity is enhanced by a factor of $2n^2$ inside the medium. The unidirectional radiation at the aperture is however only n^2. Two types of light trap are presented. The first one employs concentrated radiation incident on a small volume light trap. It is shown that efficiency depends on the ratio (solar cell area)/(input area). A more detailed analysis shows that under regular conditions part of the light is absorbed directly after entering the trap which results in higher efficiencies. We show that a trapping efficiency above 90% is obtainable.

The second type of trap is based on a photonic structure covering the surface of the medium. It has high angular selectivity and broad spectral transmission. An analysis of efficiency and loss mechanisms is presented. If both types of trap are combined even higher efficiency is possible. Consequences for solar cell technology are investigated. It is further shown that the light trapping principle can also be applied to large area stationary modules.

© 2008 Elsevier B.V. All rights reserved.

1. Introduction

1.1. Background

The efficiency of a solar cell consisting of a single semiconductor material is limited theoretically to about 40% [1]. In order to reach higher efficiency, the solar spectrum has to be subdivided and converted by different solar cells with optimized band gaps. The best approach at present is to use multijunction cells stacked above each other such that the top cell converts the shortest wavelength fraction while being transparent to the longer wavelengths that are in turn converted by other solar cells lower in the stack. In concentrating systems, those multijunction cells consist of monolithically grown III–V compounds. Thin film double or triple junction cells have so far only been realized in amorphous-microcrystalline cells but efficiencies are moderate. The multijunction approach has so far yielded the highest efficiencies but has some limitations. To achieve high efficiencies for these cells, the lattice match conditions have to be regarded. Currently, new technologies like lattice mismatched and metamorphic cells [2] are developed though that alters this limitation. Furthermore, between cells tunnel diodes have to be inserted because the cells have opposite polarity. Very stringent is the requirement that all cells have to produce equal current because the stack represents a series connection. When the spectral conditions of irradiation change current match is negatively affected. If separate individual solar cells could be used to convert the frequency bands more freedom of design and potentially higher efficiency could be expected. A well-known idea to achieve spectrum splitting for separate solar cells is the fluorescent concentrator [3].

Another very old concept to achieve this type of spectrum splitting is to use dichroic mirrors in a concentrating system that focus different parts of the solar spectrum onto separate solar cells [4]. This concept has been getting renewed attention recently [5].

In this paper, a new method is described that permits to use separate solar cells side by side without the restrictions mentioned.

1.2. The basic concept

The light trapping concept presented here has the following properties:

- A transparent volume of the trap filled with diffuse radiation.
- Solar radiation enters the trap through an input area bordering air.
- The radiation is randomized either at entering the trap or by scattering centres or by lambertian reflectors within the trap.

* Corresponding author. Tel.: +49 761 4588 5475; fax: +49 761 4588 9250.
E-mail address: marius.peters@ise.fraunhofer.de (M. Peters).

0927-0248/$ - see front matter © 2008 Elsevier B.V. All rights reserved.
doi:10.1016/j.solmat.2008.07.007

SIONYX1403000017.0009

SAMSUNG EX. 1002 - 1418/4148

- Separate solar cells with different band gaps are optically coupled to the trap.
- The surfaces of these solar cells are covered with band-pass mirrors that transmit a specific wavelength range and reflect all other light.
- Surfaces not covered by solar cells are highly reflective.

In the first part of this paper, we describe the basic principle and its application to concentrating systems. Two versions of light traps will be considered. The first is very straightforward and can be applied to existing systems; the second relies on photonic structures requiring more advanced technology.

While these concepts are designed for concentrating systems, we will show in the following part how light trapping can also be applied to non-concentrating, stationary modules.

The mechanism of the light trap is based on the thermodynamic theory of Yablonovitch [6]. Randomized light within a slab of transparent material of irregular shape and of refractive index n is enhanced in its intensity with respect to the intensity outside in air by a factor of n^2. In his paper, Yablonovitch gives a factor $2n^2$ but he defines light intensity as being bidirectional. Radiation that illuminates the surface of a solar cell is however unidirectional. Therefore, we restrict ourselves to an enhancement by n^2 due to diffuse radiation and total internal reflection. The optically coupled solar cells are exposed to this increased intensity. At the input aperture, there is a drop of intensity by n^2 vs. air. In an idealized approach, the input aperture is considered without surface (Fresnel) reflection. If necessary, this can be included but surface reflection can be minimized by antireflection measures.

We will first consider the situation with fully diffuse light within the trap and then demonstrate that the direction of the incoming light is important and that by its consideration calculated efficiencies are higher.

2. Concentration by geometric optics

2.1. The basic principle

Fig. 1 shows the first approach to the principle of light trapping.

Light is first concentrated in the usual manner by lenses or other optical means. The light trap has small openings corresponding to the focal point of the concentrating optics. The remainder of the surface is reflective. A similar concept for light confinement in bulk solar cells has been described by Luque [7,8] using micro CPCs, whereas the trap described here is fully transparent. At the bottom of the trap, there are solar cells and mirrors which may be diffuse reflectors. It has to be emphasized that diffusion of the light is essential to the concept. Exactly where the diffusion is accomplished is not important. As Yablonovitch pointed out, a diffusing surface at one point of the trap in combination with multiple reflections results in a nearly isotropic characteristic, even if the characteristic of the diffuse reflector is not lambertian itself [6].

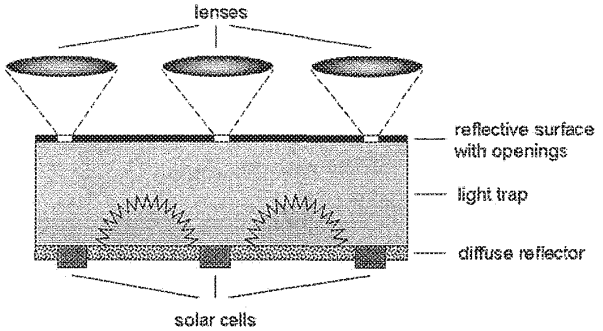

Fig. 1. Principle of a light trap. Light is concentrated by lenses or other optical means. The concentrated beam enters the light trap through a small aperture. Inside the trap the light is diffused. Solar cells with optical mirrors are optically coupled to the trap. The optical mirrors reflect all light the solar cell in question cannot use. The trap surface is reflective everywhere apart from the apertures and the solar cells. By that means light is spectrally selective concentrated onto different cells.

In a light trap with more than one solar cell, the solar cells are always combined with a band-pass mirror at the trap interface that is transparent for the light which is best used by each solar cell and reflective for all other light. As this is always the case, the mirrors were not separately included in the figures. Solar cells in the figures have always to be seen combined with band-pass mirrors or rear mirrors as described in Fig. 11.

We now estimate the efficiency of the light trap. In an idealized approach, we assume the radiation to have an isotropic characteristic and be fully uniform within the trap, the mirrors to be perfectly reflective and the solar cells to be perfectly absorbing, while there is no absorption in the trap itself. In this paper, light intensities are generally defined as being unidirectional. Let I_{int} be the internal radiation intensity, then the loss through the input aperture A_i is $I_{int}A_i/n^2$ (the input area A_i is normally somewhat larger than the illuminated area because of tolerances in focussing). The radiation absorbed by the solar cells with area A_s is $I_{int}A_s$. The trapping efficiency η_{trap} is now obtained simply by setting up the energy balance within the trap:

$$\eta_{trap} = \frac{I_{int}A_s}{I_{int}A_s + I_{int}(A_i/n^2)}$$

and

$$\eta_{trap} = \frac{1}{1+(A_i/A_s n^2)} = \frac{1}{1+(1/Fn^2)} \tag{1}$$

From Eq. (1), we see that efficiency depends on the ratio $F = A_s/A_i$. That means we can control efficiency by adjusting this ratio. In Fig. 2, efficiency is plotted vs. this ratio for $n = 1.5$ and 2.0. For example, for equal area and $n = 1.5$, $A_s/A_i = 1$: $\eta_{trap} = 0.69$ and for $A_s/A_i = 2$: $\eta_{trap} = 0.82$. In practice, this means that if we want to achieve high trapping efficiency, we have to concentrate the light first and then deconcentrate it in the light trap. It should also be kept in mind that Eq. (1) applies to every fraction of the solar spectrum separately. Therefore, the total area of solar cells is the product of the number of spectral subdivisions and the area of the solar cells. In other words if, for instance the spectrum is split into three parts, the total cell area is $3A_s$ (assuming equal area solar cells).

We can also estimate the radiation intensity in the light trap. Qualitatively we can state that the light intensity I_{int} should drop with increasing A_s/A_i and efficiency should rise because emission through A_i is lowered. If I_{inc} is the concentrated radiation impinging on A_i, then without solar cells (for $A_s = 0$) $I_{inc} = I_{int0}/n^2$. I_{inc} is the concentrated radiation averaged over the entire input area. When solar cells with area A_s are added we obtain

$$\frac{A_i I_{int}}{n^2} + A_s I_{int} = A_i I_{inc} = A_i \frac{I_{int0}}{n^2}$$

$$\frac{I_{int}}{I_{int0}} = \frac{1}{1+n^2(A_s/A_i)} \tag{2}$$

or

$$\frac{I_{int}}{I_{inc}} = \frac{1}{(1/n^2)+(A_s/A_i)} = \frac{1}{(1/n^2)+F} \tag{3}$$

SIONYX1403000017.0010

SAMSUNG EX. 1002 - 1419/4148

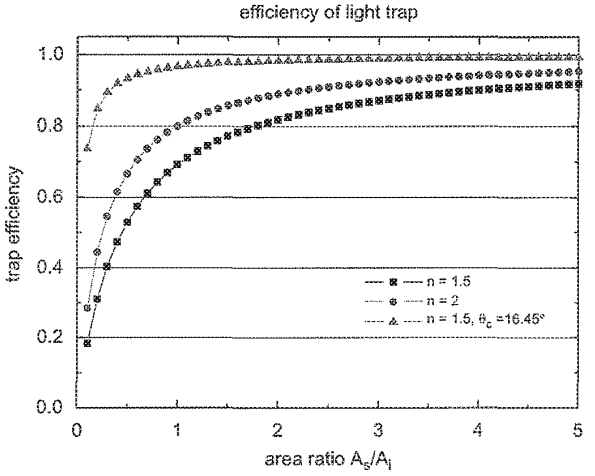

Fig. 2. Trapping efficiency vs. A_s/A_i for two values of the refractive index. The top curve is for the combination of the light trap with a photonic structure in a concentrating system as described in Section 3.3. The angular selective structure restricts the angular acceptance range to an angle of 16.45°. For high area ratios high efficiencies are reached.

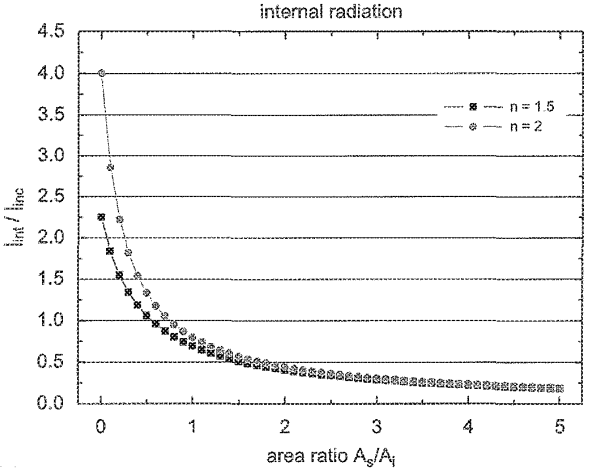

Fig. 3. Internal radiation density vs. area ratio for two different refractive indices of the trap $n = 1.5$ and 2. For larger ratios of A_s to A_i, the refractive index of the trap has less and less influence on the ratio I_{int}/I_{inc}.

The internal radiation density is shown in Fig. 3 against area ratio A_s/A_i. It shows that the refractive index becomes less important at larger area ratios.

2.2. Optimization of the geometric concentration light trap

The light trap sketched in Fig. 1 has the same area as the concentrating elements. There is no reason for the light trap to be so large. On the contrary, imperfect mirrors cause losses. This leads us to the design shown in Fig. 4.

In final consequence, we end up with a light trap that is entirely covered by solar cells (with exception of the input opening). As an example see Fig. 5. The light trap is a cube with A_i

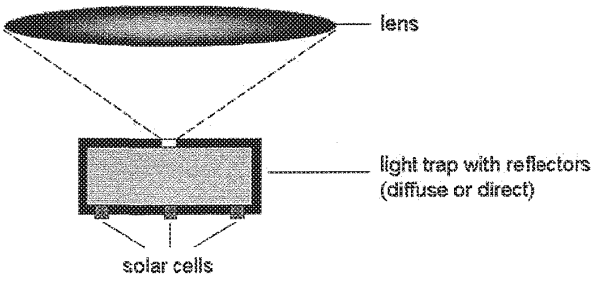

Fig. 4. Reduced area light trap. The area of the light trap may be chosen smaller than the area of light incidence. In the figure, the area of incidence is the lens area. A smaller light trap is advantageous when considering losses caused by imperfect reflections.

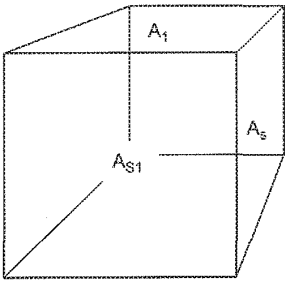

Fig. 5. Reduced size light trap. All sides A_s apart from the top A_1 are covered with solar cells. The length of a side of the cube being a, the solar cell area is $5a^2$. In this case the entire top face is the input with an area of a^2. Assuming a splitting of the light into three parts, we get $F = 5/3$ and $\eta_{trap} = 0.79$.

being the input and A_{S1}, A_{S2}, etc. being the solar cell areas. A small light trap has also other advantages:

- Absorption losses within the trap are minimized.
- Assuming perfect diffusivity, the light intensity is more uniform.
- Because of the small volume it is possible to use an expensive, highly refractive material for the trap.

The entire solar cell area of the cube in Fig. 5 is $5a^2$ with a as the dimension of the cube. If the solar spectrum is split into three parts, $A_s/A_i = 5/3$ and $\eta_{trap} = 0.79$. So even with very small light traps high efficiency can be achieved.

Similar concepts to the one given above have been proposed by Luque et al. [9] or Ortabasi [10]. In the concept of Luque a light confining cavity resembling an integrating sphere is used to reflect back the photons reflected by the solar cell. This system has already been examined closely [11,12] and high efficiencies have been predicted [8,13]. Ortabasi proposed to use a cavity into which the sunlight is concentrated. The cavity is covered on the inside with different solar cells and diffuse mirrors. In our terms, these systems would be described with a refractive index of the light trap of $n = 1$.

2.3. The effect of initial absorption

After understanding the basic principle of the light trap system, we are now able to consider initial absorption. Consider a light trap as in Fig. 5, with all the walls but A_i covered with one type of perfectly absorbing solar cells. The trapping efficiency should be $\eta_{trap} = 100\%$, as all the incoming light is absorbed by solar cells. However, this result is not given by Eq. (1). The conclusion is that we have to take the direction of the

SIONYX1403000017.0011

SAMSUNG EX. 1002 - 1420/4148

radiation into account, as the light is not randomized immediately. Light is absorbed by the solar cells already before it is randomized and fills the trap. We call this absorption "initial absorption". After the initial absorption, the light is randomized. The intensity of the diffuse light inside the trap in equilibrium with I_{inc} is denoted I_{int}. We know from [5] that the diffuse radiation with the intensity I_{int} impinging from the inside of the trap onto the surface which is coupled out equals I_{int}/n^2. The rest is totally internally reflected. However, this loss and the internal reflection can only occur for the light which actually reaches the surface again. Therefore, the intensity of the light from which the loss has to be calculated is reduced by the initial absorption.

We define an effective reflection coefficient R_{trap} as the fraction of light that actually reaches the incoupling surface after a "round trip" through the trap. The absorption $(1-R_{trap})$ includes light absorbed after multiple reflections and all light absorbed before the reflected light arrives again at the incoupling surface. As in Section 2.1, R_{trap} applies to each frequency band separately. R_{trap} depends on the geometry of the trap and the degree of spectrum splitting. It is advantageous if the bottom of the trap is diffusely reflecting (besides being absorbing for part of the spectrum) because then more light will be reflected to the vertical sides and have a chance to be absorbed. The efficiency of this light trap will now be calculated.

The relevant quantities are defined in Fig. 6. I_{inc} is the incident radiation and the incident energy is $E_{inc} = I_{inc}A_i$. It is assumed that the light traverses the trap surface without loss but is diffused when entering the trap. The energy reflected back towards the surface is

$$E_R = I_{inc}R_{trap}A_i \tag{4}$$

Eq. (4) can be seen as a definition of R_{trap} (according to the above definition of R_{trap}, it refers to the input area and not cell areas).

The energy absorbed by the solar cells is

$$E_{abs} = I_{inc}(1 - R_{trap})A_i + I_{int}A_s \tag{5}$$

The energy emitted by the trap is

$$E_{esc} = \frac{I_{int}A_i}{n^2}$$

Setting up the energy balance and solving for I_{int}

$$E_{inc} = I_{inc}A_i = E_{esc} + E_{abs} = \frac{I_{int}A_i}{n^2} + I_{inc}(1 - R_{trap})A_i + I_{int}A_s \tag{6}$$

$$I_{int} = \frac{I_{inc}R_{trap}}{(1/n^2) + F} \tag{7}$$

where $F = A_s/A_i$.

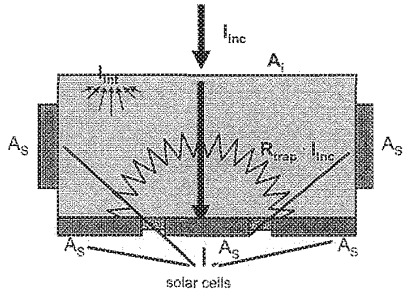

Fig. 6. Definition of quantities used in calculation of efficiency. I_{inc} is the incident intensity outside the trap. It enters the trap through an incident area A_i. In the trap, a fraction of the light is initially absorbed by solar cells with an area A_s. The rest is reflected, so that the reflected intensity is $R_{trap}I_{inc}$. R_{trap} denotes the effective reflection of the trap. The intensity of the diffuse light inside the trap that is in equilibrium with I_{inc} is called I_{int}.

Then

$$E_{esc} = \frac{I_{int}A_i}{n^2} = \frac{I_{inc}R_{trap}A_i}{1 + n^2F}$$

and

$$\eta_{tot} = \frac{E_{inc} - E_{esc}}{E_{inc}} = \frac{I_{inc}A_i - (I_{inc}R_{trap}A_i)/(1 + n^2F)}{I_{inc}A_i} = 1 - \frac{R_{trap}}{1 + n^2F} \tag{8}$$

We now check the validity of these relations.

When $R_{trap} = 0$, then $I_{int} = 0$ and $\eta_{tot} = 1$. In this case, all radiation is absorbed in the trap as was postulated above.

When $R_{trap} = 1$, then $\eta_{tot} = \eta_{trap}$; this is the case in which all incident light in the trap is diffuse as was assumed in Eq. (1). Normally, $R_{trap} = 1$ implies fully reflecting walls which also requires $\eta_{trap} = 0$. It is obvious that immediate conversion of the incoming radiation to diffuse radiation in a trap with partly absorbing walls can only be realized with scattering centres inside the trap. Therefore, the initial considerations in Section 2.2 are useful for understanding the light trap but do not fully describe the light trapping mechanism.

If we compare Eq. (6) with Eq. (3), we see that it differs by the factor R_{trap} as we expect from the the definition of R_{trap}.

In Fig. 7, η_{tot} is plotted vs. F for different values of R_{trap} and $n = 1.5$. This figure shows the strong influence of R_{trap} on the efficiency. The dashed lower curve in Fig. 7 ($R = 1$) represents the fully diffuse case that was also presented in Fig. 2. It is significantly below the curves with lower R.

3. The photonic light trap

3.1. The principle of the photonic light trap

In this section, the second concept for light trapping is described. This concept uses a photonic structure with a distinct angular selectivity in combination with a scattering reflector.

Photonic structures have recently been considered for improvement of thermophotovoltaic conversion [14]. Among the

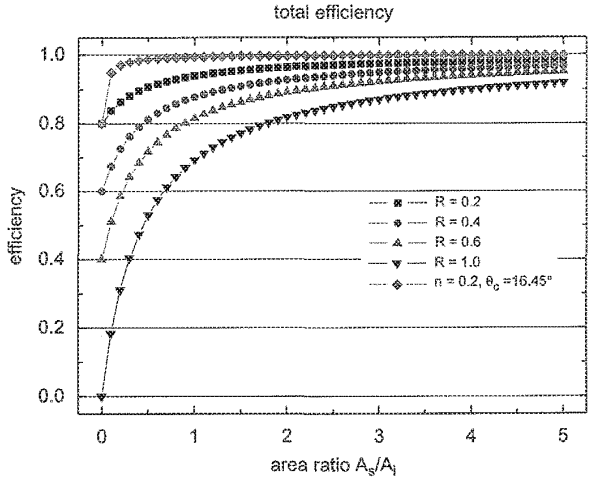

Fig. 7. Total efficiency including internal absorption of first pass of light for different values of trap reflectivity vs. coverage factor $F = A_s/A_i$. The lower dashed curve is the case without consideration of primary absorption; the top curve is with photonic structure at the input (see Fig. 8). The angular selective structure restricts the angular acceptance range to an angle of 16.45°.

SIONYX1403000017.0012

SAMSUNG EX. 1002 - 1421/4148

photonic crystals, optical elements with unique optical properties [15] exhibiting spectral and angular selectivity can be found.

In Fig. 8, the principle of a light trap with an angular selective filter is sketched. A transparent light trap with refractive index n is covered with the photonic structure. The optimum photonic structure for this purpose has the following properties:

- Broad spectral bandwidth to transmit all or most of the solar spectrum for an angular range close to perpendicular incidence.
- Narrow angular selectivity to reflect all light that impinges on the filter under an angle greater a critical angle Θ_c.

With these properties, a light trap can function as a concentrator without other optical components. As in the preceding sections, the photonic concentrating trap can only accept direct radiation and has to track the sun. Light that impinges on the trap under perpendicular incidence can traverse the filter and enter the trap. The light is than scattered into a certain angular characteristic that is assumed to be lambertian in the following. This is realized by the application of diffuse reflectors and multiple reflections [6]. Furthermore, we assume a critical angle of $\Theta_c = 1°$ which is compatible with the angle subtended by the sun of $\Theta_c = 0.27°$ and with the tracking accuracy of present trackers [16].

The opening angle of the acceptance is modified by refraction upon entry into the light trap. In that way, the angular range Θ_c under which light can leave the trap and the filter is confined to a very narrow escape cone characterized by Θ_{int}. Rays outside this cone are reflected either by total internal reflection inside the trap or at the filter.

This concept has already been applied to the increase of the path length of light in solar cells [17]. The solar cells are optimized for spectral selectivity and are covered with spectrally selective mirrors.

The optical properties of the photonic light trap are now analyzed. For an idealized treatment, we first assume perfect transmission of the light trap, perfect reflectivity of the mirrored surfaces, uniformity of diffuse radiation and perfect absorption of the solar cells. The concept is for large area devices. For the clarity of the presentation, we therefore neglect the edge surfaces in our calculations.

The internal escape cone angle is

$$\Theta_{int} = \arcsin\left(\frac{\sin\Theta_c}{n}\right) \tag{9}$$

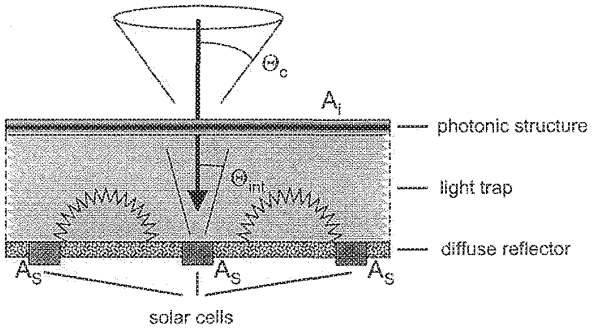

Fig. 8. Principle of light trap with angular selective photonic structure. The photonic structure has a critical acceptance angle Θ_c. Light that is scattered after diffusion into an angle greater than Θ_c is trapped. The solar cells are optimized for spectral selectivity and are covered with spectrally selective mirrors.

The escaping intensity is

$$I_{esc} = A_i \int_0^{2\pi} \int_0^{\Theta_{int}} B_{int} \cos(\vartheta) \sin(\vartheta)\, d\vartheta\, d\phi = \pi B_{int} \tag{10}$$

where A_i is the entire surface area of the trap and B_{int} is the internal radiation density per steradian. We now relate B_{int} to the internal unidirectional radiation intensity at the boundaries of the light trap:

$$I_{int} = \int_0^{2\pi} \int_0^{\pi/2} B_{int} \cos(\vartheta) \sin(\vartheta)\, d\vartheta\, d\vartheta\phi = \pi B_{int} \tag{11}$$

Therefore,

$$I_{esc} = A_i I_{int} \sin\left(\arcsin\left(\frac{\sin\Theta_c}{n}\right)\right)^2 = \frac{A_i I_{int}}{n^2} \sin(\Theta_c)^2 \tag{12}$$

The light absorbed by the solar cells is $I_{int}A_S$. Now we can calculate the efficiency of the photonic light trap by setting up the energy balance between incoming radiation and light absorbed by solar cells and light reemitted from the surface:

$$I_{inc}A_i = \frac{A_i I_{int}}{n^2} \sin(\Theta_c)^2 + I_{int}A_S \tag{13}$$

Solving for I_{int},

$$I_{int} = \frac{I_{inc}}{(\sin(\Theta_c)^2/n^2) + F} \tag{14}$$

with $F = A_S/A_i$.

The trapping efficiency is

$$\eta_{trap} = \frac{I_{int}A_S}{I_{inc}A_i} = \frac{1}{(\sin(\theta_c)^2/n^2F) + 1} \tag{15}$$

The efficiency depends strongly on the acceptance angle (Fig. 9).

The concentration is

$$C = \frac{I_{int}}{I_{inc}} = \frac{1}{(\sin(\Theta_c)^2/n^2) + F} \tag{16}$$

High concentration can only be reached with small acceptance angles.

$1/F$ can be interpreted as the geometric concentration (presently known angular selective filters do not yet show a spectrally independent characteristic. The development of structures

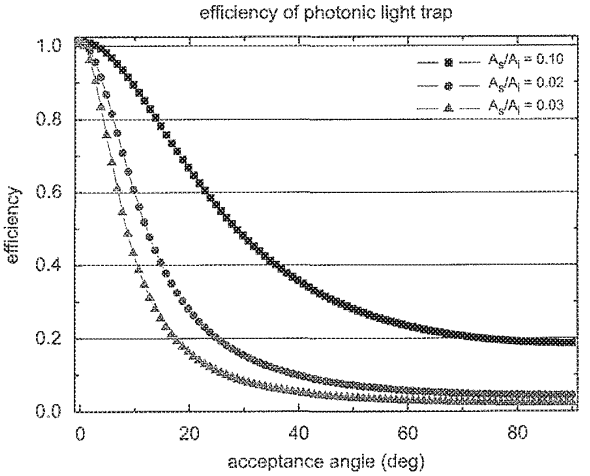

Fig. 9. Efficiency of photonic trap vs. opening angle Θ_c by restricting the acceptance angle of the photonic structure, the efficiency of the light trap is increased significantly. The maximum possible restriction is to the appearance angle of the sun of 0.27°.

SIONYX1403000017.0013

SAMSUNG EX. 1002 - 1422/4148

with an adjusted angular characteristic is probably the most difficult part of this concept).

3.2. More realistic systems

The photonic trap does not require optical elements for concentration. Concentration occurs inside the trap. This type of trap therefore has to have a large area which means that reflection losses and absorption play a crucial role. Also, the solar cells may not be fully absorbing. All these factors will now be considered.

If the reflecting areas have a reflection factor R, then the amount of light lost is

$$E_{\mathrm{refl}} = A_i I_{\mathrm{int}}(1-R)(1-F)$$

There will also be absorption in the volume. The amount of light lost in a trap with thickness W and absorption coefficient α is

$$E_{\mathrm{abs}} = \iint \alpha B_{\mathrm{int}}\,\mathrm{d}V\,\mathrm{d}\Omega = \int_0^{2\pi}\int_0^{\pi} \alpha B_{\mathrm{int}} W A_i \sin\vartheta\,\mathrm{d}\vartheta\,\mathrm{d}\phi = 4 I_{\mathrm{int}}\alpha W A_i$$

In the case of volume absorption, we have to take the bidirectional intensity $2I_{\mathrm{int}}$.

If the solar cell absorption is $\eta_{\mathrm{abs,cell}}$, then the light absorbed by the cell is

$$E_{\mathrm{abs,cell}} = I_{\mathrm{int}}\eta_{\mathrm{abs,cell}} A_s$$

Again we can equate the gains and the losses:

$$I_{\mathrm{inc}}A_i = \frac{A_i I_{\mathrm{int}}}{n^2}\sin(\Theta_c)^2 + I_{\mathrm{int}}A_s\eta_{\mathrm{abs,cell}} + A_i I_{\mathrm{int}}(1-R)(1-F) + 4 I_{\mathrm{int}}\alpha W A_i$$

In analogy to Eqs. (12)–(14), this results in the trapping efficiency:

$$\eta_{\mathrm{trap}} = \frac{\eta_{\mathrm{abs,cell}}F}{(\sin(\Theta_c)^2/n^2) + \eta_{\mathrm{abs,cell}}F + (1-R)(1-F) + 4\alpha W} \tag{17}$$

3.3. Combination of geometric concentration and photonic light trap

Optimal efficiency is obtained by combining both concepts described so far. In Section 2, we have implicitly assumed that the light entering the trap is coming from the full half space as it would at very high concentration. In reality, the light arriving at the trap from a concentrating lens has a limited opening angle. In Fig. 10, the situation in a real system (Flatcon) [18] is shown true to scale (the situation considered here is not compatible with secondaries).

In this case, the opening angle is $\Theta_c = 16.45°$. If a photonic structure with this acceptance angle is placed on the surface of the trap no light will be lost. On the other hand, light coming from the inside of the trap can only escape within the same angle modified by refraction. Inserting this value into Eq. (14), we obtain the upper curve in Fig. 2. Efficiency for this structure is very high. This combination has several advantages:

- The light trap is very small, so the losses due to absorption and reflective surfaces are negligible.
- Solar cell area can be of the same size as the input area, so efficiency is much higher.
- The surface area of the trap is small, so the cost of the photonic structure is tolerable.

The combination light trap probably cannot have a diffusing entry aperture. Randomization of the light can be achieved by diffusing reflectors or forward scattering centres close to the surface.

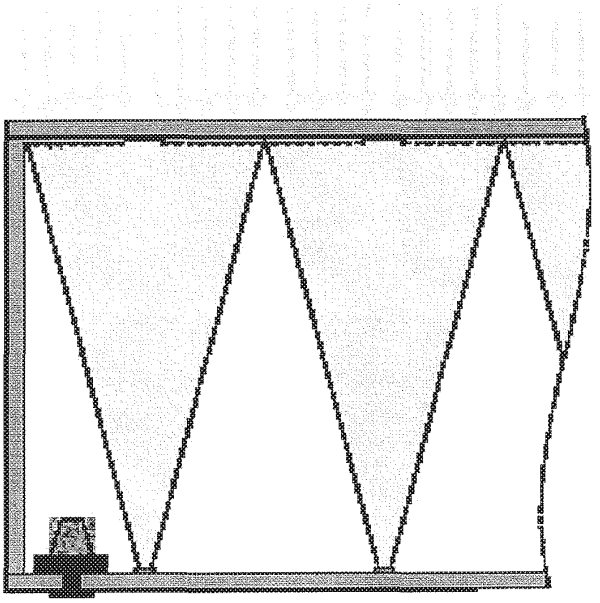

Fig. 10. Cross-section of a Flatcon concentrating system. Light is concentrated by Fresnel lenses onto highly efficient solar cells. The opening angle here is $\Theta_c = 16.45°$. Typical concentrations reached are in the order of 500.

The photonic system can also be analyzed with inclusion of initial absorption (Section 2.3). In order to calculate its efficiency, we modify Eq. (6) by inserting Eq. (14):

$$\eta_{\mathrm{tot}} = 1 - R_{\mathrm{trap}}\left(1 - \frac{1}{(\sin(\theta_c)^2/n^2F) + 1}\right) \tag{18}$$

The upper curve in Fig. 7 is the efficiency for a reflection of $R = 0.5$. Even in this case, the light trap is practically lossless.

4. Solar cell technology for light trapping

The advantage of light trapping is that solar cells of different band gaps can be placed side by side at the light trap. This offers several advantages:

- The solar cells can consist of different semiconductor materials.
- They do not have to be grown monolithically with very small lattice mismatch.
- More abundant materials can be used.
- No tunnel diodes between the cells are needed.

On the other hand, light trapping is not 100% efficient. Furthermore, the solar cells have to be equipped with selective mirrors.

The selective reflection can be simplified if it is taken into account that semiconductors are transparent for sub-band-gap light. This light can be reflected by a mirror at the back of the solar cell. In Fig. 11, this is outlined for an example with three different solar cells. The largest gap cell only has a mirror at the rear of the cell. The middle cell has a mirror for the long wavelengths and an edge filter for the short wavelengths. It should be noted that the edge mirror only has to have a sharp cut off reflection but can extend far into the ultraviolet. Such mirrors are easier to realize than band reflecting mirrors. The low gap cell finally only has an edge mirror for the shorter wavelengths.

SIONYX1403000017.0014

SAMSUNG EX. 1002 - 1423/4148

Another advantage for solar cells in conjunction with light traps is that since the cells are only thin, single semiconductor cells, wrap through technology can be used for contacts. In this way, shading of the front side by contacts is avoided.

Considering the selective mirrors, they do not have to be absolutely perfect regarding reflectivity and wavelength sensitivity. Reflected rays have a chance to be returned to the solar cell albeit at lower efficiency. High-energy photons absorbed by a lower gap cell are not lost but only converted at lower efficiency.

5. Stationary modules

So far only light traps for concentrating systems were analyzed. They permit high concentration although deconcentration by a factor of two or three is advantageous for high trapping efficiency. These systems are best suited for climates with high direct radiation intensity.

It is desirable to use the light trapping principle also for moderate climates with a high fraction of diffuse radiation. How this can be accomplished will be described now. In this paper, only stationary modules are considered. Low concentration or linear tracking systems might also be possible but will not be included here. In a first approach, the transparent superstrate of the module serves as the light trap (Fig. 12). In this case, the input aperture A_i is the entire module area. The surface of the module is structured to diffuse the light. If we consider a division of the solar spectrum by two (which is most feasible for stationary systems), the geometry of Fig. 12 results. ($A_s = A_i/2$) The lateral dimension of the solar cells should be of the order of the superstrate thickness or smaller. Otherwise the assumption of uniform light distribution breaks down.

The ratio $A_s/A_i = F$ is $F = 0.5$ and $R = 0.5$. From Eq. (6), we derive a trapping efficiency of $\eta_{tot} = 0.765$. This type of light trap can be improved by equipping the solar cells with a rough surface. There are however limits to this. Unlike the outer surface which is transmissive and will only randomize the incident radiation, a rough absorbing surface will lead to non-uniformity of the diffuse radiation. On the other hand, even a very modest structuring of the solar cell surface will improve efficiency noticeably. If the surface area is increased by a factor of 1.5, $F = 0.75$, then $\eta_{tot} = 0.814$. Better efficiency is possible with more complex geometries.

Some of them are outlined here: again deconcentration is employed. The solar cell area has to be larger than the module aperture. Many geometries can be imagined to accomplish this. Fig. 13 shows two examples namely saw tooth and parallel bars.

These geometries are particularly well adapted to thin film solar cells. Some aspects of the first two geometries will now be discussed.

Saw tooth: If the apex angle of the saw tooth is 45°, then thin film cells could be evaporated from the two sides as shown by the arrows in Fig. 13. The total efficiency is estimated as follows: $A_s/A_i = 2^{1/2} = 1.41$. R can be estimated to be about $R = 0.4$, then $\eta_{tot} = 0.9$.

Bars: For the bar $A_s/A_i = 3/2 = 1.5$, R could be exactly calculated for instance by ray tracing but is only estimated here. It is about $R = 0.25$. Then efficiency $\eta_{tot} = 0.943$. For manufacturing purposes, many bars could be placed side by side in a deposition chamber, rotated after deposition and again deposited. Finally, they could be placed in a module with the open side up. Here, just as for the saw tooth the usual thin film technologies for series connection could be used and contact could be made at the end of the bar. The structuring of the solar cell surface could of course also be applied to the geometries just mentioned.

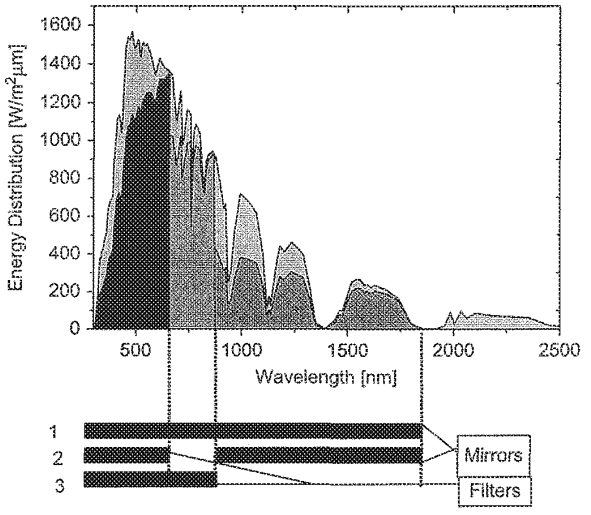

Fig. 11. Solar spectrum and spectral range of selective and regular mirrors for three stages 1–3. The first solar cell absorbs light with a wavelength lower than 700 nm. Higher wavelengths are transmitted and are reflected by a mirror. The second cell absorbs light with a wavelength smaller than 900 nm. To it a filter is attached that reflects light with a wavelength smaller than 700 nm. The mirror on the backside reflects the transmitted light. The third solar cell absorbs light with a wavelength smaller than 1800 nm. To it a filter is attached that reflects all light with a wavelength lower than 900 nm. By that means a spectrum splitting is realized. The shaded areas are schematic and only give losses due to band-gap energy.

6. Estimate of achievable conversion efficiency

6.1. Solar cell efficiency

We first consider solar cell efficiency and then look at influences of the optical system.

Starting with the thermodynamic limit, we know that efficiency increases significantly with the number of solar cells i.e. the degree of spectrum splitting. Table 1 gives the thermodynamic limit of efficiency vs. number of cells [19].

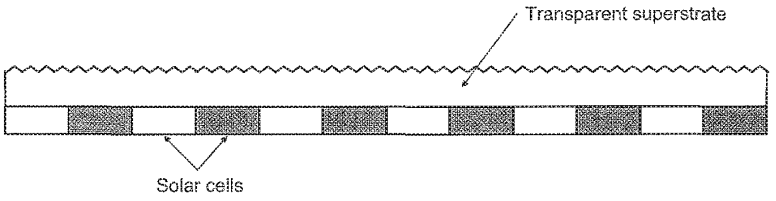

Fig. 12. Flat panel module with half-spectrum solar cells. The solar cells can either be small squares or, more practically, elongated strips. In the figure, two kinds of solar cells are shown, splitting the spectrum into two parts. Selective mirrors or reflectors as in Fig. 11 are not shown.

SIONYX1403000017.0015

SAMSUNG EX. 1002 - 1424/4148

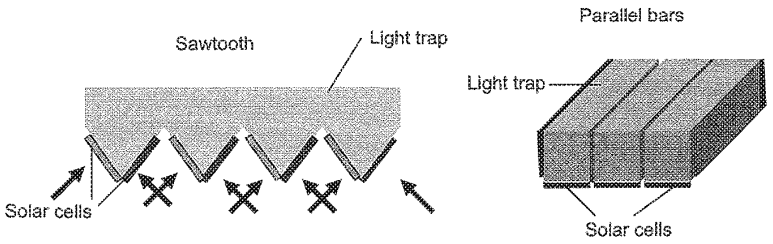

Fig. 13. Two versions of deconcentration in a flat plate module: (a) saw tooth and (b) parallel bars.

Table 1
Dependence of thermodynamic efficiency limit vs. number of cells

Number of cells	1	2	3	4	5
Efficiency	41.1	54.6	61.9	65.6	67.9

We see that these efficiencies are very high. The biggest increase occurs when going from one cell to two cells. Those ultimate efficiencies can of course not be reached in practice.

Barnett [5] estimates for a similar system practical efficiency by using derating factors. Higher band-gap cells are less derated than those with lower band gap. They estimate that for six junctions in four optical bins $\eta = 53.5\%$ can be achieved. Best experimental result so far is for three junctions in three optical bands $\eta = 42.8\%$, estimated from separate cell measurements under the conditions of their system.

With our light trap similar results can be anticipated. In order to limit the complication on the electrical side, it is suggested here that for high efficiency dual junction devices should be used for each optical band.

6.2. *Efficiency of light trap for concentrators*

As outlined in Sections 2 and 3, trapping efficiency can be very high if optimal geometrical and optical conditions are chosen, in particular if the light trap is combined with a photonic structure. Thus, the ultimate efficiency of the system light trap-solar cells can be very close to the values given above.

At this time, it is very difficult to estimate more realistic efficiencies. The following factors have to be considered:

(a) Absorption within the trap. This effect can be kept small because highly transparent materials are available and the trap can be made very small.
(b) The absorption of solar cells may be less than 100%.
(c) Efficiency of selective mirrors. Required are no parasitic absorption and good spectral selectivity as well as good reflectivity at all incidence angles.
(d) The requirement to create diffuse radiation is difficult to reconcile with selective mirrors and photonic structures. If this is not possible non-selective lambertian mirrors will have to be included. They should have very high reflectivity.

The overall system efficiency is further influenced by the efficiency of the optical concentration system as in conventional systems.

6.3. *Efficiency of the photonic structure light trap*

The photonic structure light trap as described in Section 3 is large area and does not need optical components. Concentration occurs within the trap. That means very high light intensity within the trap. Some loss factors are very severe:

(a) Absorption within the trap. When using very highly transparent material absorption could be tolerable.
(b) Reflectivity of mirrors. If high concentration is desired, a large fraction of the rear surface of the trap is covered by reflectors. Reflectivity has to be extremely good to enable high efficiency.
(c) Reflectivity of the photonic structure outside the escape cone. We assume total internal reflection but this has not yet been demonstrated (photonic structures can be as good as total internal reflection in principle).
(d) Efficiency of selective mirrors and absorption of solar cells have already been discussed in the previous paragraph.

6.4. *Stationary flat panel modules*

For the light trapping flat plate modules described in Section 5 the same solar cell efficiencies as discussed in Section 6.1 can be anticipated if optimal solar cells are used. Dependent on the geometry, lower efficiency of the light trap has to be taken into account. Optimal solar cells, however, may be too expensive for this application. Thin film cells are less costly and could be deposited onto the light traps. Amorphous Si is probably not capable of higher efficiency as the past development has shown. Better prospects are connected with micromorph films consisting of amorphous and microcrystalline films. Their efficiency is expected to be higher if used separately and not in a stacked cell. Even more efficiency can be foreseen for chalcogenides. The theoretical efficiency for two gaps has been estimated to be $\eta = 36.6\%$ [20]. In practice, $\eta = 20\%$ can be expected for a two gap system. Compared with concentrating systems flat plates have higher yield because they also utilise diffuse light.

7. Conclusions

The light trapping principle, based on diffuse radiation inside a transparent matrix, has been shown to offer many interesting aspects. It can be used for concentrating, tracking systems but also for stationary modules. The possibility to employ solar cells consisting of different materials and band gaps offers a much wider design space and holds hope to achieve higher conversion efficiency. The present paper presents mainly the basic principle and fundamental theory. Much experimental work is probably required to explore the practical applicability of this concept. Initial experiments are under way.

Acknowledgement

We acknowledge valuable discussions with Dr. Andreas Gombert and Dr. Benedikt Bläsi.

SIONYX1403000017.0016

SAMSUNG EX. 1002 - 1425/4148

References

[1] W. Shockley, H.J. Queisser, Detailed balance limit of efficiency of p–n junction solar cells, J. Appl. Phys. 32 (3) (1961) 510–519.
[2] A.W. Bett, et al., Metamorphic GaInP-GaInAs layers for photovoltaic applications, Mater. Res. Soc. Symp. Proc. 836 (2005) L6.4.1–L6.4.12.
[3] A. Goetzberger, W. Greubel, Solar energy conversion with fluorescent collectors, Appl. Phys. 14 (1977) 123–139.
[4] A.G. Imenes, D.R. Mills, Spectral beam splitting technology for increased conversion efficiency in solar concentrating systems: a review, Sol. Energy Mater. Sol. Cells 84 (19) (2004) 19–69.
[5] A. Barnett, Milestones toward 50% efficient solar cell modules, in: Proceedings of the 22nd European Photovoltaic Solar Energy Conference, Milan, Italy, 2007.
[6] E. Yablonovitch, Statistical ray optics, J. Opt. Soc. Am. 72 (7) (1982) 899–907.
[7] A. Luque, Performance of front contact silicon solar cells under concentration, Prog. Photovolt. 12 (2004) 517–528.
[8] A. Luque, The confinement of light in solar cells, Sol. Energy Mater. 23 (2–4) (1991) 152–163.
[9] A. Luque, et al., Angle-limited cavities for silicon solar cells, in: Proceedings of the 22nd IEEE Photovoltaic Specialists Conference, Las Vegas, NV, USA, 1991, pp. 99–104.
[10] U. Ortabasi, First experiences with a multi-bandgap photovoltaic cavity converter (PVCC) module for ultimate solar-to-electricity conversion efficiency, in: Proceedings of the 19th European Photovoltaic Solar Energy Conference, Paris, France, 2004, pp. 2256–2560.
[11] J.C. Minano, A. Luque, I. Tobias, Light-confining cavities for photovoltaic applications based on the angular-spatial limitation of the escaping beam, Appl. Opt. 31 (16) (1992) 3114–3122.
[12] A. Luque, J.C. Minano, Optical aspects in photovoltaic energy conversion, Sol. Cells 31 (3) (1991) 237–258.
[13] P.A. Davies, et al., Calculations of efficiencies achievable using gallium arsenide and silicon cells mounted together in cavities illuminated by single-stage concentration, Sol. Energy Mater. Sol. Cells 26 (3) (1992) 203–215.
[14] M. Florescu, et al., Improving solar cell efficiency using photonic band-gap materials, Sol. Energy Mater. Sol. Cells 91 (2007) 1599–1610.
[15] E. Yablonovitch, Inhibited spontaneous emission in solid-state physics and electronics, Phys. Rev. Lett. 58 (20) (1987) 2059–2062.
[16] I. Luque-Heredia, in: A. Luque, V. Andreev (Eds.), Concentrator Photovoltaics, Springer, Berlin, 2007, pp. 221–251.
[17] M. Peters, et al., Photonic crystals for the efficiency enhancement of solar cells, in: EOS Topical Meeting on Diffractive Optics, Barcelona, Spain, 2007.
[18] A.W. Bett, H. Lerchenmüller, in: A. Luque, V. Andreev (Eds.), Concentrator Photovoltaics, Springer, Berlin, 2007, pp. 301–319.
[19] A.W. Bett, F. Dimroth, G. Siefer, in: A. Luque, V. Andreev (Eds.), Concentrator Photovoltaics, Springer, Berlin, 2007, pp. 67–87.
[20] H.J. Lewerenz, H. Jungblut, Photovoltaik: Grundlagen und Anwendungen, Springer, Berlin, 1995.

SIONYX1403000017.0017

SAMSUNG EX. 1002 - 1426/4148

Evaluation of a Small Negative Transfer Gate Bias on the Performance of 4T CMOS Image Sensor Pixels.

Hyungjun Han, Hongjoo Park, Parker Altice, Woonil Choi, Younsub Lim, Sangjoo Lee, Seok Kang, Jaeyeong.kim, Kwangho Yoon and Jerry Hynecek
MagnaChip Semiconductor Ltd. Hyangjeong-dong, Heungdeok-gu, Cheongju-si, Chungcheongbuk-do, 361-725 Korea; E-mail: hyungjun.han@magnachip.com

I. Introduction.

From the early development of Virtual Phase CCD Image sensors it became well known that the negative bias applied to the CCD gates results in accumulation of holes at the interface [1, 2]. This leads to quenching of the interface states at the Si-SiO_2 interface under the poly-silicon gates and a significant reduction of dark current. In modern 4T CMOS image sensors the similar effect is typically accomplished by placing a suitable p-type doping implant under the transfer gate of the pixel. However, due to very thin gate oxides, which are typically used in today's CMOS image sensors; it is not possible to completely saturate the interface states with holes by using only the implants, since undesirable problems such as the large threshold voltage shift result. For this reason other methods have been developed and are typically used. This paper presents evaluation of application of a small negative bias to the transfer gate of a high performance CMOS image sensor pixel as one possible solution to the problem. The small negative gate bias is easily generated on chip without any difficulty by using simple negative charge pump circuits. A suggested circuit block diagram for the generation of the suitable negative bias on-chip is also shown for completeness. This paper presents data of the negative charge pump effects on the dark current, dynamic range and blooming characteristics. The tested 2 Megapixel imager has 2.2um x 2.2um 2T pixels and operates with 2.8V analog drain bias as is typical in mobile applications. The negative charge pump circuit can provide bias from 0.0V to -0.5V.

II. Motivation for using the negative charge pump.

During formation of pinned photo diode to minimize the dark current, a suitable p-type doping implant is also used under the gate of the charge transfer transistor in order to fill the interface states with holes in this region. The interface potential should be kept close to 0V. However due to the N+ doped poly-silicon gate typically used for this transistor a build in potential difference of approximately Ec – Ev is applied through a very thin gate oxide to this region. As a result a small potential bending occurs at the silicon surface, leading to the depopulation of the interface states of holes and generation of the dark current. Fig.1.0 shows the drawing of the approximate potential profile under the gate. To achieve a flat band condition and repopulation of the interface states by holes and consequently the dark current reduction a negative charge pump is used to apply a small negative bias to the gate.

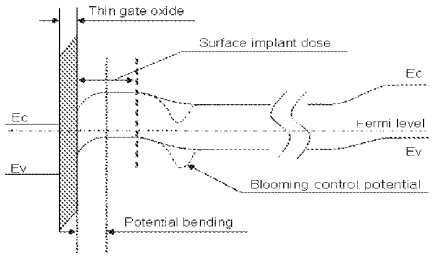

Fig.1.0. Energy band diagram under the charge transfer transistor.

In the CMOS image sensor it is also necessary to take care of the charge overflow to neighboring pixels called blooming. To prevent the blooming effects several approaches are usually used one of them being, for example, a blooming control implant. A dotted line

SIONYX1403000017.0018

SAMSUNG EX. 1002 - 1427/4148

in Fig.1.0 indicates the energy band diagram where the implant was used. When the negative charge pump is turned on, the potential profile shouldn't significantly change in order to maintain a good blooming control. For a better understanding of the device structure Fig.1.1 shows the drawing of the device cross section under the transfer gate region.

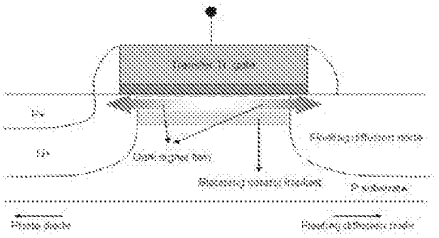

Fig.1.1. Cross section of the transfer gate region showing the interface states generated dark current flow and the blooming control implant location.

A portion of the interface states generated dark current flows into the floating diffusion and remainder flows into the photo diode. When the charge transfer transistor is turned off and a negative bias is applied to the gate holes are accumulated at the interface. This results in a significant reduction of dark current generation. Fig.1.2 shows the block diagram of the on chip negative charge pump circuit.

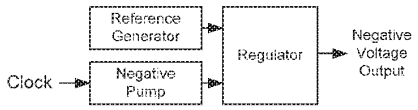

Fig.1.2. Block diagram of on chip negative charge pump circuit.

The circuit consists of the reference generator, negative bias charge pumping circuit and a regulator. The output is used as a ground level Vss-bias of the transfer gate driver-buffer. The resulting low level voltage applied to the gate of the transfer transistor thus becomes negative. The negative voltage range, which the circuit can generate, is from 0V to -0.5V with 0.05V steps.

III. Measurements and results.

Fig.1.3 shows the dark current measurement results. The dark current decreases with the negative charge pump bias. When the bias of -0.5V was applied to the gate, the dark current decreases as much as 37% in comparison to the 0V bias. However at the -0.05V bias a small increase has been noticed, which is not fully understood at this time and is currently being investigated.

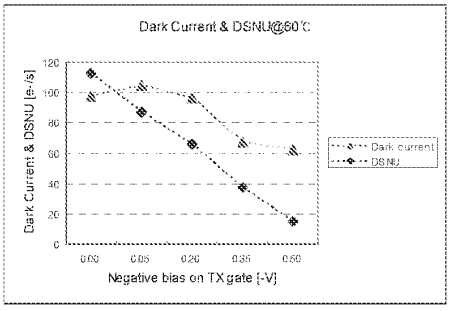

Fig.1.3. Dark current trend as function of the negative charge pump voltage.

Fig.1.4 shows the graph of the dynamic range as function of the negative charge pump bias.

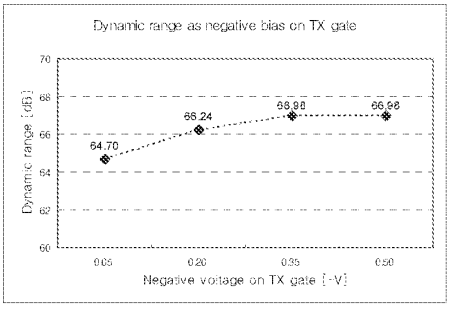

Fig.1.4. Dynamic Range as function of the negative charge pump voltage.

Since the blooming potential level can be affected by the negative gate bias it is necessary to confirm the

SIONYX1403000017.0019

SAMSUNG EX. 1002 - 1428/4148

blooming performance of the pixel. This is shown in the photographs in Fig.1.5.

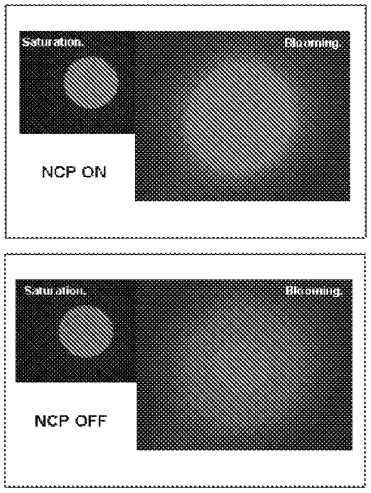

Fig.1.5. blooming image as function of the negative charge pump ON & OFF

An optical fiber was used as a light source for the generation of regular pattern and a module lens was used for the focused image. In case of the negative charge pump being turned off, the light pattern is noticed. The wider spot corresponds to bloomed area. When a lower light intensity is used no blooming pattern is found. With high intensity illumination the image intensity graph shown in Fig.1.6 is measured.

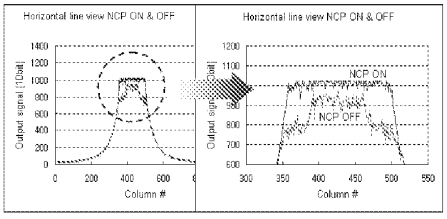

Fig 1.6. Blooming image horizontal view.

When a negative charge pump is turned off the pixel charge output is smaller than the full allowable analog swing voltage of the ADC converter. When the negative charge pump is turned on the blooming pattern could not be clearly recognized due the signal clipping by the ADC. However, when these two graphs are compared the over all shape of the graphs did not change only the output signal has increased. Fig.1.6 is showing the intensity graphs of the horizontal cross section of image in Fig.1.5. For the case of the negative charge pump turned off the signal is clipped off and only the blooming region remains. Concluding from the results shown in Fig.1.5 and Fig.1.6 it can be stated that the blooming control is working correctly. This means that the negative charge pump bias did not significantly affect the potential profile under the transfer gate.

IV. Conclusions

In this paper the effect of a small negative bias of the charge transfer gate on the CMOS sensor performance was evaluated. It was found that a small bias generated by the negative charge pump is useful for decreasing the dark current and increasing the sensor dynamic range. By using the negative charge pump, the blooming barrier was slightly lowered but the blooming characteristic was not significantly changed. The negative charge pump worked up to -0.5V and it showed approximately 37% decrease in dark signal and 0.24V increase of the saturation level.

Acknowledgements:

The authors would like to thank the ISD Device Team of MagnaChip Semiconductor Ltd. for support with the device fabrication and the Project Team III for including the Negative Charge Pump ckt. on the Sensor.

References:

[1] A. J. Theuwissen, "The Hole Role in Solid-State Imagers," IEEE Tr. Electron Devices, vol. ED-53, no. 12, pp. 2972-2979, December 2006.

[2] J. Hynecek, "Virtual Phase CCD Technology," in IEDM Tech. Dig. 1979, pp. 611-614.

SIONYX1403000017.0020

SAMSUNG EX. 1002 - 1429/4148

Light trapping effects in thin film silicon solar cells

F.-J. Haug, T. Söderström, D. Dominé, C. Ballif
École Polytechnique Fédérale de Lausanne (EPFL), Institute of Microengineering (IMT),
Photovoltaics and thin film electronics laboratory (PVLab),
Rue A.-L. Breguet 2, 2000 Neuchâtel, Switzerland

ABSTRACT

We present advanced light trapping concepts for thin film silicon solar cells. When an amorphous and a microcrystalline absorber layers are combined into a micromorph tandem cell, light trapping becomes a challenge because it should combine the spectral region from 600 to 750 nm for the amorphous top cell and from 800 to 1100 for the microcrystalline bottom cell. Because light trapping is typically achieved by growing on textured substrates, the effect of interface textures on the material and electric properties has to be taken into account, and importantly, how the surface textures evolve with the thickness of the overgrowing layers. We present different scenarios for the n-i-p configuration on flexible polymer substrates and p-i-n cells on glass substrate, and we present our latest stabilized efficiencies of 9.8% and 11.1%, respectively.

INTRODUCTION

Light scattering at textured interfaces has become a decisive feature for high efficiency thin film silicon solar cells. It allows using thinner absorber layers because the scattering enhances the effective light path in the absorbing film. While this is certainly important for production throughput, light trapping is also mandatory because of inherent material properties; in case of amorphous silicon, the impact of light induced degradation can be reduced in thinner films, in microcrystalline silicon it can, to some extent, compensate the low absorption of the indirect band gap. Light scattering is typically achieved at surface textures of the substrate or of the electric contact layer that precedes the silicon deposition [1]. For superstrate (p-i-n) devices, the transparent front contacts are either directly grown under conditions that favour preferential growth and faceting [2, 3], or they are structured by etching after growth [4]. Similar concepts are followed in substrate (n-i-p) devices for achieving textured metallic back contacts, e.g. the well known surface roughening of silver when it is grown on heated substrates [5]. Typical textures for amorphous silicon solar cells should have a root mean square (rms) surface roughness in the range from 50 to 90 nm, and a lateral feature size which varies between 300 and 500 nm.

For microcrystalline cells, the light trapping range lies between 800 and 1100 nm because of its lower band gap compared to amorphous cells. Empirical data suggest that the lateral feature size should be in the range from 1000 to 1400 nm, while higher rms roughness than in the amorphous case is not necessarily beneficial for the solar cell efficiency [6]. The latter observation might be related to the growth mechanism of microcrystalline silicon which often results in defective material above steep, V-shaped depressions [7, 8].

SAMSUNG EX. 1002 - 1430/4148

In micromorph tandem cells, where a microcrystalline and an amorphous absorber are combined in the same device, it becomes a challenging task to devise light scattering strategies that can effectively serve the different spectral ranges of the two individual cells. The first step to achieve this goal is the introduction of an intermediate reflector layer between the two cells, because light trapping in the amorphous top cell is quite simply impossible without reflection of light at its back surface; after its first realization with a thin film of ex-situ ZnO between the cells [9], in-situ solutions with P-doped SiOx have been realized [10], and the intermediate reflector is now established in production of micromorph tandem modules [11].

In this paper, we discuss the possibility of implementing different length scales for light trapping, either in the same interface by overcoating a large structure with smaller features, or by varying the texture between the individual interfaces. This approach must also take into account how a given surface structure evolves during the growth of amorphous and microcrystalline absorber layers, respectively.

EXPERIMENTAL

n-i-p cells

The n-i-p cells presented here are grown on a flexible polyethylene substrate. The surface of the substrate is textured with a periodic sinusoidal structure which is embossed into the surface by a roll-to-roll process [12]. The substrate is covered conformally by sputtering of a bilayer of silver and zinc oxide with thickness of 80 and 60 nm, respectively. The silicon layers are deposited at 180°C by very high frequency plasma enhanced CVD (PE-CVD) from a mixture of silane (SiH_4) and hydrogen (H_2), phosphine (PH_3) and tri-methyl-boron ($B(CH_3)_3$, TMB) are used as doping gases. The front contact consists of a 3.8 µm thick ZnO layer deposited by low pressure CVD (LP-CVD) which results in naturally textured growth [3]. The layer is lightly boron doped in order to suppress free carrier absorption [13]. In the n-i-p tandem cells shown here we use the same LP-CVD process for the deposition of the intermediate ZnO reflector with a thickness of 1.6 µm [14].

p-i-n cells

The p-i-n cells are grown on AF45 borosilicate glass substrates from Schott. First, the substrates are covered with a transparent front contact of LPCVD-ZnO; two different conditions are used, strongly doped films with a thickness of 1.9 µm (type A), and lightly doped films with a thickness of 4.8 µm. The sheet resistance of both substrates is 10 Ω/sq, their surface roughnesses are 66 and 180 nm, respectively. The thicker ZnO layer is subjected to a plasma treatment which changes the initial V-shaped morphology to U-shaped morphology which is better suited for the growth of microcrystalline silicon (type C) [13]. Depending on the duration of the treatment, the roughness can be reduced as much as down to 120 nm [15]. The amorphous and microcrystalline layers are deposited by VHF-PECVD under similar conditions to those of the previous section, but deposition temperatures up 220°C are tested. The intermediate reflector in the presented p-i-n cells is

SAMSUNG EX. 1002 - 1431/4148

made from P-doped SiO_x (SOIR) by in-situ processing [10]. The back contact of p-i-n cells consists again of LPCVD-ZnO, covered with a white reflector.

Characterization

The illuminated current voltage characteristics of all cells are measured in standard test conditions (25°C, AM1.5g spectrum, 100 mW/cm^2) with a dual source solar simulator (Wacom). The current density is determined independently by a measurement of the external quantum efficiency (EQE). Red and blue light bias is applied for measuring top- and bottom cells, respectively, and the photocurrent is determined by integration of the EQE weighted by the spectral photon density of the AM1.5g spectrum.

RESULTS AND DISCUSSION

n-i-p cells

As starting consideration for tandem development, we test the realistically attainable total current of the device by studying the dependence of the photocurrent on the bottom cell thickness. Figure 1 presents the EQEs of a series of microcrystalline cells on the 2D grating substrate. When the i-layer thickness increases from 1.1 µm to 2 µm, we observe a large increase in photocurrent from 23 mA/cm^2 to 24.5 mA/cm^2, but for thicker absorber layers the photocurrent tends to saturate at about for i-layers thicker than 2.5 µm. When the thickness is increased further, the electric performance degrades significantly which leads us to the conclusion the saturation reflects a problem with the collection of carriers rather than the limit of light trapping; with improved processing of the microcrystalline i-layer still higher current densities should be possible with our substrate texture.

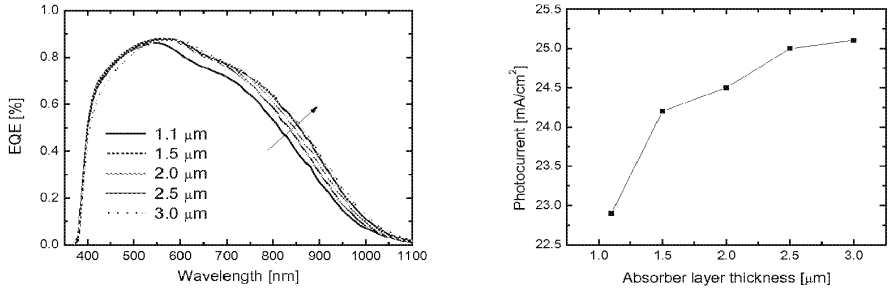

Figure 1: External quantum efficiency of microcrystalline solar cells on the periodic texture (left) and the dependence of photocurrent on the i-layer thickness (right).

Taking a limiting value of the total current of 25 mA/cm^2 for the time being, we can hope to get a matched tandem cell with a current of 12.5 mA/cm^2. However, even this current density is an ambitious goal for the amorphous top cell. If we consider a case where the amorphous top cell is stacked onto the microcrystalline bottom cell without any further enhancement, we can assume no more than one single pass through the

SAMSUNG EX. 1002 - 1432/4148

amorphous absorber layer. After passing through the top cell, the remaining light has ample chance to be absorbed in the bottom cell where it can make one passes through a thick absorber layer, undergo diffusion at the back contact and make another pass before it could reach again the amorphous cell. Thus, the top cell in such a tandem does not benefit from the back reflector. The thickness series of top n-i-p amorphous cells in Figure 2 shows that we require an i-layer thickness of more than 600 nm to obtain a photocurrent of more than 12 mA/cm^2. Clearly, such a thickness is not desirable in terms of light induced degradation.

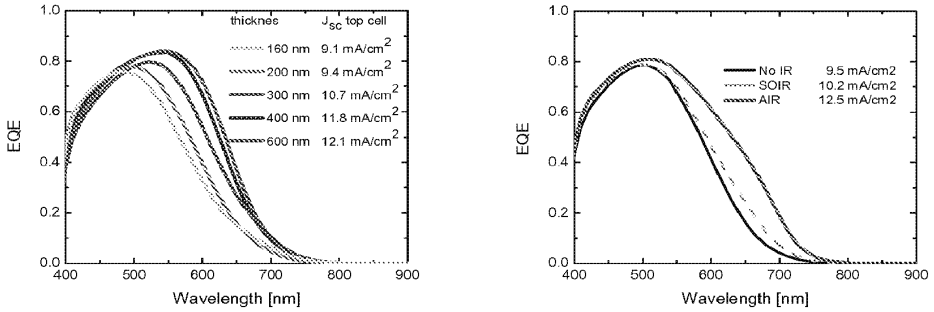

Figure 2: EQEs of the top cell in n-i-p/n-i-p tandem cells on the flexible substrate. The left panel illustrates the variation of i-layer thickness, the right panel illustrates the importance of a textured intermediate reflector layer (i-layer thickness: 200 nm).

By introducing a layer of lower refractive index between the bottom cell and the top cell, we can establish an interference condition where poorly absorbed light in the range between 600 and 750 nm is selectively reflected back into the amorphous absorber layer. The right panel in Figure 2 shows that a 100 nm thick, nominally flat SOIR improves the current in a 200 nm thick top cell from 9.5 mA/cm^2 to 10.2 mA/cm^2.

However, we are still far from the targeted photocurrent of 12.5 mA/cm^2, for two reasons. First, the periodic substrate with its period of 1200 nm is well matched to the requirements of the microcrystalline bottom cells, but not necessarily to amorphous cells. In 270 nm thick single junction amorphous cells deposited directly on this reflector, we obtained photocurrents between 12.8 and 14.4 mA/cm^2 [12], but the reflection at the SOIR in the tandem is very likely to be much inferior to the ZnO/Ag back contact. Second and more importantly, the texture of the back contact is changed by the growth of the microcrystalline bottom cell. Figure 3 shows a cross section image through a tandem cell on the periodic reflector. We observe that the amplitude of the substrate texture is reduced towards the top of the microcrystalline layer, and the sinusoidal shape is changed towards a mostly flat interface with small depressions located along the minima of the initial structure. Thus, the reflection at the SOIR can yield a second pass of light through the top cell, but we expect only little scattering of light at the flattened interface. Correspondingly, the top cell compares well to flat reference cells on a good reflector (e.g. 11 mA/cm^2 for a 270 nm thick cell [16]).

In order to achieve a real light scattering in the top cell, we introduce an asymmetric intermediate reflector (AIR) grown by LPCVD-ZnO [17]. Inherent to the growth process, LPCVD ZnO develops a textured surface regardless whether the

SAMSUNG EX. 1002 - 1433/4148

substrate is flat or mildly textured, and it is well documented that this surface texture is well adapted to amorphous solar cells [18]. Figure 3 shows that a 1.6 µm thick LPCVD-ZnO layer completely fills the small depressions in the surface of the microcrystalline layer, and develops its own typical pyramidal texture independent of the original periodicity.

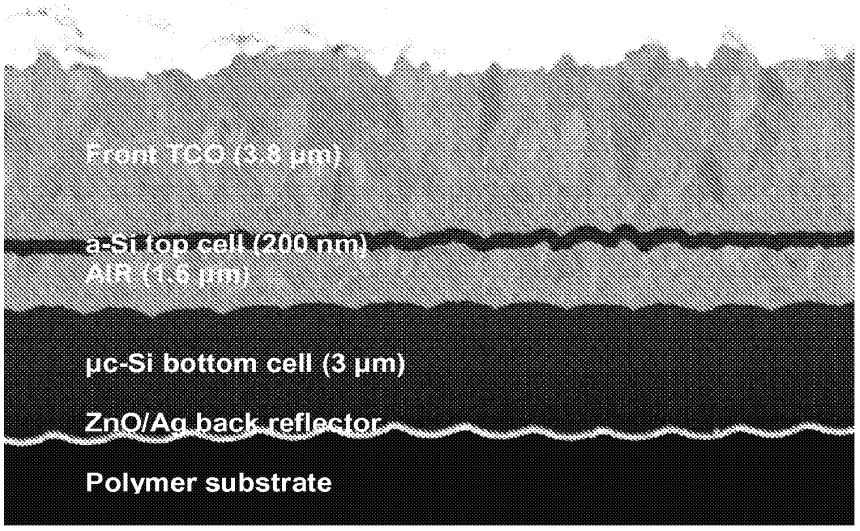

Figure 3: Cross section image through a micromorph tandem cell with LPCVD-ZnO AIR on the periodically textured polymer substrate.

Figure 2 shows that the asymmetric intermediate reflector results in a massive improvement of the top cell current, indeed, we achieve the goal of 12.5 mA/cm^2 in a 200 nm thick amorphous cell. The best cell of the AIR development showed an initial efficiency of 11.2%. After 1000 h of light soak, the efficiency stabilized at 9.8%.

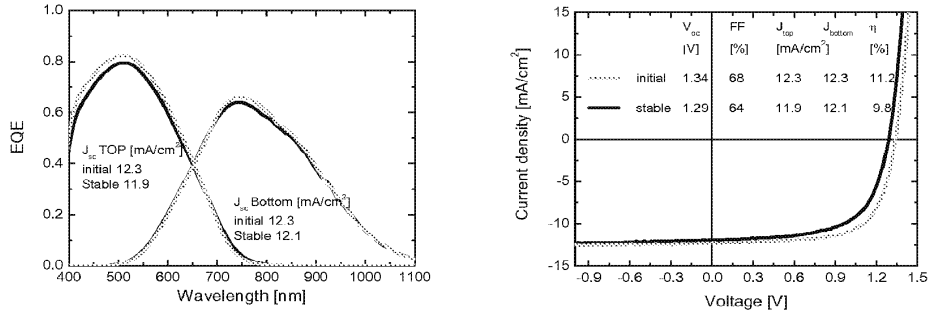

Figure 4: External quantum efficiency (left) and current voltage characteristic (right) of micromorph tandem cells with AIR on flexible polymer substrate in initial and stabilized state (1000 h light soak at 50°C and an illumination density of 100 mW/cm^2)

SAMSUNG EX. 1002 - 1434/4148

p-i-n cells

The p-i-n cell development is carried out on glass substrates covered with an LPCVD-ZnO front contact. Figure 5 shows typical surface morphologies for type A and type C substrates. Type A substrates consist of randomly distributed pyramids with a typical lateral feature size of 300 nm and clearly defined facets, whereas the surface treated type C substrates consist of large features (about 800 to 1000 nm) with rounded out bottoms of U-shape.

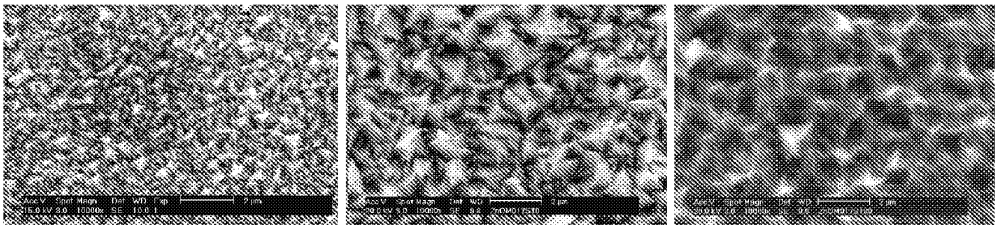

Figure 5: Surface morphology of type A substrate (left). Thicker films show similar shape, but bigger features (middle). A surface treatment yields type C substrate (right).

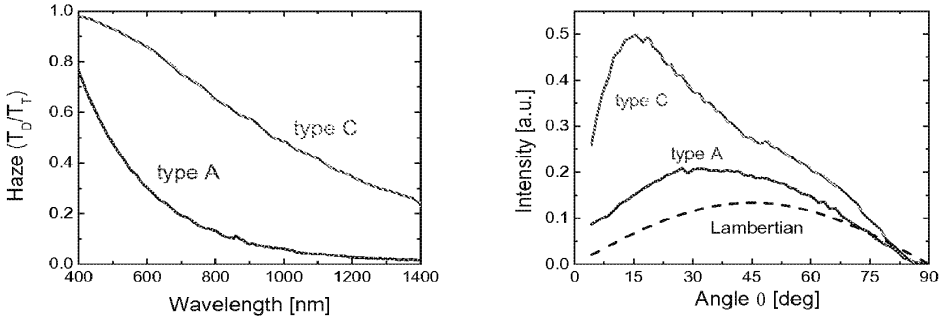

Figure 6: Spectral haze of type A and type C substrates (left panel). The right panel shows the sin-weighted ARS, the dotted line illustrates ideal Lambertian scattering.

Figure 6 compares the optical characteristics of the two layers; the haze is defined as ratio of diffuse to total transmission $H=T_D/T_T$, the angle resolved scattering (ARS) is the intensity scattered into angles between 0 and 90° for a fixed wavelength. For randomly rough surfaces with a correlation length much smaller than the wavelength, scalar scattering theory predicts the following relation between haze and wavelength [19, 20].

$$H = 1 - \exp\left\{-\left(\frac{2\pi\sigma}{\lambda}\left|n_1\cos\theta_1 - n_2\cos\theta_2\right|\right)^{\beta}\right\}$$

The angles θ_1 and θ_2 represent the incident beam and the direction of the scattered beam, respectively; n_1 and n_2 are the corresponding refractive indices. The exponent β

SAMSUNG EX. 1002 - 1435/4148

should be equal to 2, but different values have been reported experimentally [20, 21]. The haze data are shown in the left panel of Figure 6; we find β values of 2.8 and 2 for the type A substrate and the type C substrate, respectively [22]. The ARS data in the right panel are plotted after weighting with the sinus of the scattered angle which provides the shape of the probability density function associated to the angular distribution. The type A substrate shows a maximum a 40° which is very close to the behaviour of an ideal Lambertian diffuser (maximum at 45°), indicating that it scatters effectively into high angles. The type C substrate scatters into a narrow angular distribution, the most probable scattering angle being only 20°. Assuming rotational symmetry with respect to surface normal (ARS not dependent on the polar angle φ), the integrated areas under the curves are proportional to the diffuse part of the transmittance T_D. Their variation reflects the different haze values for the wavelength of the ARS measurement, in this case at 543 nm.

$$T_D \sim \iint ARS \cdot \sin\theta \cdot \mathrm{d}\varphi\,\mathrm{d}\theta = 2\pi \cdot \int ARS \cdot \sin\theta \cdot \mathrm{d}\theta$$

Figure 7 compares EQEs of tandem cells on the two different types of LPCVD ZnO front contacts; the top and bottom cell thicknesses are 290 nm and 3.0 µm, respectively. The cells without intermediate reflector in the left panel show identical top cell currents of 10.9 mA/cm^2, but the moderately doped type C substrate yields better bottom currents because of the lower free carrier absorption in the TCO and because the large grained type C structure is better suited for light trapping in the bottom cell. The behaviour of the EQEs in the top cells suggests that the current is essentially produced in one single pass through the amorphous absorber. The right panel shows the situation after the introduction of a SOIR with 150 nm thickness. Both top amorphous cells gain in current because of reflection at the SOIR, but we observe a larger gain in the device with the type A front contact (2.6 mA/cm^2 compared to 2.1 mA/cm^2 on the type C substrate). We can understand the observations in terms of the optical measurements shown in Figure 6 when we assume that, when multiple reflections can occur within the top cell, the broad ARS of the type A substrate can offset its lower haze values. We have to keep in mind though, that the optical measurements in air are different from the situation in the cell where the actual scattering interface is between ZnO and silicon, not between ZnO and air.

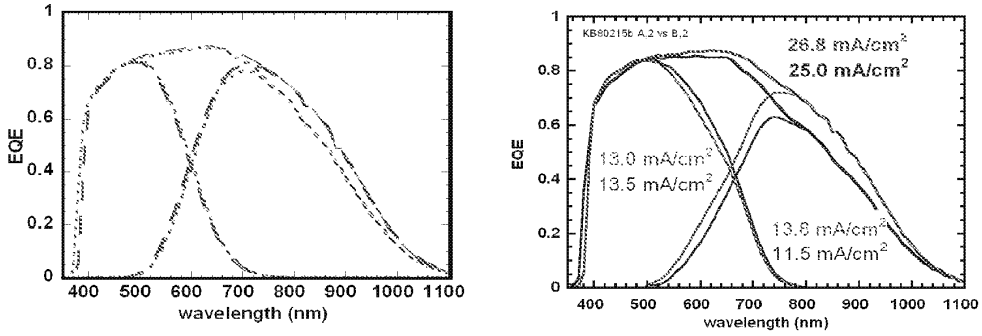

Figure 7: External quantum efficiencies of tandem solar cells on type A and type C substrates; left: no SOIR, right: with 150 nm thick SOIR.

SAMSUNG EX. 1002 - 1436/4148

We tried to combine the beneficial scattering effects of both types of substrates in a dedicated experiment by growing ZnO of type A on top of a substrate similar to type C. With this approach we intended to supply small features of type A for light scattering into the top cell. Furthermore, we anticipate that the flattening of the small features during the growth of the amorphous absorber should still maintain the larger features for scattering into the bottom cell. We compare a set of four different substrates including a type C substrate as reference (sample D3). The A3 sample is similar to the type C, but thinner; consequently it shows smaller features. The details of the substrate fabrication sequence are given in Table 1, further details can be found in [23].

Table 1: Design of the substrates for the double layer test

	A3	B3	C3	D3
Thickness 1st layer (μm)	3.6	3.6	3.6	4.5
SiOx layer		yes	no	
Thickness 2nd layer (μm)	-	1.1	1.1	
σ_{rms} (nm)	100	102	152	159
Comment:	"thin" type C	Figure 8 right	Figure 8 left	type C

The samples B3 and C3 are double structures, but care must be taken because the two constituent layers are made from the same material, ZnO. Thus, it turned out that simple stacking with surface treatment in-between just resumes the growth of the large grained ZnO in a form of local epitaxy, resulting in the formation of preferred surface facets very similar to the type C substrate before the surface treatment (c.f. left panel of Figure 8 compared to middle panel of Figure 5). The insertion of a thin SiOx layer using the same conditions as the SOIR layer, but only 5 nm thick, can effectively break the local epitaxy and force the ZnO to nucleate new grains. The right panel of Figure 8 shows that the result is a double structure that resembles to some extent the recently developed Asahi W structure [24].

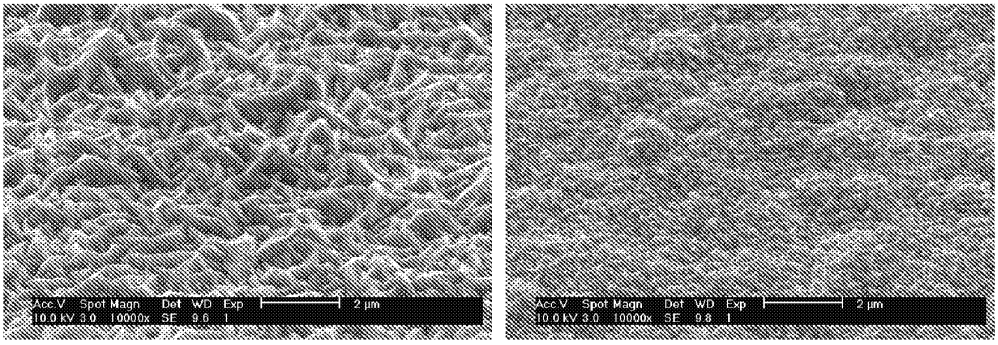

Figure 8: Stacking of type A ZnO on type C ZnO. In the left panel no interface treatment was used resulting in resumed grain growth and large features (sample C3), in the right panel a thin layer of SiOx was inserted, breaking the grain growth (sample B3).

SAMSUNG EX. 1002 - 1437/4148

Figure 9 compares the ARS of the four different substrates listed in Table 1. As expected, the single layer samples A3 and D3 are similar; their behaviour in the shallow angle range is identical, but we observe that D3 shows more scattering into large angles. The double structure without the SiOx treatment (sample C3) shows the best scattering into high angles, resembling in fact the type A structure of Figure 6. Surprisingly, the sample B3 with its clearly distinguishable double structure shows very poor scattering into high angles, but strong contributions into small angles around ~15°.

The EQEs of tandem cells with SOIR on the four different samples are shown in the right panel of Figure 9. We observe that the sample B3 shows poor light trapping in the bottom cell for wavelengths greater than 750nm, while the EQEs of the other samples are identical in this range. In the visible range between 550 and 700 nm, the inset shows that the top cell EQEs are higher in the double structures (samples B3 and C3) than in the single structures (samples A3 and D3). In the same range, the bottom EQEs of samples B3 and C3 are lower, indicating an efficient redistribution of light into the top cell. At this stage of development, it appears that among the double structures the configuration of sample C3 is preferable to B3, even though on that sample the character of a double structure is not obvious from Figure 8.

The poor performance of the B3 sample could possibly be explained by the poor ARS of this sample, but for the other substrates in this test the correspondence is much less evident. We should keep in mind that the measurement in air does not necessarily reflect the real light scattering properties in the cell. Recently, we proposed an optical model based on a Fourier approach [25] which is capable of predicting the behaviour of the ARS on the basis of AFM surface profile data [23]. We are confident that this tool will be useful in our further development of double structures because the calculations can be benchmarked against measured ARS data, and they can more reliably predict the behaviour in solar cells using realistic refractive indices.

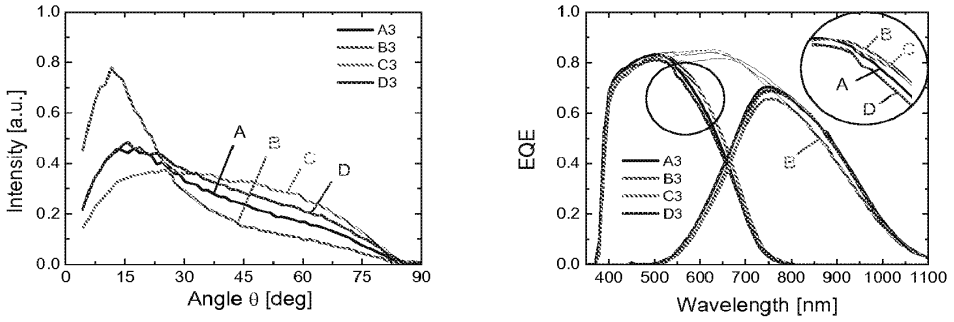

Figure 9: Comparison sin-weighted ARS data of a double layer test (left panel, layer types explained in text). The right panel shows the EQEs of tandem solar cells with SOIR on the different structures, the inset gives the details of the top cell EQEs.

After this brief outlook on new, but not yet fully conclusive double structures, we conclude this section on p-i-n tandem solar cells by reverting to the type C substrate; Figure 10 shows data on the electric performance of a configuration combining a top cell thickness of 300 nm, a bottom cell thickness of 3µm, and a SiOx intermediate reflector

SAMSUNG EX. 1002 - 1438/4148

layer of 150 nm thickness. In this configuration, and without anti-reflection coating, we obtain an initial efficiency of 12.6% which shows a relative degradation of 12% after 1000 h of light soaking, reaching a stabilized efficiency of at 11.1%. The area of this cell is 1.2 cm^2.

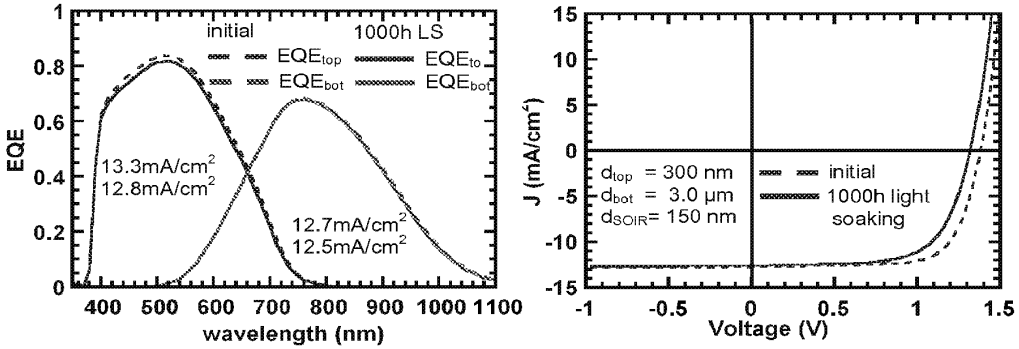

Figure 10: EQE and current voltage characteristics of a micromorph tandem solar cell with SOIR on the type C substrate in its initial and stabilized state (cell size 1.2 cm^2, no anti-reflection coating).

CONCLUSIONS

We presented thin film silicon tandem cells in n-i-p and p-i-n configuration. High efficiencies necessitate matched current densities higher than 12.5 mA/cm^2, but at the same time their thickness should not exceed 300 nm in order to avoid light induced degradation. Currently, an intermediate reflector between the top and bottom cells is the most successful route towards high top cell current densities. In n-i-p tandems, we observed that growth of the thick bottom cell results in adverse changes of the surface morphology, resulting in an almost flat interface. The potential of the intermediate reflector is very limited in these circumstances. By introducing surface texture into the intermediate reflector layer itself, we were able to supply to the top cell its very own light scattering interface, and we are at liberty to use a structure that is experimentally well proven for this purpose. We are able, on plastic substrate to apply that scheme to reach close to 10% stable efficiency micromorph cell, with an initial matched current of 12.3 mA/cm2 . We tried to apply the same line of arguments to the related case of p-i-n cells; a structure that combines small and large features should provide the fine features for light diffusion in the top cell while the flattening effect of growing the amorphous layer should not affect too seriously large features which could then diffuse longer wavelengths for light trapping in the bottom cell. We could successfully fabricate ZnO surfaces that show textures on two different length scales, but so far their application into tandem solar cells did not show a clear improvement. Single structure large grain TCO still leads to the best stable efficiencies over 11% with 12.5 mA/cm2 current.

SAMSUNG EX. 1002 - 1439/4148

ACKNOWLEDGEMENTS

Funding by the EU projects Flexcellence (contract No. 019948) and Athlet (contract No. 019670) as well as support from the Swiss Federal Office for Energy (OFEN) under project No. 101191 are thankfully acknowledged.

REFERENCES

1. H. W. Deckman, C. R. Wronski, H. Witzke, and E. Yablonovitch, *Optically Enhanced Amorphous-Silicon Solar-Cells*. Applied Physics Letters, 1983. **42**(11): p. 968-970.
2. M. Kambe, M. Fukawa, N. Taneda, Y. Yoshikawa, K. Sato, K. Ohki, S. Hiza, A. Yamada, and M. Konagai. *Improvement of light-trapping effect on microcrystalline silicon solar cells by using high haze transparent conductive oxide films*. in *Proc. 3rd World PVSEC*. 2003. Osaka. p. 1812-1815
3. S. Fay, J. Steinhauser, N. Oliveira, E. Vallat-Sauvain, and C. Ballif, *Opto-electronic properties of rough LP-CVD ZnO:B for use as TCO in thin-film silicon solar cells*. Thin Solid Films, 2007. **515**(24): p. 8558-8561.
4. O. Kluth, B. Rech, L. Houben, S. Wieder, G. Schöpe, C. Beneking, H. Wagner, A. Löffl, and H. W. Schock, *Texture etched ZnO: Al coated glass substrates for silicon based thin film solar cells*. Thin Solid Films, 1999. **351**(1-2): p. 247-253.
5. A. Banerjee and S. Guha, *Study of Back Reflectors for Amorphous-Silicon Alloy Solar-Cell Application*. Journal of Applied Physics, 1991. **69**(2): p. 1030-1035.
6. R. Franken, R. Stolk, H. Li, C. van der Werf, J. Rath, and R. Schropp, *Understanding light trapping by light scattering textured back electrodes in thin film n-i-p-type silicon solar cells*. Journal of Applied Physics, 2007. **102**: p. 014503.
7. M. Python, E. Vallat-Sauvain, J. Bailat, D. Dominé, L. Fesquet, A. Shah, and C. Ballif, *Relation between substrate surface morphology and microcrystalline silicon solar cell performance*. Journal of Non-Crystalline Solids, 2008. **354**(19-25): p. 2258-2262.
8. H. Li, R. Franken, J. Rath, and R. Schropp, *Structural defects caused by a rough substrate and their influence on the performance of hydrogenated nano-crystalline silicon n–i–p solar cells*. Solar Energy Materials and Solar Cells, 2009.
9. D. Fischer, S. Dubail, J. D. Anna Selvan, N. Pellaton Vaucher, R. Platz, C. Hof, U. Kroll, J. Meier, P. Torres, H. Keppner, N. Wyrsch, M. Goetz, A. Shah, and K.-D. Ufert. *The micromorph solar cell: extending a a-Si:H technology twoards thin film crystallline silicon*. in *Proc. 25th IEEE PVSC*. 1996. Washington D. C. p. 1053-1056
10. P. Buehlmann, J. Bailat, D. Domine, A. Billet, F. Meillaud, A. Feltrin, and C. Ballif, *In situ silicon oxide based intermediate reflector for thin-film silicon micromorph solar cells*. Applied Physics Letters, 2007. **91**(14): p. 143505.
11. K. Yamamoto, A. Nakajima, M. Yoshimi, T. Sawada, S. Fukuda, T. Suezaki, M. Ichikawa, Y. Koi, M. Goto, and T. Meguro, *A high efficiency thin film silicon solar cell and module*. Solar Energy, 2004. **77**(6): p. 939-949.

SAMSUNG EX. 1002 - 1440/4148

12. F.-J. Haug, T. Söderström, M. Python, V. Terrazzoni-Daudrix, X. Niquille, and C. Ballif, *Development of micromorph tandem solar cells on flexible low cost plastic substrates*. To be published in Sol. En. Mat., 2009.
13. J. Bailat, D. Dominé, R. Schlüchter, J. Steinhauser, S. Faÿ, F. Freitas, C. Bücher, L. Feitknecht, X. Niquille, R. Tscharner, A. Shah, and C. Ballif. *High efficiency pin microcrystalline and micromorph thin film silicon solar cells deposited on LPCVD ZnO coated glass substrates*. in *Proc. 4th World PVSEC*. 2006. Hawaii. p. 1533-1536
14. T. Söderström, F. J. Haug, X. Niquille, V. Terrazoni-Daudrix, and C. Ballif, *Asymmetrid intermediate reflector for tandem micromorph thin film silicon solar cells*. Applied Physics Letters, 2009. **94**: p. 063501.
15. D. Dominé, P. Buehlmann, J. Bailat, A. Billet, A. Feltrin, and C. Ballif. *High-efficiency micromorph silicon solar cells with in-situ intermediate reflector depositd on various rough LPCVD-ZnO*. in *Proc. 23rd European PVSEC* 2008. Valencia. p. 2091-2095
16. T. Söderström, F. J. Haug, V. Terrazzoni-Daudrix, and C. Ballif, *Optimization of amorphous silicon thin film solar cells for flexible photovoltaics*. Journal of Applied Physics, 2008. **103**(11): p. 114509-114509.
17. T. Söderström, *Single and multi-junction thin film silicon solar cells for flexible photovoltaics*, PhD Thesis, University of Neuchatel, 2009
18. J. Meier, J. Spitznagel, U. Kroll, C. Bucher, S. Faÿ, T. Moriarty, and A. Shah, *Potential of amorphous and microcrystalline silicon solar cells*. Thin Solid Films, 2004. **451**: p. 518-524.
19. C. K. Carniglia, *Scalar scattering theory for multilayer optical coatings*. Optical Engineering, 1979. **18**(2): p. 104–115.
20. M. Zeman, R. Van Swaaij, J. W. Metselaar, and R. E. I. Schropp, *Optical modeling of a-Si: H solar cells with rough interfaces: Effect of back contact and interface roughness*. Journal of Applied Physics, 2000. **88**: p. 6436.
21. H. Stiebig, T. Brammer, T. Repmann, O. Kluth, N. Senoussaoui, A. Lambertz, and H. Wagner. *Light Scattering in Microcrystalline Silicon Thin Film Solar Cells*. in *Proc. 16th EU-PVSEC*. 2000. Glasgow. p. 549-552
22. D. Domine, P. Buehlmann, J. Bailat, A. Billet, A. Feltrin, and C. Ballif, *Optical management in high-efficiency thin-film silicon micromorph solar cells with a silicon oxide based intermediate reflector*. Physica Status Solidi (RRL)-Rapid Research Letters, 2008. **2**(4).
23. D. Domine, *The role of front electrodes and intermediate reflectors in the optoelectronic properties of high-efficiency micromorph solar cells*, PhD Thesis, University of Neuchatel, 2009
24. T. Oyama, M. Kambe, N. Taneda, and K. Masumo. *Requirements for TCO substrate in Si-based thin film solar cells - toward tandem*. in *MRS Spring Meeting*. 2008. San Francisco. p. KK02-01
25. J. E. Harvey and A. Krywonos. *A Global View of Diffraction: Revisited*. in *Proc. SPIE AM100-26*. 2004. Denver. p.

SAMSUNG EX. 1002 - 1441/4148

ultrashort laser pulses allow the machining of well-defined structures and high-aspect-ratio holes under atmospheric pressure.

The production of metallic and organic stents (see Fig. 2) for the medical industry will be presented as a second industrial application for this novel machining technique.

This work was supported by the German Ministry of Science, Education, Research, and Technology (BMBF, 13N6590/0 and 13N7053/0).

1. W. Kautek, J. Krüger, SPIE Proc. **2207**, 600 (1994).
2. S. Preuss, A. Demchuk, M. Stuke, Appl. Phys. A **61**, 33 (1995).
3. C. Momma, B.N. Chichkov, S. Nolte, F. von Alvensleben, A. Tünnermann, H. Welling, B. Wellegehausen, Opt. Commun. **129**, 134 (1996).
4. B.N. Chichkov, C. Momma, S. Nolte, F. von Alvensleben, A. Tünnermann, Appl. Phys. A **63**, 109 (1996).
5. S. Nolte, C. Momma, H. Jacobs, A. Tünnermann, B.N. Chichkov, B. Wellegehausen, H. Welling, J. Opt. Soc. Am. B **110**, 2716 (1997).

CFD4 **9:00 am**

Avalanche ionization and dielectric breakdown in silicon with ultrafast laser pulses

P.P. Pronko, P.A. Van Rompay, C. Horvath, X. Liu, T. Juhasz, G. Mourou, *Center for Ultrafast Optical Science and the Department of Electrical Engineering and Computer Science, University of Michigan, Ann Arbor, Michigan 48109-2099*

Data are presented that demonstrate electron production by avalanche ionization as the dominant mechanism for laser breakdown, and subsequent surface damage in silicon, for laser pulse durations in the range of 80 fs to 9 ns. Experiments are performed at 786 nm and 1.06 μm exhibiting the correct wavelength dependence for an avalanche process. These data are correlated with plasma absorption to arrive at a model for the process. Associated electric-field breakdown potentials are observed that range from 0.3 to 40 MV/cm with avalanche ionization coefficients ranging from 1e10 to 1e14/s. These data are discussed in relation to semiempirical DC ionization rate theory and more recent AC Monte Carlo avalanche calculations. The trend of the ionization coefficients is shown to agree with the AC model throughout the optical fields studied and to converge to the DC case at the highest field strengths. Correlations are obtained between electron collision times and associated ionization rates by combining the Drude AC conductivity model with Monte Carlo and semiempirical DC avalanche theory. It is observed that the ratio of scattering to ionizing collisions varies from several thousand to approximately 50 across the field strengths investigated. For very high fields, the ionization collision times converge to the DC rates while the scattering collision times become subfemtosecond. Understanding these concepts provides insight into the modeling and use of ultrafast laser pulses for precision machining and cutting processes.

CFD5 **9:15 am**

Submicron lines in thin metal films micromachined by an ultrafast laser oscillator

X. Liu, *Center for Ultrafast Optical Science, The University of Michigan, 2200 Bonisteel Blvd., Room 1014, Ann Arbor, Michigan 48109-2099; E-mail: monkey@eecs.umich.edu*

Ultrashort laser pulses have been shown to hold great potential for high-precision micromachining applications. The laser-induced breakdown at high laser field and extremely short interaction time lead to high accuracy ablation threshold and effectively eliminate heat diffusion into the material. With the intensity-dependent and precise ablation threshold, one can control the incident laser intensity profile so that just a small central part of the focus spot is above the ablation threshold. One important consequence of this unique characteristic of ultrafast laser micromachining is its ability to machine sub-laser-spot-size holes and lines, overcoming laser wavelength-dependent minimum focus spot achievable. Indeed, sub-spot-size and even submicron holes micromachined by ultrafast lasers have been reported.[1-3]

In the studies where sub-spot-size holes were machined,[1-3] amplified pulses from a chirped-pulse amplification ultrafast laser system were used. However, we point out here that amplified pulses are not necessary when machining metal films. At ultrashort pulse widths, the ablation thresholds for most metal films are ~0.1–0.3 J/cm^2.[2] With a Ti:sapphire ultrafast laser emitting at 0.8 μm, we can focus the laser beam to a spot diameter ~1 μm when a high-numerical-aperture focusing lens is used. We then realize that the pulse energy needed to achieve a fluence of 0.3 J/cm^2 is only 2.4 nJ when the beam is focused to a 1-μm diameter (measured at $1/e^2$ width). Therefore, an ultrafast laser oscillator alone can provide the necessary pulse energy for submicron micromachining.

To the best of our knowledge, we demonstrate submicron micromachining with an ultrafast laser oscillator for the first time. The laser used was a 100-fs Ti:sapphire laser with an output power of 0.35 W operating at 89 MHz. A Faraday isolator was used to reject any backreflection from the work piece. A wave plate and polarizer combination was used to vary the laser power incident on target. The laser beam was focused by an f = 3.1 mm, 0.68 N.A. aspheric lens onto the surface of a metal film coated on Si wafer. Figure 1 plots the focused spot intensity profile measured by the scanning knife edge method, showing a $1/e^2$ diameter of 1.7 μm. Figure 2 shows the SEM picture of lines machined in 100-nm-thick Ni film deposited on Si wafer. The laser power was 65 mW (0.72 nJ/pulse), and the sample was translated at a linear speed of 0.1 mm/s. The width of the line is approximately 0.3 μm.

There are a number of improvements that can be made to our experiment that may result in even finer lines. Smaller focused spot size should be realizable with better focusing optics and by matching the input beam size to the focusing lens diameter. Better control in sample positioning and the use of a microscope imaging system should give better focus on target. We believe 0.1-μm linewidth should be achievable with ultrafast lasers. Advantages of using a femtosecond laser oscillator as opposed to a CPA system include system simplicity, compactness, stability, and much reduced cost. It may find important applications in semiconductor microelectronics, such as laser dry etching of IC circuits.

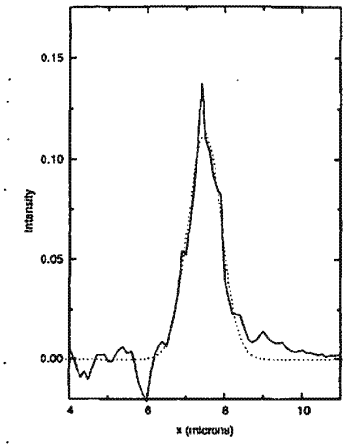

CFD5 Fig. 1. Laser beam profile at the focus of f = 3.1 mm, 0.68 N.A. lens. The Gaussian fit has a $1/e^2$ diameter of 1.7 μm. The input laser beam slightly underfilled the focusing lens.

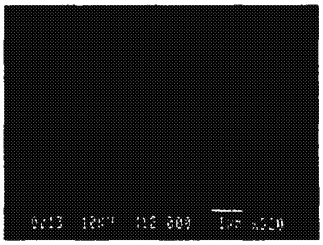

CFD5 Fig. 2. SEM picture of ultrafast laser oscillator machined lines in 100-nm-thick nickel film deposited on silicon wafer.

1. X. Liu, D. Du, G. Mourou, IEEE J. Quantum Electron. **33**, 1706–1716 (1997).
2. P. Pronko, S. Dutta, J. Squier, J. Rudd, D. Du, G. Mourou, Opt. Commun. **114**, 106–110 (1995).
3. E.N. Glezer, M. Milosavljevic, L. Huang, R.L. Finlay, H.-H. Her, J.P. Callan, E. Mazur, Opt. Lett. **21**, 2023–2025 (1996).

CFD6 **9:30 am**

Novel conical microstructures created in silicon with femtosecond laser pulses

Tsing-Hua Her, Richard J. Finlay, Claudia Wu, Eric Mazur, Shrenik Deliwala, *Harvard University, 9 Oxford St., Cambridge, Massachusetts 02138*

Silicon wafers are mounted inside a vacuum chamber backfilled with Cl_2, SF_6, N_2, or He

Authorized licensed use limited to: IEEE Xplore. Downloaded on November 24, 2008 at 10:40 from IEEE Xplore. Restrictions apply.

SIONYX1403000017.0033

SAMSUNG EX. 1002 - 1442/4148

and then irradiated with 800-nm pulses from a regeneratively amplified Ti:sapphire laser. Following laser treatment, the samples are removed from the chamber and analyzed with a scanning electron microscope (SEM).

Figure 1(a) shows the dramatically structured surface following irradiation in SF_6. The surface is covered in conical spikes. The tops of the spikes are at the same level as the surrounding unirradiated silicon surface. In the center of the micrograph, where the laser fluence was highest (10 kJ/m^2), the spikes are 35-μm tall. There is an approximately 1-μm spherical cap on each spike below which the spikes broaden. The spikes are always aligned parallel to the k vector of the laser pulse. At the edges of micrograph, where the laser fluence was lower, the surface remains highly structured, but the tall conical spikes are not observed.

The ambient gas is essential to the spike formation. Spikes such as those in Fig. 1(a) are produced in atmospheres of Cl_2 or SF_6. We repeated the experiments in atmospheres of N_2, He, and air. Figure 1(b) shows that although the surfaces produced in these gases are structured, they do not have the regular sharp spikes produced by treatment in atmospheres containing halogens.

Figure 2 shows the dependence of spike size on laser pulse duration at 10 kJ/m^2. The spike size falls precipitously as the pulse duration increases from 100 fs to 1 ps.

Many surfaces irradiated with laser pulses at fluences at or above the melting threshold become structured.[1-3] The structuring can be influenced by photostimulated chemical reaction between the surface and an ambient gas.[4,5] However, no spikes like those shown in Fig. 1(a) have been reported.

No physical model exists that can explain the spike formation we observe. A model must account for the strong dependence on laser intensity, the regular shape of the spikes, and the spherical caps. We are currently studying whether the ambient gas is directly excited by the laser pulse or whether reaction with the ambient gas is determined by the substrate excitation.

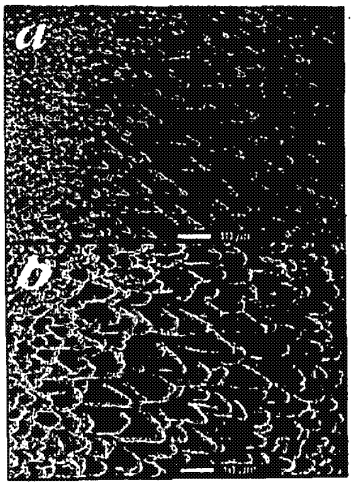

CFD6 Fig. 1. SEM micrographs of the silicon surfaces after 500 laser pulses of 100-fs duration, 10-kJ/m^2 fluence in 500-Torr SF_6 (a) or vacuum (b). This view is 45° from the surface normal. A 10-μm scale is shown. The FWHM of the laser spot was 200 μm.

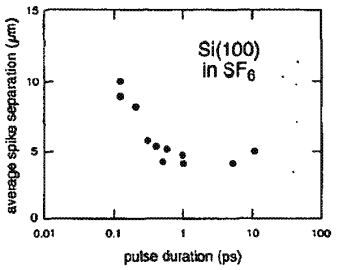

CFD6 Fig. 2. The sizes of the spikes fall rapidly with increasing pulse duration when the laser fluence is 10 kJ/m^2. High-intensity excitation is required to produce the tallest spikes. The average distance between spikes is the square root of the average area occupied by each spike. The distance between the spikes is correlated with their height because of the regular shape of the spikes.

1. *Laser Ablation*, E. Fogarassy, D. Geohegan, M. Stuke, eds. (Elsevier, Amsterdam, 1996), Vol. 55.
2. D. von der Linde, K. Sokolowski-Tinten, J. Bialkowski, Appl. Surf. Sci. **109/110**, 1 (1997).
3. Y.K. Jhee, M.F. Becker, R.M. Walser, J. Opt. Soc. Am. B **2**, 1626 (1985).
4. M. Müllenborn, H. Dirac, J.W. Petersen, App. Surf. Sci. **86**, 568 (1995).
5. H. Baumgärtner, W. Jiang, I. Eisele, Appl. Surf. Sci. **106**, 301 (1996).

CFD7 9:45 am

Advanced laser microjoining for MEMS applications

Arnold Gillner, *Fraunhofer-Institute for Laser Technology, Steinbachstrasse 15, D-52074 Aachen, Germany*

Microsystems technology requires packaging and interconnection technologies, which meets the demands of flexible production with still small lot sizes and, in contrast to microelectronics applications, often with different materials. Additionally, depending on the application of the micro parts, the joint has to withstand high temperatures, aggressive fluids, and mechanical forces constantly without degradation and negative long-term effects. The laser technology offers appropriate solutions for packaging and interconnection using processes that have been approved for a long time in fine mechanics and joining applications.

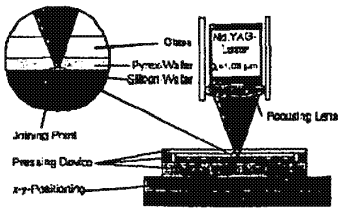

CFD7 Fig. 1. Principle setup of silicon glass joining with laser beams.

With new developments, laser joining can be used also for packaging and assembly of fluidic systems made from silicon, glass, and polymers in conjunction with metals. In Table 1, different laser-joining technologies are listed that are suitable for microsystem packaging.

As can be seen from the table, laser joining is especially suitable for applications at high temperatures and harsh atmospheres and surroundings, such as sensors and other electric components for the use in automotive parts.

The main advantage of laser joining is the high precision and the long-term stability of the joint. Especially in joining optoelectronic components, a joining technology is required that does not influence the optical quality of the subcomponents by splashes or recondensation of evaporated solubles from adhesives. But also laser joining has to be improved with respect to higher quality and smaller welding geometry. First attempts have been made to reduce the size of the weld spot with the aim of increasing the assembling accuracy. A newly developed fiber laser has been tested for micro joining optolectronic components like pigtailed laser diodes. This laser, producing a few micron focal point is able to reduce the energy impact and thus the distortion of the subcomponents to a minimum. Submicron accuracy is achieved for fiber pigtailing where displacement shifts for round parts can be minimized by using three weld spots simultaneous, which are positioned symmetrically around the axis of the part.

Besides laser beam microwelding, alternative joining techniques like the well-known soldering process can be used for joining electronic components. Especially in conjunction with high-power diode lasers, new joining tools can be developed, where both laser and gripping devices are integrated into a modular assembly device.

For joining different material composites, a new type of laser welding process has been developed. With the use of the specific advantages of laser radiation, a scaling and joining technology can be performed without the dis-

CFD7 Table 1. Laser Microjoining Technologies

Technology	Temperature range	Material	Laser power	Joining time
Laser soldering	<300°C	copper, steel precious materials	10–50 W Diode lasers	10–100 ms
Laser brazing	800–1100°C	copper, steel, refractive materials	50–500 W Diode and Nd:YAG-lasers	50 500 ms
Laser welding	>1500°C	all	>1 kW Nd:YAG-lasers	1–10 ms

Authorized licensed use limited to: IEEE Xplore. Downloaded on November 24, 2008 at 10:40 from IEEE Xplore. Restrictions apply.

SIONYX1403000017.0034

SAMSUNG EX. 1002 - 1443/4148

Appl. Phys. A 70, 383–385 (2000) / Digital Object Identifier (DOI) 10.1007/s003390000406

Applied Physics A
Materials
Science & Processing

Femtosecond laser-induced formation of spikes on silicon

T.-H. Her*, R.J. Finlay, C. Wu, E. Mazur**

Division of Engineering and Applied Sciences and Department of Physics, Harvard University 9 Oxford St., Cambridge, MA 02138, USA
(Fax: +1-617/495-2362, E-mail: mazur@physics.harvard.edu)

Received: 10 September 1999/Accepted: 7 January 2000/Published online: 8 March 2000 – © Springer-Verlag 2000

Abstract. We find that silicon surfaces develop arrays of sharp conical spikes when irradiated with 500-fs laser pulses in SF_6. The height of the spikes decreases with increasing pulse duration or decreasing laser fluence, and scales nonlinearly with the average separation between spikes. The spikes have the same crystallographic orientation as bulk silicon and always point along the incident direction of laser pulses. The base of the spikes has an asymmetric shape and its orientation is determined by the laser polarization. Our data suggest that both laser ablation and laser-induced chemical etching of silicon are involved in the formation of the spikes.

PACS: 61.80.B; 79.20.D; 82.65.J

Various micron-sized surface features have been observed on silicon surfaces after ion beam or pulsed laser irradiation. For example, mounds and columns are formed when silicon is sputtered by energetic Ar ions [1,2]. When irradiated by nanosecond laser pulses with fluence close to the melting threshold, silicon surfaces develop ripples with submicron periodicity [3]. Laser pulses with even higher fluence can induce laser ablation of silicon, leaving a crater on the surface surrounded by irregular cones protruding above the surface [4]. Previously we reported that silicon surfaces spontaneously develop arrays of conical spikes when repeatedly irradiated with high-fluence fs laser pulses in SF_6 or Cl_2 [5]. Similar structures have recently been reported with ns laser irradiation [6]. The spikes we observe have a high aspect ratio, a quasi-periodic spatial distribution, and are only formed in an atmosphere containing a halogen. Besides their scientific interest, the silicon spikes are of interest because of their potential applications as light absorbers [7] for solar cells and photodetectors, and as microneedles for transdermal drug delivery [8]. In this paper, we characterize the surface morphology and study the effect of laser fluence and pulse duration on the spikes.

**Current address:* Lawrence Berkeley National Laboratory, ms 2-300, 1 Cyclotron Rd., Berkeley, CA 94720, USA. (Fax: +1-510/486-5530, E-mail: thher@lbl.gov)

***Current address:* Northern Telecom, P.O. Box 3511 Stn. C Ottawa, ON, K1Y 4H7 Canada

1 Experimental

We carried out our experiments on *n*-type (arsenic-doped) Si(100) wafers with resistivity less than $5 \times 10^{-5}\ \Omega$ m. Each wafer is cleaned with trichloroethylene, rinsed in acetone, and then rinsed in methanol. The wafer is mounted on a three-axis translation stage in a vacuum chamber with a base pressure of less than 10^{-4} Torr. During the experiments, the chamber is backfilled with 500-Torr SF_6.

The laser system, consisting of a Ti:sapphire oscillator and a chirped-pulse-regenerative amplifier, produces a 1-kHz train of 100-fs, 0.5-mJ pulses at 800 nm. Longer pulses are obtained by adjusting the pulse compressor. The laser pulses are focused with a 0.1-m focal-length lens and, except where noted, incident normal to the sample. The spatial profile of the laser pulse is nearly Gaussian, with a fixed beam waist of 200 μm at the sample. The fluence (energy per unit area) varies over the laser spatial profile; values quoted below refer to the fluence at the center of the spatial profile. The fluence is controlled by changing the total incident energy with a half-wave plate and a polarizer. The polarization of the laser pulse is controlled by a second half-wave plate. Each spot on the sample surface is exposed to 500 laser pulses. We translate the sample by approximately 1 mm between runs. Following irradiation, the sample is analyzed with a scanning electron microscope (SEM).

2 Results and discussion

Figure 1 shows planar and cross-sectional views of the sharp conical spikes on silicon produced with 100-fs pulses at a fluence of $10\ \mathrm{kJ/m^2}$ in 500-Torr SF_6. The spike size varies across the irradiated region, reflecting the variation of the fluence across the laser spatial profile. The spikes are up to 40 μm tall and have a subtended angle of approximately 20°.

SIONYX1403000017.0035

SAMSUNG EX. 1002 - 1444/4148

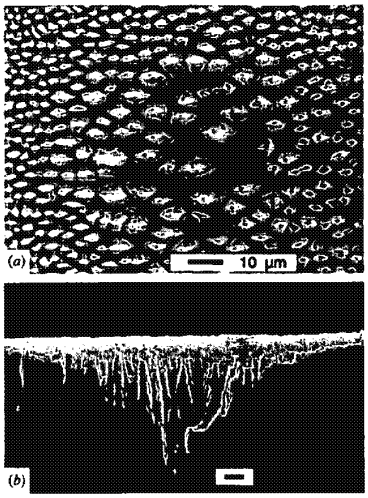

Fig. 1a,b. Sharp conical spikes produced on Si(100) by 500 laser pulses of 100-fs duration and 10-kJ/m^2 fluence in SF_6 at a pressure of 500 Torr viewed **a** from the surface normal, and **b** parallel to the surface

The base of the spikes has an asymmetric shape. When we rotate the laser polarization, the orientation of the base rotates accordingly. We find that the short axis of the base is always parallel to the laser polarization.

We determined the atomic structure of each individual spike by performing backscattering Kikuchi diffraction [9]. The diffraction pattern obtained from the spike shows the same Kikuchi lines as those taken from a flat undamaged surface next to the irradiated areas. This indicates that the spike is crystalline and has the same crystallographic orientation as bulk silicon.

We also observed similar sharp spikes on Si(111) with the laser at normal incidence and Si(100) with the laser incident at 20° off the surface normal. In all cases, the spikes point along the incident laser direction, independent of the crystallographic orientation of the substrate.

Figure 1 shows that the distribution of the spikes reflects the intensity variation over the spatial profile of the laser beam. At the center of the irradiated area, the spikes are wider, taller, and more sparsely spaced, whereas at the edges they are narrower, shorter, and more closely packed. We determined the relation between spike height and spike separation from Fig. 1 by measuring the spike height h as a function of the distance from the center of the irradiated region Fig. 1b and the average separation between spikes d from Fig. 1a. The average spike separation is obtained from the number density of the spikes within a $20 \times 20\,\mu m$ square area. Figure 2 shows that the spike height scales nonlinearly with the spike separation. The solid line in Fig. 2 is a least-squared fit of a power law, $h \propto d^p$ to the data, yielding a power law exponent $p = 2.4 \pm 0.1$. When the spike separation drops below 1.5 μm, the surface is corrugated but no sharp spikes are observed.

Figure 3 shows the dependence of the spike separation on laser fluence with 100-fs pulses. To avoid any problems associated with fluence variations over the beam profile, we obtained these data by measuring the average spike separation at the center of the laser profile for different fluences. The

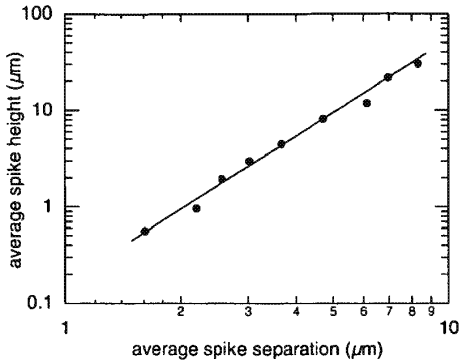

Fig. 2. Dependence of average spike height on average spike separation, determined from Fig. 1a,b. The *solid straight line* is a least-squared fit to a power law dependence

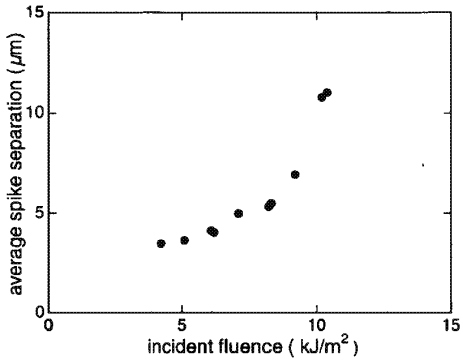

Fig. 3. Dependence of average spike separation on laser fluence for laser pulses of a fixed pulse duration of 100 fs

spike separation increases sharply with increasing laser fluence: as the fluence increases from 5 to 10 kJ/m^2, the spike separation increases by a factor of three. Using the power law fit from Fig. 2, this yields a twelve-fold increase in spike height. Below 2 kJ/m^2, the surface shows ripples of sub-μm periodicity and no spikes are observed. At 1 kJ/m^2, the surface remains intact even after 500 laser pulses.

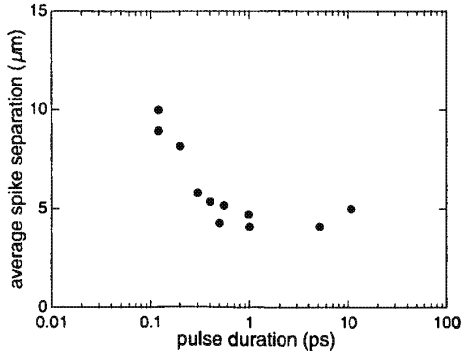

Fig. 4. Dependence of average spike separation on laser pulse duration for laser pulses of a fixed fluence of 10 kJ/m^2

SIONYX1403000017.0036

SAMSUNG EX. 1002 - 1445/4148

Figure 4 shows the dependence of the spike separation on pulse duration for laser pulses at a fixed fluence of 10 kJ/m^2. The spike separation decreases sharply as the pulse duration increases from 0.1 to 1 ps, and remains approximately constant between 1 and 10 ps. At 250 ps, the surface is corrugated but no sharp spikes are observed.

Cones with a morphology similar to the ones we observe on silicon have been seen on metals, dielectrics, and oxides after ion or ns laser sputtering [10, 11]. These cones also have the same crystallographic orientation as the bulk and point along the incident beam direction. Their formation has been attributed to shielding of the underlying substrate by sputtering-resistant impurities on the surface, leaving the cones behind as the surrounding material is removed by the sputtering particles. A similar argument can be used to explain the formation of the spikes on silicon reported here. Initial fluctuations [12] give rise to preferential removal of material at certain locations, explaining the observed crystallographic orientation and pointing of the spikes we observe on silicon.

Because more silicon is removed in areas where more energy is deposited, a difference in light absorption on different sides of the spikes would explain the asymmetric shape of their bases visible in Fig. 1a. Indeed, the laser pulses in Fig. 1a are polarized along the x axis; therefore, they are p-polarized on the sides of spikes oriented along the yz plane, and s-polarized on the sides of spikes oriented along the xz plane. Because absorption of p-polarized light is larger than that of s-polarized light, the sides of spikes oriented along the yz plane absorb more energy, causing the spikes to become narrower in the x direction. Our observations are therefore consistent with a mechanism involving the removal of silicon substrate that is dependent on the local energy absorption.

In a previous paper we reported the effect of ambient gases on spike formation [5]. The observation of blunt spikes in vacuum and sharp spikes in halogen-containing gases suggests that both laser ablation and laser-induced chemical etching are involved in the removal of substrate material. Both of these processes could explain the strong dependence of the spike separation on laser fluence and pulse duration we observe. On one hand, studies of the sub-ps laser ablation of materials have shown that ablation depends strongly on the laser fluence and pulse duration [13, 14]. On the other hand, multiphoton ionization caused by the fs laser pulses can produce reactive fluorine radicals or SF_6 plasmas [15], which are known to etch silicon [16, 17]. Recent studies have also shown that the cross sections of fs laser-induced surface reactions increase dramatically as a function of fluence and pulse duration [18, 19]. Additional experiments will be needed to determine which of these two processes is responsible for the observed phenomena.

Acknowledgements. We thank Professor Mike Aziz for valuable discussions and Dr. Daniel Mumm for help with the backscattering Kikuchi diffraction. This work was supported by the Army Research Office.

References

1. I.H. Wilson: Radiat. Eff. **18**, 95 (1973)
2. H.G. Craighead, R.E. Howard, D.M. Tennant: Appl. Phys. Lett. **37**(7), 653 (1980)
3. P.M. Fauchet, A.E. Siegman: Appl. Phys. Lett. **40**, 824 (1982)
4. J.E. Rothenberg, R. Kelly: Nucl. Instrum. Methods Phys. Res., Sect. B **1**, 291 (1984)
5. T.-H. Her, R.J. Finlay, C. Wu et al.: Appl. Phys. Lett **73**(12), 1673 (1998)
6. A.J. Pedraza, J.D. Fowlkes, D.H. Lowndes: Appl. Phys. Lett. **74**(16), 2322 (1999)
7. P.B. Clapham, M.C. Hutley: Nature **244**, 281 (1973)
8. S. Henry, D. McAllister, M. Allen et al.: J. Pharm. Sci. **87**, 922 (1998)
9. D.J. Dingley, D.P. Field: Mat. Sci. Tech. **13**(1), 69 (1997)
10. I.H. Wilson, J. Belson, O. Auciello: In *Ion Bombardment Modification of Surfaces: Fundamentals and Applications*, Vol. 1, ed. by O. Auciello, R. Kelly (Elsevier, New York 1984) p. 225
11. S. Foltyn: In *Pulsed Laser Deposition of Thin Films*, ed. by D.B. Chrisey, G.K. Hubler (Wiley, New York 1994)
12. M.F. von Allmen, S.S. Lau: In *Laser Annealing of Semiconductors*, ed. by J.M. Poate, J.W. Mayer (Academic Press, New York 1982) p. 564
13. M. Lenzner, J. Krüger, S. Sartania et al.: Phys. Rev. Lett. **80**(18), 4076 (1998)
14. W. Kautek, J. Krüger: Mater. Sci. Forum **173-174**, 17 (1995)
15. F. Raksi, K. Wilson, Z. Jiamg et al.: J. Chem. Phys. **104**(15), 6066 (1996)
16. T.J. Chuang: Surf. Sci. Rep. **3**, 1 (1983)
17. K. Suzuki, S. Okudaira, S. Nishimatsu et al.: J. Electrochem. Soc. **129**, 2764 (1982)
18. J.A. Misewich, A. Kalamarides, T.F. Heinz et al.: J. Chem. Phys. **100**, 736 (1994)
19. T.-H. Her, R.J. Finlay, C. Wu et al.: J. Chem. Phys. **108**(20), 1673 (1998)

SIONYX1403000017.0037

SAMSUNG EX. 1002 - 1446/4148

Microstructuring of silicon with femtosecond laser pulses

Tsing-Hua Her,[a] Richard J. Finlay,[b] Claudia Wu, Shrenik Deliwala,[c] and Eric Mazur
Harvard University, Cambridge, Massachusetts 02138

(Received 2 December 1997; accepted for publication 17 July 1998)

We report that silicon surfaces develop an array of sharp conical spikes when irradiated with 500 laser pulses of 100-fs duration, 10-kJ/m^2 fluence in 500-Torr SF_6 or Cl_2. The spikes are up to 40-μm tall, and taper to about 1-μm diam at the tip. Irradiation of silicon surfaces in N_2, Ne, or vacuum creates structured surfaces, but does not create sharp conical spikes. © *1998 American Institute of Physics.* [S0003-6951(98)01238-8]

We created arrays of sharp conical spikes by repeatedly irradiating silicon surfaces with femtosecond laser pulses in SF_6 or Cl_2. The spikes form spontaneously without the use of any masks. The production of sharp spikes using femtosecond laser pulses is in contrast to reports that femtosecond laser pulses can create very smooth holes, trenches, and cavities.[1–3] While there are reports that semiconductor, metal, and dielectric surfaces become structured when irradiated with lasers, to the best of our knowledge[4–9] there have been no reports of the sharp spikes we observe.

The (100) silicon wafers are *n* type (arsenic doped) with resistivity less than 5×10^{-5} Ω m. The wafers are cleaned with trichloroethylene, rinsed in acetone, and then rinsed in methanol. The wafers are mounted on a three-axis translation stage in a vacuum chamber with a base pressure less than 10^{-4} Torr. The chamber is backfilled with 500-Torr Cl_2, SF_6, N_2, or He.

The samples are irradiated with 500-μJ, 800-nm pulses from a regeneratively amplified Ti:sapphire laser. Except where noted, the laser pulses are incident normal to the sample surface. The laser pulses are focused with a 0.1-m focal-length lens. The spatial profile of the laser pulse is nearly Gaussian, with a 200-μm beam waist at the sample and a fixed fluence (energy per unit area) of 10-kJ/m^2 at the center of the spatial profile. Each spot on the sample surface is exposed to a run of 500 laser pulses. We translate the sample by approximately 1 mm between runs. Following irradiation, the sample is analyzed with a scanning electron microscope. The surface structures resulting from the irradiation are reproducible.

Figure 1 shows the sharp conical spikes produced in SF_6 at 500 Torr viewed at an angle of 45° from the surface normal and viewed parallel to the surface of a cleaved sample. The spikes are roughly aligned in rows. Their direction always coincides with the direction of the incident light and is independent of the direction of gravity. The spikes, which are up to 40-μm tall, have a cross section of about 6 $\times10$ μm^2 near the base tapering down to a diameter of about 0.8 μm near the tip. The spikes, the tops of which are approximately at the same level as the surrounding surface of the wafer, are capped by a 1.5-μm ball.

Figure 2(a) shows the sharp spikes of Fig. 1 at a lower magnification. The spike size varies across the irradiated region, reflecting the spatial profile of the laser pulse. In regions of low fluence, towards the edges of the figure, the spikes are smaller and denser than in the center. We obtained similar sharp spikes in 500-Torr Cl_2 gas.

Irradiation in vacuum produces blunt spikes with irregu-

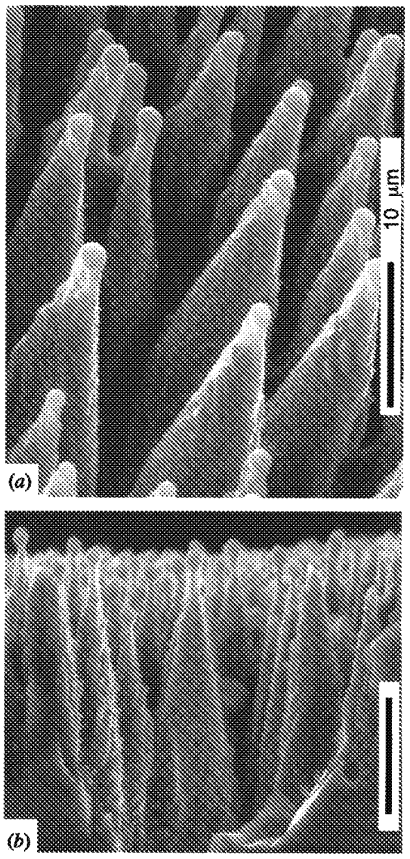

FIG. 1. Sharp conical spikes produced on Si(100) by 500 laser pulses of 100-fs duration, 10-kJ/m^2 fluence in SF_6 at a pressure of 500 Torr viewed (a) 45° from the surface normal, and (b) parallel to the surface.

[a]Electronic mail: tsing-hua_her@lucifer.harvard.edu
[b]Permanent address: Northern Telecom, P.O. Box 3511 Stn. C Ottawa, ON, K1Y 4H7 Canada.
[c]Permanent address: Science Research Laboratory, Inc., 15 Ward Street, Somerville, MA 02143.

 © 1998 American Institute of Physics

SIONYX1403000017.0038

SAMSUNG EX. 1002 - 1447/4148

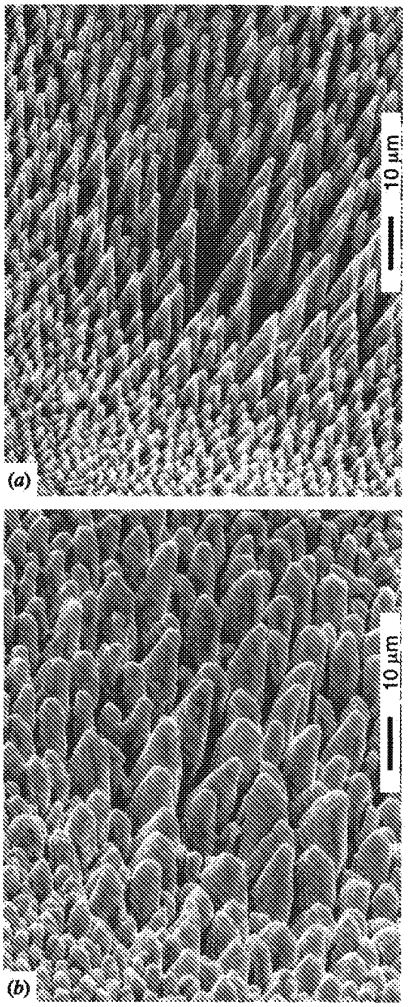

FIG. 2. Comparison of Si(100) surfaces irradiated in the presence of (a) SF_6 and (b) vacuum viewed at an angle of 45° from the surface normal. The laser spot size is 200 μm in diameter.

lar sides and rounded tops, as shown in Fig. 2(b). In the central region, the spikes taper towards the top, reaching 3–5 μm diam. We obtained similar blunt spikes in 500-Torr N_2 or He.

As Fig. 2 shows, the influence of the ambient gas on the surface morphology is striking. The spikes are sharper and narrower in SF_6 or Cl_2 than in vacuum. At the low-fluence edges of Fig. 2, it is especially clear that irradiation in SF_6 or Cl_2 results in a finer structure than irradiation in vacuum. Though the surface irradiated in vacuum, N_2, or He is very structured, it does not exhibit the sharp spikes produced in Cl_2 or SF_6.

Beyond the region shown in Fig. 2, the surface shows ripples of submicrometer periodicity. Other authors have also observed rippling with a spatial period close to the laser wavelength when a semiconductor surface is irradiated at approximately 1-kJ/m^2.[6,7] The rippling has been attributed to scattering from surface roughness and to reradiation from surface defect sites.[10,11] Interference between all incident, radiated, or scattered electromagnetic fields causes periodic variation in substrate heating and ultimately periodic surface structure. The sharp spikes in the middle of Fig. 2, however, have a mean separation much larger than the laser wavelength, very different from the ripples observed beyond the region shown in Fig. 2.

Blunt spikes similar to those we observe in vacuum, N_2, or He, have been reported by several groups.[2,4,9,12] According to one model, the spikes are formed from super-cooled liquid silicon as the recrystallization front propagates towards the surface at different rates in different locations.[8]

A striking feature of the spikes created in SF_6 and Cl_2 is the spherical cap. To see if the top of the spherical cap is a remnant of the native-oxide layer, we rinsed some samples in an aqueous solution of 2% HF to remove the native-oxide layer immediately before putting them in the vacuum chamber. The spherical caps, however, appear regardless of the presence of a native-oxide layer. The spherical shape of the caps suggests that they are due to resolidification of a liquid-silicon drop before the liquid can wet the sharp spike.

The influence of the ambient gas on the shape of the spikes indicates that chemical reaction between SF_6 or Cl_2 and silicon contributes to the formation of the sharp spikes. If the role of the gas were purely physical, such as an influence due to pressure or heat conduction, then sharp spikes should also form in He or N_2, not just in SF_6 or Cl_2. Several reactions between silicon surfaces and halogenated gases are known. High-intensity femtosecond laser pulses can dissociate SF_6,[13] and the resulting radicals may etch silicon by forming volatile SiF_4.[14] The laser pulses could also produce vibrationally excited SF_6, which has an enhanced reactivity with the silicon surface.[14] Alternatively, the laser pulses can melt silicon,[15,16] and the liquid silicon can be etched by Cl_2.[17]

We also studied spike formation using doped Si(100) samples with dopant concentrations corresponding to resistivities in the range 5×10^{-5}–1×10^{1} Ω m. However, even at the highest dopant concentration, the initial photoinduced carrier density of about 10^{27} m^{-3} exceeds the 10^{25} m^{-3} carrier density due to the dopants. Indeed, we did not find any dependence on dopant concentration.

The sharp spikes have interesting potential applications. Arrays of tips with similar dimensions to these spikes can act as field-emission sources for plasma displays.[18] Below the limit for field emission, it may be possible to influence the chemical reaction near the spikes by taking advantage of the concentration of the electric field at the tips. Finally, this is a simple way of roughening micrometer-sized patches of a Si surface to improve adhesion of other materials to the surface.

In summary, we have observed the formation of sharp conical spikes on a silicon surface irradiated by a series of high-fluence, femtosecond laser pulses in SF_6 or Cl_2. The sharp spikes do not form in vacuum, N_2, or He, suggesting that chemical reaction is essential to their formation. The cause of the sharp spikes, including their spherical caps, is unknown.

The authors would like to acknowledge valuable discussions with Dr. Yuka Tabe and Professor Frans Spaepen. One of the authors (C.W.) gratefully acknowledges a graduate fellowship from the Cusanuswerk. This work was supported by the Army Research Office.

SIONYX1403000017.0039

SAMSUNG EX. 1002 - 1448/4148

[1] C. Momma, S. Nolte, B. N. Chichkov, F. v. Alvensleben, and A. Tünnermann, Appl. Surf. Sci. **109/110**, 15 (1997).
[2] W. Kautek and J. Krüger, Mater. Sci. Forum **173-174**, 17 (1995).
[3] E. N. Glezer, M. Milosavljevic, L. Huang, R. J. Finlay, T.-H. Her, J. P. Callan, and E. Mazur, Opt. Lett. **21**, 2023 (1996).
[4] B. Dam, J. H. Rector, J. Johansson, S. Kars, and R. Griessen, Appl. Surf. Sci. **96-98**, 679 (1996).
[5] B. Hopp, M. Csete, K. Révész, J. Vinkó, and Zs. Bor, Appl. Surf. Sci. **96-98**, 661 (1996).
[6] J. F. Young, J. S. Preston, H. M. van Driel, and J. E. Sipe, Phys. Rev. B **27**, 1115 (1983).
[7] P. M. Fauchet and A. E. Siegman, Appl. Phys. Lett. **40**, 824 (1982).
[8] M. F. von Allmen and S. S. Lau, in *Laser Annealing of Semiconductors*, edited by J. M. Poate and J. W. Mayer (Academic, New York, 1982), p. 564.
[9] Y. K. Jhee, M. F. Becker, and R. M. Walser, J. Opt. Soc. Am. B **2**, 1626 (1985).
[10] Z. Guosheng, P. M. Fauchet, and A. E. Siegman, Phys. Rev. B **26**, 5366 (1982).
[11] J. E. Sipe, J. F. Young, J. S. Preston, and H. M. van Driel, Phys. Rev. B **27**, 1141 (1983).
[12] J. Carvalho, I. Ferreira, B. Fernandes, J. Fidalgo, and R. Martins, Mater. Res. Soc. Symp. Proc. **358**, 915 (1995).
[13] F. Raksi, K. Wilson, Z. Jiamg, A. Ikhlef, C. Y. Cote, and J. Kieffer, J. Chem. Phys. **104**, 6066 (1996).
[14] T. J. Chuang, J. Chem. Phys. **74**, 1453 (1981).
[15] P. P. Pronko, P. A. Vanrompay, R. K. Singh, F. Qian, D. Du, and X. Liu, Mater. Res. Soc. Symp. Proc. **397**, 45 (1995).
[16] K. Sokolowski-Tinten, J. Bialkowski, and D. von der Linde, Phys. Rev. B **51**, 14 186 (1995).
[17] D. J. Ehrlich, Jr., R. M. Osgood, and T. F. Deutsch, Appl. Phys. Lett. **38**, 1018 (1981).
[18] V. V. Zhirnov, E. I. Givargizov, and P. S. Piekhanov, J. Vac. Sci. Technol. B **13**, 418 (1994).

SIONYX1403000017.0040

SAMSUNG EX. 1002 - 1449/4148

Impact of surface topography and laser pulse duration for laser ablation of solar cell front side passivating SiN_x layers

Sonja Hermann,[1,a)] Tara Dezhdar,[1] Nils-Peter Harder,[1,2] Rolf Brendel,[1,3] Michael Seibt,[4] and Sandra Stroj[5]

[1]*Institut für Solarenergieforschung Hameln/Emmerthal (ISFH), Am Ohrberg 1, D-31860 Emmerthal, Germany*

[2]*Institut für Materialien und Bauelemente der Elektronik, Universität Hannover, Schneiderberg 32, D-30167 Hannover, Germany*

[3]*Institute of Solid-State Physics, University of Hannover, Appelstrasse 2, D-30167 Hannover, Germany*

[4]*IV. Physikalisches Institut der Universität Göttingen, Friedrich-Hund-Platz 1, D-3707z Göttingen, Germany*

[5]*Forschungszentrum Mikrotechnik, Fachhochschule Vorarlberg, Hochschulstraße 1, A-6850 Dornbirn, Austria*

(Received 19 April 2010; accepted 26 August 2010; published online 13 December 2010)

Local contact openings in SiN_x layers that passivate the front side of solar cells offer an attractive alternative to the current standard "fire-through" screen printing process for front grid fabrication. Additionally, this technology can be used for enabling a selective emitter. In the present paper, we investigate laser ablation of SiN_x layers on planar and textured silicon surfaces for various laser wavelengths and pulse durations in the nanosecond (ns) to femtosecond (fs) range. We characterize the dark *J-V* characteristics of diodes with laser contact openings in the SiN_x layer passivating the emitter. Our results show that on alkaline textured surfaces the ablation by a ns laser produces less damage than by an ultrashort pulse laser. The dark currents of alkaline textured diodes treated with picosecond (ps) or fs lasers are one order of magnitude higher than those of ns laser treated diodes. High ideality factors furthermore indicate crystal damage in the ~500 nm deep space charge region of the diodes. Scanning electron microscope and transmission electron microscope images of textured samples, confirm the presence of extensive and deep crystal damage after ps laser ablation, which are not observed in laser treated samples with planar surfaces. Correspondingly, for planar surfaces we find for both, ns and for ps laser ablated regions, emitter saturation current densities $J_{0e,abl}$ of ~2 pA/cm^2. The recombination in textured samples in contrast differs vastly for ns and ps laser ablation. The ns laser results in an only slightly increased value of 3.7 pA/cm^2 while the ps laser treated sample was not evaluable due to severe crystal damage leading to effective lifetimes of <5 μs. © *2010 American Institute of Physics*. [doi:10.1063/1.3493204]

I. INTRODUCTION

An efficient strategy for minimizing recombination losses of solar cells is to reduce the metal-semiconductor interface area at the contacts and passivating the remaining surface area by dielectric layers. Beside the example of this strategy on the rear side of passivated emitter and rear cell (PERC) solar cells,[1] local contact openings also offer various advantages on the front side of any front contacted solar cell. Local front contact openings enable the decoupling of contacted and metalized cell area, the implementation of a selective emitter and the development of alternative metallization processes to the established screen printing.[2] In order to obtain highly efficient and low-cost solar cells, it is crucial to use a reliable technology for realizing precise openings in the SiN_x passivating and antireflection layer without damaging the underlying silicon. Photolithography, as used in laboratories to fabricate highly efficient solar cells,[3] is not suitable for low-cost mass production. An attractive alternative for industrial applications is the direct laser ablation of the SiN_x layer that does not require any wet chemical post treatment. To our knowledge, this technique was applied for the first time by Dube and Gonsiorawski[4] in 1990. Laser ablation processes were also applied for the formation of local contact openings on the passivated rear side of PERC solar cells.[5,6] Recently, the use of the technique in the local removal of SiN_x layers on the textured front side of solar cells has come into focus. There have been reports of ablating UV-absorbing SiN_x layers without appreciable damage to the silicon substrate using UV (λ=355 nm) nanosecond (ns) laser pulses on planar and textured surfaces.[7–9] We also reported in a previous work that 532 and 1064 nm picosecond (ps) laser radiation applied for SiN_x layer ablation on 500 nm deep phosphorus doped n^+-emitters leads to moderate emitter saturation current densities in case of planar surfaces.[10] However, we showed in the same work that alkaline textured surfaces exhibit more than one order of magnitude higher emitter saturation current densities after ps laser treatment. Recently, solar cell results were published comparing ns and ps lasers for the formation of front side local contact openings on alkaline textured surfaces.[2] The results showed a 17 mV higher open circuit voltage in case of the ns laser application, which was explained by emitter profile modifications and varying metallization fractions.

In this work, we investigate the impact of laser radiation

a)Electronic mail: hermann@isfh.de.

 © 2010 American Institute of Physics

Downloaded 17 Dec 2010 to 18.82.0.30. Redistribution subject to AIP license or copyright; see http://jap.aip.org/about/rights_and_permissions

SIONYX1403000017.0041

SAMSUNG EX. 1002 - 1450/4148

occurring during SiN_x ablation by ns to femtosecond (fs) laser pulses on planar as well as textured surfaces. For availability reasons, these lasers differ in their wavelengths. Besides investigating the effect of laser pulse duration we also examine the impact of a flat-top profiled ns laser in comparison to a Gaussian shaped laser of same pulse duration range. In addition to scanning electron microscope (SEM) and transmission electron microscope (TEM) images for crystal defect investigations, we show dark *J-V* characteristics of diodes with 4% area fraction of laser contact openings in SiN_x layers that passivate the n^+-emitter of the diodes. Furthermore, we compare saturation current densities of ns and ps laser treated emitters with planar and textured surfaces. Our results show, that ultrashort laser pulses cause severe damage to alkaline textured surfaces.

II. EXPERIMENTAL

We examine the impact of laser ablation of plasma-enhanced chemical-vapor deposition (PECVD) SiN_x layers with a refractive index $n \approx 2.1$ on planar and textured Si surfaces. We distinguish between laser pulses in the ns range and ultrashort laser pulses in the ps and fs range. Ultrashort laser pulses are known for their minor heat-affected zone and thus are expected to be well suited for precise layer ablation involving a low level of crystal damage in the underlying silicon.[11] We investigate ps laser induced crystal damage by microscopy studies.

In order to characterize the impact of laser induced crystal defects on the performance of silicon semiconductor devices, like wafer-based solar cells, we prepare planar and textured diodes and use laser ablation for perforating the emitter passivating SiN_x layer. We measure the dark *J-V* characteristics of the laser treated diodes and compare them to diodes with wet chemically etched local contact openings. This comparison detects the impact of the total laser induced crystal damage on the performance of solar cells, including a possible removal of the thin emitter layer, damages in the space charge region (SCR), and within the base and emitter volume.

Furthermore, we investigate the surface-near damage in the diffused emitter as produced by our Gaussian ns and ps lasers by determining emitter saturation current densities in planar and textured laser treated areas.

A. Microscopy studies

We investigate the surface modifications due to SiN_x ps laser ablation on planar (100) oriented and alkaline textured silicon surfaces by SEM. In order to determine the nature of silicon crystal defects after laser treatment we additionally prepare TEM cross sectional images of the laser spots. In these images, crystal defects like dislocations or other crystal defects can be detected. Figure 2 shows SEM images of a planar (a) and textured (b) and (c) Si surface after SiN_x layer ablation by a 532 nm ps laser. Before preparation of the later thin (<200 nm) TEM lamella, a Pt:C composite protective layer is deposited onto the areas of interest of the laser treated samples [see Figs. 2(a) and 2(c)]. The TEM lamella is subsequently excavated using standard focused ion beam (FIB) techniques.[12] This preparation technique ensures that the TEM lamellas show the centered cross section of the planar laser spot [white arrow in Fig. 2(a)] and of a pyramid including the tip within a textured laser spot, respectively. In the first instance, the planar TEM lamella is investigated by energy-dispersive x-ray spectroscopy (EDX) in scanning TEM (STEM) mode. We use the EDX signal to identify the different materials in the lamella [Si, SiN_x, and Pt:C, Fig. 3(a)]. In addition, TEM images of the cross sectional wafer surface region within the planar laser spot are assembled in order to show an overview of the surface [Fig. 3(b)]. In case of the textured surface, single cross section images are shown (Fig. 4).

FIG. 1. (Color online) Cross sectional schemes of the laser treated diodes. The emitter passiviating SiN_x layer is removed on 4% area fraction by laser ablation or wet chemical etching.

B. Dark *J-V* characteristics of laser treated diodes

The laser induced crystal damage inflicted to the sample during the ablation of a SiN_x passivating layer becomes also apparent in dark *J-V* curves of laser treated diodes. *J-V* measurements of laser-processed diodes allow characterizing the impact of the laser damage for conditions relevant to solar cell operation. We prepare diodes on (2.5×2.5) cm^2 1.5 Ω cm p-type FZ-Si wafers with a 40 Ω/sq n^+-emitter formed by a $POCl_3$ furnace diffusion. The *p-n* junction is located in a depth of ~500 nm. The diodes are passivated by a thermally grown SiO_2 layer on the base and by a PECVD SiN_x layer ($n \approx 2.1$) on the emitter side. The diodes differ in their emitter surface topographies: Half of the diodes exhibit a planar surface and the second half an alkaline textured emitter surface with random pyramids. Cross sectional schemes of the diodes are shown in Fig. 1. The SiN_x layer thickness was adjusted for both surface types, resulting in a dark blue appearance for both cases (65 nm on planar and 100 nm vertically on textured surfaces). Single pulse laser ablation with equal spot distances in x- and y- direction on the P-diffused side creates local contact openings in the SiN_x layer on an area fraction of ~4%. Four different pulsed laser systems with varying wavelengths, pulse durations and beam profiles are used to compare the impact on the performance of the diodes

- $\lambda_1 = 532$ nm, $\tau_{p1} = 8$ ns, flat-top profile,
- $\lambda_2 = 355$ nm, $\tau_{p2} = 20$ ns, Gaussian profile,
- $\lambda_3 = 532$ nm, $\tau_{p3} = 9$ ps, Gaussian profile,
- $\lambda_4 = 1035$ nm, $\tau_{p4} = 400$ fs, Gaussian profile.

It has been shown previously that for fs laser pulses on silicon the wavelength is not a decisive parameter for the absorption process and ablation.[13] The fs laser pulses with the rather long wavelength of 1035 nm can therefore be well compared to the shorter wavelength pulses of the ps and ns lasers. For ablation, the pulse energies are chosen slightly

Downloaded 17 Dec 2010 to 18.82.0.30. Redistribution subject to AIP license or copyright; see http://jap.aip.org/about/rights_and_permissions

SIONYX1403000017.0042

SAMSUNG EX. 1002 - 1451/4148

higher than the ablation threshold of each laser process. Parallel to the laser treated diodes we also prepare reference samples with damage free local contact openings. These diodes are processed by inkjetting an etch mask prior to etching in an HF solution. The inkjet etch mask also features openings on 4% area fraction. After metalizing both diode sides by means of aluminum evaporation (~5 μm), the base contacts are formed by laser fired contacts (LFC).[14] The area coverage of the LFC contacts is ~0.2% in order to minimise their contribution to the total recombination of the diodes. The dark *J-V* curves of the diodes are measured without any thermal treatment (annealing) of the diodes. This avoids the full area front side metallisation to form contacts through the possibly pinhole containing SiN_x layer in the nonablated front areas. The *J-V* characteristics describe the voltage dependent recombination currents of the diodes and we compare and fit these characteristics with the widely used two-diode model[15]

$$J_{\mathrm{dark}}(V) = J_{01}(e^{q(V-R_sJ_{\mathrm{dark}})/kT\times n_1} - 1) + J_{02}(e^{q(V-R_sJ_{\mathrm{dark}})/kT\times n_2} - 1) + \frac{V - R_sJ_{\mathrm{dark}}}{R_{\mathrm{sh}}}, \quad (1)$$

involving the elementary charge q, the Boltzmann's constant k, the diode temperature T, the diode lumped series resistance R_s, and parallel resistance R_{sh}. The prefactors J_{01} and J_{02} display the saturation current density and the parameters $n_1=1$ and $n_2=2$ the ideality factor of the so called first and second diode, respectively. This simple model describes the total diode current as a sum of three current paths, related to certain mechanisms, such as recombination in the quasineutral base and emitter volume (first term, ideality factor $n_1=1$), recombination in the SCR of the *p-n* junction (second term, ideality factor $n_2 \approx 2$) of the diode and shunts (short-circuits) within the device (third term). Analyzing and comparing *J-V* characteristics of diodes with the help of this model allows making statements concerning the dominating recombination mechanism occurring in the specific device. According to superposition principle these statements can be transferred to the recombination losses occurring in correspondingly processed solar cells. However, it shall be emphasized that this "two-diode model" is highly simplifying. Therefore, it can only provide rough guidelines for physical interpretation and consequently is often observed to fail for detailed reproduction of experimental data.

C. Local emitter saturation current densities

For further investigations of the crystal damage within the emitter of ns and ps laser treated diodes we determine local emitter saturation current densities $J_{0e,abl}$ in SiN_x ablated regions of phosphorous diffused test structures. We use planar and alkaline textured p-type 1.5 Ω cm FZ-Si wafer (2.5×2.5 cm^2) and use a $POCl_3$ diffusion process for the formation of an n^+-emitter with 40 Ω/sq sheet resistance on both sides. Subsequently, we passivate the surfaces of the wafer with a PECVD SiN_x layer ($n \approx 2.1$). Prior to the laser treatment we measure the injection dependent effective charge carrier lifetime in high level injection by means of the quasisteady-state photoconductance method.[16–19] From the measured effective lifetimes we extract the emitter saturation current density for the fully passivated case $J_{0e,pass}$ as proposed in Ref. 16. Afterwards, we uniformly ablate the SiN_x on a large area fraction (>20%) on both sides of the wafer without spot overlap. For these samples, we use the Gaussian ns and ps laser as applied to above described diodes. We then measure the effective lifetime of the samples after laser treatment and extract the emitter saturation current density $J_{0e,eff}$, which contains contributions from the passivated ($J_{0e,pass}$) and the laser ablated areas ($J_{0e,abl}$). We determine the local emitter saturation current density in the ablated areas using the relation $J_{0e,abl}=[J_{0e,eff}-(1-f)\times J_{0e,pass}]/f$, where f is the laser-opened area fraction of each sample.

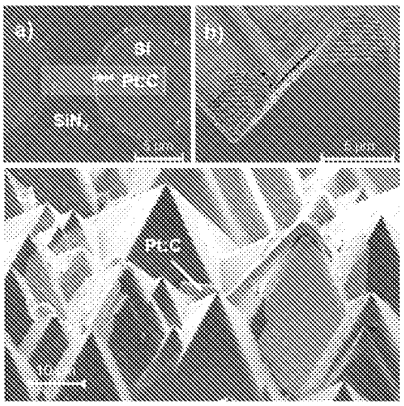

FIG. 2. (Color online) (a) SEM image of a ps laser spot ($\lambda=532$ nm) after SiN_x ablation (top view). This sample was used for TEM investigations (Fig. 3). In order to protect surface-near regions against ion damage during FIB preparation, a Pt:C layer is deposited at the area of interest. The white arrow marks the position of the lamella, which is excavated by FIB technology. (b) SEM image of a spot caused by the same laser on textures Si surface (cross section, slightly tilted). Ripple structures are clearly visible. (c) SEM image of another textured sample treated by the same laser. The areas of ablated SiN_x in this image are marked by a transparent orange coloring. This sample was used for TEM investigations. The deposited Pt:C layer is marked by green coloring and shows the position of the later TEM lamella.

III. RESULTS

A. SEM and TEM-images of ps laser treated silicon

Figure 2(a) shows an SEM image of a ps laser spot ($\lambda=532$ nm) after SiN_x ablation on a planar silicon surface. The laser spot appears to have a well-defined boundary and a smooth surface. Laser damage within the laser spot is not apparent. Only at the spot boundary, some silicon humps can be observed. In order to investigate crystal defects that are invisible in SEM images we prepare cross sectional TEM images of the laser spot. The white arrow in Fig. 2(a) marks the position of the later TEM lamella. Image (b) in Fig. 2 shows an SEM image of an alkaline textured silicon surface, treated with the same laser as used for the planar sample in image (a). Ripple structures are visible on the pyramidal texture. Such ripples or so called laser induced periodic surface structures (LIPSS) are well known in the literature and were observed on textured Si surfaces after single pulse SiN_x ablation before.[20] LIPSS in general are observed also on various planar materials in case of irradiation by intense single

Downloaded 17 Dec 2010 to 18.82.0.30. Redistribution subject to AIP license or copyright; see http://jap.aip.org/about/rights_and_permissions

SIONYX1403000017.0043

SAMSUNG EX. 1002 - 1452/4148

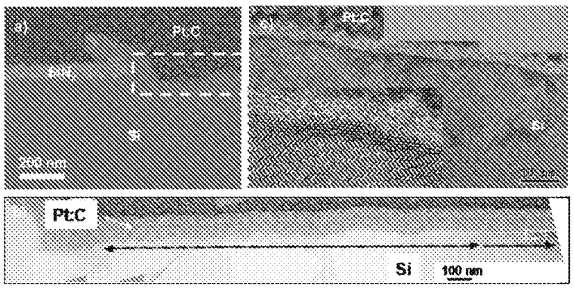

FIG. 3. (Color online) (a) STEM-EDX signals of a cross sectional TEM lamella at the boundary of a ps laser spot after SiN_x ablation on a planar Si wafer. (b) TEM image of the cross section of a ps laser spot surface. The position of the investigated area in the laser spot is marked by the white arrow in Fig. 2(a) and by the white frame in (a). Left side of the image: boundary of the laser spot; right side: toward the center of the laser spot. Dark contrasts toward the spot center indicate crystal damage. (c) Enlargement with an image detail of the dark contrasts in the TEM image by means of HRTEM. In the magnification the contrasts visible in (b) can be identified as amorphous silicon.

or multiple polarized laser pulses.[21,22] The generally accepted explanation of these periodic modulations is interference between the incident light and some form of an electromagnetic surface wave, generated by scattering. This interference leads to inhomogeneous energy deposition into the irradiated material. The nature of the scattered wave has been the subject of some controversy. A theory for describing the LIPSS phenomenon was suggested by Emmony *et al.*[23] and further developed by various authors.[21,24–26] Today, the theory considers the interaction of an electromagnetic wave with a microscopically rough surface and includes the possible excitation of surface plasmon polaritons. It predicts possible LIPSS wave vectors of the surface as a function of the laser parameters (angle of incidence, polarization direction, and wave vector of incident radiation) and surface parameters (dielectric function and surface roughness).[24] Additionally intrapulse alterations of the complex refractive index of the irradiated material due to generation of free charge carriers (Drude model) and the nonlinear Kerr-effect are considered.[26] Our textured surfaces are produced by KOH etching and feature random pyramids with an average size of 10 μm. Thus, the textured surfaces of our samples are very rough surfaces. Suitable combinations of laser incidence angle (varies due to scanner optics in the used laser system) and pyramids arrangement lead to such precisely defined ripples after a single laser pulse as shown in Fig. 2(b). These ripples are 100–200 nm deep and their spacing amounts to about 400 nm. Such deep ripples are not found in case of ns laser pulses on textured surfaces. However, Fig. 2(c) shows that these ripples do not occur in such a clear characteristic in all ps laser spots either. Rather shallow periodic structures are observable at the laser treated areas (marked by transparent orange coloring) in this image. We use the sample shown in Fig. 2(c) for TEM investigations. The position of the final cross sectional TEM lamella of this sample is marked by the Pt:C protective layer [green coloring in Fig. 2(c)].

We also perform space-resolved EDX measurements of the planar TEM lamella. Figure 3(a) shows the EDX map of the laser spot boundary of the planar sample. Each color in the image represents a signal that is specific for a certain chemical element. The image shows the arrangement of Si (red), N (green), and Pt (blue). These signals reveal a very interesting fact. The SiN_x layer is abruptly ablated from the silicon substrate. There is no gradual transition of the SiN_x thickness visible as one expects for an absorbing and directly ablated SiN_x layer after Gaussian irradiation. That means that the ablated layer (refractive index $n \approx 2.1$, band gap energy $E_{gap} \approx 3.5$ eV) is not gradually removed with increasing laser intensity, i.e., it is not directly ablated for 532 nm (photon energy: 2.33 eV) ps laser radiation. Due to the optical properties of the SiN_x layer, linear absorption is not expected anyway. However, this finding proves that also nonlinear absorption does not take place in the layer. This leads to the conclusion that the layer is removed by the expansion of the underlying absorbing silicon substrate as has already been found for SiO_2 layer ablation.[27] The white dashed frame in Fig. 3(a) marks the position of the left edge of the TEM overview in Fig. 3(b). The uplifted silicon at the boundary of the laser spot is well recognizable in the EDX map and is also identified in the TEM overview. The lateral dimension of the overview of the laser spot surface amounts ~ 2 μm and corresponds to the position marked by the white double arrow in Fig. 2(a). The laser treated silicon shown in the TEM images exhibits a waved surface, which indicates that the silicon substrate was molten during the laser process. However, the silicon crystal underneath the surface at the outer border of the laser spot in this image does not show any TEM detectable dislocations or other defects. This can be interpreted by assuming epitaxial crystallization of the molten silicon. Only close to the spot center at the right edge of the TEM overview, the microscope image shows some dark contrasts. An enlarged image of the marked contrast area (dashed white frame) is shown in Fig. 3(c), which displays a high-resolution TEM (HRTEM) lattice image. In this magnification, minor crystal defects within a depth of ~ 20 nm are found. Similar defects are also observed within a depth of ~ 5 nm in the nonablated, still SiN_x-covered area close to the laser spot border (not shown is this work). This allows two hypotheses: (1) the defects could be based on hydrogen induced lattice disturbances caused by the PECVD-deposition of the SiN_x layer.[28] Even though the Si surface within the laser spot [Fig. 3(c)] was molten during the ablation process, hydrogen could still be present, leading to defective crystal growth during otherwise epitaxial solidification. (2) The damage within and close to the border outside the laser spot is laser induced as the Gaussian laser intensity distribution continues over the border of the ablated laser spot.

Yet, the region covered by the TEM images does not cover the center of the laser spot, which is the position of highest laser intensity during the Gaussian shaped irradiation. In order to be able to exclude further defects at the spot center further investigations are needed.

Besides the planar sample, we also investigated crystal defects by cross sectional TEM images of a texture pyramid after SiN_x ablation by a single ps laser pulse ($\lambda = 532$ nm) [see run of the Pt:C cover layer in Fig. 2(c)]. The TEM images of the left hand pyramid side-wall show at the base of

Downloaded 17 Dec 2010 to 18.82.0.30. Redistribution subject to AIP license or copyright; see http://jap.aip.org/about/rights_and_permissions

SIONYX1403000017.0044

SAMSUNG EX. 1002 - 1453/4148

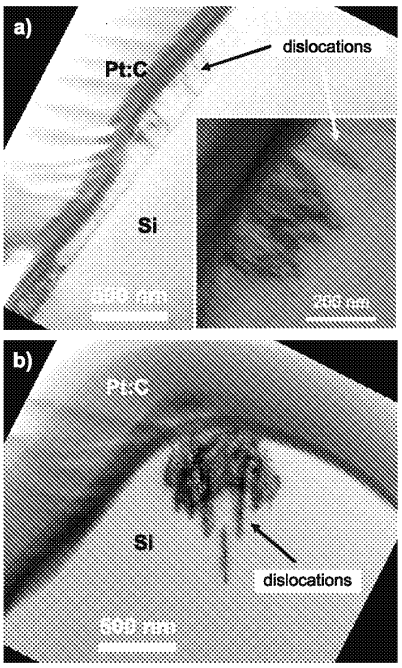

FIG. 4. (a). TEM images of the cross section of a texture pyramid after SiN_x ablation by a single ps laser pulse (λ=532 nm). (a) The surface of the left hand side side wall of the pyramid. Dislocations are clearly visible, running perpendicular to the side walls surface. (b) The apex of the pyramid. Vertical dislocations can be observed.

the pyramid a defect-free SiN_x covered Si surface (images not shown here). In 2 μm distance from the laser ablated spot border, few shallow dislocations underneath the SiN_x layer are observed. As no defects are found in larger distance to the laser spot, the dislocations are proven to be caused by the laser treatment. An impact of the SiN_x deposition or lamella preparation in this case is excluded. Inside the laser spot a very dense dislocation distribution is found with increasing expansion into the wafer bulk approaching the laser spot center. The maximal defect depth amounts to ~150 nm. Finally, the density of dislocations rapidly decreases and the defects vanish close to the apex [see Fig. 4(a)]. As shown in Fig. 4(a), the observed dislocations within the ablated laser spot exhibit a V-shaped appearance and set in at a very defined depth below the original pyramid surface. In this defined depth defects are observed forming a fine line of dark contrast in Fig. 4(a). To our opinion, this line marks the depth of molten silicon during laser irradiation. V-shaped defects have been observed in TEM investigations of laser treated {111} oriented Si surfaces before and consists according to Cullis *et al.*[29] mainly of microtwin lamellas. Please note that the pyramid side walls of alkaline textured Si wafers usually are {111} oriented. Microtwins were proven by various works to correlate with the recrystallization of {111} oriented (planar) Si wafer surfaces (see references in Ref. 30). Additionally, the epitaxial growth rate was found to be an order of magnitude slower for {111} oriented Si than for {100} wafers.[30] For both effects, the microtwinning and the slow growth rate, a model has been proposed, assuming bond arrangements of the different surfaces to cause these effects.[31] While on {100} surfaces an atom can add anywhere to form undistorted bonds, on {111} surfaces three neighboring atoms are required to nucleate a growth step. According to the model, these three atoms then can add in the correct position or in a twin orientation. Thus, the formation of microtwin lamellas is clearly correlated with the orientation of the crystallization plane. In contrast to this, the formation of above mentioned periodic surface structures (LIPSS) is correlated with a rough irradiated surface. Thus, both effects occur independently and have different origins.

However, in our TEM image [Fig. 3(a)] besides V-shaped defects with straight and well-oriented edges also contrasts with bent edges and slightly different orientation are observed [white arrow in Fig. 4(a)]. To our interpretation, these crystal defects are so called hairpin dislocations. These dislocations usually are associated with the solid-phase epitaxial regrowth of amorphous Si layers during annealing afterwards ion implantation. Hairpin dislocations are understood to nucleate when the growing amorphous/crystalline interface intersects small microcrystallites that are slightly misoriented with respect to the bulk crystalline material.[29] These dislocations propagate in V-shape with the a-Si/c-Si interface until they encounter to the surface. In our laser process we expect to have a liquid-solid interface propagating toward the Si surface rather than an a-Si/c-Si interface. However, the mechanism in forming hairpin dislocations could be the same for an epitaxially regrowing c-Si front intersecting misoriented microcrystallites. Thus, possibly the fine dark line parallel to the Si surface in Fig. 4(a) is formed by the same defects leading to nucleation of hairpin dislocations in our laser treated pyramid surface.

However, we do not find any of these defects in the cross section of the ps laser ablated laser spot on our (100) oriented planar wafer [Fig. 3(b)]. As mentioned above, this is related to the different crystal orientation. As found in Refs. 29 and 32, the solidification interface velocity has to be as low as 5–6 m/s to suppress defect formation in crystallizing {111} Si. On (001)-oriented Si-Wafers in opposite, defect-free crystal growth was observed at interface velocities as high as 18 m/s. According to these references, to decrease the crystal growth velocity and thus to obtain defect-free recrystallization on {111} Si, longer pulse durations have to be used.

Figure 4(b) shows the apex of the pyramid, which was located close to the Gaussian beam center during ps laser irradiation. Even more tremendous crystal defects are observed here. Interestingly, in the apex we find dislocations that are orientated vertically in the image and reach more than 1 μm deep into the silicon. Typical diffused emitters of solar cells are some 100 nm deep. Such textured emitters and the corresponding SCRs of the *p-n* junctions would thus be damaged to a large extend by our ps laser pulse. Moreover, even a considerable fraction of the nondiffused volume would severely be damaged by this laser pulse. The vertical orientation of the dislocations might be caused by thermomechanical stresses propagating symmetrically from the side walls and meeting in the apex.

Downloaded 17 Dec 2010 to 18.82.0.30. Redistribution subject to AIP license or copyright; see http://jap.aip.org/about/rights_and_permissions

SIONYX1403000017.0045

SAMSUNG EX. 1002 - 1454/4148

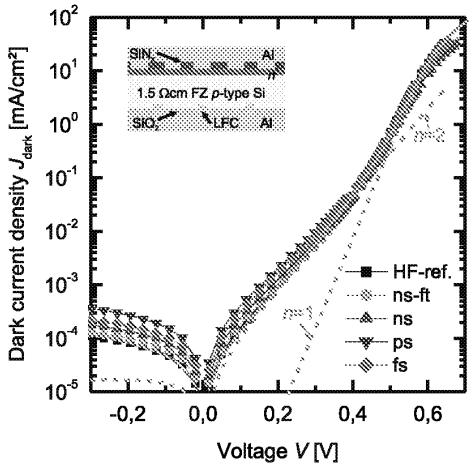

FIG. 5. (Color online) Measured dark *J-V* curves of laser treated diodes (non-square symbols) in direct comparison to a wet chemically treated diode (square symbols). A schematic cross section of the diodes is shown in the graph. Local emitter contact openings on 4% area fraction on the planar emitter side are realized by various laser technologies in the ns- to fs-range (see legend) and by inkjet technology plus selective HF etching (HF-reference). The abbreviation ft stands for flat-top beam profile.

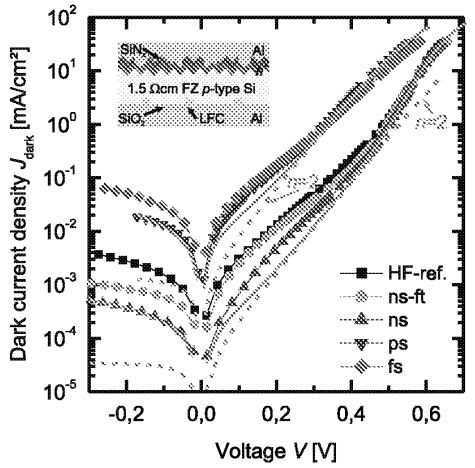

FIG. 6. (Color online) (a). Measured dark *J-V* curves of laser treated diodes (non-square symbols) in direct comparison to a wet chemically treated diode (square symbols). A schematic cross section of the diodes is shown in the graph. The local emitter contact openings on 4% area fraction on the textured emitter side were realized by various laser technologies in the ns- to fs-range (see legend) and by inkjet technology plus selective HF etching (HF-reference). The abbreviation ft stands for flat-top beam profile.

Thus, to our opinion, the distinct crystal damage in case of textured Si surfaces, which we do not find on our planar sample might be based on three circumstances. (1) The crystal orientation of the pyramid side walls ({111}) has different solidification properties as the planar (100) surface. (2) Thermal stresses occur and might interact in the apex in a fatal manner due to geometrical circumstances in a pyramid. And/or (3) the above described interference effects might lead to locally strongly varying temperature gradients and thus impact the crystal lattice even without leading to a clear ripple formation.

B. Dark *J-V* characteristics of laser treated diodes

1. Laser treatment on planar surface

Figure 5 shows measured dark *J-V* curves of planar diodes with a 40 Ω/sq emitter, treated with various types of laser pulses (see Sec. II A and legend in the graph, symbols). Also shown is the *J-V* characteristic of the diode with wet chemically processed local emitter contact openings (HF-reference, black symbols). Please note, that reverse currents are plotted as positive values. A schematic of the cross section of the diodes is shown in the graph. As can be seen in Fig. 5, no significant differences in the *J-V* characteristics of wet chemically and laser treated diodes can be observed. Thus, the laser induced damage resulting from ns lasers as well as from ultrashort pulse lasers is negligible from the perspective of diode or solar cell operation. This result is in line with the observation of minor crystal defects in a depth of only 20 nm in the TEM ps laser spot cross section in Fig. 3(b). Using the two-diode model [Eq. (1)] for describing the curves in Fig. 5 results for laser treated as well as wet chemically treated diodes in the fit parameters $J_{01}=1.3$ pA/cm^2, $J_{02}=17$ nA/cm^2, and $R_s=0.8$ Ω cm^2. The parallel resistance of the diodes varies in the range from $R_{sh}=3000$ kΩ cm^2 for the wet chemically treated diode to 800 kΩ cm^2 for the ps laser treated diode. However, parallel resistances of this magnitude do not significantly affect the electrical behavior of diodes or solar cells. The functions of the first and second term of Eq. (1) (dashed lines) as well as the entire function of Eq. (1) (line) according to the parameters of the wet chemically treated diode are plotted in the figure. From these functions we find, that the curves of the diodes are well described by the applied model. Thereby, high value of the parallel resistance R_{sh} and the identical saturation current densities for laser and wet chemically treated diodes imply that the emitter of the laser treated diodes is hardly affected by induced crystal damage.

2. Laser treatment on textured surface

In accordance with the microscopy results, we find a completely different situation in case of laser treating alkaline textured surfaces. Figure 6 shows the *J-V* curves of alkaline textured diodes. Apart from the textured emitter surface they were prepared and laser treated in an identical manner as the planar diodes whose *J-V* curves are shown in Fig. 5. For the textured diodes, we find distinct differences between the laser sources with respect to their impact on the *J-V* curves. There is a clear difference between the ultrashort pulse laser treated diodes (ps laser: blue and fs laser: green symbols) and the ns laser treated diodes (flat-top: orange and Gaussian beam profile: pink symbols), independently from the particular wavelength. The difference in curve progression of ultrashort pulse lasered diodes is significant over the total voltage range. These curves (ps and fs) suffer from one order of magnitude higher current densities compared to the HF-reference. This becomes also apparent by fitting the curves with the two-diode model [Eq. (1)]. For the ps laser treated diode values of $J_{02}=1.3$ μA/cm^2, $R_s=0.8$ Ω cm^2, and $R_{sh}=9$ kΩ cm^2 have to be chosen in order to roughly

Downloaded 17 Dec 2010 to 18.82.0.30. Redistribution subject to AIP license or copyright; see http://jap.aip.org/about/rights_and_permissions

SIONYX1403000017.0046

SAMSUNG EX. 1002 - 1455/4148

represent the progression of the curve by this model. A value for J_{01} is not definable as the *J-V* curve is dominated in the entire measured voltage range by a current with high ideality factor. According to the common interpretation of the simple two-diode model such current with high ideality factor is ascribed to recombination within the SCR of the diode. This SCR recombination is quantified by the second term of Eq. (1) with the parameters J_{02} and the ideality factor $n=2$. This term is plotted in Fig. 6 (upper dashed line). The value of $J_{02}=1.3\ \mu A/cm^2$ meanwhile is two orders of magnitude higher than the one parameterizing the SCR recombination after ps laser ablation of SiN_x layers in case of the planar diode. Thus, severe crystal damage in the in the SCR of the diode has to be assumed. This result correlates to the findings in the TEM microscopy studies of the laser induced crystal damage on textured surfaces as shown in Fig. 4. The low value of the parallel resistance of 9 $k\Omega\ cm^2$ compared to 900 $k\Omega\ cm^2$ for the ps laser treated planar diode indicates a locally removed emitter layer. This result correlates to the findings of SEM microscopy investigation of the surface modifications on a textured Si surface after ps laser ablation as shown in Fig. 2(b). Elevated current densities at low voltages can furthermore be associated to a high defect density within the SCR leading to further recombination effects like for example trap assisted tunnelling.[33] Such effects are not considered by the two-diode model, or only qualitatively described by the shunt resistance. The progression of the fit function (upper line in Fig. 6) shows that the measured *J-V* data of the ps laser treated diode are not well described by the two-diode model, particularly, in the low voltage range. This shows that the laser induced crystal damage in our diodes after short pulse laser ablation leads to recombination currents, which cannot be described in terms of the highly simplifying two-diode model. These different or additional effects might also influence the determination of the J_{02}-value. This has to be taken in to account when interpreting the differences of the J_{02} fit parameter value of the planar diodes to the one of the textured diodes.

However, the *J-V* curve fit parameters of the ns laser treated diode in Fig. 6 have values of $J_{01}=1.2\ pA/cm^2$, $J_{02}=34\ nA/cm^2$, $R_s=0.8\ \Omega\ cm^2$, and $R_{sh}=600\ k\Omega\ cm^2$. These values are very similar to the values obtained for the planar diodes. Also for the *J-V* characteristics of this diode, we inserted the fit result (lower line) and the function of the second term of Eq. (1) (lower dashed line) into the graph in Fig. 6. Small differences in the current density at lower voltages of ns laser and wet chemically (black symbols) treated diodes as well as the increase in the accordant J_{02}-value of the ns laser treated diode by a factor of 2 compared to the planar diodes have to be ascribed to handling induced defects at the sensitive textured front side. As stated above, {111} oriented (texture pyramid) Si surfaces are found to crystallize with less or even no defects only for lower solidification velocities, that means for longer pulse durations. This explains the distinct differences between the ns laser and the short pulse laser sources with respect to their impact on the *J-V* curves. We also find that the performance of the ns laser treated diodes is not affected by using a flat-top beam profile.

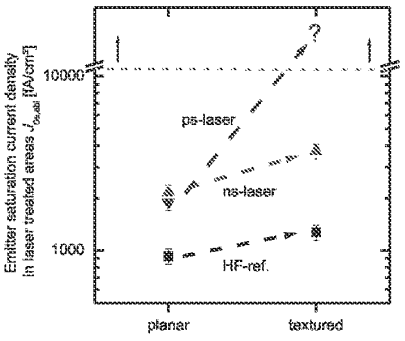

FIG. 7. (Color online) Local emitter saturation current densities in laser ablated areas after ns (triangle symbols) and ps (inverted triangle symbols) laser ablation of a SiN_x layer. Reference values for wet chemically treated samples are also displayed (square symbols).

This matches the observations we obtain for ns laser treatment in comparison to short pulse laser ablation.

C. Emitter saturation current densities in laser treated areas

Figure 7 shows emitter saturation current densities in laser treated areas of in Sec. II C. described lifetime test structures. These test structures were treated with comparable pulse energies as the Gaussian ns and ps laser treated diodes in Figs. 5 and 6. Figure 7 uses the same color code for ns laser (pink), ps laser (blue), and the HF-reference sample (black). In this investigation we compare the crystal damage related $J_{0e,abl}$ values again of planar and textured surfaces (*x*-axis).

We find moderate emitter saturation current densities in case of SiN_x laser ablation (ns and ps) on planar emitters of $\sim 2\ pA/cm^2$. This means an increase in approximately a factor of 2 compared to damage free wet chemically treated emitter regions with $\sim 0.93\ pA/cm^2$. Also on alkaline textured surfaces the ns laser ablation leads to only slightly increased $J_{0e,abl}$-values of $\sim 3.7\ pA/cm^2$, which means approximately a factor of 3 compared to the $\sim 1.2\ pA/cm^2$ of wet chemically prepared contact openings. However, we find that ps laser treatment on textured lifetime samples leads to strongly reduced effective charge carrier lifetimes of less than 5 μs. From these injection dependent lifetime measurements we cannot reliably extract the recombination in the emitter, i.e., the $J_{0e,eff}$-values as proposed by Ref. 16. In accordance with the microscopy results, this could be due to significant crystal damage and thus injection dependent recombination in the SCR and the bulk volume. However, we assume a $J_{0e,abl}$ value for this case well above 10 pA/cm^2 as for other laser treated samples of the same bulk material $J_{0e,abl}$-values of up to 50 pA/cm^2 were obtained from effective lifetimes exceeding 100 μs (not shown is this work here). However, such severe damage of the Si wafer substrate is clearly not acceptable for the fabrication of highly efficient solar cells.

Thus, the saturation current density results confirm the findings of the analysis of the *J-V* characteristics of laser treated diodes. On planar surfaces ns and ultrashort laser pulses are suitable for SiN_x ablation without significantly

Downloaded 17 Dec 2010 to 18.82.0.30. Redistribution subject to AIP license or copyright; see http://jap.aip.org/about/rights_and_permissions

SIONYX1403000017.0047

SAMSUNG EX. 1002 - 1456/4148

affecting the performance of silicon solar cells. However, we find that on alkaline textured surfaces short pulse laser ablation is not advisable for preparing contact openings in SiN_x anti-reflection (AR)-and passivation layers. On the other hand, ns laser pulses seem to be well suited for this purpose and do not inflict excessive damage to the laser processed wafer or solar cell.

IV. CONCLUSIONS

The shallow heat-affected zone of ultrashort pulse laser has nourished hopes for virtually damage free ablation of dielectric layers from silicon. While this technique has proven to be suitable for processing planar surfaces of solar cells, our results on alkaline textured surfaces provide a different picture. We show that in contrast to ns laser pulses the application of ps or fs laser ablation for the formation of local contact openings on textured solar cell front sides produces severe crystal damage and degradation of the electronic device properties. TEM imaging, diode *J-V* characteristics and emitter saturation current density evaluations support this finding in this work.

However, the performance of ps laser ablation on textured surfaces might be improvable. Possibly better results could be achieved for a reduced depth of energy deposition and thus of crystal defects in this process, e.g., by decreasing the applied laser wavelength. Even though LIPSS were also observed for circularly polarized multipulse laser radiation[21] other publications report about ripples on silicon solely for linearly polarized laser radiation[34,35] Thus, the application of circular radiation by inserting a lambda quarter plate into the beam path might lead to a further decrease in the crystal damage on the treated surface. In this field, further investigation needs to be done.

However, if the dislocation density at the pyramid {111} side walls rather than the defect depth at the walls or the apex is the limiting factor in this laser process, only an increase in pulse duration will lead to a stable process improvement.

Without improvement, the observed damage on textured surfaces resulting from short pulse ablation processes is so severe that we find ps and fs laser ablation of dielectric layers from textured emitter surfaces to be inapplicable for fabricating efficient solar cells. Thus, so far, ns lasers are a suitable tool for this laser process. Thereby, Gaussian beam profiles seem to be as suitable as flat-top profiles.

ACKNOWLEDGMENTS

The authors would like to thank the Fraunhofer-Centre of Silicon-Photovoltaics (CSP) for excellent TEM-images of the texture pyramid (Fig. 4) and J. Bonse for fruitful discussions about LIPSS. Funding was provided by the State of Lower Saxony and the German Federal Ministry for the Environment, Nature Conservation and Nuclear Safety (BMU) under Contract No 0327547A.

[1]A. W. Blakers, A. Wang, A. M. Milne, J. Zhao, and M. A. Green, Appl. Phys. Lett. **55**, 1363 (1989).
[2]A. Knorz, M. Aleman, A. Grohe, R. Preu, and S. W. Glunz, Proceedings of the 24th European Photovoltaic Solar Energy Conference, Hamburg, Germany, 21–25 September 2009, pp. 1002–1005.
[3]J. Zhao, A. Wang, and M. A. Green, Prog. Photovoltaics **7**, 471 (1999).
[4]C. E. Dubé and R. C. Gonsiorawski, Proceedings of the 21st IEEE Photovoltaic Specialists Conference, Kissimmee, Florida, 21–25 May 1990, pp. 624–627.
[5]R. Preu, S. W. Glunz, S. Schäfer, R. Lüdemann, W. Wettling, and W. Pfleging, Proceedings of the 16th European Photovoltaic Solar Energy Conference, Glasgow, UK, 1–5 May 2000, pp. 1181–1184.
[6]S. W. Glunz, R. Preu, S. Schäfer, E. Schneiderlöchner, W. Pfleging, R. Lüdemann, and G. Willeke, Proceedings of the 28th Photovoltaic Specialists Conference, Anchorage, Alaska, 15–22 September 2000, pp. 168–171.
[7]P. Engelhart, N.-P. Harder, T. Horstmann, R. Grischke, R. Meyer, and R. Brendel, Proceedings of the Fourth World Conference on Photovoltaic Energy Conversion, Waikoloa, HI, 7–12 May 2006, pp. 1024–1027.
[8]A. Knorz, A. Grohe, C. Harmel, R. Preu, and J. Luther, Proceedings of the 22nd European Photovoltaic Solar Energy Conference, Milan, Italy, 3–7 September 2007, pp. 1488–1491.
[9]A. Knorz, M. Peters, A. Grohe, C. Harmel, and R. Preu, Prog. Photovoltaics **17**, 127 (2009).
[10]S. Hermann, T. Neubert, B. Wolpensinger, N.-P. Harder, and R. Brendel, Proceedings of the 23rd European Photovoltaic Solar Energy Conference, Valencia, Spain, 1–5 September 2008, pp. 1204–1208.
[11]J. Krüger and W. Kautek, Laser Phys. **9**, 30 (1999).
[12]L. A. Giannuzzi and F. A. Stevie, *Introduction to Focused Ion Beams* (Springer, New York, 2005).
[13]S. Zoppel, J. Zehetner, and G. A. Reider, Appl. Surf. Sci. **253**, 7692 (2007).
[14]E. Schneiderlöchner, R. Preu, R. Lüdemann, S. W. Glunz, and G. Willeke, Proceedings of the 17th European Photovoltaic Solar Energy Conference, Munich, Germany, 22–26 October 2001, pp. 1303–1306.
[15]A. Goetzberger, B. Voß, and J. Knobloch, *Sonnenenergie: Photovoltaik-Physik und Technologie der Solarzelle*, (Teubner, Stuttgart, 1994), p. 91.
[16]R. Sinton and A. Cuevas, Appl. Phys. Lett. **69**, 2510 (1996).
[17]A. Cuevas, M. Stocks, D. Macdonald, and R. Sinton, Proceedings of the Second World Conference on Photovoltaic Energy Conversion, Vienna, 6–10 July 1998, Austria, pp. 1236–1241.
[18]H. Nagel, C. Berge, and A. G. Aberle, Appl. Phys. Lett. **86**, 6218 (1999).
[19]D. E. Kane and R. M. Swanson, Proceedings of the 18th IEEE Photovoltaic Specialists Conference, Las Vegas, Nevada, 21–26 October 1985, pp. 578–583.
[20]V. Rana, Z. Zhang, C. Lazik, R. Mishra, T. Weidman, and C. Eberspacher, Proceedings of the 23rd European Photovoltaic Solar Energy Conference, Valencia, Spain, 1–5 September 2008, pp. 1942–1944.
[21]Z. Guosheng, P. M. Fauchet, and A. E. Siegman, Phys. Rev. B **26**, 5366 (1982).
[22]H. M. van Driel, J. E. Sipe, and J. F. Young, Phys. Rev. Lett. **49**, 1955 (1982).
[23]D. C. Emmony, R. P. Howson, and L. J. Willis, Phys. Lett. **23**, 598 (1982).
[24]J. E. Sipe, J. F. Young, J. S. Preston, and H. M. van Driel, Phys. Rev. B **27**, 1141 (1983).
[25]J. Bonse, M. Munz, and H. Sturm, J. Appl. Phys. **97**, 013538 (2005).
[26]D. Dufft, A. Rosenfeld, S. K. Das, R. Grunwald, and J. Bonse, J. Appl. Phys. **105**, 034908 (2009).
[27]S. Hermann, N.-P. Harder, D. Herzog, H. Haferkamp, and R. Brendel, Appl. Phys. A: Mater. Sci. Process. **99**, 151 (2009).
[28]N. M. Johnson, F. A. Ponce, R. A. Street, and R. J. Nemanich, Phys. Rev. B **35**, 4166 (1987).
[29]A. G. Cullis, N. G. Chew, and H. C. Webber, Phys. Rev. Lett. **49**, 219 (1982).
[30]K. S. Jones, S. Prussin, and E. R. Weber, Appl. Phys. A: Mater. Sci. Process. **45**, 1 (1988).
[31]J. Washburn, in *Defects in Semiconductors*, edited by J. Narayan and T. Y. Tan (North-Holland, Amsterdam, 1981), p. 209.
[32]A. G. Cullis, N. G. Chew, H. C. Webber, and D. J. Smith, J. Cryst. Growth **68**, 624 (1984).
[33]O. Breitenstein, P. Altermatt, K. Ramspeck, and A. Schenk, Proceedings of the 21st European Photovoltaic Solar Energy Conference, Dresden, Germany, 4–8 September 2006, pp. 625–628.
[34]M. Oron and G. Sørensen, Appl. Phys. Lett. **35**, 782 (1979).
[35]P. M. Fauchet and A. E. Siegman, Appl. Phys. Lett. **40**, 824 (1982).

Downloaded 17 Dec 2010 to 18.82.0.30. Redistribution subject to AIP license or copyright; see http://jap.aip.org/about/rights_and_permissions

SIONYX1403000017.0048

SAMSUNG EX. 1002 - 1457/4148

High-performance technologies for advanced biomedical applications

PerkinElmer®
precisely

SIONYX1403000017.0049

SAMSUNG EX. 1002 - 1458/4148

table of contents

Imaging Components

- Amorphous Silicon 2
- Cooled CCD Sensors & Cameras 4
- Buffered Multiplexers 8
- Image Tubes 9
- Line Scan Imagers 10
- CMOS Photodiode Arrays 12
- TDI Imagers 14

Xenon Lighting & Spectrophotometer Platforms

- Cermax Xenon Lighting 16
- Guided Arc Pulsed Xenon Lighting 20
- UV/Vis/NIR Spectrophotometers 26

Photo Detectors

- Photon Counting Modules 28
- Channel Photomultipliers 30
- Photodiodes 34
- Thermopile Detectors 42

Medical CO_2 Sensors 44

Consistent with PerkinElmer Optoelectronics' policy of continually updating and improving its products, the type designation and data are subject to change, unless otherwise arranged. No obligations are assumed for notice of change of future manufacture of these devices or materials.

Copyright©2004 PerkinElmer Optoelectronics. All rights reserved. Lumex is a registered trademark of EASTMAN KODAK COMPANY. Windows 98, Windows 2000 and Windows NT are registered trademarks of Microsoft Corporation.

Information furnished by PerkinElmer Optoelectronics is believed to be accurate and reliable. However, no responsibility is assumed by PerkinElmer Optoelectronics for its use; nor for any infringements of patents or other rights of third parties which may result from its use. No license is granted by implication or otherwise under any patent or patent right of PerkinElmer, Inc.

One source for industry-leading OEM products.

PerkinElmer Optoelectronics offers a wide selection of complete, high-performance technologies, making us a valuable partner for all your biomedical applications. Our component and subsystem solutions play a critical role in patient monitoring, functional genomics, proteomics, cellomics, diagnostics, molecular identification, and therapy monitoring and procedures.

From design to product launch, PerkinElmer Optoelectronics consistently delivers performance-driven, high reliability solutions for demanding applications. With a full range of complete solutions from Gamma to Infrared, customization capabilities and extensive experience, PerkinElmer provides customers with faster time to market and significantly reduced manufacturing, test and calibration costs. Every product is engineered to meet stringent performance requirements in extreme environments. The entire product family is backed by PerkinElmer's exceptional ISO 9001 - certified design, production and test capabilities with more than 50 years of experience in hardware, software, and system solutions integration.

PerkinElmer Optoelectronics is a global technology leader providing market-driven, integrated solutions for biomedical and industrial applications. Our technologies, services and support fuel the medical, genomic and digital revolutions by enhancing our Customers' productivity, optimizing their performance, and accelerating their time-to-market.

We leverage our global engineering and manufacturing Centers of Excellence to provide products, custom qualified solutions, and exceptional service to our Customers around the world.

SIONYX1403000017.0051

SAMSUNG EX. 1002 - 1460/4148

amorphous silicon

Features
* Self contained digital camera
* Monolithic sensor
* Mega pixel resolution
* Pixel resolution 200 µm, 400 µm and 800 µm
* Over 65,000 shades of grey
* Ultra high sensitivity
* Electronic zoom
* Live images @ 3fps and 7fps
* Compatible with all standard image processing software
* Compatible with all Windows-based PCs with a PCI slot

Typical Applications
* Portable Radiography
* Densitometry
* PCB Inspection
* Pipeline inspection
* NDT
* Portal Imaging
* Veterinary Medicine
* Foreign Material Detection

Principle of Operation
Unique flat panel technology offers a new approach to medical, industrial and scientific imaging applications.

Datasheets available upon request

Description
All Amorphous Silicon X-Ray Detectors (XRD) work as a digital x-ray camera. The detectors are each based on a single solid state amorphous silicon sensor operating as a two-dimensional photodiode array. The cameras are well suited to perform digital image acquisitions and include all drive and readout processing electronics including an x-ray interlock. X-rays are converted to light by using different scintillators. The information is digitized in 16 bit (65,536 grey levels).

XRD 512-400 Family
The XRD 512-400 family has 512 x 512 pixels at a resolution of 400 µm pitch forming 262,144 discrete pixels on an active area of 204.8 x 204.8 mm². The base frame rate is 7 fps. The XRD 512-400 is available in different configurations allowing the user to apply x-ray energies from 30 keV up to 15 MeV. Different scintillators allow the user to customize to their specific applications and respective x-ray dosage.

XRD 18xx family
The XRD 18xx family is based on a single amorphous silicon substrate of 16 x 16 inch². The family has three branches XRD 1620, XRD 1640 and XRD 1680, presented by their pixel resolution of 200, 400 and 800 µm pitch respectively.

XRD 1640 Branch
The major member of the XRD 1640 branch is the XRD 1640 AL1, a camera having 1024 x 1024 pixels at a resolution of 400 µm pitch forming 1,046,576 discrete pixels on an active area of 409.6 x 409.6 mm². The camera uses a fast, Lanex® scintillator. The frame rate is 3 fps. Higher frame rates are available upon request. The unique design of the XRD 1640 AL1 allows the user to apply x-ray energies from 30 keV up to 15 MeV.

XRD 1680 Branch
In the specific XRD 1680 version, the detector allows the user to collect image data of 512 x 512 pixels at a resolution of 800 µm forming 262,144 discrete pixels on an active area of 409.6 x 409.6 mm². The lower resolution is well suited to perform 3-D image reconstruction applications.

XRD 1620 Branch
With the XRD 1620 version, the detector allows the user to collect image data of 2048 x 2048 pixels at a resolution of 200 µm pitch forming 4,194,304 discrete pixels on an active area of 409.6 x 409.6 mm².

SIONYX1403000017.0052

SAMSUNG EX. 1002 - 1461/4148

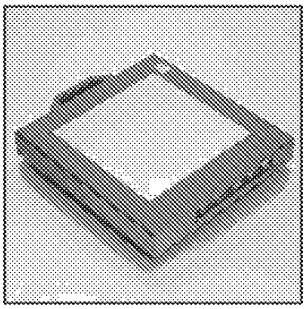

Digital X-ray Cameras—XRD 512-400

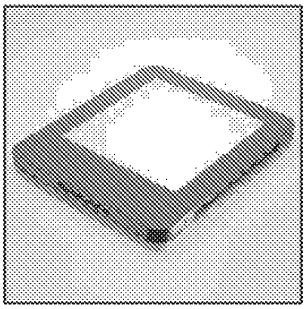

Digital X-ray Cameras—XRD 16xx

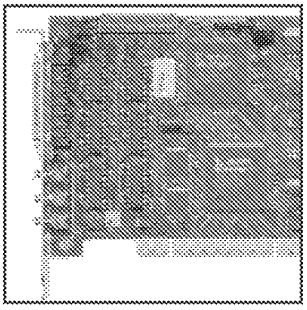

PCI Frame Grabber II

Detector Specifications

Part Number	Pixel Number	Pixel Pitch	Active Area (mm)	Photodiode Capacitance	Saturation Charge @ 10 V	Scintillator	Radiation Energy
512-400 AL1	512 x 512	400 µm	204.8 x 204.8	0.4 pF	84 pC	Lanex® fast	30–220 kV
512-400 AL2	512 x 512	400 µm	204.8 x 204.8	0.4 pF	84 pC	Lanex fine	30–220 kV
512-400 AL3	512 x 512	400 µm	204.8 x 204.8	0.4 pF	84 pC	CsI	30–220 kV
512-400 AS1	512 x 512	400 µm	204.8 x 204.8	0.4 pF	84 pC	Lanex fast	30–220 kV
512-400 BL1	512 x 512	400 µm	204.8 x 204.8	0.4 pF	84 pC	Lanex fast	30–220 kV
512-400 EL1	512 x 512	400 µm	204.8 x 204.8	0.4 pF	84 pC	Lanex fast	30 keV–15 MeV
1040 AL1 (ES)	1024 x 1024	400 µm	409.6 x 409.6	0.4 pF	84 pC	Lanex fast	30 keV–15 MeV
1040 AL2 (ES)	1024 x 1024	400 µm	409.6 x 409.6	0.4 pF	84 pC	Lanex fine	30 keV–15 MeV
1040 AL3 (ES)	1024 x 1024	400 µm	409.6 x 409.6	0.4 pF	84 pC	CsI	30 keV–15 MeV
1040 AS1 (ES)	1024 x 1024	400 µm	409.6 x 409.6	0.4 pF	84 pC	Lanex fast	30 keV–15 MeV
1620 AJ1	2048 x 2048	200 µm	409.6 x 409.6	0.1 pF	21 pC	Lanex fast	30 keV–15 MeV
1620 AJ3	2048 x 2048	200 µm	409.6 x 409.6	0.1 pF	21 pC	CsI	30 keV–15 MeV

Electronics Specifications

Part Number	Charge Amplifier (fC/LSB)	ADC 16-bit, 250 kHz	Saturation Charge @ 400 fC/LSB	Non-linearity	Minimum Integration Time
512-400 AL1	6 x 128	8	3 pC	<±1%	133 ms
512-400 AL2	6 x 128	8	3 pC	<±1%	133 ms
512-400 AL3	8 x 128	8	3 pC	<±1%	133 ms
512-400 AS1	6 x 128	8	3 pC	<±1%	133 ms
512-400 BL1	6 x 128	8	3 pC	<±1%	133 ms
512-400 EL1	6 x 128	8	3 pC	<±1%	133 ms
1640 AL1 (ES)	16 x 128	16	3 pC	<±1%	284 ms (142 ms)
1640 AL2 (ES)	16 x 128	16	3 pC	<±1%	284 ms (142 ms)
1640 AL3 (ES)	16 x 128	16	3 pC	<±1%	284 ms (142 ms)
1640 AS1 (ES)	16 x 128	16	3 pC	<±1%	284 ms (142 ms)
1620 AJ1	16 x 256	16	2 pC	<±1%	333 ms
1620 AJ3	16 x 256	16	2 pC	<±1%	333 ms

Detector Specifications

Part Number	Dynamic Range	Linearity (10% -90% of FSR)	Image Lag	Frame Rate	Detector Binning Mode
512-400 AL1	>80 dB	<±2%	<5%	7 fps	512 x 512 x 4b
512-400 AL2	>80 dB	<±2%	<5%	7 fps	512 x 512 x 4b
512-400 AL3	>80 dB	<±2%	<5%	7 fps	512 x 512 x 4b
512-400 AS1	>80 dB	<±2%	<5%	7 fps	512 x 512 x 4b
512-400 BL1	>80 dB	<±2%	<5%	7 fps	512 x 512 x 8b
512-400 EL1	>80 dB	<±2%	<5%	7 fps	128 x 128 x 4b
1640 AL1 (ES)	>80 dB	<±2%	<5%	3.5–7 fps	672 x 368 x 8b
1640 AL2 (ES)	>80 dB	<±2%	<5%	3.5–7 fps	672 x 368 x 8b
1640 AL3 (ES)	>80 dB	<±2%	<5%	3.5–7 fps	672 x 368 x 8b
1640 AS1 (ES)	>80 dB	<±2%	<5%	3.5–7 fps	672 x 368 x 8b
1620 AJ1	>80 dB	<±2%	<5%	3 fps	672 x 368 x 8b
1620 AJ3	>80 dB	<±2%	<5%	3 fps	672 x 368 x 8b

Frame Grabber Technical Specifications

Physical Dimensions	PCI Compliant	DMA	DMA Architecture	PCI Power Supply	PCI Bus	Sustained Throughput	Operating System
20 x 107 mm	2.2	Bus master	Scatter-gather	5 V, 0.5 A (typ.) 0.7 A (max) 3.3 V, 0.18 A (typ.) 0.2 A (max)	32 bit 33 MHz	>96 MB/s	Windows NT 4.0, Windows 2000, Windows 98, Windows XP

SIONYX1403000017.0053

SAMSUNG EX. 1002 - 1462/4148

cooled ccd sensors

Features

- 363,000 picture elements (pixels) in a 1100x330 configuration
- 24 µm square pixels
- 2-phase buried channel process
- On-chip amplifier for low noise and high-speed readout
- Dynamic range greater than 25,000:1
- On-chip temperature sensor
- Two-stage TE cooler integrated into the package
- Hermetically sealed
- 100% fill factor
- 10MHz data rate

Typical Applications

- Spectroscopy
- Fluorescence Microscopy
- Luminescence
- Protein Quantification

Datasheet available upon request

Description

The RA1133J is a full-frame CCD sensor with reset capabilities designed specifically for use in spectroscopy, biomedical imaging and related scientific imaging applications. The package for the array is designed with an integrated two-stage thermoelectric cooler. This enables the device to be run 40°C below ambient temperature, -15°C when compared to room temperature. Its combination of very low noise and low dark current make the RA1133J ideal for low-light, high dynamic range, and high-resolution applications.

The imager is structured with a single-output register at one end of the imaging columns. A lateral reset drain is located adjacent to this readout register, which enables the dumping of accumulated charge from the array. Two-phase clocks are needed to drive the readout register, and three-phase clocks are needed to drive imaging cells. The array is available in a 30-pin metal package with an integrated TE cooler.

Table 1: Electro-Optical Specifications

Parameter	Symbol	Min	Typ	Max	Units
Format			1100x330		
Pixel Size			24x24		µm
Imaging Area			26.4x7.92		mm
Dynamic Range	DR		25,000:1		
Full Well Charge	Q_{FWC}	250	300		Ke-
Saturation Voltage	V_{sat}	100	120		mV
Dark Current MPP	DR		1	3	pA/cm2
Photo Response Non Uniformity	PRNU		2	10	±%
Dark Signal Uniformity	DSNU		2	5	±%
Charge Transfer Efficiency	CTE	>0.9999	>0.99999		
Output Amplifier Gain			4		uV/e-
Operating Frequency	pixels			10	MHz
Read Noise			10		e-

Dynamic Range: Full well/read noise, MPP mode
Full Well Charge: Measured at 5 V bias, MPP mode
Dark Current MPP: MPP mode at -15°C
Read Noise: Measured at 500 KHz at -15°C

Absolute Maximum Ratings

Storage Temperature: -55°C min. to 65°C max.
Operating Temperature: 0°C min. to 55°C max.

SIONYX1403000017.0054

SAMSUNG EX. 1002 - 1463/4148

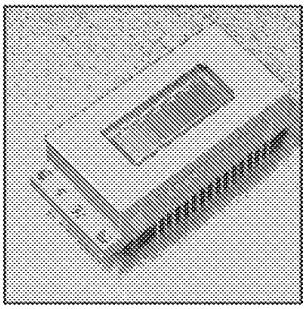

Cooled CCD Sensor—
24 µm sq. pitch,
1100x330 pixel configuration

Principle of Operation
A major source of dark current in devices such as these originates in surface states at the Si-SiO_2 interface. A unique design and process enables the RA1133J to be run in "multi-pinned phase" or MPP mode of operation. This helps eliminate dark current generation in the interface surface states. By holding the vertical clocks at negative potential during integration and horizontal signal readout, the surface will not be depleted and the surface state will not generate dark current.

Architecture & Performance

Part Number	Format	Pixel Size µm	Image Area mm	Saturation Voltage mV typ.	Dark Current MPP pA/cm²	Dynamic Range	Pixel Image
RA1133LBE-912	1100x330	24x24	26.4x7.92	1200	1	>27,000:1	16e-

Dynamic Range: Full well/read noise, MPP mode
Dark Current MPP: MPP mode at -15°C
Pixel Rate: Measured at 500 kHz at -15°C
Storage Temperature: -55°C min. to +85°C max.
Operating Temperature: 0°C min. to 50°C max.

Quantum Efficiency

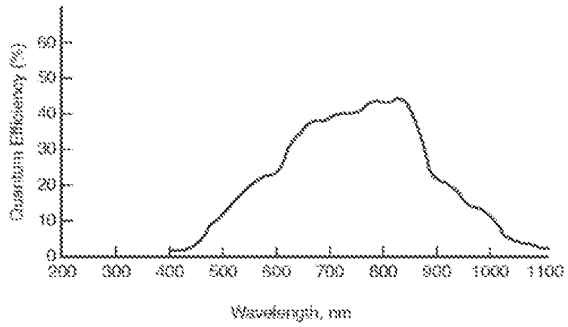

SIONYX1403000017.0055

SAMSUNG EX. 1002 - 1464/4148

cooled ccd cameras

Features
- 3,214,848 picture elements (pixels) in a 2184 x 1472 configuration
- 6.8 µm square pixels
- USB 2.0 interface
- Peltier cooling to -30°C at 25°C ambient
- 16-bit output depth with 8 electrons noise typical
- Up to 16 x 16 binning (asymmetric)
- Hermetically sealed sensor head reduces risk of contamination
- Varying readout rates (1250 kHz max)
- 300–1000 nm spectral range
- Includes power supply and software

Typical Applications
- Protein Quantification
- Fluorescence Microscopy
- Luminescence
- Sequencing

Description

PerkinElmer Optoelectronics ColdBlue™ series of cooled CCD camera systems offer scientific-grade CCD technology integrated with the latest in camera electronics to offer the user an unparalleled solution for advanced imaging applications. Featuring the Eastman Kodak KAF-3200ME image, the PD2114KNU offers pixel resolutions of 2184 x 1472 (6.8 µm x 6.8 µm pixel size). The modular sensor head design allows the camera system to be customized with different sensors at a minimum of design time.

To eliminate contamination and moisture within the sensor package, the package that surrounds the sensor has been hermetically-sealed under vacuum. The sensor head has been sealed against light and dust.

The camera is supplied with a Win32.dll, Windows drivers library, regulated power supply, and cables necessary for operation.

The PD2114 also features an integrated Thermo-Electric (TE) cooler, which cools the sensor to -30°C. This reduction in temperature allows for almost a 1000X reduction in dark current. Additionally, Area of Interest readout and binning are supported within the camera.

PD2114KNU-CP-TT-USB

Parameter	Symbol	Min.	Typ.	Max.	Units
Format			2184 x 1472		
Pixel Size			6.8 x 6.8		µm
Imaging Area			14.85 x 10.26		mm
Noise (typical)			8		e-
Image Full Well	Q_{MAX}		55		ke-
Interface Style			USB 2.0		
Gain Settings			8		
Quantum Efficiency			55		%
Spectral Range		300		1000	nm
Exposure Time		52 µs		3.2 hrs	
Binning		1 x 1		16 x 16	
Operating Temperature		0		30	°C
Storage Temperature		0		50	°C

Windows is a registered trademark of Microsoft.

SIONYX1403000017.0056

SAMSUNG EX. 1002 - 1465/4148

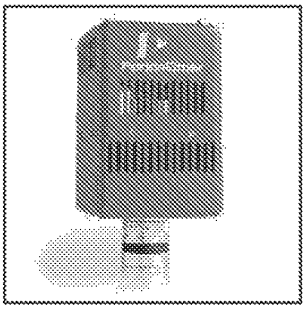

Cooled CCD Camera

Principle of Operation

The Perkinelmer ColdBlue series incorporates high performance, high resolution area image sensors. Each pixel within the sensor converts light into discrete charge packets, that are then converted to an analog voltage.

The analog voltage is then processed as a single channel of sampled-and-held, raster order analog video data. Analog processing circuitry provides adjustable gain levels, allowing the accomodation of user's unique lighting and application requirements. Once the signal is processed, it is then digitized to 16-bit depth and formatted for ouput.

Technical Specification

Part Number	Format	Pixel Size µm	Image Area mm	Saturation Voltage mV/µm	Dark Current µA/cm²	Dynamic Range	Read Noise
FU2114KNU-011	Cooled Area	6.8µm x 6.8µm	14.80mm x 15.80mm	N/A	0.015 e-/pixel/sec @ -35C	76 dB minimum, unbinned	8 e- typical

Dynamic Range: Full well/read noise, MPP mode
Dark Current MPP: MPP mode at -15°C
Read Noise: Measured at 500 kHz at -15°C
Storage Temperature: -55°C min. to +85°C max.
Operating Temperature: 0°C min. to 55°C max.

Quantum Efficiency

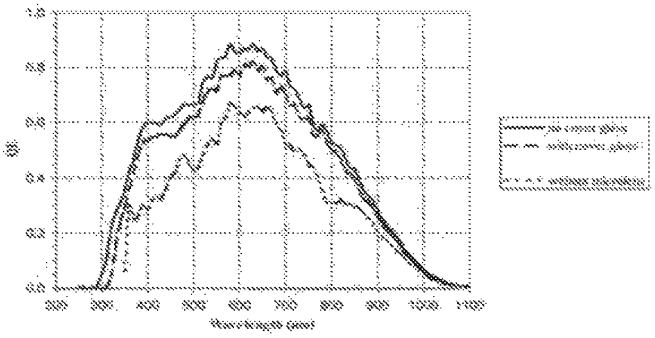

SIONYX1403000017.0057

SAMSUNG EX. 1002 - 1466/4148

buffered multiplexers

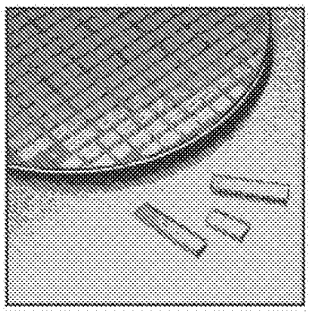

XL-1 Variable-Gain Multiplexers

Description

PerkinElmer Optoelectronics' CMOS buffered multiplexers offer the ideal solution to the increasing demand for low noise amplification and multiplexing applications. They are designed to interface with a variety of photosensitive arrays constructed from materials such as amorphous silicon, gallium arsenide, germanium or mercury cadmium telluride. These devices, available in 64, 128 and 256 channel models, are widely used in medical, scientific, and industrial applications to read electrical signals generated by x-ray, infrared, and other radiation beyond the direct detection range of silicon.

XL-1 Variable-Gain Multiplexers

These advanced devices offer a versatile solution to the increasing demand for low noise amplification and multiplexing. They are designed to interface with linear photosensitive arrays, such as those made of gallium arsenide, germanium or amorphous silicon, or any of several special purpose infrared-sensitive materials. Each channel of the multiplexer consists of a charge amplifier in series with two separate buffered sample-and-hold paths for correlated double sampling (CDS). A broad range of electrically selectable integrating capacitors provide accommodation for charge packets from a wide range of sensor materials, pixel sizes and exposure levels.

XL-1 multiplexers are available in 64, 128 or 256 active channels, all with 100µm channel-to-channel spacing. They offer a dynamic range in excess of 90 db, low offset voltage, bidirectional readout, and integrated calibration facilities.

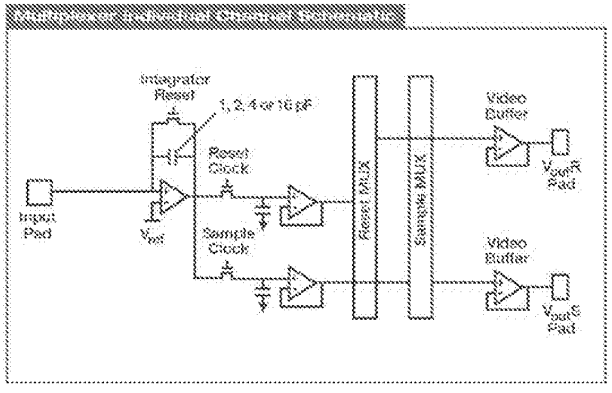

SIONYX1403000017.0058

SAMSUNG EX. 1002 - 1467/4148

image tubes

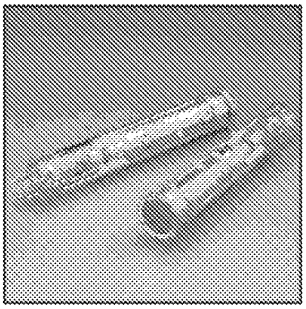

High-Resolution Image Tubes

Description

The use of image tubes in special applications is indispensable. The camera tube is superior to solid-state image sensors in high-resolution television systems with high frame-repetition rates. The essential characteristics of the camera tubes, such as absolute and spectral sensitivity, resolution and lag are determined by the photoconducting material (target) and the electron optical parameters of the scanning electron beam.

Resistron Tubes

These are universally applied low cost image tubes. The target material is Antimony Trisulfide (Sb_2S_3) which provides good resolution and integration of quantum noise.

Saticon Tubes

Saticon Tubes with a Selenium storage layer (SeAsTe) are suited for acquiring fast moving images, especially in medical applications. Their typical characteristics: low lag, excellent resolution and signal uniformity.

Newvicon Tubes

Worldwide, these tubes have been taken out of production. We offer Resistron tubes as a close equivalent to replace Newvicons.

Industrial and Surveillance 2/3" Tubes

Technical Specification

Part Number	Version	Characteristics	Length mm	Diameter mm	Focept. Temperature °C	Dark Current nA	Illumination lx
XQ1308	Resistron	electrostatic focusing	108	19.8	30+/-2	20	10
XQ1371	Resistron	large dyn. range, gr.1	108	19.8	30+/-2	20	10
XQ1372	Resistron	gr.2	108	19.8	30+/-2	20	10

Industrial and Surveillance 1" Tubes

Technical Specification

Part Number	Version	Characteristics	Length mm	Diameter mm	Focept. Temperature °C	Dark Current nA	Illumination lx
XQ1292	Resistron	large dyn. range, gr.1	162	28.6	30+/-2	20	10
XQ1293	Resistron	gr.2	162	28.6	30+/-2	20	10

Special TV 2/3" Tubes

Technical Specification

Part Number	Version	Characteristics	Length mm	Diameter mm	Focept. Temperature °C	Dark Current nA	Illumination lx
XQ13713F	Resistron	radiation resistant	108	19.8	30+/-2	20	10
XQ13720F	Resistron	radiation resistant	108	19.8	30+/-2	20	10
XQ1300F	Saticon	radiation resistant	108	19.8	30+/-2	<1	10

Special TV 1" Tubes

Technical Specification

Part Number	Version	Characteristics	Length mm	Diameter mm	Focept. Temperature °C	Dark Current nA	Illumination lx
XQ1292F	Resistron	fiberoptic faceplate	162	28.6	30+/-2	20	10
XQ1292SF	Resistron	radiation resistant	162	28.6	30+/-2	20	10
XQ1292RF	Resistron	with articles	162	28.6	30+/-2	20	10

Medical 1" Tubes

Technical Specification

Part Number	Version	Characteristics	Length mm	Diameter mm	Focept. Temperature °C	Dark Current nA	Illumination lx
XQ1290	Resistron	high sensitivity + resolution	162	28.6	30+/-2	30	1.7
XQ1395	Resistron	high resolution / line no.	162	28.6	30+/-2	30	1.7
XQ1560	Saticon	short lag / high beam	162	28.6	30+/-2	<1	1.7
XQ1670	Saticon	low lag / high beam	162	28.6	30+/-2	<1	1.7
XQ1870	Saticon	with diode gun structure	162	28.6	30+/-2	<1	1.7

SIONYX1403000017.0059

SAMSUNG EX. 1002 - 1468/4148

line scan imagers

Features
* 2500:1 dynamic range
* Ultra-low image lag
* Electronic exposure control
* Antiblooming control
* Square pixels with 100% fill factor
* Extended spectral range—250-1000 nm

Typical Applications
* High-Speed Document Reading
* Web Inspection
* Mail Sorting
* Production Measurement
* Position Sensing
* Spectroscopy

Principle of Operation
Line scan sensors are ideal for imaging objects in motion on webs or conveyors.

Datasheet available upon request

Description
Line scan sensors are ideal for imaging objects in motion on webs or conveyors. Applications range from inspection of lead frames and labels to scanning mail and parcels.

P-Series Linear Photodiode Array Imagers
In P-series linear imagers, PerkinElmer has combined the best features of high-sensitivity photodiode array detection and high-speed, charge-coupled scanning to offer an uncompromising solution to the increasing demands of advanced imaging applications. These high-performance imagers feature low noise, high sensitivity, impressive charge-storage capacity, and lag-free dynamic imaging in a convenient 1-output architecture. The 14 µm square contiguous pixels in these imagers reproduce images with minimum information loss and artifact generation, while their unique photodiode structure provides excellent blue response extending below 250 nm in the ultraviolet.

The two-phase CCD readout registers require only modest clocking voltages, yet achieve excellent charge-transfer efficiency. Additional electrodes provide independent control of exposure and antiblooming. Finally, high-sensitivity readout amplifiers provide a large-output signal to relax the noise requirements on the camera electronics that follow. These versatile imagers are available in array lengths of 512 to 2048 elements with either low-cost glass or UV-enhanced fused silica windows. PerkinElmer Optoelectronics also maintains capabilities to manufacture line scan imagers up to 8192 pixels combined with 4 outputs and 7 or 14µm pixels with existing designs. Contact PerkinElmer for more information.

SIONYX1403000017.0060

SAMSUNG EX. 1002 - 1469/4148

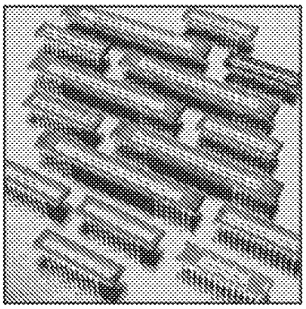

Line Scan Imagers—P Series

P Series

Technical Specification

Part Number	Pixel Count elements	Pixel Size µm	Number of Outputs	Spectral Response Range nm	Pixel Data Rate MHz	Dynamic Range	Horizontal Clocking typ.
RL0512P	512	14x14	1	250-1000	40	2500:1	2 ø @ 5 V
RL1024P	1024	14x14	1	250-1000	40	2500:1	2 ø @ 5 V
RL2048P	2048	14x14	1	250-1000	40	2500:1	2 ø @ 5 V

Operating Temperature: 0°C min. to +55°C max.
Storage Temperature: -25°C min. to +55°C max.
Lag: <1%
Saturation Voltage: 600 mV

Spectral Sensitivity Curve

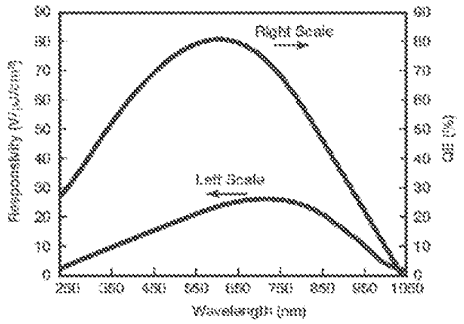

SIONYX1403000017.0061

SAMSUNG EX. 1002 - 1470/4148

cmos photodiode arrays

Features
* 2.5 mm photodiode aperture
* Extremely low dark leakage current
* Low power dissipation
* Clock-controlled sequential readout at rates up to 1 MHz
* Single-supply operation with HCMOS-compatible inputs
* Single shift register design
* Wide dynamic range
* Differential video output for clock noise cancellation
* High saturation charge 10 pC (25 µm) or 20 pC (50 µm)
* Antiblooming function for low crosstalk
* Line Reset Mode for simultaneous reset of all photodiodes
* Wide spectral response 300 to 1000 nm
* Polished fused silica window
* On-chip diodes (two) for temperature monitoring

Typical Applications
* Spectroscopy
* Colorimetry

Datasheet available upon request

Description
For nearly thirty years, PerkinElmer Optoelectronics has been a leader in the development of sensors for spectroscopy. In spectroscopy and other instrumentation applications, large pixels, very high charge storage capacity, low readout noise and dark current, and direct access to the charge packet are all critical to delivering the high dynamic range and linear response demanded. The CMOS photodiode array architecture meets all of these needs in a way no other sensor technology can match.

L-Series Visible Range Spectroscopy Arrays
PerkinElmer Optoelectronics' L-series CMOS linear photodiode arrays offer a high-quality, low-cost solution for spectroscopy and colorimetry applications in the 300-1000 nm range. The L-Series family's combination of high sensitivity, low dark current, low switching noise and high saturation charge provides excellent dynamic range and great flexibility in setting integration time.

L-series sensors consist of a linear array of silicon photodiodes, each connected to a MOS switch for readout controlled by an integrated shift register scanning circuit. Under external clock control, the shift register sequentially enables each of the switches, directing the charge on the associated photodiode to an output line. A dummy output provides clock noise cancellation. L-series devices are mounted in ceramic side-brazed, 22-pin, dual-inline packages with ground and polished fused silica windows and are pin-compatible with earlier PerkinElmer SB and TE-series sensors.

L-series models are available with pixel spacings of 25 µm and 50 µm and lengths from 128 to 1024 pixels. All models feature a 2500 µm pixel aperture to simplify alignment in spectroscopic instruments.

SIONYX1403000017.0062

SAMSUNG EX. 1002 - 1471/4148

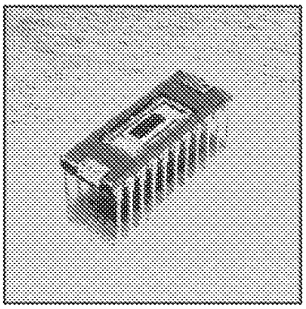

L-Series Linear CMOS Spectroscopy Sensor— 25 or 50 µm pitch, 2.5 mm aperture

- 128, 256, 512 or 1024 photodiode elements with 25 µm center-to-center spacing
- 128, 256, or 512 photodiode elements with 50 µm center-to-center spacing

L Series

Electro-Optical Specifications

Part Number	Video Capacitance @ 0 V bias pF	Video Capacitance @ 2.5 V bias pF	Sensitivity V/J/cm²	Saturation Exposure nJ/cm²	Saturation Charge pC	Dynamic Range	Dark Current typ. fA
RL1201	---	6.7	2x10⁹	50	10	76,000	0.2
RL1202		10.2	2x10⁹	50	10	76,000	0.2
RL1206	---	15.4	2x10⁹	50	10	76,000	0.2
RL1210		20.7	2x10⁹	50	10	76,000	0.2
RL1601	0.1	---	4x10⁹	50	20	156,000	0.4
RL1602	3.5		4x10⁹	50	20	156,000	0.4
RL1606	25	---	4x10⁹	50	20	156,000	0.4

Sensitivity Exposure/ Saturation Charge: Measured at 2.5 V video line bias average 600-700 nm, includes 8% window loss

Dark Current: Maximum dark current ±1.5 x average dark current

Spectral Response Peak: 650 nm. Range: 320-1060 nm typ.

Operating Temperature: 0°C min. to 55°C max.

Storage Temperature: -25°C min. to +85°C max

Center-to-center spacing: RL12XX, 25 µm
RL16XX, 50 µm

Quantum Efficiency

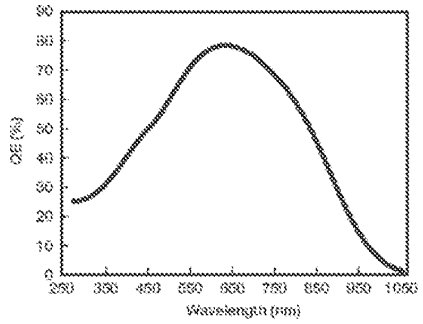

SIONYX1403000017.0063

SAMSUNG EX. 1002 - 1472/4148

tdi imagers

PT1109AAQ-711 Features
- 1024 pixel x 96 stage
- Unidirectional operation
- 20 MHz data rate
- High dynamic range (>5000:1)
- Line rates to 19 kHz
- Quantum efficiency of 42% at 700 nm
- 13 µm x 13 µm pixel size
- >0.99995 horizontal, >0.9999 vertical CTE at maximum saturation exposure

Typical Applications
- Semiconductor Inspection
- Wafer Inspection
- Sorting Applications

Datasheets available upon request

Description
The PT1109AAQ Time Delay Integration (TDI) imagers combine the best features of photodiode array detection and TDI operation to offer an uncompromising solution to the increasing demands of high-speed imaging applications.

PT 1109AAQ
The PT1109AAQ is a high-performance TDI imager featuring a unique 13 µm x 13 µm-square TDI pixel architecture. The chip has 96 stages with 1024 pixels per stage, allowing for stable imaging in both fast and low-light applications. Eight extra stages are present at the front end of the sensor, allowing for adequate dark balancing. Full well capacity of the sensor is >400,000 electrons, and readout noise is <70 electrons, allowing for a >5000:1 dynamic range.

SIONYX1403000017.0064

SAMSUNG EX. 1002 - 1473/4148

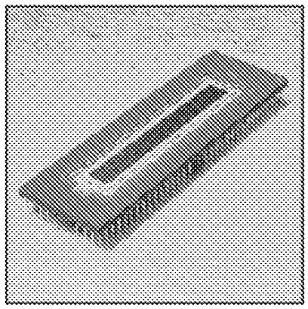

TDI Imagers—PT 1109AAQ

Technical Specification	
	PT1109AAQ-711
Pixel Count*	1024 active elements
Extra Stages*	0
Pixel Size	13x13 mm
Number of Directions	1
Integration Stages**	96
Extra Stages**	1
Number of Outputs	1
Pixel Rate	20 kHz
Line Output Rate (max.)	18.1 kHz
Pixel Fill Factor	100%
Net Quantum Efficiency	>42% at 700 nm
Power Dissipation	—
Well Capacity	>400,000 electrons per pixel
RMS Noise	—
Dynamic Range	>3000:1
CTE @ Q_{sat}	>0.9998 (horizontal) >0.9993 (vertical)
Photo Response Non-Uniformity (PRNU)	+/-10%
Spectral Response	400 to 1000 nm
Dark Current	—
Sensitivity	3 µV/electron
Operating Temperature	0 to 35°C
Package Type	32 pin ceramic

Operating Temperature: 0°C min. to 30°C max.
* In readout direction
** In TDI direction

SIONYX1403000017.0065

SAMSUNG EX. 1002 - 1474/4148

cermax xenon lighting

Features
* Very robust ceramic body
* Integrated reflector
* Broad band xenon emission spectrum
* CW operation
* Instant ON

Typical Applications
* Tunable Excitation Source for Fluorescence Applications
* Photo-Activation Source for Photo Therapy Applications
* Medical Fiber Optic Illuminators Used for Endoscopy, Surgical Headlamp, Surgical Microscopy
* Spectroscopy
* UV Curing
* Video Projection

Available Related Products
Power supplies, accessories and complete fiber optic systems

Datasheets available upon request

Description
PerkinElmer Optoelectronics' Cermax® xenon short arc lamps and associated operating equipment are a unique and innovative approach to many challenging and demanding lighting applications.

Utilizing an integrated parabolic or ellipsoidal reflector, Cermax® lamps produce high intensity, collimated or focused light output. Due to the xenon lamps broad color spectrum, the lamp is filtered to emit either visible, UV or IR light depending on application or usage. With their internal reflector and rugged ceramic body and seal construction, Cermax® lamps are a safe and compact alternative to conventional quartz xenon lamps making them ideal for such applications as medical endoscopy, fiber optic illumination and video projection.

SIONYX1403000017.0066

SAMSUNG EX. 1002 - 1475/4148

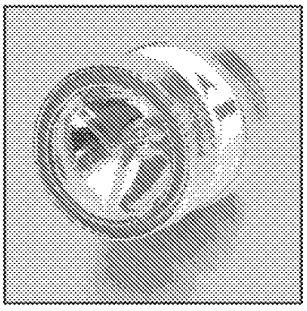

Cermax® Xenon Arc 1.5" Lamps

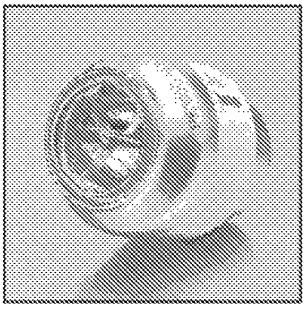

Cermax® Xenon Arc 1.0" Lamps

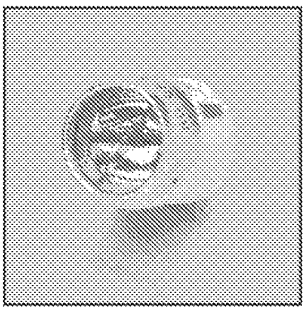

Cermax® Xenon Arc Mini Lamps

Cermax® Xenon Arc Lamps

Technical Specification

Part Number	Power Watts	Operating Current Amps (Hz)	Ignition Voltage Vdc	Voltage KV min.	Temperature	Arc Gap	Reflector	Window Diameter
PE80AF/AUV	85–100	7–10	10.5–13.5	26	120°C	.025"	Parabolic	.770"
PE80A-10F/AUV	85–100	7–10	10.5–13.5	26	120°C	.025"	Ellipsoidal	.770"
PE80A-13F/AUV	85–100	7–10	10.5–13.5	26	120°C	.025"	Ellipsoidal	.770"
PE150AF/AUV	100–150	10–14	10–13.8	26	120°C	.032"	Parabolic	.770"
PE150A-10F/AUV	100–150	10–14	10–13.8	26	120°C	.032"	Ellipsoidal	.770"
PE150A-13F/AUV	100–150	10–14	10–13.8	26	120°C	.032"	Ellipsoidal	.770"
PE125BF	75–150	7–14	9.5–12.5	23	150°C	.044"	Parabolic	1"
PE125BUV	75–150	8–14	9.5–12.5	23	150°C	.044"	Parabolic	1"
PE125B-10F/UV	75–150	7–14	10–12.5	23	150°C	.038"	Ellipsoidal	1"
PE175BF	150–200	12–16	11–14	23	150°C	.045"	Parabolic	1"
PE175BUV	150–200	13–16	11–14	23	150°C	.045"	Parabolic	1"
PE175B-10F/UV	150–200	12–16	10.5–13.5	23	150°C	.038"	Ellipsoidal	1"
PE300BF	180–320	10–22	13–16	23	150°C	.046"	Parabolic	1"
PE300BUV	180–320	11–22	13–16	23	150°C	.045"	Parabolic	1"
PE300B-10F/UV	175–305	13–23	11.5–15	23	150°C	.038"	Ellipsoidal	1"
PE300C-10F/UV	175–305	13–23	11.5–15	23	150°C	.045"	Ellipsoidal	1"
PE300C-13F/UV	175–300	13–23	11.5–15	23	150°C	.045"	Ellipsoidal	1"
PE500C-10F/UV	350–525	23–35	14–16.5	30	150°C	.045"	Ellipsoidal	1"
PE500C-13F/UV	350–525	23–35	14–16.5	30	150°C	.045"	Ellipsoidal	1"
PE700C-10F/UV	600–750	35–46	15.5–18	35	150°C	.045"	Ellipsoidal	1"
PE700C-13F/UV	600–750	35–46	15.5–18	35	150°C	.045"	Ellipsoidal	1"
PE500DF/DUV	340–675	20–32	16–21	35	150°C	.090"	Parabolic	2"
PE1000DF/DUV	850–1050	46–54	18.5–22	35	150°C	.090"	Parabolic	2"
PE1000D-10F/UV	600–1050	30–56	15–24	28	150°C	.062"	Ellipsoidal	1.375"
PE1000D-13F/UV	600–1050	30–56	15–24	28	150°C	.062"	Ellipsoidal	1.375"
PE1200D-10F/UV	950–1250	45–70	17–22	28	160°C	.067"	Ellipsoidal	1.375"
PE1200D-13F/UV	950–1250	45–70	17–22	28	160°C	.067"	Ellipsoidal	1.375"
PE1500D-10F/UV	900–1550	45–80	17–23	28	160°C	.075"	Ellipsoidal	1.375"
PE1500D-13F/UV	900–1550	45–80	17–23	28	160°C	.075"	Ellipsoidal	1.375"

PE=PerkinElmer
A=0.75"
B=1"
C=1.4"
D=2"
E=3"
F=UV Filtered Output
UV=Enhanced Output
-10=f/1 reflector (elliptical)
-13=f/1.3 reflector (elliptical)

SIONYX1403000017.0067

SAMSUNG EX. 1002 - 1476/4148

cermax xenon lighting

Features
* Output of 3480 lumens
* Input voltage: 90–264VAC, 50/60 Hz, auto select
* Line cord: IEC320, 6', US and European options
* ACMI fiber optic adapter—Storz, Olympus, Wolf, ACMI, or Liquid Light Guide
* Mechanical shutter: continuously adjustable from front panel knob, 0–100%
* Main power switch: located on rear panel
* AC power connector: located n rear panel, dual fuses
* Warranty: 12 months, excluding lamp

Typical Applications
* Tunable Excitation Source for Fluorescence Applications
* Photo-activation Source for Photo Therapy Applications
* Medical Fiber Optic Illuminators used for Endoscopy, Surgical Microscopy, and Surgical Headlamp
* Spectroscopy
* Dental Curing

Datasheets available upon request

Description
The XL-2000 fiber optic light source is a superior choice for machine vision, endoscopy, boroscopy, microscopy, minimally invasive surgery, headlamps, and dental curing. This is a high performance light source, which is light weight, compact and cost competitive with lower performing light sources.

This light source utilizes the latest in Cermax® technology, the PE300C-10F, 300 watt xenon lamp. This lamp sets new standards in optical efficiency and ease of use. As with all Cermax® lamps the PE300C-10F has an integral reflector, extremely high brightness, excellent color rendering, stable color over life and operating range, instant-on operation, and modulation capability.

The XL-2000 Fiber Optic Light Source can be supplied with fiber optic adapters for Storz, Olympus, Wolf, ACMI or Liquid Light Guides. A manually operated mechanical shutter allows the output intensity to be continuously adjusted from 0–100% without affecting color temperature. Additionally, this unit can be customized to individual specifications to meet all customer needs.

Optional Features
* Constant output: Optical feedback
* Electronic shutter
* Remote on/off
* Turret fiber optic adapter—Storz, Olympus, Wolf, ACMI, or Liquid Light Guide
* Hour meter
* Lamp aging/Over voltage indicator
* Dental adaptation—filters, EPROM, switches, membrane control panel
* Alternate fiber optic adapters—Storz, Olympus, Wolf, Liquid Light Guide, turret or custom.

SIONYX1403000017.0068

SAMSUNG EX. 1002 - 1477/4148

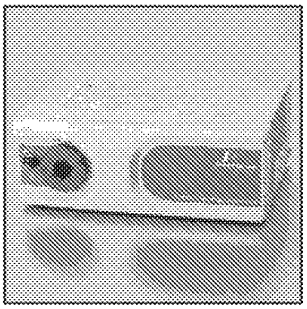

Fiber Optic Light Source—
XL-2000

XL-2000 Fiber Optic Light Source

Technical Specification

Part Number	Dimensions Inches	Weight lbs.	Operating Temperature	Storage Temperature	Humidity non-condensing	Noise
XL-2000	11.5W x 4.5L x 8.5H	8.75	0–40°C	20–+65°C	0%–85%	<45 dB

Spectral Output

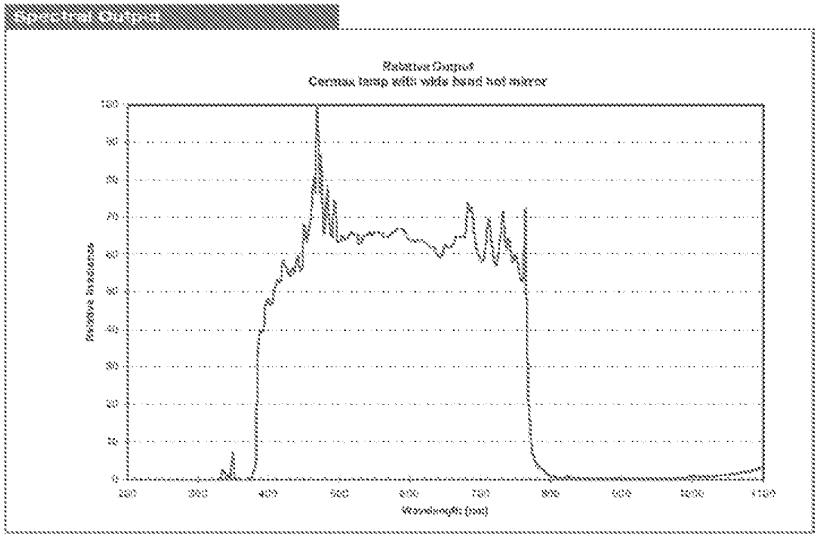

SIONYX1403000017.0069

SAMSUNG EX. 1002 - 1478/4148

guided arc pulsed xenon lighting

Features
* Small size
* High radiant intensity
* Continuous spectrum UV-VIS-IR
* Long life
* Adjustable intensity control
* Ozone free windows and collimating lens options
* Metal enclosure for improved EMI performance
* Optional SMA fiber optic connector
* Customization available

Typical Applications
* Absorption Analysis
* Clinical Chemistry Analysis
* Liquid Chromatography
* Immunoassay Systems
* Fluorimetry
* Gas Chromatography
* Colorimetry
* Machine Vision
* Particle Sizing
* Portable Instrumentation

Principle of Operation
Miniature xenon flashlamp systems that offer exceptional arc stability, microsecond flash duration and long life characteristics.

Datasheets available upon request

Description
The RSL2100 is a miniature, pulsed xenon system with broadband spectrum from UV to IR. The system operates at up to 2 watts and produces high peak intensities from 200–1100+ nm.

The RSL3100 offers SMA connector flexibility, intensity control and reduced EMI, all in a small package designed to meet CE directives. Along with a standardized "D-Sub" connector, various window options and optimized lamp alignment, the new RSL3100 meets the most demanding system requirements. The RSL3100 operates at up to 2 watts and offers high radiant, broad-band optical energy with the long life customers have grown to expect.

SIONYX1403000017.0070

SAMSUNG EX. 1002 - 1479/4148

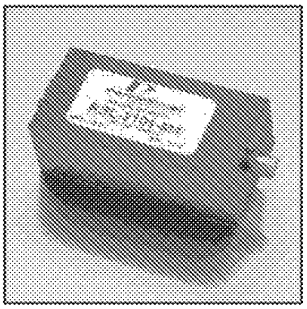

RSL2100

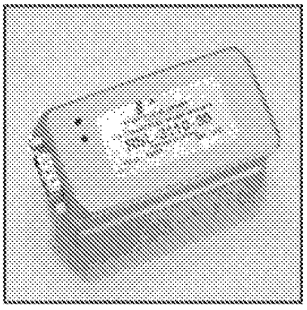

RSL3100

Input Specifications

Part Number	Voltage	DC Current	Peak Current	Trigger	Input Connector
RSL2100	11–15 VDC	0.2 amps RMS	1.0 amps	TTL	9-pin sub-D
RSL3100	11–28 VDC	0.2 amps RMS	1.0 amps	TTL	9-pin sub-D

Opto-Isolated, +5 V TTL Compatible, 20–50 mA Peak Input, 10–100 µsec Pulse Width, Leading Edge Trigger, Internal Resistor 150 ohms.

Expected Output

Part Number	Voltage	Power Under Dwell	Standard Discharge Capacitor	Flash Rate Hz
RSL2100	400–600 VDC	2 Watts max	0.047 min. µfd	$F_{MAX}=2/E$
RSL3100	400–600 VDC	2 Watts max	0.047 min. µfd	$F_{MAX}=2/E$

E=J/CV².

Power=Joules x Flash Rate

Light Output

Part Number	Spectral Range	Stability CV	Lifetime
RSL2100	190–4,000 nm	<3%	>1 x 10^8 Flashes
RSL3100	190–3,000 nm	<3%	>1 x 10^8 Flashes

CV or Coefficient of Variation is Defined as: CV%=(standard deviation of 20 flashes) ÷ (mean of 20 flashes)

Operating Temperature: 32 to 104°F (0 to 40°C)

Storage Temperature: -40 to 194°F (-40 to 90°C)

Humidity: 95% RH, Non-condensing

Shock and Vibration: 15G, 5–250 Hz (MIL-STD-810C)

Safety and EMI Compliance: Designed to Meet EN61010

Spectral Output

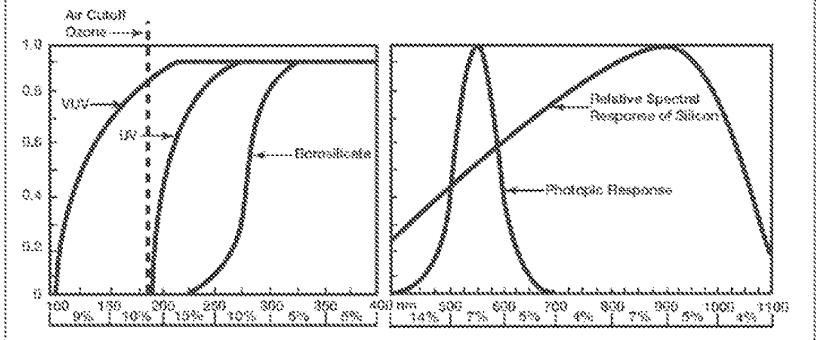

SIONYX1403000017.0071

SAMSUNG EX. 1002 - 1480/4148

guided arc pulsed xenon lighting

Features
* Exceptional arc stability
* High radiant intensity
* Continuous spectrum UV-VIS-IR
* Long life
* High repetition flash rates
* Low heat radiation
* Microsecond flash durations
* Various envelope materials
* No warm up period
* High efficiency output in the blue
* Simple fiber optic coupling
* Small size

Typical Applications
* Absorption Analysis
* Clinical Chemistry Analysis
* Liquid Chromatography
* Immunoassay Systems
* Fluorimetry
* Gas Chromatography
* Colorimetry
* Machine Vision
* Particle Sizing

Available Related Products
Power Supplies:
PS-1105
PS-1110
PS-1120
FlashPacs:
LS-1102
LS-1130
Lite-Pac® Trigger Modules:
PYD-1101
PYD-1104
PYD-113-
PYD-1150
PYD-1153

Datasheets available upon request

Description
The 1100 Series short arc xenon flashlamps are unconfined arc flashlamps which produce microsecond duration pulses of broadband light of high radiant intensities. Capable of operating at high repetition rates, these small flashlamps generate light over a continuous spectrum from ultraviolet to infrared. Exceptional arc stability and life characteristics will make the 1100 Series Flashlamps indispensable in precision photometry, radiometry, and spectroradiometry. When coupled with the 1100 Series Trigger Modules and highly regulated-low ripple power supplies, the short arc flashlamps make ideal sources of pulsed light for absorption analysis, immunoassay systems, fluorescent photometers, spectroradiometry, liquid chromatography, gas chromatography, colorimetry and ultraviolet applications.

A broad range of flashlamp, trigger modules, and power supply configurations are available to satisfy the most demanding application.

The FX-1160 Reflector Lamp has greater than 40% more usable light intensity than our standard FX-1150 and is completely interchangeable. PerkinElmer customers have the option of either taking advantage of the greatly increased light output or they can operate the FX-1160 at a reduced input energy. Lower energy operation equates to increased lamp life and stability.

The hemispherical reflector internal to the FX-1160 should not be confused with competitive types employing parabaloids or ellipsoids in which all of the forward direct light is nonrecoverable and becomes a serious source of optical scattering. PerkinElmer's FX-1160 has an electrode orientation which does not block the forward light emission and therefore does not cause a "black hole" in the output beam profile.

The optical design of the FX-1160 is ideal for use with lenses and fiber bundles, and provides the additional advantage of reduced optical noise by preventing back-plane scattering caused by the pin base. Applications that will benefit from this new PerkinElmer product introduction include: Absorption Spectroscopy, Fluorimetry, HPLC and Machine Vision.

SIONYX1403000017.0072

SAMSUNG EX. 1002 - 1481/4148

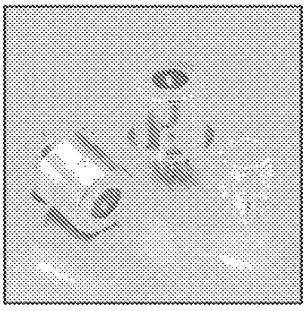

1100 Series Flashlamps

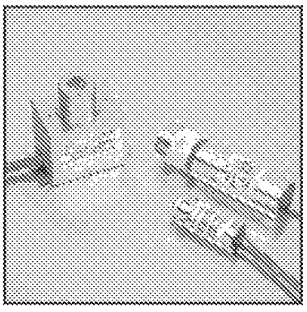

LitePac Trigger Modules with Pulsed Xenon Flashlamps

1100 Series Pulsed Xenon Flashlamps

Typical Specifications

Part Number	Pulse Load	Arc Length mm	Spectral Distribution nm	Window Material	Energy Per Flash joules max.	Average Power W max.	Voltage Vdc	Flash Rate Hz max.	Life Pulses
FX 1101	Low	1.5	225~1100+	Borosilicate	0.15	10	350~1000	300	>1 x 10⁹
FX 1102	Low	1.5	150~1100+	UV	0.15	10	350~1000	300	>1 x 10⁹
FX 1103	Low	1.5	120~1100+	VUV	0.15	10	350~1000	300	>1 x 10⁹
FX 1104	Low	3.0	225~1100+	Borosilicate	0.15	10	350~1000	300	>1 x 10⁹
FX 1105	Low	3.0	150~1100+	UV	0.15	10	350~1000	300	>1 x 10⁹
FX 1106	Low	3.0	120~1100+	VUV	0.15	10	350~1000	300	>1 x 10⁹
FX 1130	Medium	1.5	225~1100+	Borosilicate	0.25	15	350~1000	300	>1 x 10⁹
FX 1131	Medium	1.5	150~1100+	UV	0.25	15	350~1000	300	>1 x 10⁹
FX 1132	Medium	1.5	120~1100+	VUV	0.25	15	350~1000	300	>1 x 10⁹
FX 1180	Medium	3.0	225~1100+	Borosilicate	0.5	20	350~1000	300	>1 x 10⁹
FX 1181	Medium	3.0	150~1100+	UV	0.5	20	350~1000	300	>1 x 10⁹
FX 1182	Medium	3.0	120~1100+	VUV	0.5	20	350~1000	300	>1 x 10⁹
FX 1183	Medium	3.0	225~1100+	Borosilicate	0.5	20	350~1000	300	>1 x 10⁹
FX 1184	Medium	3.0	150~1100+	UV	0.5	20	350~1000	300	>1 x 10⁹
FX 1185	Medium	3.0	120~1100+	VUV	0.5	20	350~1000	300	>1 x 10⁹
FX 1160	High	1.5	225~1100+	Borosilicate	0.5	20	350~1000	300	>1 x 10⁹
FX 1161	High	1.5	150~1100+	UV	0.5	20	350~1000	300	>1 x 10⁹
FX 1162	High	1.5	120~1100+	VUV	0.5	20	350~1000	300	>1 x 10⁹
FX 1163	High	3.0	225~1100+	Borosilicate	0.5	20	350~1000	300	>1 x 10⁹
FX 1164	High	3.0	150~1100+	UV	0.5	20	350~1000	300	>1 x 10⁹
FX 1165	High	3.0	120~1100+	VUV	0.5	20	350~1000	300	>1 x 10⁹

Arc Stability Light Output: 1%

Arc Stability Spatial Movement: <0.1 mm

Spectral Output

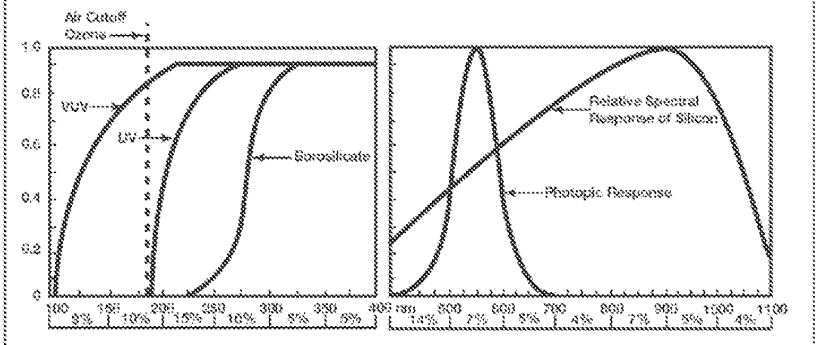

SIONYX1403000017.0073

SAMSUNG EX. 1002 - 1482/4148

guided arc pulsed xenon lighting

Features
* Up to 20x the output intensity of traditional xenon style lamps
* Exceptional arc stability
* Long life
* Continuous spectrum UV-VIS-IR
* Collimated output beam
* Ideal for use with optical lenses and fiber bundles
* Low optical noise
* Microsecond flash durations
* Various window materials transmissions ranging from 160 nm to 20 microns)
* High repetition flash rates
* No warm-up period required
* Compact size

Typical Applications
* Absorption Analysis
* Clinical Chemistry Analysis
* Liquid Chromatography
* Immunoassay Systems
* Pinorimetry
* Gas Chromatography
* Colorimetry
* Machine Vision
* Particle Sizing

Available Related Products
Power Supplies:
PS-4400

Datasheets available upon request

Description
The new FX-4400 light source from PerkinElmer Optoelectronics is a compact, high-output, long-life pulsed xenon flashlamp that offers exceptional arc stability, microsecond pulse durations and a high-intensity continuous line spectrum from the deep UV to the far IR.

The lamp utilizes an integral parabolic reflector to provide a collimated output beam and is capable of operating at up to 60 Watts average power. This new design measures approximately the same size as our traditional pulsed xenon lamps, yet provides up to 20X the light output intensity. This allows customers the option of either taking advantage of the greatly increased light output or operating the FX-4400 at a reduced input energy for increased lamp life and stability.

Lamp life exceeds 1 billion flashes, when operating at an input energy of up to 0.5 joules per flash. The maximum flash rate is 1 kHz for an input energy of 60 milli Joules. Several window materials are available to provide customers with transmission output ranging from 160nm to 20 microns.

PerkinElmer will work closely with OEM's to customize the light source and related electronics to meet the most demanding applications. Also, our broad technical expertise in light sources, optics, detectors, light management and signal processing allows us to work with and provide OEM's with unique Sensor solutions that generate, control and measure light.

SIONYX1403000017.0074

SAMSUNG EX. 1002 - 1483/4148

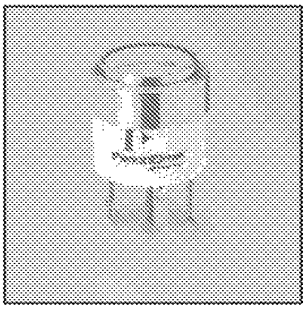

High Output Xenon Flashlamp—FX-4400

FX-4400 Series High Output Xenon Flashlamp

Technical Specification

Part Number	Energy Per Flash Joules* max.	Average Power W**	Voltage volts	Flash Rate Hz***	Life Flashes****	Output Stability*****	Spectral Distribution	Window Material
FX-4400	1.0	60	400–1000	1000	>1 x 10⁶	<3%	275–2000+	Borosilicate
FX-4401	1.0	60	400–1000	1000	>1 x 10⁶	<3%	190–2000+	UV Glass
FX-4402	1.0	60	400–1000	1000	>1 x 10⁶	<3%	160–4000	Sapphire
FX-4403	1.0	60	400–1000	1000	>1 x 10⁶	<3%	600–20,000	ZnSe

* Input Energy or $E=1/2\ CV^2$ where
E=Discharge Energy (joules)
C=Discharge Capacitor Value
V=discharge Voltage

The lamp is capable of an input energy higher than 1.0 J/flash but long life cannot be guaranteed.

** Maximum Average Power or $P_{AVG}=EF$ where
P_{AVG}=Average Power (watts)
E=Discharge Energy
F=Rate of flashes in pulses per second

Additional cooling required when operating above 40 watts.

*** Flash rate must be set so as not to exceed 60-watts Average Power. To operate the lamp at greater than 1000 Hz consult with a PerkinElmer Product Specialist.

**** Life is primarily a function of input energy per flash ($E=1/2\ CV^2$) but is also influenced by average power and peak current.

*****Typical for most operating conditions. Lamp output stability is dependent on a number of variables including input energy, flash rate, optics design, Life Pac and Power Supply.

Spectral Output

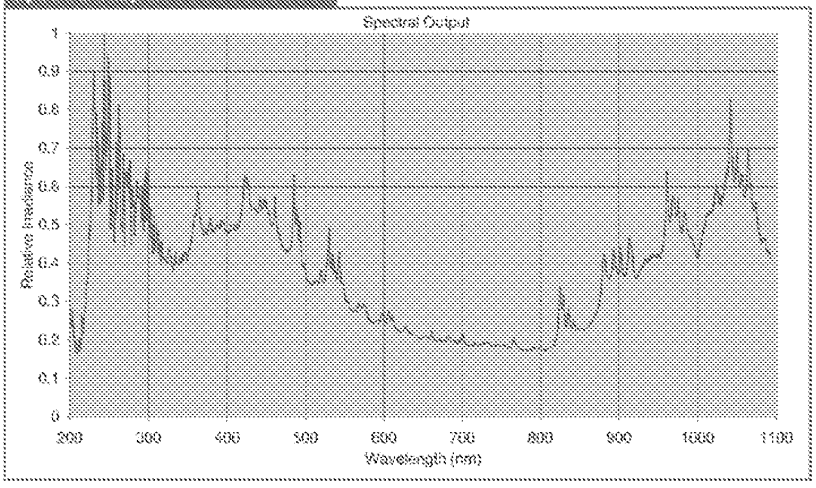

SIONYX1403000017.0075

SAMSUNG EX. 1002 - 1484/4148

UV/Vis/NIR spectrophotometers

Features
* Custom OEM design solutions
* Designs from 190–1,950 nm
* High resolution
* Low stray light
* Fast data acquisition (10 ms)
* Spectral calibration
* Built-in scan control and data acquisition
* Small footprint
* Deuterium, Xenon and Tungsten sources
* Photodiode array, photodiode, CPM, SPCM or PMT type detectors
* Cuvette, fiber or gas sampling
* Solid state design
* Vibration tolerant

Typical Applications
* Molecular Spectroscopy
* Materials Analysis
* Process Control

Datasheets available upon request

Description
PerkinElmer's spectrophotometer platforms are rugged, high performance modules that can be customized for a variety of applications in the field of Analytical Chemistry, Clinical Diagnostics, Colorimetry, Process Monitoring, Food and Agriculture, Gas Chromatography and many others. The Cross Czerny-Turner design utilizes high performance optics to minimize stray light and maximize optical performance. The modules include an integrated, miniature UV-Vis or NIR light source that provide extremely stable, high-intensity broad band output to ensure maximum signal to noise. The modules also feature compact size, high speed, solid state design and RS232/USB interface.

Companies depend on PerkinElmer for their unique ability to design and manufacture precision electro-optical OEM subsystems. In doing so, we call upon our broad technical expertise in emitters, detectors, optics design, circuit design, embedded programming and signal processing. Specializing in managing light within complex optical systems, we work with OEM teams to ensure minimum lead times, maximum value and superior performance.

SIONYX1403000017.0076

SAMSUNG EX. 1002 - 1485/4148

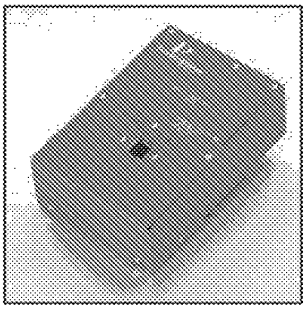

Cuvette Based UV/Vis Spectrophotometer

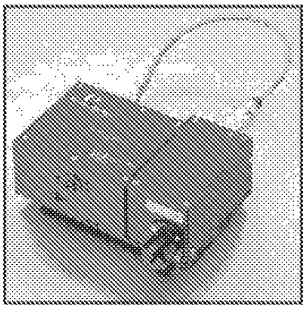

Fiber Coupled UV/Vis Spectrophotometer

	UV-Vis	NIR
Spectral Range*	190–800 nm	800–1700 nm
Spectral Resolution*	<2 nm	5 nm
Detector	1024 Si	256 InGaAs
Source	Pulsed Xenon	Tungsten
A/D Converter	16-bit	16-bit
Photometric Accuracy	±0.01A @1 AU	±0.02A @1 AU
Photometric Repeatability	±0.005 @1 AU	±0.01A @1 AU
Photometric Noise	0.00[illegible] @0 AU, 220 nm	0.0[illegible] @0 AU, 1400 nm
Stray Light	<0.1% @ 220 nm	<0.1%
Photometric Range	0–3 AU	0–3 AU
Minimum Scan Speed	0.005 seconds	0.035 seconds
Wavelength Reproducibility	0.1 nm	0.5 nm
Wavelength Accuracy	0.2 nm	0.8 nm
Outputs*	USB or RS232	USB or RS232
Computer Capability	700 MHz Pentium or equiv.	700 MHz Pentium or equiv.
Power Requirements	12 V	12 V
Size (excluding light source)	5" x 4" x 2"	8" x 4" x 2"
Weight	2 lbs.	2 lbs.

* Configurable for application specific requirements

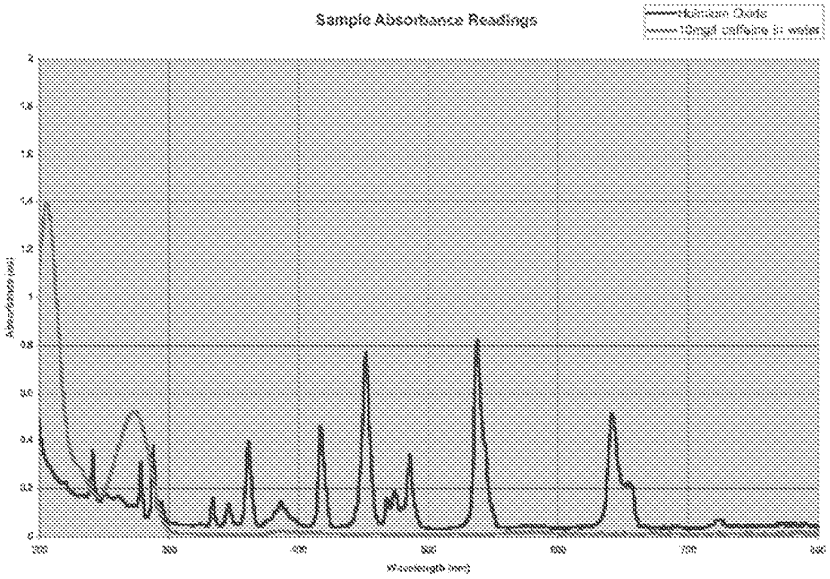

SIONYX1403000017.0077

SAMSUNG EX. 1002 - 1486/4148

photon counting modules

Features
* Peak Photon-Detection Efficiency @ 650 nm: 65% Typical
* Active Area: SPCM-AQE-1X: 175 µm
* User Friendly
* Gated Input
* Single +5 V Supply

Typical Applications
* LIDAR
* Photon-Correlation Spectroscopy
* Astronomical Observation
* Optical Range Finding
* Adaptive Optics
* Ultra-Sensitive Fluorescence
* Particle Sizing

Datasheets available upon request

Description
PerkinElmer Optoelectronics provides photon-counting modules based on both APDs and innovative Channel Photomultipliers.

APD Based Single-Photon Counting Modules
The Single-Photon Counting Module (SPCM) is a self-contained photon counter which covers the wavelength range from 400 nm to 1100 nm, with photon detection efficiencies exceeding 60% at 650 nm. It has an integral 2-stage TE cooler, cooler controller, amplifier, discriminator and TTL output driver. It also contains a high-voltage DC-to-DC converter and is powered from a single 5 V source. The module utilizes a patented active-quench circuit which allows it to count over 10 million photons per second. The photosensitive area is 0.2 mm, and units are available with dark-count rates less than 25 counts/second.

SPCM-AQ4C Single-Photon Counting Array
The SPCM-AQ4C is a 4-channel photon-counting card capable of detecting single photons of light over a wavelength range from 400 nm to 1060 nm. Each channel is independent from the others. The SPCM-AQ4C utilizes a unique silicon avalanche photodiode (SiPM™) with a circular active area whose peak photon-detection efficiency exceeds 60% at 650 nm. Each photodiode is both thermoelectrically cooled and temperature controlled, ensuring stabilized performance despite changes in the ambient temperature.

SIONYX1403000017.0078

SAMSUNG EX. 1002 - 1487/4148

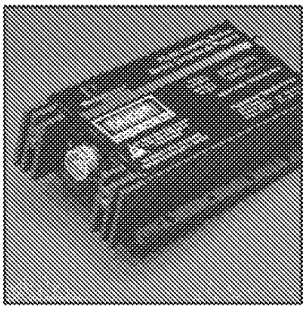

Single-Photon Counting Module—SPCM

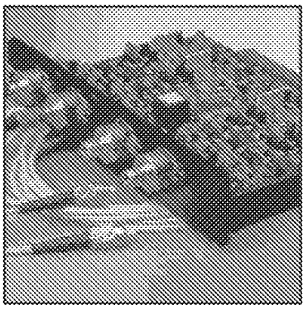

SPCM-AQ4C Single-Photon Counting Array

SPCM-AQR-1X Series

Technical Specification

Parameter	Typical	Parameter	Typical
Supply current	0.5 Amps	Supply voltage	5 V
Power cable total resistance	0.2 Ω	Case operating temperature	5-40°C
Active area (diameter) @ min. Pd	175 µm		
Photon detection efficiency (Pd) @ 400 nm 650 nm 830 nm 1060 nm	5% 65% 45% 2%	Output pulse width	35ns
Pd variation at constant case temperature (2 h @ 25° C)	±1-±5%	Pd variation 5° C to 40° C case temperature	±4-±10%
Dark count (cps) = SPCM-AQR-12 SPCM-AQR-13 SPCM-AQR-14	250-500 150-250 50-100	Dark count (cps) = SPCM-AQR-15 SPCM-AQR-16	50 max. 25 max.
Average dark count variation at constant case temperature (6 hrs @ 25°C) SPCM-AQR-12/13 SPCM-AQR-14/15/16	±10% max. ±1σ max.	Average dark count variation at 5°C to 40°C case temperature SPCM-AQR-12/13 SPCM-AQR-14/15/16	±20% max. ±2σ max.
Single-photon timing resolution	Contact Factory	Dead time (Count rates below 5 Mc/s)	50 ns
Output count rate before saturation	15 Mc/s	Afterpulsing probability	0.5%
Linearity correction factor @200 kc/s @1 Mc/s @5 Mc/s	1.05 1.08 1.4	Gating turn on/off (50 Ω output) Disable = TTL Low Enable = TTL High	2 ns 47 ns
Settling time following power up (1% stability) @ 1 meg counts/sec and 25°C	15 S	Threshold setting required on counter for digital output pulse (terminate in 50 Ω)	1 V
Gate threshold voltage: (@ V_{supply} = 5 V) Low level (sink current >60 mA)	0 V-0.4 V	Gate threshold voltage: (@ V_{supply} = 5 V) High level (sink current >30 mA)	3.5-5.25 V

Test Conditions: T=22°C

SPCM-AQ4C

Technical Specification

Parameter	Typical	Parameter	Typical
Supply currents: @+2 V @+5 V @+30 V	1 Amp 0.25 Amps 0.01 Amps	Maximum power consumption: @+2 V @+5 V @+30 V	Counts/Second 6 Watts max. 5 Watts max. 1.2 Watts max.
Supply voltage	1.95 V-2.05 V 4.75 V-5.25 V 29 V-31 V	Photon detection efficiency (per channel) @400 nm @650 nm @830 nm	5% 65% 25%
Operating temperature (heatsink)	5°C-40°C	Dark count (per channel)	500 counts/sec.
Average dark count variation per channel @ constant heatsink temp.	10%	Average dark count variation per channel @ 5° to 40°C heatsink temp.	20%
Timing resolution	Contact Factory	Dead time	50 ns
Output pulse width	25 ns	Maximum count rate*	4 Mc/s
Continuous	1.5 Mc/s	Afterpulsing probability	0.5%
Gate threshold voltage: (@ V_{supply} = 5 V) Low level (sink current >60 mA)	0 V-0.4 V	Gate threshold voltage: (@ V_{supply} = 5 V) High level (source current >30 mA)	3.5 V-5.25 V

Test Conditions: T=22°C *500 ns duration, 25% duty cycle

SIONYX1403000017.0079

SAMSUNG EX. 1002 - 1488/4148

channel photomultipliers

CPM Features

- Ultra-high anode sensitivity up to 10^7 A/W
- Extremely low dark current, typically 3 pA @ 10^8 gain
- Very low equivalent noise input (down to 10^{-17} W)
- High stability in dark current ("no bursts")
- High gain exceeding 10^8
- Compact dimensions
- High dynamic range
- Wide spectral response through multiple window materials
- High resolution
- Fast response time
- High immunity to magnetic fields
- Rugged design

Module Features

- High dynamic range
- No cooling required
- Very high stability in noise level
- Adjustable gain
- Active quenching circuit for high light protection
- Gateable CPM input
- Optical fiber read-out possible
- 5 volts operating voltage
- Monitor voltage output

Typical Applications

- Photon Detection and Counting
- Fluorescence Measurements
- Analytical and Clinical Instrumentation
- Bioluminescence
- High-Energy Physics

Available Related Products

CPM:

1/8" C930 Series
1/2" C1300 Series
3/4" C1900 Series

CPM Modules:

MD Series
MP Series
MH Series
MP 96X-2, MP 97X-2

High Voltage Power Supply:

C1V 30N
C1V 30P

Datasheets available upon request

Description

PerkinElmer Optoelectronics' Channel Photomultiplier (CPM) is an ultra-high sensitivity optical detector capable of replacing conventional photomultipliers (PMTs). This device uses a proprietary detector principle to produce ultra-high gain and dynamic range, extremely low noise, and fast response within a compact form factor. These detectors are available as components or in complete modules designed for DC operation and photon counting. All modules are gateable by an external TTL pulse for time-resolved measurements.

Modules

- MD Series DC-Module—contains the CPM, a high-voltage power supply, an amplifier with I/U conversion, and an active quenching circuit for high light protection.
- MP Series Photon Counting Module—The Photon Counting Head MP 900 contains the Channel Photomultiplier, a high-voltage power supply, a discrimination amplifier and a pulse shaper for fast output pulses.
- MH Series Channel Photomultiplier Head Module—The Channel Photomultiplier module MH 900 series is designed for both photon counting and dc operating modes. it contains an adjustable high-voltage supply and a Channel Photomultiplier of the C900 series.
- MP 96X-2, MP 97X-2 Single Photon Counting Module— These modules are specially designed for particle measurement with 630 nm and 632 nm lasers. Based on the standard multialkali photocathode, the sensitive diameter is reduced to 2 mm in order to achieve an excellent low dark-count performance.

Power Supply

- C1V 30N—A self-contained high-voltage supply specially designed for the Channel Photomultipliers CPM C930, C1300 and C1500. It provides the matching voltages for the cathode, channel entrance, and channel end.
- C1V 30P—The equivalent power supply for positive high voltage.

All given values are nominal/typical at 20°C ambient temperature; specifications are subject to change without notice.

Principle of Operation

The CPM converts a very low light level into photoelectrons through a semitransparent photocathode deposited on the inner surface of the entrance window. On their way from the cathode to the anode, the photoelectrons pass through a narrow semiconductive channel. Each time the electrons hit the inner surface of the curved channel, multiple secondary electrons are emitted. This effect occurs multiple times along the path, leading to an avalanche effect with a gain exceeding 10^8. The curved shape of the glass tube improves the multiplication effect.

SIONYX1403000017.0080

SAMSUNG EX. 1002 - 1489/4148

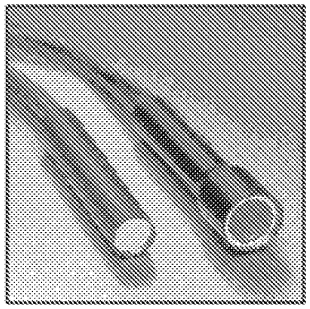

Channel Photomultipliers—
CPM Formats 1/2" and 3/4"

CPM—1/3" C 906 Series

Technical Specifications

Spectral Response Type	Model	47 ID mm 3/16	40.26 mm 5/16	40.80 mm 3/8	40.50 mm 5/8	ENI (W)	Dark Current nA	Model	Dark Counts Per Second (cps)
115-200	C911	8x10⁶				1x10⁻¹⁷	2	C911P	0.1
115-200	C921		7x10⁶			1x10⁻¹⁷	10	C921P	
185-320	C922		3x10⁶			5x10⁻¹⁷	10	C922P	1
185-320	C942			2x10⁶		5x10⁻¹⁷	80	C942P	10
185-650	C963			3x10⁶		1x10⁻¹⁶	80	C963P	10
185-650	C964			8x10⁶		1x10⁻¹⁶	80	C964P	10
185-730	C952			2x10⁶		2.5x10⁻¹⁶	250	C952P	40
185-730	C953			5x10⁶		2.5x10⁻¹⁶	250	C953P	40
185-850	C962				8x10⁶	4x10⁻¹⁶	1000	C962P	100
185-850	C963				2x10⁷	4x10⁻¹⁶	1000	C963P	100
185-890	C972				2x10⁶	3.5x10⁻¹⁶	3000	C972P	500
185-900	C973				5x10⁶	3.5x10⁻¹⁶	3000	C973P	500
185-650	C962			3x10⁶		8x10⁻¹⁷	25	C962P	3
185-650	C963			8x10⁶		8x10⁻¹⁷	25	C963P	3
185-730	C952			2x10⁶	2x10⁶	1x10⁻¹⁶	80	C952P	5
185-730	C953			5x10⁶	5x10⁶	1x10⁻¹⁶	80	C953P	5

Useful Area: Min. 5 mm
Window Material: MgF_2, Quartz or UV Glass
Electron Multiplication: Channel Electron Multiplier
Current Amplification: 5x10⁷
Bias Current (μA): 50
Anode Current: Max. 10 μA (Max. 30 sec.)
Single Photo Electron gain: 2x10⁶
Ambient Temperature (°C): Max. 50

Photocathode Material: CsI, CsTe, Low-noise Bialkali, Bialkali, Low-noise Multialk., Multialk, Extended Red Multialk, or yellow enhanced.
Supply Voltage (V): 2400 (Max. 3000)
Linear Anode Current: Max. (DC Linearity limit) 10% of Bias Current
Response Time Rise Time (ns): 5
Pulse Width/FWHM (ns): 8
Peak to Valley: 10:1

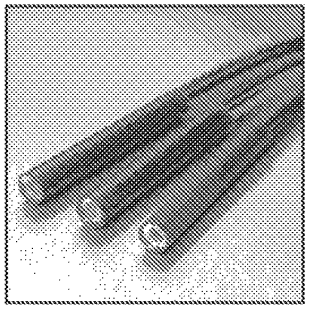

Channel Photomultipliers—
CPM Format 1/3"

CPM—1/2" C 1360 Series

Technical Specifications

Spectral Response Type	Model	50.80 mm 2"	50.80 mm 2"	50.80 mm 2"	50.80 mm 2"	ENI (W)	Dark Current nA	Model	Dark Counts per Second (cps)
115-200	C1311	8x10⁶				2x10⁻¹⁷	8	C1311P	0.4
115-320	C1321		1x10⁶			2x10⁻¹⁷	40	C1321P	2
185-320	C1322		1x10⁶			2x10⁻¹⁷	40	C1322P	4
185-650	C1342			2x10⁶		2x10⁻¹⁶	320	C1342P	40
185-650	C1343			8x10⁶		2x10⁻¹⁶	320	C1343P	40
300-650	C1344			2x10⁶		2x10⁻¹⁶	320	C1344P	40
185-750	C1352			2x10⁶		4x10⁻¹⁶	1000	C1352P	100
185-750	C1353			5x10⁶		4x10⁻¹⁶	1000	C1353P	100
185-850	C1362				2x10⁶	8x10⁻¹⁶	4000	C1362P	400
185-850	C1363				5x10⁶	8x10⁻¹⁶	4000	C1363P	400
185-890	C1372				2x10⁶	8x10⁻¹⁶	20000	C1372P	2000
185-900	C1373				5x10⁶	8x10⁻¹⁶	20000	C1373P	2000
185-650	C1382			8x10⁶		1x10⁻¹⁶	100	C1382P	10
185-650	C1383			2x10⁷		1x10⁻¹⁶	100	C1383P	10
185-750	C1392			2x10⁶	2x10⁶	2x10⁻¹⁶	250	C1392P	20
185-750	C1393			5x10⁶	5x10⁶	2x10⁻¹⁶	250	C1393P	20

Useful Area: Min. 9 mm
Window Material: MgF_2, Quartz, UV Glass or Borosil.
Supply Voltage (V): 2400 (Max. 3000)
Bias Current (μA): 50
Response Time Rise Time (ns): 5
Pulse Width/FWHM (ns): 8
Peak to Valley: 10:1

Photocathode Material: CsI, CsTe, Low-noise Bialkali, Bialkali, Low-noise, Multialk., Multialk, Extended Red Multialk, or yellow enhanced.
Current Amplification: 5x10⁷
Linear Anode Current: Max. (DC Linearity limit) 10% of Bias Current
Anode Current: Max. 10 μA (Max. 30 sec.)
Single Photoelectron gain: 2x10⁶
Ambient Temperature (°C): Max. 50

SIONYX1403000017.0081

SAMSUNG EX. 1002 - 1490/4148

channel photomultipliers

CPM—3/4" C 1900 Series

Technical Specification

Spectral Response /nm	Model	@140 nm A/W	@200 nm A/W	@400 nm A/W	@800 nm A/W	ENI (W)	Dark Current pA	Model	Dark Counts per Second (cps)
115-200	C1911	5x10⁴				3x10⁻¹⁷	25	C1911P	1
115-320	C1921		1x10⁴			3x10⁻¹⁷	100	C1921P	10
185-320	C1922		1x10⁴			3x10⁻¹⁷	100	C1922P	10
165-650	C1942			3x10⁴		3x10⁻¹⁷	800	C1942P	100
165-850	C1943			3x10⁴		3x10⁻¹⁷	800	C1943P	100
300-850	C1944			3x10⁴		3x10⁻¹⁷	800	C1944P	100
185-750	C1952			3x10⁴		8x10⁻¹⁷	2500	C1952P	400
165-750	C1953			3x10⁴		8x10⁻¹⁷	2500	C1953P	400
165-850	C1962				2x10⁵	1x10⁻¹⁷	10000	C1962P	1000
185-850	C1963				2x10⁵	1x10⁻¹⁷	10000	C1963P	1000
185-900	C1972				2x10⁵	3x10⁻¹⁷	30000	C1972P	3000
165-900	C1973				2x10⁵	3x10⁻¹⁷	30000	C1973P	3000
165-850	C1982			3x10⁴		2x10⁻¹⁷	250	C1982P	25
185-850	C1983			3x10⁴		2x10⁻¹⁷	250	C1983P	25
185-750	C1992			3x10⁴	2x10⁵	3x10⁻¹⁷	500	C1992P	50
165-750	C1993			3x10⁴	2x10⁵	3x10⁻¹⁷	500	C1993P	50

Useful Area: Min. 15 mm
Window Material: MgF_2, Quartz, UV Glass or Borosil.
Electron Multiplication: Channel Electron Multiplier
Current Amplification: 5x10⁶
Bias Current (pA): 50
Anode Current: Max. 10 nA (Max. 30 sec.)
Single Photoelectron gain: 5x10⁶
Ambient Temperature (°C): Max. 50

Photocathode Material: Cs1, CsTe, Low-noise Bialkali, Bialkali, Low-noise Multiall , Multiall, Extended Red Multiall, or yellow enhanced.
Supply Voltage (V): 2400 (Max. 3000)
Linear Anode Current: Max. (DC linearity limit) 10% of Bias Current
Response Time Rise Time (ns): 3
Pulse Width/FWHM (ns): 6
Peak to Valley: 10:1

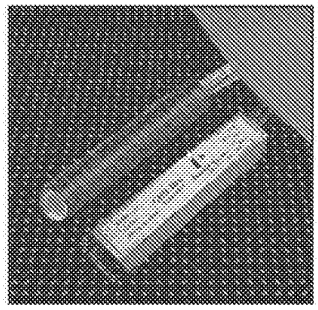

Power Supply
CHV30N, CHV30P

Power Supply—CHV30N

Technical Specification

Part Number	Voltage Channel Entrance	Voltage Cathode	Output Current	Long Term Stability typ.	Output Ripple typ.	Supply Voltage
CHV30N	-2900 V max.	-3000 V max.	100 nA max.	< 1E-5	< 50 mV_{pp}	5 V

Test conditions: T = 20°C
Voltage channel entrance: V_{SET}=0-2.6 V
Voltage cathode: V_{gate}=low at open
Long-term stability @ V_{SET} <<1 E-5
Weight: 45 g
Operating temperature: 0-50°C
Storage temperature: -20-60°C

Power Supply—CHV30P

Technical Specification

Part Number	Voltage Anode	Voltage Cathode typ.	Voltage Channel Entrance typ.	Output Current	Long Term Stability typ.	Output Ripple typ.	Supply Voltage
CHV30P	+3000 V max.	0 V	140 V	100 nA max.	< 1E-5	< 30 mV_{pp}	5 V

Test conditions: T = 20°C
Voltage Anode: @ V_{SET}=0-3 V
Voltage cathode: 100 V—when gated
Voltage channel entrance: @ V_A ≥1400 V
Long-term stability @ V_{SET} <<1 E-5
Weight: 45 g
Operating temperature: 0-50°C
Storage temperature: -20-60°C

SIONYX1403000017.0082

SAMSUNG EX. 1002 - 1491/4148

CPM Module—1/2" 900 Series

Preferred Specifications

Spectral Response nm	Model	Dark Current/Offset Voltage @ G=1.0E6 Gain RH (R)	S-1 (200 nA	Model	Dark Counts per Second (cps)	Model	Dark Current pA @2x10⁶ Gain	Model	RH (R)	Dark Counts per Second (cps)
165-650	MD 942	1x10¹⁰	3 pA/120 µV	MP 942	10	MH 942	80	MH 942P	1x10¹⁰	10
185-650	MD 943	1x10¹⁰	3 pA/120 µV	MP 943	10	MH 943	80	MH 943P	1x10¹⁰	10
165-730	MD 952	2.5x10¹⁰	10 pA/500 µV	MP 952	40	MH 952	250	MH 952P	2.56x10¹⁰	40
185-730	MD 953	2.5x10¹⁰	10 pA/500 µV	MP 953	40	MH 953	250	MH 953P	2.56x10¹⁰	40
165-850	MD 962	4x10¹⁰	30 pA/1.5 mV	MP 962 MP 962-2	100 40	MH 962	1000	MH 962P	4x10¹⁰	100
185-850	MD 963	4x10¹⁰	30 pA/1.5 mV	MP 963 MP 963-2	100 40	MH 963	1000	MH 963P	4x10¹⁰	100
165-855	MD 972	1.5x10¹⁰	200 pA/10 mV	MP 972 MP 972-2	500 160	MH 972	5000	MH 972P	1.5x10¹⁰	466
185-855	MD 973	1.5x10¹⁰	200 pA/10 mV	MP 973 MP 973-2	500 160	MH 973	5000	MH 973P	1.5x10¹⁰	466
165-630	MD 982	6x10¹⁰	1 pA/50 µV	MP 982	8	MH 982	25	MH 982P	6x10¹⁰	8
185-630	MD 983	6x10¹⁰	1 pA/50 µV	MP 983	8	MH 983	25	MH 983P	6x10¹⁰	8
165-750	MD 992	1x10¹⁰	2 pA/100 µV	MP 992	8	MH 992	50	MH 992P	1x10¹⁰	8
185-750	MD 993	1x10¹⁰	2 pA/100 µV	MP 993	8	MH 993	50	MH 993P	1x10¹⁰	8

Photocathode Diameter: 8 mm (MP 9xx-2 types: 2 mm)
Window Material: Quartz or UV Glass
Additional models on request

Photocathode Material: Low-noise Bialkali, Bialkali, Low-noise Multialk., MultiAlk, Extended Red Multialk, or yellow enhanced.
Quantum Efficiency: 20% typical (Ext. Red MA: 10% typical)

CPM Module—1/2" 1300 Series

Preferred Specifications

Spectral Response nm	Model	Dark Current/Offset Voltage @ G=1.0E6 Gain RH (R)	S-1 (200 nA	Model	Dark Counts per Second (cps)	Model	Dark Current pA @2x10⁶ Gain	Model	RH (R)	Dark Counts per Second (cps)
165-650	MD1342	2x10¹⁰	12 pA/600 µV	MP1342	40	MH1342	320	MH1342P	2x10¹⁰	40
185-650	MD1343	2x10¹⁰	12 pA/600 µV	MP1343	40	MH1343	320	MH1343P	2x10¹⁰	40
165-730	MD1352	4x10¹⁰	40 pA/2 mV	MP1352	160	MH1352	1000	MH1352P	4x10¹⁰	146
185-730	MD1353	4x10¹⁰	40 pA/2 mV	MP1353	160	MH1353	1000	MH1353P	4x10¹⁰	146
165-850	MD1362	8x10¹⁰	120 pA/6 mV	MP1362	466	MH1362	4000	MH1362P	8x10¹⁰	600
185-850	MD1363	8x10¹⁰	120 pA/6 mV	MP1363	466	MH1363	4000	MH1363P	8x10¹⁰	600
165-905	MD1372	2x10¹¹	600 pA/40 mV	MP1372	2000	MH1372	20000	MH1372P	3x10¹¹	2000
185-905	MD1373	2x10¹¹	600 pA/40 mV	MP1373	2000	MH1373	20000	MH1373P	3x10¹¹	2000
165-650	MD1382	1x10¹⁰	8 pA/200 µV	MP1382	16	MH1382	100	MH1382P	1x10¹⁰	16
185-650	MD1383	1x10¹⁰	8 pA/200 µV	MP1383	16	MH1383	100	MH1383P	1x10¹⁰	16
165-730	MD1392	2x10¹⁰	8 pA/400 µV	MP1392	20	MH1392	200	MH1392P	2x10¹⁰	20
185-730	MD1393	2x10¹⁰	8 pA/400 µV	MP1393	20	MH1393	200	MH1393P	2x10¹⁰	20

Photocathode Diameter: Min. 8 mm
Window Material: Quartz or UV Glass
Additional models on request

Photocathode Material: Low-noise Bialkali, Bialkali, Low-noise Multialk., Multialk, Extended Red Multialk, or yellow enhanced.
Quantum Efficiency: 20% typical (Ext. Red MA: 10% typical)

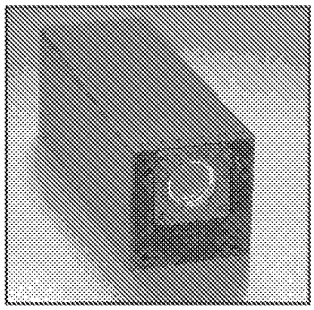

CPM Modules—
3/4" 1900 Series

CPM Module—3/4" 1900 Series

Preferred Specifications

Spectral Response nm	Model	Dark Current/Offset Voltage @ G=1.0E6 Gain RH (R)	S-1 (200 nA	Model	Dark Counts per Second (cps)	Model	Dark Current pA @2x10⁶ Gain	Model	RH (R)	Dark Counts per Second (cps)
165-650	MD1942	8x10¹⁰	30 pA/1.5 mV	MP1942	100	MH1942	800	MH1942P	8x10¹⁰	100
185-650	MD1943	8x10¹⁰	30 pA/1.5 mV	MP1943	100	MH1943	800	MH1943P	8x10¹⁰	100
165-730	MD1952	8x10¹⁰	100 pA/5 mV	MP1952	400	MH1952	2500	MH1952P	8x10¹⁰	400
185-730	MD1953	8x10¹⁰	100 pA/5 mV	MP1953	400	MH1953	2500	MH1953P	8x10¹⁰	400
165-850	MD1962	1x10¹¹	300 pA/15 mV	MP1962	1000	MH1962	10000	MH1962P	1x10¹¹	1000
185-850	MD1963	1x10¹¹	300 pA/15 mV	MP1963	1000	MH1963	10000	MH1963P	1x10¹¹	1000
165-900	MD1972	3x10¹¹	2 nA/100 mV	MP1972	5000	MH1972	50000	MH1972P	3x10¹¹	5000
185-900	MD1973	3x10¹¹	2 nA/100 mV	MP1973	5000	MH1973	50000	MH1973P	3x10¹¹	5000
165-650	MD1982	2x10¹⁰	10 pA/500 µV	MP1982	25	MH1982	250	MH1982P	2x10¹⁰	25
185-650	MD1983	2x10¹⁰	10 pA/500 µV	MP1983	25	MH1983	250	MH1983P	2x10¹⁰	25
165-750	MD1992	3x10¹⁰	30 pA/800 µV	MP1992	50	MH1992	500	MH1992P	3x10¹⁰	50
185-750	MD1993	3x10¹⁰	30 pA/800 µV	MP1993	50	MH1993	500	MH1993P	3x10¹⁰	50

Photocathode Diameter: Min. 15 mm
Window Material: Quartz or UV Glass
Additional models on request

Photocathode Material: Low-noise Bialkali, Bialkali, Low-noise Multialk., Multialk, Extended Red Multialk, or yellow enhanced.
Quantum Efficiency: 20% typical (Ext. Red MA: 10% typical)

SIONYX1403000017.0083

SAMSUNG EX. 1002 - 1492/4148

photodiodes

Features
* Low-cost visible and near-IR photodetector
* Excellent linearity in output photocurrent over 7 to 9 decades of light intensity
* Fast response times
* Available in a wide range of packages including epoxy-coated, transfer-molded, cast, and hermetic packages, as well as in chip form
* Low noise
* Mechanically rugged, yet compact and lightweight
* Available as duals, quads or as linear arrays
* Usable with almost any visible or near-infrared light source such as solid state laser diodes, neon, fluorescent, incandescent bulbs, lasers, flame sources, sunlight, etc.
* Can be designed and tested to meet the requirements of your application

Typical Applications
* Fiber-Optic Communications
* Instrumentation
* High-Speed Switching
* Spot Position Tracking and Measurement
* Photometry
* Data Transmission
* UV Light Meters
* Fluorescent Light Detection
* Laser Range Finding
* Barcode Scanning
* Laser Safety Scanning
* Distance Measurement

Datasheets available upon request

Description
PerkinElmer Optoelectronics offers a broad array of Silicon and InGaAs PIN and APDs.

InGaAs Avalanche Photodiodes
The high-quality InGaAs avalanche photodiodes (APDs) are packaged in hermetically sealed TO cans and ceramic blocks designed for the 900 to 1700 nm wavelength region.

InGaAs PIN Photodiodes
High-quality Indium Gallium Arsenide photodiodes designed for the 900 to 1700 nm wavelength region, these photodiodes are available in standard sizes ranging from 50 microns to 5 mm in diameter. Packages include ceramic submount, TO packages, and chip form.

Silicon Avalanche Photodiodes
These are reliable, high-quality detectors in hermetically sealed TO packages designed for high-speed and high-gain applications. A "reach-through" structure is utilized which provides very low noise performance at high gains, and a full range of active areas is available.

Silicon PIN Photodiodes
Offered for low- to high-speed applications, these PINs are designed for the 250 nm to 1100 nm range. Standard sizes range from 100 microns to 10 mm in diameter.

Silicon PN Photodiodes
This format includes a variety of high-volume, low-cost silicon photodiodes that meet the demanding requirements of today's commercial and consumer markets.

Alternate Source/Second Source Photodiodes
PerkinElmer's nearest equivalent devices are selected on the basis of general similarity of electro-optical characteristics and mechanical configuration. Interchangeability in any particular application is not guaranteed, suitability should be determined by the customer's own evaluation.

Detector Modules
Preamplifier modules are hybrid devices with a photodiode and a matching amplifier in a compact hermetic TO package. An integral amplifier allows for better ease of use and noise bandwidth performance. 14-pin, DIL, and/or fibered packaged modules are available on a custom basis.

SIONYX1403000017.0084

SAMSUNG EX. 1002 - 1493/4148

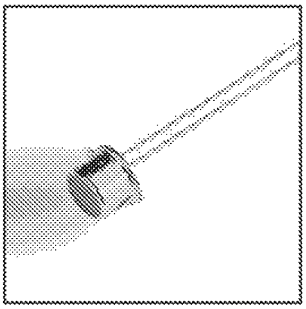

Indium Gallium Arsenide PIN Photodiodes, Large-Area, and Small-Area Indium Gallium Arsenide APDs

- High Responsivity
- Low Capacitance for High Bandwidths
- Available in Various Hermetic Packages

InGaAs APDs—900 nm to 1700 nm

Technical Specification

Part Number	Standard Package	Photo Sens. Diam. (µm)	Resp. A/W @1300 nm	Resp. A/W @1550 nm	Dark Curr. Id (nA)	Spect. Noise Curr. Dens. in (pA/√Hz)	Cap. @100 kHz Cd (pF)	Bandwidth GHz into 50 W	NEP @ 1500 nm (pW/√Hz)	VOP for Gain=10 V
C30644E	TO window	50	8.4	9.4	8	0.15	1	2	0.03	40-90
C30644ECER	Ceramic	50	8.4	9.4	5	0.15	0.8	2	0.03	40-90
C30645E	TO window	80	8.4	9.4	10	0.25	1.2	1	0.13	40-90
C30645ECER	Ceramic	80	8.4	9.4	10	0.25	1	1	0.13	40-90
C30662E	TO window	200	8.4	9.4	200	1.4	2.5	0.2	0.15	40-90
C30662ECER	Ceramic	200	8.4	9.4	200	1.4	2.5	0.2	0.15	40-90
C30733ECER	Ceramic	30	8.4	9.4	5	<0.1	0.25	3	0.01	40-90

Test conditions: T = 22°C

InGaAs PIN Large-Area—900 nm to 1700 nm

Technical Specification

Part Number	Standard Package	Photo Sens. Diam. (mm)	Resp. A/W @1300 nm	Resp. A/W @1550 nm	Dark Curr. Id (nA)	NEP @ 1300 nm (pW/√Hz)	Cap. @100 kHz Cd (pF)	Bandwidth MHz into 50 W	Max. Power for 3.5 dB Linearity (dBm)	Bias Volt for Stress Spec. V
C30619G	TO-18	0.5	0.2	0.85	0.95	5	<0.1	6	350	>+13	5
C30641G	TO-18	1	0.2	0.85	0.95	5	<0.1	40	75	>+13	2
C30642G	TO-5	2	0.2	0.85	0.95	10	0.1	350	20	+11	0
C30665G	TO-5	3	0.2	0.85	0.95	25	0.2	1000	3	+11	0
C30723G	TO-8	5	0.2	0.85	0.95	30	0.3	2500	2.5	+11	0

Test conditions: T = 22°C

InGaAs PIN Small-Area—900 nm to 1700 nm

Technical Specification

Part Number	Standard Package	Photo Sens. Diam. (µm)	Resp. A/W @1300 nm	Resp. A/W @1550 nm	Dark Curr. Id (nA)	Spect. Noise Curr. Dens. in (pA/√Hz)	Cap. @100 kHz Cd (pF)	Bandwidth GHz into 50 W	NEP @ 1550 nm (pW/√Hz)	Bias Volt for Stress Spec. V
C30616ECER	Ceramic	50	0.86	0.95	0.5	<0.02	0.35	>3.5	<0.02	5
C30627ECER	Ceramic	75	0.86	0.95	0.5	<0.02	0.4	3.5	<0.02	5
C30617ECER	Ceramic	100	0.86	0.95	1	<0.02	0.55	3.5	<0.02	5
C30617B	Full wire	100	0.8	0.9	1	<0.02	0.8	3.5	<0.02	5
C30618ECER	Ceramic	350	0.86	0.95	2	0.02	4	0.8	0.02	5
C30618G	TO window	350	0.86	0.95	2	0.02	4	0.8	0.02	5

Test conditions: T = 22°C

SIONYX1403000017.0085

SAMSUNG EX. 1002 - 1494/4148

photodiodes

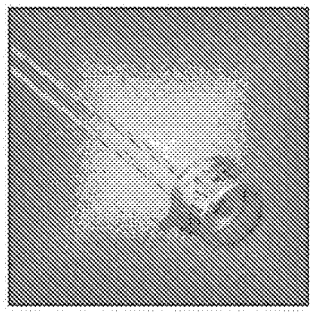

Silicon Avalanche Photodiodes
* Hermetically Sealed Packages

Si APD—Standard Types–400 nm to 1100 nm

Technical Specification

Part Number	Standard Package	Photo Sens. Diam. mm	Resp. @900 nm A/W	Dark Curr. Id (nA)	Spect. Noise Curr. Dens. In (pA/√Hz)	Cap. @100 kHz Cd (pF)	Resp. Time tr (ns)	NEP @ 900 nm W/√Hz	VOP Range V
C30817E	TO-5	0.8	75	50	0.5	2	2	7	275-425
C30872E	TO-5	1	45	100	0.5	10	2	13	275-425
C30902E	TO-18	0.5	77 (@ 650 nm)	15	0.25	1.8	0.05	3 (@ 630 nm)	180-250
C30902E	TO-18	0.5	125 (@ 810 nm)	15	0.15	1.5	0.05	0.86 (@ 810 nm)	180-250
C30916E	TO-5	1.5	70	100	0.5	3	2	8	275-425

Test conditions: T = 22°C

Si APD—Arrays Quadrant and Linear–400 nm to 1100 nm

Technical Specification

Part Number	Standard Package	Photo Sens. Diam. mm	Resp. @930 nm A/W	Dark Curr. Id (nA)	Spect. Noise Curr. Dens. In (pA/√Hz)	Cap. @100 kHz Cd (pF)	Resp. Time tr (ns)	NEP @ 930 nm W/√Hz	VOP Range V
C30927E-01	TO-8	1.5 total	62 (@900 nm)	25	0.25	1	5	16 (@900 nm)	275-425
C30927E-02	TO-8	1.5 total	62 (@900 nm)	25	0.25	1	5	16 (@900 nm)	275-425
C30927E-03	TO-8	1.5 total	62 (@900 nm)	25	0.25	1	5	16 (@900 nm)	275-425
C30965E	Custom	0.3 pitch	31	1	0.3	0.5	2	7	250-425

Test conditions: T = 22°C

Si APD—Low Cost, High Volume–400 nm to 1000 nm

Technical Specification

Part Number	Standard Package	Photo Sens. Diam. mm	Resp. @900 nm A/W	Dark Curr. Id (nA)	Spect. Noise Curr. Dens. In (pA/√Hz)	Cap. @100 kHz Cd (pF)	Resp. Time tr (ns)	NEP @ 900 nm W/√Hz	VOP Range V
C30724F	TO-18	0.5	9 (@ M=15)	25	0.1	1	5	11	120-200
C30724P	Plastic	0.5	9 (@ M=15)	25	0.1	1	5	11	120-200
C30737E	TO-18	0.5	47 (@ 1-800 nm M=100)	25	0.3	2.5	0.3	5.4 (@ 800 nm M=100)	120-200

Test conditions: T = 22°C

Si APD—TE-Cooled

Technical Specification

Part Number	Standard Package	Photo Sens. Diam. mm	Resp. @930 nm A/W	Dark Curr. Id (nA)	Spect. Noise Curr. Dens. In (pA/√Hz)	Cap. @100 kHz Cd (pF)	Resp. Time tr (ns)	NEP @ 930 nm W/√Hz	AGF VOP Range V
C30902S-TC	TO-66	0.3	128	2	0.04	1.6	0.3	0.3	160-200
C30902S-DTC	TO-66	0.3	128	1	0.02	1.8	0.3	0.18	160-200

Test conditions: T = 0°C for -TC and -20°C for -DTC AGF VOP Range: temperature dependent

SIONYX1403000017.0086

SAMSUNG EX. 1002 - 1495/4148

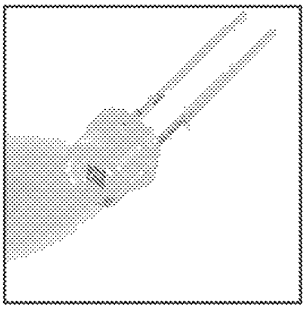

Silicon Avalanche Photodiodes
* Low Cost, High Volume

Si APD—NIR-Enhanced-400 nm to 1100 nm

Technical Specification

Part Number	Standard Package	Photo Sens. Diam. mm	Resp. @1000 nm A/W	Dark Curr. Id (nA)	Spect. Noise Curr. Dens. In (pA/√Hz)	Cap. @100 kHz Cd (pF)	Resp. Time tr (ns)	NEP @ 900 nm mW/√Hz	VOP Range V
C30964E	TO-5	0.8	38	50	0.5	2	2	14	275-425
C30955E	TO-5	1.5	14	100	0.5	3	2	15	275-425
C30956E	TO-8	3	25	100	0.5	10	3	20	275-425

Test conditions: T = 22°C

Si APD—Lightpipe

Technical Specification

Part Number	Standard Package	Photo Sens. Diam. mm	Resp. @830 nm A/W	Dark Curr. Id (nA)	Spect. Noise Curr. Dens. In (pA/√Hz)	Cap. @100 kHz Cd (pF)	Resp. Time tr (ns)	NEP @ 830 nm fW/√Hz	VOP Range V
C30921E	TO-18	0.5	77	15	0.23	1.6	0.55	3	180-250
C30921S	TO-18	0.5	128	15	0.11	1.6	0.55	0.09	180-250

Test conditions: T = 22°C

Si APD—Radiation Detection

Technical Specification

Part Number	Photo Sens. Diam. mm	Resp. A/W	Dark Curr. Id (nA)	Spect. Noise Curr. Dens. In (pA/√Hz)	Cap. @100 kHz Cd (pF)	Resp. Time tr (ns)	NEP @ Peak fW/√Hz	VOP Range V
C30625	3x5	22 (@900 nm)	250	0.3	30	5	23 (@900 nm)	275-425
C30703	10x10	16 (@800 nm)	10	0.7	120	5	40 (@800 nm)	275-425

Test conditions: T = 22°C

SIONYX1403000017.0087

SAMSUNG EX. 1002 - 1496/4148

photodiodes

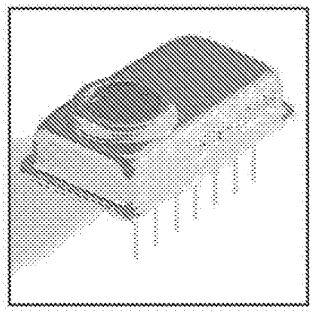

Silicon PIN Photodiodes and Modules

- Broad Range of Photosensitive Areas
- Low Operating Voltage
- Hermetically Sealed Packages

Si PINs—Window and Lightpipe Packages, Fast Response-400 nm to 1100 nm

Technical Specification

Part Number	Standard Package	Photo Sens. Diam. mm	Resp. @900 nm A/W	Dark Curr. Id nA	Spect. Noise Curr. Dens. in (fA/√Hz)	Cap. @100 kHz Cd (pF)	Resp. Time tr (ns)	NEP @ 900 nm fW/√Hz	Bias Volt for Three Specs. V
C30871E	TO-18	0.5	0.5	10	57	1.8	0.3	113	100
C30871EL	TO-18 Lightpipe	0.25	0.5	10	57	1.0	0.3	113	100

Test conditions: T = 22°C.

Si PINs—Large Area, Fast Response-400 nm to 1100 nm

Technical Specification

Part Number	Standard Package	Photo Sens. Diam. mm	Resp. @900 nm A/W	Dark Curr. Id nA	Spect. Noise Curr. Dens. (fA/√Hz)	Cap. @100 kHz Cd (pF)	Resp. Time tr (ns)	NEP @ 900 nm fW/√Hz	Bias Volt for Three Specs. V
FFD-100	TO-5	2.5	0.58	2	25	6.5	3.5	44	15
FFD-200	TO-8	5.1	0.58	4	36	30	5	52	15

Test conditions: T = 22°C.

Si PINs—Quadrant-220 nm to 1100 nm

Technical Specification

Part Number	Standard Package	Photo Sens. Diam. mm	Resp. @900 nm A/W	Dark Curr. Id nA	Spect. Noise Curr. Dens. in (fA/√Hz)	Cap. @100 kHz Cd (pF)	Resp. Time tr (ns)	NEP @ 900 nm fW/√Hz	Bias Volt for Three Specs. V
C30845E	TO-5	8	0.6	7	47	8	6	79	45
UV-140BG-4	TO-5	[illegible]	[illegible]	—	4	24	<1 psec	[illegible]	0
YAG-444-4A	Custom	11.4	0.4 @1.06 µm	40	118	9	23	295	180

Test conditions: T = 22°C.

Si PINs—Standard N-Type-400 nm to 1100 nm

Technical Specification

Part Number	Standard Package	Photo Sens. Diam. mm	Resp. @900 nm A/W	Dark Curr. Id nA	Spect. Noise Curr. Dens. in (fA/√Hz)	Cap. @100 kHz Cd (pF)	Resp. Time tr (ns)	NEP @ 900 nm fW/√Hz	Bias Volt for Three Specs. V
C30807E	TO-18	1	0.6	1	18	2.5	3	30	45
C30808E	TO-5	2.5	0.6	3	31	6	5	52	45
C30822F	TO-8	5	0.6	5	40	17	7	67	45
C30809E	TO-8	8	0.6	7	47	35	10	79	45
C30810E	Custom	11.4	0.6	20	98	70	12	163	45

Test conditions: T = 22°C.

SIONYX1403000017.0088

SAMSUNG EX. 1002 - 1497/4148

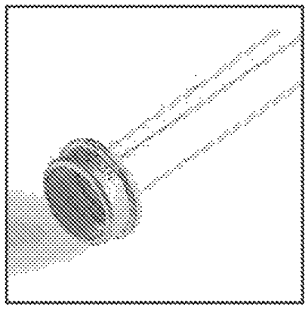

Silicon PINs—UV Enhanced

Si PINs—UV Enhanced, Low Noise–220 nm to 1100 nm

Electrical Specifications

Part Number	Standard Package	Photo Sens. Diam. mm	Resp. A/W @220 nm	Resp. A/W @632 nm	Shunt Resist. MΩ Min.	Shunt. Noise fA/√Hz Max.	Cap. @ 0V, 1 MHz pF Typ.	NEP @ 632 nm W/√Hz Typ.
UV-040BQ	TO-8	1	0.12	0.58	2000	3	25	5
UV-100BQ	TO-5	2.5	0.12	0.58	1000	4	120	7
UV-218BQ	TO-8	5.4	0.12	0.58	250	8	450	25
UV-245BQ	TO-8	8.5 x 8.5	0.12	0.58	175	9	675	30
UV-1408Q-2	TO-8	2.5x1.3 (x2)	0.12	0.58	1000	4	60	7
UV-1408Q-4	TO-8	2.5 x 2.5 (x4)	0.12	0.58	1000	4	60	7

Test conditions: T = 22°C

Si PIN Modules—Low Bandwidth–1 kHz to 50 kHz

Electrical Specifications

Part Number	Standard Package	Photo Sens. Diam. mm	Resp. A/W @ 900 nm	@ 960 nm	Shunt. Noise fA/√Hz Max.	NEP @ 632 nm W/√Hz Typ.	Bandwidth kHz into 50 Ω	Rise time to Theor. Typical
HUV-2000B	Custom	5.4	24	136	2.5	0.02	8	9
HUV-11000B	TO-5	2.5	23	126	20	0.17	20	3

Test conditions: T = 22°C

Si PIN Modules—High Bandwidth–40 MHz to 100 MHz

Electrical Specifications

Part Number	Dk. @ 900 nm Min.	Standard Package	Photo Sens. Diam. mm	Resp. A/W @ 900 nm	Cap. Volt. Dep. Delay (ns)	Speed, Noise Volt. Grade fA/√Hz Typ.	NEP @ 900 nm W/√Hz Typ.	Bandwidth MHz @ 50 Ω into 50 Ω	Photo. Rise Time Typ. ns
C30665E	C30971	TO-5	0.5	32 (@ 830 nm)	0.7	60	1.8 (@ 830 nm)	50	12
C30950-1550-R2A	C30662	TO-5	0.2	0.9 @ 1.55 µm	0.1	25	0.1 (@ 1.55 µm)	50	3.5
C30809E	C30817	TO-8	0.8	550	0.7	30	.036	50	275-425
C30810E	C30817	Custom	0.8	550	0.7	25	.033	50	275-425

Test conditions: T = 22°C

SIONYX1403000017.0089

SAMSUNG EX. 1002 - 1498/4148

photodiodes

Silicon PN Photodiodes

Table Key

I_{SC}	Short-Circuit Current H=100 fc, 2850 K
TC I_{SC}	I_{SC} Temperature Coefficient, 2850 K
V_{OC}	Open-Circuit Voltage H=100 fc, 2850 K
TC V_{OC}	V_{OC} Temperature Coefficient, 2850 K
I_D	Dark Current H=0, VR=10, 50, 100 V
R_{SH}	Shunt Resistance H=0, V=10 mV
C_J	Junction Capacitance H=0, V=0, 3, 15 V
R_E	Responsivity 850-940 nm
S_R	Sensitivity @ Peak
λ_{range}	Spectral Application Range
λ_P	Spectral Response @ Peak
V_{BR}	Breakdown Voltage

Table Key

I_{SC}	Short-Circuit Current H=1000 lux, 2850 K
TC I_{SC}	I_{SC} Temperature Coefficient H=1000 lux, 2850 K
I_D	Dark Current H=0, VR=100 mV
TC I_D	ID Temperature Coefficient H=0, VR=100 mV
R_{SH}	Shunt Resistance H=0, VR=10 mV
C_J	Junction Capacitance H=0, V=0 V, 1 MHz
S_R	Sensitivity @ 400 nm
R_E	Responsivity 400 nm, 0.10 A/W
t_R/t_F	Rise/Fall Time @ 1 KΩ load VR=1 V, 830 nm
V_{OC}	Open-Circuit Voltage H=1000 lux, 2850 K
TC V_{OC}	V_{OC} Temperature Coefficient H=1000 lux, 2850 K

Silicon PN—VTP Series

Part Number	I_{SC} µA	TC I_{SC} %/°C	V_{OC} mV	TC V_{OC} mV/°C	I_D nA max.	R_{SH} GΩ	C_J pF	R_E A/W min.	S_R A/W	λ_{range} nm	λ_P nm	V_{BR} V
VTP100	55	0.24	390	-2	30	0.35	50 max.	0.047	0.5	725-1150	925	340
VTP100D	70	0.2	420	-2	20	0.25	50 max.	0.06	0.55	725-1150	925	150
VTP1012	17	0.2	350	-2	7	0.5	8 max.	0.014	0.55	400-1150	925	140
VTP1112	18	0.2	360	-2	7	0.5	7 max.	0.014	0.55	400-1150	925	140
VTP11883	330	0.2	510	-2	30	67	180	—	0.55	400-1100	925	—
VTP1232	100 min.	0.2	437 min.	-2	20	—	100 max.	0.09	0.5	400-1100	925	—
VTP3210LA	18	0.2	350	-2	35	1.0	25 max.	0.015	0.55	400-1150	925	140
VTP3411LA	22	0.2	360	-2	35	1.0	27 max.	0.017	0.55	400-1150	925	140
VTP4086	300	0.2	510	-2	150	3	350	—	0.55	400-1100	925	—
VTP4085C	300	0.2	510	-2	75	6	350	—	0.55	400-1100	925	—
VTP5200	70	0.2	350	-2	15	0.25	84 max.	0.05	0.55	400-1150	925	140
VTP5300	250	0.2	350	-2	35	1.0	30 max.	0.14	0.55	400-1150	925	140
VTP7110	9	0.2	350	-2	35	7	25 max.	0.015	0.55	400-1150	925	340
VTP7210	7	0.2	350	-2	35	7	22 max.	0.012	0.55	400-1150	925	140
VTP7340	70	0.2	525	-2	20	0.25	40 max.	—	0.55	725-1150	925	1,010 mA
VTP8300	60	0.2	450	-2	20	1.0	70 max.	0.07	0.55	400-1150	925	140
VTP8440	55	0.2	350	-2	15	0.5	15 max.	0.025	0.55	400-1150	925	340
VTP8551	70	0.2	525	-2	10	0.25	50 max.	0.05	0.55	725-1150	925	150
VTP8651	55	0.24	500	-2	50	0.35	50 max.	0.045	0.5	725-1150	925	140
VTP9412	17	0.2	350	-2	7	0.4	7 max.	0.011	0.55	400-1150	925	140

Electro-optical characteristics @ 25°C

Silicon PN—VTS Series

Part number	I_{SC} mA	TC I_{SC} %/°C	I_D nA	TC I_D %/°C	R_{SH} MΩ	C_J nF	S_R A/W	R_E A/W min.	t_R/t_F µsec	V_{BR} V	TC V_{BR} mV/°C
VTS__60	1	0.2	200	+11	0.3	7.3	0.2	0.7	13	0.45	-2.6
VTS__61	1.5	0.2	100	+11	0.5	4.8	0.2	0.18	8.5	0.45	-2.6
VTS__62	0.69	0.2	50	+11	1.2	3.75	0.2	0.16	3.5	0.45	-2.6
VTS__63	0.35	0.2	20	+11	2.5	1.75	0.2	0.15	1.5	0.45	-2.6
VTS__66	0.33	0.2	40	+11	1.5	1	0.2	0.07	1.8	0.45	-2.6
VTS__65	0.16	0.2	20	+11	3	0.5	0.2	0.08	1.2	0.45	-2.6
VTS__66	0.040	0.2	10	+11	6	0.25	0.2	0.03	0.75	0.45	-2.6

Electro-optical characteristics @ 25°C

SAMSUNG EX. 1002 - 1499/4148

Table Key

I_{SC}	Short-Circuit Current 940 nm, H=0.5 mW/cm² (VTD205, VTD206) H=5 mW/cm², 2850 K (VTD31AA, VTB Series) 100 Lux, 2850 K (VTD34, VTD205K) 100 Lux, 2850 K (VTD206K)
TC I_{SC}	I_{SC} Temperature Coefficient 2850 K (VTD31AA, VTD34, VTD34F, VTB Series) 2850 K (VTD205, VTD205K, VTD206, VTD206K)
V_{OC}	Open-Circuit Voltage 940 nm, H=0.5 mW/cm² (VTD 205, VTD205K, VTD206, VTD206K) 2850 K (VTD31AA, VTD34, VTD34F)
TC V_{OC}	V_{OC} Temperature Coefficient 2850 K (VTD31AA, VTD34, VTD34F, VTB Series) 2850 K (VTD205, VTD205K, VTD206, VTD206K)
I_D	Dark Current H=0, V_R=2 V (VTB Series) H=0, V_R=10 V (VTD34, VTD34F, VTD205, VTD205K, VTD206, VTD206K, VTB100) H=0, V_R=15 V (VTD31AA)
R_{SH}	Shunt Resistance H=0, V=10 mV (VTB Series)
TC R_{SH}	R_{SH} Temperature Coefficient H=0, V=10 mV (VTB Series)
C_J	Junction Capacitance H=0, V_R=0 V, 1 MHz (VTD205, VTD205K, VTD206, VTD206K) @ 1 MHz, V_R=0 V (VTD34, VTD34F) H=0, V=0 V (VTD31AA, VTB Series)
t_R/t_F	Rise/Fall Time @ R_L=50 Ω, V_P=5 V, 850 nm (VTD205, VTD205K, VTD206, VTD206K) @ R_L=1 kΩ Load, V_R=10 V, 633 nm (VTD34, VTD34F)
S_P	Sensitivity @ Peak 365 nm (VTB Series)
λ_{range}	Spectral Application Range
λ_P	Spectral Response @ Peak
V_{BR}	Breakdown Voltage

Silicon PN—VTD Series

Part Number	I_{SC} (μA)	TC I_{SC} (%/°C)	V_{OC} (mV)	TC V_{OC} (mV/°C)	I_D (pA max.)	C_J (pF)	S_P (A/W)	λ_{range} (nm)	λ_P (nm)	V_{BR} (V)
VTD31AA	150-225	0.2	330	-2	50	500 max.	---	0.55	400-1150	860	5 min.
VTD34	75	0.2	330	-2	30	90	50	0.6	400-1150	900	30 min.
VTD34F	---	---	330	-2	30	90	50	0.6	725-1150	940	30 min.
VTD205	80	0.2	360	-2.6	30	72	20	0.6	400-1100	925	30
VTD205K	80	0.2	365	-2.6	30	72	20	0.6	405-1100	925	30
VTD206	80	0.2	360	-2.6	30	72	20	0.6	400-1100	925	30
VTD206K	80	0.2	365	-2.6	30	72	20	0.6	400-1100	925	30

Electro-optical characteristics @ 25°C.

Silicon PN—VTB Series

Part Number	I_{SC} (μA)	TC I_{SC} (%/°C)	V_{OC} (mV)	TC V_{OC} (mV/°C)	I_D (pA max.)	R_{SH} (GΩ)	TC R_{SH} (%/°C)	C_J (pF)	S_P (A/W)	λ_{range} (nm)	λ_P (nm)	V_{BR} (V)
VTB100	65	0.12	490	-2	500	1.8	-8	2 max.	0.1	320-1100	920	40
VTB1012	10	0.12	490	-2	100	0.25	-8	0.31	0.08	320-1100	920	40
VTB1012B	1.8	0.02	420	-2	100	0.25	-8	0.31	---	330-720	380	40
VTB1013	10	0.12	490	-2	20	7	-8	6.31	0.08	320-1100	920	40
VTB1013B	1.8	0.02	420	-2	20	7	-8	6.31	---	330-720	380	40
VTB1112	60	0.12	490	-2	100	0.25	-8	0.31	0.13	320-1100	920	40
VTB1112B	8	0.02	420	-2	100	0.25	-8	0.31	---	330-720	380	40
VTB1113	60	0.12	490	-2	20	7	-8	6.31	0.13	320-1100	920	40
VTB1113B	8	0.02	420	-2	20	7	-8	6.31	---	330-720	380	40
VTB4081	200	0.12	490	-2	250	0.56	-8	3	0.1	320-1100	920	40
VTB5081	150	0.12	490	-2	250	0.56	-8	3	0.1	320-1100	920	40
VTB5081B	15	0.02	420	-2	250	0.56	-8	3	---	330-720	380	40
VTB5081J	150	0.12	490	-2	250	0.56	-8	3	0.1	320-1100	920	40
VTB5081JV	150	0.12	490	-2	250	0.56	-8	3	0.1	320-1100	920	40
VTB5081JV2	150	0.12	490	-2	250	0.56	-8	3	0.1	320-1100	920	40
VTB8061	350	0.12	490	-2	2000	0.1	-8	8	0.1	320-1100	920	40
VTB8061B	35	0.02	420	-2	2000	0.1	-8	8	---	330-720	380	40
VTB8081CS	10	---	---	---	4000	0.1	-8	8	---	475-925	725	---
VTB8081J	350	0.12	490	-2	2000	0.1	-8	8	0.1	320-1100	920	40
VTB8081JV	350	0.12	490	-2	2000	0.1	-8	8	0.1	320-1100	920	40
VTB8081JV2	350	0.12	490	-2	2000	0.1	-8	8	0.1	320-1100	920	40
VTB8341	20	0.12	490	-2	100	1.8	-8	1	0.1	320-1100	920	40
VTB8440	45	0.12	490	-2	2000	0.07	-8	1	0.1	320-1100	920	40
VTB8440B	5	0.02	420	-2	2000	0.07	-8	1	---	330-720	380	40
VTB8441	65	0.12	490	-2	100	1.8	-8	1	0.1	320-1100	920	40
VTB8441B	5	0.02	420	-2	100	1.8	-8	1	---	330-720	380	40
VTB8612	10	0.12	490	-2	100	0.25	-8	0.31	0.08	320-1100	920	40
VTB8612B	1.8	0.02	420	-2	100	0.25	-8	0.31	---	330-720	380	40
VTB8613	10	0.12	490	-2	20	7	-8	6.31	0.08	320-1100	920	40
VTB8613B	1.8	0.02	420	-2	20	7	-8	6.31	---	330-720	380	40

SIONYX1403000017.0091

SAMSUNG EX. 1002 - 1500/4148

thermopile detectors

Features
* Available in TO-39 and TO-18 housings
* Integrated signal processing ASIC available (TPMI)
* Single, dual or quad elements
* 8 element line arrays and 4x4 matrix arrays with various lens optics and integrated ASIC with multiplexer
* Various filters for optical broadband or narrow-band applications
* Excellent repeatability of electro-optical parameters
* Ambient temperature reference (thermistor) included
* High sensitivity of several 10 V/W; DC radiation sensitive
* Extremely low temperature coefficient of sensitivity and resistivity
* Constant response over the infrared spectrum
* The absence of microphonic noise effects
* Low susceptibility to electromagnetic pulses (EMP) due to the low internal resistance (<100 kΩ)
* Rugged construction based on CMOS silicon micromachining technology

Typical Applications
* Remote Temperature Sensing, Hand-Held or Industrial Pyrometers
* Ear or Body Thermometers
* Temperature-Sensor Modules in Microwave Ovens, Hair Dryers, Cookers, Toasters
* Sensor Modules for Control of Air Condition Systems (Heat Management, Home, Automotive)
* Temperature Control in Copiers and Printers
* Sensor Arrays for Spatial Temperature Measurements (Imaging Applications)
* Sensors with Infrared Bandpass Filters for Gas Detection by Infrared Absorption

Datasheets available upon request

Description
Thermopile detectors directly sense thermal radiation, providing the perfect device for remotely measuring temperatures without the need for any mechanical chopper. PerkinElmer's proprietary and innovative Si-based micromachining technology guarantees a new generation of components: extreme long-term stability, very low temperature coefficient in sensitivity, and excellent repeatability of electro-optical parameters.

Thermopile sensors allow remote temperature sensing at a low system cost. The sensor does not require cooling, and can reach an accuracy of ±1°C, dependent on the measurement range. For narrow temperature ranges, as in body temperature measurement, a precision of 0.1°C is possible.

Single-Element Thermopile Detectors: TPS series
The different available chip sizes and packaging types, together with the variety in window openings with and without a silicon lens, enable the adaptation of the PerkinElmer thermopiles to virtually every application where a remote temperature measurement or control is needed.

Dual- and Quad-Element Types: TPS 2, TPS 4 series
PerkinElmer offers thermopile detectors with two or four channels, each of which can be equipped with one of the many available infrared spectral bandpass filters. The main application of multiple channel thermopiles is gas detection through IR absorption. Prominent gases to be detected are CO_2, hydrocarbons and CO.

Thermopile Modules
with Integrated signal processing: TPMI series
For convenient use, PerkinElmer offers thermopile sensors with an integrated electronic circuit for the necessary signal condition and ambient temperature compensation – the TPMI. This very compact and miniature thermopile module is offered as a fully calibrated, ready-to-go sensor. Various temperature ranges and optics are available.

Thermopile Line and Matrix Arrays: TPL, TPA series
The latest PerkinElmer thermopile technology development features more than a single hot spot. The new TPA- (matrix array) and TPL- (line array) series offer multi-element thermopile arrays combined with an optical lens, amplifier, and interface electronics (multiplexer, ambient temperature sensor) in a compact TO-39-type housing. This combines solid-state, non-chopperad temperature measurement without the need for in-field calibration.

Typically, the array sensors are sold as a modular type, i.e. on a PCB with external data memory. These TPA- and TPL-Modules are p ecalibrated with the data stored in an EEPROM. In an application, the associated micro controller (µC) reads this calibration information and converts the sensor signals to the object temperatures.

SIONYX1403000017.0092

SAMSUNG EX. 1002 - 1501/4148

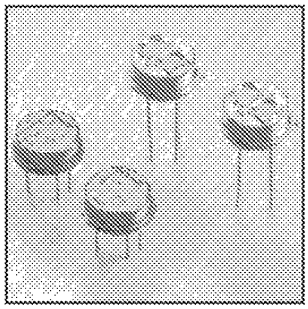

Dual and Quad Element Thermopile Detectors

General Data
Tc of sensitivity (absolute value):
0.02%/K
Tc of resistance (absolute value):
0.02%/K
Max. operating temperature: -20 to 100°C
Max. storage temperature: -40 to 100°C
Thermistor BETA: 3964 K
Option for all types: 6-14 um
Pyrometry filter: G9

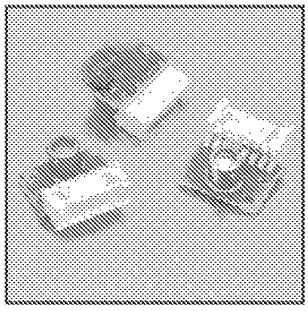

Thermopile Arrays

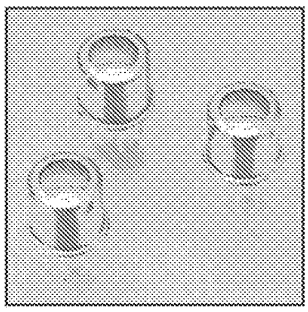

Thermopile TPMI Modules

Single Element Thermopile Detectors

Technical Specification

Part Number	Housing	Field of View	DC Sensitivity V/W	Time Constant ms	Active Area mm²	TP Chip Resistance kΩ	Noise nV/√Hz	NEP nW/√Hz	D* cm√Hz/W	Thermistor (25°C) kΩ
TPS333	TO-18	100°	35	25	0.7x0.7	75	35	1	0.7x10⁸	100
TPS334	TO-39	60°	35	25	0.7x0.7	75	35	1	0.7x10⁸	30
TPS334LB.6	TO-39**	7°	55	25	0.7x0.7	75	35	0.6	1.1x10⁸	30
TPS434	TO-39	55°	35	20	0.5x0.5	35	24	0.7	0.7x10⁸	30
TPS434IRA	TO-39***	15°	55	20	0.5x0.5	35	24	0.4	1.1x10⁸	30
TPS534	TO-39	60°	20	35	1.2x1.2	50	20	1.4	0.8x10⁸	30
TPS535	TO-39	60°	20	35	1.2x1.2	50	20	1.4	0.8x10⁸	30

Test conditions: T = 25°C
Field of view: at 50% intensity points
Noise: r.m.s., 200 K

* 500 K black body
** with 5.5 mm lens
*** with int. reflector

Dual and Quad Thermopile Detectors

Technical Specification

Part Number	Housing	Field of View	DC Sensitivity V/W	Time Constant ms	Active Area mm²	TP Chip Resistance kΩ	Noise nV/√Hz	NEP nW/√Hz	D* cm√Hz/W	Thermistor (25°C) kΩ
TPS2534	TO-39**	2x90°	42	35	1.2x1.2	50	20	0.7	1.8x10⁸	30
TPS4339	TO-39***	4x60°	75	35	0.7x0.7	75	35	0.5	1.5x10⁸	100

Test conditions: T = 25°C
Field of view: at 50% intensity points
Noise: r.m.s., 200 K
Above data are referenced without the hp filter. Option for all types: individual hp filters for each channel

* 500 K black body
** with 2 channels
*** with 4 channels

Line and Matrix Arrays

Technical Specification

Part Number	Housing	Number of Pixels	Field of View	Optics	Output Voltage V (NTC object, 20°C ambient)	Object temperature	Noise mV/√Hz (1.5-20Hz)
TPLM086L5.6	TO-39 on PCB	6 element line	41°x6°	f/1 optics, f=5.5 mm	0.95	-20-100°C	0.4
TPLM086L3.9	TO-39 on PCB	6 element line	51°x6°	f/1 optics, f=3.9 mm	0.95	-20-100°C	0.4
TPAM168L3.9	TO-39 on PCB	4x4 matrix	41°x32°	f/1 optics, f=3.9 mm	0.95	-20-100°C	0.4

Test conditions: T = 25°C

Operating voltage: 5 V
Operating current: 1 mA
Zero signal offset: Vpp/2
Output resistance: 200 Ω
Power up time: 0.3 s

Sample frequency: 3 kHz
Max. operating temperature: -20-100°C
Max. storage temperature: -40-100°C
Temperature reference slope: 10 mV/K
Temperature reference offset: 0 mV

TPMI Modules

Technical Specification

Part Number	Housing	Optics	Field of View
a2TPMI 334	TO-39	window opening 2.5 mm	60°
a2TPMI 334 LB.6	TO-39	integrated Si lens, 5.5 mm focal length	7° (DtS = 6:1)
a2TPMI 334 IRA	TO-39	internal mirror	15° (DtS = 4:1)

For further details please contact us.

SIONYX1403000017.0093

SAMSUNG EX. 1002 - 1502/4148

medical sensors

Features
- Designed to meet ASTM standards for capnometers
- Neonatal, Pediatric and Adult use
- Low-flow design
- Fast rise time for high respiration rates
- Compatible with standard sampling disposables
- Easy-to-interface RS232 Digital Output
- Rugged solid-state sensor—no moving parts
- Low power consumption
- Fast warm-up time
- Long life
- Small footprint
- Custom packaging available

Typical Applications
Real-time breath-to-breath quantitative end-tidal CO_2 measurement

Datasheets available upon request

Digital Sidestream CO_2 Bench
The PerkinElmer Digital Sidestream CO_2 Bench represents a breakthrough in solid-state technology. These sensors achieve the highest levels of accuracy and reliability while having no moving parts. The low power consumption and compact design set a new standard in sidestream monitoring. The bench incorporates our latest advances in component design and signal processing.

All design requirements of ASTM standards have been met or exceeded. The measurement technique is non-dispersive infrared absorption, which utilizes a unique infrared emitter design in conjunction with state-of-the-art detector technology. Output from the bench is a digitized voltage function of CO_2 concentration within the sampling cell. The sidestream sensor is on a printed circuit board with a single low-cost connector, has added pneumatics circuit, and uses standard sampling disposables.

Digital Mainstream CO_2 Sensor
PerkinElmer introduces a significant advancement in mainstream CO_2 sensing. Output from the sensor is a digitized voltage function of CO_2 concentration, providing a low noise signal and easy interfacing. All processing electronics are self-contained within the compact and rugged sensor head. The solid-state design incorporates our latest advances in component innovation and signal processing, and ensures high accuracy and long life.

All design requirements of ASTM standards have been met or exceeded. The measurement technique is non-dispersive infrared absorption, which utilizes a unique infrared emitter design in conjunction with state-of-the-art detector technology. This sensor has self-contained electronics on a flex circuit, a cable, and uses low-cost disposable airway adapters.

SIONYX1403000017.0094

SAMSUNG EX. 1002 - 1503/4148

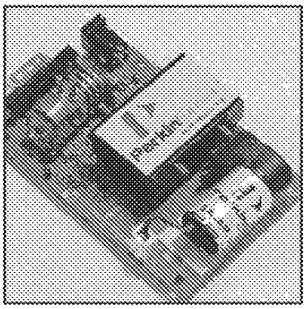

CO_2 Sidestream Sensors

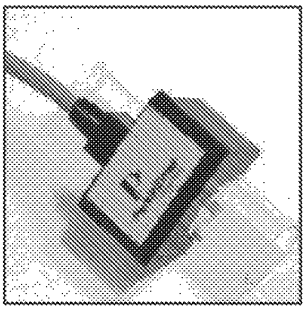

Mainstream CO_2 Sensors

Technical Specifications

	Digital Sidestream CO_2 Sensor	Digital Mainstream CO_2 Sensor
Method	Non-dispersive Infrared Absorption	Non-dispersive Infrared Absorption
Calibration	3-point calibration	3-point calibration
Respiration Rate	150 bpm	150 bpm
Input Voltage	5 V	5 V
Power Consumption	1.0 W typical, 1.5 W max	1.0 W typical, 1.5 W max
Output	Digital Serial RS232	Digital Serial RS232
Measurement Range	0-76 mmHg	0-76 mmHg
Accuracy	±2 mmHg plus ± 5% of reading	±2 mmHg plus ± 5% of reading
Resolution	1 mmHg	1 mmHg
Rise Time	Less than 200 ms*	Less than 200 ms
Flow Rate	50 ml/min ± 10 ml/min	N/A
Warm-up Time	≤ 1 minute to ASTM Standards ≤5 minutes to published specifications	≤ 1 minute to ASTM Standards ≤5 minutes to published specifications
Mechanical Shock	N/A	100 G 1/2 sine wave
Temperature	10-40°C (operating) -40-75°C (storage)	10-40°C (operating) -40-75°C (storage)
Relative Humidity	15-95% non-condensing (operating) 10-95% non-condensing (storage)	15-95% non-condensing (operating) 10-95% non-condensing (storage)
Physical Dimensions	33x50x77.5 mm (1.3x2.32x3.05")	35x30x22.3 mm (1.38x1.06x0.88")
Cable	N/A	10-foot standard length
Connector	10 pin, dual in-line	Standard or custom

*with PerkinElmer recommended algorithms

SIONYX1403000017.0095

SAMSUNG EX. 1002 - 1504/4148

Beratung und Verkauf durch:

Hutmacher+Schlund AG
Postfach 70
5023 Biberstein
Telefon 062 837 80 55
Fax 062 837 80 56
info@hus.ch
www.hus.ch

SIONYX1403000017.0096

SAMSUNG EX. 1002 - 1505/4148

sics Research ... A275 (1989) 536
North-Holland, Amsterdam

Nuclear Instruments and Methods in Physics Research A275 (1989) 537–541
North-Holland, Amsterdam

SILICON *

FABRICATION OF DETECTORS AND TRANSISTORS ON HIGH-RESISTIVITY SILICON

Steve HOLLAND

Lawrence Berkeley Laboratory, University of California, Berkeley, CA 94720, USA

A new process for the fabrication of silicon p–i–n diode radiation detectors is described. The utilization of backside gettering in the fabrication process results in the actual physical removal of detrimental impurities from critical device regions. This reduces the sensitivity of detector properties to processing variables while yielding low diode reverse-leakage currents. In addition, gettering permits the use of processing temperatures compatible with integrated-circuit fabrication. P-channel MOSFETs and silicon p–i–n diodes have been fabricated simultaneously on 10 kΩ cm ⟨100⟩ silicon using conventional integrated-circuit processing techniques.

1. Introduction

The complexity and scale of many new applications for charged particle detectors, notably in high-energy physics, require well-controlled fabrication techniques. Local front-end and readout circuitry is essential for these systems, and monolithic integration of at least part of this circuitry would greatly simplify the readout system and increase performance and reliability [1]. Even on a smaller scale, devices such as the semiconductor drift chamber [2] would also benefit greatly from integrated front-ends by reducing the circuit capacitance in order to exploit the extremely low capacitance of these detectors. Hence, a modern detector process should offer minimum sensitivity to process-induced contaminants and ideally would be compatible with contemporary integrated-circuit (IC) fabrication techniques.

However, typical fabrication processes for radiation detectors do not fulfill either of these goals. While in one notable case outstanding results have been achieved [3], the process used is incompatible with conventional IC fabrication and is very sensitive to the temperature at which the implanted dopants are annealed [4]. This is due to the extreme sensitivity of detector leakage current to impurities that introduce energy levels near the center of the silicon bandgap [5].

In this work fairly conventional integrated-circuits processing techniques are used to realize low-leakage p–i–n diode detectors. The process developed for the detector fabrication relies on the formation of a gettering layer on the back side of the wafer. By utilizing gettering techniques that actively counteract the presence of harmful impurities in the active volume of the device, the sensitivity of the process to variations in the fabrication environment is greatly reduced. In addition, the use of relatively high processing temperatures is an integral part of the process; this removes a major obstacle to monolithic integration of front-end electronics with the detector. The process described here is fully compatible with conventional IC processing. Data are presented on radiation detectors that demonstrate the effects of gettering and also on p-channel MOSFETs that were fabricated on the same wafer as a first step towards monolithically integrated detector–readout systems.

2. Processing considerations

A major goal in detector fabrication is the minimization of the diode reverse-leakage current, which contributes shot noise and can limit the dynamic range of the input amplifier. High quantity float-zone refined silicon is required in order to achieve the high generation lifetime necessary for low reverse-leakage currents. The leakage current of a reverse-biased p–n junction is due to the generation of minority carriers in the device. These minority carriers can arise from the undepleted neutral region, the depletion region, and the surface [5]. In silicon diodes the leakage current is often dominated by generation in the depletion region. This component of leakage current is greatly enhanced by the presence of impurities that introduce energy levels near the center of the silicon bandgap. Such impurities are often referred to as lifetime killers since they also decrease the generation lifetime. Typical examples are the transition metals [6,7]. These are rather ubiquitous contaminants and great care is needed in the fabrication of devices in order to achieve low leakage currents.

However, the total elimination of these contaminants has proven to be impractical due to the pervasiveness of such elements and the sensitivity of the leakage current to extremely small concentrations, typically part per billion or less [8–10]. This has led to the development of techniques, collectively known as gettering, which ren-

0168-9002/89/$03.50 © Elsevier Science Publishers B.V.
(North-Holland Physics Publishing Division)

SIONYX1403000017.0097

SAMSUNG EX. 1002 - 1506/4148

der any lifetime-killing impurities electrically inactive [11]. The basic concept of gettering relies on the fact that at typical integrated-circuit processing temperatures in silicon (approximately 900–1100 °C) most harmful impurities have relatively high diffusivities and hence are very mobile [12]. Therefore suitable impurity sinks can be incorporated in electrically inactive regions.

Two general classes of gettering are commonly employed. In "intrinsic" gettering, the bulk of the wafer forms the impurity sink with a relatively thin, defect-free region near the surface where the active devices reside. The technique is often applied to Czochralski-grown substrates and relies on the formation of oxygen precipitates in the bulk of the wafer [11]. While perfectly adequate for conventional IC processing, intrinsic gettering is not compatible with thick p–i–n diode detectors, where the depletion region often extends to the backside contact of the wafer. Thus the second class of gettering, "extrinsic" gettering, is utilized in this work. Extrinsic gettering relies on the formation of a gettering layer on the back side of the wafer, away from the active region of the device, e.g. the depletion region of detector diodes. Typical extrinsic gettering techniques include phosphorus doping [8], ion implantation [13], and deposition of thin films such as polysilicon [14] and silicon nitride [15]. Gettering techniques have been applied to detector fabrication, but no details of the actual method used were given [16,17].

3. Experimental procedures / results

Fig. 1 shows the detector processing sequence used in this work. The technique shown has been applied to both 1 kΩ cm ⟨111⟩ and 10 kΩ cm ⟨100⟩ n-type starting substrates with similar results. Initially a layer of polysilicon, in situ doped with phosphorus, is deposited at 650 °C by chemical vapor deposition on the backside of the wafer. This layer, which is approximately 1 μm thick, serves both as the gettering layer and as the backside contact. The gettering properties of this layer are due to the presence of both the polysilicon and phosphorus. Polysilicon consists of small grains of single crystal material separated by highly disordered regions called grain boundaries. These grain boundaries act as impurity sinks and hence polysilicon itself is an efficient gettering material [14,18]. In addition, phosphorus also getters impurities by an ion-pairing mechanism [19] and the combination of both methods has been shown to yield synergistic results [20].

After deposition the polysilicon layer is capped by a low-temperature oxide formed by chemical vapor deposition at 450 °C. This layer minimizes the oxidation of the polysilicon during subsequent processing. A passivating oxide is then thermally grown, followed by

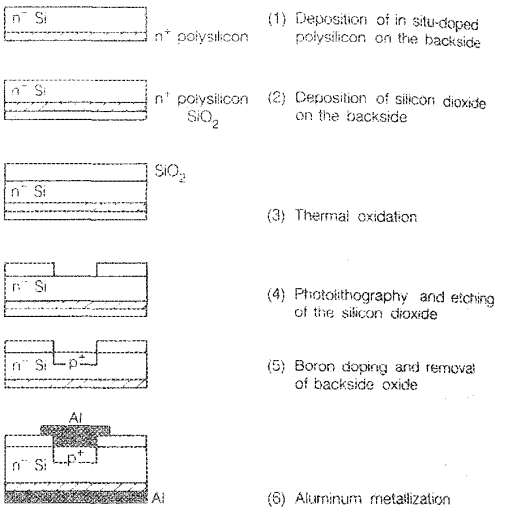

Fig. 1. The fabrication process used in this work.

selective removal of the oxide in the areas where boron is desired. For this experiment, the boron was diffused at 900 °C from a B_2O_3 source in order to avoid any crystalline damage at the p–n junction associated with ion implantation. In order to unambiguously determine the effectiveness of the gettering layer, some of the wafers received the backside polysilicon gettering on one half of the wafer only, while the other half received implantation of arsenic to form the back contact. After implantation the wafers were annealed at 900 °C for 15 min in oxygen followed by a 2 h anneal at the same temperature in nitrogen. Conventional aluminum metallization followed by a 400 °C/450 °C (⟨100⟩/⟨111⟩) anneal in forming gas (80% nitrogen, 20% hydrogen) completes the processing.

The detector diodes used in this work were circular in area with a 1 mm radius. In addition, the diodes were surrounded by a circular guard ring consisting of a p⁺ region contacted by metallization. The inner radius of the guard ring measured from the center of the diode was 1.1 mm, and the outer radius was 1.4 mm. For the diode current–voltage measurements, the bias voltage was applied to the substrate with the top contact and guard ring grounded.

Fig. 2 compares the reverse-leakage currents of gettered and ungettered devices from the same wafer (⟨100⟩, 10 kΩ cm). The gettered sample exhibits a substantially reduced leakage current relative to the sample that did not receive the gettering. The current is reduced by a factor of nearly 400 at low voltages and even more at higher voltages where the ungettered sample exhibits a soft breakdown characteristic. The leakage current density at 100 V, which corresponds to an

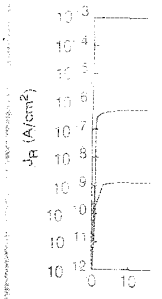

ig. 2. The detector
ith backside getteri
ere fabricated on
device

werdepleted dete
hickness), is on th
ares very favoral
lowever, the Ker
mperatures to 60
striction is necess
rrents for that
corporate higher
ocess has been r
nt significantly, e
on width after ani
vices shown in fi
at 900 °C after
intaining low l
oids the major
mely the high she
d resulting incor
n of active devic
The current of
ely insensitive t
rrent is limited by
m the undeplet
face leakage curr
pletion region. T
ded to increase
ion, which is in t
Similar results
ates. However, a
kage current is o
order of 3–12
m electrically act
ide interface. It c
a metal–oxide-
ded between the
ed-diode structur
is suppressed, t
rents on the orde
higher surface

SIONYX1403000017.0098

SAMSUNG EX. 1002 - 1507/4148

(1) Deposition of in situ-doped polysilicon on the backside

(2) Deposition of silicon dioxide on the backside

(3) Thermal oxidation

(4) Photolithography and etching of the silicon dioxide

(5) Boron doping and removal of backside oxide

(6) Aluminum metallization

rocess used in this work.

le in the areas where boron ent, the boron was diffused irce in order to avoid any -n junction associated with o unambiguously determine ttering layer, some of the le polysilicon gettering on hile the other half received rm the back contact. After annealed at 900 °C for 15 a 2 h anneal at the same Conventional aluminum 400 °C/450 °C ((100)/ (80% nitrogen, 20% hydro- g.

in this work were circular n addition, the diodes were rd ring consisting of a p^+ ation. The inner radius of m the center of the diode adius was 1.4 mm. For the irements, the bias voltage with the top contact and

verse-leakage currents of ices from the same wafer ttered sample exhibits a e current relative to the e gettering. The current is y 400 at low voltages and where the ungettered sam- characteristic. The leakage which corresponds to an

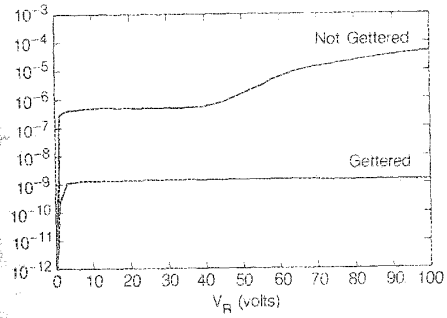

2. The detector diode reverse-leakage current for a device ith backside gettering compared to one without. The devices are fabricated on 10 kΩ cm ⟨100⟩ substrates, and both devices are from the same wafer.

verdepleted detector (≈ 250 μm depletion region ickness), is on the order of 1–2 nA/cm^2, which com- ares very favorably with the result of Kemmer [3]. owever, the Kemmer process limits the processing mperatures to 600 °C after the initial oxidation. This striction is necessary in order to maintain low leakage rrents for that process, and in fact an attempt to corporate higher anneal temperatures into a similar ocess has been reported to increase the leakage cur- nt significantly, e.g. 420 nA/cm^2 per 100 μm deple- on width after annealing at 900 °C [4]. In contrast, the vices shown in fig. 2 have undergone approximately 3 at 900 °C after the initial oxide was grown, while aintaining low leakage currents. Thus this process oids the major drawbacks of the Kemmer process, amely the high sheet resistance of the implanted layers nd resulting incompatibility with monolithic integra- on of active devices.

The current of the gettered device in fig. 2 is rela- ively insensitive to voltage, which implies that the rrent is limited by either diffusion of minority carriers om the undepleted regions of the diode, or from rface leakage currents, but not from generation in the pletion region. The bulk generation current is ex- cted to increase with the volume of the depletion gion, which is in turn bias-voltage dependent [5].

Similar results were observed for the ⟨111⟩ sub- rates. However, a significant surface component of akage current is observed on the ⟨111⟩ substrates (on e order of 3–12 nA/cm^2) [21]. This current arises om electrically active states at the silicon–silicon di- xide interface. It can be suppressed by proper biasing a metal–oxide–semiconductor (MOS) capacitor cated between the diode and guard ring, similar to a ted-diode structure [5]. Once the surface leakage cur- nt is suppressed, the gettered devices achieve leakage rrents on the order of 1 nA/cm^2 as shown in fig. 3. e higher surface current for the ⟨111⟩ substrates is consistent with the higher density of surface states on oxidized ⟨111⟩ substrates as compared to the ⟨100⟩ orientation [22].

A significant aspect of the gettering process is the fact that the diodes were fabricated at typical integrated-circuit processing temperatures. Thus monolithic integration of detectors and active devices can be investigated with the use of a process employing gettering, and MOS devices on high-resistivity silicon have been reported [23]. In order to pursue this further, polysilicon-gate p-channel MOS transistors were fabricated simultaneously with detector diodes on high-resistivity silicon. The only additional steps required for the transistor fabrication consisted of the growth of a 36.5 nm gate oxide in steam at 800 °C followed by the chemical vapor deposition of polysilicon at 610 °C to form the gate of the transistor. The source/drain regions of the transistor are self-aligned to the gate to minimize the gate to drain overlap capacitance [22].

In order to determine directly the effect of this additional processing on the detector properties, detector diodes were fabricated on the same substrates. This was accomplished by using a mask aligner which steps nine separate 1 cm^2 fields. Five of these fields were devoted to the transistor array and the other four contained the diodes described previously. The polysilicon and gate oxide were completely removed from the diode fields prior to boron doping, which simultaneously formed the source/drain regions of the transistors and the top contact of the diode.

Fig. 4 shows typical output current–voltage characteristics of a p-channel MOSFET fabricated on 10 kΩ cm silicon. The channel width and length for this device are 26 μm and 5 μm, respectively. Due to the high-resistivity material the devices behave normally even with a large bias (100 V in fig. 4b) applied to the substrate as

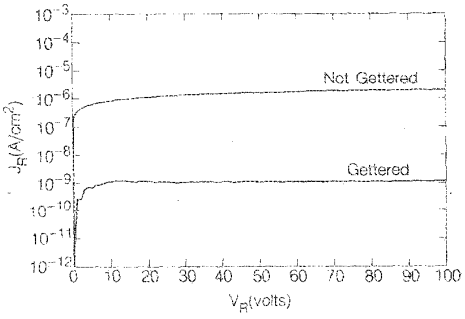

Fig. 3. The detector diode reverse-leakage current for a device with backside gettering compared to one without. The devices were fabricated on 1 kΩ cm ⟨111⟩ substrates, and both devices are from the same wafer. For the gettered device the surface leakage current has been suppressed by biasing an MOS capacitor located between the diode and guard ring at −5 V.

SIONYX1403000017.0099

SAMSUNG EX. 1002 - 1508/4148

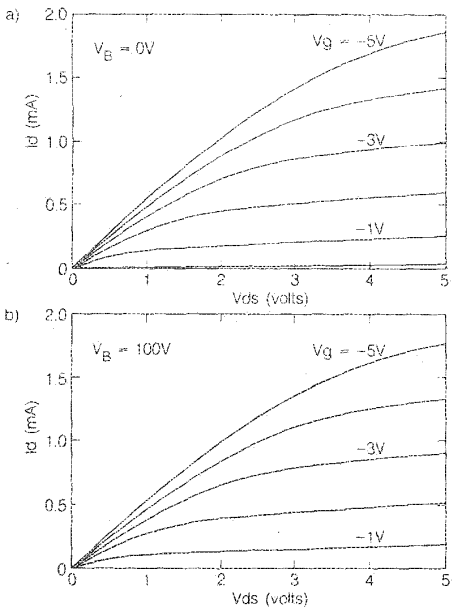

Fig. 4. Current–voltage characteristics of a p-channel MOSFET fabricated on 10 kΩ cm silicon. The transistor gate oxide thickness is 36.5 nm, and the channel width to length ratio is 26 μm/5 μm. (a) 0 V substrate bias. (b) 100 V substrate bias.

has been reported earlier [23]. The change in device threshold voltage due to the substrate bias is proportional to the square root of substrate doping [22] and hence is very small in this case.

The I–V characteristic of a p–i–n diode fabricated on the same wafer is shown in fig. 5. The leakage current is on the order of 1–3 nA/cm^2, comparable to the results shown in figs. 2 and 3. Hence no significant

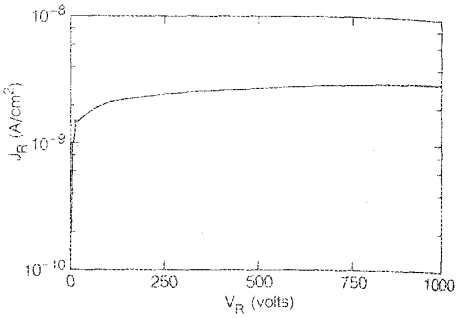

Fig. 5. Detector diode reverse-leakage current of a device fabricated on the same substrate with p-channel MOSFETs.

degradation in the detector diode properties result from the additional processing necessary to fabricate p-channel transistors. The fact that the devices were processed at 900 °C for nearly 3 h while maintaining low leakage current is significant and offers the prospect that CMOS or JFET circuits can be integrated directly with the detector on high-resistivity silicon.

Fig. 6 shows the response of a detector fabricated on ⟨100⟩ silicon to an ^{241}Am source [24]. The full width at half maximum for the 59.4 keV gamma ray is approximately 1.7–1.8 keV yielding an energy resolution of approximately 3%, which is limited by the noise of the signal-processing electronics.

4. Conclusion

A silicon detector process has been developed that is compatible with standard IC processing. Extrinsic gettering of lifetime-killing impurities yields leakage current densities in the range 1–3 nA/cm^2 at depletion

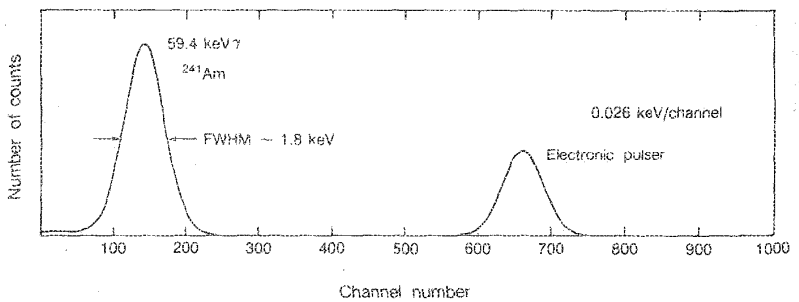

Fig. 6. The response of a detector fabricated on ⟨100⟩ silicon to an ^{241}Am source. The peak at lower channel numbers is the detector response to the 59.4 keV gamma ray whereas the peak at higher channel numbers corresponds to a voltage pulser applied directly to the input of the preamplifier. The full width at half maximum is approximately the same for both implying that the detector response is dominated by the noise in the signal processing electronics. The diode bias was 30 V and the integration time was 0.8 μs. The counting period was approximately 8 h and the measurements were performed at room temperature. The sensitivity is approximately 0.026 keV per channel.

region thicknesses of 2
processing temperatures
fabrication, and reduces
detrimental impurities. T
sary to fabricate p-chan
cantly degrade the detect
effective use of gettering
readout electronics on th
tector diode with potenti
remains to be seen if varia
applied to devices which
both sides of the wafer su
[2]. However, good getteri
using a patterned silicon
hope that drift chambers
could also benefit from ge

Acknowledgements

The devices used in this
University of California-Be
ty. Helpful conservations
Spieler of the Lawrence E
Bosisio of INFN (Pisa, It
edged. Special thanks are
Lawrence Berkeley Laborat
the detector response to
sponsored by the U.S. De
contract number DE-AC03-

References

[1] G. Zimmer, Nucl. Instr. an
[2] E. Gatti, P. Rehak and J.
Meth. 226 (1984) 129.
[3] J. Kemmer, Nucl. Instr. and
[4] P.J. Van Wijnen and W.R. T
Meth. A253 (1987) 351.
[5] A.S. Grove, Physics and T
Devices (Wiley, 1967).
[6] E.R. Weber, Appl. Phys. A3
[7] S.M. Sze, Physics of Semi
(Wiley, 1981) p. 21.
[8] A. Goetzberger and W. Shoc
1821.
[9] K.J. Rawlings, Nucl. Instr. a
[10] P. Eichinger, Nucl. Instr. and
[11] A recent review paper on
Materials Issues in Silicon I
Mater. Res. Soc. Symp. Proc.,
Stimmell and M. Strathman
p. 3.
[12] S.M. Sze, Physics of Semic
(Wiley, 1981) p. 68.
[13] T.M. Buck, K.A. Pickar, J.M
Appl. Phys. Lett. 21 (1972) 48

SIONYX1403000017.0100

SAMSUNG EX. 1002 - 1509/4148

gion thicknesses of 250–300 μm. Gettering allows processing temperatures consistent with typical IC fabrication, and reduces the sensitivity of the process to detrimental impurities. The additional processing necessary to fabricate p-channel MOSFETs did not significantly degrade the detector leakage current. Hence, the effective use of gettering provides a path to integrating readout electronics on the same substrate with the detector diode with potentially high fabrication yields. It remains to be seen if variations of this technique can be applied to devices which require junction formation on both sides of the wafer such as the silicon drift chamber [3]. However, good gettering results have been reported using a patterned silicon nitride film [25] thus offering hope that drift chambers and other two-sided devices could also benefit from gettering.

Acknowledgements

The devices used in this work were fabricated at the University of California-Berkeley microfabrication facility. Helpful conservations with D.R. Nygren and H.G. Spieler of the Lawrence Berkeley Laboratory and L. Rossio of INFN (Pisa, Italy) are gratefully acknowledged. Special thanks are due J.T. Walton of the Lawrence Berkeley Laboratory for the measurement of the detector response to ^{241}Am. This research was sponsored by the U.S. Department of Energy under contract number DE-AC03-76SF00098.

References

[1] G. Zimmer, Nucl. Instr. and Meth. 226 (1984) 175.
[2] E. Gatti, P. Rehak and J.T. Walton, Nucl. Instr. and Meth. 226 (1984) 129.
[3] J. Kemmer, Nucl. Instr. and Meth. 226 (1984) 89.
[4] P.J. Van Wijnen and W.R. Th. Ten Kate, Nucl. Instr. and Meth. A253 (1987) 351.
[5] A.S. Grove, Physics and Technology of Semiconductor Devices (Wiley, 1967).
[6] E.R. Weber, Appl. Phys. A30 (1983) 1.
[7] S.M. Sze, Physics of Semiconductor Devices, 2nd ed. (Wiley, 1981) p. 21.
[8] A. Goetzberger and W. Shockley, J. Appl. Phys. 31 (1960) 1821.
[9] K.J. Rawlings, Nucl. Instr. and Meth. A260 (1987) 201.
[10] P. Eichinger, Nucl. Instr. and Meth. A253 (1987) 313.
[11] A recent review paper on gettering is T.F. Seidel, in: Materials Issues in Silicon Integrated Circuit Processing, Mater. Res. Soc. Symp. Proc., vol. 71, eds. M. Wittmer, J. Stimmell and M. Strathman (MRS, Pittsburgh, PA, 1986) p. 3.
[12] S.M. Sze, Physics of Semiconductor Devices, 2nd ed. (Wiley, 1981) p. 68.
[13] T.M. Buck, K.A. Pickar, J.M. Poate and C.-M. Hsieh, Appl. Phys. Lett. 21 (1972) 485.
[14] S.M. Hu, U.S. Patent 4,053,335 (Oct. 11, 1977).
[15] P.M. Petroff, G.A. Rozgonyi and T.T. Sheng, J. Electrochem. Soc. 123 (1976) 565.
[16] T.E. Hansen, Nucl. Instr. and Meth. A235 (1985) 249.
[17] M. Caccia et al., Nucl. Instr. and Meth. A260 (1987) 124.
[18] S.M. Hu, in: Semiconductor Silicon/1986, Proc. 5th Int. Symp. on Silicon Mater. Sci. and Tech., vol. 86-4, eds. H.R. Huff, T. Abe and B. Kolbesen (The Electrochem. Soc., Pennington, NU, 1986) p. 722.
[19] D. Lecrosnier, J. Paugam, F. Richou and G. Pelous, J. Appl. Phys. 51 (1980) 1036.
[20] D.E. Hill, in: Proc. Symp. on Defects in Silicon, vol. 83-9, eds. W.M. Bullis and L.C. Kimerling (The Electrochem. Soc., Pennington, NJ, 1983) p. 433.
[21] S. Holland, to be published.
[22] R.S. Muller and T.I. Kamins, Device Electronics for Integrated Circuits, 2nd ed. (Wiley, 1986).
[23] G. Vanstraelen, I. DeBusschere, C. Claeys and G. Declerck, Proc. London Conf. on Position-Sensitive Detectors, University College, London (Sept. 7–11, 1987) Nucl. Instr. and Meth. A273 (1988) 625.
[24] Measurement courtesy of J.T. Walton, Lawrence Berkeley Laboratory.
[25] Y. Mada, Jpn. J. Appl. Phys. 21 (1982) L683.

Questions

Q. (G. Hall, Imperial College): Have you tested some of your diodes as detectors to look at the influence of the gettering on the charge collection?

A.: We plan to do this in the future.

Q. (G. Hall, Imperial College): Could your gettering also be done if not the complete backside is available, like with drift detectors?

A.: I have not investigated it with my technique but there are people who tried it with Si_3N_4.

Q. (K. Rawlings, Harwell): You used a P-diffusion for your n^+ regions. Have you tried out implantation?

A.: No, we used diffusion to avoid a spiking problem.

Q. (G. Vanstraelen, IMEC): Did you look at the stability of your devices on the longer term, after introducing the extra processing step?

A.: The diodes are the same now as when they were fabricated six months ago, but we didn't try any stressing.

Q. (G. Declerck, IMEC): Did you observe any wafer warpage or breaking due to the polysilicon on the backside

A.: No, we have seen no warpage, because the poly is only 1 μm thick. We have seen breaking, but we assume this is because the wafers are only 250 μm thick and not because of the poly.

Q. (G. Declerck, IMEC): If you increase the doping level too much, then wafer breakage may increase?

A.: I think this kind of stress would manifest itself in the leakage current, and we have not observed this.

SIONYX1403000017.0101

SAMSUNG EX. 1002 - 1510/4148

Cryogenic Processed Metal–Semiconductor–Metal (MSM) Photodetectors on MBE Grown ZnSe

Hyesook Hong and Wayne A. Anderson, *Senior Member, IEEE*

Abstract— **Molecular beam epitaxy grown 0.5-μm and 2.0-μm thick undoped ZnSe on semi-insulating (100) GaAs substrates were prepared for metal–semiconductor–metal (MSM) photodetector devices. The MSM photodetectors consisted of interdigitated metal fingers with 2, 3, and 4 μm width/spacing on a wafer. A multilayer resist process was employed using polyimide and SiO_2 thin films before the pattern generation to aid in a special low temperature (LT) lift-off process. Dark current–voltage ($I-V$), DC photo $I-V$, high-frequency $I-V$, spectral response, and frequency response techniques were employed for testing the device performance. The cryogenic processed metallization provided an improved interface between metal and semiconductor interface. The breakdown voltage in these devices is dependent on the electrode width/spacing and not on film thickness. Dark current remained at around 1 pA for a bias of ± 10 V. The devices exhibited a high spectral responsivity of 0.6 (A/W) at a wavelength of 460 nm at 5 V applied bias. A maximum spectral responsivity of 1 (A/W) at an applied bias of 5 V was obtained in these devices indicating an internal gain mechanism. This internal gain mechanism is attributed to hole accumulation in ZnSe epilayers.**

I. Introduction

WIDE bandgap compound semiconductors such as those in the ZnSe family and GaN family are very attractive materials for future electro-optic devices such as deep ultraviolet (DUV) light sources, electro-optic displays, short distance communications, high density optical recorders and readers. This is especially true for ZnSe since it is closely lattice matched to GaAs hence facilitating optoelectronic integrated circuits (OEIC) on GaAs. Of special interest are the metal–semiconductor–metal photodetectors (MSM-PD's) since they are useful for monolithically integrated optoelectronic receivers in free space optical interconnects due to their easy fabrication and compatibility with planar stacked optics and with field effect transistors (FET's) [1], [2]. MSM-PD's consist of a semiconductor absorbing layer between two electrodes deposited to form back-to-back Schottky contacts on the semi-insulating substrate.

Controlling the Schottky barrier height is an important issue in fabrication of MSM photodetectors on covalent bonding semiconductors. Moreover, compound semiconductors, such as GaAs, InAs, and ZnS_xSe_{1-x}, show Fermi level pinning at the metal/semiconductor interface which limits the device characteristics. Previous studies [3]–[5] show that low temperature (LT) metallization resulted in an enhanced Schottky barrier height and reduced carrier trapping at the metal/semiconductor interface. Increasing the barrier height leads to low dark currents which are in turn critical for improving the minimum detectable power. Improving the metal/semiconductor interface leads to high speed devices and improved detector sensitivity. Many MSM-PD's in III–V compound semiconductors have been studied for optical communication at 1.3 and 1.55 μm [1]–[2], [6]–[8] wavelengths. These have good saturation characteristics which are attributed to narrow electrode width/spacing (submicron range), defined by e-beam lithography, and small active area (usually 50×50 μm^2) achieved by reducing the contact area at the metal/semiconductor interface. In this study, by employing optical lithography, low dark currents were obtained on LT processed ZnSe MSM-PD's. Due to the lower dark currents in these ZnSe MSM-PD's, higher voltages can be applied to obtain better charge collection as necessary for radiation detector applications. This paper will present photoluminescence (PL), the fabrication procedure for LT processed ZnSe MSM-PD's, dark current–voltage ($I-V$) characteristics, continuous wave (CW) photocurrent–voltage characteristics, high-frequency photocurrent–voltage characteristics, frequency response, and spectral response of these devices.

II. Experimental

Elemental sources of Zn and Se were used for the MBE growth of ZnSe in a Riber MBE 32P system. The epilayer growth of samples was monitored using 10 keV reflection high-energy electron diffraction (RHEED) to optimize the growth conditions. The background pressure during growth was around 10^{-9} Torr. On initiating growth, the streaky RHEED pattern of the GaAs surface changes immediately into dim spots for a brief period, indicating an initial three-dimensional nucleation. The spots then elongate, and within a few minutes, the streaks are reestablished. This implies a layer-by-layer growth once a smooth surface has been established. 0.5 μm and 2.0 μm thick undoped ZnSe epilayers were grown on semi-insulating GaAs(100) at 300 °C. After growth, the undoped ZnSe was cleaned in acetone, methanol, and deionized (DI) water, etched in HCl:DI H_2O (1:1) for 1 min, etched in HF:DI H_2O (1:1) for 1 min, rinsed in DI water, and dried with N_2 gas.

The fabrication procedure for LT processed MSM-PD's is depicted in Fig. 1. Samples were placed on a spinner and cleaned with acetone followed by isopropanol at 4000 r/min for 30 s. An adhesion promoter, Probimide QZ3289:QZ3290 (1:9) was applied and allowed to sit for 10 s before spinning

Manuscript received August 26, 1998; revised December 22, 1998. The review of this paper was arranged by Editor P. K. Bhattacharya.

The authors are with the Department of Electrical and Computer Engineering, State University of New York at Buffalo, Amherst, NY 14260 USA.

Publisher Item Identifier S 0018-9383(99)04208-2.

0018–9383/99$10.00 © 1999 IEEE

SIONYX1403000017.0102

SAMSUNG EX. 1002 - 1511/4148

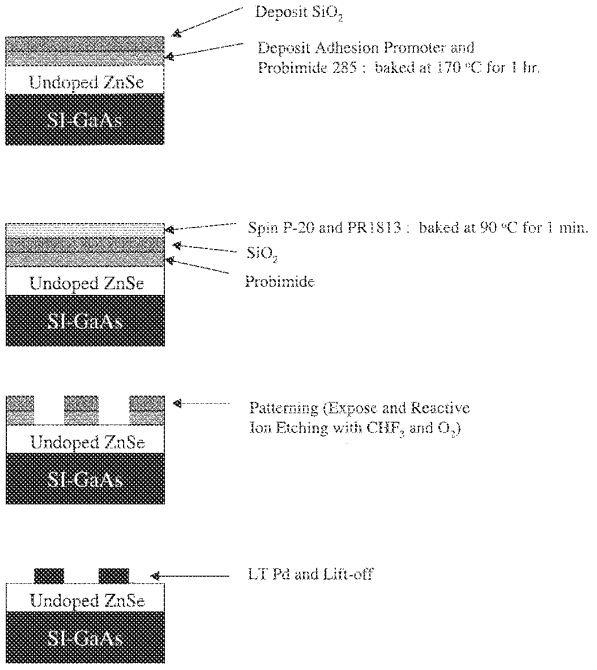

Fig. 1. Fabrication steps of low-temperature processed MSM-PD's.

at 5000 r/min for 30 s. Polyimide 285 was applied and spun at 4000 r/min for 2 min. Curing was done at 170 °C for 1 h.

A 1200 Å SiO_2 film was deposited on top of the Polyimide by plasma enhanced chemical vapor deposition (PECVD) at a substrate temperature of 150 °C. P-20 (20% hexamethyldisiazane) primer was applied to the sample, allowed to sit for 10 s, and spun until the primer was dry, usually at 4000 r/min for 30 s. Next, Shipley 1813 resist was applied to the sample and immediately spun at 4000 r/min for 30 s. Photolithography was done using a GCA 5:1 g-line stepper. After exposure, the resist was developed in MF312:DI H_2O (1:1) for 45 s, rinsed and blown dry.

The exposed area was etched into SiO_2 by reactive ion etching (RIE) in CHF_3 and into polyimide by RIE in O_2. This O_2 etch removed the remaining resist, leaving only the pattern of SiO_2/polyimide/ZnSe. Before metallization, the samples were etched in HCl:DI H_2O (1:1) for 30 s and HF:DI H_2O (1:1) for 30 s to remove any damage caused to ZnSe after RIE and oxide layer patterning. The polyimide/SiO_2 patterning scheme adopted here facilitates lift-off and linewidth integrity when metallization is performed at liquid N_2 temperatures. Subsequently, the sample was transferred to a metal evaporation system capable of a 1×10^{-7} Torr base pressure. The substrate temperature is then lowered to 80 K using a modified holder cooled with liquid N_2. Once the temperature stabilized, Pd was deposited and the substrate holder temperature was raised back to room temperature using DC heating. Control samples were also fabricated by depositing Pd at room temperature (RT). Lift-off was done in 1165 remover which dissolved the polyimide layer over a period of 5–10 h. Fig. 2 shows the scanning electron micrograph (SEM) prior to metallization and a cross section of the MSM-PD.

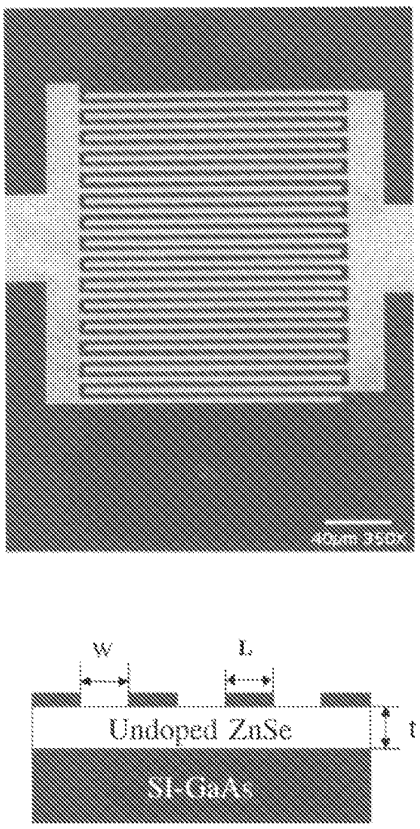

Fig. 2. SEM prior to metallization and a cross section of the ZnSe MSM-PD structure with a 4 μm/4 μm electrode width/spacing.

TABLE I
LT PROCESSED ZnSe MSM-PDs WITH DIFFERENT DESIGN PARAMETERS

MSM PD #	Thickness of ZnSe epilayer : T (μm)	Electrode width and space : w (μm)	Detector area (μm^2)
A	2.0	3	200 x 200
B	2.0	4	200 x 200
C	0.5	3	200 x 200
D	0.5	2	200 x 200
E	0.5	3	50 x 200

III. RESULTS AND DISCUSSION

Table I lists the design information about all LT processed MSM-PD's fabricated on the undoped ZnSe/SI-GaAs substrates to be discussed here. Fig. 3 shows the dark $I-V$ data for LT processed MSM-PD's fabricated on 2.0-μm thick ZnSe epilayers with 3-μm and 4-μm electrode width/spacing, on 0.5-μm thick ZnSe epilayers with 2 μm and 3 μm electrode width/spacing, and a RT processed MSM-PD, fabricated on 2.0-μm thick ZnSe epilayers with 2-μm electrode

SIONYX1403000017.0103

SAMSUNG EX. 1002 - 1512/4148

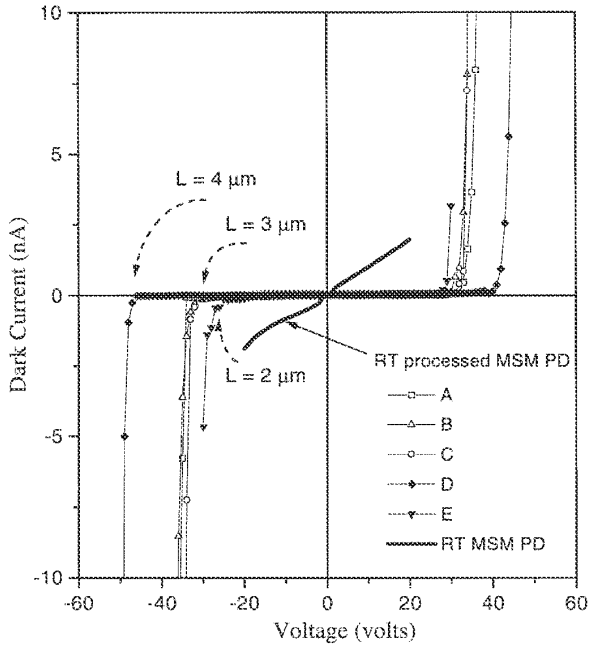

Fig. 3. Dark $I-V$ characteristics of ZnSe MSM-PD's for various electrode width/spacing.

width/spacing. Dark currents were generally less than 1 pA up to a bias of 10 V for all ZnSe MSM-PD's fabricated by the LT process. However MSM-PD's processed by RT metallization are leaky. Dark currents obtained from LT processed MSM-PD's are low compared to the other reports on InGaAs [9] or GaN [10] MSM-PD's.

Dark $I-V$ can be expressed by (1) for MSM-PD's if the simplest thermionic emission model [7] is used as

$$J = A_n^* T^2 \exp(-q\phi_{bn}/kT)\exp(q\Delta\phi_n/kT) + A_p^* T^2 \exp(-q\phi_{bp}/kT)\exp(q\Delta\phi_p/kT) \quad (1)$$

where A_n^* and A_p^* are the effective Richardson constants for the electrons and holes, respectively, $\phi_{n,p}$ are the respective barrier heights, q is electron charge, k is Boltzman constant, and T is absolute temperature in Kelvin. $\Delta\phi_n$ is the image force lowering term at the cathode, and $\Delta\phi_p$ is at the anode. Using a Richardson factor of 25.2 A cm^{-2} T^{-2} for electrons and 72 A cm^{-2} T^{-2} for holes, a barrier height of 1.3 eV for electrons and holes was obtained. Barrier height values were also confirmed by measuring single Schottky devices. Since the barrier heights obtained are about half the bandgap of ZnSe, the dark leakage current should be at a theoretical minimum [9]. Fig. 3 also shows a sharp breakdown voltage for all values of different electrode width/spacing. In contrast to ZnSe *pin* photodetectors which showed a breakdown voltage dependence on the i-layer thickness [11], breakdown voltages here exhibit a linear dependence on only the electrode width/spacing of ZnSe MSM-PD's. Breakdown voltages of 25 V, 36 V, and 50 V are obtained for the 2 μm, 3 μm, and 4 μm electrode width/spacings, respectively.

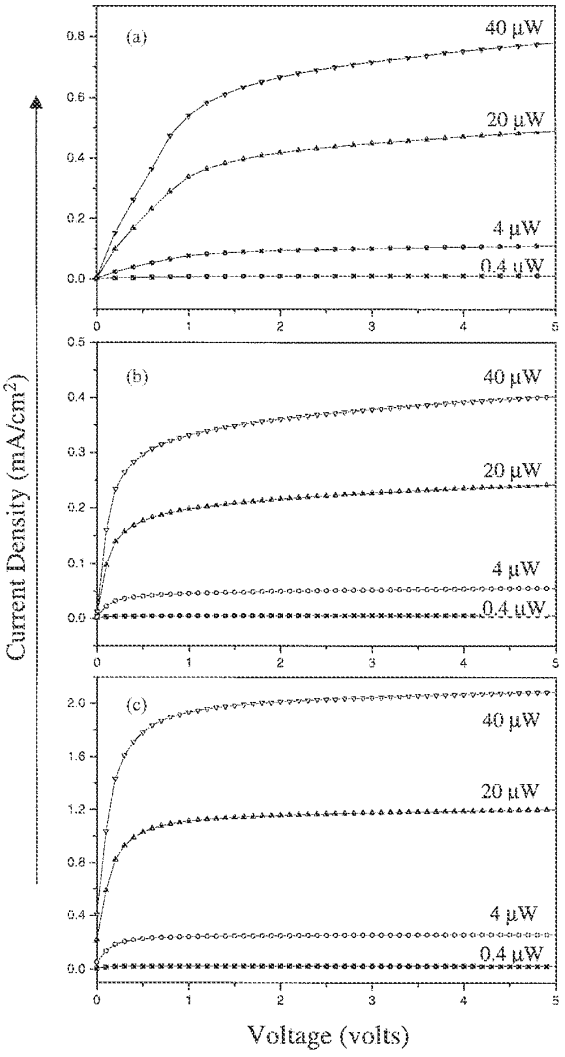

Fig. 4. CW Photocurrent–voltage characteristics of MSM-PD's (a) #A, (b) #C, and (c) #E.

Fig. 4 shows continuous wave (CW) photo $I-V$ characteristics of MSM-PD's #A, #C, and #E in Table I. These MSM-PD's were uniformly illuminated using a quartz tungsten halogen lamp (CW light source) at various optical power levels. In Fig. 4(a), the $I-V$ curve consists of two regions; the photocurrent first rapidly increases as bias increases, and then saturates. This rapid increase of photocurrent in the low bias region is due to the expansion of the depletion region in the reverse bias Schottky junction and the improved internal quantum efficiency [1]. The shoulder or the knee voltage, where the photocurrent starts to saturate, locates between 0.7 and 1.5 V depending on the extent of the incident optical power. Up to the shoulder voltage, the increasing carrier collection efficiency as the bias increases can be explained in terms of the finite carrier lifetime model [6]. Above the shoulder voltage, if photocurrent does not increase with applied voltage, it indicates that all the photoexcited carriers reach

SIONYX1403000017.0104

SAMSUNG EX. 1002 - 1513/4148

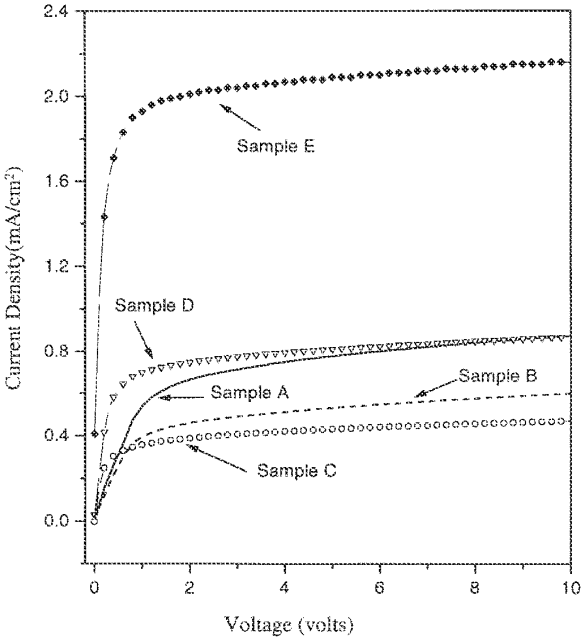

Fig. 5. Comparison for threshold voltage and transimpedance with thickness and electrode line width/spacing in MSM-PD's at a optical level of 40 μW.

the opposite side electrodes before they recombine [12] or the carrier generation rate is higher than the carrier sweep-out rate [13]. However, perfect saturation of the photocurrent is not seen in Fig. 4(a), which can be explained by an internal gain mechanism [1]. Although the exact internal gain mechanism is moot, it has been postulated that when photo-generated holes are accumulated at the valence-band peak near the cathode, these positive charges increase electron tunneling current and a similar effect takes place at the anode [6]. It is also possible that this effect is caused by long lifetime traps located either at the metal/semiconductor interface or bulk layer [1], [3], [8]. The ZnSe MSM-PD #C in Table I, having 0.5 μm thickness and 3 μm electrode width/spacing with the same active area as #A showed the improved saturation current in Fig. 4(b). This result supported the theory that the internal gain mechanism is associated with traps in the bulk layer. However the photocurrent (detector sensitivity) in Fig. 4(b) at the same incident optical power is less than in Fig. 4(a). It might be that the detector did not absorb most of the incident light due to thin layers. Fig. 4(c) shows the DC photo $I-V$ characteristics for MSM-PD #E, having an 0.5 μm thick ZnSe epilayer with the same electrode width/spacing (3 μm), but with four times smaller active area (50 μm $\times$ 200 μm) than MSM-PD #A and #C. Compared to PD #A, the photo $I-V$ of PD #E exhibits excellent saturation behavior indicating less internal gain as a result of reduction in area and the layer thickness. However, PD #E did not demonstrate a better saturation behavior than PD #C by reducing the contact area indicating that the gain mechanism is associated with bulk layer traps. For MSM-PD's fabricated with conventional room temperature metallization, saturation current characteristics were not observed.

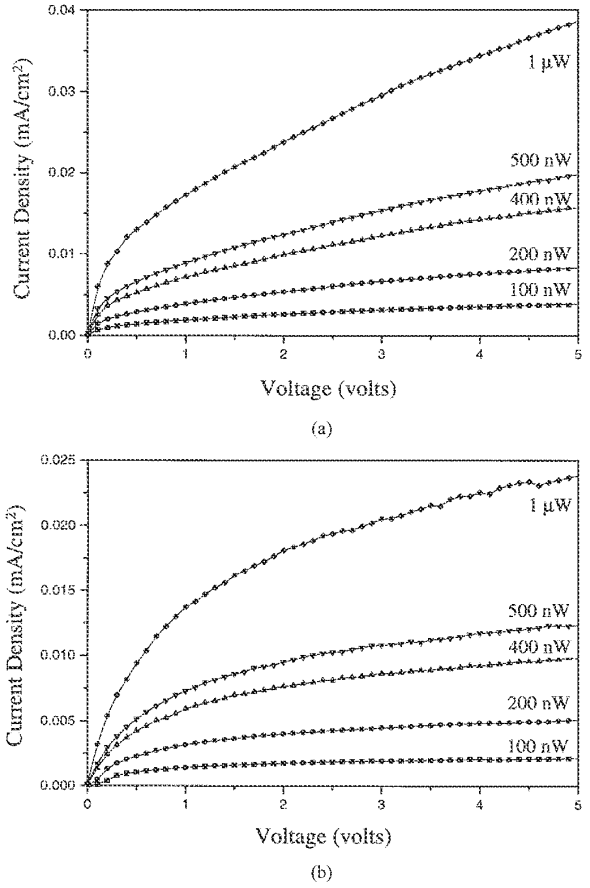

Fig. 6. Photocurrent–voltage characteristics of MSM-PD's (a) #A and (b) #C using 100 fs pulsed Ti:Sapphire mode-locked laser at a wavelength of 448 nm.

The saturation current behavior is a major feature for applying an active impedance load such as FET's to design photoreceiver circuits in the integrated optoelectronic devices. So, the large differential output transimpedance within the saturation current region enables the practical use of FET's because the $I-V$ characteristics of MSM-PD's are so similar to the output characteristics of a FET. Fig. 5 shows a comparison of photo $I-V$ for photo-transimpedance and shoulder voltage associated with flat band voltages among MSM-PD's #A, #B, #C, #D, and #E at a 40 μW optical power level. Photo-transimpedance is given by dV/dI at a certain optical power level (analogous to the gate bias of a FET). All ZnSe MSM-PD's showed high transimpedance ranging from 20 to 70 kΩ at 40 μW optical power level in the saturation region. As another comparison between PD's, the shoulder voltage is correlated with semiconductor epilayer thickness not with the device electrode width/spacing in this study, in contrast to the other study [1], [14].

Fig. 6 shows the high frequency photo $I-V$ characteristics of MSM-PD's #A and #D (Table I). Here a Spectra Physics Tsunami Ti:Sapphire 100 fs pulsed laser with 80 MHz repetition rate was used. The mode locked laser beam was passed through a barium borate (BBO) crystal for frequency doubling

SIONYX1403000017.0105

SAMSUNG EX. 1002 - 1514/4148

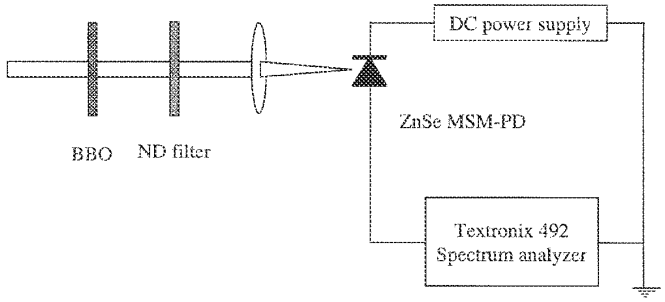

Fig. 7. Experimental setup for frequency response for ZnSe MSM-PD's using a 100 fs pulsed/frequency doubled Ti:Sapphire laser through the BBO crystal.

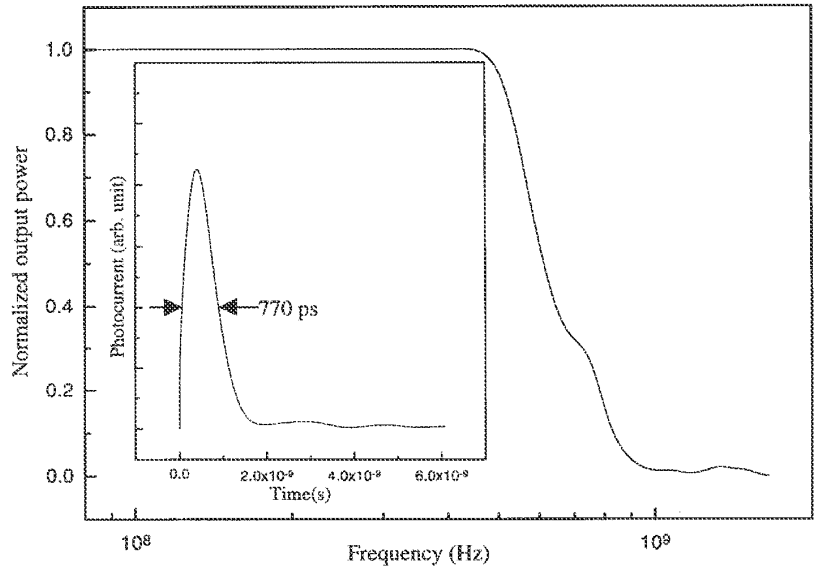

(a)

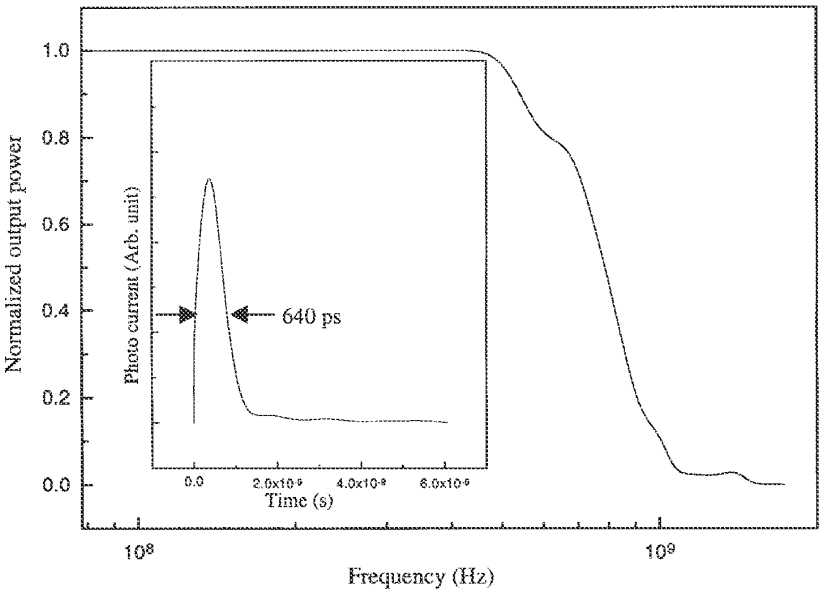

(b)

Fig. 8. Frequency response of ZnSe MSM-PD's (a) #C and (b) #D using 100 fs pulsed Ti:Sapphire mode locked laser at a wavelength of 448 nm.

SIONYX1403000017.0106

SAMSUNG EX. 1002 - 1515/4148

leading to a wavelength of 448 nm, above the ZnSe bandgap energy. The full width half maximum (FWHM) of laser beam size is around $492 \times 481\ \mu m^2$, which is six times larger than the active area of the MSM-PD's. Therefore, optical power captured by the detector is smaller than the power mentioned in Fig. 6. Comparing this to the CW photo $I-V$ characteristics, the saturation behavior at higher bias voltage in Fig. 6(a) is not good. Reducing the thickness of the bulk layer showed a little better saturation behavior but still worse than in the CW photocurrent saturation data. However, reducing the electrode width/spacing did not improve the saturation (internal gain was not influenced) for the high frequency photoresponse. This result again supports the theory that the internal gain in the ZnSe MSM-PD's may be due to long lifetime traps in the bulk layer rather than at the metal/semiconductor interface.

Fig. 7 shows the schematic experimental setup for frequency response based on impulse response with the assumption of the input optical signal as a train of delta functions. Impulse response of the MSM-PD's was obtained by optical excitation with a 100 fs pulsed mode locked Ti:Sapphire laser at a wavelength of 448 nm. The output signal was detected by a Tektronix 492 spectrum analyzer. Taking Fourier transformation, the temporal response for the MSM-PD's can be obtained.

Fig. 8 shows the frequency response of ZnSe MSM-PD's (a) #C and (b) #D and their Fourier transformed temporal response in insets to the 100 fs pulse laser input having 80 MHz repetition rate. The 3 μm MSM-PD showed a 3 dB frequency of 620 MHz and its associated temporal pulse width (FWHM) of 770 ps. The 2 μm device demonstrated a 3 dB frequency of 800 MHz and its corresponding pulse width of 640 ps. FWHM's of pulse width were obtained by taking the Fourier transform of frequency response. The frequency response showed that the 2 μm device had improved device speed due to the short carrier transit time between electrodes.

Fig. 9 shows the experimental setup for spectral response at a low optical frequency of 300 Hz chopper speed. The monochromatic wave was extracted from a xenon white light source through the monochrometer. Monochromatic light was focused onto the device under test (DUT) to obtain maximum output signal at the given incident optical power. The light source was first calibrated by a commercial silicon p-i-n photodetector. The output signals from DUT and silicon p-i-n photodetector were taken by using a lock-in amplifier. For all the MSM-PD's, a reverse bias of -5 V was applied. Fig. 10 shows spectral response of ZnSe MSM-PD's #A, #C, and #D. However, since the lenses had a cutoff wavelength at 300 nm, spectral response below 300 nm could not be obtained in this experiment. The device shows a cutoff wavelength of 460 nm at room temperature. Responsivities of $\sim$1 A/W are obtained at a wavelength of 380 nm from these PD's #A and #D, without an anti-reflecting coating, signifying an internal gain mechanism to be present. For PD #C, increasing the bias voltage (>5 V) did not result in a dramatic increase of responsivity, indicating the reduced

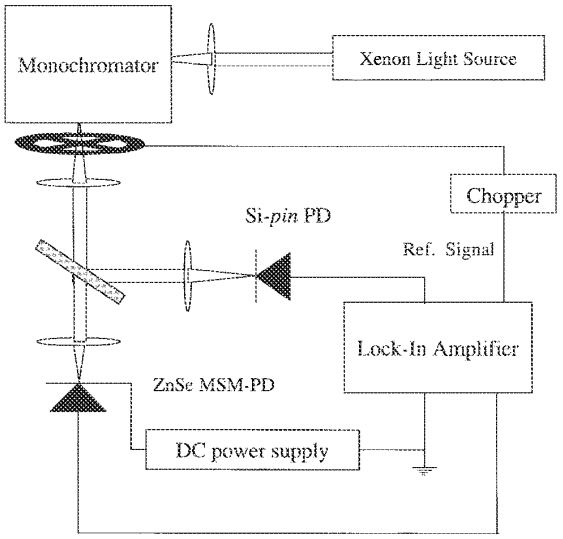

Fig. 9. Experimental setup for spectral response of LT processed ZnSe MSM-PD's using a Xenon white light source.

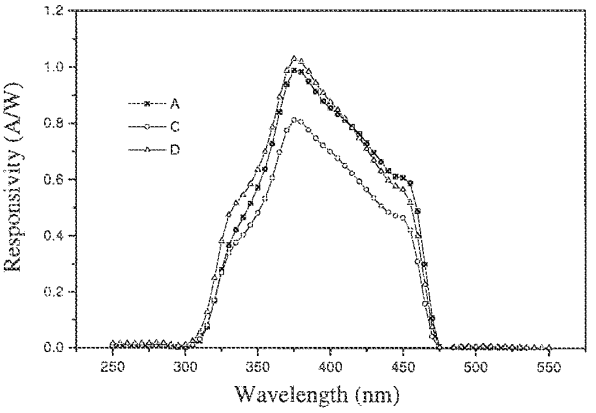

Fig. 10. Spectral response of LT processed ZnSe MSM-PD's #A, #C, and #D at a bias of 5 V using a Xenon light source modulated at 300 Hz.

internal gain by reducing the epilayer thickness. Such internal gain can be seen in photoconductor type of photodetectors. Internal gain ranges from 2.6 to 3.6 in LT processed ZnSe MSM-PD's.

Photoluminescence (PL) spectra were taken at 10 K on MBE grown undoped 2.0 μm and 0.5 μm thick ZnSe/SI-GaAs (100). Fig. 11 shows PL spectra of undoped a) 2.0 μm thick, b) 0.5 μm thick ZnSe samples. Fig. 11(a) shows a strong free exciton (Fx) signal at an energy of 2.803 eV and free-to-bound exciton (Bx) peak at an energy of 2.79 eV similar to those seen in a typical undoped ZnSe/GaAs (100) PL spectra [15], [16]. A strong Fx peak indicates an undoped layer with a high crystalline quality. This PL spectra possibly shows a longitudinal optical (LO) phonon signal related to the Bx at 2.76 eV (about 30 meV). Also, at a lower energy level near 2.6 eV called the Y-line, a sharp signal can normally be

SIONYX1403000017.0107

SAMSUNG EX. 1002 - 1516/4148

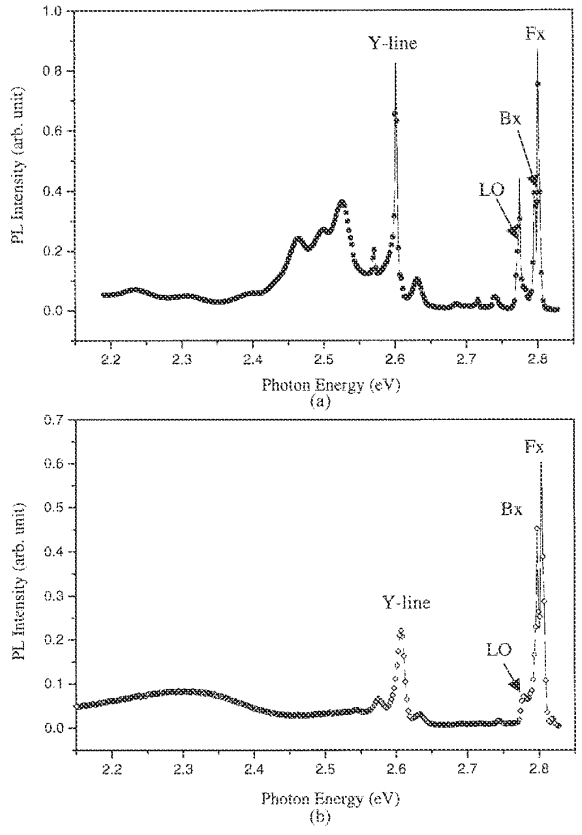

Fig. 11. The 10 K PL intensity of (a) 2.0 μm and (b) 0.5 μm thick undoped ZnSe/SI-GaAs.

seen in ZnSe samples. There is broad luminescence below the Y-line attributed to the unintentional impurity during growth. Fig. 11(b) shows a Fx, Bx, LO phonon, and Y-line like in Fig. 11(a). But the Fig. 11(b) shows that the 0.5 μm thick ZnSe sample had less impurity in the bulk layer and supported the internal gain mechanism involved in these devices.

IV. Conclusion

Cryogenic processed MSM-PD's were fabricated by defining the SiO_2 hard mask and using a lift-off technique. Low temperature (LT) processed ZnSe MSM-PD's showed a low dark current of less than 1 pA, at a bias of 10 V, and high breakdown voltage. The breakdown voltage in low temperature processed ZnSe MSM-PD's is dependent on the electrode width/spacing. Gain in the detectors for measurement at 80 MHz is higher than that obtained for DC measurements which indicates transition time limited devices. The frequency response measurements using the 100 fs Ti:Sapphire mode locked laser at a wavelength of 448 nm demonstrated that the 3 μm device had 620 MHz bandwidth correlated with a FWHM of 770 ps pulse width and the 2 μm device had 800 MHz bandwidth corresponding to a FWHM of 640 ps pulse width. From spectral response of ZnSe MSM-PD's, the responsivity of 1 (A/W) at a wavelength of 380 nm and 0.6 (A/W) at a wavelength of 450 nm and at a bias of 5 V were obtained without any anti-reflecting coating layers.

Acknowledgment

The authors wish to thank H. Luo of the Physics Department, for providing samples, A. Petrou of the Physics Department, for PL measurement, and A. Cartwright of the Electrical Engineering Department, for allowing the use of a Ti:Sapphire laser. The assistance provided by M. Skvarla for the part of this work carried out at the Cornell Nanofabrication Facility is also acknowledged.

References

[1] J. B. D. Soole and H. Schumacher, "InGaAs metal–semiconductor–metal photodetectors for long wavelength optical communications," *IEEE J. Quantum Electron.*, vol. 27, pp. 737–752, Mar. 1991
[2] E. H. Böttcher, D. Kuhl, F. Hieronymi, E. Dröge, T. Wolf, and D. Bimberg, "Ultrafast semiinsulating InP:Fe-InGaAs:Fe-InP:Fe MSM photodetectors: Modeling and performance," *IEEE J. Quantum Electron.*, vol. 28, pp. 2343–2357, Oct. 1992.
[3] J. W. Palmer, W. A. Anderson, D. T. Hoelzer, and M. Thomas, "Cross-sectional TEM of Pd/InP and Au/InP interfaces formed at substrate temperatures near 300 and 77 K," *J. Electron. Mat.*, vol. 25, no. 10, pp. 1645–1651, Oct. 1996.
[4] Z. Q. Shi, R. L. Wallace, and W. A. Anderson, "High-barrier height schottky diodes on N-InP by deposition on cooled substrates," *Appl. Phys. Lett.*, vol. 59, no. 4, pp. 446–448, July 1991.
[5] A. Z. H. Wang, W. A. Anderson, and M. A. Haase, "Electrical properties of schottky contacts to *N*-type $ZnS_{0.07}Se_{0.93}$ epilayers," *J. Appl. Phys.*, vol. 77, no. 7, pp. 3513–3517, Apr. 1995.
[6] M. Klingenstein, J. Kuhl, J. Rosenzweig, C. Moglestue, A. Hulsmann, Jo. Schneider, and K. Kohler, "Photocurrent gain mechanisms in metal–semiconductor–metal photodetectors," *Solid State Electron.*, vol. 37, no. 2, pp. 333–340, 1994.
[7] W. Wohlmuth, M. Arafa, P. Fay, and I. Adesida, "InGaAs metal–semiconductor–metal photodetectors with a hybrid combination of transparent and opaque electrodes," *Appl. Phys. Lett*, vol. 70, no. 22, pp. 3026–3028, June 1997.
[8] S. Y. Chou and M. Y. Liu, "Nanoscale tera-hertz metal–semiconductor–metal photodetectors," *IEEE J. Quantum Electron.*, vol. 28, pp. 2358–2368, Oct. 1992.
[9] W. A. Wohlmuth, M. Arafa, A. Mahajan, P. Fay, and I. Adesida, "InGaAs metal–semiconductor–metal photodetectors with engineered Schottky barrier heights," *Appl. Phys. Lett.*, vol. 69, no. 23, pp. 3578–3580, Dec. 1996.
[10] J. C. Carrano, P. A. Grudowski, C. J. Eiting, R. D. Dupuis, and J. C. Campbell, "Very low dark current metal–semiconductor–metal ultraviolet photodetectors fabricated on single-crystal GaN epitaxial layers," *Appl. Phys. Lett.*, vol. 70, no. 15, pp. 1992–1994, Apr. 1997.
[11] H. Hong, W. A. Anderson, S. Nagarathnam, A. Cartwright, E. H. Lee, H. C. Cheng, M. H. Na, and H. Luo, "PIN photodiodes using nitrogen ion implantation on ZnSe/GaAs heterostructure," in *Proc. IEEE 24th Int. Comp. Semi. Symp.*, 1997, pp. 163–166.
[12] R. B. Darling, H. J. Yoon, and K. J. Kuhn, "Use of active loads with MSM photodetectors in digital GaAs MESFET photoreceivers," *J. Lightwave Technol.*, vol. 10, no. 11, pp. 1597–1605, Nov. 1992.
[13] P. T. Chan, H. S. Choy, C. Shu, and C. C. Hsu, "High-performance $InP/Ga_{0.47}In_{0.53}As/InP$ metal–semiconductor–metal photodetectors with a strained $Al_{0.1}In_{0.9}P$ barrier enhancement layer," *Appl. Phys. Lett.*, vol. 67, no. 12, pp. 1715–1717, Sept. 1995.
[14] P. Bhattacharya, *Semiconductor Optoelectronic Devices*. 1994, p. 399.
[15] K. Ohkawa, A. Ueno, and T. Mitsuyu "Molecular-beam epitaxial growth of *p*- and *n*-type ZnSe homoepitaxial layers," *J. Cryst. Growth*, vol. 117, nos. 1–4, pp. 375–384, Feb. 1992.
[16] J. Gutowski and G. Kudlek, "Optical properties of ZnSe epilayers and films," *Phys. Stat. Sol (a)*, vol. 120, pp. 11–59, 1990.

SIONYX1403000017.0108

SAMSUNG EX. 1002 - 1517/4148

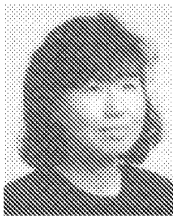

Hyesook Hong received the B.S. degree in electronics engineering from Sung Kyun Kwan University, Suwon, Korea, in 1983, the M.S. degree in electrical engineering from the University of Colorado, Boulder, in 1991, and the Ph.D. degree in electrical engineering from State University of New York at Buffalo in 1998. Her Ph.D. work focused on characterization, fabrication, and applications of ZnSe devices.

From 1983 to 1989, she was with the Korea Telecommunication Authority as a Software Engineer. In 1998, she joined Headway Technologies, Inc., Milpitas, CA. Her current interests are fabrication, modeling, and characterization for semiconductor devices.

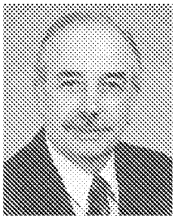

Wayne A. Anderson (S'68–M'70–SM'82) received the Ph.D. in electrical engineering in 1970, with an emphasis in semiconductors and microwaves.

His experience includes industrial R&D (1962–1965), and university teaching (1966–present) with eight years at Rutgers University and the remaining at State University of New York at Buffalo. His present research interests include thin-film resistors and capacitors, thin-film silicon for solar cells and flat panel displays, and metallization of wide-bandgap semiconductors. He has supervised the completion of 44 M.S. or Ph.D. theses/dissertations and coauthored over 200 conference presentations as well as over 150 journal articles.

Prof. Anderson is a member of APS and MRS.

SIONYX1403000017.0109

SAMSUNG EX. 1002 - 1518/4148

Focal-Plane-Arrays and CMOS Readout Techniques of Infrared Imaging Systems

Chih-Cheng Hsieh, Chung-Yu Wu, *Senior Member, IEEE*, Far-Wen Jih, and Tai-Ping Sun

Abstract— **A discussion of CMOS readout technologies for infrared (IR) imaging systems is presented. First, the description of various types of IR detector materials and structures is given. The advances of detector fabrication technology and microelectronics process technology have led to the development of large format array of IR imaging detectors. For such large IR FPA's which is the critical component of the advanced infrared imaging system, general requirement and specifications are described. To support a good interface between FPA and downstream signal processing stage, both conventional and recently developed CMOS readout techniques are presented and discussed. Finally, future development directions including the smart focal plane concept are also introduced.**

Index Terms— **Detector, focal plane array, infrared imaging, readout circuit, thermal image.**

I. Introduction

SINCE the 1950's, the infrared (IR) imaging system technology has been developed for various applications including IR search and track, medical examination [1], astronomy [2], [3], forward-looking infrared (FLIR) systems, missile guidance, and other strategic equipment [4], [5]. Recently, a dual-use technology concept has been proposed which emphasizes the integration of commercial and military IR imaging systems to meet both economic and defense challenges [6]. This concept has led to the increasing research and development efforts in applying the commercial CMOS very large scale integration (VLSI) technologies in the design of IR imaging systems. Incorporating the rapid advancement in CMOS VLSI with the progress in infrared focal-plane array (IR FPA) technologies like detector material, sensing structure, optics, coolers, readout electronics, image enhancement, and intelligent signal processing results in the revolution of IR image systems to a new generation with significant performance improvement.

In general, the IR FPA can be divided into two major parts, namely the detector array and the readout electronics. As compared to the conventional discrete design, the IR FPA has the inherent advantages of high packing density, low cost, reduced signal leads through the dewar, high feasibility on-chip signal processing, and high flexibility for system integration. In the high-sensitivity applications, the IR FPA's are typically fabricated with narrow bandgap semiconductor detectors and silicon multiplexer and operated in the cryogenic environment. Thus, very challenging technologies for detection materials and system interface are required. Moreover, high-performance and low-temperature mixed-mode circuit design are also required for the readout electronics [7]. To achieve the optimal overall performance of the IR FPA's, suitable tradeoff among circuit performance, power dissipation, chip area, and image resolution should be made. A number of readout structures have been developed for different system applications and concerns.

In this paper, the CMOS readout techniques for IR image system are presented and discussed. The IR detector materials and structures for used in thermal image are described in Section II. In Section III, the architectures and operational requirements of IR FPA are discussed. In Section IV, the CMOS readout techniques for IR detectors are discussed including the state-of-the-art structure. In Section V, future directions for IR sensor readout are presented. Finally, a summary is given.

II. Infrared Detectors for Use in Thermal Imaging

All real objects are thought to exist at temperatures above absolute zero, which means that the thermal radiation exists always. The infrared radiation which is detected just above the visible spectrum was found in 1900 as a function of temperature and wavelength [8]. Since then, various infrared detectors have been developed to convert incident infrared radiation, directly or indirectly, into electrical signals. Among these detectors, two major classes known as photon detectors and thermal detectors are discussed here.

In the photon detectors, photons are converted directly into free current carriers by photoexciting electrons across the energy bandgap of the semiconductor to the conduction band. This produces a current, voltage, or resistance change of the detectors. The photoexcitation is caused by the sufficiently short wavelength radiation interacting directly with the lattice sites. Therefore, the temperature of the detector must be low enough so that the number of carriers thermally excited across the bandgap is less significant. To maintain a low temperature, the cooling system or the dewar is required, which increases the system cost. Generally, the sensitivity of photon detectors depends on the spectral absorption and photoexcitation. The spectral response of photon detectors depends on the energy

Manuscript received September 30, 1996; revised January 31, 1997. This paper was recommended by Guest Editors B. Sheu, C.-Y. Wu, H.-D. Lin, and M. Ghanbari.

C.-C. Hsieh and C.-Y. Wu are with the Integrated Circuits and Systems Laboratory, Department of Electronics Engineering and Institute of Electronics, National Chiao Tung University, Hsinchu, Taiwan 300, R.O.C.

F.-W. Jih and T.-P. Sun are with the Chung Shang Institute of Science and Technology, Lung-Tan, Taiwan, R.O.C.

Publisher Item Identifier S 1051-8215(97)05894-1.

1051–8215/97$10.00 © 1997 IEEE

SIONYX1403000017.0110

SAMSUNG EX. 1002 - 1519/4148

TABLE I
GENERAL PROPERTIES OF PHOTON AND THERMAL DETECTORS

Parameter	Photon Detector	Thermal Detector
Response time	Fast	Slow
Spectral responsively	Narrow and selective	Wide and flat
Sensitivity	High	Low
Operating temperature	Cryogenic	Room
Cost	Expensive	Economical
System requirement	Cooling System	Optical Chopper

gap of the semiconductor as well as the optical radiation wavelength.

In the thermal detectors, the incident radiation absorbed by the crystal lattice leads to a temperature change which changes the physical or electrical property of the detector. Most thermal detectors are operated at room temperature and have a wide spectral response. Since the operation of thermal detectors involves a change in temperature, they have a inherently slow response and a relatively low sensitivity compared to photon detectors [9]. The response time and sensitivity of a thermal detector are influenced by the heat capacity of detector structure as well as the optical radiation wavelength. In some applications of thermal detectors, an optical chopper is also needed [10], [11]. Some comparisons between photon detectors and thermal detectors are summarized in Table I.

In the following subsections, the most commonly used IR radiation sensing structures of photon detectors in arrays, namely, photovoltaic detectors, photoconductive detectors, and Schottky barrier detectors are described. Moreover, two mostly used structures of thermal detectors, pyroelectric detectors and bolometers, are also discussed.

A. Photovoltaic (PV) Detectors [12]–[14]

The structure of a photovoltaic (PV) detector is based on a P–N junction device as shown in Fig. 1(a). The reflective coating on the bottom of the detector provides the double chances (injection and reflection) of photon absorption. Under the IR radiation, the potential barrier of the P–N junction leads to the photovoltaic (PV) effect. An incident photon with the energy greater than the energy band gap of the junction generates electron-hole pairs and the photocurrent is excited. The resultant I-V curve of the PV detector when exposed to IR radiation is similar to that of normal P–N junction device but shifted downward as shown in Fig. 1(b). The amount of the photon excited current is denoted by I_p, the photocurrent. Normally, the photovoltaic detector is operated under zero or near zero biasing condition to obtain a large output shunt resistance without the device breakdown treat. The output shunt resistant of PV detectors is expressed as R_oA where R_o is the shunt resistance normalized to the detector area A under zero bias. Generally, high value of R_oA is an important requirement for PV detectors to achieve a good sensitivity and a good input injection. Due to the zero biasing condition of PV detectors, the power consumed is nearly zero and the heat generation problem can be avoided.

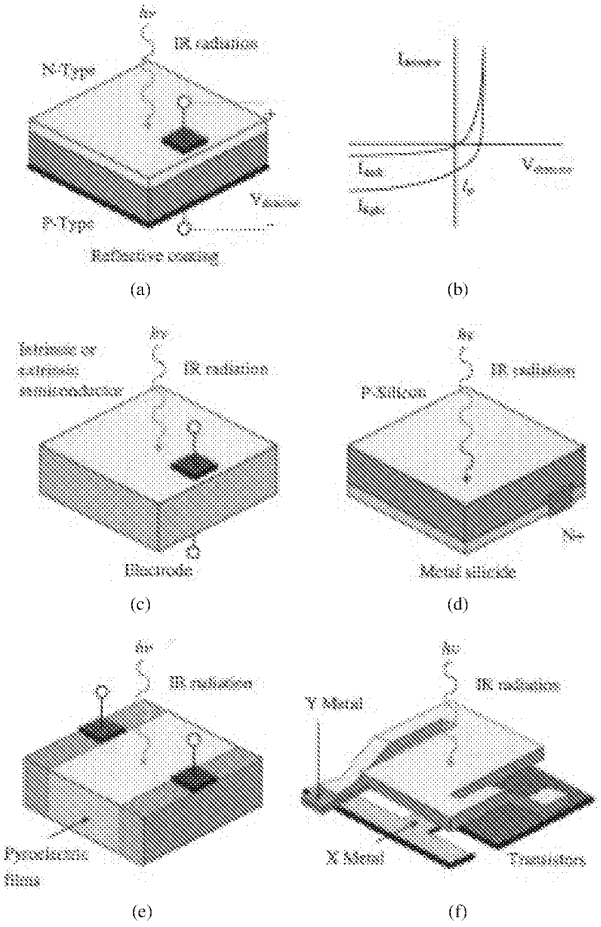

Fig. 1. (a) The device structure of photovoltaic detector, (b) the I-V curve of the PV detector, (c) the device structure of the photoconductive detector, (d) the device structure of the Schottky barrier detector, (e) the device structure of the pyroelectric detector, and (f) the device structure of the bolometer.

The thermal noise and the $1/f$ noise are the major noise sources of the PV detector, which degrade the detector performance. The ultimate performance of an ideal detector is defined as the background-limit-IR-performance (BLIP) [15], which is only affected by the photon noise due to the fluctuation of the incident optical radiation. All other noises in detectors should be kept below the photon noise to achieve the BLIP performance. In long-wavelength IR (LWIR) detection, the fabrication of the low-noise PV detector using narrow bandgap materials is quite challenging [16], [17].

B. Photoconductive (PC) Detectors [12], [18]

The mechanism of photoconductive (PC) detectors is to produce the conductance change under the IR radiation. In PC detectors, the increase of the conductance of photoconductive material under an applied constant electric field is caused by the free carriers generated by the photon energy. The structure of PC detectors is shown in Fig. 1(c). The detector material

SIONYX1403000018.0001

SAMSUNG EX. 1002 - 1520/4148

can be either an intrinsic or an extrinsic semiconductor. The spectral response of a semiconductor material can be controlled by the doping of the intrinsic semiconductor to make PC detectors applicable in LWIR detection [16], [19]. In the case of intrinsic semiconductor, the incident IR radiation is absorbed to generate holes and electrons. In the case of extrinsic semiconductors, the photon energy is absorbed by the impurity, and only the majority carriers are excited. Under the applied constant bias, the resultant current level is proportional to the incident photon flux.

In PC detectors, the photoconductive gain is defined as the ratio of carrier lifetime to detector transit time. The gain usually varies from 0.5 to greater than unity. If carrier lifetime is longer than transit time, the free carriers can transit cross the detector without recombination and the current gain is greater than one. Since the current flows under a constant electric field, the photoconductive detector consumes power and generates heat. This makes it not suitable for large IR array applications. Moreover, an additional noise source called the generation-recombination noise exists in PC detectors besides the thermal and the $1/f$ noise sources.

C. Schottky Barrier Detectors [20]–[22]

The structure of Schottky barrier detectors with the silicide (PtSi) thin film which can be fabricated by using the conventional CMOS process is shown in Fig. 1(d). The IR radiation photons injected from the backside of the silicon substrate are absorbed in the silicide layer. Fractions of the excited carriers are emitted over the Schottky barrier into the silicon. Since the carrier recombination can be avoided due to the Schottky barrier, charges are accumulated in the silicide layer. The accumulated charges can be transferred out through a structure like the charge-coupled device (CCD). Due to the process compatibility of Schottky barrier detectors with CMOS, it is easy to merge detector arrays with readout circuits and other VLSI circuits or systems monolithically [23], [24]. The problems of bonding and hybrid process can be solved in high-density IR FPA applications [25]. However, low quantum efficiency and low spectral response limit the applications of Schottky barrier detectors on the medium wavelength IR (MWIR) image detection [22]. Recently, new technology of Schottky barrier detectors for LWIR have been under development [26].

D. Pyroelectric Detectors [27], [28]

The basic structure of the pyroelectric detector is shown in Fig. 1(e). The pyroelectric material is a special dielectric material with spontaneous and permanent polarization. In the pyroelectric material, the change of dielectric constant is proportional to the temperature dependent spontaneous polarization. When IR radiation is incident and absorbed, the resultant heating makes a change in electrical polarization which causes charges to flow to the connected external readout circuit. Since the polarization is temperature dependent, a chopper is needed to cut the heat source, i.e., the photon flux and reset the polarization condition. Some techniques have been proposed to improve the influence of nonideal chopper effect on the nonuniformity in uncooled pyroelectric staring array systems [10], [11]. The ambient operating temperature and the flat spectral response make the pyroelectric detector useful in some IR image detection applications. However, slow response time and low sensitivity result in the limitation on readout performance. New process technology, new material, and improved structure of pyroelectric detectors are under development to improve performance of pyroelectric detectors [29]–[31].

E. Bolometer Detectors [32], [33]

The operating principle of bolometer detectors is that the temperature change caused by the absorption of IR radiation leads to a change in electrical resistance of the material. Unlike the photoconductive detectors, the resistance change in bolometer detectors is caused directly by the heating of material instead of direct photon-lattice interaction and carrier generation. The general detector structure of bolometer detectors using the micromaching technology is shown in Fig. 1(f). The X–Y metals are used as interconnection tracks and the transistor switch beneath each pixel enables addressing. As a thermal detector, larger conductivity in bolometer detectors ensures faster response but higher temperature change which lowers the sensitivity. This makes a tradeoff on the structure design of bolometer detectors. The application of superconducting materials on bolometer detectors is also under development. The dramatic resistance change versus temperature in superconducting materials leads to a high sensitivity of bolometer detectors [34]–[36].

III. Structures and Operational Requirements of IR FPA

A. IR FPA Structures

Recently, the development of IR FPA technologies has made the design of high-sensitivity, high-density, large-format, and high-spectral-resolution IR image systems quite feasible. Moreover, the progress on VLSI techniques and detector fabrication technologies dramatically reduce complexity and cost of IR systems. The application of various developed technologies on the design of IR FPA's has resulted in the advantages of simplified electrical interconnection, reduced signal number leads through the dewar, higher performance reliability, and simplified package. Some commonly used structures of the three major classes of IR FPA's, namely, hybrid array, monolithic array, and pseudomonolithic array, are discussed below.

1) Hybrid Array: The most commonly used IR FPA structures in the hybrid array [37] are flip-chip and Z-plane technologies [38] as shown in Fig. 2(a) and (b), respectively. In Fig. 2(a), the IR detector array chip and silicon readout chip are compounded by the indium bump grown on the aligned pixels of both chips. This is the most used structure in the hybrid array technology. In the Z-plane technology shown in Fig. 2(b), the readout chips are stacked one on top of another and then the detector array is mounted to the third-dimensional plate on the edge. In the Z-plane structure, one readout chip is

SIONYX1403000018.0002

SAMSUNG EX. 1002 - 1521/4148

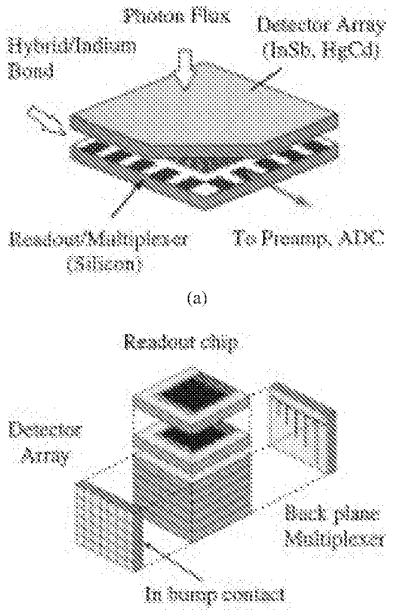

Fig. 2. The technologies of the hybrid array structures: (a) the flip-chip array technology [5] and (b) the Z-plane technology [4].

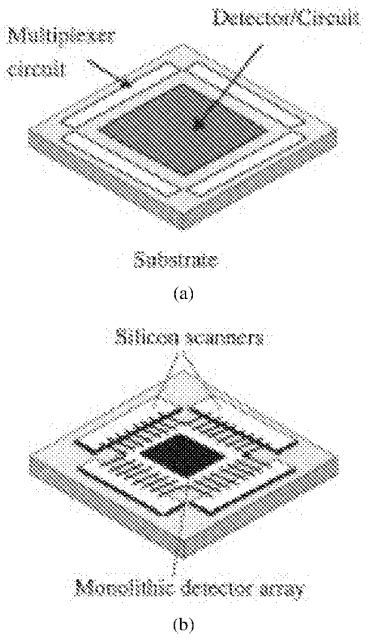

Fig. 3. (a) The structure of monolithic array technology [4] and (b) the structure of pseudomonolithic array technology [4].

used by one channel of detectors so that many electrical circuit techniques like complex input circuit, gain offset correction, A/D converter, filter, smart, and neural function, as well as image signal processing stage can be implemented on the readout chip [39]. However, the image resolution is limited by the readout chip thickness. In the application of hybrid array technology, uniformity of indium bumps, chip alignment, as well as thermal expansion effect and mechanical damage on the detectors should be considered during the hybridization process [40].

2) Monolithic Array: The monolithic array technology is currently developed to solve the hybrid process problems by building IR detectors like PtSi Schottky barriers [22], micromachining bolometers [41], [42], or extrinsic detectors on the silicon substrate [43]. Thus, both IR detectors and readout circuits can be fabricated in a monolithic chip as shown in Fig. 3(a). Both production and reliability of IR FPA's can be improved under monolithic design. However, the detector types and materials must be compatible with the silicon process. This limits the applications of the monolithic array on IR image systems.

3) Pseudomonolithic Array: As an alternative method to the indium-bumping hybrid array and monolithic array technologies, the readout chip and detector chip can be compounded through the via-hole technique [44], in the so-called pseudomonolithic array as shown in Fig. 3(b). Both readout chip surface and detector chip surface must be polished to achieve a precise flatness and parallelism before combining as a single chip. Then some detector fabrication processes and routing metallization processes are applied on the combined single chip. The pseudomonolithic technology retains some advantages of silicon-like processing, but its reliability still needs to be optimized.

B. Operational Requirements for IR FPA

In different applications of IR image systems, there exist certain specific requirements for the design of IR FPA's. In general, the requirements involve a broad range of electrical circuit and detector array parameters like detector bias control, injection efficiency, charge storage capacity, integration time, noise, dynamic range, readout rate, array size and pitch, power, and operating temperature. Some general discussions of these requirements are summarized below.

1) Detector Bias Control: The dark current, injection efficiency, detector $1/f$ noise, and reponsivity are affected by the detector bias. Moreover, operation ability and linearity of spectral response are also affected directly by the bias. Therefore, a strict and stable detector bias control is necessary in IR FPA's.

2) Injection Efficiency and Bandwidth: The injection efficiency is defined as the ratio of the current flowing into the readout circuit to the detector current. High injection efficiency and wide input bandwidth lead to good responsibility and readout performance. To achieve high injection efficiency and wide bandwidth, the input impedance of the interface circuit should be lower than the shunt resistance of IR detectors.

3) Charge Storage Capacity: In most readout structures of IR FPA's, the photon excited carriers are accumulated on the integrating capacitor and transferred to voltage outputs. Therefore, the charge storage capacity is determined by both background and dark current levels of IR detectors as well as the value of the integrating capacitor. Maximum charge

SIONYX1403000018.0003

SAMSUNG EX. 1002 - 1522/4148

storage capacity can be achieved by keeping background and dark currents small and by using a large integrating capacitor. However, the capacitance value is limited by pixel size and the chip area of readout circuit.

4) Noise: The temporal noise sources in IR FPA's include the photon noise, the detector noise, and the noise from readout electronics. The random and time-invariant noise source associated with the fabrication process of detectors and readout circuits is the fixed-pattern noise (FPN). Those noise sources contributed by readout electronics such as transistor white noise and reset noise (KTC or clocking noise) must be minimized so that their levels are below the background photon noise to achieve the BLIP. Generally, layout arrangement and circuit techniques can be used to reduce the noise level of readout circuits.

5) Dynamic Range: The dynamic range is defined as the ratio of maximum charge capacity to noise floor. The required dynamic range of IR FPA's is determined by the ratio of the brightest signal level to the weakest. Larger dynamic range is preferred but limited by storage capacitance, linearity, and noise level.

6) Readout Rate: The readout rate is chosen according to the specific IR system requirement and limited by the allowable chip power dissipation as well as the circuit operation speed. Usually a higher readout rate is needed for multiple sampling applications in image compensation function. Higher readout rate is also needed to avoid the saturation of the signal after integration.

7) Integration Time: Like the readout rate, the integration time is chosen according to the application consideration. Generally, the saturation frequency of the integrating capacitor and the detector sensitivity determine the proper length of integration time.

8) Array Size and Pitch: The array size and pitch are usually determined by the IR FPA technology. Higher image resolution requires larger array size and smaller pixel pitch. However, a larger pixel size is needed to increase the integration capacitance and improve the performance of charge capacity and dynamic range. Thus, the optimal design tradeoff should be made between the application flexibility and resolution performance.

9) Power Dissipation: This is a typical requirement in the applications of the IR FPA using a photon detector instead of a thermal detector. Power dissipation is limited by the heat loading of the cryogenic cooling system which determines the system cost.

10) Operating Temperature: The operating temperature is determined by the detected wavelength range and the material of IR detectors. For each detector, there is a unique operating temperature.

It is important to determine the operational requirements in the design of an IR FPA for specific applications. A complete analysis of operational parameters like IR background radiation level, spectral response band, operating temperature, detector structure, signal contrast ratio, sensitivity, and resolution should be set before the design tradeoff. Therefore, all the operational requirements discussed above have unique optimized orientations for IR image systems in different applications.

IV. CMOS Readout Techniques for IR Detectors

In the development of IR FPA's, the readout circuit electronics are the second major part next to the IR detector array. Readout electronics are deigned to support a good interface between IR detectors and the following signal processing stage. Different circuit techniques have been developed for IR FPA's with different materials and structures. In the following discussion, only the circuit techniques based on silicon CMOS VLSI technology are addressed.

Generally, the pixel pitch of IR FPA's is reduced with the increasing array size and resolution. Moreover, the total power dissipation of IR FPA's is limited by the image system. These two major factors often put constraints on circuit design space and complexity. Thus, the design of IR FPA readout electronics requires a tradeoff between circuit performance and complexity.

Some simple readout structures like source-follower per detector (SFD) [45], [46], direct injection (DI) [47]–[49], and gate-modulation input (GMI) [45], [50] are still commonly used in large staring IR FPA's because of the small pixel area and power consumption. In addition, more complex circuit techniques like buffered direct injection (BDI) [47], [51] and capacitive transimpedance amplifier (CTIA) [52], [53] have been developed to provide excellent bias control, high injection efficiency, linearity, and noise performance. Simple and high-performance circuit techniques have been a challenging work in the design of readout circuits for IR FPA's. Recently, some new readout structures like the share-buffered direct injection (SBDI) [54], [55], switch current integration (SCI) [56], and buffered gate modulation input (BGMI) [57], have been proposed to achieve better compromise between pixel pitch limitation and readout performance.

In the following, some of the commonly used CMOS readout techniques as well as the state-of-the-art structures will be presented. The noise reduction strategies used to improve IR image performance are also discussed.

A. Readout Circuits

1) Source-Follower Per Detector [45], [46]: A simple readout circuit called the source-follower per detector (SFD) is shown in Fig. 4 where an NMOS source-follower composed of MNI and MNL, a reset PMOS gate M-Rst, and a multiplexing NMOS device M-Sel are used in each cell. The integration capacitance is the summation of detector shunt capacitance C_{detector} and input node capacitance of the SFD. The integration capacitor is reset to high and then discharged by the photocurrent I_{detector}. After an integration period, the cell voltage signal is sampled to the output stage serially through the device M-Sel controlled by the clock *Select*. The simple structure of the SFD makes it suitable for the applications of high density, large format, and low power IR FPA. However, since the photon excited carrier charges are integrated on the input node capacitance of the detector directly, the detector bias voltage changes through integration.

SIONYX1403000018.0004

SAMSUNG EX. 1002 - 1523/4148

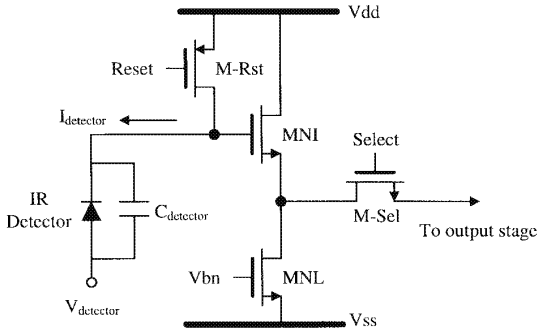

Fig. 4. The source follower per detector (SFD) readout circuit.

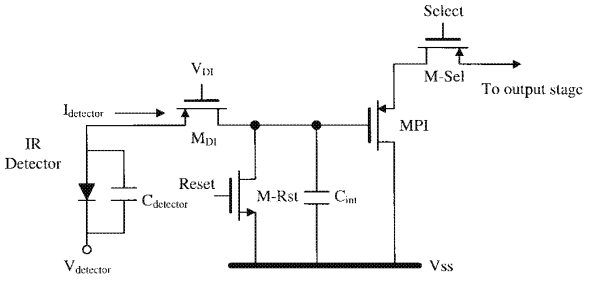

Fig. 5. The direct injection (DI) readout circuit.

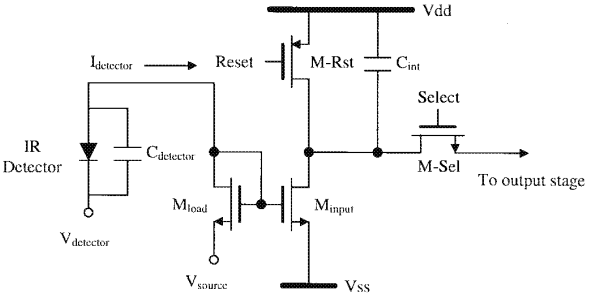

Fig. 6. The gate modulation input (GMI) readout circuit.

It can result in variations of detector characteristics and nonlinearity of readout current, which limit the application of SFD. Moreover, the SFD is susceptible to KTC noise induced by the integration-and-reset function and fixed pattern noise (FPN) caused by the process-dependent threshold voltage variations. Usually, a correlated double sampling (CDS) stage is used to reduce the KTC noise of the SFD readout circuit.

2) Direct Injection [47]–[49]: Another simple readout circuit called the direct injection (DI) is shown in Fig. 5. In the DI circuit, a common-gate PMOS device $M_{\rm DI}$ is used to bias and sense the current of the IR detector. The detector current $I_{\rm detector}$ passing through the gate $M_{\rm DI}$ is further integrated on the integration capacitor $C_{\rm int}$ which can be reset by the NMOS device M-Rst. The integrated voltage is readout through the PMOS source follower MPI and the multiplexing device M-Sel. In the DI circuit, a better bias control than the SFD during integration is supported by the common gate device $M_{\rm DI}$. Like the SFD circuit, the DI circuit has a simple structure and no active power dissipation. This makes it suitable for high-density IR FPA applications. The injection efficiency of a readout circuit is defined as the ratio of the current flowing into the readout circuit to the detector photocurrent $I_{\rm detector}$. The injection efficiency of the DI is determined by the ratio of detector shunt resistance to input resistance of $M_{\rm DI}$. Thus, a lower input resistance means a higher injection efficiency and better detectivity since the input resistance of the PMOS device $M_{\rm DI}$ is proportional to its overall current including the background current level. Thus, the DI is not suitable for the applications of low-background IR image readout. Moreover, a stable and low noise dc bias $V_{\rm DI}$ is needed in the DI circuit. Both threshold voltage nonuniformity and KTC noise are still problems of the DI readout circuit.

3) Gate-Modulation Input [45], [50]: The gate modulation input (GMI) readout circuit has a current-mirror configuration with the tunable source bias $V_{\rm source}$ to control the current gain as shown in Fig. 6. The injection current flowing into the master device $M_{\rm load}$ is mirrored and amplified by the slave device $M_{\rm input}$ and integrated on the integration capacitor $C_{\rm int}$ with the reset PMOS device M-Rst. The current gain of the current mirror $M_{\rm load}$ and $M_{\rm input}$ is tunable by the adjustable bias $V_{\rm source}$. Similar to that in the DI circuit, the injection efficiency of the GMI is dependent on the ratio of detector shunt resistance to input resistance of $M_{\rm load}$. However, the inherent current gain of the GMI leads to higher detection sensitivity and reduced input referred noise as compared to the DI. Moreover, the adaptive current gain in the GMI can be controlled by the background level and thus the realizable background suppression leads to a higher dynamic range. However, both injection efficiency and current gain of the GMI are sensitive to the variations of $V_{\rm source}$ and threshold voltages. To obtain a large total dynamic range in the GMI circuit, the current gain should be kept high and uniform. This leads to strict requirements on MOSFET threshold-voltage uniformity and dc bias stability of $V_{\rm source}$ which are difficult to be controlled.

4) Buffered Direct Injection [47], [51]: A complex readout circuit called the BDI circuit is shown in Fig. 7 where the circuit structure is similar to the DI except that an additional inverted gain stage with the gain $-A$ is connected between gate node of the common-gate input device $M_{\rm BDI}$ and detector node. The input impedance can be decreased by a factor of A due to the negative feedback structure. Thus, the injection efficiency is increased to near unity. Usually, the inverted gain stage can be implemented by a differential pair or inverter. The detector bias control of the BDI is more stable than those of SFD and DI due to the virtual-short property of the gain stage. Moreover, both equivalent input referred noise and operational bandwidth can also be improved as compared to the DI circuit. Since the detector bias is controlled by the input voltage $V_{\rm com}$ of the differential pair instead of $V_{\rm DI}$ and gate-to-source voltage of $M_{\rm DI}$ in the DI circuit, both the threshold voltage nonuniformity problem and strict low-noise bias requirement of the DI are immune. However, the additional gain stage consumes active power during integration. This additional power loading can be reduced by proper design of the gain

SIONYX1403000018.0005

SAMSUNG EX. 1002 - 1524/4148

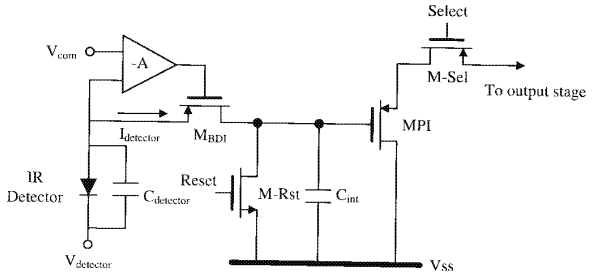

Fig. 7. The buffered direct injection (BDI) readout circuit.

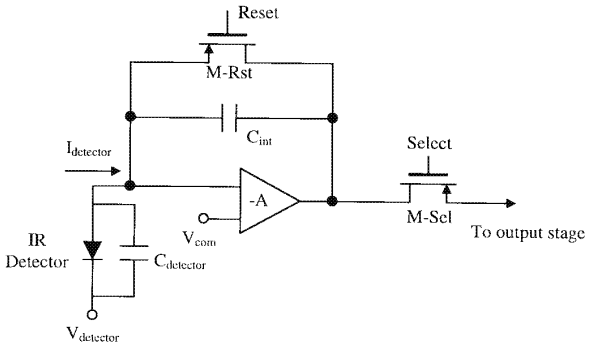

Fig. 8. The capacitive transimpedance amplifier (CTIA) readout circuit.

stage with low bias current. Generally, the BDI is suitable for those applications which require high readout performance and can afford additional circuit complexity, chip area, and power dissipation.

5) Capacitive Transimpedance Amplifier [52], [53]: The schematic of the capacitive transimpedance amplifier (CTIA) is shown in Fig. 8 where the integration capacitor $C_{\rm int}$ is placed on the feedback loop of the amplifier with a reset device M-Rst to discharge the integration capacitor and reset the amplifier output to the reference voltage $V_{\rm com}$. The detector bias is also controlled by $V_{\rm com}$ through the virtual-short feature of the amplifier. Thus, a good detector-bias control can be obtained in the CTIA as the BDI. Due to the Miller effect on the integration capacitor, its capacitance can be made extremely small to obtain low-noise and high-sensitivity performance. Unlike DI and BDI, the input impedance of the CTIA is independent of detector current. However, the feedthrough effect of the reset clock can be coupled to the detector node and affect the stability of both detector bias and amplifier operational point. Moreover, additional area and power consumption of the inverted gain stage are needed in the CTIA. Usually, the inverted gain stage is implemented by a differential amplifier to provide low detector bias offset and a CDS stage is used to eliminate the KTC noise.

6) Share-Buffered Direct Injection [54], [55]: Recently, an improved BDI readout circuit called the SBDI has been proposed. In the SBDI, the gain stage is implemented by the differential pair with the shared half circuit techniques as shown in Fig. 9. The differential pair consists of the common left-half circuit Mb, MNS, and MPS which is shared by all the cells in the same row and the two MOS devices MP and MN which are implemented in each cell circuit. The source node of MP and the gate node of MN are biased by the shared half circuit through two global lines. Under this arrangement, both chip area and power dissipation of the amplifier in the SBDI can be reduced to nearly 50% of those in BDI or CTIA circuits. But high injection efficiency, good detector bias control, threshold voltage variation immunity, and low noise performance of the BDI circuit can be maintained in the SBDI. In the SBDI circuit of Fig. 9, a dynamic discharging output stage is also introduced to save the static power dissipation and improve readout speed by applying a dynamic discharging gate MNDy and clock Dyrst. The discharging gate MNDy controlled by clock Dyrst is dynamically turned on to overcome the speed bottleneck of output stage at discharging phase and consumes only dynamic power. Generally, the SBDI can offer a better tradeoff between circuit area, power consumption, and circuit performance. This makes it more suitable for high density, large-array, and high-performance applications in IR FPA's.

7) Switch Current Integration [56]: A new readout structure called the SCI is shown in Fig. 10 where the integration capacitors are put outside the FPA and shared by the cells in the same column. The detector current $I_{\rm detector}$ is selected row by row, switched to the shared integration capacitor through the row select switch MR-Sel, and integrated. Thus, the structure performs the current switching and integration as its name implies. As shown in Fig. 10, the shared buffer technique is used to realize the gain stage of the SCI. Therefore, good performance of both SBDI and BDI can be retained in the SCI readout structure. The cascode current mirror M_1–M_4 acts as the current buffer before the select switch and offers a current mode gain determined by the dimension ratio of M_2 and M_4. This current gain can improve the detection sensitivity and reduce the input referred noise. When the row-select signal R-Sel is low, each cell in the same row is selected through MR-Sel and connected to the shared integration capacitor stage. The switched current is integrated on the shared capacitor and then sampled to the output stage through MC-Sel controlled by the column-select signal C-Sel. Since the integration capacitor is moved out of the cell circuit and the focal plane, the pixel size limitation of the readout circuit can be released. Moreover, both dynamic range and charge capacity can be increased by making a large integration capacitor along the column direction in the shared off-focal-plane integration capacitor stage. The integration time of the SCI readout structure is limited by one row processing time. This could lead to the reduced detection sensitivity. But the reduced sensitivity can be compensated by increasing the current gain of the current mirror.

8) Buffered Gate Modulation Input [57]: In the GMI circuit of Fig. 6, the amplified background current is integrated directly, and thus a large amount of charges must be accommodated within a unit cell. Under this situation, a large integrating capacitor is required to avoid saturation. However, the realization of a large capacitor is a problem in the design of high-density large IR FPA system. To solve this problem, the improved circuit of the GMI called the BGMI is proposed as shown in Fig. 11 where a current-mode background sup-

SIONYX1403000018.0006

SAMSUNG EX. 1002 - 1525/4148

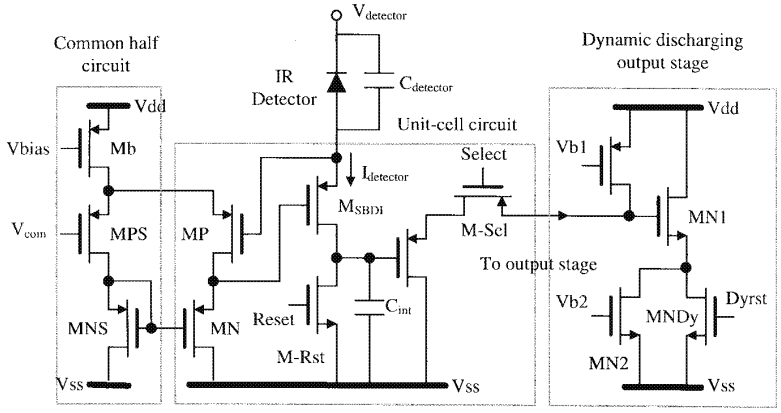

Fig. 9. The SBDI readout circuit with dynamic discharging output stage.

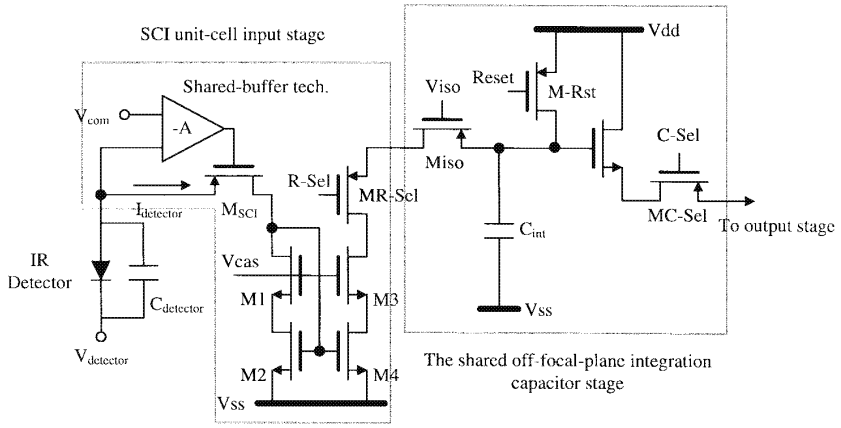

Fig. 10. The unit-cell input stage and off-FPA shared integration capacitor stage of the SCI readout structure.

pression circuit is incorporated with the SCI circuit to achieve higher dynamic range and better readout performance. Thus, a large integrating capacitor can be achieved. As shown in Fig. 11, the unit-cell circuit of the BGMI consists of a shared buffer as the input stage, the unbalance current mirror M_1 and M_2, and the row select switch $M_{\text{R-Sel}}$. The shared-buffer technique provides a good bias control for the IR detector, whereas the unbalance current mirror has a large current gain due to the threshold voltage difference between M_1 and M_2 caused by the intentional device channel-length unbalance. Through the use of the threshold voltage difference, the strict requirement of low- noise tunable dc source bias V_{source} in the GMI and the inevitable FPN due to the threshold voltage process dependent variation can be avoided.

As shown in Fig. 11, the detector current is switched from the BGMI unit-cell input stage to the shared off-FPA integration capacitor stage. In the shared integration capacitor stage, the amplified current from the cell is mirrored through a cascade current mirror and subtracted by a dc tunable current before being integrated on the capacitor C_{int}. Thus, the current-mode background suppression is achieved. To generate the dc tunable current, the threshold-voltage compensated current source [5] M_{B1}, M_{B2}, and M_{B3} is used with the adjustable voltage V_{Tune} added to the source node of M_{B2}. This current source can generate a dc current nearly independent of MOS threshold voltages. Thus, the background pedestal removal of IR FPA readout with good immunity from threshold-voltage variations can be achieved. The resultant input referred spatial noise is relatively small and the strict requirement of threshold-voltage uniformity can be released. The suppression current is also adjustable through the voltage V_{Tune}. After the background suppression, the signal current is integrated on the integration capacitor, and the integrated signal voltage is alternatively sampled to the common output stage through the P-type source follower as a buffer.

Since only one row of the integration capacitor stage is needed in the whole chip and the infrared background current is low, the additional power dissipation of background suppression circuits is still tolerable. The good readout performance and adaptive gain control make BGMI suitable for the IR FPA readout applications with large background level range.

B. Noise Reduction of IR Image

Temporal noise and pattern noise are two main noise types of IR image systems. The temporal noise sources include shot, thermal, $1/f$ (flicker), generation-recombination, KTC,

SIONYX1403000018.0007

SAMSUNG EX. 1002 - 1526/4148

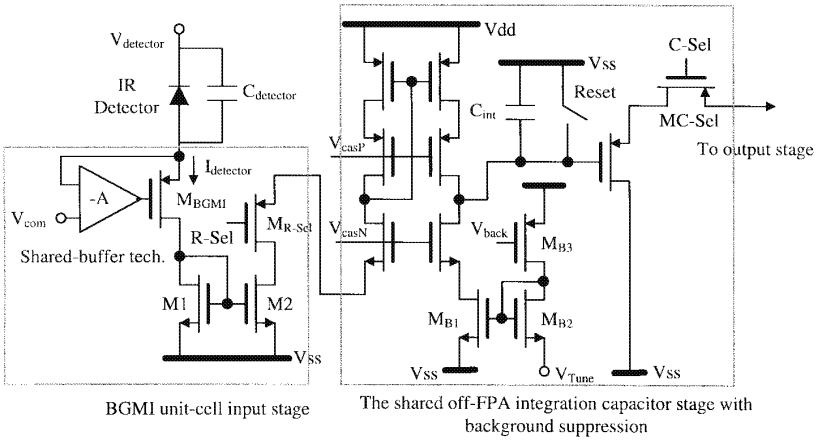

Fig. 11. The BGMI readout structure with adaptive current gain control and background suppression.

and photon noise which are contributed by detectors and readout circuits. The pattern noise is caused by the process dependent variations which produce offset drifts among detector channels. Usually, the temporal noise can be reduced by detector technology, operational condition, circuit techniques, and system arrangement, whereas the fixed pattern noise can be reduced by calibration techniques [59], [60]. The two-point and multipoint calibrations are commonly used to reduce the FPN [16], [61]. The required number of calibration points is dependent on the infrared radiation determined by the range of object temperature variations. A larger radiation means a larger output voltage swing and more nonuniformity of response. For the same range of temperature variations, the infrared radiation of the MWIR detector is larger than that of the LWIR detector. Thus, the number of calibration points of MWIR readout is usually more than that of LWIR readout. The noise sources contributed by readout circuits should be carefully reduced to achieve a BLIP. Some general strategies of noise reduction for readout circuits like CDS [62], modified CDS [63], multiple correlated sample read (MCS) [64], and chopper-stabilized input circuit (CSI) [65] have been proposed.

V. Future Directions

In the future, the performance of thermal imaging systems with cooled or uncooled FPA technologies will be further enhanced by the development of new detection methodologies and signal processing techniques. Moreover, the concept of military and commercial dual-use technology in IR imaging systems will lead to the cost-driven and application-oriented development. In this section, some advanced development directions on IR imaging systems such as on-FPA signal processing, optical link, background suppression, and smart-FPA concept are discussed briefly.

A. On-Chip A/D Conversion

The on-chip A/D conversion is an advanced circuit technology which is applied to IR FPA chips more recently [66], [67]. Through the conversion, instead of analog, the digital output signal of IR FPA chips avoids noise coupling during the transfer out of cooling systems and dewars. Thus, the system design can be simplified and the cables and IC chip counts can be reduced. However, the additional power and area consumption on the FPA may not be acceptable in some applications. Thus, the on-chip A/D conversion is usually used in high-performance scanning array applications. Some new structures of on-chip A/D conversion have been proposed for the design of staring arrays by using sigma–delta modulation or semi-parallel architectures [68].

B. Optical Link

The loading of cable capacitance in a readout chip, the loading of parasitic heat from thermal detectors, and the noise coupling effect degrade the system performance seriously. This can be improved by optical link techniques [69]. An analog optical modulator on the FPA is designed to transfer output signals to the laser diodes outside the dewar through optical fibers. In this configuration, all the noise, loading, and coupling effects of the conventional cables can be avoided. The optical signals can also be digitized before sending to the optical link. This can further improve performance at the expense of additional power dissipation.

C. Background Suppression

The background suppression is used to improve detection sensitivity, dynamic range, and application range. High background charges could saturate the finite integration capacitance and cause malfunction of IR image systems. Typically, the background suppression is done in the charge domain which cannot solve the above problem. New current-mode background suppression like BGMI described above and current memory structure [68] have been proposed to achieve a better performance of IR image readout.

D. Smart Focal Plane Array

The on-FPA signal processing technologies are used to support a front-end signal processing which can significantly reduce the downstream system loading and improve readout performance [70], [71]. Some smart functions such as

SIONYX1403000018.0008

SAMSUNG EX. 1002 - 1527/4148

bad pixel substitution [72], pixel averaging [73], and neural-FPA concept [74] have been introduced in the IR FPA. The bad pixel substitution by using quad-cell readout and pixel averaging techniques can improve both yield and signal-to-noise ratio of FPA's [72]. Neural network concept can be applied to achieve the on-chip image extraction and motion detection. Recently, a new sensing structure has been proposed to implement CMOS silicon retina systems using multi-emitter bipolar junction transistors (BJT's) [75]. The new BJT-based silicon retina can perform some smart functions like edge detection, pattern recognition, and motion detection in simple and compact detector arrays [76]. Thus, it is suitable for the development of IR smart FPA. Other image processing functions including contrast and quality enhancement, image compensation, and nonlinearity fix may be implemented on-chip to achieve smart FPA's. The development of smart functions can satisfy the needs of IR image applications in system performance, productivity, availability, and specific requirement.

VI. Summary

In this paper, IR detectors, FPA structures and requirements, CMOS readout techniques, and the future development trend of IR imaging systems are presented and discussed. All the structures and technologies discussed above have their uniqueness and features for different applications. Due to the development of commercial uncooled IR imaging systems and the fast advancement of submicrometer CMOS technologies, a high-performance and low-cost IR imaging system will be developed through the inventions of new circuit techniques and structure. Moreover, the emerging technologies of CMOS visible-light imaging systems [77]–[80] will share the advantages of the developed IR imaging systems due to their similarities. Both will be driven by rapid development and wide applications of multimedia systems. A new generation of CMOS imaging systems is highly expected.

Acknowledgment

The authors would like to thank their colleagues at the Chung Shang Institute of Science and Technology and the Chip Implementation Center of the National Science Council for their valuable discussions, suggestions, and support.

References

[1] R. J. Dempsey, D. G. Davis, R. G. Jr. Buice, and R. A. Lodder, "Biological and medical applications of near infrared spectrometry," *Appl. Spectr.,* vol. 50, no. 2, pp. 18A–34A, Feb. 1996.

[2] N. Itoh, K. Yanagisawa, T. Ichikawa, K. Tarusawa, and H. Kataza, "Kiso observatory near-infrared camera with a large format array," in *Proc. SPIE, Infrared Technology XXI,* 1995, vol. 2552, pp. 430–437.

[3] D. C. Murphy, S. E. Persson, M. A. Pahre, A. Sivaramakrishnan, and S. G. Djorgovski, "An infrared camera for the Palomar Observatory 60-inch telescope," *Publications Astronomical Soc. of the Pacific,* vol. 107, pp. 1234–1242, 1995.

[4] D. A. Scribner, M. R. Kruer, and J. M. Killiany, "Infrared focal-plane array technology," *Proc. IEEE,* vol. 79, no. 1, pp. 66–85, 1991.

[5] E. R. Fossum and B. Pain, "Infrared readout electronics for space science sensors: State of the art and future directions," in *Infrared Technology XIX, Proc. SPIE 2020,* 1993, pp. 262–285.

[6] L. S. Johns, "Dual-use technology programs," in *Infrared Technology XX, Proc. SPIE 2269,* 1994, pp. 2–7.

[7] R. K. Kirshchman, *Low-Temperature Electronics.* New York: IEEE Press, 1989.

[8] E. L. Dereniak and D. G. Crowe, *Optical Radiation Detectors.* New York: Wiley, 1984.

[9] L. J. Kozlowski, J. M. Arias, and W. E. Tennant, "Experimental comparison of staring IR sensor technologies including PV HgCdTe, PV InGaAs, and quantum well GaAs/AlGaAs," in *Solid State Crystals: Materials Science and Applications, Proc. SPIE,* Oct. 1994, vol. 2373, pp. 354–360.

[10] C. Hanson, "Uncooled thermal imaging at Texas Instruments," in *Infrared Technology XIX, Proc. SPIE,* July 1993, vol. 2020, pp. 330–339.

[11] J. Koepernik, H. Budzier, and G. Hofmann, "Influence of nonideal chopper design on nonuniformity in uncooled pyroelectric staring array systems," in *Infrared Technology XXI, Proc. SPIE,* July 1995, vol. 2552, pp. 624–635.

[12] L. Goldminz, B. Sabbah, Z. M. Friedman, and Y. Nemirovsky, "Mercury-cadmium-telluride photovoltaic and photoconductive focal-plane arrays," *Opt. Eng.,* vol. 32, pp. 952–957, May 1993.

[13] H. Zogg, A. Fach, C. Maissen, J. Masek, and S. Blunier, "Photovoltaic lead-chalcogenide on silicon infrared sensor arrays," *Opt. Eng.,* vol. 33, pp. 1440–1449, May 1994.

[14] H. Zogg, A. Fach, J. John, J. Masek, P. Muller, C. Paglino, and S. Blunier, "Photovoltaic IV–VI on Si infrared sensor arrays for thermal imaging," *Opt. Eng.,* vol. 34, pp. 1964–1969, July 1995.

[15] R. L. Petritz, "Fundamentals of infrared detectors," *Proc. IRE,* vol. 47, pp. 1458–1467, 1959.

[16] H. Zogg, A. Fach, J. John, J. Masek, P. Muller, C. Paglino, and W. Buttler, "Pb/sub 1-x/Sn/sub x/Se-on-Si LWIR thermal imaging system," in *Infrared Technology XXI, Proc. SPIE,* July 1995, vol. 2552, pp. 404–410.

[17] V. Gopal, "Spatial noise limited NETD performance of a HgCdTe hybrid focal plane array," *Infrared Phys., Technol.,* vol. 37, pp. 313–320, 1996.

[18] L. J. Kozlowski, J. M. Arias, and W. E. Tennant, "Experimental comparison of staring IR sensor technologies including PV HgCdTe, PV InGaAs, and quantum well GaAs/AlGaAs," in *Solid State Crystals: Materials Science and Applications, Proc. SPIE,* Oct. 1994, vol. 2373, pp. 354–360.

[19] J. Wolf, "Low-background far-infrared detectors and arrays," *Opt. Eng.,* vol. 33, pp. 1492–1500, May 1994.

[20] T. Seto, A. Mori, R. Ishigaki, S. Itoh, N. Yutani, M. Kimata, N. Tubouchi, A. Akiyama, and T. Sasaki, "Performance of 1M-IRCSD imager with PtSi Schottky-barrier detectors," in *Infrared Technology XIX, Proc. SPIE,* July 1993, vol. 2020, pp. 404–414.

[21] A. Akiyama, T. Sasaki, T. Seto, A. Mori, R. Ishigaki, S. Itoh, N. Yutani, M. Kimata, and N. Tubouchi, "1040 × 1040 infrared charge sweep device imager with PtSi Schottky-barrier detectors," *Opt. Eng.,* vol. 33, pp. 64–71, Jan. 1994.

[22] M. Kimata, H. Yagi, N. Yutani, K. Endo, and M. Nunoshita, "Schottky-barrier infrared focal plane arrays," *J. Japan Soc. Infrared Sci. Technol.,* vol. 5, pp. 33–42, 1995.

[23] H. Yagi, N. Yutani, J. Nakanishi, M. Kimata, M. Nunoshita, T. Seto, and M. Kamei, "Monolithic photovoltaic IV–VI-on-Si infrared sensor array with integrated readout electronics," *IEEE Trans. Electron Devices,* vol. 39, p. 2676, Nov. 1992.

[24] ———, "Monolithic Schottky-barrier infrared image sensor with 71% fill factor," *Opt. Eng.,* vol. 33, pp. 1454–1460, 1994.

[25] M. Kimata, H. Yagi, N. Yutani, K. Endo, and M. Nunoshita, "1040 × 1040 infrared charge sweep device imager with PtSi Schottky-barrier detectors," *Opt. Eng.,* vol. 33, pp. 64–71, 1994.

[26] R. L. Petritz, "Blocking injected dark current in impurity-band-conduction photodetectors using a PtSi Schottky barrier," *Appl. Phys. Lett.,* vol. 67, pp. 774–776, 1995.

[27] N. M. Shorrocks, A. Patel, M. J. Walker, and A. D. Parsons, "Uncooled pyroelectric arrays for contactless temperature measurements," in *Smart Focal Plane Arrays and Focal Plane Array Testing, Proc. SPIE,* 1995, vol. 2474, pp. 98–109.

[28] ———, "Integrated thin film PZT pyroelectric detector arrays," *Microelectron. Eng.,* vol. 29, pp. 59–66, 1995.

[29] P. W. Kruse, "Uncooled IR focal plane arrays," in *Infrared Technology XXI, Proc. SPIE,* July 1995, vol. 2552, pp. 556–563.

[30] N. Neumann, R. Kohler, R. Gottfried-Gottfried, and N. Hess, "Pyroelectric sensors and arrays based on P(VDF/TrFE) copolymer films," in *Seventh Int. Symp. Integrated Ferroelectrics,* Mar. 1995, vol. 11, pp. 1–14.

[31] N. M. Shorrocks, A. Patel, M. J. Walker, and A. D. Parsons, "Integrated thin film PZT pyroelectric detector arrays," in *1st European Meeting on Integrated Ferroelectrics,* July 1995, vol. 29, pp. 59–66.

[32] N. Butler, R. Blackwell, R. Murphy, R. Silva, and C. Marshall, "Low cost uncooled microbolometer imaging system for dual use," in *Infrared Technology XXI, Proc. SPIE,* July 1995, vol. 2552, pp. 583–591.

SIONYX1403000018.0009

SAMSUNG EX. 1002 - 1528/4148

[33] A. Tanaka, S. Matsumoto, N. Tsukamoto, S. Itoh, T. Endoh, A. Nakazato, Y. Kumazawa, M. Hijikawa, H. Gotoh, T. Tanaka, and N. Teranishi, "Silicon IC process compatible bolometer infrared focal plane array," in *8th Int. Conf. Solid-State Sensors and Actuators and Eurosensors IX,* 1995, vol. 2, pp. 632–635.
[34] N. Bluzer and M. G. Forrester, "Superconducting quantum detectors," *Opt. Eng.,* vol. 33, pp. 697–703, Mar. 1993.
[35] B. R. Johnson, M. C. Foote, H. A. Marsh, and B. D. Hunt, "IEpitaxial YBa/sub 2/Cu/sub 3/O/sub 7/ superconducting infrared microbolometers on silicon," in *Advanced Microdevices and Space Science Sensors, Proc. SPIE,* July 1994, vol. 2267, pp. 24–30.
[36] F. M. Tong, N. M. Ravindra, L. Ganapathi, S. Giles, and R. Rao, "High T/sub c/ YBa/sub 2/Cu/sub 3/O/sub 7-delta/superconducting transition-edge microbolometers," *Infrared Phys. Technol.,* vol. 36, pp. 1053–1058, Dec. 1995.
[37] D. H. Pommerenig, D. D. Enders, and T. E. Meinhardt, "Hybrid silicon focal plane array development: An update," in *Proc. Society Pho-Opt. Instrumentation Engineering,* vol. 267, pp. 23–30, 1981.
[38] J. C. Carson, "Application of advanced 'Z' technology focal plane architectures," in *Proc. Society Pho-Opt. Instrumentation Engineering,* 1988, vol. 930, pp. 164–182.
[39] E. T. Young, M. Scutero, G. H. Rieke, E. E. Haller, and J. W. Beeman, "High performance Ge:Ga arrays for the far infrared," in *Infrared Detectors and Instrumentation, Proc. SPIE,* Apr. 1993, vol. 1946, pp. 68–77.
[40] V. Gopal, "Spatial noise limited NETD performance of a HgCdTe hybrid focal plane array," *Infrared Phys. Technol.,* vol. 37, pp. 313–320, Apr. 1996.
[41] M. Ueno, O. Kaneda, T. Ishikawa, K. Yamada, A. Yamada, M. Kimata, and M. Nunoshita, "Monolithic uncooled infrared image sensor with 160 × 120 pixels," in *Infrared Technology XXI, Proc. SPIE,* July 1995, vol. 2552, pp. 636–643.
[42] A. Tanaka, S. Matsumoto, N. Tsukamoto, S. Itoh, T. Endoh, A. Nakazato, Y. Kumazawa, M. Hijikawa, H. Gotoh, T. Tanaka, and N. Teranishi, "Silicon IC process compatible bolometer infrared focal plane array," in *8th Int. Conf. Solid-State Sensors and Actuators and Eurosensors IX, Dig. Tech. Papers,* 1995, vol. 2, pp. 632–635.
[43] J. Wolf, "Low-background far-infrared detectors and arrays," *Opt. Eng.,* vol. 33, pp. 1492–1500, May 1994.
[44] I. M. Baker and R. A. Ballingall, "Photovoltaic CdHgTe-silicon hybrid focal planes," in *Proc. Society Pho-Opt. Instrumentation Engineering,* 1984, vol. 510, pp. 121–129.
[45] A. M. Fowler, R. G. Probst, J. P. Britt, R. R. Joyce, and F. C. Gillett, "Evaluation of an indium antimonide hybrid focal plane array for ground-based infrared astronomy," *Opt. Eng.,* vol. 26, pp. 232–240, 1987.
[46] N. Lum, J. Asbrock, R. White, R. Kelchner, L. Lum, L. Pham, C. McCreight, M. McKelvey, R. Jr. McMurray, W. Forrest, and J. Garnett, "Low-noise, low-temperature, 256 × 256 Si:As IBC staring FPA," in *Infrared Detectors and Instrumentation, Proc. SPIE,* Apr. 1993, vol. 1946, pp. 100–109.
[47] N. Bluzer and R. Stehlik, "Buffered direct injection of photocurrents into charge coupled devices," *IEEE Trans. Electron Devices,* vol. 25, no. 2, pp. 160–166, 1978.
[48] J. T. Longo, D. T. Cheung, A. M. Andrewheung, A. M. Andrews, C. C. Wang, and J. M. Tracy, "Infrared focal planes in intrinsic semiconductors," *IEEE Trans. Electron Devices,* vol. 25, no. 2, 1978.
[49] K. Chow, J. P. Rode, D. H. Seib, and J. D. Blackwell, "Hybrid infrared focal-plane arrays," *IEEE Trans. Electron Devices,* vol. 29, no. 1, 1982.
[50] L. J. Kozlowski, W. V. McLevige, S. A. Cabelli, A. H. B. Vanberwyck, D. E. Cooper, E. R. Blazejewski, K. Vural, and W. E. Tennant, "Attainment of high sensitivity at elevated operating temperatures with staring hybrid HgCdTe-on-Sapphire focal plane arrays," *Opt. Eng.,* vol. 33, no. 3, pp. 704–715, 1994.
[51] P. Norton, "Infrared image sensors," *Opt. Eng.,* vol. 30, no. 11, pp. 1649–1660, 1991.
[52] L. Kozlowski, S. Cabelli, R. Kezer, and W. Kleinhans, "10 × 132 CMOS/CCD readout with 25 μm pitch and on-chip signal processing including CDS and TDI," in *Infrared Readout Electronics, Proc. SPIE,* 1992, vol. 1684, pp. 222–230.
[53] C. Staller, L. Ramiirez, C. Niblack, M. Blessinger, and W. Kleiinhans, "A radiation hard, low background multiplexer design for spacecraft imager applications," in *Infrared Readout Electronics, Proc. SPIE,* 1992, vol. 1684, pp. 175–181.
[54] C. Y. Wu, C. C. Hsieh, F. W. Jih, T. P. Sun, and S. J. Yang, "A new share-buffered direct-injection readout structure for infrared detector," in *Infrared Technology XIX, Proc. SPIE,* 1993, vol. 2020, pp. 57–64.
[55] C. Y. Wu and C. C. Hsieh, "New design techniques for a complementary metal-oxide semiconductor current readout integration circuit for infrared detector arrays," *Opt. Eng.,* vol. 34, no. 1, pp. 160–168, Jan. 1995.
[56] C. C. Hsieh, C. Y. Wu, F. W. Jih, T. P. Sun, and S. J. Yang, "A new switch-current integration readout structure for infrared focal plane array," in *Infrared Technology XX, Proc. SPIE,* July 1994, vol. 2269, pp. 718–726.
[57] C. C. Hsieh, C. Y. Wu, F. W. Jih, T. P. Sun, and H. Chang, "A new CMOS readout circuit design for the IR FPA with adaptive gain control and current-mode background suppression," in *IEEE Proc. ISCAS'96,* May 1996, vol. 1, pp. 137–140.
[58] S. Y. Chin and C. Y. Wu, "A 10-b 125-MHz CMOS digital-to-analog converter (DAC) with threshold-voltage compensated current sources," *IEEE J. Solid-State Circuits,* pp. 1374–1380, Nov. 1994.
[59] M. D. Nelson, J. F. Johnson, and T. S. Lomheim, "General noise processes in hybrid infrared focal plane arrays," *Opt. Eng.,* vol. 30, no. 11, pp. 1682–1700, 1991.
[60] I. M. Mason, P. H. Sheather, J. A. Bowles, and G. Davies, "Blackbody calibration sources of high accuracy for a spaceborne infrared instrument: The along track scanning radiometer," *Appl. Opt.,* vol. 35, no. 4, pp. 629–639, 1996.
[61] A. Lambrecht, M. Tschirschwitz, R. Grisar, U. Schiessl, J. Wolf, and D. Lemke, "Sub-threshold operated lead-salt lasers for calibration of IR-astronomy detectors," *Infrared Phys. Technol.,* vol. 37, no. 1, pp. 173–179, 1996.
[62] R. J. Kansy, "An response of a correlated double sampling circuit to $1/f$ noise," *IEEE J. Solid-State Circuits,* vol. 15, pp. 373–375, 1980.
[63] H. M. Wey and W. Guggenbuhl, "An improved correlated double sampling circuit for low noise charge-couple devices," *IEEE J. Solid-State Circuits,* vol. 37, no. 12, pp. 1559–1565, 1990.
[64] E. T. Young, M. Scutero, G. Rieke, T. Milner, F. J. Low, P. Hubbard, J. Davis, E. E. Haller, and J. Beeman, "Far-infrared focal plane development for SIRT," in *Infrared Readout Electronics, Proc. SPIE,* Apr. 1992, vol. 1684, pp. 63–74.
[65] A. Lockwood and W. Parrish, "Predicted performance of indium antimonide focal plan arrays," *Opt. Eng.,* vol. 26, no. 3, pp. 228–231, 1987.
[66] W. J. Mandl, "Focal plane analog-to-digital conversion development," in *Smart Focal Plane Arrays and Focal Plane Array Testing, Proc. SPIE,* Apr. 1995, vol. 2474, pp. 63–71.
[67] U. Ringh, C. Jansson, C. Svensson, and K. Liddiard, "CMOS analog to digital conversion for uncooled bolometer infrared detector arrays," in *Smart Focal Plane Arrays and Focal Plane Array Testing, Proc. SPIE,* Apr. 1995, vol. 2474, pp. 88–97.
[68] B. Pain, S. Mendis, R. Schober, R. Nixon, and E. Fossum, "Low-power, low-noise analog circuits for on focal-plane signal processing of infrared sensors," in *Infrared Detectors and Instrumentation, Proc. SPIE,* 1993, vol. 1946, pp. 365–374.
[69] A. R. Johnston, D. T. H. Liu, S. Forouhar, G. F. Lutes, J. Maserjian, and E. R. Fossum, "Optical links for cryogenic focal-plane array readout," in *Infrared Detectors and Instrumentation, Proc. SPIE,* 1993, vol. 1946, pp. 375–383.
[70] P. Bauer, L. Audaire, P. Rambaud, M. Pirot, F. Bauer, and J. Simonne, "On the way to a smart infrared sensor," *ESSCIRC'95, 21st European Solid-State Circuits,* Sept. 1995, pp. 330–333.
[71] C. Jansson, U. Ringh, and K. Liddiard, "On-chip analog-to-digital conversion suitable for uncooled focal plane detector arrays employed in smart IR sensors," in *Smart Focal Plane Arrays and Focal Plane Array Testing, Proc. SPIE,* Apr. 1995, vol. 2474, pp. 72–87.
[72] R. Cannata, "Introduction to infrared focal plane electronics," *The SPIE Short Course Note,* San Diego, CA, July 1993.
[73] R. Panicacci, S. Kemeny, L. Matthies, B. Pain, and E. R. Fossum, "Programmable multiresolution CMOS active pixel sensor," in *Int. Soc. Optical Engineering, Proc. SPIE,* Feb. 1996, vol. 2654, pp. 72–79.
[74] H. H. Thodberg, "Review of bayesian neural networks with an application to near-infrared spectroscopy," *IEEE Trans. Neural Networks,* vol. 7, no. 1, pp. 56–72, 1996.
[75] C. Y. Wu and C. F. Chiu, "A new structure of the 2-D silicon retina," in *IEEE J. Solid-State Circuits,* vol. 30, pp. 890–897, Aug. 1995.
[76] C. F. Chiu and C. Y. Wu, "The design of rotation-invariant pattern recognition using the silicon retina," *IEEE J. Solid-State Circuits,* vol. 32, pp. 526–534, Apr. 1997.
[77] R. H. Nixon, S. E. Kemeny, C. O. Staller, and E. R. Fossum, "256 × 256 CMOS active pixel sensor camera-on-a chip," in *ISSCC Dig. Tech. Papers,* 1996, pp. 178–179.
[78] C. H. Aw and B. A. Wooley, "A 128 × 128-pixel standard-CMOS image sensor with electronic shutter," in *ISSCC Dig. Tech. Papers,* 1996, pp. 180–181.

SIONYX1403000018.0010

SAMSUNG EX. 1002 - 1529/4148

[79] A. Bakker and J. H. Huijsing, "Micropower CMOS temperature sensor with digital output," in *IEEE J. Solid-State Circuits,* vol. 31, no. 7, pp. 933–937, 1996.
[80] K. S. Szajda, C. G. Sodini, and H. F. Bowman, "A Low-noise, high-resolution silicon temperature sensor," *IEEE J. Solid-State Circuits,* vol. 31, no. 9, pp. 1308–1313, 1996.

Chih-Cheng Hsieh was born in Taichung, Taiwan, R.O.C., in 1967. He received the B.S. degree from the Department of Electronics Engineering, National Chiao-Tung University, Hsinchu, Taiwan, in 1990.

Since 1991, he has been working toward the Ph.D. degree at the Institute of Electronics, National Chiao-Tung University, Hsinchu, Taiwan. His research interests include analog integrated circuits and system design and infrared readout integrated circuits design.

Chung-Yu Wu (M'75–SM'96), for a photograph and biography, see this issue, p. 574.

Far-Wen Jih was born on February 25, 1961 in Taiwan. He received the B.S. and M.S. degrees in electronics engineering from National Chiao-Tung University, Hsinchu, Taiwan, in 1983 and 1985, respectively.

He is currently an Assistant Scientist at the Opto-Electronics Devices Section in Chung-Shang Institute of Science & Technology, Taiwan. His research interests include infrared device readout technology, image readout IC design, and thermal image system.

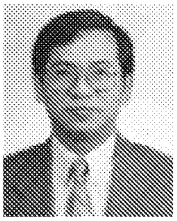

Tai-Ping Sun was born in Taiwan in 1950. He received the B.S. degree in electrical engineering from Chung Cheng Institute of Technology, Taiwan, in 1974, the M.S. degree in material science engineering from National Tsing Hua University, Taiwan, in 1977, and the Ph.D. degree in electrical engineering from National Taiwan University, Taiwan, in 1990.

He joined the Material Science & Research Center, Chung Shan Institute, Taiwan, in 1977. Until 1987, he was engaged in the development of infrared devices and circuits and systems since 1990. He is currently a Section Head of Opto-Electronic Devices of Material R&D Center of CSIST in charge of infrared FPA detectors and imaging systems.

SIONYX1403000018.0011

SAMSUNG EX. 1002 - 1530/4148

SOLAR CELLS

From Basics to Advanced Systems

SCIENTIFIC LIBRARY
JUN 14 1984
PAT. & T.M. OFFICE

Chenming Hu
Richard M. White
University of California, Berkeley

Harman,
, Ronald A.
nan, John G.

McGraw-Hill Book Company

New York St. Louis San Francisco Auckland Bogotá Hamburg
Johannesburg London Madrid Mexico Montreal New Delhi
Panama Paris São Paulo Singapore Sydney Tokyo Toronto

SIONYX1403000018.0012

SAMSUNG EX. 1002 - 1531/4148

TK
2960
H8
1983
c.2

This book was set in Times Roman by Interactive Composition Corporation.
The editor was T. Michael Slaughter;
the production supervisor was Leroy A. Young.
The cover was designed by Mark Wieboldt.
Project supervision was done by Joan Stern of Interactive Composition Corporation.
Halliday Lithograph Corporation was printer and binder.

SOLAR CELLS
From Basics to Advanced Systems

Copyright © 1983 by McGraw-Hill, Inc. All rights reserved. Printed in the United States of America. Except as permitted under the United States Copyright Act of 1976, no part of this publication may be reproduced or distributed in any form or by any means, or stored in a data base or retrieval system, without the prior written permission of the publisher.

1 2 3 4 5 6 7 8 9 0 HALHAL 8 9 8 7 6 5 4 3

ISBN 0-07-030745-8

Library of Congress Cataloging in Publication Data

Hu, Chenming.
Solar cells.

(McGraw-Hill series in electrical engineering.
Power, and energy)
Includes bibliographies and index.
1. Solar cells. I. White, Richard M., date
II. Title. III. Series.
TK2960.H8 1983 621.31'244 83-975

Pref

Part 1 Sola

1 Ove
Box:
1.1 How
1.2 Types
1.3 How
Refer
Proble

2 Natu
2.1 The S
Box:
2.2 Atmo
2.3 Solar
2.4 Geog
2.5 Effect
2.6 Sumn
Refer
Proble

3 Princ
3.1 Eleme
3.2 Semic

SIONYX1403000018.0013

SAMSUNG EX. 1002 - 1532/4148

In this chapter we shall explore the principles of operation, the electrical characteristics, and the limits of efficiency of solar cells. Silicon *pn*-junction solar cells will often be used as examples, but the principles presented here are general. The choices of cell materials and structures will be discussed in more detail in later chapters.

Mathematics is kept to a minimum in this chapter. The occasional long equations are included for reference purposes and may be bypassed by the reader. It is hoped that a conceptual, physical, and intuitive understanding of the operation of solar cells will emerge from studying this chapter. For more rigorous, mathematical, and formal treatments of this subject, readers should consult technical journals or other books, for example, Hovel (1975).

3.1 ELEMENTS OF SOLAR CELL OPERATION

Figure 3.1 illustrates the basic operation of a solar cell. Light photons are absorbed by the semiconductor and in the process generate electric-charge carriers called *electrons* and *holes*. Electrons and holes diffuse to a "junction," either a *pn* junction as illustrated in Fig. 3.1 or some other type of junction where a strong internal electric field exists. Electrons and holes are separated by the field and give rise to electric voltage and current in the external circuit. This scenario involves several topics that will now be discussed individually: semiconductors, light absorption and carrier generation, *pn* junction, cell current, cell voltage, and efficiency of energy conversion.

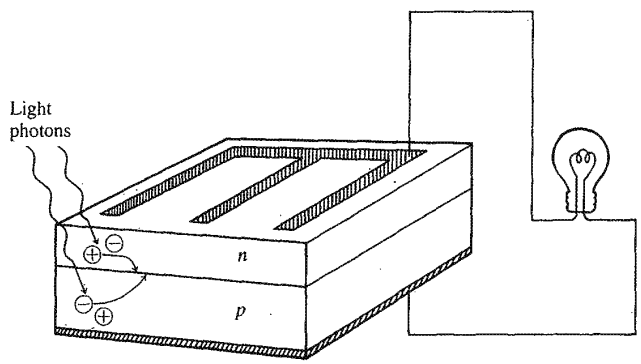

Figure 3.1 Positive and negative charge carriers are generated in a semiconductor as light photons are absorbed. These carriers, when collected by a *pn* junction, give rise to an electric current in the external circuit. Here, the current is shown to power a light bulb.

SIONYX1403000018.0014

SAMSUNG EX. 1002 - 1533/4148

Microstructured silicon photodetector

Zhihong Huang
Microelectronics Research Center, Department of Electrical and Computer Engineering, The University of Texas at Austin, Austin, Texas 78758

James E. Carey
Department of Physics, Harvard University, Cambridge, Massachusetts 02138 and Division of Engineering and Applied Sciences, Harvard University, Cambridge, Massachusetts 02138

Mingguo Liu and Xiangyi Guo
Department of Electrical and Computer Engineering, School of Engineering and Applied Science, University of Virginia, Charlottesville, Virginia 22904-4743

Eric Mazur[a)]
Department of Physics, Harvard University, Cambridge, Massachusetts 02138 and Division of Engineering and Applied Sciences, Harvard University, Cambridge, Massachusetts 02138

Joe C. Campbell[b)]
Department of Electrical and Computer Engineering, School of Engineering and Applied Science, University of Virginia, Charlottesville, Virginia 22904-4743

(Received 15 December 2005; accepted 14 June 2006; published online 20 July 2006)

Photodetectors fabricated on microstructured silicon are reported. The photodetectors exhibited high photoresponse; at 3 V bias, the responsivities were 92 A/W at 850 nm and 119 A/W at 960 nm. At wavelengths longer than 1.1 μm, the photodetectors still showed strong photoresponse. A generation-recombination gain mechanism has been proposed to explain the photoresponse of these photodiodes. From measurements of the noise current density, the calculated gain was approximately 1200 at 3 V bias. © *2006 American Institute of Physics*. [DOI: 10.1063/1.2227629]

Silicon-based photodetectors are attractive owing to their monolithic integratibility with low-cost complementary metal oxide semiconductor (CMOS) technology. Conventional silicon (Si) photodetectors achieve high responsivity at wavelengths shorter than 850 nm.[1] For longer wavelengths, the absorption coefficient of Si is less than 10^3 cm^{-1}. In order to increase the responsivity, a long absorption region is required. The band gap of Si limits operation to wavelengths <1.07 μm, which makes it unsuitable for many near-infrared applications. In order to extend the operating wavelength of Si-based photodetectors, germanium (Ge) on Si photodetectors and wafer bonded photodetectors on Si substrates have been reported and have achieved high responsivity and high speed.[2–4] Recently, laser-etched microstructured Si has been developed. This material exhibits low reflectance and high absorption across a broad wavelength spectrum extending to 2 μm.[5–9] These properties could extend the application potential for Si-based optoelectronic devices and make them attractive for applications such as infrared imaging, infrared microbolometers, and biomedical and chemical sensors.[10–12] In this letter, photodetectors fabricated with microstructured Si are reported. These photodetectors exhibit high photoresponse in a wide spectral range (600 nm$<\lambda<$1100 nm). Photoresponse at 1.31 and 1.55 μm was observed as well.

The device structure was prepared by irradiating n-doped Si (111) wafers (ρ=8–12 Ω cm) with a regeneratively amplified Ti:sapphire laser that delivered a 1 kHz train of 100 fs laser pulses at normal incidence in a 6.7×10^4 Pa atmosphere of sulfur hexafluoride (SF_6). The laser pulses were focused by a 0.25 m focal length lens and struck the silicon surface with an average fluence of 4 kJ/m^2. The experimental setup was described in Ref. 9. Irradiation creates an array of structures on the sample surface only in the region illuminated by the laser. In order to structure an area larger than the laser spot size, the Si substrate was translated relative to the laser beam at a speed such that any given spot on the surface was exposed to an average of 200 laser pulses. Following irradiation, the sample was thermally annealed at 825 K in vacuum for 30 min. This resulted in a surface covered with microstructures that were 2–3 μm tall and spaced by 2–3 μm. The shape of the pillars depends heavily on the scanning conditions such as laser fluence, shot number, gas pressure, gas species, and pulse duration.[6,13,14] Figure 1 is the scanning electron microscope (SEM) picture of the microstructured surface. The surface layer was heavily doped with sulfur, approximately 1 at. %. The microstructured layer has higher doping concentration due to the fact that sulfur can act as a dopant in the laser-etched layer. Hall measurements

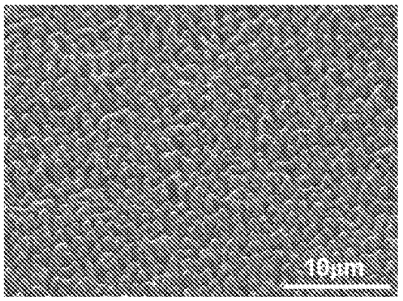

FIG. 1. Scanning electron micrographs of microstructured Si surface.

[a)]Electronic mail: mazur@physics.harvard.edu
[b)]Electronic mail: jcc7s@virginia.edu

 © 2006 American Institute of Physics

SIONYX1403000018.0015

SAMSUNG EX. 1002 - 1534/4148

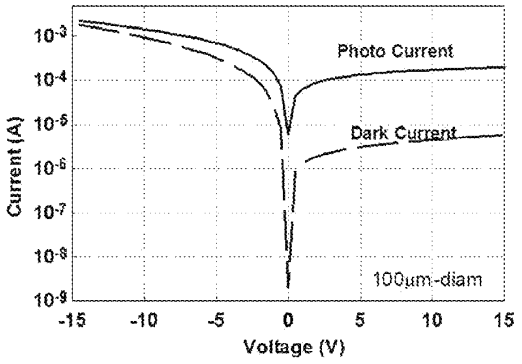

FIG. 2. Photocurrent and dark current vs voltage characteristics for a 100-μm-diam microstructured Si photodetector.

of this surface layer showed a higher electron concentration than the substrate and electron mobility on the order of 100 $cm^2\ V^{-1}\ s^{-1}$. Laser irradiation thus creates an n/n^+ heterojunction between the undisturbed crystalline substrate and the disordered surface layer.[9]

The wafer was fabricated into mesa devices by lithography, etching, and metallization processes. Mesas having diameters from 50 to 500 μm were wet etched by polysilicon etchant down to the Si substrate and were passivated with 200 nm of SiO_2 by plasma enhanced chemical vapor deposition (PECVD). Ti/Au (35 nm/125 nm) metal contacts were deposited by e-beam evaporation. The contact on the n-type Si substrate is Schottky, while on the microstructured silicon it is Ohmic.

Figure 2 shows the dark current and the photocurrent versus voltage characteristics for a 100-μm-diam device. Between the n-type silicon and its metal contact, a metal-semiconductor Schottky barrier is formed. In this case, reverse bias is defined with the n-type Si substrate biased negative with respect to the microstructured Si. At 1 and 3 V reverse bias, the dark currents were 1.3 and 2.3 μA for a 100-μm-diam device, respectively. This was more than one order of magnitude lower than the forward-biased dark current at the same voltages. The resistivity of the microstructured Si is estimated to be 0.17 Ω cm using the transmission-line method. The capacitance was ~0.2 pF at 1 V reverse bias. When the device was illuminated, the microstructured Si exhibited high photoresponse at near-infrared and visible wavelengths.

The responsivity from 0.60 to 1.60 μm was measured using a tunable monochromatic light source, a lock-in amplifier, and a calibrated Ge photodetector. A tungsten-halogen lamp filtered by a grating monochromator provided a tunable optical input. The responsivity of the photodetector under test was determined by comparing its photocurrent with that from a calibrated photodiode. The incident light was focused to a spot that was smaller than the active area of the photodetector. For wavelengths longer than 1.1 μm, a filter was used to remove higher order short wavelengths. Figure 3 shows the responsivity versus wavelength from 0.60 to 1.30 μm at 0, 1, 2, and 3 V reverse bias. Semiconductor lasers were used to measure the photoresponse at 1.31 and 1.55 μm. At 0 V, the photodetector exhibited low responsivity; however, when the photodetector was biased above 0.5 V, a high photoconductive response was observed. At 850 nm, the responsivities were 0.77 A/W at 0 V and 60, 79, and 92 A/W at 1, 2, and 3 V reverse bias, respectively. At 960 nm, the responsivities were 0.63, 88, 106, and 119 A/W at 0, 1, 2, and 3 V reverse bias, respectively. The responsivities were 0.09 and 0.02 A/W at 1.31 and 1.55 μm, respectively. The ambient gas has an important effect on the photoresponsivity. During laser irradiation the component species of the ambient gas are implanted into the silicon surface in large concentrations. In the case of SF_6, sulfur implantation is extremely important for the high photoresponsivity. Using other gases such as air, nitrogen, and hydrogen does not give the high responsivity. It has been found that selenium and tellurium incorporation also leads to the high photoresposivity.[9] However, these are difficult to use in gaseous form and thin films of each have to be evaporated onto a silicon substrate and then irradiated with the laser.

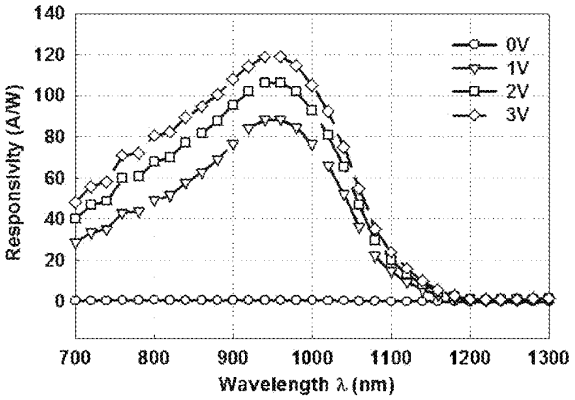

FIG. 3. Responsivity for a 250-μm-diam device under reverse bias of 0, 1, 2, and 3 V.

Figure 4 shows the frequency response of a 250-μm-diam device as determined by illumination through a chopper, whose frequency was varied. The bandwidth of the device was approximately 1200 Hz at 3 V reverse bias, and it did not vary much with device area.

In order to aid identification of the gain mechanism, the noise current density of the microstructured Si photodetector was measured with a low noise current preamplifier and a fast Fourier transform (FFT) spectrum analyzer. Figure 5(a) shows the noise current density versus frequency for a 250-μm-diam device at 3 V reverse bias with photocurrents of 0, 2, and 16 μA, respectively. The noise spectral density of the detector was obtained by subtracting the noise floor of the

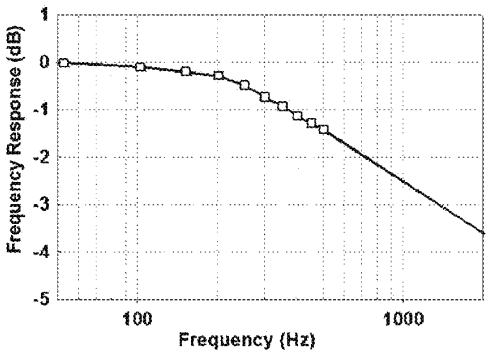

FIG. 4. Frequency response of a 250-μm-diam microstructured Si photodetector at 3 V reverse bias.

SIONYX1403000018.0016

SAMSUNG EX. 1002 - 1535/4148

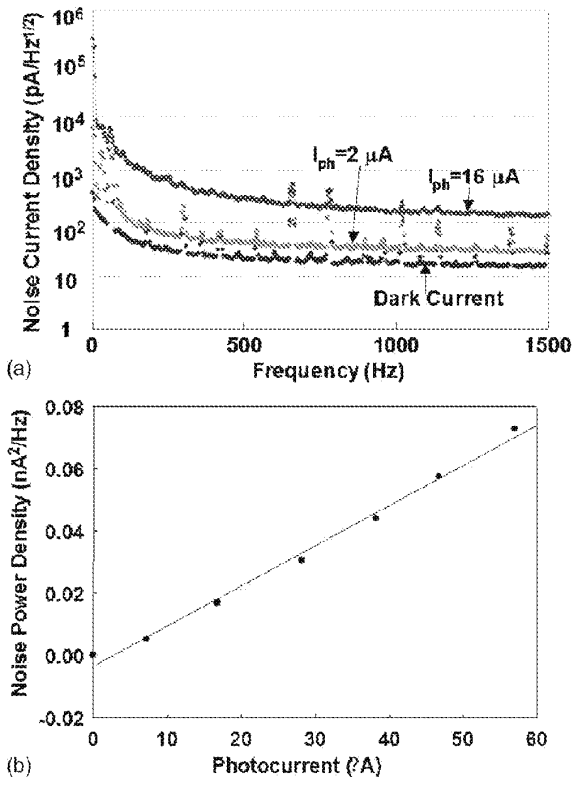

FIG. 5. (a) Noise current density vs frequency at 3 V reverse bias for a 250-μm-diam device with 0, 2, and 16 μA photocurrent. (b) Noise power density vs photocurrent at 3 V reverse bias.

test apparatus from the measured noise spectral density.[15] At low frequency to 100 Hz, the dominant noise was $1/f$ noise. However, at higher frequency, the noise current density was relatively insensitive to frequency, which is consistent with a generation-recombination gain mechanism. From the current noise density, the generation-recombination gain can be estimated. To good approximation, the photodetector gain and the noise gain are equal in a conventional photoconductor. The generation-recombination noise current can be expressed as $i_{GR}^2=4IeG\Delta f$, where I is the current and G is photoconductive gain. Using this relation, the extracted noise power density versus photocurrent is shown in Fig. 5(b); the gain was estimated to be 1200 at 3 V bias. From the measurement of noise current, we can also estimate the bandwidth of these devices. The estimated bandwidth is approximately 800 Hz which is consistent with that from the speed measurement discussed above.

In microstructured Si photodetectors, the gain mechanism is most likely to be generation-recombination that originates from random carrier generation and recombination in the high density of impurities and structural defects in the microstructure layer. The high infrared absorptance mechanism in the microstructured Si has been analyzed by Wu *et al.*[5] Sulfur impurities introduce energy states into the band gap of silicon, both near the band edge and in the middle of the band gap. In addition, the structural defects introduce infrared-absorbing states near the band edge. These energy states serve as trapping centers for photogenerated electron-hole pairs. Such band characteristics can explain the observed below-band-gap carrier generation. In the microstructured photodetector, the photogenerated electrons and holes move in opposite directions under applied bias. For example, under reverse bias, photogenerated electrons move toward the microstructured Si surface and holes toward the Si substrate. The resulting photocurrent will persist until both carriers are collected at the electrodes, or until they recombine in the bulk of the semiconductor before reaching the respective contacts. The recombination time of the minority holes is important. During transport to the cathode, they are more likely to be temporarily trapped and reexcited without recombination in the trapping centers.[16,17] At the same time, most electrons, as majority carriers, can travel to the anode within the dielectric relaxation time. The transit time differences between electrons and holes create a large photoconductive gain in microstructured photodetectors. As for all photoconductors, high gain is achieved at the cost of low bandwidth.

We have fabricated laser-microstructured Si photodetectors. The responsivities were 92 A/W at 850 nm and 119 A/W at 980 nm at 3 V reverse bias. At 1.31 and 1.55 μm, the photodetectors still exhibited photoresponse. The noise current density spectrum indicates a generation-recombination gain mechanism for these photodetectors.

The authors would like to acknowledge Dr. Hao Chen, Ariane E. Beck, Dr. Shuling Wang, and Dr. Gauri V. Karve for helpful discussions. This work is supported by MARCO through the IFC program.

[1]S. M. Csutak, J. D. Schaub, W. E. Wu, and J. C. Campbell, IEEE Photonics Technol. Lett. **14**, 516 (2002).
[2]J. Oh, J. C. Campbell, S. G. Thomas, S. Bharatan, R. Thoma, C. Jasper, R. E. Jones, and T. E. Zirkle, IEEE Photonics Technol. Lett. **38**, 1238 (2002).
[3]Z. Huang, J. Oh, and J. C. Campbell, Appl. Phys. Lett. **85**, 2386 (2004).
[4]Z. Huang, N. Kong, X. Guo, N. Duan, M. Liu, A. L. Beck, S. K. Banerjee, and J. C. Campbell, IEEE J. Sel. Top. Quantum Electron. (to be published).
[5]C. Wu, C. H. Crouch, L. Zhao, J. E. Carey, R. Younkin, J. A. Levinson, E. Mazur, R. M. Farrell, P. Gothoskar, and A. Karger, Appl. Phys. Lett. **78**, 1850 (2001).
[6]C. H. Crouch, J. E. Carey, J. M. Warrender, M. J. Aziz, and E. Mazur, Appl. Phys. Lett. **84**, 1850 (2004).
[7]M. Y. Shen, C. H. Crouch, J. E. Carey, and E. Mazur, Appl. Phys. Lett. **85**, 5694 (2004).
[8]J. E. Carey, C. H. Crouch, M. Shen, and E. Mazur, Opt. Lett. **30**, 1773 (2005).
[9]J. E. Carey, Ph.D. dissertation, Harvard University, 2004.
[10]P. J. Treado, I. W. Levin, and E. N. Lewis, Appl. Spectrosc. **48**, 607 (1994).
[11]D. S. Tezcan, S. Eminoglu, and T. Akin, IEEE Trans. Electron Devices **50**, 494 (2003).
[12]F. Fixe, V. Chu, D. M. F. Prazeres, and J. P. Conde1, Nucleic Acids Res. **32**, e70 (2004).
[13]C. H. Crouch, J. Carey, M. Shen, E. Mazur, and F. Y. Genin, Appl. Phys. Lett. **79**, 1635 (2004).
[14]R. J. Younkin, J. E. Carey, E. Mazur, J. A. Levinson, and C. M. Friend, J. Appl. Phys. **93**, 2626 (2003).
[15]Z. Ye and J. C. Campbell, Appl. Phys. Lett. **83**, 1234 (2003).
[16]E. Munoz, E. Monroy, J. A. Garrido, I. Izpura, F. J. Sanchez, M. A. Sanchez-Garcia, E. Calleja, B. Beaumont, and P. Gibart, Appl. Phys. Lett. **71**, 870 (1997).
[17]C. H. Qiu, C. Hoggatt, W. Melton, M. W. Leksono, and J. I. Pankove, Appl. Phys. Lett. **66**, 2712 (1995).

SIONYX1403000018.0017

SAMSUNG EX. 1002 - 1536/4148

LIGHT SCATTERING AND TRAPPING IN DIFFERENT THIN FILM PHOTOVOLTAIC DEVICES

J. Hüpkes[1], S. E. Pust[1], W. Böttler[1], A. Gordijn[1], N. Wyrsch[2], D. Güttler[3], A. N. Tiwari[3], Gordon[4], Y. Qiu[4]
[1] IEF5 - Photovoltaik, Forschungszentrum Jülich GmbH, 52425 Jülich, Germany
[2] Ecole Polytechnique Fédérale de Lausanne (EPFL), Institute of Microengineering (IMT), Breguet 2, 2000 Neuchâtel, Switzerland
[3] EMPA, Laboratory for Thin Films and Photovoltaics, Ueberlandstr. 129, CH-8600 Duebendorf, Switzerland
[4] Interuniversitair Micro-elektronika Centrum, Kapeldreef 75, 3001 Leuven, Belgium
corresponding author: J. Hüpkes, Phone +49 2461 61-2594 | Fax +49 2461 61-3735 | j.huepkes@fz-juelich.de

ABSTRACT: Light trapping in different thin film technologies is investigated in the context of the European integrated project ATHLET since it allows for thinner devices and thus for reduction of costs for absorber material preparation as well as for advanced multi-junction solar cells. In silicon technology, rough interfaces are typically introduced by roughening of substrates, transparent conducting oxides (TCOs) and/or reflectors at the back side to scatter the light into the absorber material. Well known rough TCOs, plasma-textured poly-Si as well as rough $Cu(In,Ga)Se_2$ (CIGS) absorbers are used as source for light scattering in microcrystalline silicon solar cells and compared regarding their surface roughness. The results prove that CIGS and poly silicon solar cells provide efficient light scattering by the surface features of the rough absorber.
Keywords: Light Trapping, Thin Film Solar Cell, Si-Films, CIGS

1 INTRODUCTION

Light trapping is an important feature of silicon thin film solar cells. Also for other thin film technologies light trapping attracts increasing attention since it allows for thinner devices, and costs for absorber material preparation have to be reduced. In silicon technology, typically, rough interfaces are introduced to scatter the light into the absorber material. This can be achieved by roughening of substrates, transparent conducting oxides (TCOs) and/or reflectors at the back side. In chalcopyrite or crystalline film silicon devices, rough features are introduced during growth or by post deposition texturing of the absorber material, respectively. However, the effectiveness of the different types of roughness for light trapping is not known in detail. This paper addresses the comparison of different light scattering features that are involved in the European integrated project, called ATHLET. We will compare the different types of roughness, namely well known rough TCOs, plasma-textured poly-silicon as well as rough CIGS absorbers. To be comparable for all these types of rough substrates we prepared hydrogenated microcrystalline silicon (µc-Si:H) solar cells in substrate configuration on top of the rough layers with a rough back contact.

We investigated the surface structure, the light scattering behavior the corresponding reflectors and performance of microcrystalline hydrogenated silicon solar cells on top of the reflectors.

2 EXPERIMENTAL

2.1 Sample preparation

As substrates for the light trapping investigation we applied CIGS absorber layers grown by an evaporation method [1], plasma-textured poly silicon [2] and as reference two often applied surface textured ZnO films, namely as-grown textured boron doped zinc oxide (ZnO:B) prepared by low pressure chemical vapor deposition (LPCVD) [3] and sputtered and texture-etched aluminum doped ZnO:Al [4]. Details on sample preparation are given in the respective references. These rough layers were used as substrates for µc-Si:H solar cells. The cells consist of the previously mentioned rough substrates, 200 nm evaporated silver film and 80 nm aluminum doped ZnO as part of the back reflector, p-i-n doped silicon films and an 80 nm aluminum doped ZnO front contact. Silver finger contacts were applied to support the conductivity of the thin TCO front contact.

All silicon and ZnO layers were co-deposited in 30x30 cm² reactors by plasma-enhanced CVD [5] and non-reactive RF sputtering from ceramic ZnO targets (1 wt% Al_2O_3) [4]. All silver films were thermally evaporated in a 10x10 cm² system. The approximately 1.2 µm thick solar cell is then illuminated through the n side.

Table I: RMS roughness data of the bare rough samples, samples with Ag and with Ag/ZnO coating, and photo current of the solar cells extracted from QE

Substrate	RMS roughness [nm]	Surface angle α [°]	J_{ph} [mA/cm²]
CIGS absorber (EMPA)	65	18	16.7
+ 200 nm Ag	-		
+ 80 nm ZnO	-		
LPCVD ZnO:B (EPFL)	80	44	16.4
+ 200 nm Ag	74		
+ 80 nm ZnO	77		
RF-sputtered, texture-etched ZnO:Al (Jülich)	130	26	18.7
+ 200 nm Ag	115		
+ 80 nm ZnO	117		
Plasma-textured poly-Si (IMEC)	240	39	13.1 (at -0.5V)
+ 200 nm Ag	202		
+ 80 nm ZnO	200		

2.2 Characterization

We investigated the surface structures by atomic force microscopy (AFM) and statistical analysis. For roughness values given in Table I a measurement error of about 5 nm was estimated. Optical reflectivity spectra

SIONYX1403000018.0018

SAMSUNG EX. 1002 - 1537/4148

were taken of the rough silver layers with and without the additional ZnO:Al film and of the solar cells on areas with only ZnO:Al front contact without silver fingers. The reflectance spectra show some artifacts at about 900 nm that must be ignored. Cell performance was evaluated by spectral response measurements to get quantum efficiency and to extract the cell current via AM1.5 spectrum.

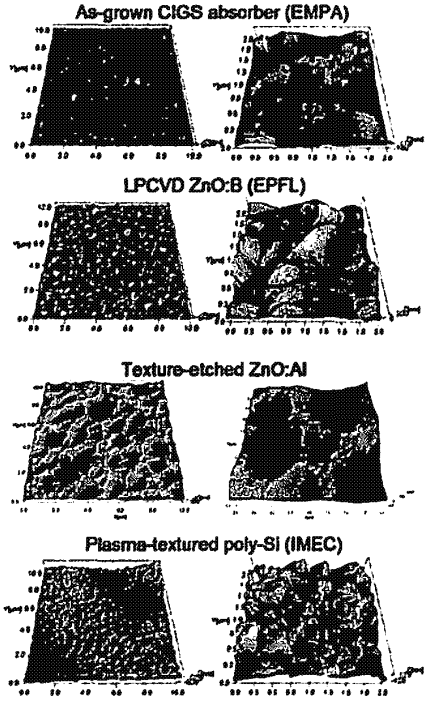

Figure 1: AFM surface images of the rough substrates before Ag layer deposition

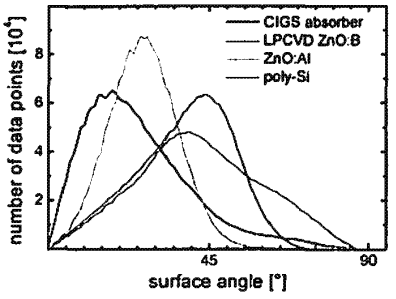

Figure 2: Histogram of the local surface tilt angle for the different substrates: CIGS (black), LPCVD ZnO (red), texture-etched ZnO:Al (green) and plasma-textured poly silicon (blue)

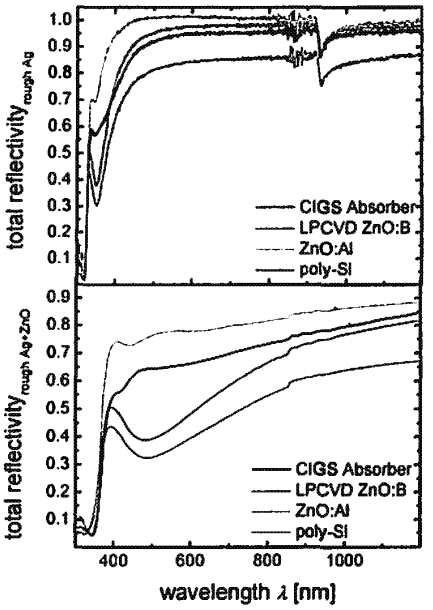

Figure 3: Reflectivity of rough Silver layers without (top) and with an additional 80 nm ZnO film

3 RESULTS AND DISCUSSION

3.1 Surface characteristics of rough samples

Figure 1 shows the AFM surface images of the roug h surfaces. The type of substrate is indicated in the figure. The corresponding statistical roughness data are provided in Table I. The data exhibit different lateral and vertical feature sizes. The roughness increases from CIGS via LPCVD and texture-etched ZnO films to the plasma-textured poly silicon film. The lateral features are largest for texture-etched ZnO:Al, followed by CIGS, LPCVD ZnO:B and plasma-textured poly silicon. Thus, the local tilt angles of the surfaces are different. These AFM data were evaluated by a self-made software [6] and the local tilt angles of the surface relative to the substrate are illustrated in Figure 2. The maxima of the distribution of surface tilt angles α are given in Table I. The CIGS absorbers and the texture-etched ZnO:Al films exhibit small values of α and also are similar in lateral surface feature size. The other two samples LPCVD ZnO:B and textured poly silicon structures consist of laterally smaller and sharp features leading to much steeper angles around 40°.

3.2 Optical reflector performance

After coating of the rough samples with silver and ZnO we performed reflectivity measurements as shown in Figure 3. The reflectivity of the rough silver shows severe minima at about 350 nm for bare silver that shift up to 500 nm after coating with the ZnO layer. These absorption peaks are discussed in literature to be propagating or localized surface plasmons [7,8,9]. Additionally, the low reflection of the rough Ag/ZnO

SIONYX1403000018.0019

SAMSUNG EX. 1002 - 1538/4148

reflector is related to strong absorption by light trapping inside the ZnO:Al layer that also enhances parasitic absorption at the rough Ag/ZnO interface. This effect is more pronounced for samples with steeper surface angles α. Here the light scattering into larger angles is much more effective [10] and the small sharp features may enhance localized plasmonic effects to cause additional absorption.

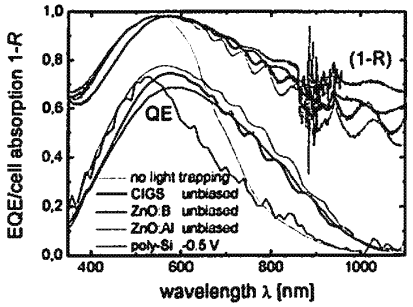

Figure 4: External quantum efficiency and total cell absorption (1-R) of μc-Si:H solar cells on different rough substrates: CIGS (black), LPCVD ZnO (red), texture-etched ZnO:Al (green) and plasma-textured poly silicon (blue). Additionally, we show absorption of 2.4 μm silicon corresponding to no light trapping and ideal front side anti-reflection and back side reflector

3.3 Solar cells

Standard p-i-n solar cells were prepared in substrate configuration and illuminated through the n side. The cell performance in terms of efficiency was strongly limited by the fact of a non-optimized process for substrate configuration and for μc-Si:H growth on these different rough substrates. However, there were a few solar cells with acceptable fill factor, open circuit voltage and current (not shown), proving that the deposition process worked well. Spectral response measurements of the solar cells on different rough substrates were taken and the corresponding quantum efficiency QE is given in **Figure 4**. The figure also contains cell absorption data calculated from total cell reflection. The absorption of 2.4 μm silicon corresponds to a cell with no light trapping, no parasitic absorption and ideal front side antireflection and back side reflector. The calculated photocurrent is given in Table I. Note that the electrical properties of the μc-Si:H cell on the poly-silicon substrate were poor, so the photocurrent could only be collected at reverse bias. The different and partially poor QE of the solar cells especially in the blue region is attributed to imperfect homogeneity of the antireflective front contact and of n-layer thickness. It may also be limited by the quality of μc-Si:H, grown on rough substrates [11]. However, reverse bias did not significantly change the QE data for the cells on ZnO and CIGS.

At about 550 nm the cell absorption is nearly 100% caused by an effective antireflection effect of the transparent front contact. Below this wavelength, strong primary reflection occurs. The amount of secondary reflection in the NIR depends on light trapping and parasitic absorption inside the cells. In the long wavelength region, the QE reveals severe light trapping in cells prepared on CIGS and the two kinds of ZnO. The light absorption is strongly enhanced as compared to the absorption calculated for light passing twice the silicon thickness (no light trapping, ideal reflector). For both rough ZnO one would expect enhanced red response, since the surface features are known to provide good light trapping in silicon thin film solar cells when applied at the front contact. For surface features provided by the CIGS itself, the provided light trapping is an important message, since cost reduction drives CIGS development to thinner cells moreover in combination with appropriately chosen CIGS composition (for bandgap tailoring) advance multi-junction solar cells are under development [12,13]. The μc-Si:H cell on plasma-textured poly silicon substrate behaves strongly different. The QE is comparable to the curve calculated for no light trapping. However, the cell absorption is highest within this series. This hints to very strong parasitic absorption losses. This can be explained by the low reflectivity of the reflector as shown in Figure 3. However, the reflectivity measurement of the reflector was performed in air and reflectivity might change in the real cell structure, where the silicon is directly attached to the ZnO. From the roughness one would expect light trapping effect. Thus one can directly study the light trapping effect in the poly silicon cells itself. From another publication that studies the effect of plasma texturing on optical performance [2], one can extract a light trapping effect, if the QE values are compared to the case of no light trapping in analogy to **Figure 4** (not shown). This comparison reveals even in the un-textured cells a significant light trapping effect. However, the light trapping ability in the poly-silicon cells still can be improved by adjusted surface texturing and even more important by reduction of parasitic absorption [2].

4 CONCLUSIONS

Light trapping in silicon thin film solar cells is very important. It might also be important for CIGS technology if the absorber thickness is reduced for cost reasons. The rough CIGS absorber already provides light scattering to enhance the optical performance, even though, it is not important due to the strong absorption of CIGS, but with tailored bandgap and thickness the concepts are attractive for applications in multi-junction (tandem) solar cells. In this context a-Si as top cell and CIGS as intermediate or bottom cell are suitable. By our approach a judgment of light trapping in poly silicon cells is not possible. Other publications indicate a light trapping effect even in the un-textured cells. That means that light trapping is available in different thin films PV technologies and will be an important factor to boost the efficiency, even for material systems that did not require light trapping so far.

ACKNOWLEDGEMENTS

We thank our colleagues for assistance in solar cell preparation and characterization. The authors also thank the project partners O. Salomon, J. Palm and T. Dalibor for their support of our experimental work by discussions and with additional test samples. Financial support by the European Commission (ATHLET project, contract 019670) is gratefully acknowledged.

SIONYX1403000018.0020

SAMSUNG EX. 1002 - 1539/4148

REFERENCES

[1] D. Rudmann, D. Brémaud, A.F. da Cunha, G. Bilger, A. Strohm, M. Kaelin, H. Zogg, A. N. Tiwari, Thin Solid Films 480, 55 (2005).

[2] I. Gordon, L. Carnel, D. Van Gestel, G. Beaucarne, and J. Poortmans, Progress in Photovoltaics: Research and Applications 2007; 15: 575-586

[3] S. Faÿ, L. Feitknecht, R. Schlüchter, U. Kroll, E. Vallat-Sauvain, A. Shah, Solar Energy Materials and Solar Cells 90 (2006) 2960-2967

[4] M. Berginski, J. Hüpkes, M. Schulte, G. Schöpe, H. Stiebig, B. Rech, M. Wuttig, J. Appl. Phys. 101 (2007) 74903

[5] T. Repmann, T. Kilper, W. Appenzeller, C. Zahren, H. Stiebig, B. Rech, 2005 In Proceedings of the 31st IEEE Photovoltaic Specialist Conference, Orlando, Florida, USA, S. 1383 – 1388

[6] H. Stiebig, M. Schulte, C. Zahren, C. Haase, B. Rech. P. Lechner, Proceedings SPIE Photonics for Solar Energy Systems, 6197, Strasbourg, France, (2006)

[7] J. Springer, B. Rech, W. Reetz, J. Müller, M. Vanecek, Solar Energy Materials & Solar Cells 85 (2005) 1–11

[8] D. Sainju, P.J. van den Oever, N.J. Podraza, M. Syed, J.A. Stoke, J. Chen, X. Yang, X. Deng, R.W. Collins. Proceedings of the 4th World PVSEC (Hawaii) 2006; 2: 1732–1735

[9] U. W. Paetzold, C. Haase, H. Stiebig, this conference

[10] M. Schulte, C. Zahren, H. Stiebig, Proceedings of the 21th EUPVSEC (2006)

[11] J. Bailat, D. Dominé, R. Schlüchter, J. Steinhauser, S. Faÿ, F. Freitas, C. Bücher, L. Feitknecht, X. Niquille, T. Tscharner, A. Shah, C. Ballif, Proc. of the 4th WCPEC Conf., (2006), Hawaï, 1533

[12] S. Nishiwaki, S. Siebentritt, P. Walk, M. Ch. Lux-Steiner, Progress in Photovoltaics: Research and Applications, 11 243 – 248, (2003)

[13] S. Seyrling, S. Calnan, S. Bücheler, J. Hüpkes, S. Wenger, D. Brémaud, H. Zogg, A. N. Tiwari, Thin Solid Films, 517, 2411 (2009)

SIONYX1403000018.0021

SAMSUNG EX. 1002 - 1540/4148

BULLETIN OF THE POLISH ACADEMY OF SCIENCES
TECHNICAL SCIENCES
Vol. 53, No. 2, 2005

Defect states in the CIGS solar cells by photocapacitance and deep level optical spectroscopy

M. IGALSON* and A. URBANIAK

Faculty of Physics, Warsaw University of Technology, 75 Koszykowa Str., 00-662 Warsaw, Poland

Abstract. Thin film solar cells based on multinary compound Cu(In,Ga)Se_2 show record photovoltaic conversion efficiency approaching 20%. Investigation on defect physics in this compound is crucial for making further progress in the technology. In this work we present the results on photocapacitance (PC) and deep level optical spectroscopy (DLOS) for two types of cells – high efficiency Cu(In,Ga)Se_2 cell with about 20% of gallium and pure gallium $CuGaSe_2$ device. We show that PC and DLOS, employed as the techniques complimentary to deep level transient spectroscopy DLTS and admittance spectroscopy, are useful methods in providing information on defect levels in solar cells. In particular they are helpful in differentiating between levels belonging to the bulk of absorber and to the interface states. We tentatively assign some of the observed deep levels to In_{Cu} or Ga_{Cu} antisites and Cu interstitials.

Key words: solar cells, CIGS, photocapacitance, deep levels.

1. Introduction

Solar cells with Cu(In,Ga)Se_2 (CIGS) chalcopyrite semiconducting compound as an absorber are among thin film devices of highest photovoltaic efficiency, which currently is close to 20% for laboratory cells and 12% for modules [1,2]. The successful development of this technology took place despite of relatively low level of knowledge about fundamental properties of CIGS compounds, especially about defects controlling photovoltaic performance of these devices. The lack of this knowledge appears now as more and more severe limitation in the pursuit of higher efficiencies and simpler, cheaper technology of CIGS-based solar cells.

CIGS compounds are well known for their ability to accommodate large deviations from stoichiometry without impediment of their photovoltaic properties. This makes possible to use relatively simple technology for preparation of the absorber layer, without the need of very strict control over its composition. Material used for photovoltaic application is fabricated with the excess of indium In/Cu > 1 (excess of copper results in separation of Cu_2Se phase in grain boundaries and short-cutting of the device). Thus the most probable defects are V_{Cu} and In_{Cu}. The first one gives shallow acceptors responsible for p-type conductivity. Antisites In_{Cu} are compensating donors, which make the compound a compensated material with a degree of compensation estimated as 1:100 [3].

The methods well known for their usefulness on providing information on defect states in semiconductors are capacitance techniques – DLTS and admittance spectroscopy. While the experiment itself and the interpretation of results are quite straightforward in simple structures and well known materials, it is not so for the complicated photovoltaic structure with many interfaces, non-ideal diode behaviour and presence of non-thermal processes of carrier emission. Additional obstacle, making both experiments and their interpretation difficult, are metastable phenomena in the electrical characteristics of these devices, which are induced by illumination and/or biasing of a device at temperatures around 300 K. Our current understanding of these phenomena relates them to special defect states, with the electronic properties similar to DX centers or "dangling bonds" in amorphous compounds [3,4]. Changes of the occupation of these defects cause the metastable changes in the doping level of absorber, which persist for days. The consequences are persistent changes of the electric field strength in the absorber and of the potential distribution within the device. This in turn influences the spectra of levels revealed by capacitance spectroscopy. One example is the so called N1 level observed in most devices in the DLTS and admittance spectra at low temperature. Its apparent thermal activation energy depends on the state of the sample. Thus N1 has been interpreted initially as the response belonging to the continuous distribution of interface electron traps, depending on the position of the Fermi level in the vicinity of the heterointerface [5,6]. Illumination or voltage bias shifts the Fermi-level, hence the activation energy is different for various states of the sample.

However, the evidences have been accumulating recently that N1 (at least in the annealed cells) belongs rather to bulk single level [7–9]. The metastabilities in the activation energy are according to [8] caused by two factors: various contribution of the electric field-enhanced tunneling to the emission rates and the changes of the po-

*e-mail: igalson@if.pw.edu.pl

SIONYX1403000018.0022

SAMSUNG EX. 1002 - 1541/4148

sition of the Fermi-level at the hetrointerface which cause that some levels situated in the upper half of the bandgap appear or disappear in the admittance and DLTS spectra.

In this contribution we will show the results obtained by photocapacitance (PC) and deep level optical spectroscopy (DLOS), which unambiguously show that the N1 levels in the baseline CIGS devices are situated in the bulk of absorber. The same methods also have been used for investigation of the cells based on the wide band-gap $CuGaSe_2$ compound and provided some new information on the spectrum of bulk levels in this material.

2. Samples

Historically first cells with chalcopyrite semiconductor as absorber have been based on ternary compound $CuInSe_2$. Addition of gallium widens the energy gap of this material, which should increase the efficiency of the cells. However, in contrary to the expectations, the highest photovoltaic efficiency has been obtained for relatively low gallium content: Ga/(In + Ga) = 0.2. Up to date there is no commonly accepted explanation why higher addition of gallium in the absorber leads to the lower efficiency of the cells – whether it is a question of a specific defect spectrum or heterointerface properties [10].

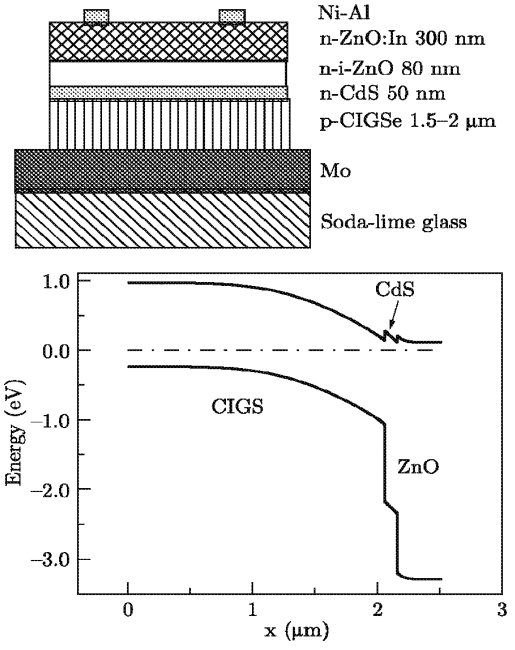

Fig. 1. Schematic of the ZnO/CdS/CIGS photovoltaic structure and its band diagram

In this contribution we present the results for high efficiency solar cells with absorbers of low gallium content (Ga/(In + Ga) = 0.2) prepared in Ångström Solar Center, Uppsala and cells with $CuGaSe_2$ wide band-gap absorbers fabricated in Hahn-Meitner Institute, Berlin. Comparison of the defect spectra for these two cells could perhaps provide some insight into the defect-related causes of efficiency losses in the wide band-gap cells.

Both types of cells have been prepared according to the similar recipe [11,12]. Absorbers have been deposited by co-evaporation of elements in so called three stage process on heated molybdenum-covered soda-lime glass. Then CdS buffer has been obtained by chemical bath deposition, followed by sputtered ZnO window (80 nm of i-ZnO and about 300 nm of ZnO:In). The structure has been completed by the evaporation of a Ni-Al grid (Fig. 1). Photovoltaic conversion efficiency of CIGS devices is about 14%, and of CGS cells – 8%.

3. Experimental details

In the DLTS measurements we used a DLTS-E82 apparatus in the frequency scan mode (emission rate window was swept quasi-continuously in the range 0.5–5000 s^{-1} while temperature was kept constant). We rather employed reverse-pulse DLTS (RDLTS) – a modification of the standard DLTS since RDLTS is particularly sensitive to traps in the interface region of the cell while providing essentially the same information on thermal emission rate as DLTS [13]. In the RDLTS measurement a voltage pulse is applied in the reverse direction (e.g. −1 V pulse to the junction kept at 0 V). In this mode a capture of carriers, not thermal emission is observed, so the sign of the signal should be opposite to that of the DLTS – negative for the minority carrier traps.

In the photocapacitance measurements (PC) a computer-controlled spectrometer with halogen lamp calibrated by use of a pyroelectric sensor has been used. Phase-sensitive detection by use of the SR810 lock-in amplifier has been employed to measure spectral distribution of the photocapacitance.

In the deep level optical spectroscopy (DLOS) experiments [14] we have registered a change of the DLTS signal corresponding to the specific DLTS peak induced by a weak sub-bandgap light. It has been recorded as a function of wavelength at the fixed emission rate widow. Similar method have been used for investigation of the CIGS cells by Heath *et al.* [15].

4. Experimental results

4.1. $Cu(In,Ga)Se_2$ cells. In Fig. 2 the typical Arrhenius plots of the emission rates characteristic for N1 level derived from admittance spectroscopy and RDLTS are presented. As reported already in [7–9] the emission rates depend on the state of the sample. Typical feature is also a decreasing activation energy from the trap level with decreasing temperature. This has been discussed in detail in [8] and attributed to the contribution of the electric-field assisted tunnelling to the emission process from levels crossing the Fermi-level close to the heterointerface. This contribution is most significant at low temperature and

SIONYX1403000018.0023

SAMSUNG EX. 1002 - 1542/4148

low emission rates in the region accessed by RDLTS. Thus the activation energies obtained from admittance spectroscopy are less distorted and should provide more reliable information on the level distance from the conduction band. The activation energy derived from the admittance data for the baseline CIGS cell is equal to about 0.24 eV after annealing at 330 K without voltage bias. After annealing with reverse bias, the energy increases to 0.32 eV [5].

Now we will check, how the sub-bandgap light affects the capacitance of the CIGS cell. Generally it might transfer carriers captured in the trap levels to the bands or fill empty trap states. At low temperature, when the thermal emission rates are slow, these processes will cause an increase or decrease of the junction capacitance, depending on the sign of the captured/released charge. Spectrum of the photocapacitance measured in the baseline device after annealing at 330 K and normalized by the photon flux is shown in Fig. 3. At low temperature two steps are observed, with energies about 0.86 and 1.0 eV (derived from the inflection points). They correspond to the increase of the negative charge in the absorber, so they belong to the transition of electrons into the empty trap states in the upper half of the band-gap. These transitions disappear from the spectrum at temperatures above 180 K, hence we conclude, that the thermal rates characteristic for the traps involved become too fast and electrons transferred by light are immediately emitted to the conduction band.

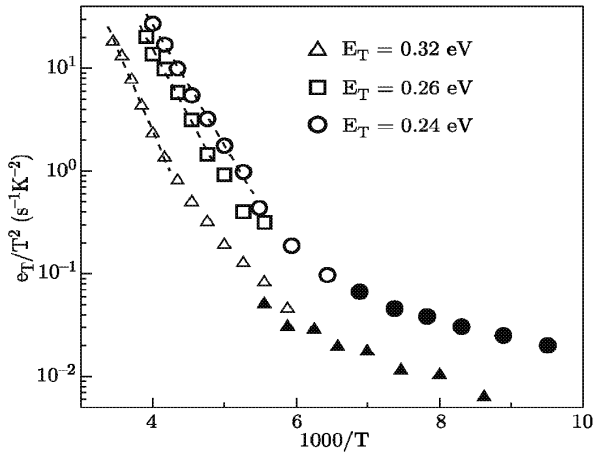

Fig. 2. Arrhenius plots of the emission rates from traps revealed in the admittance and RDLTS in the CIGS device (circles – measured after annealing at 0 V, triangles – after annealing at −2 V); and in the CGS cell (annealed at 0 V – squares). Full symbols are the data derived from RDLTS, open symbols – from admittance

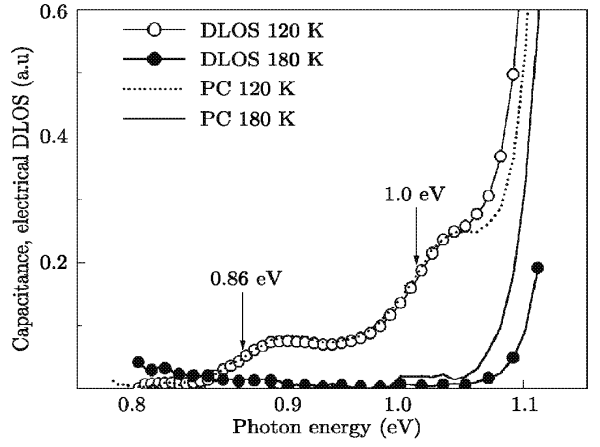

Fig. 3. Photocapacitance (continuous line) and DLOS spectra (circles) measured at 120 K and 180 K in the CIGS cell

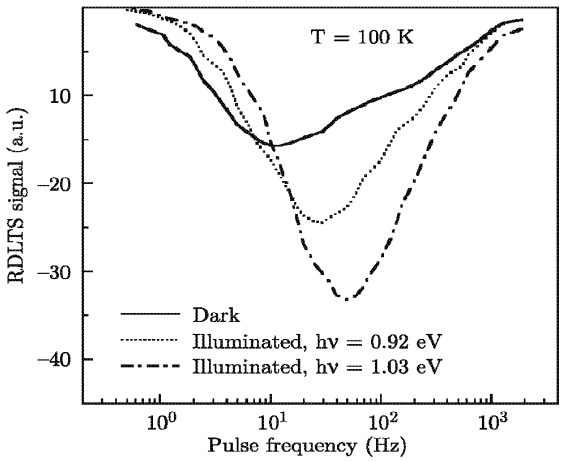

Fig. 4. RDLTS spectrum at 100 K in the frequency scan mode measured in the cell annealed under reverse bias prior to the experiment: measurement taken in the dark – continuous line, under illumination with photons of energy slightly above the first and second step – broken lines

By performing DLOS experiment we are able to check, whether sub-bandgap light influences a capture/emission process involving one specific level. In Fig. 4 the RDLTS spectrum of the sample annealed with reverse bias prior to the experiment is shown. It features the deep 0.34 eV peak with some shoulder belonging to the shallower 0.24 eV. Under sub-bandgap illumination we see an increase of the capture rate. We have to remember though that the capture rate is equal to the emission rate in our case, since only levels from the vicinity of the cross-point of the Fermi-level and trap level respond here [13]. The peak magnitude also increases, which is a natural consequence of the increasing capture rate for a fixed (and short) pulse length. Spectral distribution of the DLTS signal increment, measured at the fixed emission rate window

SIONYX1403000018.0024

SAMSUNG EX. 1002 - 1543/4148

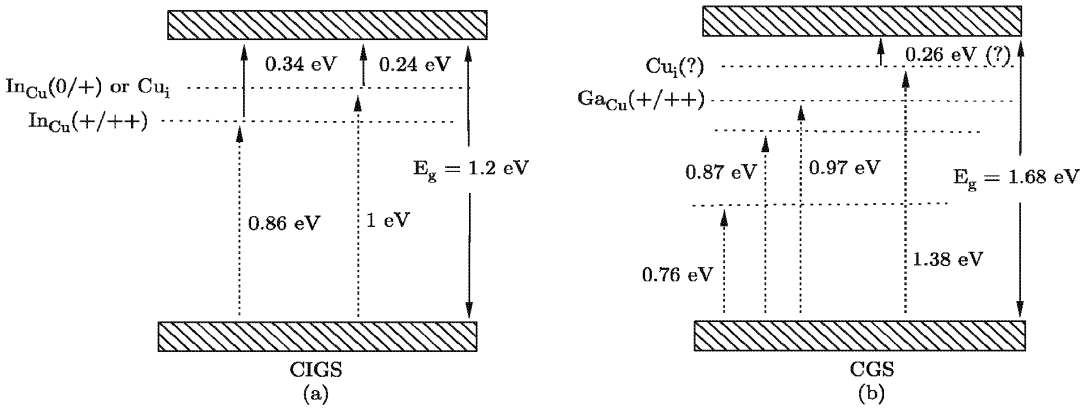

Fig. 5. Schematic of thermal (continuous lines) and optical (dotted lines) transitions observed in CIGS (a) and CGS (b) cells with tentative assignment of levels to intrinsic defects

(close to the RDLTS maximum) and normalized to the photon flux is exactly the same as the photocapacitance spectrum (see Fig. 3). Again the characteristic transition steps disappear at higher temperatures, when the thermal emission rates from both trap levels, 0.24 eV and 0.32 eV become faster than the emission rate window used in DLOS experiment.

The optical and thermal transitions observed in our measurements are illustrated in Fig. 5a. The sum of thermal and optical activation energies for both levels observed as N1 peak in the two analyzed states of the cell is close to the CIGS band-gap energy (1.2 eV) in our samples. All this findings lead us to the conclusion, that the optical transitions observed in PC and DLOS spectra involve the same N1 traps as revealed in admittance and DLTS spectroscopy. This result supports strongly the hypothesis that N1 levels in the annealed cells are discrete donor-type states in the bulk of absorber, and not the interface states at the CdS/CIGS heterointerface.

4.2. $CuGaSe_2$ cells. These cells exhibit much worse photovoltaic performance and, as it is usually the case, also worse diode behaviour – their I–V characteristics show large leakage currents and tunneling-like mechanism of current transport [16]. It is quite typical, that in these circumstances capacitance spectroscopy is not so efficient in revealing defect levels. Thus in the DLTS spectrum we observe only continuous distribution of the emission rates, and no peaks which could be attributed to the transitions to single levels. In the admittance spectrum a single level of energy 0.26 eV (see Fig. 2.) has been revealed, and two or three shallower and hardly discernible levels (not shown).

The photocapacitance spectrum of the CGS cell is relatively rich – at least four steps could be distinguished (Fig. 6). All revealed transitions originate from the transfer of electrons to the empty deep electron traps. The interpretation of these levels is here more difficult, since no DLOS experiment could be performed due to the absence of DLTS peaks in the spectrum up to 330 K. We may only notice that the sum of the energies of the PC step of 1.4 eV and thermal transition of 0.26 eV revealed by admittance is close to the bandgap energy of CGS (1.68 eV), so they might involve the same level (see Fig. 5b). The question arises why we do not observe in DLTS or admittance the other levels revealed by photocapacitance. Possible explanation is that they might be too deep (close to midgap) to be seen in the DLTS spectrum within the experimental range of temperatures (40–330 K) and emission rate windows (0.5–5000 s^{-1}).

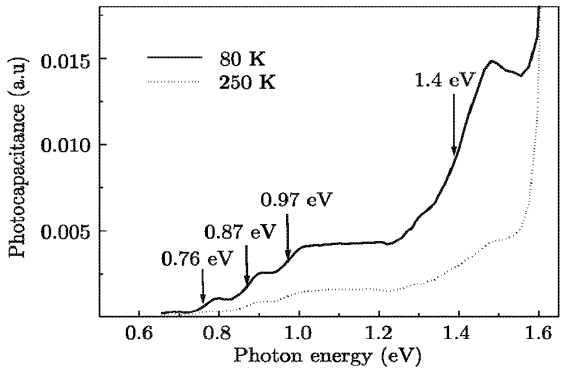

Fig. 6. Photocapacitance spectra in 80 K and 250 K measured in the CGS cell

5. Discussion and conclusions

In the CIGS samples we have observed the optical transitions of electrons from the valence band to trap levels and have been able to correlate them with the thermal transitions revealed by DLTS and admittance spectroscopies. We have concluded that these optical and thermal transitions involve the same bulk compensating donor states. The values of energies derived from our experiments match very closely the theoretical predictions for

SIONYX1403000018.0025

SAMSUNG EX. 1002 - 1544/4148

In_{Cu} 0/+ and ++/+ level (0.25 eV and 0.34 eV below conduction band correspondingly [17]). Another bulk compensating donor, which may be taken under consideration as a candidate for the shallower of those two levels is Cu interstitial with its theoretical value of energy equal to 0.20 eV below the conduction band. This defect might be present in large concentration in the interface region of the absorber, since according to [18] its creation energy decreases in the regions, where the Fermi-level is situated close to the conduction band.

The experimental data on the levels in the CGS sample are collected in Fig. 5b. They are not so complete as for CIGS cells, since no DLTS peaks have been observed in the measurement temperature range and DLOS measurements could not be performed. In contrary to the findings of Heath *et al.* [15], we have not registered any change of the non-thermally activated DLTS signal by the sub-bandgap illumination. The optical transition of 1.4 eV and thermal of 0.26 eV, observed in admittance might involve the same level, but, as no confirmation by DLOS have not been obtained, this agreement could be only the circumstantial coincidence.

Comparing the spectrum of levels observed in CGS by photocapacitance with theoretical calculations of Zhang *et al.* [18] we notice that the step at the energy of 0.97 eV might involve a ++/+ level of Ga_{Cu} antisite (0.69 eV below the conduction band edge). Other levels with energies close to the midgap might be responsible for the reduced photovoltaic performance of this device. It is also worth noting, that Cu_i level according to [17] should be situated at the same energy below conduction band in CIS and CIGS compound. This is an argument in favour of assigning of the 0.24 eV level in CIGS and the 0.26 eV level in CGS to the copper interstitials as they feature very similar emission rates in the CIGS and CGS material.

Summing up, our experiments show that the investigation of the influence of sub-bandgap illumination on the cell capacitance can provide data helping to interpret the spectra of deep levels in the complicated photovoltaic structures. This is particularly true if the photocapacitance measurements are combined with deep level optical spectroscopy. That gives the possibility of observing at one time both types of transitions – thermal and optical to a particular level. In the photocapacitance spectrum also the levels, which for some reasons are not observed in the admittance and DLTS measurements, might be revealed.

Acknowledgements. Authors are grateful to the colleagues from the Ångström Solar Center and the Hahn-Meitner Institute for providing samples used in that study.

References

[1] J. A.M. Abushama, S. Johnston, T. Moriarty, G. Teeter, K. Ramanathan, and R. Noufi, "Properties of ZnO/CdS/$CuInSe_2$ solar cells with improved performance", *Prog. Photov.: Res. Appl.* 12, 39–45 (2004).

[2] B. Dimmler, M. Powalla, and H.W. Schock, "CIS-based thin-film photovoltaic modules: potential and prospects", *Prog. Photov.: Res. Appl.* 10, 149–57 (2002).

[3] U. Rau and H.W. Schock, "Electronic properties of Cu(In,Ga)Se_2 heterojunction solar cells-recent achievements, current understanding, and future challenges", *Appl. Phys.* A69, 131–47 (1999).

[4] M. Igalson and H.W. Schock, "The metastable changes of hole and electron trap spectra of $CuInSe_2$-based photovoltaic devices", *J. Appl. Phys.* 80, 5765–9 (1996).

[5] A. Niemegeers, M. Burgelman, R. Herberholz, U. Rau, D. Hariskos, and H.W. Schock, "Model for electronic transport in Cu(In,Ga)Se_2 solar cell", *Prog. Photovolt.: Res. Appl.* 6, 407–21 (1998).

[6] P. Zabierowski, U. Rau and M. Igalson, "Classsification of the metastabilities in the electrical characteristics of ZnO/CdS/Cu(In,Ga)Se_2 devices", *Thin Solid Films* 387, 147–50 (2001).

[7] M. Igalson, M. Bodegård, L. Stolt, and A. Jasenek, "The defected layer" and the mechanism of the interface-related metastable behavior in the ZnO/CdS/Cu(In,Ga)Se_2 devices", *Thin Solid Films* 431–432C, 153–157 (2003).

[8] P. Zabierowski and M. Edoff, "Laplace-DLTS analysis of the minority carrier traps in the Cu(In,Gas)Se_2-based solar cells", *Thin Solid Films* 480–481C, 301–306 (2005).

[9] M. Igalson and P. Zabierowski, "Electron traps in Cu(In,Ga)Se_2 absorbers of thin film solar cells studied by junction capacitance techniques", *Opto-Electron. Rev.* 11, 261–267 (2003).

[10] S. Siebentritt, "Wide gap chalcopyrites: material properties and solar cells", *Thin Solid Films* 403–404, 1–8 (2002).

[11] J. Kessler, M. Bodegård, J. Hedström, and L. Stolt, "Baseline Cu(In,Ca)Se_2 device production: control and statistical significance", *Sol. Ener. Mat. Sol. Cells* 67, 67–76 (2001).

[12] S. Schuler, S. Nishiwaki, M. Dziedzina, R. Klenk, S. Siebentritt, and M.C. Lux-Steiner, "Solar cells based on PVD grown $CuGaSe_2$ absorber and device properties", *Mater. Res. Soc. Symp. Proc.* Warrendale, PA, USA 668, H5.14.1–6. (2001).

[13] M. Igalson and P. Zabierowski, "Transient capacitance spectroscopy of defect levels in CIGS devices", *Thin Solid Films* 361–362, 371–7 (2000).

[14] P. Blood and J.W. Orton, *The Electrical Characterization of Semiconductors*, pp. 698–704, Academic Press Ltd, London, 1992.

[15] J.T. Heath, J.D. Cohen, W.N. Shafarman, D.X. Liao, and A.A. Rockett, "Effect of Ga content on defect states in $CuIn_{1-x}Ga_xSe_2$ photovoltaic devices", *Appl. Phys. Lett.* 80, 4540–4542 (2002).

[16] J. Malmström, J. Wennerberg, and L. Stolt, "A study of the influence of the Ga content on the long-term stability of Cu(In,Ga)Se_2 thin film solar cells", *Thin Solid Films* 431–432, 436–442 (2003).

[17] S.B. Zhang, S.H. Wei, A. Zunger, and H. Katayama-Yoshida, "Defect physics of the $CuInSe_2$ chalcopyrite semiconductor", *Phys. Rev.* B57, 9642–9656 (1998).

[18] S.H. Wei, S.B. Zhang, and A. Zunger, "Effects of Ga addition to $CuInSe_2$ on its electronic, structural, and defect properties", *Appl. Phys. Lett.* 72, 3199–3201 (1998).

SIONYX1403000018.0026

SAMSUNG EX. 1002 - 1545/4148

SpringerLink

Try the new SpringerLink Beta

Institutional Login

Recognized as:

U.S. Patent & Trademark Office, Scientific & Technical (665-54-532)

US Patent and Trademark 2007

3686.002 (911-40-100)

Welcome!

To use the personalized features of this site, please log in or register.

If you have forgotten your username or password, we can help.

My Items

Marked Items

Alerts

Order History

Saved Items

All

Favorites

Infrared absorption by sulfur-doped silicon formed by femtosecond laser irradiation

Journal	Applied Physics A: Materials Science & Processing
Publisher	Springer Berlin / Heidelberg
ISSN	0947-8396 (Print) 1432-0630 (Online)
Issue	Volume 79, Number 7 / November, 2004
DOI	10.1007/s00339-004-2676-0
Pages	1635-1641
Subject Collection	Physics and Astronomy
SpringerLink Date	Wednesday, June 23, 2004

Add to marked items

Add to saved items

Permissions & Reprints

Recommend this article

PDF (455.8 KB)

C.H. Crouch[1, 2], J.E. Carey[2], M. Shen[2], E. Mazur[1, 2] ✉ and F. Y. Génin[3]

(1) Department of Physics, Harvard University, 9 Oxford St., Cambridge, MA, 02138, UK

(2) Division of Engineering and Applied Sciences, Harvard University, 9 Oxford St., Cambridge, MA, 02138, UK

(3) Lawrence Livermore National Laboratory, Livermore, CA, USA

Received: 13 August 2003 **Accepted:** 4 February 2004 **Published online:** 23 June 2004

Abstract We microstructured silicon surfaces with femtosecond laser irradiation in the presence of SF_6. These surfaces display strong absorption of infrared radiation at energies below the band gap of crystalline silicon. We report the dependence of this below-band gap absorption on microstructuring conditions (laser fluence, number of laser pulses, and background pressure of SF_6) along with structural and chemical characterization of the material. Significant amounts of sulfur are incorporated into the silicon over a wide range of microstructuring conditions; the sulfur is embedded in a disordered nanocrystalline layer less than 1 μm thick that covers the microstructures. The most likely mechanism for the below-band gap absorption is the formation of a band of sulfur impurity states overlapping the silicon band edge, reducing the band gap from 1.1 eV to approximately 0.4 eV.

PACS 78.68.+m; 81.15.Fg; 81.40.Tv; 81.65.Cf; 85.60.Gz

Find more

... Go

Within all content

Within this journal

Within this issue

Export this article

Export this article as RIS | Text

Referenced by

6 newer articles

1. Liu, Y. (2008) Broad band enhanced infrared light absorption of a femtosecond laser microstructured silicon. *Laser Physics* 18(10) [CrossRef]
2. Tabbal, Malek (2007) Formation of single crystal sulfur supersaturated silicon based junctions by pulsed laser melting. *Journal of Vacuum Science & Technology B Microelectronics and Nanometer Structures* 25(6) [CrossRef]
3. Zabotnov, S. V. (2007) Formation of nanoparticles on the silicon surface under the effect of femtosecond laser pulses. *Semiconductors* 41(8) [CrossRef]
4. Zorba, V. (2006) Silicon electron emitters fabricated by ultraviolet laser pulses. *Applied Physics Letters* 88(8)

SIONYX1403000018.0027

SAMSUNG EX. 1002 - 1546/4148

✉ **E. Mazur**
Email: mazur@physics.harvard.edu
Fax: +1-240/255-4622

References

1. T.-H. Her, R.J. Finlay, C. Wu, S. Deliwala, E. Mazur: Appl. Phys. Lett. **73**, 1673 (1998)

2. C. Wu, C.H. Crouch, L. Zhao, J.E. Carey, R. Younkin, J.A. Levinson, E. Mazur, R.M. Farrell, P. Gothoskar, A. Karger: Appl. Phys. Lett. **78**, 1850 (2001)

3. M. Sheehy, L. Winston, J.E. Carey, E. Mazur, C.M. Friend: unpublished results

4. A.J. Pedraza, J.D. Fowlkes, D.H. Lowndes: Appl. Phys. Lett. **74**, 2322 (1999)

5. C.H. Crouch, J.E. Carey, J.M. Warrender, M.J. Aziz, E. Mazur: Appl. Phys. Lett. **84**, 1850 (2004)

6. R. Younkin, J.E. Carey, E. Mazur, J.A. Levinson, C.M. Friend: J. Appl. Phys. **93**, 2626 (2003)

7. J.E. Carey, C.H. Crouch, M. Shen, M.A. Sheehy, E. Mazur: unpublished results

8. The laser beam has a Gaussian spatial profile; the fluence reported here is the average fluence determined over the entire laser spot, and the peak fluence (in the center of the spot) is twice the average fluence

[CrossRef]

5. Kim, T. G. (2006) Strong sub-band-gap infrared absorption in silicon supersaturated with sulfur. *Applied Physics Letters* 88(24)
[CrossRef]

6. Reinhardt, C. (2007) Replica molding of picosecond laser fabricated Si microstructures. *Applied Physics A*
[CrossRef]

SIONYX1403000018.0028

SAMSUNG EX. 1002 - 1547/4148

9. The average number of laser pulses used to structure a sample is defined as $\langle N \rangle = df/s$, where d= the FWHM of the Gaussian beam profile, f= the frequency of the laser pulse train, and s= the scan speed. The natural frequency of the laser pulse train is 1 kHz, but we can reduce the frequency to 150 Hz or less using a fast mechanical shutter

10. Z.R. Zanatta, I. Chambouleyron: Phys. Rev. B **53**, 3833 (1996)

11. www.genplot.com

12. The RBS spectra may be affected slightly by the changing morphology of the surface, as the surface area of the samples changes as processing conditions change. However, the microstructures made with 2, 3, and 5 laser pulses are similar in size and shape, as are the microstructures made with 3, 4, and 5 kJ/m^2, so the sulfur concentrations for those samples can be confidently compared. As the shape of the microstructures is unchanged by annealing, the concentrations before and after annealing can also be compared with confidence

13. E. Janzen, R. Stedman, G. Grossmann, H.G. Grimmeiss: Phys. Rev. B **29**, 1907 (1984)

14. W. Fahrner, A. Goetzberger: Appl. Phys. Lett. **21**, 329 (1972)

15. J.I. Pankove: *Optical Processes In Semiconductors* (New York: Dover Publications, Inc. 1971) p. 9

16. The diffusion length of S in c-Si in 30 minutes at 775 K was estimated to be 25 nm by extrapolation from data In: S.M. Sze: *Physics of Semiconductor Devices*, 2nd ed. (New York: Wiley & Sons 1981) p. 68, In microcrystalline or amorphous silicon, the diffusion length may be somewhat different but is unlikely to increase more than threefold

17. Annealing temperatures that completely eliminate the below-band gap absorptance are much lower than the temperatures at which significant grain growth would be expected in microcrystalline or polycrystalline silicon. See S. Roorda, S. Saito, W.C. Sinke: Mat. Res. Soc. Symp. Proc. **100**, 417 (1988)

18. R. Wilson: J. Appl. Phys. **53**, 3490 (1984)

SIONYX1403000018.0029

SAMSUNG EX. 1002 - 1548/4148

19. P. Keblinski, S.R. Phillpot, D. Wolf, H. Gleiter: Phys. Lett. A **226**, 205 (1997)

20. F.A. Trumbore: Bell System Tech. J. **39**, 205 (1960)

21. V.I. Emel`yanov, D.V. Babak: Appl. Phys. A **74**, 797 (2002)

22. D. von der Linde, K. Sokolowski-Tinten, J. Bialkowski: Appl. Surf. Sci. **109/110**, 1 (1997)

23. P.G. Carey, T.W. Sigmon: Appl. Surf. Sci. **43**, 325 (1989)

24. R. Reitano, P.M. Smith, M.J. Aziz: J. Appl. Phys. **76**, 1518 (1994)

Frequently asked questions | General information on journals and books | Send us your feedback | Impressum | Contact

© Springer, Part of Springer Science+Business Media

Privacy, Disclaimer, Terms and Conditions, © Copyright Information

MetaPress Privacy Policy

Remote Address: 151.207.242.4 • Server: mpweb08
HTTP User Agent: Mozilla/4.0 (compatible; MSIE 6.0; Windows NT 5.1; SV1; .NET CLR 1.1.4322; InfoPath.1; .NET CLR 2.0.50727)

SIONYX1403000018.0030

SAMSUNG EX. 1002 - 1549/4148

Mat. Res. Soc. Symp. Proc. Vol. 719 © 2002 Materials Research Society

DOPING OF OXIDIZED FLOAT ZONE SILICON BY THERMAL DONORS - A LOW THERMAL BUDGET DOPING METHOD FOR DEVICE APPLICATIONS ?

R. JOB[1], A.G. ULYASHIN[1], Y.L. HUANG[1], W.R. FAHRNER[1], E. SIMOEN[2], C. CLAEYS[2, 3], F.-J. NIEDERNOSTHEIDE[4], H.-J. SCHULZE[4], G. TONELLI[5]
[1] University of Hagen, P.O. Box 940, D-58084 Hagen, Germany
[2] IMEC, Kapeldreef 75, B-3001 Leuven, Belgium
[3] Electr. Eng. Dept., KU Leuven, Kasteelpark Arenberg 10, B-3001 Leuven, Belgium
[4] Infineon AG, P.O. Box 80 09 49, D-81609 Munich, Germany
[5] IFN, Via Livornese 1291, I-56010 Pisa, Italy

ABSTRACT

Thermal donor formation was studied in oxygen enriched high resistive float zone silicon (FZ Si:O_i). Such substrates are used e.g. for radiation hard detectors or high voltage devices. RF Plasma hydrogenation (110 MHz, 50 W) was carried out at 250°C for 1 hour. Subsequent annealing was done at 450°C/air for up to 50 h. The plasma treated and annealed FZ Si:O_i samples were analyzed by spreading resistance probe, capacitance-voltage and DLTS measurements. It is shown that a rapid formation of donors can be observed in oxidized FZ Si:O_i, but in a somewhat different way than in Czochralski (Cz) Si. While in Cz Si the hydrogen enhanced formation of 'old' thermal double donors occurs under the applied processes, in FZ Si:O_i most probably the formation of new hydrogen related shallow donors can be assumed.

1. INTRODUCTION

Hydrogen enhanced formation of oxygen related 'old' thermal double donors (TDDs) can be observed in Cz Si after applying a plasma hydrogenation at 250°C (60 min) and a subsequent annealing in air at 450°C (≥ 20 min) [1-4]. TDD concentrations up to ~ 10^{16} cm^{-3} were observed. Therefore, in p-type Cz Si a counter doping by TDDs and the formation of deep p-n junctions occur if the acceptor concentration is below 10^{16} cm^{-3}. In n-type material deep regions with a graded doping can be created by the TDDs [5]. The controlled TDD formation can be used for a low thermal budget fabrication of devices with deep p-n junctions and/or graded doping profiles (e.g. high voltage or radiation detectors) [6, 7]. Normally highly resistive FZ substrates are used for such applications. By oxygen enrichment FZ Si can be made radiation hard [8-10]. But to obtain acceptable radiation hardness properties, the oxygen has to be located mainly at interstitial lattice sites. In Cz Si interstitial O_i is a major constituent of TDDs. Therefore, hydrogen enhanced TDD formation might play a role also in FZ Si:O_i, as we have recently speculated in [11]. On the other hand, hydrogen could be involved in the formation of other thermal donors species, i.e. the shallow thermal donors (STDs) [12-20], which are single donors. Oxygen most probably is also a constituent of these complexes. We will show that under the applied hydrogenation/annealing treatments in FZ Si:O_i the formation of new hydrogen related shallow donors occurs and not a hydrogen enhanced TDD formation, as was observed in Cz Si.

2. EXPERIMENTAL

The investigations were done on two kinds of oxidized n-type FZ silicon substrates with high resistivity, i.e. nominal 5 kΩcm and 500 Ωcm wafers. In case of the 5 kΩcm FZ Si, oxygen was incorporated into the material by the following procedure: i) oxygen enrichment of the wafer surfaces by 15 h dry

SIONYX1403000018.0031

SAMSUNG EX. 1002 - 1550/4148

oxidation at 1000°C (the temperature ramps were driven in a N_2 ambient), ii) annealing at 1150°C for 24 h. The first step results in a typically 340 nm thick oxide layer and during the second one, oxygen diffuses into the wafer bulk. Finally, the capping oxide layer was removed by HF etching. This annealing procedure was repeated three times in order to achieve a uniform oxygen doping across the 400 µm thick substrates. As was proven by Fourier Transform Infrared (FTIR) absorption measurements the average oxygen concentration was $1 \cdot 10^{17}$ cm^{-3} ($\pm$ $0.05 \cdot 10^{17}$ cm^{-3}). No precipitate bands were observed. Secondary Ion Mass Spectrometry (SIMS) profiles showed that over a depth of 30 µm the oxygen content in FZ Si:O_i was rather uniform. It is also important to mention that the oxygenation preserved the high resistivity of the material, which is important for device applications.

The 500 Ωcm substrates were loaded with oxygen by the wet-oxidation method, which was applied at 1150°C. Three different samples were prepared with treatment times of either 6, 12, or 21 hours. Oxygen was incorporated into the wafers bulk by in-diffusion from the surface oxide. After the oxidation procedure the oxide cap on the wafers top was removed by etching.

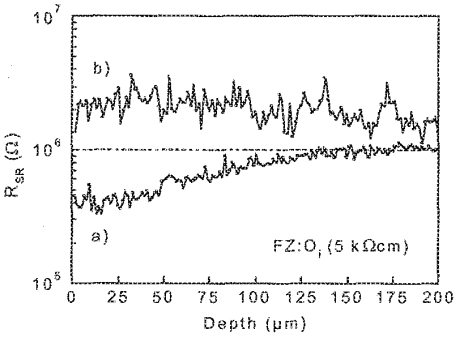

Fig. 1: a) SRP profile of a H-plasma treated (60 min, 250 °C) and annealed oxidized FZ Si (30 min at 450 °C/air); b) FZ Si, which was only annealed at 450 °C for 30 min, no H-plasma exposure was done The oxidation procedure of the FZ Si is described in the text.

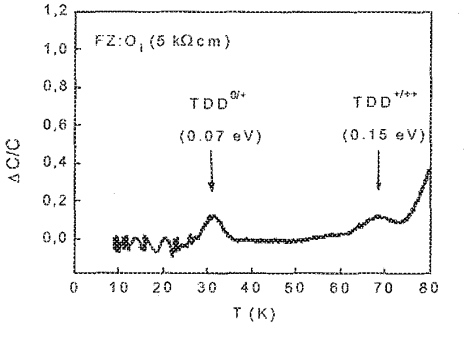

Fig. 2: DLTS spectrum of oxidized FZ Si after H-plasma treatment (60 min, 250°C) and 30 min 450°C/air annealing.

As previously reported [11], the FZ Si:O_i samples were hydrogenated by a RF (110 MHz) H-plasma exposure in a PECVD system, where the plasma was applied for 1 h at a substrate temperature of ~ 250°C. Subsequent annealing was done at 450°C in air. The samples were analyzed by spreading resistance probe (SRP) measurements on beveled samples to study qualitatively the donor concentration profiles. Beveling was done on a rotating quartz plate (typical angles to the wafer surface: 5° or 10°). Capacitance-voltage/ -temperature, C(V), C(T), and deep level transient spectroscopy, DLTS, measurements were also carried out. C(V), C(T) and DLTS were applied on circular Au Schottky barriers.

3. RESULTS AND DISCUSSION

In Fig. 1 the SRP profiles obtained on the 5 kΩcm FZ Si:O_i material are shown. Curve a) corresponds to a sample, which was treated by the H-plasma at 250°C for 60 min and a subsequent annealing at 450°C/air for 30 min. For comparison, curve b) shows the SRP profile of a sample, which was only annealed at 450°C/air for 30 min. No H-plasma treatment was applied in this case. The H-plasma treated sample, which was annealed for 30 min (curve a)), exhibits a significant decrease of the spreading resistance profile towards the surface. The bulk value for a

SIONYX1403000018.0032

SAMSUNG EX. 1002 - 1551/4148

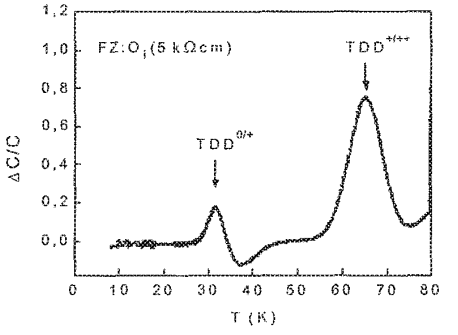

Fig. 3: DLTS spectrum of oxidized FZ Si after 50 hours annealing at 450°C/ air. No H-plasma treatment was carried out.

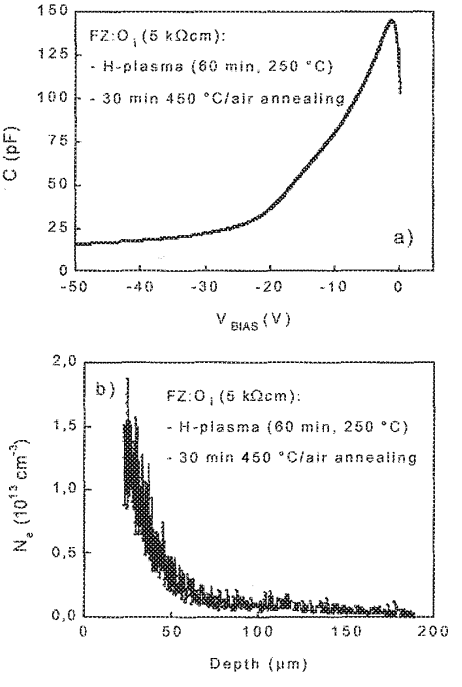

Fig. 4: a) C(V) measurements: H-plasma treated (60 min, 250°C) and annealed (30 min 450°C/air) 5 kΩcm FZ Si:O$_i$. b) From the derivative of d(1/C^2) vs. the depth the carrier concentration was calculated.

depth deeper than ~ 130 μm was ~ $1 \cdot 10^6$ Ω, while near the surface a resistance of ~ $4 \cdot 10^5$ Ω could be observed. The SRP profiling of a similar substrate, which was only annealed for 30 min at 450 °C/air (curve b)), did not show a donor introduction near the surface above the donor concentration of the starting material (i.e. a flat profile was found). In addition, it can be seen that the overall resistance of the flat profile was slightly higher than the bulk value of curve a).

In order to verify the presence of oxygen related TDDs a DLTS characterization was applied. DLTS was done with a bias pulse from -4 to 0 V, the emission constant window was 6 ms. In Fig. 2 a spectrum is shown, which was obtained on a H-plasma treated (1 h, 250°C) and annealed (30 min, 450 °C/air) 5 kΩcm FZ Si:O$_i$ sample. Fig. 3 exhibits the DLTS results measured on the 5 kΩcm FZ Si:O$_i$ sample, which was only annealed for 50 h at 450°C/air. After plasma hydrogenation and 30 min annealing at 450°C/air only very small signals occur, which can be attributed to TDDs. The DLTS signal corresponding to TDDs is increased for the case of the 50 h annealed sample (without previous H-plasma treatment), as can be seen in Fig. 3. However, it is to underline that the observed TDD concentrations are rather low. TDD concentrations were estimated from the saturation peak height of the TDD$^{+/++}$ level for three samples: [TDD] ≈ $2 \cdot 10^{10}$ cm^{-3} for plasma treated and 30 min annealed FZ Si:O$_i$ (Fig. 2); [TDD] ≈ $1.4 \cdot 10^{12}$ cm^{-3} for 50 h annealed FZ Si:O$_i$ (Fig. 3); and [TDD] ≈ $2.7 \cdot 10^{12}$ cm^{-3} for a plasma treated and 50 h annealed FZ Si:O$_i$ (not shown).

Figure 4a exhibits the C(V) curve of the sample, which was H-plasma treated for 1 h at 250°C and annealed for 30 min at 450°C. The depth dependence of the carrier concentration can be derived via the equation:

$$N_e = \frac{2}{HqA^2\varepsilon_{Si}},$$

where q is the elementary charge, A the contact area (A = 0.2827 cm^2 for the case shown in Fig. 4), ε_{si} is the permittivity of Si ($\varepsilon_{si} \approx 1.035 \cdot 10^{-12}$ F/cm). H is the derivative of the 1/C^2 vs. V_{BIAS} curve. The depth D can be calculated from the C(V) curve by:

SIONYX1403000018.0033

SAMSUNG EX. 1002 - 1552/4148

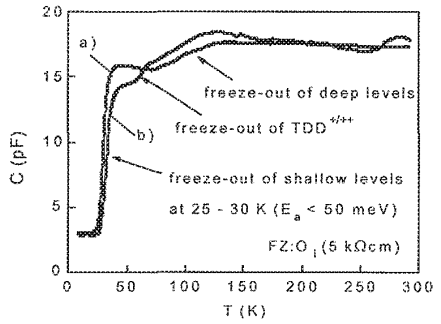

Fig. 5: C(T) measurements of oxidized FZ Si: a) after H-plasma treatment (60 min, 250 °C) and annealing (30 min at 450 °C/air); b) after H-plasma treatment and 50 h annealing at 450 °C/air.

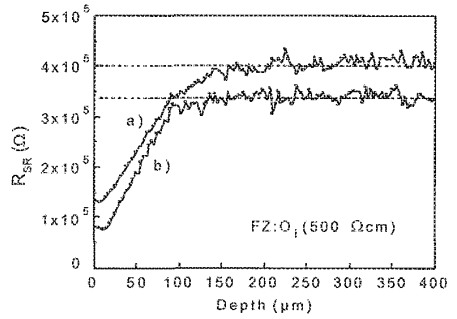

Fig. 6: SRP profiles of oxidized FZ Si (12 h wet-oxidation at 1150°C): a) 60 min H-plasma treatment at 250°C (as plasma treated); b) H-plasma treatment and subsequent 30 min annealing at 450°C/air.

$$D(V_{BIAS}) = \frac{\varepsilon_{Si} \cdot A}{C(V_{BIAS})}.$$

As can be seen in Fig. 4b the free carrier concentration N_e (electrons) is enhanced near the wafers surface, where a value of ~ $1.3 \cdot 10^{13}$ cm^{-3} can be calculated for the plasma treated and 30 min annealed FZ Si:O_i sample. The bulk free carrier concentration is ~ $1 \cdot 10^{12}$ cm^{-3}, and can be found in wafer regions deeper than 80 μm below the surface. Similar results were obtained for the 50 h annealed sample (without H-plasma treatment) and the plasma treated and 50 h annealed samples. Except for the 50 h annealed sample, C(V) analysis reveals a carrier concentration, which was significantly higher than the corresponding TDD concentration measured by DLTS. It has to be mentioned that the doping density of a non-treated 5 kΩcm FZ Si:O_i sample was about $3.6 \cdot 10^{12}$ cm^{-3} [11], i.e. a value comparable with the bulk value of the H-plasma treated and 30 min annealed sample.

The TDD concentrations, which were introduced by H-plasma treatments and subsequent annealing in FZ Si:O_i are not comparable with the TDD concentrations, observed recently in p-type Cz Si, which was treated under similar conditions (plasma hydrogenation at 250°C and subsequent annealing at 450°C/air for t ≥ 20 min). These Cz Si samples were doped with rather high acceptor concentrations ([B] ~ $1 \cdot 10^{15}$ cm^{-3}). Due to the observed counter doping of initial p-type Cz Si material and the formation of p-n junctions by a hydrogen enhanced TDD formation, one can conclude that by such treatments the TDD concentrations are significantly higher than $1 \cdot 10^{15}$ cm^{-3}, and even can reach values of ~ $1 \cdot 10^{16}$ cm^{-3} near the wafer surface [1-4]. The carrier concentrations near the surface of the plasma hydrogenated and annealed FZ Si:O_i are about 2-3 orders of magnitude lower.

The question arises, which donor species are responsible for the increased carrier densities of the plasma treated and annealed FZ Si:O_i samples? More insight can be obtained from C(T) measurements. In Fig. 5 the C(T) curves of H-plasma treated FZ Si:O_i samples are shown, which were annealed for 30 min and 50 hours at 450°C. In both cases a capacitance freeze-out can be observed below 30 K, i.e. a carrier emission from shallow donors with activation energies < 100 meV occurs. In addition, the freeze-out of deep levels around 125 K and of the TTD$^{+/++}$ level can be seen (the latter one only for the case of 50 h post-hydrogenation annealing).

SIONYX1403000018.0034

SAMSUNG EX. 1002 - 1553/4148

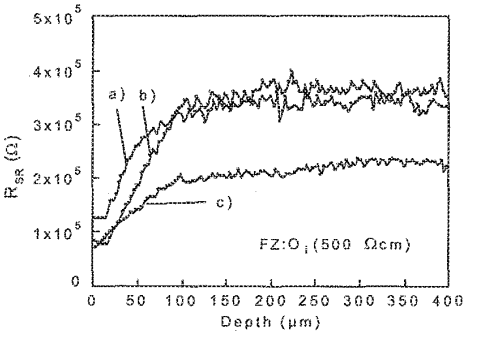

Fig. 7: SRP profiles of oxidized FZ Si after H-plasma treatment (60 min, 250°C) and 30 min annealing at 450°C/air: a), b), c) 6, 12, 21 hours wet-oxidation at 1150°C, respectively.

Now a second question arises: can the shallow donors observed by the C(T) curves in Fig. 5 be attributed to the STDs? STDs with an ionization energy of ~ 35-37 meV are found in as-grown Cz Si in a wide temperature range. They are created at ~ 470 °C. Due to model assumptions they are related to NO_x species (with x = 2-4) [20]. Nitrogen might be incorporated into the FZ Si from the inert gas ambient during crystal growth. Oxygen was introduced later by the oxidation procedures. However, as can be seen from SRP profiles obtained on 500 Ωcm FZ Si:O_i samples (Fig. 6), already directly after the H-plasma exposure at 250°C, an enhanced doping can be observed towards the wafer surface. In deep wafer regions (≥ 150 μm) the flat bulk doping profile is found. Post-hydrogenation annealing for 30 min at 450°C does not significantly change this profile. Only the bulk resistance is somewhat reduced (i.e. a weak hydrogen supported TDD formation?). Moreover, in Fig. 7 the SRP profiles of H-plasma exposed and annealed 500 Ωcm FZ Si:O_i samples are shown, which were pre-treated by 6 h, 12 h, and 21 h wet-oxidation. It is evident that an increasing oxygen concentration does not significantly alter the graded doping near the surface of the samples. Also it can be seen (especially for the sample with 21 h wet-oxidation) that the bulk resistance is slightly reduced probably due to the formation of TDDs. We conclude that neither TDDs nor STDs are responsible for the increased graded doping near the surface of H-plasma treated and annealed FZ Si:O_i samples, since even post-hydrogenation annealing is not necessary to create the graded doping region. It is more reasonable to assume that hydrogen plays the major role for the creation of the observed shallow levels.

4. SUMMARY AND CONCLUSIONS

Shallow donor formation during plasma hydrogenation and subsequent annealing of highly resistive oxidized FZ Si was studied by SRP, DLTS, C(V), and C(T) measurements. H-plasma treatments at 250°C with (even without subsequent annealing at 450°C/air) provided a graded doping near the wafers surface. Deep in the bulk of the treated FZ Si:O_i samples the original doping concentration was retrieved. Although a rapid low temperature doping occurs in the plasma hydrogenated and annealed FZ Si:O_i, it is to underline that it occurs in a different way than in Cz Si. While in Cz Si 'old' TDDs are created by the H-plasma exposure at 250°C and subsequent annealing at 450°C/air [1-4], in FZ Si:O_i there is no clear evidence for such a hydrogen supported TDD formation. Only after long annealing times (i.e. 50 hours) TDD formation could be observed in FZ Si:O_i (similar after long time furnace annealing of Cz Si). But the TDD concentration was also rather low in this case (which can be explained by a lower concentration of interstitial oxygen in FZ Si:O_i as compared to Cz Si). Also the formation of STDs can be ruled out under the applied process conditions. A more reasonable explanation of the experimental results is the formation of new hydrogen related shallow donors with an activation energy below 100 meV. Since the mechanism of hydrogen supported TDD formation is not working in FZ Si:O_i, the state of in-diffused oxygen might be different than the one of grown-in oxygen in Cz Si. In other words, there might be different nuclei present in Cz Si, which interact with hydrogen

SIONYX1403000018.0035

SAMSUNG EX. 1002 - 1554/4148

to form the TDDs, and such nuclei are not present in FZ Si:O_i. Graded doping profiles might be favorable for an improvement for certain device applications, for instance in case of high-voltage diodes or radiation detectors. The performance of such devices can be improved by deep graded doping profiles, since by the internal electrical field gradient the device operation (e.g. sensitivity of detectors) can be optimized. The discussed formation of graded doping in FZ Si:O_i by plasma hydrogenation with or without additional annealing might be a promising approach to develop a low thermal budget technology for such applications.

ACKNOWLEDGEMENT

This work has been partially performed in the frame of the European Network on Defect Engineering of Advanced Semiconductor Devices (ENDEASD - ERB 4061 PL 97-0645) and was also partially supported by the F.W.O.-G.0051.97 project.

REFERENCES

1. R. Job, D. Borchert, Y.A. Bumay, W.R. Fahrner, G. Grabosch, I.A. Khorunzhii, A.G. Ulyashin, MRS Symp. Proc. Series **469**, 101 (1997).
2. A.G. Ulyashin, Y.A. Bumay, R. Job, G. Grabosch, D. Borchert, W.R. Fahrner, A.Y. Diduk, Solid State Phenomena **57-58**, 189 (1997).
3. R. Job, W.R. Fahrner, N.N. Kazuchits, A.G. Ulyashin, MRS Symp. Proc. Series **513**, 337 (1998).
4. A.G. Ulyashin, Y.A. Bumay, R. Job, W.R. Fahrner, Appl. Phys. A **66**, 399 (1998).
5. R. Job, A.G. Ulyashin, W.R. Fahrner, V.P. Markevich, L.I. Murin, J.L. Lindström, V. Raiko, J. Engemann, in: High Purity Silicon VI, Electrochem. Soc. Proc. **2000-17**, 209 (2000).
6. R. Job, A.G. Ulyashin, W.R. Fahrner, F.J. Niedernostheide, H.J. Schulze, E. Simoen, C.L. Claeys and G. Tonelli, in: Proc. of the XIth Int. Workshop on the Physics of Semicond. Devices (IWPDS '2001), p. 405 (2002).
7. R. Job, W.R. Fahrner, A.G. Ulyashin, Mater. Sci. Engineer. B **73**, 197 (2000).
8. A. Ruzin, G. Casse, M. Glaser, F. Lemeilleur, Nucl. Instr. and Meth. in Phys. Res. A **426**, 94 (1999).
9. A. Ruzin, G. Casse, M. Glaser, F. Lemeilleur, R. Talamonti, S. Watts, A. Zanet, Nucl. Phys. B (Proc. Suppl.) **78**, 645 (1999).
10. B. Dezillie, Z. Li, V. Eremin, W. Chen, L.J. Zhao, IEEE Trans. Nucl. Sci. **47**, 1892 (2000).
11. R. Job, A. G. Ulyashin, W. R. Fahrner, E. Simoen, C. Claeys, G. Tonelli, Nucl. Instr. and Meth. B **186**, 116 (2002).
12. J. Hartung, J. Weber, Phys. Rev. B **48**, 14161 (1993).
13. S.A. McQuaid, R.C. Newman, E.C. Lightowlers, Semicond. Sci. Technol. **9**, 1736 (1994).
14. V.P. Markevich, M. Suezawa, K. Sumino, L.I. Murin, J. Appl. Phys. **76**, 7347 (1994).
15. Yu. V. Martynov, T. Gregorkiewicz, C.A.J. Ammerlaan, Phys. Rev. Lett. **74**, 2030 (1995).
16. H.J. Stein, J.W. Medernach, J. Appl. Phys. **79**, 2337 (1996).
17. R.C. Newman, J.H. Tucker, N.G. Semaltianos, E.C. Lightowlers, T. Gregorkiewicz, I.S. Zevenbergen, C.A.J. Ammerlaan, Phys. Rev. B **54**, R6803 (1996).
18. Y. Tokuda, A Ito, H. Ohshima, Semicond. Sci. Technol. **13**, 194 (1998).
19. Yu. V. Gorelkinskii, N.N. Nevinnyi, K.A. Abdullin, J. Appl. Phys. **84**, 4847 (1998).
20. V.V. Voronkov, M. Porrini, P. Collareta, M.G. Pretto, R. Scala, R. Falster, G.I. Voronkova, A.V. Batunina, V.N. Golovina, L.V. Arapkina, A.S. Guliaeva, M.G. Milvidski, J. Appl. Phys. **89**, 4289 (2001).

SIONYX1403000018.0036

SAMSUNG EX. 1002 - 1555/4148

Development of a Production-Ready, Back-Illuminated CMOS Image Sensor with Small Pixels

Tom Joy, Sunggyu Pyo[#], Sunghyung Park[#], Changhoon Choi, Chintamani Palsule, Hyungjun Han[#], Chen Feng, Sangjoo Lee[#], Jeff McKee, Parker Altice, Chris Hong, Christian Boemler, Jerry Hynecek, Michael Louie, Juil Lee[#], Daebyung Kim[#], Homayoon Haddad and Bedabrata Pain*

Magnachip Semiconductor America, Advanced Pixel Research Center, Lake Oswego, Oregon
Tel: +1(408) 213-2561, Email: tom.joy@magnachip.com
[#]Magnachip Corporation, Seoul, Korea and Cheongju, Korea
*Jet Propulsion Laboratory, California Institute of Technology, Pasadena, California

Abstract

A back-illuminated 2 megapixel CMOS sensor utilizing mature wafer manufacturing operations is described. Sensitivity, dark current and other key pixel performance measures are compared against an equivalent conventional sensor. Aspects of the process integration that make the technology manufacturable are described. Simulations that predict the performance of a full color sensor are discussed.

Introduction

Back-illuminated imaging is receiving increasing interest as a solution to some of the problems that limit imager performance as pixel size decreases. Several examples of SOI-based back illuminated sensors have been demonstrated in previous publications (1-5). In this work, we focus on the development of a production-worthy monolithic sensor with 2.2um pixels, as a platform to extend the CMOS pixel roadmap into the sub-micron range. It was built using low-cost standard fabrication techniques, and with performance predictable from simulation. We describe a production process for these sensors using available mature technology modules, and present results from a 2 megapixel (MP) sensor exhibiting comparable dark current and noise but much higher quantum efficiency (QE) and sensitivity than a conventional sensor.

Optical Advantages of BSI Configuration

Figure 1 depicts a conventional front-side illuminated (FSI) stack and a BSI stack. The optical stack height is much lower for the BSI pixel, leading to significant advantages in the effective pixel f number. On top of this, the high refractive index of silicon causes light to converge to the center of the pixel, as shown in Figures 2(a) and (b). These are finite difference time domain (FDTD) analyses of energy coupling into the silicon at 550nm, showing the stark contrast in coupling efficiency into the target pixel for FSI and BSI cases at this pixel size (1.75um). At smaller pixel sizes, the differences are even more pronounced and present a practical limit to how small conventional CMOS pixels can be using conventional technology.

Production-Ready Integration

Figure 3 is a schematic representation of the demonstration black and white imager. The fabrication process begins with a specially tailored SOI wafer that allows accurate backside thinning using oxide as an etch-stop (1-3). We use a special SOI layer configuration to suppress dark current generation at the BOX interface, to prevent QE loss at short wavelengths, to reduce cross-talk, and to provide a low resistance back-plane. An imager-compatible bulk-CMOS process (not an SOI process) was used for fabrication. Prior to thinning, a handle wafer was attached to the processed wafer for mechanical support using a low temperature oxide-oxide bonding process (6). Compared to adhesive bonding, this method allows more flexibility for subsequent processing, including higher temperature anneal steps. The acoustic micrograph of the wafer stack (figure 4) built using this process demonstrates void free bonding.

To connect the front-side metals to the bond pads on the backside (i.e. the exposed side), the fabrication process used W-filled and liner oxide isolated through-silicon vias. However, unlike that in "3D" stacked technologies (4), neither multi-wafer vias nor bonding of multiple wafers with sub-micron alignment is needed, resulting in enhanced manufacturability. Figure 5 is a SEM cross-section of the finished SOI wafer. Subsequent wafer-level thinning (backgrind to remove most of the silicon, followed by a dry silicon etch) produced a thinned monolithic imager with a planar back surface, important for subsequent color filter and microlens processing. Backside bond pads connected to the through-vias, standard oxide/nitride passivation and hydrogen anneal complete the wafer process. No special AR coating was applied. Die assembly utilized a simple wire-bonded package – similar to that utilized for an FSI part, as indicated in figure 6 that shows the pictures of two packaged black and white FSI and BSI sensors.

Demonstration Vehicle

The vehicle used to demonstrate the technology was a 2MP, 2.2um pixel pitch sensor with a two-way multiplexed pinned

1-4244-0439-X/07/$25.00 © 2007 IEEE

SIONYX1403000018.0037

SAMSUNG EX. 1002 - 1556/4148

photodiode, and with an average of 2.5 transistors per pixel. The photodiodes are fully depleted and use conventional transfer gate readout. The conventional version of this sensor, which features column-parallel ADCs and full ISP, is one of our standard products and has been optimized to achieve industry standard FSI performance. No mask or process changes (including implants) were made in the pixel area for this demonstration. The only additional masks were for through vias, backside bond pads and backside passivation. Device simulation with the unchanged imager fabrication process clearly shows the tradeoff between crosstalk and sensitivity as device thickness is varied. The 3.3um we chose for this demonstration is close to our FSI epi thickness.

Performance Summary

Table 1 is a summary comparison between the front-illuminated and back-illuminated versions of the sensor (with the same fabrication process). Neither sensor has color filters. Table 1 clearly indicates the advantages of BSI. Unlike in previous work (5), broadband QE (81% for BSI) improved 2.7x over FSI. Other imaging parameters (such as dark current, full-well, PRNU) of the BSI sensor are comparable to or better than that of the FSI sensor. The mean dark current value and the hot pixel counts were similar for BSI and FSI devices, indicating a high quality back interface has been achieved without any post-thinning backside treatment.

Figure 7 compares standard images taken at varying illumination conditions. Note that a BSI image is nearly as bright as a corresponding FSI image with three times the incident illumination. Figure 8 shows the relative spectral response of the BSI sensor compared with the simulated transmission characteristics of the passivation/oxide/silicon stack on the backside. The shape of the relative QE curve is due to the non-optimized stack on the back side of the wafer, as shown by the similarity in shapes of the two curves. We attribute the difference in peak locations to the slight discrepancy between the actual sample stack thicknesses and nominal thicknesses used in the simulation. Figure 9 shows the estimated internal quantum yield (IQE), calculated by dividing the measured response by the stack transmission. As expected, IQE drops off with wavelength due to an increasing optical penetration depth.

Simulation shows that without any additional process optimization, electrical cross-talk of BSI would be inferior to that of FSI. This was also noted by (3), and is due to the absence of inter-pixel isolation, traditionally available in form of STI and implants for FSI, where the bulk of photoelectrons are generated near the front surface of the wafer. The deterioration in BSI MTF is obvious in figure 10, and is shown as a function of primary color in figure 11. As expected from simulation, shorter wavelengths exhibit higher cross-talk - a reversal of the conventional situation. Work is ongoing to improve BSI MTF.

Optical Considerations for BSI Sensors

The optimization techniques that apply to FSI sensors clearly have to be modified for BSI sensors. One example is optimization of optical transmission into the backside. As seen in the previous section, the presence of the BOX/silicon layer in the SOI wafer presents a fresh challenge for BSI. Creating an optically ideal backside AR stack without compromising dark current is a challenging requirement and is one area of ongoing work.

The quantum efficiency measured on a black and white BSI sensor without microlenses, as in the example presented here, is the upper limit of what can be achieved. It could be argued that the addition of microlenses and color filters will only serve to decrease the measured quantum efficiency on a BSI sensor. In a front side sensor, the expectation is that the addition of a microlens above the pixel increases quantum efficiency due to concentration of photons into the photodiode area and away from the metal lines that would otherwise block much of the illumination. In our demonstration (black and white) BSI sensor, all of the incident photons that are converted to electrons are counted as part of the signal, even those that are collected by pixels that are neighbors of the target pixel. Therefore there will not be a sensitivity advantage when microlenses are added – only a cross talk reduction advantage. In fact, there will be a sensitivity penalty since the optical efficiency of a microlens is rarely over 95%.

However, in practice we have found that microlens effectiveness is limited for conventional pixel sizes of 2.2um and below. The addition of a microlens and color filter increases sensitivity by less than 10% for a 2.2um pixel, implying that the microlens barely compensates for the signal loss due to the color filter material. A major reason for this is that diffraction effects at smaller pixel sizes limit the classical advantage of a microlens, as shown in the earlier optical section.

Conclusion

Manufacturing feasibility of a black and white BSI CMOS image sensor has been demonstrated using a special SOI starting wafer, with no degradation in dark current and sensitivity increase as expected. Differences in optical considerations between FSI and BSI and potential advantages of BSI have been analyzed.

References

1. B. Pain, *Proc. 2005 Workshop on CCD/AIS*, p 105-6, 2005.
2. B. Pain et al., *Proc. 2007 Intl. Image Sensor Workshop*, p. 158-61, 2007.
3. J. Prima et al., *Proc. 2007 Intl. Image Sensor Workshop*, p 5-8, 2007.
4. V. Suntharalingam et al., *Tech. Dig. ISSCC*, vol. 48, p. 356-7, 2005.
5. S. Iwabuchi et al., *Tech Dig. ISSCC*, vol. 49, p. 302-3, 2006.
6. US patent 6,902,987, June 7, 2005

SIONYX1403000018.0038

SAMSUNG EX. 1002 - 1557/4148

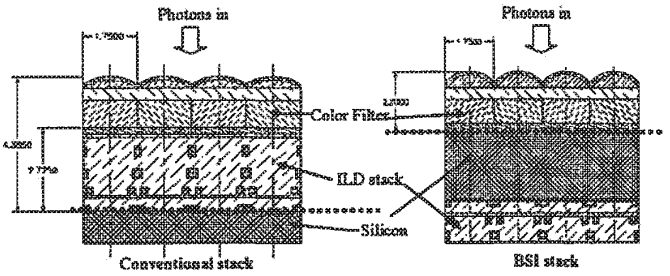

Figure 1: Schematic cross-sections of a front-illuminated (Conventional) and a back-illuminated imager (BSI) showing the optical stacks. The effective optical stack height (distance between microlens and absorbing silicon layer) is much smaller in the BSI case. The dotted line indicates the depth at which photon absorption begins. Dimensions are in microns.

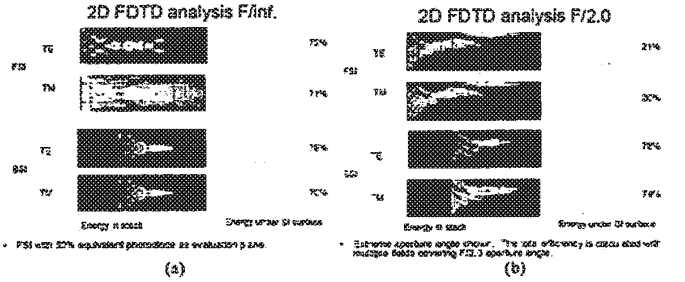

Figure 2: FDTD simulation of optical energy coupling into silicon conventional (FSI) and back-illuminated (BSI) imager under (a) normal incidence and (b) maximum incident angle for f/2.0 illumination. Even at the extreme edges of f/2.0 illumination, optical energy is well contained within the target pixel in the BSI case

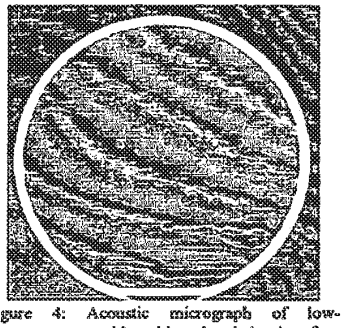

Figure 4: Acoustic micrograph of low-temperature oxide-oxide bonded interface between two 200 mm diameter wafer, revealing void-free bonding (courtesy of Ziptronix, Inc.)

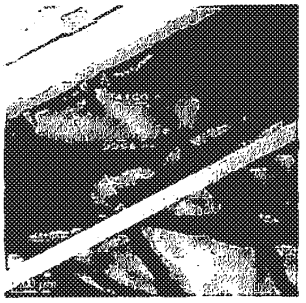

Figure 5: XSEM showing device, dielectric stack, BOX, and substrate layers of the finished SOI wafer, before removal of substrate silicon

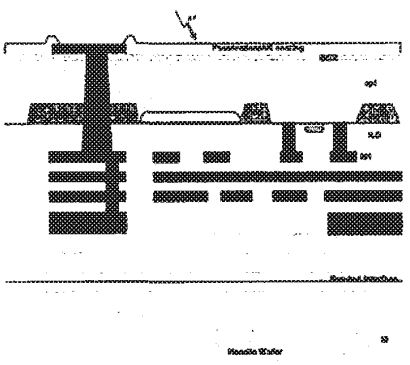

Figure 3 – Schematic cross-section of a black and white BSI sensor. The key features are the thermal oxide defining the end of the SOI device layer, the through-via providing electrical face-up connection, and the bonded handle wafer for mechanical support

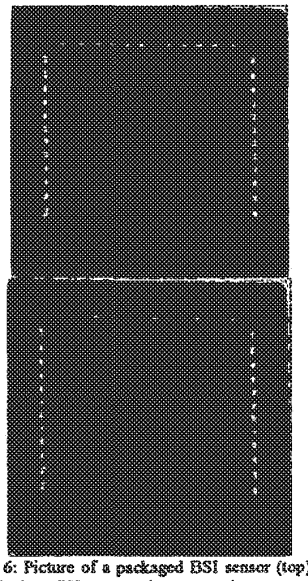

Figure 6: Picture of a packaged BSI sensor (top) next to equivalent FSI sensor (bottom) using most of the same masks. The wire bond patterns are mirror images of each other

Table 1: Measured Performance of the 2 Megapixel Back-Illuminated Imager

Parameter	BSI	FSI	Change	Units
Sensitivity (@FD, 3000°K)	1.83	0.74	2.5x increase	V/lux-sec
QE (3000°K)	81	30	2.7x increase	%
Full-well (linear)	16.5	13.0	26% increase	Ke⁻
Dark Current (@ 60°C)	126	116	8% increase	e⁻/pixel
Read noise	12.7	13.1	3% reduction	e⁻
PRNU (@ 50% full-well)	1.85	1.83	unchanged	%
Dynamic Range	62.3	59.9	2.4 dB improvement	dB
Max SNR	42.2	41.1	1.1 dB improvement	dB

SIONYX1403000018.0039

SAMSUNG EX. 1002 - 1558/4148

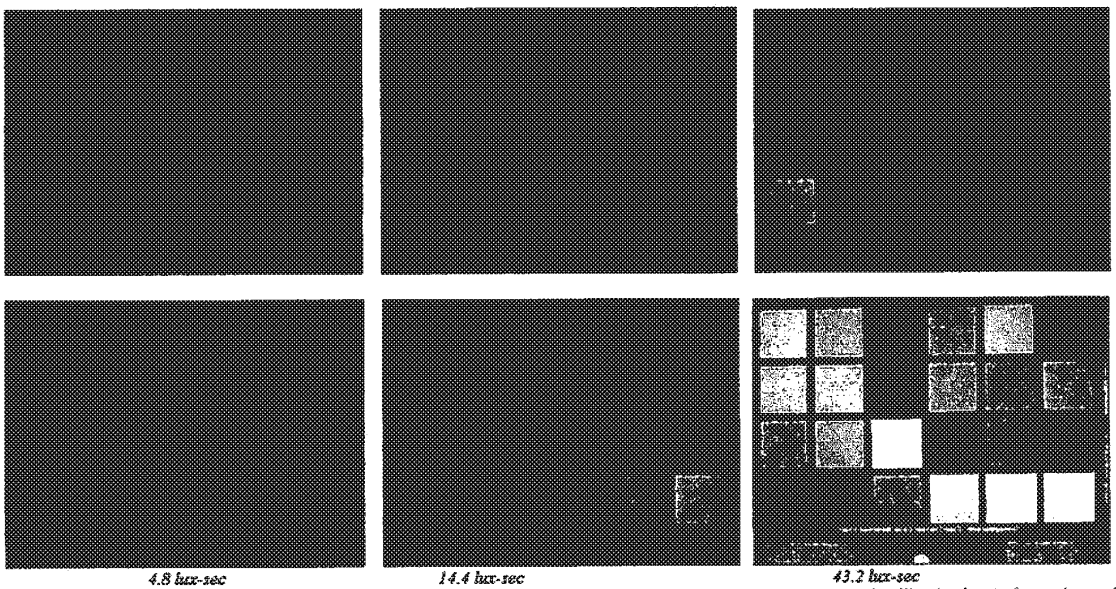

Figure 7: Comparison of images of standard target patterns using a 2MP FSI imager (top) and BSI imager (bottom) at varying illumination (unity analog and digital gain). Note that a BSI image is about as bright as an FSI image at 3X the illumination.

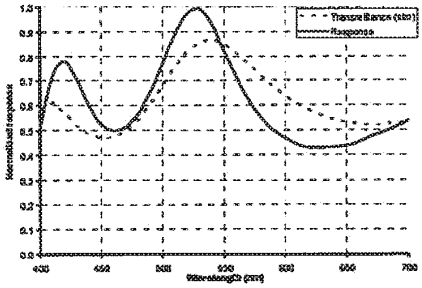

Figure 8: Relative spectral response of the BSI sensor (solid line) compared with the simulated transmission characteristics of the passivation/oxide/silicon stack (dashed line). The difference in peak locations is likely due to film thickness error in the simulation.

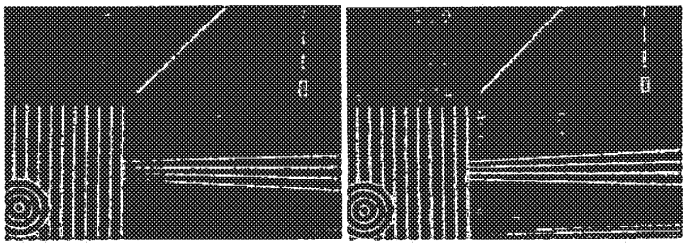

Figure 10: Resolving power comparison of BSI (left) and a FSI sensor (right). Note that BSI image is comparatively blurred (due to diffusion crosstalk).

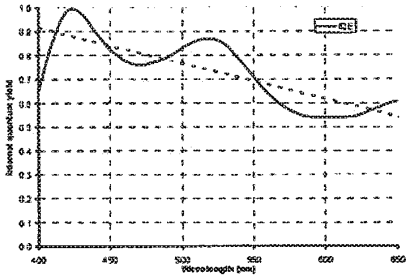

Figure 9: Relative internal quantum yield, after compensating for transmission characteristics. The dashed line is the simulated decrease in QE with wavelength, commensurate with device layer thickness

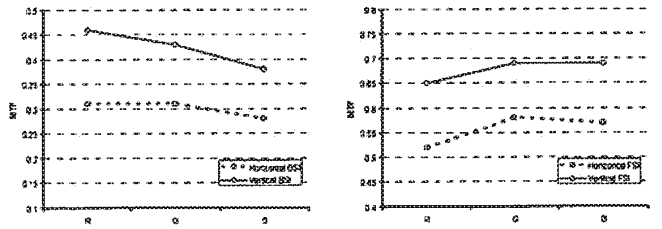

Figure 11: Horizontal and vertical components of modulation transfer function (MTF) for BSI (left) and FSI (right) as a function of illumination color

SIONYX1403000018.0040

SAMSUNG EX. 1002 - 1559/4148

Advanced Photodiode Detector For Medical CT Imaging: Design and Performance

Fan Ji, Mikko Juntunen, Iiro Hietanen
Detection Technology, Inc.
Vantaa, Finland
Email: ji.fan@deetee.com, mikko.juntunen@deetee.com

Simo Eränen
Micro and Nanoelectronics
Technical Research Center of Finland (VTT)
Espoo, Finland
Email: simo.eranen@vtt.fi

***Abstract*—This paper presents an advanced photodiode detector design for medical imaging applications, especially computerized tomography. The detector is silicon based and integrates the through-wafer interconnection technology into conventional front illuminated photodiode. The number of photodiode elements in the detector can be extended in 2D without reducing the photodiode active area. The signal of each photodiode element can be directly read out from the backside of the detector. Moreover, detectors can be tiled together in 2D without any physical limitation. A test photodiode detector was designed and demonstrated with 3x3 photodiode matrix arrangement in this paper. Different parameters were measured and analyzed from the demonstrated chip and test structures. The results show that the detector inherits most of the performance advantages from the conventional front illuminated photodiode, and all the parameters can either meet or exceed the requirements of modern CT systems.**

I. Introduction

The principle of the X-ray Computed Tomography (CT) for medical imaging is that an X-ray source gives out a fan beam or a cone beam of X-rays with certain energy and intensity, and the attenuation of the X-ray beam having penetrated the patient is recorded by an arc of photodiode detector arrays on the opposite side of the patient. With the synchronized rotation of the X-ray source and detectors around the patient, 2D cross section image or 3D information of the desired object inside the patient can be reconstructed.

For efficient volume scanning, spiral CT has been developed, in which the patient is controlled to continuously moving during the scanning through the rotating gantry, which is the ring structure carrying X-ray source and the detector arrays sampling the signals at the certain frequency. In addition, multi-slice detectors have been introduced to increase the volume scanning speed and enhance the spatial resolution. For instance, to scan a dynamic organ like the heart, the shorter the scanning time, the less distortion into the images will be caused by the patient and organ movements during the scanning. In order to further increase the scanning speed of the multi-slice CT machines, more detector coverage in 2D is required. Moreover, the pitch of two slices is getting smaller and smaller to increase the quality of the image. Some exemplary detector geometries used in modern CT systems can be seen in Table I [1], where the slice of the detectors is defined as the physical number of the rows along the gantry circumference direction.

TABLE I
Modern CT System With Multi-Slice Detectors

Manufacture	Scanner	No. of element slices	Year
GE	VCT 64	64	2004
Philips	Brilliance 64	64	2005
Siemens	SOMATOM Sensation 64	40	2004
Toshiba	Aquilion 64	64	2004
Toshiba	Beta site	256	2006

The development trend of increasing the amount of slices in modern X-ray CT detector for medical imaging application is facing serious limitations with the conventional photodiode detectors. The signals are wired out by metal lines which consume the surface area between the active photodiode elements in the conventional photodiode detectors. Therefore, only a certain maximum amount of slices can be constructed without sacrificing too much of the detector active area. The need of wire bonding pads for all of the signals on the edge of the detector chip gives another practical limitation to increase the number the slices. Furthermore, due to the wire bonding connections from the detectors to the substrate, detectors can not be fully tiled in 2D side by side. In addition to these limitations, once the detector elements exceed certain amount slices, the performance of the detector starts to decrease by parasitic factors like coverage efficiency, cross talk, electrical noise, etc.

Back illuminated Photodiode (BIP) detector has been reported to overcome the limitations encountered by conventional detectors [2] [3], but it has some drawbacks in both fabrication and operation. In order to effectively collect the photo current, very thin wafers and chips (typically 100μm thickness) have to be handled in the processing and assembly. On the other hand, the photo current is collected by carrier diffusion from the BIP's working principle, which slows down the operational speed and increases the cross talk between the adjacent elements. By introducing slot structures [2], BIP detector can minimize the cross talk to some level, but it

1-4244-0755-9/07/$20.00 ©2007 IEEE

Authorized licensed use limited to: IEEE Xplore. Downloaded on March 5, 2009 at 16:26 from IEEE Xplore. Restrictions apply.

SIONYX1403000018.0041

SAMSUNG EX. 1002 - 1560/4148

deteriorates the mechanical stability and the productivity as side effect.

In order to achieve fully tileable detector arrays for medical imaging application without decreasing the productivity and performance of the detector, an advanced structure is presented in this paper. It integrates the through-wafer interconnection (TWI) technology [4] into the conventional front illuminated photodiode (FIP) detector. With the incoming light on the front surface of the detector, each signal of the detector elements can be extracted directly from the back side of the detector through TWI, meanwhile, keeping most of the performance advantages from FIP.

II. Design And Fabrication

A test photodiode detector with the 3x3 photodiode elements and the corresponding amount of TWIs were designed and demonstrated in this paper. The geometry of each photodiode element is designed and optimized for the application in the medical CT imaging. The photodiode element has an active area about $1mm^2$ and the pitch of approximately 1.25mm. The TWI for each photodiode element is located outside the active area and has the dimension of ϕ50μm. Each TWI consists of the isolated side wall and the conductive filling plug. The length of the TWI is that of the final thickness of the detector. The distance between the photodiode active area and the TWI is about 100μm. The anode of each photodiode element is connected to the top end of the TWI by a metal line on the front side. The corresponding contact pad for the anode on the back side is located directly on top the other end of the TWI. The cathode contact of each photodiode element is connected to the silicon bulk from the back side as well. The size of the contact pads is about 160μmx160μm. The cross section of individual photodiode element can be seen in Fig. 1. The light impacts on the front surface of the photodiode, and the generated photo current is collected by the anode and thereafter extracted out through the TWI from the pad on the back side.

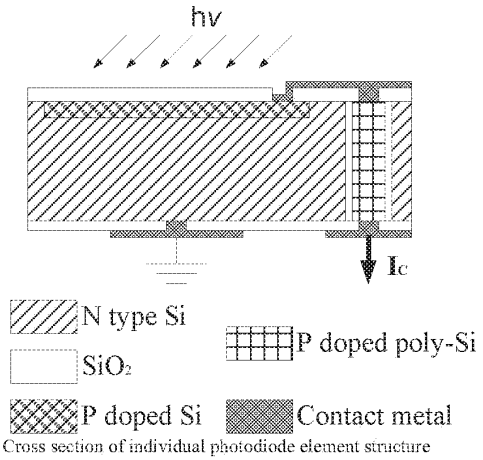

Fig. 1. Cross section of individual photodiode element structure

N type silicon wafer with suitable resistivity was selected as the substrate. The fabrication process started with the formation of TWIs. Inductively coupled plasma etching (ICP), thermal oxidation, in-situ doped polycrystalline silicon filling, grinding and chemical mechanical polishing (CMP) were used sequentially to fabricate the TWIs on the wafer. More details can be found in [4]. Since the structure and material of the interconnections are totally compatible with the standard silicon processing, photodiodes can be readily processed onto the pre-processed wafers already with TWIs. The p-type implantation was carried out to create active areas (anodes) on the front side, and the additional n-type implantation was carried to form better cathode contacts on the back side. Contact openings were etched out on the front side for both anode and TWI, and aluminum metallization was sputtered and patterned for the connection between the anode and the top end of the TWI. Contact openings were also etched on the back side for the cathode and TWI, followed by aluminum sputtering and patterning. Additionally, under bump metallization might be needed based on the selected packaging method. The simplified processing flow can be seen in Fig. 2. After the whole processing, the final detector thickness is about 300μm, which can be easily increased to 400μm.

The cross section of one processed photodiode with TWI can be seen in Fig. 3, where the PN junction area of the photodiode element was marked afterwards, because the implantation areas are not visible by the picture from microscopy. On the other hand, the TWI structure can be clearly seen. The serrated side wall close to the bottom is caused by the local etching in the ICP process. As long as it is protected by reasonable thickness of isolation, it will not affect the performance of the photodiode.

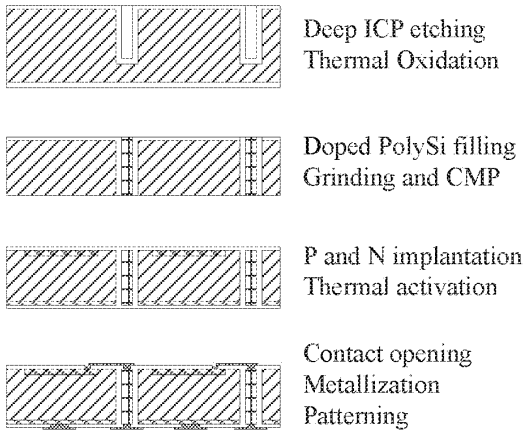

Fig. 2. Processing flow of the detector

Authorized licensed use limited to: IEEE Xplore. Downloaded on March 5, 2009 at 16:26 from IEEE Xplore. Restrictions apply.

SIONYX1403000018.0042

SAMSUNG EX. 1002 - 1561/4148

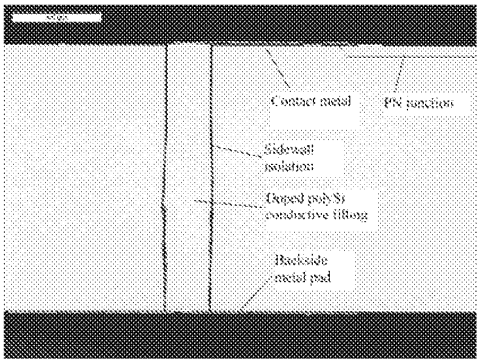

Fig. 3. Microscopy picture of the processed photodiode element structure

III. Methods And Results

A. *Current versus voltage characteristics*

Within a Karl SÜSS dark probe station, the current to voltage characteristics of all photodiode elements on the sample detectors were measured by using a HP semiconductor parameter analyzer. The current to voltage behaviors of nine photodiode elements on one sample chip can be seen in Fig. 4. The leakage current, series resistance, shunt resistance and breakdown voltage can be extracted from the measurement data.

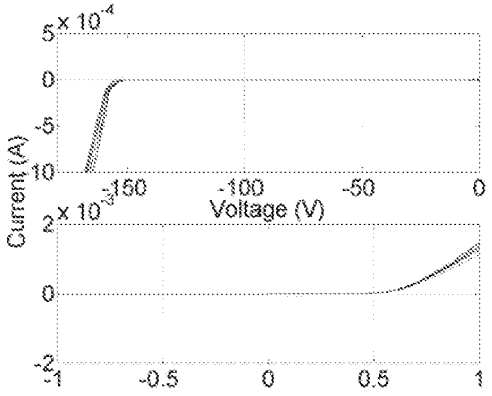

Fig. 4. The dark current of the photodiode elements under the bias voltage browsing from -180V to 1V at room temperature.

The leakage current is one of the important parameters for medical CT imaging, which partly influences the noise of the system. The average leakage current of the photodiode elements is about 0.5pA at the room temperature under 10mV reverse bias. The distribution of leakage currents of one tested chip is shown in Fig. 5. The sources of the leakage current in PN diode devices are well known mainly from the space charge region, bulk quasi natural region and surface interface region in terms of the saturation current, generation-recombination current and the surface current [5]. The design presented in this paper is such that the TWI is far enough outside the active area of the photodiode. Therefore, the TWI induced space charge region and surface interface are separated from photodiode active area by quasi natural regions and the isolation side wall. This results in the TWI having very small impact on the photodiode leakage current.

By commonly used definition of shunt resistance, the shunt resistance of the photodiode can be evaluated by the voltage current ratio under 10mV reverse bias. According to the leakage current data in Fig. 5, the average shunt resistance is about 20GΩ.

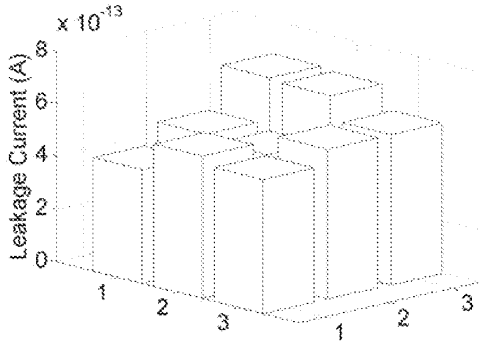

Fig. 5. The leakage current of individual photodiode element under 10mV reverse bias at room temperature.

The series resistance of the photodiode is another important parameter for CT system. The total resistance of a conventional photodiode element includes two contact resistances, silicon bulk resistance and the wire resistance. The length of a standard wire in conventional multi-slice FIP detector from center to the edge can be about 30mm with 6μm width, which gives 250Ω with aluminum sheet resistance of 50mΩ/□. This will cause a relatively large resistance difference between the center elements and edge elements of a conventional FIP detector. The uniformity of series resistances can be greatly improved by extracting signal through TWI besides each photodiode element. In the forward bias situation [6], considering the voltage falls on the series resistor, the series resistance of the photodiode can be deduced in the form of (1), where dV/dI is the dynamic series resistance measured under 1V forward bias, k is the Boltzmann's constant, T is the temperature in Kelvin, q is the electronic charge, I is the dynamic current under 1V forward bias and n_f is the ideality factor. The calculated series resistance value of the demonstrated photodiode detector in this paper is shown in Fig. 6 by assuming the ideality factor of 1.5. This gives about 230Ω on the average.

$$R_s = \frac{dV}{dI} - \frac{n_f kT}{qI} \qquad (1)$$

Authorized licensed use limited to: IEEE Xplore. Downloaded on March 5, 2009 at 16:26 from IEEE Xplore. Restrictions apply.

SIONYX1403000018.0043

SAMSUNG EX. 1002 - 1562/4148

The average breakdown voltage of each photodiode element is about 160V reverse bias, which can also be seen in Fig. 4. This is much higher than the requirement for the CT application. In addition, the breakdown voltage measured from individual TWI was over 200V reverse bias under the same measurement condition. Consequently, the TWI structure has no negative effect on photodiode breakdown characteristic.

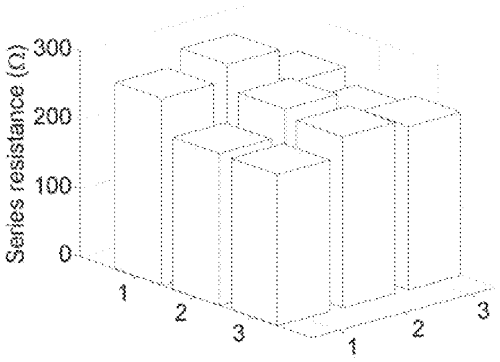

Fig. 6. The dynamic series resistance of individual photodiode element under 1V forward bias at room temperature.

B. Capacitance versus voltage characteristic

The capacitance of conventional FIP element consists of PN junction capacitance, line capacitance and bonding pad capacitance under normal working conditions of CT system. The metal lines induce not only parasitic capacitance to the silicon bulk, but also a small parasitic capacitance to each other. According to Schaper and Amey's model [7], the same metal line as discussed in the series resistance section can cause about 10pF parasitic capacitance, which proportionally increases the noise in the following preamplifier stage of the CT system. For the photodiode detector presented in this paper, the TWI capacitor replaces the wire capacitor in each photodiode element. The total capacitance of the photodiode elements with TWIs were measured by Keitheley CV analyzer and the results are shown in Fig. 7, where the dotted line presents the measured capacitance, and the "o" line is the calculated capacitance from the PN junction and contact pad with proper material parameters and dimension values. The capacitance of the pad capacitor can be calculated by using parallel plate model. The capacitance of a quasi PIN junction introduced by depletion region can be calculated by (2) according to [6], where A_j is the junction area, ε_s is the silicon permittivity, ϕ_i is the junction build-in potential, V is the bias voltage, N_d is the doping density in quasi intrinsic N type region, W indicates the width of the depletion region and W_i indicates the width of the quasi intrinsic region. The calculated capacitance might have bigger error under low reverse bias voltage, because one side abrupt junction is assumed instead of the real variation of the doping concentration in the quasi intrinsic region. But the calculated capacitance is more accurate under high reverse bias voltage because the extended depletion width can be neglected once the depletion width reaches the edge of the quasi intrinsic region. Therefore, the difference between two curves at high bias voltage point gives more precisely about the capacitance of the TWI, which is about 0.1pF under 5V reverse bias. It is fairly small when comparing to the pad and the junction capacitance.

$$\begin{cases} C_j = A_j\sqrt{\dfrac{q\varepsilon_s N_d}{2(\phi_i - V)}} & W < W_i \\ C_j = A_j\varepsilon_s / W_i & W \geq W_i \end{cases} \quad (2)$$

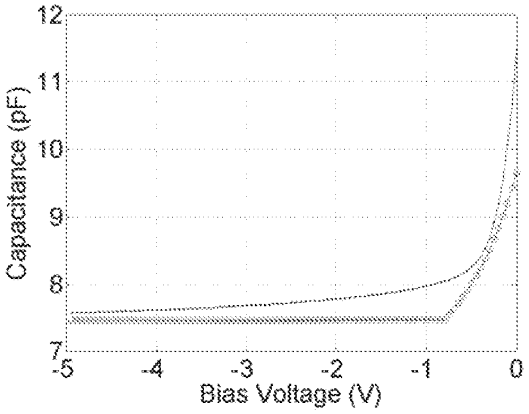

Fig. 7. Total capacitance measured from demonstrated photodiode element at 1MHz under room temperature with dotted line. The "o" line is the calculated capacitance of PN junction and contact pad at room temperature with assumption and certain material parameters.

C. Light responsivity

Light responsivity, also called light sensitivity, is defined in (3) according to [5], where η is the quantum efficiency, λ is the wavelength of the incident light, h is the Planck's constant, c is the light speed and q is the electronic charge. In the measurement setup, a monochrometer was used to scan over a spectral range from 320nm to 1040nm of a mercury lamp source. The outcoming light was collimated to the active area of the photodiode. The light current of both specimen and a calibrated photodiode were measured from the amperometer at zero bias voltage. The power of the incoming light was calculated by using the known properties of the calibrated photodiode. In order to make the incident light safely fall into the active area of the photodiode, a 25mm^2 monitor diode with the TWI taken from the same processed wafer was used as the sample diode. In addition to the sample diode, another monitor diode with the 25mm^2 active area but without the TWI taken from the same processed wafer was also measured. The measured responsivity data can be seen in Fig. 8, where the

Authorized licensed use limited to: IEEE Xplore. Downloaded on March 5, 2009 at 16:26 from IEEE Xplore. Restrictions apply.

SIONYX1403000018.0044

SAMSUNG EX. 1002 - 1563/4148

two curves from two monitor diodes show that the TWI has nearly no effect on the light responsivity. The straight line in Fig. 8 gives the ideal light responsivity with the quantum efficiency of 100%. The quantum efficiency is close to 80% for the demonstrated sample diodes under the wavelength from 500nm to 840nm by using (3). The quantum efficiency can be further improved by using additional antireflection layers.

$$\frac{I_{opt}}{P_{opt}} = \eta \frac{q\lambda}{hc} \tag{3}$$

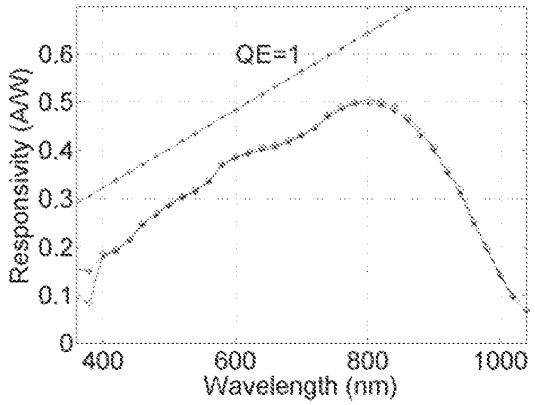

Fig. 8. Light responsivity from the sample diodes at room temperature. The "o" line is measured from sample diode with TWI, the "*" line is measured form sample diode without TWI, and most of the "o" line and "*" line is overlapped each other. The "+" line is the ideal reponsivity calculated by assuming quantum efficiency equal to 100%.

D. Rise time and fall time

The rise time of the photodiode is defined as the output signal rising from 10% to 90% of the steady state value, and fall time is defined in the opposite direction, output signal falling from 90% to 10%. The circuit of the measurement setup can be seen in Fig. 9, where I_{ph} is the photo current generated in the photodiode under testing by using a laser LED illumination driven with square waveform at low frequency, C_D is the total capacitance of the photodiode including junction capacitance, TWI capacitance and terminal capacitance, R_S is the series resistance of the photodiode including the diode resistance, TWI resistance and terminal resistance, R_f is the feedback resistance in the operational amplifier circuit and R_{sh} is the shunt resistance of the photodiode. The output can be calculated by using (4), assuming that the shunt resistance is infinite.

$$V_{out} = \frac{R_f}{1 + j2\pi f C_D R_S} I_{ph}. \tag{4}$$

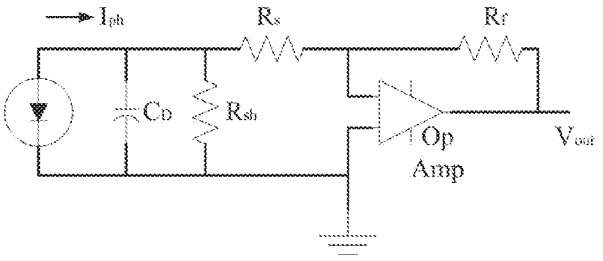

Fig. 9. Modeling of photodiode and operational amplifier circuit.

It can be seen from (4) that the total capacitance and series resistance contribute to the RC delay time, which is given by

$$t_1 = 2.2 R_S C_D. \tag{5}$$

In addition to the RC delay time, there are two additional delay time due to photo current being collected by carrier drifting within the space charge region, and by carrier diffusion within the quasi natural region. The delay time caused by drifting can be evaluated by (6), where W is the depletion width of the junction, μ_p is the drift mobility of holes in the space charge region. The delay time caused by the diffusion can be evaluated by (7), where L is the diffusion length from the quasi natural region to the edge of the space charge region and D_p is the diffusion coefficient of holes in the quasi natural region. Both drifting delay time and diffusion delay time are very small compared to the RC delay time when using the material parameters and dimensions of the demonstrated samples.

$$t_2 = \frac{W^2}{\mu_p(\phi_i - V)} \tag{6}$$

$$t_3 = \frac{L^2}{2D_p} \tag{7}$$

Therefore, the total delay time combining all three components can be given by

$$t = \sqrt{t_1^2 + t_2^2 + t_3^2} \approx t_1. \tag{8}$$

The same 25mm^2 active area samples used in light responsivity measurement were also used in the rise and fall time testing. Applying the delay time analysis above, the rise and fall times of the samples can be estimated. The photodiode sample in the package with the TWI structure has the capacitance of about 227pF and the series resistance of about 242Ω, which gives to the calculated rise and fall times of about 124ns.

Authorized licensed use limited to: IEEE Xplore. Downloaded on March 5, 2009 at 16:26 from IEEE Xplore. Restrictions apply.

SIONYX1403000018.0045

SAMSUNG EX. 1002 - 1564/4148

Utilizing the laser LED with the dominant wavelength of about 637nm to illuminate the test diode with the TWI at 25kHz frequency, the rise and fall times of about 125ns were measured. This shows that the test result matches very well with the theoretical analysis. On the other hand, the sample photodiode without TWI has the measured rise and fall times of about 60ns. The difference between the two measured results gives the effect of the TWI resistance on the rise and fall times. In practice, functional photodiode elements in real detectors will have much shorter rise and fall times, because the PN junction area and related capacitance will be much smaller. Meanwhile, the CT systems are using the scintillation layer on top of the detector to convert the X-rays to the visible light spectra. Therefore the requirement on the rise and fall times of the detector is in the range of micro second.

IV. Conclusions

The advanced photodiode detector presented in this paper shows that it achieves a true 2D extension ability for medical imaging, especially X-ray CT application, by integrating TWI technology into the conventional front illuminated photodiode structure. The photocurrent signal can be wired out from the back side of the detector, which gives possibility of building up arbitrarily large area detectors for CT equipments. The measurement results of the demonstrated detectors and samples presented in this paper show that the performance essentially meets or exceeds the requirements of the modern CT systems.

Acknowledgment

The authors would like to thank Kimmo Henttinen and Tuula Virolainen of VTT for their contributions to the TWI processing reported in this paper. The authors would like to acknowledge Wang Yong, Zeng Ying, Mikael Kroneld and Sami Juottonen at Detection Technology Inc. for their support in photodiode design and testing. As a Ph.D student, the author would also like to thank Prof. Harri Lipsanen from Micro and Nanosciences Laboratory, Helsinki Univeristy of Technology for reviewing the paper.

References

[1] W. A. Kalender, Computed tomography, Publicis Corporate Publishing, Erlangen, 2005, pp. 58.

[2] R. Luhta, R. Mattson, N. Taneja, P. Bui, R. Vasbo, "Back Illuminated Photodiodes for Multislice CT," Medical Imaging 2003: Physics of Medical Imaging, Proceedings of the SPIE, Vol. 5030, pp. 235-245 (2003).

[3] R. Luhta, M. Chappo, B. Harwood, R. Mattson, D. Salk, C. Vrettos, "A new 2D-tiled detector for multislice CT," Medical Imaging 2006: Physics of Medical Imaging, Proceeding of SPIE, Vol. 6142, pp. 275-286 (2006).

[4] F. Ji, S. Leppävuori, J. Luusua, S. Eränen, I. Hietanen, M. Juntunen, "Fabrication of Silicon Based Through-wafer Interconnects for Advanced Chip Scale Packaging", Proceedings of Eurosensors Conference XX, Vol I, pp. 188-189 (2006).

[5] M. Fukuda, Optical semiconductor devices, John Wiley & Sons, 1999, pp. 211-219.

[6] P. Bhattacharya, Semiconductor optoelectronic devices, Prentice-Hall International, Inc., 1994, pp. 171-175.

[7] L. W. Schaper, D. I. Amey, "Improved electrical performance required for future MOS packaging," IEEE Transactions On Components, Hybrids, And Manufacturing Technology, Vol. CHMT 6, No. 3, pp. 283-289 (1983).

Authorized licensed use limited to: IEEE Xplore. Downloaded on March 5, 2009 at 16:26 from IEEE Xplore. Restrictions apply.

SIONYX1403000018.0046

SAMSUNG EX. 1002 - 1565/4148

APPLIED PHYSICS LETTERS 88, 241902 (2006)

Strong sub-band-gap infrared absorption in silicon supersaturated with sulfur

T. G. Kim, Jeffrey M. Warrender,[a] and Michael J. Aziz
Division of Engineering and Applied Sciences, Harvard University, Cambridge, Massachusetts 02138

(Received 25 January 2006; accepted 27 April 2006; published online 12 June 2006)

Silicon supersaturated with up to 0.6 at. % sulfur in solid solution was fabricated by ion implantation and pulsed-laser-melting-induced rapid solidification. The optical absorption coefficient over the range of 1200–2500 nm is uniformly high at $\sim 2.5 \times 10^4$/cm, which is at least an order of magnitude greater than the maximum value attributable to free carriers. High crystal quality was confirmed by transmission electron microscopy and ion channeling. The absorption coefficient decreases markedly with subsequent furnace annealing over the range of 200–600 °C. We propose that the high absorptivity is due to a broad distribution of sulfur-related localized states within the band gap. © *2006 American Institute of Physics*. [DOI: 10.1063/1.2212051]

Repeated pulsed laser irradiation of silicon in the presence of sulfur-bearing gases has been used to create microstructured silicon surfaces that exhibit high optical absorptance in the near infrared (1100–2500 nm).[1–3] These materials have potential applications as photodetectors[4] and light emitters.[5] The incorporation of sulfur in the laser-irradiated surfaces was found necessary to induce high sub-band-gap absorptance,[3] but the relative roles and potential interactions of sulfur, surface topography, and crystallographic disorder have yet to be established. Although the properties of dilute sulfur-bearing silicon are known,[6–8] they do not explain the observed absorptance of sulfur-bearing microstructured silicon. Here we report the optical properties of unstructured silicon supersaturated with sulfur, prepared by ion implantation and pulsed-laser-melting-induced rapid solidification. Despite the absence of any detectable surface microstructure or interior extended defects, this material exhibits high infrared absorptance. These results permit us to clarify the origin of the high absorptance and to measure the magnitude of the absorption coefficient. Additionally, these results indicate the possibility of infrared (IR) applications for sulfur-bearing silicon in thin film form, which is compatible with a wide variety of device architectures.

Si(111) (*n*-type, phosphorus-doped, 1.2 kΩ cm, 300 μm thick, single-side polished) wafers were ion implanted with 200 keV $^{32}S^+$ to a dose of 1×10^{16} ions/cm^2. During implantation the sample was nominally at room temperature, but we expect some amount of uncontrolled heating from the ion beam to have occurred. The ion implanted samples were irradiated by a spatially homogenized pulsed $XeCl^+$ excimer laser beam [308 nm, 25 ns full width at half maximum (FWHM), 50 ns total pulse duration] with fluences of 1, 1.4, or 1.8 J/cm^2. In order to process a sufficiently large area (1.5×1.5 cm^2) for spectroscopic measurements of optical reflection and transmission, the $\sim 3 \times 3$ mm^2 excimer laser spot was tiled across the area by moving 1.27 mm vertically or horizontally between pulses; consequently the average point on the surface was irradiated by four to five laser pulses. Time-resolved reflectivity of a low-power Ar^+ ion laser (488 nm) was used to determine that the surface remained optically flat and to monitor the duration over which the surface was molten.[9]

Rutherford backscattering spectrometry in channeling mode (c-RBS) and cross-sectional transmission electron microscopy (TEM) were carried out in order to investigate the crystal quality of the samples. 2 MeV He^+ ions were used for c-RBS and channeling was performed down the [111] axis. c-RBS of the as-implanted and the 1.0 J/cm^2 irradiated samples revealed a high amount of dechanneling from the top ~300 nm, indicating the presence of amorphous or highly defective crystalline material. c-RBS of the 1.4 and 1.8 J/cm^2 irradiated samples revealed a minimum backscattered yield χ_{min} of 3% of that from a random direction, which indicates that these samples are indistinguishable by ion channeling from perfect single-crystal Si. Cross-sectional TEM (XTEM) examination was performed at 200 kV using a JEOL 2010F TEM, with lattice imaging obtained along the Si⟨110⟩ direction. XTEM of the as-implanted samples revealed an amorphous layer near the peak of the sulfur implant (~230 nm) buried beneath a heavily damaged crystalline surface layer. XTEM of the 1.0 J/cm^2 irradiated sample revealed a reduction in damage of the surface layer but still large amounts of extended defects were evident. XTEM of the 1.4 and 1.8 J/cm^2 irradiated samples revealed perfect single-crystalline material throughout the surface region, with zero extended defects observed.

Total hemispherical specular and diffuse reflectance R and transmittance T over the range of 900–2500 nm were measured using a Hitachi U-4001 UV-VIS spectrophotometer equipped with an integrating sphere detector.[1,2] The total absorptance ($A = 1 - T - R$) was determined from directly measured transmittance and reflectance. In order to follow the change of IR absorptance with heat treatment, a 1.4 J/cm^2 irradiated sample was furnace annealed in an argon atmosphere for 30 min periods sequentially from 200 to 700 °C in 100° intervals. The sulfur content in some samples was determined by secondary ion mass spectroscopy (SIMS) performed on a Physical Electronics 6650 quadrupole mass spectrometer using 4 keV Cs^+ primary beam at an incident angle of 60° from the surface normal and monitoring the $^{28}Si^-$ and $^{32}S^-$ secondary ions.

In Fig. 1 we show the optical absorption spectra. All laser irradiated samples exhibit strong, broad absorption at wavelengths longer than ~1100 nm, which corresponds to

[a]Present address: Fatigue and Fracture Analysis Branch, Benet Laboratories, Watervliet, NY 12189.

 © 2006 American Institute of Physics
Downloaded 16 Jul 2006 to 128.103.60.225. Redistribution subject to AIP license or copyright, see http://apl.aip.org/apl/copyright.jsp

SIONYX1403000018.0047

SAMSUNG EX. 1002 - 1566/4148

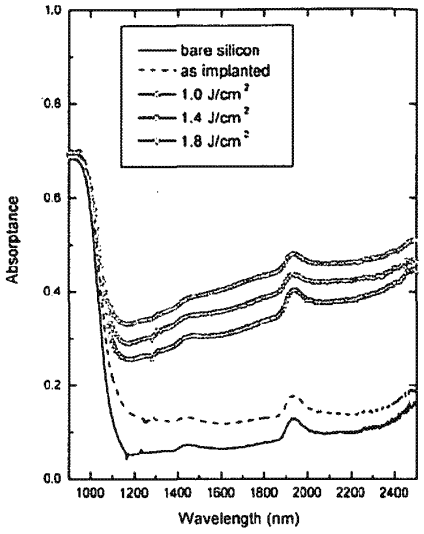

FIG. 1. (Color online) IR absorptance data from samples irradiated with 1.0, 1.4, and 1.8 J/cm^2: as implanted (---) and bare silicon (—). The peak at ~1900 nm is from water.

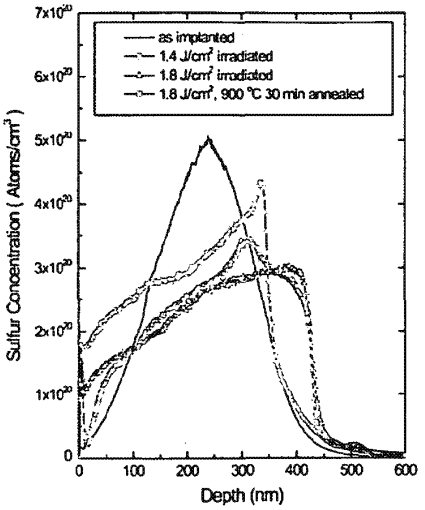

FIG. 2. (Color online) SIMS depth profiles. Retained sulfur doses ($\times 10^{16}$ S/cm^2) calculated from integrating profiles are implanted, 1.09; 1.4 J/cm^2 irradiated, 1.13; 1.8 J/cm^2 irradiated, 1.02; and annealed at 900 °C for 30 min after 1.8 J/cm^2 irradiation, 1.02.

the indirect band gap of pure Si. The 1.4 J/cm^2 irradiated samples are slightly higher in absorptance than those irradiated with either the lower or the higher fluence. Extended defects may contribute to the absorptance of the as-implanted and the 1.0 J/cm^2 irradiated samples, but they are absent from, and therefore cannot be the cause of the high absorptance of, the samples irradiated with the higher fluences.

In Fig. 2 we show sulfur concentration-depth profiles determined by SIMS. We interpret the abrupt drop in sulfur concentration at 350 and 450 nm for the 1.4 and 1.8 J/cm^2 irradiated samples, respectively, as the depths of maximum penetration of the melt front. These maximum melt depths are roughly consistent with the results of heat-flow simulations of melting and solidification, constrained to match the measured melt duration.[9] Subsequent rapid solidification is known to cause solute trapping, resulting in high substitutional supersaturations of dopants in silicon.[9,10] The average sulfur concentration in the melted region of the 1.4 J/cm^2 irradiated sample is 3×10^{20} at./cm^3, which is at least four orders of magnitude above the maximum solubility limit.[8,11] That the 1.4 J/cm^2 irradiated sample appears to have a 4% higher dose than the implanted sample may indicate a slight lateral nonuniformity in the implant. The ratio of the absorptance of 1.8 to 1.4 J/cm^2 irradiated sample is experimentally indistinguishable from the ratio of retained doses, 0.9, consistent with the notion that the absorptance in the laser melted samples is simply proportional to the areal density of sulfur. However, there may be some contribution to the absorption from point defects, at concentrations or sizes below the detection limit of c-RBS and lattice-resolution TEM, lying just below the position of maximum melt front penetration in the 1.4 J/cm^2 irradiated sample: note the tail of the sulfur distribution below this depth.

The absorption coefficient α at 2300 nm wavelength was calculated from the measured reflectance and transmittance using[12] $\alpha=(1/d)\ln[(1-R)/T]$, where d is the thickness of the melted and solidified layer. The absorption coefficient of the implanted, 1.4 J/cm^2 pulsed laser irradiated, unannealed sample is 2.3×10^4 cm^{-1}. This is much greater than the value reported by Spitzer and Fan[13] for heavily arsenic doped silicon of ~200 cm^{-1} for this wavelength when the free electron concentration is 1×10^{19}/cm^3. Spitzer and Fan also reported that the absorption coefficient at this wavelength is linearly proportional to the free electron concentration for arsenic and phosphorus doping and identified the predominant absorption mechanism as interband transitions of free electrons. If we assume a maximum possible free electron concentration in our 1.4 J/cm^2 irradiated sample of two electrons per sulfur atom, i.e., 6×10^{20}/cm^3, our measured absorption coefficient remains an order of magnitude above the value anticipated from extrapolating Spitzer and Fan's data to this value; if our free electron concentration turns out to be smaller, due to incomplete activation, then the discrepancy is even larger. We conclude that the mechanism of absorption in sulfur-doped silicon is quite different from the absorption by free carriers in silicon doped with shallow donors.

At low sulfur concentrations (~3×10^{16} S/cm^3), four impurity levels in the band gap have been identified experimentally and attributed to isolated sulfur and sulfur dimers.[7,14] At higher concentrations, impurity levels from sulfur-related complexes have also been identified.[14] The deepest of all these levels is the transition of sulfur monomers from singly ionized to doubly ionized donors at 613 meV below the conduction band edge. Our absorption spectra show no sharp features at wavelengths corresponding to transitions involving any of these levels; in particular, no step is seen at 2.05 μm corresponding to a transition from the deepest level to the conduction band edge. We propose that the absence of sharp features is due to the formation of bands from these levels at high concentration.

The total absorptance in our samples is somewhat lower than that in silicon microstructured in a sulfur-bearing atmosphere,[2] the topography of which can be described as spikes tens of microns in height with surface slopes >1. These spiked silicon materials have sulfur concentrations in the top ~100 nm that are similar to the concentrations in our samples, and the thickness of the sulfur-bearing layer ap-

Downloaded 16 Jul 2006 to 128.103.60.225. Redistribution subject to AIP license or copyright, see http://apl.aip.org/apl/copyright.jsp

SIONYX1403000018.0048

SAMSUNG EX. 1002 - 1567/4148